Thermal Management of Heat-Generating Automotive Powertrain Hardware using Spray Evaporative Cooling

A dissertation submitted to University of Sussex for the degree of Doctor of Philosophy in Engineering

April 2021

Alireza Sarmadian
Registration Number: 21815678

School of Engineering and Informatics

Statement

I hereby declare that this thesis has not been and will not be, submitted in whole or in part to another University for the award of any other degree.

Signature: …… ……

Summary

Thermal management of heat generating powertrain hardware in automotive vehicles is examined using spray evaporative cooling, particularly taking account of the effect of vehicle vibration and agitation. The heat transfer characteristics of spray evaporative cooling of vibrating surfaces are important for both automotive and aerospace applications but this thesis content focuses on automotive applications involving highly-boosted IC engines, power electronics, batteries, and electrical machines.

The fundamental physics of highly complex two-phase spray evaporative cooling is currently computationally intractable, therefore the thesis addresses (for the first time) construction and calibration of correlation models of spray evaporative cooling involving vibrating surfaces. Suitable correlation models are constructed using dimensional analysis involving the Generalized Buckingham Π-Theorem. Two nondimensional parameters are introduced in the form of Acceleration Number and Vibrational Reynold Number to account for dynamic effects resulting in models which accommodate the combined effects of vibration amplitude and frequency. The correlation models are fitted to experimentally-measured spray evaporative cooling data taken from an experimental test rig which includes instrumented test-pieces vibrated by a shaker to amplitudes and frequencies appropriate for real (on-road) vehicle conditions. The models provide dynamic predictions of heat flux in the nucleate boiling regime, and predictions of the Critical Heat Flux and its associated temperature. The experimental measurements alone show that dynamic effects do indeed influence heat transfer.

Thermal management in the nucleate boiling regime using a feedback control system for flat and curved surfaces with, and without vibration, has been subsequently studied in the thesis using simulation and experimental hardware. The performance of a PID controller within a thermal management system has been examined using the calibrated correlation models to provide an approximate description of the 'plant' physics. A detailed examination is made of the effect of the PID controller gains on the performance of a thermal management system in terms of stability and practical response requirements with, and without vibration.

The results of the study confirm that thermal management of heat-generating automotive powertrain hardware is a definite practical possibility using evaporative spray cooling.

Acknowledgments

I would like to offer my special thanks to my supervisor Professor Julian Dunne for his invaluable supervision and continuous support during the course of my PhD. I would like to express gratitude to Dr Christopher Long, Mr Jean-Pierre Pirault, and Dr Jisjoe Thalackottore Jose for their technical support which was really influential in shaping my experimental methods and critiquing my results. My gratitude extends to the Doctoral School, the University of Sussex for the Chancellor's International Research Scholarship (CIRS) 2018 to undertake my studies. I would also like to thank my second supervisor, Dr Kun Liang, for his support to achieve this scholarship. I would like to thank Ms Emily Clifford-Brown for proofreading my research manuscripts. My appreciation also goes out to my family for their love, encouragement, and support all through my studies.

Contents

List of Tables

List of Figures

Nomenclature

R_t	mean roughness height (μm)
$\dot{m}$	mass flow rate (kg/s)
$\bar{\vec{v}}$	average volumetric spray flux, $\bar{\vec{v}} = \frac{v}{\pi(Htan(\frac{\alpha}{2}))^2}$ (m^3s^{-1}/m^2)
A	surface area (m^2)
a	amplitude of vibration (m)
Ac	dimensionless acceleration, $Ac = \omega^2 a/g$ (-)
Bo	Boiling number, $Bo = qH/\mu_l h_{fg}$ (-)
C_p	specific heat (kJ/kg k)
d	diameter(mm)
D	derivative gain
e	error
f	frequency (Hz)
d_{05}	mass or volume median diameter (m)
d_{32}	Sauter mean diameter (m)
G	mass velocity (kg/m^2s)
h	specific enthalpy (kJ/kg)
h	heat transfer coefficient ($kW/m^2\ K$)
H	height (m)
I	current (A)
I	integral gain
Ja	Jakob number, $Ja = C_l \Delta T/h_{fg}$ (-)
k	thermal conductivity (W/m K)
L	length (mm)
P	pressure (kPa)
P	proportional gain
Pr	Prandtl number, $C_p \mu/k$ (-)
q	heat flux (kW/m^2)
Re	Reynolds number, $Re_V = \rho_l a \omega d_H/\mu_l$ (-)
St	Strouhal number, $St = \frac{fd}{v}$ (-)
T	temperature (K)
t	time (s)
u	velocity
V	voltage (V)
We	Weber number, $We = \rho_l(u_m^2 or \bar{\vec{v}}^2)d_{32}/\sigma$ (-)
Bi	Biot number, $Bi = {xh}/{k}$ (-)

Fo	Fourier number, $Fo = {\alpha t}/{x^2}$ (-)
Q	heat (kW)
x	position (m)
$\acute{v}$	local volumetric spray flux (m^3s^{-1}/m^2)

Greek symbols

μ	dynamic viscosity (Kg/m s)
ΔT	temperature difference (K)
v	volumetric flow rate (m^3/s)
Δp	pressure drop (kPa)
α	thermal diffusivity, $\alpha = \frac{k}{\rho C_p}$ (m^2/s)
ϑ	spray cone angle
γ	efficiency factor
δ	liquid film thickness (m)
ρ	density ($\mathrm{kg/m}^3$)
σ	surface tension (N/m)
ω	angular velocity (Hz)
ϖ	power (W)

Subscripts

am	ambient
at	atmospheric
Ch	chamber
c	coolant
d	droplet
f	liquid phase
g	vapour phase and gravitational force
H	heating surface
i	grid point
l	liquid
lat	latent
m	modified
n	time step
o	orifice
ref	reference temperature
sat	saturation
sub	subcooling
tot	total

V	vibration
w	wall

Acronyms

CHF	critical heat flux
COP	coefficient of performance
FIR	finite impulse response
GUI	graphical user interface
HMI	human-machine interface
ICE	internal combustion engine
MSE	mean square error
PID	proportional integral derivative
IGBT	Insulated-Gate-Bipolar-Transistor
PHEV	plug-in hybrid electric vehicle

EXECUTIVE SUMMARY

The overarching aim of this study is to address the climate change by reducing CO_2 emissions from transport. Emissions from transportation, that account for 28% of all greenhouse gas emissions in the United States, increased more in absolute terms between 1990 and 2018 than from any other sector. Existing vehicle cooling and thermal management systems are nearing their thermal limits because they use forced convection-based heat transfer. This limit restricts the performance of spark ignition (SI) hybrid electric vehicles, and the range of both hybrid and battery electric vehicles. Evaporative cooling is of considerable interest to automotive vehicle manufacturers. Many see the great potential of evaporative cooling over conventional convective systems, to achieve improved IC engine fuel economy, reduced CO2 emissions, and extended range for Electric Vehicles. The heat transfer characteristics of spray evaporative cooling applied to vibrating surfaces is important in several application areas, in particular, those exposed to dynamic conditions such as automotive and aerospace industry. Applications including thermal management of electric and hybrid vehicles, highly-boosted IC engines, power electronics, batteries, and hydrogen technologies are all significant.

This dissertation has examined the potential of spray evaporative cooling for use on electronic components and electric powertrain of Hybrid Electric Vehicles (HEV), as well as highly boosted Internal Combustion (IC) engines. The main objective of the thesis is to examine the effects of vibrating flat and curved surfaces on the heat removal capabilities and stability of controlled evaporative cooling for representative coolant jacket test pieces, electronic component heat sinks, and electric motors. This has assisted in understanding the physics of spray evaporative cooling, that is helpful in the development of robust control strategies to handle what is considered to be a very effective but potentially unstable heat transfer mechanism. An actual control system has been implemented in hardware. This has allowed the effectiveness of robust control in the presence of surface vibration to be experimentally assessed and verified.

Spray evaporative cooling, even with impingement on static surfaces, involves highly complex two-phase physics which is currently way beyond the capabilities of numerical simulation. Since at present, even high performance computing power is still orders of magnitudes too small to simulate fully evaporative 2-phase spray cooling. For this reason, several empirical correlation models have been developed and calibrated for predicting the spray evaporative cooling characteristics of static surfaces. No such correlations existed to characterise heat transfer associated with spray evaporative cooling applied to vibrating surfaces. This dissertation addresses for the first time, correlation model requirements for spray evaporative cooling of vibrating surfaces. Prediction models have been constructed to investigate the effect of vibrating surfaces on the nucleate boiling regime, critical heat flux (CHF) and its associated temperature in spray evaporative cooling.

Dimensional analysis has been used to construct the models to account for the influence of key dynamic parameters. Experimental measurements have been obtained from a flat, electrically-heated, copper test-piece, located inside a spray-chamber mounted on top of a shaker. A wide range of large-amplitude and high frequency measurements have been obtained which correspond to test conditions for a piece of hardware mounted on board a light duty automotive vehicle with vibration amplitudes ranging from 0 to 12 mm and frequencies from 0 to 400 Hz. Different nozzle types have been fed with distilled water at flow rates ranging from 55 to 200 ml/min being used to cool with subcooling degrees ranging from

10℃ to 45℃. Measured data for both static and dynamic cases has been used to explore the influence on the nucleate boiling, CHF and the surface-to-fluid saturation temperature at which CHF occurs, of subcooling degrees, surface vibration amplitude and frequency, vibrational Reynolds Number and vibrational Acceleration Number. The measured data has also subsequently been used to calibrate the predictive models for use in thermal management systems.

For the nucleate boiling regime, the results show that surface dynamic effects certainly influence nucleate boiling, but they also show that surface vibration does not have the same effect for all excess temperatures - dynamic effects can either increase or decrease heat transfer depending on the heat transfer mechanism. These new models are important for thermal management in several areas, particularly involving batteries, power electronics, and electrical machines in automotive and aerospace applications.

For the CHF, static measurements (without vibration) show that the influence of flow rate, volumetric flux, and subcooling are largely in agreement with published literature. For dynamic cases, the influence of vibration is best explained in terms of the nondimensional parameters: Vibration Reynolds Number and Acceleration Number. The effect of vibration on CHF and associated temperature is assessed in detail for three nozzle types of PJ8, PJ10 and MW145 at different flow rates and degrees of subcooling. Predictions of CHF and associated excess temperature, using the calibrated correlation models for the dynamic conditions, are very reasonable, and suitable for the intended purpose of ensuring safe operation of thermal management systems using spray evaporative cooling.

By exploiting an experimentally calibrated dynamic correlation model to represent spray evaporative cooling of a flat test-piece, a PID controller has been adopted with emphasis focused on the choice of gain parameters to ensure both stability of temperature control, and favourable responses in terms of relevant performance measures. Optimum linearisation of the correlation model has been achieved by solving an appropriate Wiener-Hopf equation, mainly to undertake a practical stability assessment of the closed-loop temperature control system. To assess the effects of different PID controller gains on the thermal performance of the thermal management system, a coefficient of performance (COP) is used, defined as the ratio of heat power removal to the required pumping power. To achieve a reduction in the settling time and an increase the rise time of stable control, a PID controller with a negative proportional gain showed most promising results. A 10.5% increase in COP was achieved in comparison to a PID controller with positive gains. This information is useful for the design and optimization of a thermal management system using evaporative spray cooling.

The spray evaporative cooling thermal performance for vibrating three-dimensional surfaces has also been investigated using temperature ratio. The deteriorating effect of vibration was consistent with the results of the flat test-piece. An updated version of the actual control system for the flat test-piece has been implemented in hardware to thermally-manage the ¼-cylinder test-piece. The study shows that within the thermal inertia and mass limitations of the ¼-cylinder test-piece, temperature control is indeed achievable in practice.

1. INTRODUCTION

Designing compact, efficient, and safe thermal management systems is important for the development of future low-emission electric and plug-in hybrid vehicles [1]. Thermal management plays a pivotal role in the electrification of both automotive vehicles [1] and aircraft [2, 3]. In these applications, high heat-flux levels have increased the need for high energy conversion efficiency to meet stricter regulatory targets (such as those set by the EU for 2030 [4, 5]) to speed-up progress towards with zero CO_2 emission transport systems [6]. This need has focused attention on electrification of vehicle powertrain and aircraft propulsion, with the aim of reducing their carbon footprint [7-9]. To meet the thermal management demand of high heat removal under controlled conditions, highly optimized cooling systems are needed. Addressing this need, Jafari et al. [10] reviewed state-of-the-art evaporative cooling systems for internal combustion engines, showing that there was considerable interest in spray evaporative cooling [11]). The heat transfer characteristics of spray evaporative cooling applied to vibrating surfaces is important in several application areas. Applications including automotive transport (electric [12] and hybrid vehicles [13]), thermal management of highly-boosted IC engines [11], power electronics (e.g. cooling high-power LEDs [14], IGBTs [15], high-heat flux heat sinks for IGBTs [16], and MEMS [17]), batteries (for improving thermal performance [18], or to achieve optimised lifespan [19]), and hydrogen technologies [20] (cooling of storage tanks [21] in hydrogen-powered road vehicles and aircraft) are all significant.

In recent years, there has been an increasing interest in spray cooling mechanisms for different cooling purposes [22] including high-flux with low-temperature [23] and high-temperature cooling requirements [24]. The evaporative spray cooling method has several advantages in comparison to the conventional forced convective cooling. First, two-phase spray cooling benefits from higher heat transfer rates due to its latent heat compared to the sensible heat transfer mechanism in conventional

single-phase methods. Therefore, such a method is feasible enough to cover all the extra heat removal demands induced by the downsizing of internal combustion (IC) cylinders in modern hybrid cars. Moreover, the two-phase flow mechanism itself provides a more uniform temperature across the cylinder head and therefore enhances knock control in internal combustion engines. Second, spray cooling requires much lower mass flow rates, and therefore, it will result in a substantial reduction in the required coolant mass and consequently the pumping power which can give rise to reduced emissions.

Spray evaporative cooling offers a significant increase in heat flux compared with single-phase convection used in automotive industry [25, 26]. This is demonstrated in Figure 1-1a, which shows the variation of heat flux with 'excess temperature' (T_{wall} - T_{sat}) obtained from single-phase convection with two different bulk velocities (i.e. ranges related to automotive operating conditions), and for an evaporative spray of the type used in [27]. Also shown on Figure 1-1a is a pool boiling curve for water [28]. The convection cooling curves [29, 30] in Figure 1-1, use 50/50 water/glycol, whereas all the other curves are for pure water. Spray cooling, compared with flow boiling heat transfer, also offers significantly greater heat flux for a lower flow rate [31, 32]. This point is evident from Figure 1-1b which shows heat flux per unit mass-flow-rate (i.e. specific heat flux) as a function of excess temperature. Figure 1-1b shows that spray evaporative cooling has specific heat flux several orders of magnitude higher than single-phase convection. Lower mass-flow rates are advantageous because they result in a substantial reduction in the required pumping power [33].

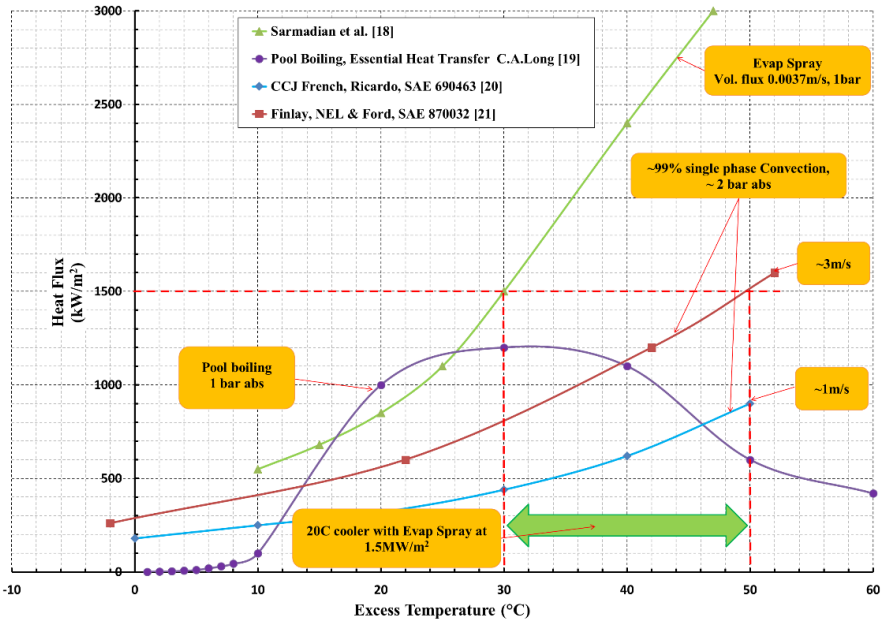

(a)

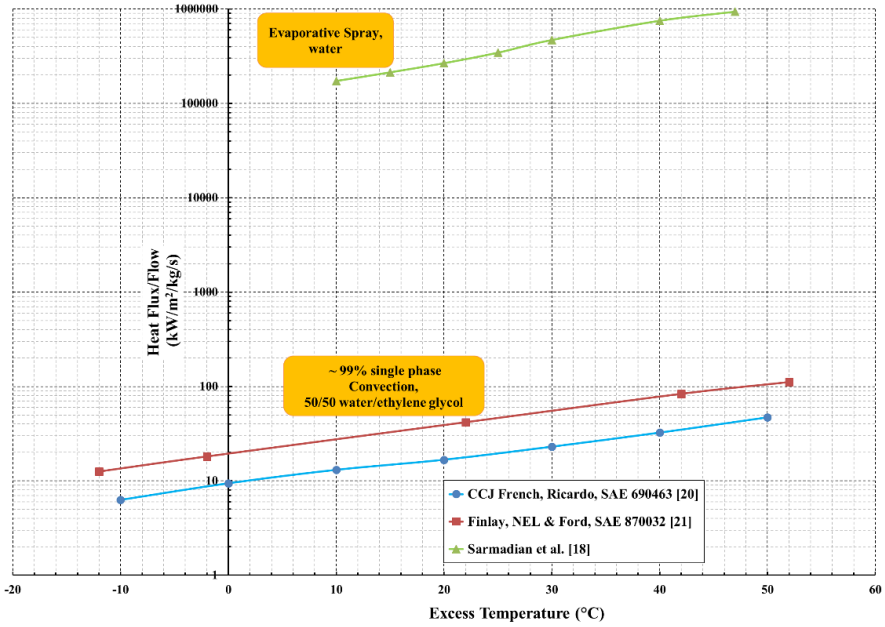

(b)

Fig. 1-1. Comparison between spray evaporative cooling and single-phase convection cooling related to automotive: (a) variation of heat flux with excess temperature (T_{wall} - T_{sat}) including pool boiling, (b) specific heat flux (heat flux/mass-flow-rate) versus excess temperature (The convection cooling curves [29, 30] use 50/50 water/glycol; all other curves are for water only.).

Focusing on cooling of the electronic hardware in hybrid electric vehicles, Mudawar et al. [34], reported that a feasible thermal management system should be able to dissipate heat in the flux range 1.5 - 2 MW/m^2 while maintaining temperatures below 150 ˚C (i.e. the silicon-based transistors limit). Spray evaporative cooling should meet this challenge, moreover its two-phase flow helps to eliminate hot spots, by providing a uniform temperature across all cooled surfaces [35]. Uniform temperature is vital in the thermal management of electronic components and Lithium-ion battery stacks [36], where there is risk of overheating [37, 38] and fires [39]. Further applications include indirect cooling, using pre-cooled air, which improves thermal performance of lithium battery packs [18]. Li-ion batteries have a narrow optimal working temperature range, exceeding the upper limit runs the risk of thermal runaway and fire, operating below the lower limit, reduces battery life. Operating at an optimal temperature also maximizes power output, and improves charging rate, and longevity [12, 40].

Precise thermal management for the design of future cooling systems relies on the ability of the controller to either track the prescribed temperature profile or maintain values within specified thermal limits [41]. Thus, a comprehensive understanding of different flow regimes of spray cooling plays a vital role. Generally, the flow pattern associated with a spray, impinging on a surface, comprises: a nucleate-boiling mode, a transition, a critical heat flux (CHF), followed by transition, and a film-boiling regime [42]. Figure 1-2a depicts a typical flow pattern map using the coordinates of heat flux and superheat temperature (i.e. the difference between impinged surface temperature and the saturation temperature). In fact, much of the current literature on spray cooling pays particular attention to the models and correlations that can predict such heat transfer mechanisms as mentioned, which are of importance in plant model construction of control approaches. For instance, Yang et al. [43], Mudawar and Valentine [44], Cabrera [45] and Rybicki and Mudawar [46] suggested correlations for the nucleate boiling regime. Additionally, Hsieh et al. [47] developed the empirical correlation of Ghodbane et al.

[48] and claimed that their correlation is capable of predicting force convection, the onset of nucleate boiling and transition boiling modes. To predict the CHF, Mudawar and Valentine [44], Estes and Mudawar [49, 50], and Visaria and Mudawar [51, 52] also proposed correlations. Finally, for the film boiling flow regime, prediction models are suggested in [53-55].

Most potential applications of spray evaporative cooling also operate in environments where mechanically-induced vibration occurs. Vibration is considered to have an influence on heat transfer [56]. This effect can be seen through the dimensionless Vibrational Reynolds and the Acceleration Number. Vibrational Reynolds Number is a representation of the turbulence resulting from the vibrating surface [57]. It helps in understanding how vibration through the increased turbulence can affect heat transfer. Heat transfer enhancement, or deterioration, as a consequence of the vibration field (if there is any) can be explained by increased flow turbulence, a thinned or thickened boundary layer, more or less generated nucleate sites [58] and the changed wetting-angle [59]. The dimensionless Acceleration Number is helpful in considering any possible impact of experimentally-measured acceleration (using an accelerometer). The impact of acceleration on spray cooling heat transfer has been empirically investigated in the following dynamic conditions: An acceleration test bench with a rotating arm [60], a reduced gravity condition [61], and on an aircraft doing parabolic flights [62, 63]. However, there are inconsistencies in the conclusions drawn owing to the complexity of spray heat transfer mechanisms and differences in experimental conditions. Thus, acceleration which stemmed from the vibrational environment (which is different to aerospace conditions in terms of heater orientation) is also of importance to the understanding of spray cooling for all dynamic conditions such as for automotive and aerospace vehicle applications.

Although the potential exists for high rates of heat transfer with small mass flows, there are some concerns surrounding the control of a system that can operate near the required heat flux and yet remain stable. Furthermore, most of the spray evaporative cooling database in the literature has not considered more complex three-dimensional geometries and is limited to flat surface test-pieces. These factors have motivated the current study which seeks to address the lack of experimental data and investigate the design, simulation, and implementation in hardware of an appropriate spray evaporative cooling control system.

The literature review section shortly gives more in-detail explanations about spray heat transfer, first, focusing on spray dynamics and heat transfer mechanisms. Second, the nucleate boiling and critical heat flux regimes which are important in thermal management and control are comprehensively reviewed. Discussions are also made on the key parameters involved in these two important cooling modes. In addition, the literature review provides information on the sensitivity of spray cooling systems to vibration and acceleration. All the thermal management and temperature studies using evaporative spray cooling are discussed. In last section of this chapter, the outcome of the literature review is used to discuss the state-of-the-art of the subject culminating in the statements of objectives.

1.1. Literature Review

This section discusses the literature on spray physics and heat transfer mechanisms. Modeling approaches as well as developed physics-based correlations for spray cooling modes are reviewed. The literature addressing the suitability of these correlations and models for thermal management purposes are discussed, in particular temperature control of cooling systems for vehicle IC engines and power electronic components. In addition, the thermal management investigations of spray evaporative cooling systems are also reviewed to help with establishing the state-of-the-art of the subject. In

particular, the adventure of the literature review addresses spray heat transfer regimes, flow visualization, droplet impact physics, prediction correlation models of nucleate boiling and critical heat flux, sensitivity of spray cooling systems to vibration and acceleration, and finally, thermal management and temperature control. Since the single-phase cooling is not of interest to the current study owing to its low heat transfer coefficient, its models and correlations are not included in this literature review.

Spray heat transfer regimes

In heat and mass transfer, it is more convenient and acceptable for thermal engineers to start from separate description of single-phase and two-phase flows. In spray cooling, the process of heat transfer without evaporation (a phase change from liquid to vapor) is deemed to be single-phase, otherwise, it is two-phase flow since it contains a portion of vapour. Thermodynamically, both have always been considered to have some advantages and disadvantages which are mostly dependent on the application in which they are employed. In order to represent the different flow regimes, (i.e. those commonly found in the literature on spray cooling) there are two curves for boiling and quenching, each with different coordinates. A boiling curve is a plot of the heat flux versus superheat temperature, i.e. the difference between the sprayed surface temperature and the coolant saturation temperature as shown in Figure 1-2a. A quench curve is the cooled-surface temperature versus time, i.e. a plot of the transient temperature associated with these regimes during the spray cooling as shown Figure 1-2b. Usually, when it is hard to obtain the heat flux, for example by having complex three-dimensional geometries, quench curve is preferred to give the information about different regimes (which can be done by collecting the transient data of such cooling systems with the aid of thermocouples from the data acquisition system (DAQ)).

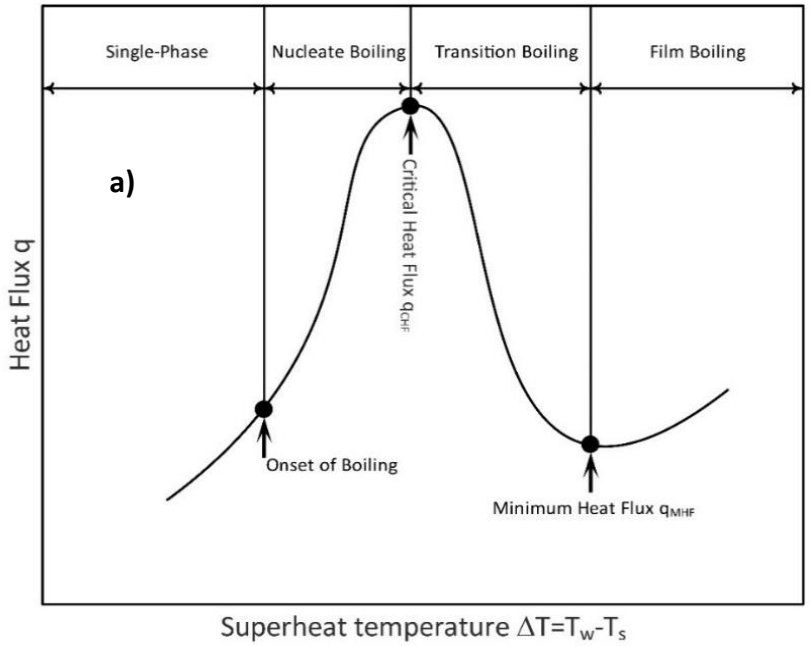

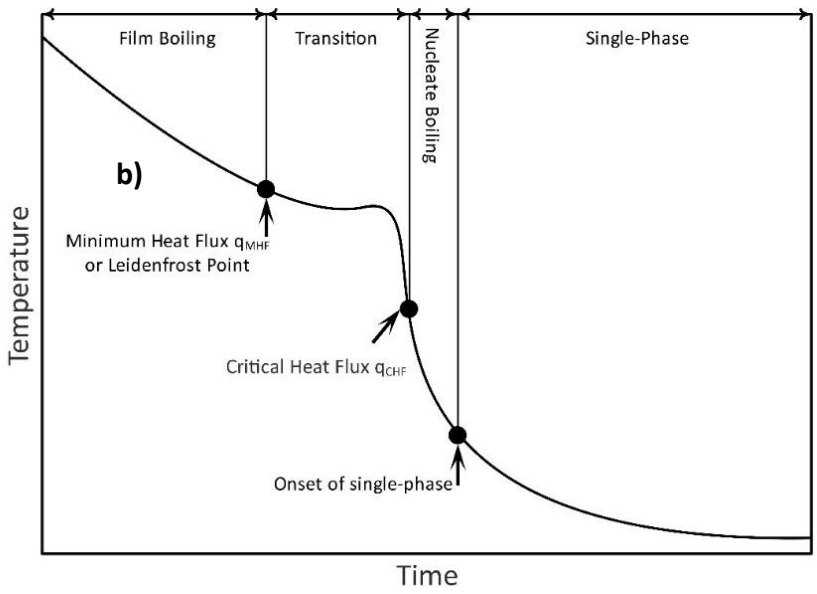

Fig. 1-2. Spray flow pattern maps; a) Boiling curve, b) Quench curve

To model the heat transfer phenomenon of each flow regime in the spray cooling, there are two approaches. One is to represent the spray impact as a simple superposition of sole droplet impact events, and the second, is to statistically model the phenomenon under some predefined parameters

with measurements and data analysis of large numbers of spray droplet impact. For single droplet impact on a surface, there are six different empirical models which are longitudinally reviewed by Cossali et al. [64]. Nevertheless, it is discussed by Tropea and Roisman [65] that such an approach (Considering single droplets) is not reliably capable of predicting the whole spray impact behavior. There are disturbing interactions between drops that are spraying onto a surface as well as fluctuations that impinging droplets impose onto the liquid film. Therefore, in this study, only those models and correlations that are more reliable (or in other words, are physics-based by considering different key parameters of spray cooling) will be reviewed.

Flow visualization

Observing the flow regimes throughout different spray cooling modes is a useful strategy to illuminate the physical phenomena and is highly beneficial for modelling. Flow visualization helps to include the flow regime behaviour in the development of flow pattern maps which are vital in both designing and control approaches. Figure 1-3 shows what happens during a spray cooling observation in terms of dynamic and heat transfer mechanisms involved in the spray flow field of a typical cooling system. The working fluid first flows through a pipeline and is injected by a nozzle orifice. Then, it breaks-up into droplets in the chamber until they impact onto the surface. The impinging droplets may accumulate, become larger slugs, and move so that they form a thin liquid film at the heating surface. The impinging droplets can move away from the surface, with splashing occurring. Such dynamic behaviour is followed by heat removal from the hot surface through different heat transfer mechanisms. As shown in Figure 1-3, there are different heat transfer modes involved, including evaporation of the liquid film, convection in both the liquid film and the spray flow field as well as the droplet impact to the liquid film (based on [66]). Furthermore, there is a nucleate boiling mechanisms [43]. This is surface nucleation stemming from bubble generation in nucleate sites of the impacted

surface. All these heat transfer modes and their interactions result in complexity in the spray cooling phenomenon. Developing correlations with such high nonlinearity in the heat transfer physics is rather difficult. Flow visualization facilitates the classification of spray cooling mechanisms so as to make the modelling process and predicting demands, much more feasible. Moreover, for both designing and controlling purposes of spray cooling systems (compared to conventional ones), having enough information about transitions to different primary heat transfer modes is of important interest to thermal engineers.

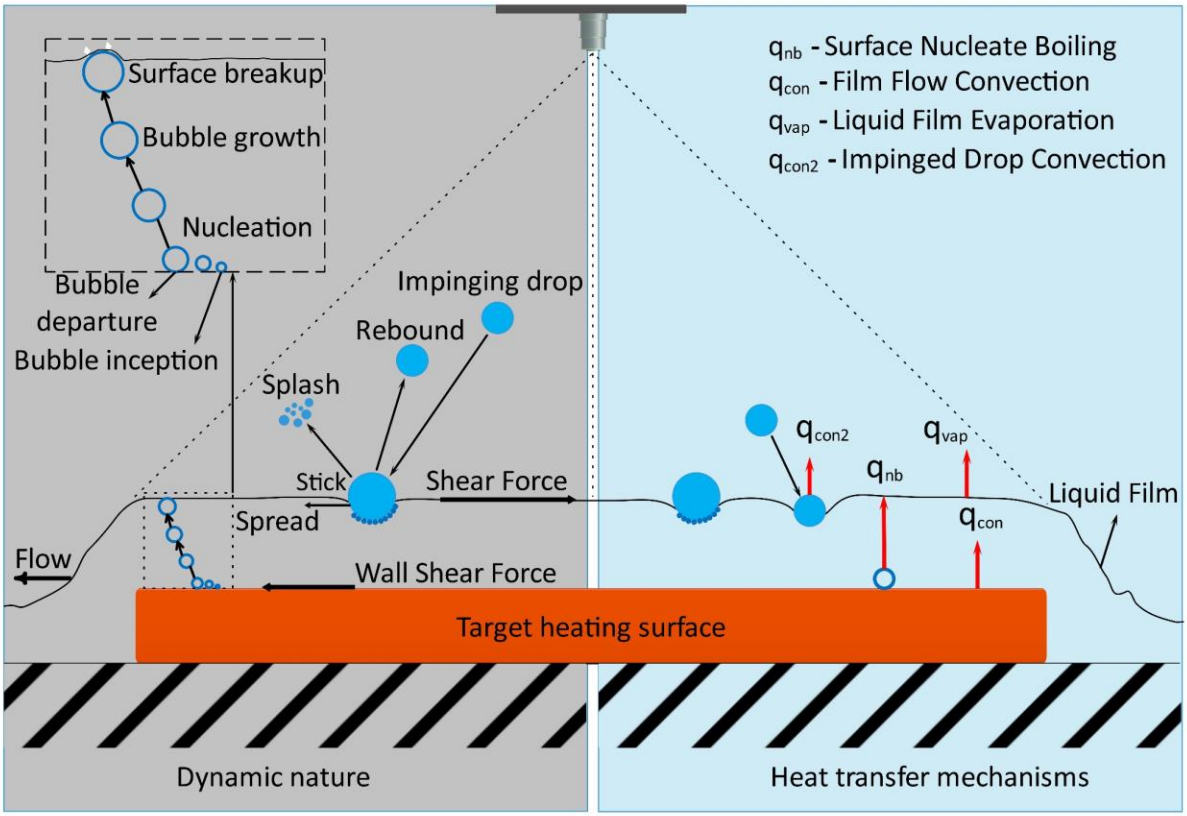

Fig. 1-3. Heat transfer and dynamic characteristics of spray cooling process

Such flow visualizations representing all spray cooling modes in terms of droplet impact behaviour has been examined by Breitenbach et al. [22]. In a review paper, they have considered single droplet impact

onto a surface as well as a liquid film, and explained the nature of impinging droplets (spray) onto a liquid film with a focus on all the flow regimes. The next part of the review pays attention to droplet impact physics and heat transfer mechanisms.

Droplet impact physics

An interesting feature of spray cooling is that droplets impacting onto surfaces are to some extent bombarding it, and this behaviour results in postponing the separation of liquid film from the surface during evaporation (bubble generation). The momentum of the impacting the droplets is dominant compared to that of bubbles growing and coming up from the bottom through boiling. The generated bubbles on return are anchored at the surface. This phenomenon is conjectured to increase the likelihood of bubble breakdown and distribution of smaller bubbles all over the surface. The impinging droplets can also be responsible for thinning the liquid film and therefore augmenting the local heat transfer coefficient. However, there are some concerns that can be raised against this explanation. One concern is the possibility of forming slugs for the suppressed (or anchored) bubbles on the thin liquid film (rather than breaking down to smaller bubbles and being distributed all over the surface). The likelihood of this slug propagation (caused by bubble accumulation) may be responsible for leading the transition from nucleate to transition boiling which is known to degrade the heat transfer coefficient. Therefore, there is a need to study such an important aspect of spray cooling which it means that flow visualization again plays an important role in identifying some unknown aspects of spray heat transfer. So far different investigators in their observations have reported that there are four main heat transfer modes in two-phase heat transfer: nucleate boiling, transition boiling, thermal atomization, and film boiling during a droplet impact onto a hot surface [67]. As illustrated in Figure 1-4, thermal atomization has also been recently observed by some researchers [68]. Therefore, thermal atomization, that can be

considered as a part of the transient mode, has also been added to Figure 1-4 to better explain the physics behind the whole cooling process with different possible flow regimes. Following on from this an explanation is given about different flow regimes observed during a droplet impact onto a hot surface with different substrate temperatures and heat loads.

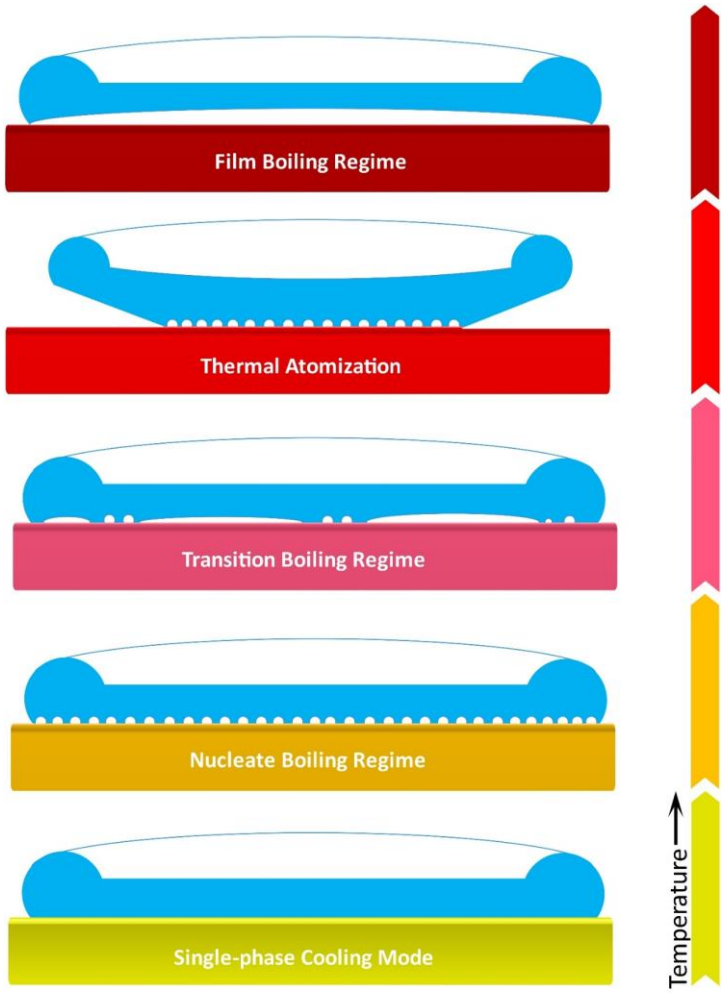

Fig. 1-4. Different flow regimes of a droplet impinging on a surface under different heat loads (Based on [22])

When the droplet impact is not accompanied by boiling, the single-phase cooling regime is observable. This happens when the superheat temperature is less than the onset of boiling (in Figure 1-2a). It means that it is not exceeding the critical point of incipient boiling and therefore the heat transfer is not governed by boiling [69]. The flow in the spreading droplet is just affected by the temperature dependence of the material properties (of both the coolant and the wall) and therefore

its physical mechanisms which determine the outcome of the droplet impact are deemed to be like when a droplet impinges onto a substrate at isothermal conditions and at room temperature. Thus, as shown in Figure 1-4, the whole drop lamella is in contact with the surface at the moment of impact, thereby the spray cooling in this flow is only accompanied by conduction in the wall and convection inside the thin liquid film.

At a higher temperature, by the onset of boiling (see also Figure 1-2a) an array of growing bubbles appears on the surface caused by heterogeneous nucleation which is called bubble inception (depicted in Figure 1-3). Then, it will be followed by bubble growth until the departure of bubbles happens. Nucleate boiling physics can be characterised by a growth rate, and the departure or residence time of bubbles, before collapsing. As it can be deduced from Figure 1-2a, nucleate boiling provides the highest heat transfer coefficients which are of interest in spray cooling system designs. That is why this regime has received much more attention compared to the other flow regimes in the literature.

By increasing the temperature above saturation, or by having an excess temperature (i.e. the difference between wall and saturation temperature), the density of nucleate sites increases, and in turn, starts to coalesce and form slugs (rather than collapsing). These slugs are stuck to the surface owing to the pressing influence of impinging droplets (or a force like a ‘thrust’ perpendicular to the surface). Then, they grow to form a vapour film which is known as the advent of film boiling. Nucleate boiling and transition can be separated, and distinguished by the critical heat flux (CHF point in Figure 1-2).

Critical heat flux is the highest achievable heat flux in spray cooling, and in fact, is a threshold for transition from nucleate boiling to more unstable heat transfer mode of transition boiling. Having a precise correlation to predict CHF has long been of interest as it is highly effective in design, modelling, and control of systems that are employing the spray cooling method. In this regard, the first serious

discussion and prediction of CHF emerged in 1989 by Mudawar and Valentine [44] and later modified for a broad range of operational conditions and spray specifications by Estes and Mudawar [49] in 1995 and [50] in 1996. In 2008, Visaria and Mudawar [51, 52] updated the previous correlations for various parameters such as spray inclination and subcooling degrees. Overall, transition boiling is accompanied by both the highest and lowest heat fluxes over a short span of superheating and therefore is highly unstable.

As it can be seen from Figure 1-4, the thermal atomization regime happens when the central part of the droplet lamella is still attached to the surface while the peripheral part of it rises and floats as a result of a rapid vapour stream ejection near to the contact line. By increasing superheating, there is a surface temperature at which all the generated bubbles and slugs accumulate to form a vapour layer between the liquid film and the surface. This temperature is called the Leidenfrost point (indicated in Figure 1-2b) which is governed by the minimum heat flux (MHF). From this point forward, the heat transfer regime is film boiling which has a lower heat flux and heat transfer coefficient in comparison to Nucleation. It is mostly because the vapour film between the liquid film and the wall is impeding the effectiveness of cooling through the insulation.

In fact, the science behind the heat transfer of spray cooling is complicated and needs to be comprehensively experimented and assessed from different points of view. For example, the main flow regimes are to some extent the same when there is a sole droplet impact onto a dry surface, wet surface, or a substrate with a liquid film on the top. Yet there is a lot of effort needed to better understand flow regimes during dilute or dense sprays, in order to model them for design purposes. In this regard, in the next sections, different models and correlations will be discussed to pave the way for thermal management approaches. Since the single-phase cooling is not of interest to the current study

owing to its low heat transfer coefficient, its models and correlations are not included in this literature review.

Two-phase spray cooling

Two-phase spray cooling has several important advantages in comparison to the conventional forced convective cooling. First, two-phase spray cooling benefits from higher heat transfer rates owing to its latent heat compared to the sensible heat transfer mechanism in conventional single-phase methods. Second, spray cooling requires much lower mass flow rates, and will therefore result in a substantial reduction in the required coolant mass and the pumping power which offers energy saving and high coefficient of performance (COP, defined as the ratio of heat power removal to the required pumping power).

In this section, all models capable of predicting the nucleate boiling and CHF characteristics are provided. This is to assess and find the best models and correlations applicable to the thermal management of vehicles and electronic components based on the desired operating conditions in both part-to-full load cooling system requirements. As heat dissipation to the spray cooling system is equal to the heat flux of non-dimensional correlations (i.e. $Q = q$), an explicit plant model needed for designing controllers can be obtained.

Although the heat transfer coefficient in nucleate boiling is known to be high, temperature at high heat flux is sometimes in danger of instability. For instance, when the bubbles in nucleate sites start to form slugs, the mechanism may lead to transition boiling which has the least local heat transfer coefficient. Therefore, CHF models are also important to be included in the thermal management designs.

Nucleate boiling correlations

In this section, all the available models and correlations for the nucleate boiling regime in the open literature are reviewed. Then, discussions about how to assess their reliability, operating conditions, and accuracy will be discussed.

To help with the understanding of modelling and correlation development process, some important information about spray specifications, terminology, and key parameters are given as follows:

Spray specifications formulas

The Sauter mean diameter d_{32} for a nozzle of exit diameter d_n, is correlated by Estes and Mudawar in [49] as follows:

$$\frac{d_{32}}{d_n} = 3.67\left(We_{d_n}^{0.5} Re_{d_n}\right)^{-0.259} \tag{1.1}$$

where We and Re are respectively Weber and Reynolds numbers. The droplet impact velocity (or droplet breakup velocity) can be obtained from an energy balance developed by Ghodbane and Holman [48], and extended by Qiao and Chandra [70], in a way to include gravitational potential energy which is formulated as follows:

$$u_m = \left(u_o^2 + \frac{2\Delta P}{\rho_l} - \frac{12\sigma}{\rho d_{05}} - 2gHsin(\alpha)\right)^{0.5} \tag{1.2}$$

where u_o, ΔP, d_{05}, ρ_l and H are mean velocity of water entering nozzle, the pressure drop across spray nozzle (Kpa), mass median droplet diameter, liquid density, and distance from the nozzle to surface, respectively. The mass median droplet diameter can be defined by the following equation:

$$d_5 = 9.5 \frac{d_n}{\Delta P^{0.37} sin\frac{\alpha}{2}} \tag{1.3}$$

where d_n and α represent the nozzle spray diameter and cone angle. The surface tension (σ) of water capable of covering the entire range of vapour-liquid saturation curve can be calculated from an equation by Vargaftik et al. [71] with an uncertainty of ±0.5% [72]:

$$\sigma = 0.2358\left(1-\frac{T}{647.096}\right)^{1.256}\left[1-0.625\left(1-\frac{T}{647.096}\right)\right]\times[Nm^{-1}] \quad (1.4)$$

Volumetric flux has been considered to play a prominent role in tracking the surface temperature and heat flux trends in spray evaporative cooling [44]. The volumetric flow rate of an infinitesimal portion of the spray impacting onto a surface divided by the same portion of the area, is called local volumetric flux and is represented by $\acute{v}$. Mean volumetric flux $\bar{\acute{v}}$, can be obtained by dividing the total volume flow rate of spray by the entire spray impact area [50] defined as:

$$\bar{\acute{v}} = \frac{v}{\pi(\mathrm{Htan}\left(\frac{\alpha}{2}\right))^2} \quad (1.5)$$

where v is volumetric flow rate. Rybicky and Mudawar [73] have claimed that the effect of flow rate (of coolant PC-5052) on nucleate boiling regime (for a fixed subcooling of 27 $^{\circ}C$) is small but perceptible compared to that for single-phase and the transition boiling.

Effects of Pressure (Nozzle and Chamber)

Chamber and nozzle pressures are considered as key parameters in spray cooling. The difference between them has a profound effect on the breakup of droplets. In addition, the pressure drop across the nozzle, changes mean diameter and mean velocity of droplets which are known to have an impact on the heat transfer characteristics [23]. Chamber pressure itself is deemed to be a control parameter which has a direct effect on saturation temperature and latent heat of the two-phase flow and consequently the surface temperature. Xu et al. [74] carried out an experimental investigation of R600-a spray cooling in a closed refrigeration loop. In their study, the influences of the chamber and nozzle inlet pressures on the surface temperature, the uniformity of surface temperature, and the heat transfer coefficient are discussed. In another empirical study, Liu et al. [75] has assessed the effects of chamber pressure on the CHF. They reported that by increasing the chamber pressure, the spray efficiency, CHF and heat transfer coefficients were increased.

Subcooling degree effect

Subcooling degree level is the difference between saturation temperature (inside a spray cooling system chamber) and the subcooled coolant (which is fed by a pump into the nozzle just before droplet breakup.) Hsieh et al [47] in their experimental investigation, revealed that the subcooling influence of water on heat transfer performance has a deteriorating effect. The slope of heat flux to superheat declines by subcooling to between 55 and 60 ℃. This impeding effect becomes more significant by reducing the Weber number (which is equivalent to the mean velocity of droplets or mass flux by the power of two).

Rybicky and Mudawar [73] in their experiments set the mass flow (for PC-5052) and changed the coolant temperature entering the chamber to assess the sensitivity of heat flux to subcooling. They reported that subcooling (due to negligible changes in viscosity and surface tension) does not have any considerable effect on single phase. However, their work suggests that subcooling can play a profound role in the nucleate boiling enhancement and CHF improvement.

Surface roughness

Surface roughness in heat and mass transfer has been always considered as one of the most effective ways of heat transfer augmentation. It is a passive method which in most cases results in a heat transfer coefficient increase compared to the smooth surfaces. However, in some applications, such as forced convection in shell and tube heat exchangers, surface roughness, in spite of having enhancement on heat transfer coefficients, has a penalty of frictional pressure drop which can adversely lead to more energy consumption for pumps. Pais et al. [76] performed an experiment of two-phase spray cooling to illuminate the effect of surface roughness on the heat transfer characteristics. In this regard, a grit size with 0.3 μm roughness, with a water-air atomizing nozzle, was considered. The results revealed

that the heat transfer rate can reach up to 12 MW/m^2. This is about ten times higher than heat transfer rates already reported for pool boiling [28]. This confirms the merits of exploiting surface roughness for spray cooling to enhance heat transfer.

Surfactants and soluble salts

Dissolving additives, such as surfactants to sprays, has long been investigated as a promising way of heat transfer enhancement. Nonetheless, its mechanism is not well understood until now. One of the earliest (1949) speculations of the reason for such an increase in the heat transfer, was made by Morgan et al. [77]. They reported that a reduction in surface tension results in nucleate boiling enhancement in all operational conditions of their experiments. Nevertheless, some other investigations years afterwards proved that adding surfactants to coolants that did not change surface tension could still promote the heat transfer coefficients [78, 79] (nucleate boiling in the latter article). It was found that a perceptible increase stemmed from surface tension reduction. The rest of the substantial change in heat transfer was from promoted nucleation by solute particles and the effect on foaming in the liquid. Despite this, there are correlations [80] in which just the effects of surface tension reduction are considered for modeling purposes. The model can successfully predict the heat removal from a hot surface to droplet impingement with the presence of additives. Some more recent work has suggested that a valid reason for the enhancement is down to an increase in local viscosity [81]. Local viscosity can change the dynamic surface tension [82] due to the different surfactant concentrations on the hot surface (where nucleation cites exist [83, 84]). Therefore, the heat transfer augmentation by surfactants is speculated to have occurred by two reasons. First, because of more nucleation sites with more liquid foaming caused by surface tension reduction. Second, due to a more effective convection mechanism [85, 86] in the liquid film that has an increased viscosity on the heated surface.

It is noteworthy that some studies have revealed that adding surfactants leads to heat transfer deterioration (e.g. sodium dodecyl sulfate (SDS) in [87]). Adding surfactants in comparison with a pure coolant, reduces the contact angle of droplets to the surface (from 90 degrees for pure water to 55 and 20 degrees for 100 and 1000 ppm SDS, respectively). The reason for this is that the more reduced contact angle occurs there will be more chances of liquid film flooding into the surface cavities. Consequently, the trapped vapour inside these cavities can suppress the nucleation. As mentioned, there are many investigations that report that surfactants enhance the nucleate boiling heat flux. These studies also proved that by increasing the surfactant concentration (for instance, from 100 ppm SDS to 1000 ppm SDS in [88]) there is just a small increase in heat transfer. In comparison to pure water, by adding 100 ppm SDS, the surface tension reduced by about 4 per cent while by increasing to 1000 ppm SDS, the surface tension reduced by more than 30 per cent (which is substantial). Therefore, it can be concluded that it is not possible to correlate nucleate boiling only with surface tension.

Mudawar and Valentine [44] conducted an experimental study on nucleate boiling regime of water spray cooling. In their measurements, they calculated local heat transfer coefficients with respect to different hydrodynamic parameters such as velocity and diameter of the droplets as well as volumetric spray flux ($\acute{v}$) with a heated area of 0.5 cm^2. During the experiments, the volumetric spray flux was varied from 0.6×10^{-3} to 9.96×10^{-3} m^3s^{-1}/m^2. The droplet diameter changed from 0.434 to 2.005 mm. The drop velocity varied from 10.6 to 26.5 m/s. Based on their results, it is concluded that the heat flux in nucleate boiling is independent on the hydrodynamic properties and is only dependent on the temperature difference between the cooling fluid (inlet water $T_{c,i}$) and the wall temperature (T_w). Therefore, the collected data is fitted to the following model:

$$q = 1.87 \times 10^{-5}(T_w - T_c)^{5.55} \quad (1.6)$$

where q is the heat flux in W/m^2. It should be noticed that this correlation is valid just for the cooling water temperature ranging from 22.5 to 23.5 $°C$. In order to facilitate presenting the quench curve, in [44] they also correlated the incipient boiling to predict the inception of nucleate boiling with the Sauter mean diameter (SMD, d_{32}) and Mass median droplet diameter (d_{05}). These models predict the surface temperature difference from the coolant temperature ($\Delta T = T_w - T_c$):

$$\Delta T = 13.43 Re_s^{0.167} Pr_f^{0.123} \left(\frac{k_f}{d_{32}}\right)^{0.22} \quad (1.7)$$

and

$$\Delta T = 13.50 Re_s^{0.172} Pr_f^{0.123} \left(\frac{k_f}{d_{05}}\right)^{0.22} \quad (1.8)$$

Qiao and Chandra [70] used the same model as Mudawar and Valentine [44]. Their model is calibrated from experimental data to predict the water spray cooling heat flux in nucleate boiling with 100-ppm surfactant (sodium dodecyl sulfate) and a mass flux of $G = 2.8\ Kg.s^{-1}/m^2$. The derived correlation is:

$$q = 0.56 \times 10^{-5}(T_w - T_c)^{6} \quad (1.9)$$

There is no information in [70] about the coolant temperature but it is reported that the surface temperature needed to start bubble nucleation is between 103 and 118 $°C$ (respectively with and without the presence of surfactant.)

Using the same relation of $q = a(T_w - T_c)^b$, Dou et al. [89] have correlated their data (full cone water spray cooling) for a flow rate range of 30 to 50 l/min to obtain:

$$q = 1.837 \times 10^{4}(T_w - T_c)^{0.69} \quad (1.10)$$

In this correlation, the water inlet temperature was fixed at 15°C and the experiments were undertaken at different nozzle pressures of 2, 3, 4, and 5 bar.

Pereira et al. [90] based on a suggestion by Yoshida et al. [61] decided to take into account the effect of saturation temperature T_{sat} on the heat flux instead of coolant inlet temperature in previous models. Yoshida et al. [61] have discussed that the heat flux is better modelled using wall superheat $\Delta T_{sat} = T_w - T_{sat}$ (i.e. the difference between the wall temperature and the saturation temperature of the coolant). Considering this, Pereira et al. [90] developed their results for a four, and a five, array of full-cone spray nozzles onto 100 cm^2 square surface with a water subcooling temperature ($\Delta T_{sub} = T_{sat} - T_c$) of 30 to 75 °$C$ as follows:

$$\mathrm{q} = 2067(\mathrm{T_w} - \mathrm{T_{sat}})^{1.57} \tag{1.11}$$

Rybicki and Mudawar [73] suggested a similar correlation to Holman and Kendall [91] (discussed shortly) modified with a density ratio multiplier for both water (downward spray) and PF-5052 (upward spray). The correlation obtained is:

$$\mathrm{q} = 4.79 \times 10^{-3} \frac{\mu_l h_{fg}}{d_{32}} \left[\frac{C_l \Delta T_c}{h_{fg}}\right]^{5.75} \left[\frac{\rho_l \bar{v}^2 d_{32}}{\sigma}\right]^{0.35} \left[\frac{\rho_l}{\rho_v}\right]^{2.5} \tag{1.12}$$

where $\bar{v}$ is mean volumetric flux obtained by dividing the total volume flow rate by the area of the sprayed test piece (Equation (1. 5)). It should be noted that in the experiments, in [73] the chamber pressure was kept at one bar with data collected when the heater temperature became steady for 10 min. Note this correlation covers subcooling degrees of 23-27 $^{\circ}C$ for PC-5052 and 76-77 $^{\circ}C$ for water. In a different study, Visaria and Mudawar [52] suggested that increasing the subcooling will delay the inception of nucleate boiling, and consequently that it leads to a reduction in the slope of nucleate boiling region in the boiling curve chart (which means it is degrading the heat transfer rate.) In addition,

the same authors in [92] modified the mean volumetric flux for two adjacent sprays when they are overlapping. Their experiments confirmed that the increment in the mean volumetric flux caused by two sprays, has a significant effect on the nucleate boiling heat transfer coefficients.

Ghodbane and Holman [48] in their experimental study have used a vertically oriented surface which is impinged by a horizontal spray. They pointed out that the heat flux is highly dependent to the subcooling degree, and for modelling purposes (in order to better fit the data to the models), they suggested it is better to use $\Delta T = T_w - T_c$ instead of subcooling. They correlated the heat flux data for Freon (R-113) to obtain:

$$q = 10.55 \frac{\mu_l h_{fg}}{H} \left[\frac{C_l \Delta T_c}{h_{fg}}\right]^{1.46} \left[\frac{\rho_l u_m^2 d_{0.5}}{\sigma}\right]^{0.6} \quad (1.13)$$

where u_m is the mean velocity of droplets (which can be obtained from Equation (1.2) by Qiao and Chandra [70]) in which the second term on the RHS is dominant (i.e. $u_m^2 = \frac{2\Delta P}{\rho_l}$). The Equation (1.13) is valid for mean droplet velocities (u_m) ranging from 5.4 to 28.5 m/s, and mass median droplet diameters ($d_{0.5}$) of 0.21 to 0.98mm. In addition, it is stated in [48] that with an increase in either volumetric heat flux, or subcooling degree, the onset of nucleate boiling and critical heat flux (CHF) is delayed.

Holman and Kendall [91] in another study have updated the Ghodbane and Holman correlation [48] with an extended droplet diameter ($d_{0.5}$) range of 0.096 to 0.98 mm in the same mean droplet velocity range ($u_m = 5.4 - 28.5\ m/s$) as follows:

$$q = 9.5 \frac{\mu_l h_{fg}}{H} \left[\frac{C_l \Delta T_c}{h_{fg}}\right]^{1.5} \left[\frac{\rho_l u_m^2 d_{0.5}}{\sigma}\right]^{0.6} \quad (1.14)$$

Hsieh et al. [47] used the correlation of Ghodbane et al. [48] for both water and R-134a and claimed that their correlation is capable of predicting forced convection, the onset of nucleate boiling, and transition boiling modes in the operating conditions of their experiments. On the LHS of their correlation, a modified boiling number of $Bo_m = qH/\mu_l h_{fg}$ was considered. There are in fact two dimensionless numbers: the Weber Number $We = \rho_l u_m^2 d_{32}/\sigma$ and the Jakob Number $Ja = C_{p,l}\Delta T_c/h_{fg}$. Their developed model is as follows:

$$\mathrm{Bo_m} = \mathrm{C(We)^m(Ja)^n} \tag{1.15}$$

where for water C, m, and n, are 15.6, 0.59, and 1.68 respectively, and for R-134a, they are 2.1, 0.66, and 1.51, respectively. By substituting the required equations for Bo_m, We, and Ja into Equation (1.15), the nucleate boiling heat flux for water can be written as:

$$\mathrm{q} = 33.595\frac{\mu_l h_{fg}}{H}\left[\frac{C_l \Delta T_c}{h_{fg}}\right]^{1.68}\left[\frac{\rho_l\left(\frac{2\Delta P}{\rho_l}\right)d_n\left(\frac{\rho_V^{0.5}\Delta P d_n^{1.75}}{\sigma^{0.5}\mu_l}\right)^{-0.259}}{\sigma}\right]^{0.59} \tag{1.16}$$

Note that in Equation (1.16), $\Delta T_c = T_{w,c} - T_c$ and $\Delta P = P_n - P_c$. For water, the correlation is valid for the Weber numbers in the range 80 to 231, and subcooling degrees of 55 to 60 °C. For R-134a, it can predict heat fluxes for Weber numbers in the range 50 to 152 and subcoolings of 2 to 4 °C.

Hsieh et al. [93] in a more recent study, equipped their test rig with a micro-particle image velocimetry (PIV) to measure the local velocity, and laser-induced fluorescence to monitor the local droplet temperature distribution. They revised the previous correlation for water with a new functional relationship for $Bo_m = c(We)^m(Ja)^n(H/L)^r$. The updated c, m, and n, are 12.3, 0.525, and 1.854. The power of the newly introduced dimensionless parameter of $(H/L)^r$ is $r = 0.924$. This parameter (H/L)

indicates how the heat flux varies with the change of nozzle distance to the surface and with the length of the impinged surface. However, this correlation is only valid for the subcooling of 77 $°C$.

Sehmbey et al. [94, 95] with an investigation of nitrogen spray cooling have proposed a new functional relationship taking into account the effect of hydraulic diameter of the surface d_H (in dimensionless parameter of d_H / d_{32}) according to:

$$q = 9.4 \frac{k_l h_{fg}}{d_H C_l} \left[\frac{C_l \Delta T_c}{h_{fg}}\right]^{1.12} \left[\frac{\rho_l u_m d_H}{\mu_l}\right]^{0.3} \left[\frac{u_m}{\bar{v}}\right]^{0.16} \left[\frac{d_H}{d_{32}}\right]^{0.24} \quad (1.17)$$

The reported operational range for this study is the mass fluxes of $16.9 - 88.9 \frac{kg}{m^2.s}$,Sauter mean diameters of $d_{32} = 14 - 29\ \mu m$, and mean droplet velocities of (u_m) 14 to 30.7 m/s. The highest heat flux achieved is 1.65 MW/m^2. The authors state that the uncertainty in heat flux measurements in the worst condition (which is near to CHF) is about ±8%. A comparison between the predicted data by the correlation and experimental data is made, however, error bands are not provided and therefore it is hard to assess the accuracy of the correlation. It is noted that the correlation is only valid for smooth surfaces.

Ortiz and Gonzalez [96] conducted an experimental study of water spray cooling to investigate the effects of surface roughness and inclination on nucleate boiling regime. They developed a correlation based on volumetric mass flow rate Q, subcooling degree ΔT_{sub}, inclination angle α, and wall superheat ΔT_{sat} as follows:

$$q = 120Q[1 + 0.25(cos\,\alpha)^{1.75}] \left[\frac{\Delta T_{sat}}{\Delta T_{sub}}\right]^{0.3} \quad (1.18)$$

The heat flux obtained from this equation is in W/cm^2, and the input for the mass flow rate is in l/h. The correlation is valid for an angle range of 0 to 90 degrees and mass flow rates between $1.48 < v < 2.91\ l/h$. As it is reported, the rough surfaces are constructed using silicon carbide abrasive paper

achieving a surface roughness of 320, 400, and 600 grit. Furthermore, a correlation for a smooth surface was developed with the same parameters except involving a different angle of inclination. The model is valid for a mass flow rate of $1.5\ l/h$ only, and is given as:

$$\mathrm{q} = 133\mathrm{v}\left[\frac{\Delta \mathrm{T_{sat}}}{\Delta \mathrm{T_{sub}}}\right]^{0.47} \tag{1.19}$$

The correlations equations (1.18) and (1.19) are claimed to be capable of predicting the entire data range within a deviation window of ±10% for smooth surface results, and ±18% for rough surfaces.

Using Freon (R-134a) in a closed loop refrigeration cycle, Tan et al. [97] carried out their experimental study on a multi-nozzle array. They reported that the region between heat fluxes of 0.35 and 1.2 MW/m^2 is associated with the nucleate boiling (the heat transfer coefficient is augmenting by increasing the mass velocity in this region.) In the region of 1.2 to 1.65 MW/m^2 the heat transfer coefficient starts to degrade which means that the point 1.2 MW/m^2 is the critical heat flux. The operating condition in this study is limited to the mean velocity of $u_m = 18.6 \text{ to } 19.6\ \mathrm{m/s}$ and Sauter mean diameters of $d_{32} = 145\ to\ 182\ \mu m$. The developed empirical correlation is:

$$\mathrm{q} = 1.7453\rho_\mathrm{l} h_\mathrm{fg} \bar{\bar{\mathrm{V}}} \left[\frac{\mathrm{C_l}\Delta \mathrm{T_{sat}}}{\mathrm{h_{fg}}}\right]^{1.5286} \left[\frac{\rho_\mathrm{l} \mathrm{u_m}^2 \mathrm{d_{32}}}{\sigma}\right]^{-0.3514} \left[\frac{\rho_\mathrm{l} \sigma \dot{\mathrm{m}}}{{\mu_\mathrm{l}}^3}\right]^{0.1643} \left[\frac{\Delta \mathrm{T_{sat}}}{\Delta \mathrm{T_{sub}}}\right]^{-0.1946} \tag{1.20}$$

which predicted experimental results within uncertainty bands of ±18%.

Cabrera and Gonzalez [98] studied water spray cooling with uniform droplet sizes and velocities (which they call 'monodisperse spray'.) In this study, the mass flux varied from 340 to 750 $\mathrm{kg/m^2 s}$, the subcooling degree was between 25 to 78°C, and the pressure inside the chamber ranged from the atmosphere to 1.8 bar. The fitted correlation obtained is:

$$q = 0.245\rho_l h_{fg} u_d \left[\frac{C_l \Delta T_{sat}}{h_{fg}}\right]^{1.038} \left[\frac{\rho_l \sigma \dot{m}}{{\mu_l}^3}\right]^{0.133} \left[\frac{\Delta T_{sat}}{\Delta T_{sub}}\right]^{-0.491} \left[\frac{R_t}{d_d}\right]^{0.0213} \left[\frac{P_{am}}{P_{at}}\right]^{0.291} \quad (1.21)$$

where R_t is the mean roughness height, which in this study is confined to a range of $5 < R_t < 79\ \mu m$. The surface roughness was obtained by polishing. The correlation accuracy is assessed by comparing the predicted results to the experimental data. It is claimed that with a confidence level of 95%, the deviations between the results are maintained within an error window of ±19.2%. The total uncertainty in the empirical heat flux measurements was around 10%.

Yang et al. [43] experimentally examined the effect of air-assist nozzles on the nucleate boiling regime of water and have correlated the results based on the effect of film thickness, δ, on the Nusselt number ($Nu = \frac{h\delta}{k_l}$) according to:

$$Nu = 1.031 \left[\bar{\bar{v}}\delta \left(\frac{C_l \mu_l}{k_l}\right)^{0.5} \frac{\rho_l g^{0.25}}{h_{fg} \sigma^{0.75} \rho_v^{1.25}}\right]^{0.655} \quad (1.22)$$

This correlation is applicable to droplet diameters in the range of 10 to 18 μm while droplet velocity is varying from 25 to 58 m/s. The flow rate varied between 0.5 to 3 l/h , the air pressure ranges from 240 to 446 KPa, and the feed water temperature was kept at 20 $°C$. It is reported that the model is capable of predicting the experimental results within bands of ±4%.

Discussions on nucleate boiling correlations

To choose an appropriate and reliable correlation for the thermal management purposes, it is first important for the correlation to be in the range of the required operating conditions. Second, the reliability of the correlation should be checked. As can be seen from Table 1-1, there are error bands in which the correlations are able to predict the experimentally measured data. These errors are generated by fitting the correlations to the database. Furthermore, precision measurement

instruments themselves add some uncertainty to the empirically measured data even before fitting a functional model to the data. Uncertainty analysis of experimental data can be undertaken by a method proposed by Moffat [99]. Table 1-1 contains most of the developed correlations for nucleate boiling regime, where offer a promising and safe mode for the design of spray cooling systems with static surfaces. This is to enable different models to be chosen based on their operating conditions, experimental uncertainties, and calibration errors.

Table 1-1. Previously undertaken studies on spray cooling in the nucleate boiling regime.

Authors	Working fluid	Only valid for: (as reported in referenced publication)	Error range of the correlations (%)	Experimental uncertainty of measured heat flux (%)	Derived experimental correlations*
Hsieh et al. (2015) [93]	**DI water**	$\Delta T_{sub} = 77\ ^{\circ}C$, $We = 30\ and\ 32.9$, $H = 170mm$, $Ja = 0.145 - 0.16$	± 20	5	(C1)
Yang et al. (1996) [43]	**water-air**	$d_d = 10 - 18\ \mu m$, $u_d = 25 - 58\ m/s$, $v = 0.5 - 3\ l/h$, $T_c = 20^{\circ}C$	± 4	10	(C2)
Cabrera and Gonzalez (2003) [45]	**water**	$G = 340 - 750$ kg/m^{2}s, $\Delta T_{sub} = 25 - 78\ ^{\circ}C$, $R_t = 5 - 79\ \mu m$, $P_{am} = 1 - 1.8\ bar$	± 19	10	(C3)
Tan et al. (2013) [97]	**R-134a**	$q = 0.35 - 1.2\ MW/m^2$, $u_m = 18.6$ to 19.6 m/s, $d_{32} = 145\ to\ 182\ \mu m$	± 18	3.3-5.1	(C4)
Ortiz and Gonzalez (1999) [96]	**water**	Roughness levels of 320, 400, and 600 grit: $\alpha = 0 - 90$, $v = 1.5 - 3\ l/h$, $d_d = 85 - 100\ \mu m$, $T_c = 24^{\circ}C$, $\Delta T_{sub} = 30\ and\ 76\ ^{\circ}C$, $q \leq 5\ MW/m^2$	± 18	≤7	(C5)
Ortiz and Gonzalez (1999) [96]	**water**	Smooth surfaces: $v = 1.5\ l/h$, $d_d = 85 - 100\ \mu m$, $T_c = 24^{\circ}C$, $\Delta T_{sub} = 30\ and\ 76\ ^{\circ}C$, $q \leq 5\ MW/m^2$, P_n~5 and 8 bar	± 10	≤7	(C6)
Sehmbey et al. (1995) [94]	**Liquid N_2**	Smooth surfaces: $G = 16.9 - 88.9$ kg/m^{2}s, $d_{32} = 14 - 29\ \mu m$, $u_m =$ 14 to 30.7 m/s, $q \leq 1.65\ MW/m^2$	-	≤8	(C7)
Hsieh et al. (2004) [54]	**water**	$\Delta T_{sub} = 55 - 60\ ^{\circ}C$, $We = 80 - 231$, $H = 60mm$, $d_{32} = 42 - 46\ \mu m$, $G = 0.178 - 0.306$ kg/m^{2}s, $P_n = 1.5 - 2.5\ bar$	-	1.05 ≤ U[1]≤ 9.06	(C8)
Hsieh et al. (2004) [54]	**R-134a**	$\Delta T_{sub} = 2 - 4\ ^{\circ}C$, $We = 50 - 152$, $H = 60mm$, $d_{32} = 42 - 46\ \mu m$, $G = 0.064 - 0.108$ kg/m^{2}s, $P_n = 6.2 - 7.2\ bar$	-	1.05 ≤ U ≤ 9.06	(C9)
Ghodbane and Holman (1990) [48]	**R-134a**	$d_{05} = 210 - 980\ \mu m$, $u_m = 5.4 - 28\ m/s$, $q = 0.001 - 0.5\ MW/m^2$, $T_c = 5 - 10^{\circ}C$, $H = 18 - 35cm$, $We = 2200 - 13750$	-	-	(C10)
Rybicki and Mudawar (2006) [46]	**water** **PF-5052**	$\Delta T_{sub} = 76 - 77\ ^{\circ}C$, $d_{32} = 109 - 151\ \mu m$, $\bar{\vec{v}} = 35 - 186$ m^{3}s^{-1}/m^2 $\Delta T_{sub} = 23 - 27\ ^{\circ}C$, $d_{32} = 109 - 151\ \mu m$, $\bar{\vec{v}} = 35 - 186$ m^{3}s^{-1}/m^2	MAE[2]=22.7	-	(C11)
Pereira et al. (2013) [90]	**water**	4-5 array of full cone nozzles: $\Delta T_{sub} = 30 - 75\ ^{\circ}C$, $G = 0.3 - 7.2$ kg/m^{2}s	MAE=10.6	1.3 ≤ U ≤ 1.7	(C12)
Dou et al. (2015) [89]	**water**	$T_c = 15 \pm 1^{\circ}C$, $P_n = 2 - 5\ bar$, $v = 30 - 50\ l/min$	±25	ARE[3]=6.3	(C13)
Qiao and Chandra (1998) [100]	**water additive**[4]	$G = 2.8$ kg/m^{2}s, $P_n = 1.38 - 2.76\ bar$, $u_m = 17 - 23$ m/s	-	-	(C14)
Mudawar and Valentine (1989) [44]	**water**	$T_c = 23 \pm 0.5^{\circ}C$, $\bar{\vec{v}} = 0.06 - 9.96$ m^{3}s^{-1}/m^2, $u_m = 10.6 - 26.7$ m/s $d_{05} = 434 - 2005\ \mu m$	-	-	(C15)

[1]Uncertainty, [2]Mean absolute error, [3]Average relative error, [4]100-ppm sodium dodecyl sulfate

Table 1-1. Continued:

*Developed correlations associated with Refs. [18][20 -31] identified by Equations C1 to C15 as appropriate:

$$Bo_m = c(We)^m(Ja)^n(H/L)^r,\ c = 12.3,\ m = 0.525,\ n = 1.854, \text{ and } r = 0.924. \quad \text{(C1)}$$

$$Nu = 1.031\left[\bar{\vec{v}}\delta\left(\frac{C_l\mu_l}{k_l}\right)^{0.5}\frac{\rho_l g^{0.25}}{h_{fg}\sigma^{0.75}\rho_v^{1.25}}\right]^{0.655} \quad \text{(C2)}$$

$$q = 0.245\rho_l h_{fg} u_d\left[\frac{C_l\Delta T_{sat}}{h_{fg}}\right]^{1.038}\left[\frac{\rho_l\sigma\dot{m}}{{\mu_l}^3}\right]^{0.133}\left[\frac{\Delta T_{sat}}{\Delta T_{sub}}\right]^{-0.491}\left[\frac{R_t}{d_d}\right]^{0.0213}\left[\frac{P_{am}}{P_{at}}\right]^{0.291} \quad \text{(C3)}$$

$$q = 1.7453\rho_l h_{fg}\bar{\vec{v}}\left[\frac{C_l\Delta T_{sat}}{h_{fg}}\right]^{1.5286}\left[\frac{\rho_l {u_m}^2 d_{32}}{\sigma}\right]^{-0.3514}\left[\frac{\rho_l\sigma\dot{m}}{{\mu_l}^3}\right]^{0.1643}\left[\frac{\Delta T_{sat}}{\Delta T_{sub}}\right]^{-0.1946} \quad \text{(C4)}$$

$$q = 120Q[1 + 0.25(\cos\alpha)^{1.75}]\left[\frac{\Delta T_{sat}}{\Delta T_{sub}}\right]^{0.3} \quad \text{(C5)}$$

$$q = 133v\left[\frac{\Delta T_{sat}}{\Delta T_{sub}}\right]^{0.47} \quad \text{(C6)}$$

$$q = 9.4\frac{k_l h_{fg}}{d_H C_l}\left[\frac{C_l\Delta T_c}{h_{fg}}\right]^{1.12}\left[\frac{\rho_l u_m d_H}{\mu_l}\right]^{0.3}\left[\frac{u_m}{\bar{\vec{v}}}\right]^{0.16}\left[\frac{d_H}{d_{32}}\right]^{0.24} \quad \text{(C7)}$$

$$q = 33.595\frac{\mu_l h_{fg}}{H}\left[\frac{C_l\Delta T_c}{h_{fg}}\right]^{1.68}\left[\rho_l\left(\frac{2\Delta P}{\rho_l}\right)d_n\left(\frac{\rho_v^{0.5}\Delta P d_n^{1.75}}{\sigma^{0.5}\mu_l}\right)^{-0.259}/\sigma\right]^{0.59} \quad \text{(C8)}$$

$$Bo_m = C(We)^m(Ja)^n,\ c = 2.1,\ m = 0.66,\ n = 1.51 \quad \text{(C9)}$$

$$q = 10.55\frac{\mu_l h_{fg}}{H}\left[\frac{C_l\Delta T_c}{h_{fg}}\right]^{1.46}\left[\frac{\rho_l u_m^2 d_{0.5}}{\sigma}\right]^{0.6} \quad \text{(C10)}$$

$$q = 4.79\times10^{-3}\frac{\mu_l h_{fg}}{d_{32}}\left[\frac{C_l\Delta T_c}{h_{fg}}\right]^{5.75}\left[\frac{\rho_l\bar{\vec{v}}^2 d_{32}}{\sigma}\right]^{0.35}\left[\frac{\rho_l}{\rho_v}\right]^{2.5} \quad \text{(C11)}$$

$$q = 2067(T_w - T_{sat})^{1.57} \quad \text{(C12)}$$

$$q = 1.837\times10^4(T_w - T_c)^{0.69} \quad \text{(C13)}$$

$$q = 0.56\times10^{-5}(T_w - T_c)^6 \quad \text{(C14)}$$

$$q = 1.87\times10^{-5}(T_w - T_c)^{5.55} \quad \text{(C15)}$$

For the aim of thermal management, even if the nozzle used is found to be the same as the reported data in the literature, owing to the undetectable variances in machining, the flow field of spray might be different, and therefore it can result in a sizeable error associated with using correlations. Thus, there are concerns about using spray flow data from one nozzle to predict heat transfer characteristics for a different nozzle even with the same geometry. Overall, the ideal solution is to use the same nozzle [44] to obtain both the hydrodynamic and heat transfer characteristics and then try to use a fitting function (or any modelling approach) to make a unique correlation for every nozzle.

As can be seen in Table 1.1, correlations are for different working fluids. These include eight correlations for water, one for water-air, three for R134-a, one for Liquid N_2, one for PF-5052, and one for water

with 100-ppm sodium dodecyl sulfate. Correlations with different coolants are not comparable against each other due to significant differences between their thermophysical properties. For correlations with R134-a, as can be seen, in the third column of Table 1.1, they are valid for totally different operating conditions (in comparison to each other), and therefore they are not comparable.

For the correlations applicable to water, correlations by Cabrera and Gonzalez (2003) [45] (C3 based on the last column of Table 1.1) as well as Ortiz and Gonzalez (1999) [96] (C5) are for rough surfaces and have different levels of roughness, so they are not comparable. They are follow-up works by the same research groups. The correlation by Ortiz and Gonzalez (1999) [96] (C6) for smooth surfaces is only for a constant volumetric flow rate of $v = 1.5\ l/h$. Pereira et al. (2013) [90] (C12) correlated results for 4-5 array of full cone nozzles, and Dou et al. (2015) [89] (C13) used nozzles with substantially high volume flow rates of $v = 30 - 50\ l/min$ (at least 20 times higher than other utilized nozzle flow rates). Mudawar and Valentine (1989) [44] (C15), in their correlation, considered the wall and coolant temperature as effective parameters and correlated their data only for a coolant temperature of $T_c = 23 \pm 0.5^{\circ}C$. Therefore, only two correlations of Hsieh et al. (2004) [54] and Rybicki and Mudawar (2006) [46] with functional forms of respectively C8 and C11 in Table 1.1 are comparable. In this regard, Figure 1-5 shows the comparisons between these two correlations.

For thermal management architecture design, after checking typical thermal management requirements and operating conditions for passenger cars (as shown in Table 1-2), it was found that the correlations of Hsieh et al. (2004), and Rybicki and Mudawar (2006), have the highest level of applicability.

Table 1-2. The required operating condition and nozzle specification [31] to compare the correlations.

Parameter	Type or value	Units
Coolant	water	None
Heat flux (part-full load)	0.2-1.6	MW/m^2
Coolant side metal T	120	℃
Refrigerant mass flow rate	1.46	g/s
Coolant temperature	95-128	℃
Chamber pressure	1-2.4	bar
Pressure drop	11.5	bar
Nozzle diameter	0.15	mm
Nozzle-to-surface distance	15	mm
Spray cone angle	90	degrees

The correlation results within the operating conditions are illustrated in Figure 1-5. The heat flux trends obtained by two correlations are, however, different from each other even with the same chamber pressures and pumping pressures (except for one point at chamber pressure 2 bar, as can be seen in Figure 1-5a). Therefore, to decide on their suitability to the experimental test rig available for this study, a verification with the available in house experimental data from preliminary investigation on nucleate boiling was undertaken. The correlation by Hsieh et al. (2004) was able to predict one experimental point at incipient boiling with an acceptable deviation of 4% which is supplied in the table below:

Table 1-3. An experimentally-measured data point against one predicted by Hsieh et al (2004).

T_{sat} (°C)	P_{sat} (bar)	T_c (°C)	T_w (°C)	q (MW/m^2)- Predicted by Hsieh et al. (2004)	q (MW/m^2)- Experimental data
103.56	1.15	85	127	0.946	0.9

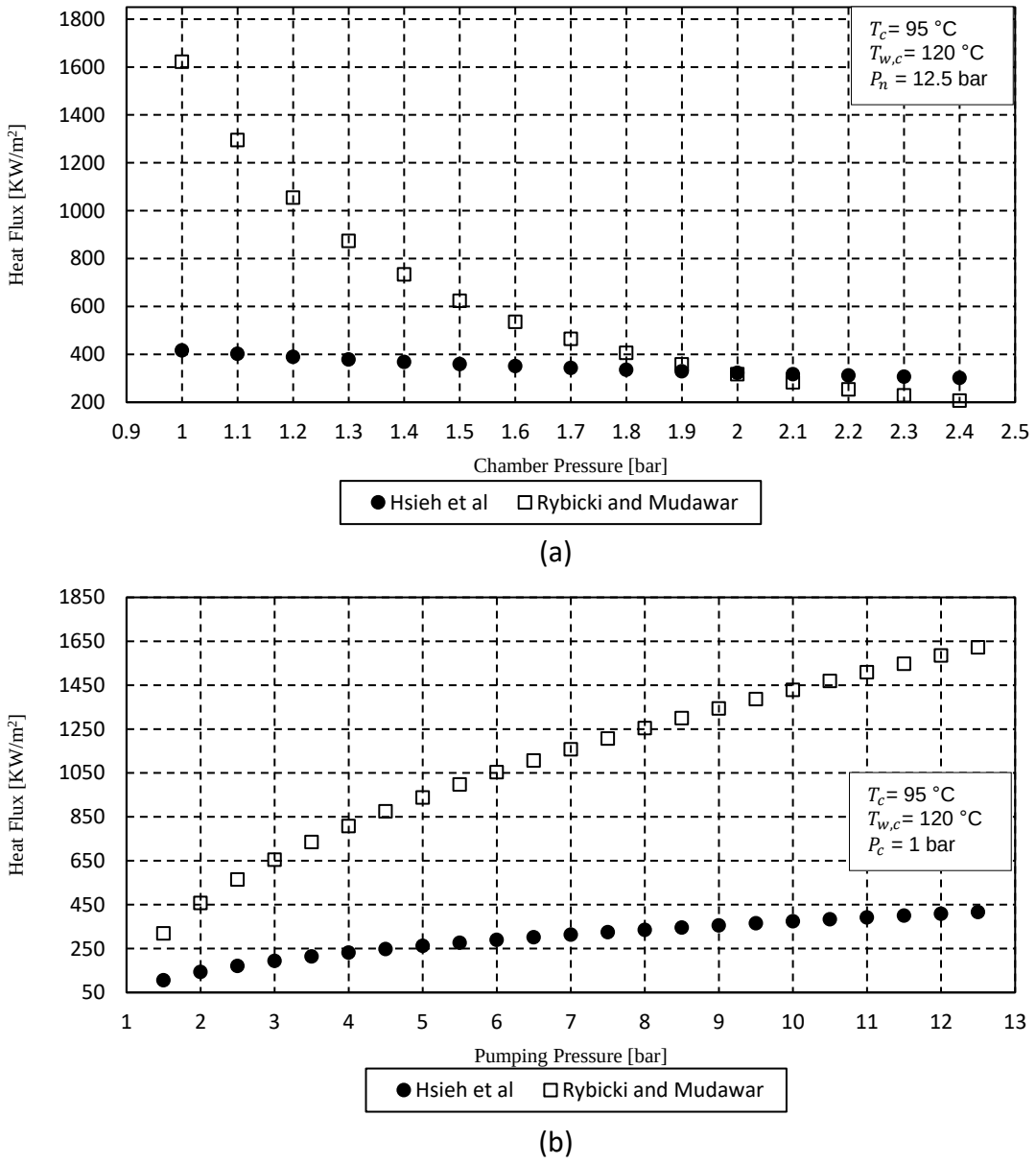

Fig. 1-5. Heat flux as a function of a) Chamber pressure, b) pumping pressure using correlations of Hsieh et al. (2004) and Rybicki and Mudawar (2006)

The correlation by Rybicki and Mudawar (2006) was not able to predict the same experimental data with acceptable accuracy (i.e. more than 100 percent deviation). This can be because of different hydrodynamic and geometrical parameters which have significant effects on the heat transfer characteristics of the spray cooling. Understanding the effects of different key parameters on evaporative spray cooling can help find the best modelling approach. Furthermore, as can be seen from

Table 1-1, there is no correlation that takes into account the effect of vibration and acceleration on the spray heat transfer characteristics (none of the cited work have included dimensionless parameters containing frequency or amplitude of vibration in formulas). One of the other major aims of this study is to investigate the heat transfer characteristics of spray cooling exposed to the dynamic conditions (which means in the presence of vibration).

Sensitivity analysis has been undertaken for the correlation by Hsieh et al. (2004) to examine the effects of different parameters including chamber pressure, pumping pressure, and coolant temperature. This has been achieved using symbolic computations by taking the partial differential of heat flux with respect to various parameters. The results are as follows:

$$\frac{\partial q}{\partial P_n} = \frac{55627 d_n^{0.32} \mu_l^{1.15} (C_l \Delta T_c)^{1.68}}{2500 H \rho_v^{0.08} \sigma^{0.51} h_{fg}^{0.68} (P_n - P_c)^{0.56}} \quad (1\text{-}23)$$

and

$$\frac{\partial q}{\partial P_c} = \frac{-55627 d_n^{0.32} \mu_l^{1.15} (C_l \Delta T_c)^{1.68}}{2500 H \rho_v^{0.08} \sigma^{0.51} h_{fg}^{0.68} (P_n - P_c)^{0.56}} \quad (1\text{-}24)$$

and

$$\frac{\partial q}{\partial T_c} = \frac{-106197 C_l d_n^{0.32} \mu_l^{1.15} (C_l \Delta T_c)^{0.68} (P_n - P_c)^{0.44}}{1250 H \rho_v^{0.08} \sigma^{0.51} h_{fg}^{0.68}} \quad (1\text{-}25)$$

By substituting the thermophysical properties taken from REFPROP (given in Table1-4), and spray specifications (given in Table 1-5 [31]),

Table 1-4. Thermophysical properties at operational condition taken from REFPROP.

T_{sat} (°C)	P_{sat} (Pa)	ρ_V (kg/m^3)	C_l (J/KgK)	μ_l (PaS)	σ (N/m)	h_{fg} (J/Kg)
99.606	100000	0.59034	4215.2	0.00028275	0.058988	2257400

Table 1-5. Proposed spray cooling specifications in [31]

T_c (°C)	$T_{w,c}$ (°C)	ΔT	P_n (Pa)	ΔP (Pa)	H(m)	d_n (m)
95	120	25	1250000	1150000	0.015	0.00015

the following functions for different parameters are obtained:

$$\frac{\partial q}{\partial T_c} = -11.61(505824 - 4215.2T_c)^{0.68} = -30223 \quad (1\text{-}26)$$

and

$$\frac{\partial q}{\partial P_n} = \frac{426.3035}{(P_n - 100000)^{0.56}} = 0.17 \quad (1\text{-}27)$$

and

$$\frac{\partial q}{\partial P_c} = \frac{-426.3035}{(1250000 - P_c)^{0.56}} = -0.17 \quad (1\text{-}28)$$

From the equations (1-26)-(1-28), it is evident that the sensitivity of heat flux to the water inlet temperature is significantly high (-30223) in comparison to influences of the remaining parameters (±0.17). These parameters can be considered as control parameters for thermal management purposes. However, owing to the thermal inertia, it is difficult to change the water temperature rapidly and therefore it cannot be a suitable control parameter in thermal management applications with high response demands.

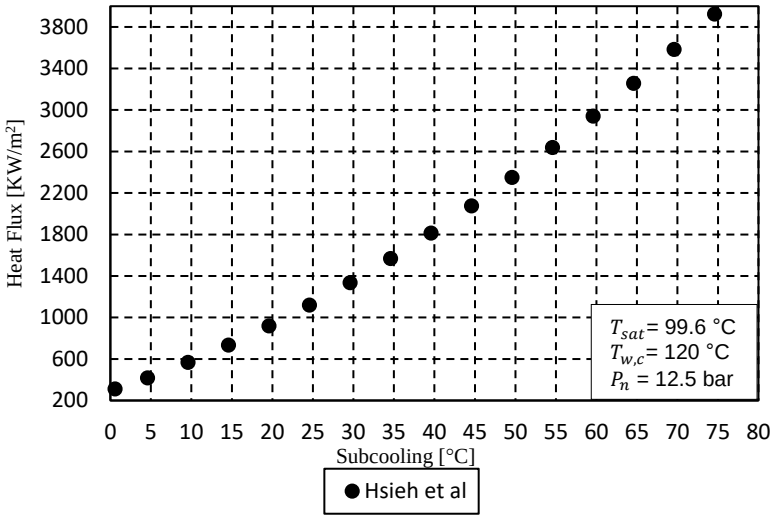

Fig. 1-6. Heat flux versus subcooling predicted by the correlation of Hsieh et al. (2004)

As shown in Figure 1-6, a spray cooling system that is required to provide part-to-full heat removals of 0.2 to 1.6 MW/m^2, the subcooling degrees of 0 to 35 $^{\circ}C$ are needed. This means that a highly efficient and compact condenser is needed. It can be expensive for a passenger car to be equipped with such heat exchangers. The magnitudes of the partial differentials giving the sensitivity of heat flux to both chamber and nozzle pressure, are low but are useful for control purposes. Either chamber pressure or nozzle pressure can be appropriate as a control parameter. However, more investigation is needed to be confident about using such correlations (in particular, the effects of other unknown factors affects the heat transfer characteristics of spray cooling, such as vibration and acceleration, which as mentioned has not yet been considered in any of the models and correlations of nucleate boiling.)

Critical Heat Flux (CHF) correlations

For safety purposes in thermal management system design, prediction of the critical heat flux just after nucleate boiling plays a pivotal role. This is because nucleate boiling is the desired two-phase spray mode (capable of many applications). Therefore staying within this regime requires prediction capabilities of transition to CHF. Mudawar and Valentine [44] reported that steady-state temperature

is difficult to obtain in the transition and film boiling regimes which occur just after the CHF point (owing to low heat flux and surface oxidation). This means that to achieve successful and secure temperature control in a thermal management system, models are required to predict both critical heat flux and the excess temperature at which CHF happens.

Owing to the complexity of heat transfer mechanisms, involvement of many different effective parameters in the prediction of CHF, (and a need for fast response models), zero dimensional models are common in the field of spray cooling. These models and the operating range in which they are valid are listed in Table 1. Furthermore, since the uncertainty of measured data, as well as data fitting methodologies, are important in both phases of thermal management and controller design, error estimation is important. To assist with this requirement columns for the experimental errors and uncertainty ranges of correlations are addressed. But prediction models are rare, for the excess temperature at which CHF occurs. This mostly stems from the presence of many contradictions concerning dynamic and heat transfer mechanisms, key parameters, and data trends. Empirical models for surface temperature at CHF by Mudawar and Valentine [44] and Dou et al. [89], and an analytical model by Baysinger et al. [62] for aerospace applications, are the examples of such models. Clearly, more careful and comprehensive experimental tests which consider different key parameters (such as vibration and acceleration) must be undertaken in the future.

The results in the literature clearly show that vibration does indeed affect heat transfer [101]. However, as can be seen in Table 1-6, there is no study in the literature that considers the effects of vibrational surfaces on CHF and its corresponding excess temperature. Therefore, experiments needed to be undertaken to reveal the influences of vibration frequency and amplitude (emulating the range present in the transportation sector). In addition, the influence of dynamics and superheat on CHF needs to be established. Vibration and acceleration are important parameters and need to be considered in thermal

management systems exposed to dynamics such as automotive vehicles [1] and aircraft [102, 103]. The effects of vibration and acceleration on spray cooling in single-phase [58], incipient boiling [104, 105], and nucleate boiling [27] modes have recently been investigated. Correlation models with CHF and excess temperature prediction capabilities also need to be developed. Such empirical correlations not only can be employed in the design of spray evaporative cooling systems but can also be used in thermal management.

Table 1-6. Studies on the prediction of Critical Heat Flux (CHF).

Authors	Working fluid	Test conditions: (as reported in referenced publication)	Error range of the correlations (%)	Experimental uncertainty of measured heat flux (%)	Derived experimental correlations*
Mudawar and Valentine (1989) [44]	**Water**	$T_c = 23 - 80\ ^\circ C$, $v^{"} = 0.6 \times 10^{-3} - 9.96 \times 10^{-3} m^3 s^{-1}/m^2$ $d_{0.5}$ = 0.434-2.005 mm, u_m =10.6-26.5 m/s	±20	-	(C1)
Estes and Mudawar (1995) [106]	**Water, FC-72, FC87**	$v = 2.52 \times 10^{-6} - 3.15 \times 10^{-5}\ m^3 s^{-1}$, $\Delta T_{sub} = 13 - 33^\circ C$	±25	-	(C2)
Mudawar and Estes (1995) [107]	**FC-72, FC87**	$v^{"} = 16.6 \times 10^{-3} - 216 \times 10^{-3} m^3 s^{-1}/m^2$, $\Delta T_{sub} = 13 - 33\ ^\circ C$	±30	-	(C3)
Jian and Dhir (2004) [108]	**Water**	$v^{"} = 2.9 \times 10^{-3} - 5.1 \times 10^{-3} m^3 s^{-1}/m^2$, $T_c = 23 - 70\ ^\circ C$	±23	±4.3	(C4)
Thiagarajan et al.(2013) [109]	**HFE-7100**	$v = 1.1 \times 10^{-6} - 15.8 \times 10^{-6}\ m^3 s^{-1}$, $\Delta T_{sub} = 0 - 30^\circ C$	±30	±6	(C5)
Thiagarajan et al. (2013) [109]	**HFE-7100**	A microporous surface: 100 μm coating, porosity of 57%.	±30	±6	(C6)
Dou et al. (2015) [89]	**Water**	$G = 6.2 - 12.4$ kg/m^{2}s, $\Delta P = 2 - 7 bar$	±20	±6.3	(C7)
Visaria and Mudawar (2008) [110]	**FC-77**	$\Delta T_{sub} = 22 - 70\ ^\circ C$, $v = 3.33 - 20.4\ cm^3 s^{-1}$	±30	-	(C8)
Sehmbey et al. (1995) [94]	**Liquid nitrogen Water**	$d_{32} = 14 - 29\ \mu m$, $G = 16.9 - 88.9$ kg/m^{2}s, $P_n = 2.8 - 8.3\ bar$	±30	±8	(C9)
Chow et al. (1996) [111]	**Liquid nitrogen Air-water R-113**	$\Delta T_{sub} = 0 - 50\ ^\circ C$, $u_m = 10 - 50\ m/s$, $G = 1.12 - 6.75$ kg/m^{2}s	±30	-	(C10)
Sawyer et al. (1996) [112]	**Water**	$u_m = 2.4 - 4.6\ m/s$, $We = 175 - 730$	±22	±5	(C11)
Silk et al. (2007) [113]	**Water Methanol Perfluorocarbons**	$Pr = 0.33$, $T_{sat} = 31 - 80$ ℃	±30	-	(C12)
Cabrera and Gonzalez (2003) [45]	**Water**	$\Delta T_{sub} = 25 - 78\ ^\circ C$, $P_n = 1 - 1.8\ bar$, $R_t = 5 - 79 \mu m$, $G = 340 - 750$ kg/m^{2}s	±15	±10	(C13)
Abbasi and Kim (2011) [114]	**PF-5060**	$\Delta T_{sub} = 11 - 31\ ^\circ C$, $P_n = 2 - 6.9\ bar$, $H = 3, 5,$ and 7 mm	±25	±6.3	(C14)
Zhao et al. (2019) [115]	**Water**	$\Delta T_{sub} = 61.3\ ^\circ C$, $\bar{v} = 2.42 - 8.04$ m^{3}s^{-1}/m^2	±12.31	±4.6	(C15)

Table 1-6. Continued:

*Developed correlations associated with Refs. [18][20 -31] identified by Equations C1 to C15 as appropriate:

$$q_{CHF} = 122.4\rho_g h_{fg} v^{"}\left[1 + 0.0118\left(\frac{\rho_g}{\rho_f}\right)^{1/4}\left(\frac{\rho_f C_{p,f}\Delta T_{sub}}{\rho_g h_{fg}}\right)\right]\left(\frac{\sigma}{\rho_f v^{"2} d_{32}}\right)^{0.198} \quad \text{(C1)}$$

$$q_{CHF} = 134.3\rho_g h_{fg} v^{"}\left[1 + 0.0118\left(\frac{\rho_g}{\rho_f}\right)^{1/4}\left(\frac{\rho_f C_{p,f}\Delta T_{sub}}{\rho_g h_{fg}}\right)\right]\left(\frac{\sigma}{\rho_f v^{"2} d_{0.5}}\right)^{0.192} \quad \text{(C1)}$$

$$q_{CHF,p} = 2.3\rho_g h_{fg} v^{"}\left(\frac{\rho_f}{\rho_g}\right)^{0.3}\left(\frac{\rho_f v^{"2} d_{32}}{\sigma}\right)^{-0.35}\left[1 + 0.0019\left(\frac{\rho_f C_{p,f}\Delta T_{sub}}{\rho_g h_{fg}}\right)\right] \quad \text{(C2-a)}$$

$$q_{CHF,p} = \frac{q_{CHF}L^2}{L^2(\pi/4)} = \frac{4}{\pi}q_{CHF} \quad \text{(C2-b)}$$

$$v^{"} = \frac{2v}{\pi L^2}\left[(1 + \cos(\frac{\theta}{2}))\cos(\frac{\theta}{2})\right] \quad \text{(C2-c)}$$

$$q_{CHF} = 1.467\rho_g h_{fg}\bar{v}^{"}\left[(1 + \cos(\frac{\theta}{2}))\cos(\frac{\theta}{2})\right]^{0.3}\left(\frac{\rho_f}{\rho_g}\right)^{0.3}\left[\frac{\rho_f \bar{v}^{"2} d_{32}}{\sigma}\right]^{-0.35}\left[1 + 0.0019\left(\frac{\rho_f C_{p,f}\Delta T_{sub}}{\rho_g h_{fg}}\right)\right] \quad \text{(C3)}$$

$$q_{CHF} = 2.3\rho_g h_{fg}\bar{v}^{"}\left(\frac{\rho_f}{\rho_g}\right)^{0.5}\left(\frac{\rho_f \bar{v}^{"2} d_o}{\sigma}\right)^{-0.2}\left[1 + 0.0019\left(\frac{\rho_f C_{p,f}\Delta T_{sub}}{\rho_g h_{fg}}\right)\right] \quad \text{(C4)}$$

$$q_{CHF} = 1.449\rho_g h_{fg}\bar{v}^{"}\left(\frac{\rho_f}{\rho_g}\right)^{0.3}\left[\frac{\rho_f \bar{v}^{"2} d_{32}}{\sigma}\right]^{-0.3371}\left[1 + 0.0058\left(\frac{\rho_f C_{p,f}\Delta T_{sub}}{\rho_g h_{fg}}\right)\right] \quad \text{(C5)}$$

$$q_{CHF} = 2.14\rho_g h_{fg}\bar{v}^{"}\left(\frac{\rho_f}{\rho_g}\right)^{0.3}\left[\frac{\rho_f \bar{v}^{"2} d_{32}}{\sigma}\right]^{-0.363}\left[1 + 0.0058\left(\frac{\rho_f C_{p,f}\Delta T_{sub}}{\rho_g h_{fg}}\right)\right] \quad \text{(C6)}$$

$$q_{CHF,p} = 2.52 \times 10^{-3}\rho_g h_{fg} v^{"}\left(\frac{\rho_f \bar{v}^{"2} d_{32}}{\sigma}\right)^{-0.4255}\left[1 + 0.013\left(\frac{\rho_f}{\rho_g}\right)^{-0.25}\left(\frac{\rho_f C_{p,f}\Delta T_{sub}}{\rho_g h_{fg}}\right)\right] \quad \text{(C7)}$$

$$q_{CHF,p} = 2.3\rho_g h_{fg} v^{"}\left(\frac{\rho_f}{\rho_g}\right)^{0.3}\left(\frac{\rho_f v^{"2} d_{32}}{\sigma}\right)^{-0.35}\left[1 + 0.005\left(\frac{\rho_f C_{p,f}\Delta T_{sub}}{\rho_g h_{fg}}\right)\right] \quad \text{(C8)}$$

$$q_{CHF} = 0.31\rho_g h_{fg}\left(\frac{\rho_f}{\rho_g}\right)^{0.5}\left(\frac{6\bar{v}^{"}\sigma}{\pi\rho_f d_{32}}\right)^{1/3} \quad \text{(C9)}$$

$$q_{CHF} = 0.38\rho_g h_{fg} u_m\left(\frac{\rho_f {u_m}^2 d_{32}}{\sigma}\right)^{-1/3}\left(\frac{\rho_f}{\rho_g}\right)^{-0.5}\left(\frac{P_a}{P_s}\right)^{-0.25} \quad \text{(C10)}$$

$$q_{CHF} = 0.166\rho_f h_{fg} u_d\left(\frac{\rho_f u_d^2 d_d}{\sigma}\right)^{-0.4138}\left(\frac{f d_d}{u_d}\right)^{0.8906} \quad \text{(C11)}$$

$$q_{CHF} = 5.3Re_d^{0.55}Pr_f^{0.33}\left[\frac{1+0.8\left(C_{p,f}\Delta T_{sub}/h_{fg}\right)}{\left(\frac{\rho_f}{\rho_g}\right)^{0.4}}\right]\left(\frac{\pi N^{+} d_{32}^3}{6}\right)^{0.09}\left(\frac{k_f}{L}\right)\left(\frac{h_{fg}}{c_{p,f}}\right) \quad \text{(C12)}$$

$$q_{CHF} = 1.623(We)^{-0.315}(S_t)^{0.0465} = 1.623Gh_{fg}\left(\frac{\rho_f u_d^2 d_d}{\sigma}\right)^{-0.315}\left(\frac{R_t}{R_d}\right)^{0.0465} \quad \text{(C13)}$$

$$q_{CHF}^{"} = 9.15 * 10^4 P^{0.4}\left(1 + 2.42\left(\frac{C_{p,f}\Delta T_{sub}}{h_{fg}}\right)\right)^{0.52} \quad \text{(C14)}$$

$$q_{CHF} = 58.0628\rho_g h_{fg}\bar{v}^{"}\left[1 + 0.00118\left(\frac{\rho_f}{\rho_g}\right)^{-0.25}\left(\frac{\rho_f C_{p,f}\Delta T_{sub}}{\rho_g h_{fg}}\right)\right]We^{-0.2054}St^{0.4462} \quad \text{(C15)}$$

Sensitivity of Spray Cooling Systems (SCS) to vibration and acceleration

In this section, the sensitivity reported in the literature of spray cooling systems to vibration and acceleration, is reviewed.

Vibration is definitely considered to have an influence on heat transfer [56]. Cooling systems, especially those used in the automotive industry, are mostly operating in dynamic conditions. Consequently, modelling should consider the effect of vibration as an externally imposed force. In the literature, there are no experimental studies addressing spray cooling involving nucleate boiling. A recent study by Sathyabhama et al. [57] investigated pool-boiling. The results of the study [7] concluded that at low frequencies (10 Hz) and amplitudes (2.5 mm), vibration has a positive influence on heat transfer coefficient (by 26%) compared to when vibration is absent. At high frequencies and amplitudes, vibration impedes boiling. This study suggests the existence of an intermediate optimum, i.e. between low and high frequencies and amplitudes. The effects of vibration and acceleration on spray cooling in incipient boiling [104, 105], and nucleate boiling [27] modes, have recently been investigated. For spray cooling in two-phase flow nucleate boiling, there is only one investigation involving a numerical study on the impact of single and multiple droplets on the surface in the presence of surface vibration [8]. This is performed by the *Volume of Fluid* (VOF) method [105]. The study contains two case studies of frequency injection. Low frequency injection generates a single droplet. A slightly higher frequency injection generates less than five droplets. The whole domain contains the impact of either single or multiple droplets on a liquid film, with a bubble sticking to the hot surface interior. A preliminary study which considers such a limited number of droplets cannot be used in modelling, thermal management, or system design of spray cooling systems, especially under dynamic conditions (e.g. automotive applications). However, it is of great importance to the theoretical understanding of the physical phenomenon. Tropea and Roisman [65] discuss that such an approach which considers such a limited

number of droplets is not capable of predicting the whole spray impact behaviour reliably. They raise concern for the disturbing interactions between droplets sprayed onto a surface. They also draw attention to the fluctuations that impinging droplets impose on the liquid film. The study [35] exposes a significant need for further research.

The vibrational effect can be seen through Vibrational Reynolds $Re_V = \rho_l a \omega d_H / \mu_l$ and dimensionless Acceleration Number $Ac = (\omega\text{^}2\ a)/g$, where, a and $\omega = 2\pi f$ are vibration amplitude and frequency respectively. In fact, Vibrational Reynolds Number is a representation of the turbulence resulting from the vibrating surface [57]. It is a metric to help understand how vibration (through increased turbulence) can affect heat transfer. Heat transfer enhancement or deterioration as a consequence of vibration can be explained by increased flow turbulence, a thinned or thickened boundary layer, more or less generates nucleate sites [58] and changes wetting-angle [59]. The dimensionless Acceleration Number is helpful in considering any possible impact of experimentally-measured acceleration (using an accelerometer). The impact of acceleration on the spray cooling heat transfer has been investigated empirically in the following dynamic conditions: An acceleration test bench with a rotating arm [60], a reduced gravity condition [61], an aircraft in parabolic flight [62, 63]. Elston et al. [116, 117] studied the effect of acceleration on the cooling performance of spray arrays using NASA's C-9 aircraft able to achieve accelerations of 0.02g to 2.02g. They reported that acceleration has an impeding effect on spray heat transfer in nucleate boiling. By contrast, Michalak et al. [118] claimed that for accelerations between 0.15g and 1.8g, the spray heat transfer enhances with increasing acceleration. There are however inconsistencies in the conclusions owing to the complexity of spray heat transfer mechanisms, and also differences in experimental conditions. Thus, acceleration stemming from vibration (which is different from aerospace operating conditions, in terms of heater orientation) is also important to the

understanding of spray cooling for all dynamic conditions (such as generally occurs in automotive and aerospace vehicle applications).

Thermal management and temperature control

In general, thermal management involves two important qualities: efficacy and safety. For the specific purpose of evaporative spray cooling, efficacy requires a thorough understanding of the dynamic and heat transfer mechanisms involved. The dynamic mechanism involve many complex relations, from the droplet impingement to rebound and splashing from the impinging surface, followed by bubble generation in the liquid film during nucleation [119]. Heat transfer consists of mechanisms such as impinged drop convection, liquid film evaporation, film flow convection, and surface and secondary nucleate boiling [66]. To better understand the combination of these mechanisms, spray cooling researchers have separated different modes of spray cooling based on achievable excess temperature and heat flux (the excess temperature is the difference between the cooled surface and saturation temperature, also known as superheat). Spray cooling modes start from single-phase with high degrees of subcooling, which is for the cooling systems with low heat-flux, low-temperature requirements. Next, the spray cooling mode is nucleate boiling with high heat-transfer rates and high surface-temperature capabilities, ideal for cooling systems with extreme thermal requirements [23]. After critical heat flux, transition boiling occurs. At the transition boiling mode the bubbles come together, forming small slugs in the liquid film resulting in partial contact of thin layer with the surface. The Leidenfrost point occurs when the heat transfer mode changes from transition boiling to film boiling, where a thermally-insulated layer forms between the hot surface and the impinging spray droplets. Film boiling gives a poor heat transfer coefficient. For safety purposes, as was mentioned, the capability of CHF and maximum temperature predictions are important.

It is worthy of note, that conventional cooling systems in gasoline engines uses smart thermostats and variable speed pumps driven by crankshafts. Modern IC engines generally run hot, that is over 80 $^{\circ}C$, in order to be more efficient and consequently reduce CO_2 emissions. On the other hand, all suggested state-of-the-art spray cooling systems have a complex physical phenomenon with different sensitive control parameters and therefore different important precautions should be inevitably considered in thermal management. Recently, JT Jose et al. [11] assessed deployment of spray cooling systems for IC engines. The important precautions in order to successfully meet the requirements, such as the need for changing the cylinder-head design, are discussed. A system was designed and simulated. However, there is still a need to investigate the thermal management of such systems under realistic operating conditions (such as those involving dynamics). This should at least examine a representative cylinder head or coolant jacket. Before closing this however, it is important to review on all the thermal management research available.

In the literature, for thermal management of spray cooling systems, two spray flow fields of 'variable' and 'intermittent' are classified. Variable flow spray cooling schemes need pump speed control. The intermittent flow spray cooling requires control of solenoid valves mounted just before a nozzle. In the next section, thermal management experiments on spray cooling with the aim of hybrid and electric cars applications will be reviewed.

Variable flow spray cooling

Wang et al. [15] established control systems in order to evaluate a spray cooling system on sintered porous wick made from copper. To keep the system within a safe working temperature, fuzzy logic and PID controllers were implemented. Based on the results, it was reported that the performance of Fuzzy-PID controller was superior to PID as it responded faster with a smaller error. Ding et al. [16] applied

PID controllers in order to keep the Insulated-Gate-Bipolar-Transistor (IGBT) junction temperature below 150 ℃ for a safe operation. A spray cooling system (working with water) was employed for cooling. The results illustrated that Fuzzy-PID is better than conventional PID for controlling the junction temperature. Sai and Reddy [120] developed a controller to keep, under control, the temperature of superheated steam in power plant. Water was considered as the working fluid in the spray cooling system. To control the temperature, a fuzzy gain scheduler and conventional PID were implemented. The results showed that the settling time and oscillations associated with peak overshoot of the PID controller, were higher. By contrast, the fuzzy gain scheduler was capable of eliminating the oscillations and reducing the time needed for settling.

Intermittent flow spray cooling

To enhance the cooling performance, a lot of attention has been paid to evaluate intermittent spray cooling systems. Generally, spray cooling systems can be divided into two categories including intermittent, and continuous spray cooling. The first category, i.e. intermittent, is used where heat loads are variable, while the second type is employed for satisfying the maximum heat loads. The continuous system utilizes a larger volume of coolant. To overcome this issue, solenoid valves have been used commonly to control two factors: duty cycle and spray frequency. When these factors are controlled by taking the heat loads into account, it should be possible to enhance the cooling efficiency. In this regard, Panao and Moreira [121] studied pulsed-spray impinging onto heated surfaces. Tests were undertaken to demonstrate the impact of injection parameters including frequency, duration, and pressure on the cooling performance. The test conditions, similar to applications in hybrid configurations, were considered. It was observed by the experiments that increasing the injection pressure results in decreasing heat flux. The data also suggested that for the range of injection

conditions for real engines, time variations of the transferred heat is more dependent on the coolant mass velocity than on the size of the droplets, and their axial velocity.

In another study, by Moreira and Panao [122], it was demonstrated that increasing the frequency within the range of 10 to 20 Hz, gives rise to an increasing in the rate of local transferred heat. However, it was also observed that by further increase in the frequency, the heat transfer rate declines. Panao and Moreira [123] also investigated a two-phase flow cooling system using several intermittent sprays. Spray characteristics, i.e. the size of drops, and their axial velocity, and the thermal features of the surface, were considered to explain the factors which have high impact on heat transfer. As a result, it was reported that injection frequency, and the temperature of the surface, have greatest effect on the amount of transferred heat, but not the spray features prior to impact. Moreira et al. [124] assessed an intermittent spray cooling system and found that under conditions of five milliseconds pulse duration, at the critical heat flux, for smaller injection frequency, cooling efficiency increases. Panao and Moreira [32] suggested an intermittent spray cooling system for thermal management purposes and investigated the influences of different parameters such as injection frequency, pressure and pulse duration. The results demonstrated that injection frequencies do not affect the spray characteristics significantly. A parameter called “duty cycle” was introduced as the percentage of cycle time associated with the injecting liquid. Smaller duty cycles were found to be effective in controlling the surface temperature. Also, higher performance was obtained when injection pressure was lower. Also, the comparison between the performance of continuous and intermittent spray cooling showed that by using the intermittent mode, a significant reduction in coolant usage is observed for similar cooling efficiency.

In another study conducted by Panao et al. [125], it was concluded that the heat transfer rates increase when a smaller period between the consecutive injection cycles was implemented. Somasundaram and Tay [126] studied spray cooling systems in continuous and intermittent conditions to reveal the influences of heat flux and mass velocity on the fluctuations of surface temperature and other parameters. The experiments showed that when the temperature of the surfaces is sufficiently superheated, the fluctuation of the surfaces is reduced. In another empirical investigation performed by Majaron et al. [127] on the intermittent cooling systems, it was observed that cooling rates increased when the duty cycle was neither high nor small. But, for smaller duty cycles, a significant decrease in the rates of heat removal was observed.

Applications

Spray cooling is receiving attention in the development of advanced thermal management systems. Spray heat transfer characteristics are ideal for high COP (defined as the ratio of the heat removed to the pumping power) [128], high-heat flux, and high-temperature [129] heat removal applications. Spray cooling applications include: i) electric vehicles [12] and hybrid electric vehicles [13], ii) power electronic components (such as high-power LEDs [14], IGBTs [15], high-heat flux heat sinks for IGBTs [16], and micro-electro-mechanical systems in aerospace [17]), iii) Lithium-ion batteries (for the specific purpose of improving thermal performance [18], or to achieve optimised lifespan [19]), IV) power plant (spray cooling of superheaters [120]), hydrogen technologies [20] (cooling storage tanks [21], catalyst surface temperature control by spray for hydrogen fuel cells [130]), and V) carbon capture technologies (i.e. water spray cooling in the CO_2 separation process results in the most cost-effective gasifier design [131]). These applications of spray cooling are in accordance with the 10-point-plan booklet published by the UK government in 2020 as part of the green industrial revolution [132]. With new regulations

emphasising the need to mitigate emission footprints to achieve 2050 net zero, the need to find highly efficient and safe thermal management systems is becoming increasingly obvious.

Researchers have undertaken studies to manage the thermal performance of power electronic hardware in different industrial systems such as automotive applications. In this regard, Mudawar et al. [34] undertook several experiments on thermal management of hybrid vehicles. During the tests, R-134a and HFE-7100 were used as coolants. According to the observations, the CHF value obtained by R-134a was much larger than the heat flux anticipated in hybrid vehicles electronics. It was reported that the R-134a performance was not satisfactory as it could not maintain the temperature of the test device below 125 ^{o}C, which was the maximum allowable temperature. By contrast, HFE-7100 performed better by keeping the surface temperature below the maximum allowed value of 125 ^{o}C for CHF higher than 200 W/cm^2.

An empirical investigation was performed by Turek et al. [133] on the thermal management of a power inverter system. For this purpose, a spray cooling system working with the mixture of two fluids, i.e. water and propylene glycol with equal volume concentrations at 100 ^{o}C temperature, was established. Results indicated that owing to the higher values of the heat transfer coefficients obtained by the spray cooling system, the power invertor was kept in a safe temperature range of operation. Turek et al. [134] also performed another study on the same experimental facility using pure water as the coolant. According to the experiments, pure water has a better performance. Results indicated that, compared to the mixture of water/propylene glycol, lower temperatures are obtained with water. The reason behind this difference in performance is that when the mixture is used, the water vaporizes significantly, while the propylene glycol concentration on the surface increases, the local boiling point increases, which in turn, adversely affects the boiling rate and performance.

Another study on managing the thermal performance of a power inverter was undertaken by Bostanci et al. [135]. Coolant was sprayed onto enhanced surfaces. Experiments revealed that a maximum heat flux value of 400 W/cm^2 is achievable with just surface superheat of 14 ^{o}C. Under these conditions, the maximum coefficient of heat transfer was 280000 W/m^2 ^{o}C. To thermally manage a surface in an electric device, and to keep its temperature below 125 ^{o}C for the proper performance of the device, Panao et al. [125] developed an empirical arrangement, using a multi-jet atomization method. The results demonstrate that implementing shorter times between injection cycles, and keeping the surface wetted (instead of appearing wet and dry surfaces frequently), results in higher heat transfer coefficients and better efficiencies. Also, it was observed that by using more impinging jets, the rates of transferred heat increase but the cooling efficiency does not improve.

In order to use environment-friendly refrigerants such as R-1234yf (instead of the traditional high GWP (global warming potential) refrigerant of R-134a in spray cooling systems) Bostanci et al. [33] performed an empirical investigation on different enhanced surfaces cooled with spray. The HTC (heat transfer coefficient) obtained, and CHF using R-134a, were higher than those obtained by R-1234yf, for all mass fluxes and surfaces. And for the mass flow rates per unit area studied i.e. between 2.5-4.5 ml/cm^{2}s, it was found that although the HTC and CHF increased by increasing the mass flow, the cooling efficiency and COP (coefficient of performance) decline, because further increment of the mass flux, the heat elimination capability does not enhance proportionally.

Temperature Control

Several attempts have been made to implement spray cooling systems for plug-in hybrid electric vehicles (PHEVs) [136]. Mudawar et al. [34] reported that a feasible thermal management system for

PHEVs should have the potential to dissipate heat in the range of 1.5-2 $\mathrm{MW/m^2}$ while the temperature must be kept below 125 $^{\circ}$C. In this regard, spray cooling is assessed and results showed that such heat removal requirements are achievable. Nevertheless, there was no discussion of the control problem. Generally, the challenges are mostly summarised in a control strategy development that is workable on an automobile cooling system considering the dynamic behaviour of such a method with a phenomenon that is not yet well known. To be more specific, nonlinearities of two-phase spray cooling stem from different hydrodynamic parameters make it difficult to select an appropriate controller. PID controller is widely used and developed in automotive applications owing to its simplicity of design and tuning of a system as well as offering promising results in handling, and robustness [137]. Jafari et al. [41], in their control strategy for spray evaporative cooling of a highly boosted internal combustion engine, had two control loops. One with a PID controller to regulate the pump pressure, and another with a look-up table to set the sub-cooling temperature of the coolant. Results first showed that the controller works well in either part-load or steady state conditions but is weak in dealing with abrupt changes of load induced by the cooling system for different driving situations. The solution was to introduce an additional reservoir, with a 3-way valve to regulate subcooling (i.e. the temperature difference between coolant temperature to its saturation temperature at ambient pressure). Even though any additional component may compromise the compactness and lightweight requirements of a modern car, the results found were much better. This suggests a need to investigate various controllers available such as Fuzzy, hybrid and those using artificial intelligence (AI) to overcome thermal management problems as well as meeting the main requirements of the performance and robustness.

1.2. The objectives of the dissertation

Having now reviewed the literature, a stage has been reached where appropriate remaining research questions can be identified. Based on the literature review, there is no experimental and numerical studies on evaporative spray cooling exposed to vibration. In particular, the effect of vibration frequency and amplitudes on nucleate boiling regime and its associated critical heat flux is not investigated. In addition, there is no published work on thermal and control performance of evaporative spray cooling systems under vibration for hybrid, electric and range extended vehicles. Owing to the complexity of heat transfer mechanisms, involvement of many different effective parameters in the prediction of nucleate boiling and its associated CHF, (and a need for fast response models), zero dimensional models are common in the field of spray cooling. Numerical models of spray evaporative cooling such as high fidelity CFD models are computationally expensive owing to non-linearity of two-phase flow governing equations and cannot be deployed for real-time control applications. (Heat transfer associated with spray evaporative cooling of vibrating surfaces is a process involving complex two-phase physics well beyond current numerical simulation capabilities.) Therefore, empirical correlation models derived by dimensional analysis and similitude are the best alternative approach for such novel subject. Black box models are not chosen owing to their deficiency in explaining the physics, so nondimensional physics-based models are constructed and fitted to address the objectives of this thesis.

The overarching aim of this dissertation is to exploit evaporative spray cooling to reduce CO_2 emissions in hybrid electric vehicles, and to extend the range of battery electric vehicles. The research questions to address this aim are summarized in the following:

1- Is it possible to create dynamic correlations to model spray evaporative cooling that will be useful for a range of automotive and aerospace applications (ICE, power electronics, batteries, electrical machines)?
2- Is it possible to design a robust control system based on an extrapolated correlation model?

A requirement to address these questions is: i) to get good dynamic spray evaporative cooling data; ii) to construct as necessary archival dynamic correlations that will be useful for design, and iii) to find the simplest control strategy that will fully meet the requirements for a variety of control application under dynamic conditions, particularly for cooling automotive electrical and electronic powertrain components. To be more specific, the objectives of the thesis can be stated as follows:

Objective 1: to investigate the effect of vibration on spray evaporative nucleate boiling for a full-cone spray impinging on a (heated) flat circular copper test piece, driven by a shaker. Experimentally-measured data is obtained and corresponding empirical correlation models are developed and fitted by exploiting dimensional analysis and similitude conditions involving the effect of vibration on the trend of the measured data in particular making use of the Vibrational Reynolds Number and a dimensionless Acceleration Number.

Objective 2: to reveal the influences of vibration, its frequency and amplitude (emulating the range present in the transportation sector), as well as acceleration on CHF and superheat. In this regard, the correlation models with CHF and excess temperature prediction capabilities are developed. Then, experimentally-measured data are fitted to the associated correlations. These empirical correlations can not only be employed in the design process of spray evaporative cooling systems but also in the thermal management of such systems.

Objective 3: to create a spray-evaporative-cooling-based thermal management system, and to experimentally verify its controllability. This is to address the concerns surrounding the temperature control of a system that can operate near the required heat flux and yet remain stable. Furthermore, most of the spray evaporative cooling database in the literature has not considered trickier three-dimensional geometries and is limited to flat surface test pieces. There is, to the authors' knowledge, no published experimental data on the effects of vibration on the heat transfer rate from an evaporative spray. These factors have motivated the current study which seeks to address the lack of experimental data and investigate the design, simulation, and implementation in hardware of an appropriate spray evaporative cooling control system.

2. DIMENSIONAL ANALYSIS AND SIMILITUDE FOR CONSTRUCTION OF EMPIRICAL MODELS OF SPRAY EVAPORATIVE COOLING

Dimensional analysis is considered one of the most important steps in modeling and pre-experimental planning [138]. It systematically reduces the number of variables in a physical relationship, eliminating the need for excessive amounts of experimentation. Implementing dimensional analysis methods such as the Buckingham Π-Theorem [139, 140], and developing only important dimensionless parameters, reduces the amount of data that needs to be taken by measurement. It also saves time, financial and budgetary resources, laboratory space and sometimes reduces the need for technical support. Furthermore, initiating dimensional analysis before quantitative analysis helps to reach an understanding of a problem with minimum complexity. This is highly beneficial when investigating novel phenomena, of which the equations and boundary conditions are not yet fully expressed [141].

2.1. Generalized Buckingham π-Theorem applied to spray evaporative cooling of surfaces with and without vibrations

In a preliminary investigation of a novel phenomenon, some independent variables exist. These define the dependent variable of interest, which have invariant values in all the case studies under consideration. For example, in spray cooling, all the experiments are supposed to be at the same pressure and equilibrium conditions. Owing to the nature of two-phase flow, some of the fluid properties (as independent variables) which define the heat flux (as a dependent variable), have the same invariant values. This is also true for spray cooling specifications while undertaking experiments with the same nozzle. To attempt to simplify this further, by neglecting quantities that have the same value during experimental measurement, will however adversely affect the dimensional analysis. Dimensional analysis must be based on a complete set of independent parameters that express the

heat flux. To prevent dimensional analysis from being affected by such an issue, the generalized Π-Theorem by Sonin [142] (a developed form of Buckingham Π –Theorem) will be expressed in the following flowchart Figure 2-1.

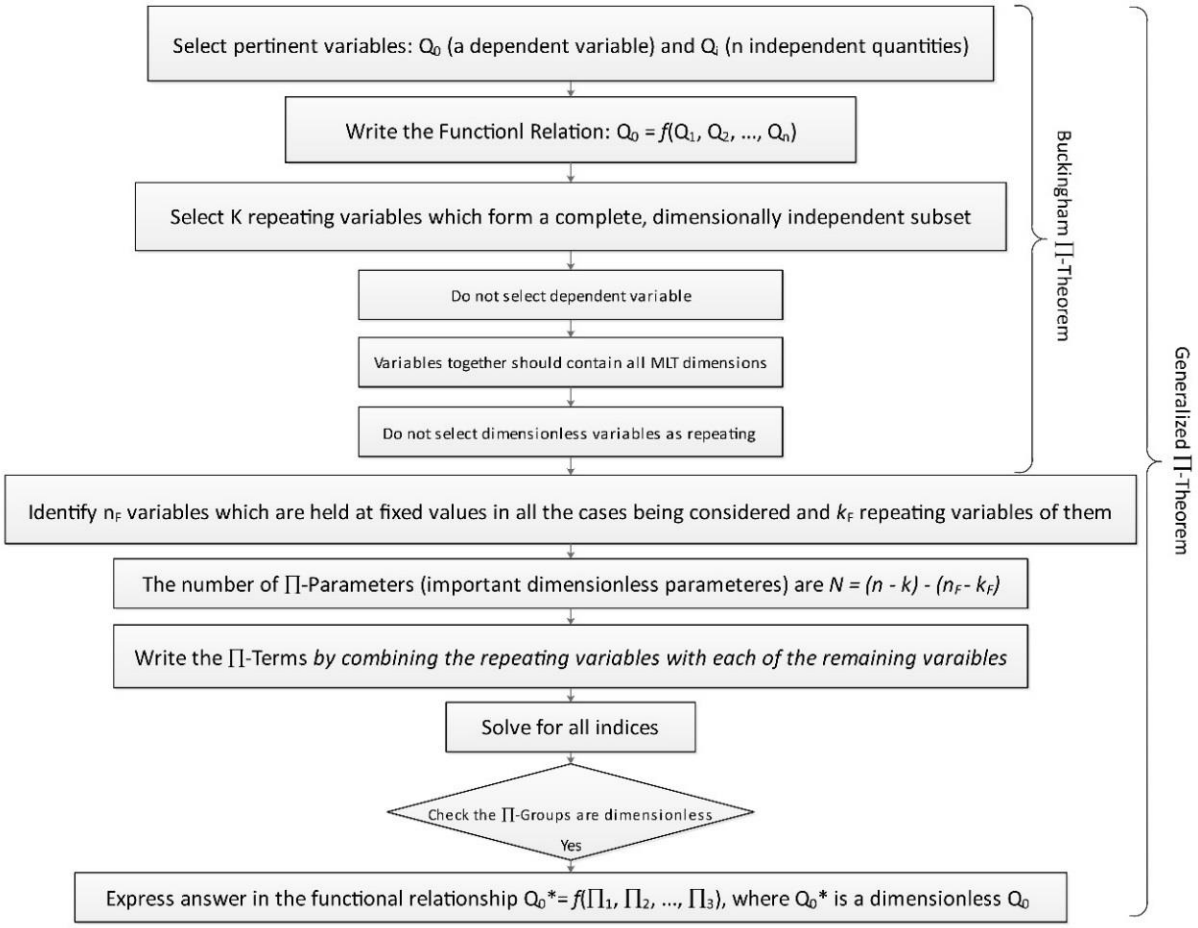

Fig. 2-1. Procedure of the Generalized Π-Theorem
(Each repeating variable must be dimensionally independent of the others, i.e. they should not be allowed to combine to form any dimensionless product.)

Based on the test rig available the configuration of the spray cooling system is schematically depicted in Figure 2-2. Measurements of the system in Figure 2-2 can be obtained either with, or without, mechanically-induced vibration. Figure 2-2 shows a test piece located in a chamber, attached to a mechanical shaker by a shaft. The test-piece and nozzle, inside the chamber, can be shaken simultaneously at different amplitudes and frequencies. A National Instrument data acquisition system

(DAQ), (precision instruments) can be used to collect data corresponding to different system states. For static measurements during nucleate boiling (as summarised in Table 1-1), heat flux as a dependent variable can be fully determined from the fluid properties, geometry, forcing, and spray specifications as provided in the functional relationship as follows:

$$q_{static} = \varphi(\rho_l, \rho_v, h_{fg}, \mu_l, C_l, \sigma, T_c, T_w, P_n, P_{ch}, \Delta T_c, \Delta T_{sat}, \Delta T_{sub}, P_{at}, u_d \text{ or } u_m, \dot{m}, d_{32}, H) \quad (2\text{-}1)$$

where in Equation (2-1), the variables $\dot{m}$ and d_{32} can be replaced by v, or d_{05} respectively. All quantities are described in Table 2-1, which accounts for both SI and MLT systems. It should be noted that all key parameters in equation (2-1) are used in different empirical correlations of spray cooling. These are available in Table 1-1 and were discussed in Chapter 1 and also [23].

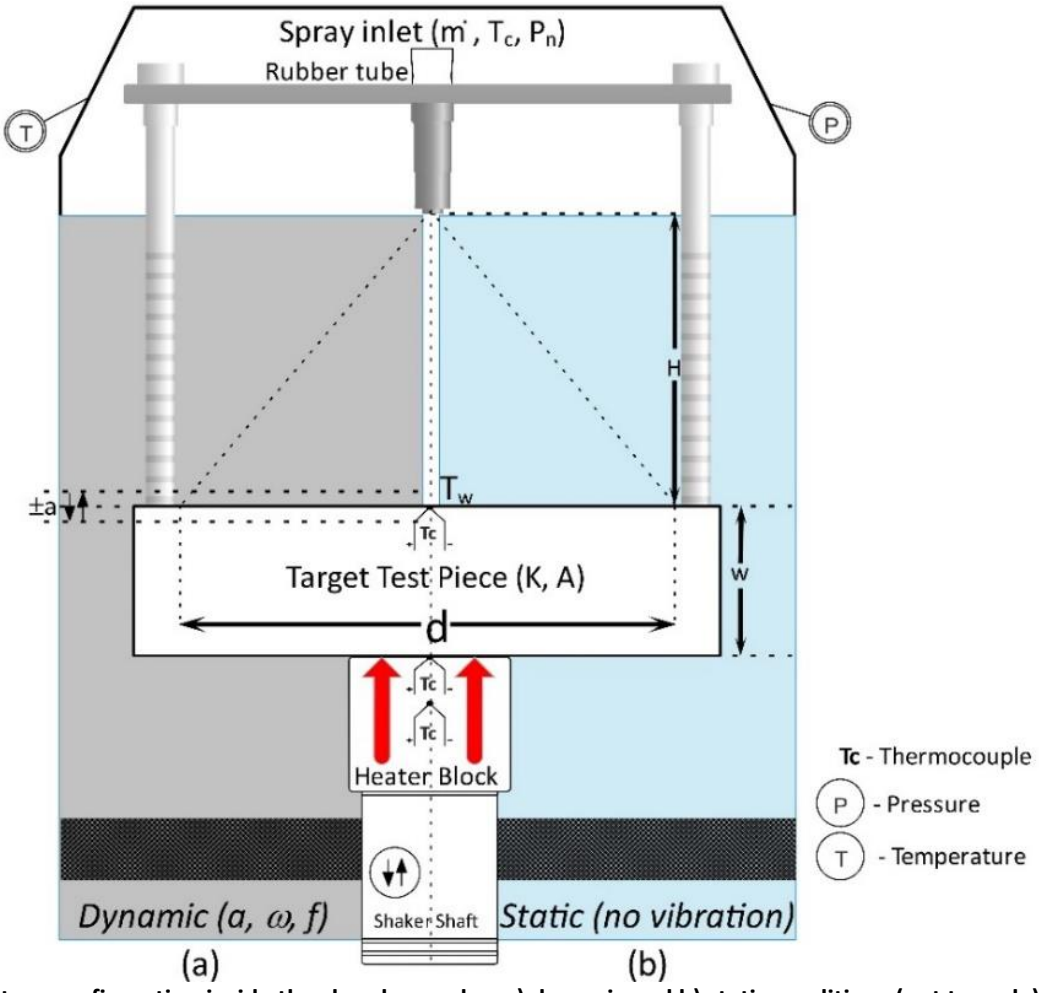

Fig. 2-2. Spray system configuration inside the chamber under: a) dynamic and b) static conditions (not to scale)

Surface roughness also affects the heat transfer coefficient. It is known that a high value of heat transfer coefficient occurs with very smooth and rough surfaces, but a lower value for surface finish that is representative of a typical machining process [23].

For prediction of critical heat flux q_{CHF} (as it was concluded from Table 1-6), it is not appropriate to consider hot metal or wall temperature T_w as an independent variable since the critical heat flux only occurs at a certain wall temperature. Thus, the functional form (2-1) can be reduced as follows:

$$q_{Statci-CHF} = \varphi(\rho_l, \rho_v, h_{fg}, \mu_l, C_l, \sigma, T_c, P_n, P_{ch}, \Delta T_{sub}, P_{at}, u_d \text{ or } u_m, \dot{m} \text{ or } v \text{ or } \bar{\vec{v}}, d_{32} \text{ or } d_{05}, H) \quad (2\text{-}2)$$

where the dimensions and description of different parameters are given in Table 2-1. In the next sections, the functional forms, obtained from the dimensional analysis for both nucleate boiling and Critical Heat Flux (CHF), are explained.

Table 2-1. Parameters with dimensions in SI and MLT systems.

		Dimensions	
Quantity	Symbol	SI	MLT
q	Heat Flux	kW/m^2	MT^{-3}
ρ	Density	kg/m^3	ML^{-3}
h_{fg}	Latent heat	kJ/kg	L^{2}T^{-2}
μ	Dynamic viscosity	Kg/m s	ML^{-1}T^{-1}
C_l	Specific heat	kJ/kg k	L^{2}T^{-2}θ^{-1}
σ	Surface tension	N/m	MT^{-2}
T	Coolant temperature	K	θ
P	Pressure	kPa	ML^{-1}T^{-2}
ΔT_{sub}	Subcooling degree	K	θ
u	velocity (u_d and $u_m^2 = \frac{2\Delta P}{\rho}$ based on [70])	m/s	LT^{-1}
$\dot{m}$	Mass flow rate	kg/s	MT^{-1}
v	Volumetric flow rate	m^3/s	L^3 T^{-1}
$\bar{\vec{v}}$	Average volumetric spray flux	m^{3}s^{-1}/m^2	LT^{-1}
d_{32}	Sauter mean diameter (correlated in [49])	m	L
d_{05}	mass or volume median diameter (correlated in [48])	m	L
d_H	Hydraulic diameter of the heating surface	m	L
H	Nozzle to surface distance	m	L
a	Amplitude	m	L
ω	Angular frequency	1/s	T^{-1}
g	Acceleration of gravity	m/s^2	LT^{-2}

[1]subscrpits v and l are respectively vapour and liquid phases.
[2]subscripts n, ch, and at represent nozzle, chamber, and atmosphere, respectively.
[3]subscripts d and m are respectively droplet and mean droplet breakup velocities

2.2. Nucleate Boiling functional forms for static and dynamic tests

As discussed in Chapter 1, there are currently no published studies which have used dimensional analysis for dynamic measurements (i.e. in the presence of vibration). Therefore, no correlation has yet been developed to predict the heat flux in nucleate boiling under dynamic conditions. There is a published numerical investigation on two-phase flow spray characteristics including vibration using the *Volume of Fluid* (VOF) method [59] to study single and multiple droplets. But to develop a dynamic relation (for the first time), fundamental fluid dynamics suggests that heat flux should at least include those independent parameters appropriate for static conditions. It should also use vibration amplitude a, and vibration frequency $\omega = 2\pi f$. Therefore, the proposed functional form for nucleate boiling is as follows:

$$q = \varphi(\rho_l, \rho_v, h_{fg}, \mu_l, C_l, \sigma, T_c, T_w, P_n, P_{ch}, \Delta T_{sat}, \Delta T_{sub}, P_{at}, u_d \text{ or } u_m, \dot{m}, d_{32}, H, a, \omega, g, d_H) \quad (2\text{-}3)$$

where also in Equation (2-3) the variables $\dot{m}$ and d_{32} can be replaced by v, or d_{05} respectively. The dimensions, and a description of different parameters, are given in the Table 2-1.

After defining independent variables (i.e. key parameters), Dimensional Analysis can now proceed. To determine the number of Π-terms in the procedure in Figure 2-1, invariant parameters in different case studies (e.g. Chamber Pressure) need to be identified. This is possible from the planned experimental measurement programme. For example, when experiments are only undertaken at atmospheric pressure. Following Dimensional Analysis, the dimensionless Π-parameters can be omitted (i.e. those which entirely comprise invariant quantities with fixed values). This results in further simplification as shown by the derived functional forms given in Table 2-2 for nucleate boiling, which corresponds to different spray evaporative cooling conditions for both dynamic and static conditions.

Table 2-2. Functional forms of spray cooling heat flux in the nucleate boiling regime

Environment	Invariant Parameter	Number of Π-terms	Measure--ments needed	Functional form
Static (No vibration)	None	5	Spray spec.[3]	$\frac{qH}{\mu_l h_{fg}} = f\left(\frac{C_l \Delta T}{h_{fg}}, \frac{\rho_l (u_m^2 or \bar{\vec{v}}^2) d_{32}}{\sigma}, \frac{\Delta T_{sat}}{\Delta T_{sub}}, \frac{P_{ch}}{P_{at}}, \frac{\rho_l}{\rho_v}\right)$
			flow rate	$\frac{qH}{\mu_l h_{fg}} = f\left(\frac{C_l \Delta T}{h_{fg}}, \frac{\rho_l \sigma \dot{m}}{{\mu_l}^3} or \frac{{\rho_l}^2 \sigma v}{{\mu_l}^3}, \frac{\Delta T_{sat}}{\Delta T_{sub}}, \frac{P_{ch}}{P_{at}}, \frac{\rho_l}{\rho_v}\right)$
	P_{ch}[1]	3	Spray spec.	$\frac{qH}{\mu_l h_{fg}} = f\left(\frac{C_l \Delta T}{h_{fg}}, \frac{\rho_l (u_m^2 or \bar{\vec{v}}^2) d_{32}}{\sigma}, \frac{\Delta T_{sat}}{\Delta T_{sub}}\right)$
			flow rate	$\frac{qH}{\mu_l h_{fg}} = f\left(\frac{C_l \Delta T}{h_{fg}}, \frac{\rho_l \sigma \dot{m}}{{\mu_l}^3} or \frac{{\rho_l}^2 \sigma v}{{\mu_l}^3}, \frac{\Delta T_{sat}}{\Delta T_{sub}}\right)$
	P_{ch}, ΔT_{sub}[2]	2	Spray spec.	$\frac{qH}{\mu_l h_{fg}} = f\left(\frac{C_l \Delta T}{h_{fg}}, \frac{\rho_l (u_m^2 or \bar{\vec{v}}^2) d_{32}}{\sigma}\right)$
			flow rate	$\frac{qH}{\mu_l h_{fg}} = f\left(\frac{C_l \Delta T}{h_{fg}}, \frac{\rho_l \sigma \dot{m}}{{\mu_l}^3} or \frac{{\rho_l}^2 \sigma v}{{\mu_l}^3}\right)$
Dynamic	None	8	Spray spec.	$\frac{qH}{\mu_l h_{fg}} = f\left(\frac{C_l \Delta T}{h_{fg}}, \frac{\rho_l (u_m^2 or \bar{\vec{v}}^2) d_{32}}{\sigma}, \frac{\Delta T_{sat}}{\Delta T_{sub}}, \frac{P_{ch}}{P_{at}}, \frac{\rho_l}{\rho_v}, \frac{a}{H}, \frac{\omega^2 a}{g}, \frac{\omega a}{u_d}\right)$
			flow rate	$\frac{qH}{\mu_l h_{fg}} = f\left(\frac{C_l \Delta T}{h_{fg}}, \frac{\rho_l \sigma \dot{m}}{{\mu_l}^3}, \frac{\rho_l a \omega d_H}{\mu_l}, \frac{\Delta T_{sat}}{\Delta T_{sub}}, \frac{P_{ch}}{P_{at}}, \frac{\rho_l}{\rho_v}, \frac{a}{H}, \frac{\omega^2 a}{g}\right)$
	P_{ch}	6	Spray spec.	$\frac{qH}{\mu_l h_{fg}} = f\left(\frac{C_l \Delta T}{h_{fg}}, \frac{\rho_l (u_m^2 or \bar{\vec{v}}^2) d_{32}}{\sigma}, \frac{\Delta T_{sat}}{\Delta T_{sub}}, \frac{a}{H}, \frac{\omega^2 a}{g}, \frac{\omega a}{u_d}\right)$
			flow rate	$\frac{qH}{\mu_l h_{fg}} = f\left(\frac{C_l \Delta T}{h_{fg}}, \frac{\rho_l \sigma \dot{m}}{{\mu_l}^3} or \frac{{\rho_l}^2 \sigma v}{{\mu_l}^3}, \frac{\rho_l a \omega d_H}{\mu_l}, \frac{\Delta T_{sat}}{\Delta T_{sub}}, \frac{a}{H}, \frac{\omega^2 a}{g}\right)$
	P_{ch}, ΔT_{sub}	5	Spray spec.	$\frac{qH}{\mu_l h_{fg}} = f\left(\frac{C_l \Delta T}{h_{fg}}, \frac{\rho_l (u_m^2 or \bar{\vec{v}}^2) d_{32}}{\sigma}, \frac{a}{H}, \frac{\omega^2 a}{g}, \frac{\omega a}{u_d}\right)$
			flow rate	$\frac{qH}{\mu_l h_{fg}} = f\left(\frac{C_l \Delta T}{h_{fg}}, \frac{\rho_l \sigma \dot{m}}{{\mu_l}^3} or \frac{{\rho_l}^2 \sigma v}{{\mu_l}^3}, \frac{\rho_l a \omega d_H}{\mu_l}, \frac{a}{H}, \frac{\omega^2 a}{g}\right)$

[1]Constant pressure, [2]Constant pressure and degree of subcooling, [3]Spray specifications

Based on the test rig capability, three different experimental measurement test plans are considered in static and dynamic conditions. The first measurement plan uses variable pressure, and the degree of subcooling (i.e. '*None'* invariant parameter in Table 2-2). The second plan uses constant pressure (with invariant P_{ch} in the second column of Table 2-2). The third plan uses constant pressure and the degree of subcooling (P_{ch}, ΔT_{sub}). To undertake experiments with constant pressure (i.e. above atmospheric only) the test rig is equipped with a control valve, which can be adjusted manually if required. In order

to control the degree of subcooling ($\Delta T_{sub} = T_{sat} - T_c$), the saturation temperature T_{sat} can be held constant by the same control valve which keeps the chamber pressure constant. This is a result of thermal equilibrium in two-phase flow. (At this stage (PID) controller for example can be used to set the inlet temperature T_c to a constant value). The third column of Table 2-2, shows that the number of Π-terms are reduced for the functional forms obtained, from '*None'* invariant parameters to those for fixed P_{ch} and ΔT_{sub}, a result of applying the Generalized Π–Theorem.

Dimensionless functional forms can also be derived by exploiting modelling requirements and expectations; designated in Table 2-2: '*spray specifications'* and '*flow rate'* (i.e. the fourth column of Table 2-2). For example if it is for a design purpose in which spray specifications are important, or a special control approach that the pumping flow rate (either $\dot{m}$ or v) plays an important role on the wall temperature control, different dimensionless Π–terms can be obtained as shown in the last column of Table 2-2. In other words, these Π–terms can simplify measurement requirements, such as *'spray specifications'*, which are usually costly and time consuming to obtain. They also make system identification easier.

Table 2-2 also shows three dimensionless numbers which are well known in fluid mechanics. These are the Boiling Number ($Bo = qH/\mu_l h_{fg}$), the Jakob Number ($Ja = C_l \Delta T/h_{fg}$), and the Weber Number $We = \rho_l(u_m^2 or \bar{\vec{v}}^2)d_{32}/\sigma$. In the functional forms corresponding to '*flow rate*' measurements, another Π–term is substituted for Weber Number. This Π–term is: '$\rho_l \sigma \dot{m}/{\mu_l}^3$ or ${\rho_l}^2 \sigma v/{\mu_l}^3$', which contains mass ($\dot{m}$) or volumetric flow rate (v) instead of spray specifications of 'u_m *or* $\bar{\vec{v}}$' and 'd_{32}' in the Weber Number. What is revealing about the functional forms associated with the dynamic condition, is that a Vibrational Reynolds Number $Re_V = \rho_l a \omega d_H/\mu_l$ is obtained. In fact, Vibrational Reynolds Number is an indication of the turbulence resulting from the vibrating surface [57]. It is a metric to help understand how vibration through augmented turbulence can affect heat transfer. Hypothetically, heat transfer

enhancement or deterioration, as a consequence of vibration can be explained by increased flow turbulence, a thinned or thickened boundary layer, more or less generated nucleate boiling sites [58], and a change to the wetting-angle [59]. In addition, there is a dimensionless Acceleration Number, $\omega^2 a/g$ in the dynamic functional forms. The dimensionless Acceleration Number is helpful in considering any possible impact of experimentally-measured acceleration (obtained using an accelerometer). The published literature shows that the impact of acceleration on spray cooling heat transfer has been empirically investigated in the following dynamic conditions: An acceleration test bench with a rotating arm [60], a reduced gravity condition [61], and on an aircraft doing parabolic flights [62, 63]. There are however inconsistencies in the conclusions obtained, owing to the complexity of spray heat transfer mechanisms and differences in experimental conditions. Thus, acceleration stemming from the vibration is important in the understanding of spray cooling for all dynamic conditions for both automotive and aerospace vehicle applications.

2.3. Functional forms of Critical Heat Flux (CHF) for static and dynamic tests

For the vibrating surfaces and dynamic-CHF, there are no published studies in the literature which have used dimensional analysis. Therefore there is no developed correlation available to predict the critical heat flux (See Table 1-6). To develop a relationship for the first time, fluid dynamics suggests that the heat flux should be determined not only based on the independent parameters already mentioned for static conditions but also with vibration amplitude (a) and angular frequency ($\omega = 2\pi f$). The proposed functional form is therefore as follows:

$$q_{CHF} = \varphi(\rho_l, \rho_v, h_{fg}, \mu_l, C_l, \sigma, T_c, P_n, P_{ch}, \Delta T_{sub}, P_{at}, u_d \text{ or } u_m, \dot{m} \text{ or } v \text{ or } \bar{\vec{v}}, d_{32} \text{ or } d_{05}, d_H, H, a, \omega, g) \quad (2\text{-}4)$$

where d_H and g are respectively hydraulic diameter of the heating surface and gravitational acceleration. After defining independent variables (key parameters) by performing dimensional

analysis, using the generalized Π-Theorem, invariant parameters for different case studies can be identified. Invariant parameters (e.g., Chamber Pressure) can be identified from the test plan. Again, when the experimental measurements are only undertaken at atmospheric pressure, then those dimensionless Π-parameters that comprise entirely invariant quantities (i.e. with fixed values) can be neglected resulting in simplification. All the derived functional forms corresponding to the different test conditions for both static and dynamic conditions are given in Table 2-3:

Table 2-3. Dimensional analysis for CHF prediction.

Surface condition	Invariant Parameter	Number of Π-terms	Measurements needed	Functional form
Static (No vibration)	None	4	Spray spec.[3]	$\frac{qH}{\mu_l h_{fg}} = f\left(\frac{C_l \Delta T_{sub}}{h_{fg}}, \frac{\rho_l (u_m^2 or \bar{\vec{v}}^2) d_{32}}{\sigma}, \frac{P_{ch}}{P_{at}}, \frac{\rho_l}{\rho_v}\right)$
			Flow rate	$\frac{qH}{\mu_l h_{fg}} = f\left(\frac{C_l \Delta T_{sub}}{h_{fg}}, \frac{\rho_l \sigma \dot{m}}{{\mu_l}^3} or \frac{{\rho_l}^2 \sigma v}{{\mu_l}^3}, \frac{P_{ch}}{P_{at}}, \frac{\rho_l}{\rho_v}\right)$
	P_{ch}	2	Spray spec.	$\frac{qH}{\mu_l h_{fg}} = f\left(\frac{C_l \Delta T_{sub}}{h_{fg}}, \frac{\rho_l (u_m^2 or \bar{\vec{v}}^2) d_{32}}{\sigma}\right)$
			Flow rate	$\frac{qH}{\mu_l h_{fg}} = f\left(\frac{C_l \Delta T_{sub}}{h_{fg}}, \frac{\rho_l \sigma \dot{m}}{{\mu_l}^3} or \frac{{\rho_l}^2 \sigma v}{{\mu_l}^3}\right)$
	$P_{ch}, \Delta T_{sub}$	1	Spray spec.	$\frac{qH}{\mu_l h_{fg}} = f\left(\frac{\rho_l (u_m^2 or \bar{\vec{v}}^2) d_{32}}{\sigma}\right)$
			Flow rate	$\frac{qH}{\mu_l h_{fg}} = f\left(\frac{\rho_l \sigma \dot{m}}{{\mu_l}^3} or \frac{{\rho_l}^2 \sigma v}{{\mu_l}^3}\right)$
Dynamic (Vibration)	None	7	Spray spec.	$\frac{qH}{\mu_l h_{fg}} = f\left(\frac{C_l \Delta T_{sub}}{h_{fg}}, \frac{\rho_l (u_m^2 or \bar{\vec{v}}^2) d_{32}}{\sigma}, \frac{P_{ch}}{P_{at}}, \frac{\rho_l}{\rho_v}, \frac{a}{H}, \frac{\omega^2 a}{g}, \frac{\omega a}{u_d}\right)$
			Flow rate	$\frac{qH}{\mu_l h_{fg}} = f\left(\frac{C_l \Delta T_{sub}}{h_{fg}}, \frac{\rho_l \sigma \dot{m}}{{\mu_l}^3} or \frac{{\rho_l}^2 \sigma v}{{\mu_l}^3}, \frac{\rho_l a \omega d_H}{\mu_l}, \frac{P_{ch}}{P_{at}}, \frac{\rho_l}{\rho_v}, \frac{a}{H}, \frac{\omega^2 a}{g}\right)$
	P_{ch}	5	Spray spec.	$\frac{qH}{\mu_l h_{fg}} = f\left(\frac{C_l \Delta T_{sub}}{h_{fg}}, \frac{\rho_l (u_m^2 or \bar{\vec{v}}^2) d_{32}}{\sigma}, \frac{a}{H}, \frac{\omega^2 a}{g}, \frac{\omega a}{u_d}\right)$
			Flow rate	$\frac{qH}{\mu_l h_{fg}} = f\left(\frac{C_l \Delta T_{sub}}{h_{fg}}, \frac{\rho_l \sigma \dot{m}}{{\mu_l}^3} or \frac{{\rho_l}^2 \sigma v}{{\mu_l}^3}, \frac{\rho_l a \omega d_H}{\mu_l}, \frac{a}{H}, \frac{\omega^2 a}{g}\right)$
	$P_{ch}, \Delta T_{sub}$	4	Spray spec.	$\frac{qH}{\mu_l h_{fg}} = f\left(\frac{\rho_l (u_m^2 or \bar{\vec{v}}^2) d_{32}}{\sigma}, \frac{a}{H}, \frac{\omega^2 a}{g}, \frac{\omega a}{u_d}\right)$
			Flow rate	$\frac{qH}{\mu_l h_{fg}} = f\left(\frac{\rho_l \sigma \dot{m}}{{\mu_l}^3} or \frac{{\rho_l}^2 \sigma v}{{\mu_l}^3}, \frac{\rho_l a \omega d_H}{\mu_l}, \frac{a}{H}, \frac{\omega^2 a}{g}\right)$
[1]Chamber pressure is constant, [2]Chamber pressure and degrees of subcooling are constant, [3]Spray specifications				

Based on invariant parameters, three different test conditions are considered either for static or dynamic cases. First, with variable pressure and degree of subcooling (Indicated as '*None*' under the invariant parameter list in column 2 of Table 2-3), second, under constant pressure (with invariant P_{ch} in column 2 of Table 2-3), and third, constant pressure and degrees of subcooling (P_{ch}, ΔT_{sub}). For present study, the functional forms with invariant P_{ch} are used. As shown, the third column of tables

2-2 and 2-3, the number of Π-terms is reduced for the functional forms obtained from '*None'* invariant parameters, to those for fixed P_{ch} and ΔT_{sub} as a result of using the Generalized Π–Theorem.

As was discussed for nucleate boiling in section 2.2, dimensionless functional forms can be derived based on modelling requirements and expectations; here '*spray specifications'* and '*flow rate'* appear in column 4 of Table 2-3. If, for a design purpose in which spray specifications are important, or special control of pumping flow rate plays an important role on the wall temperature, different dimensionless Π –terms can be obtained (see for example the last column of Table 2-3). In Table 2-3, three dimensionless groups: of the Boiling Number ($Bo = \frac{qH}{\mu_l h_{fg}}$), the Jakob Number ($Ja = \frac{C_l \Delta T_{sub}}{h_{fg}}$), and the Weber Number ($We = \frac{\rho_l (u_m^2 or \bar{v}^2) d_{32}}{\sigma}$) are also identifiable. Owing to the high dependency of CHF to subcooling, $\Delta T_{sub} = T_{sat} - T_c$ is considered for Jakob number. In the functional forms corresponding to '*flow rate*' measurements, $\frac{\rho_l \sigma \dot{m}}{{\mu_l}^3}$ is substituted for Weber number, which has spray specifications of $u_m \; or \; \bar{v}$ and d_{32}. For functional forms with invariant parameters of P_{ch} and ΔT_{sub}, the Jakob Number $Ja = \frac{C_l \Delta T_{sub}}{h_{fg}}$ stays invariant too and therefore, according to the Generalized Π–Theorem, is eliminated.

For dynamic conditions, vibrational Reynolds Number $Re_V = \frac{\rho_l a \omega d_H}{\mu_l}$, and dimensionless Acceleration Number $Ac = \frac{\omega^2 a}{g}$ have been derived.

2.4. The Conclusions of Chapter 2.

New empirical correlation models are constructed to characterise heat transfer associated with spray evaporative cooling of vibrating surfaces - a process involving complex two-phase physics well beyond current numerical simulation capabilities. The proposed correlation models, which account for dynamic, rather than just static surface conditions (as in existing models), are constructed using dimensional analysis involving the Generalized Buckingham Π-Theorem. Two nondimensional

parameters are introduced in the form of Acceleration Number and Vibrational Reynolds Number to account for dynamic effects resulting in models which accommodate the combined effects of vibration amplitude and frequency. Appropriate static and dynamic correlation models can be chosen based on three different experimental measurement test plans involving static and dynamic conditions. The first plan uses variable pressure and the degree of subcooling. The second plan uses constant pressure. The third test plan uses constant pressure and the degree of subcooling. These test plans are used to design a suitable experimental measurement programme which is explained in the next chapter.

3. EXPERIMENTAL TEST FACILITIES AND DESIGN OF EXPERIMENTAL MEASUREMENT PROGRAMME

In this section, the experimental measurement facilities and the design of the experimental test programme is thoroughly explained. First, information regarding the measurement facilities are provided. This includes the spray rig associated with a pipework, a data acquisition system (DAQ), its associated control unit, and two test-pieces that are used in subsequent sections. Cooling loop components are described in the subsection describing spray rig pipework along with the main components of the DAQ and the sensor-based control unit system. Test-piece assemblies are then described with information on the location of the nozzles, heaters, and sensors. The final section discusses the test rig capabilities, the test procedures and data reduction, uncertainty analysis and reproducibility.

3.1. Experimental measurement facilities

Figure 3-1 schematically shows the major components of the test unit, the DAQ and the control unit. These are explained in the following sections.

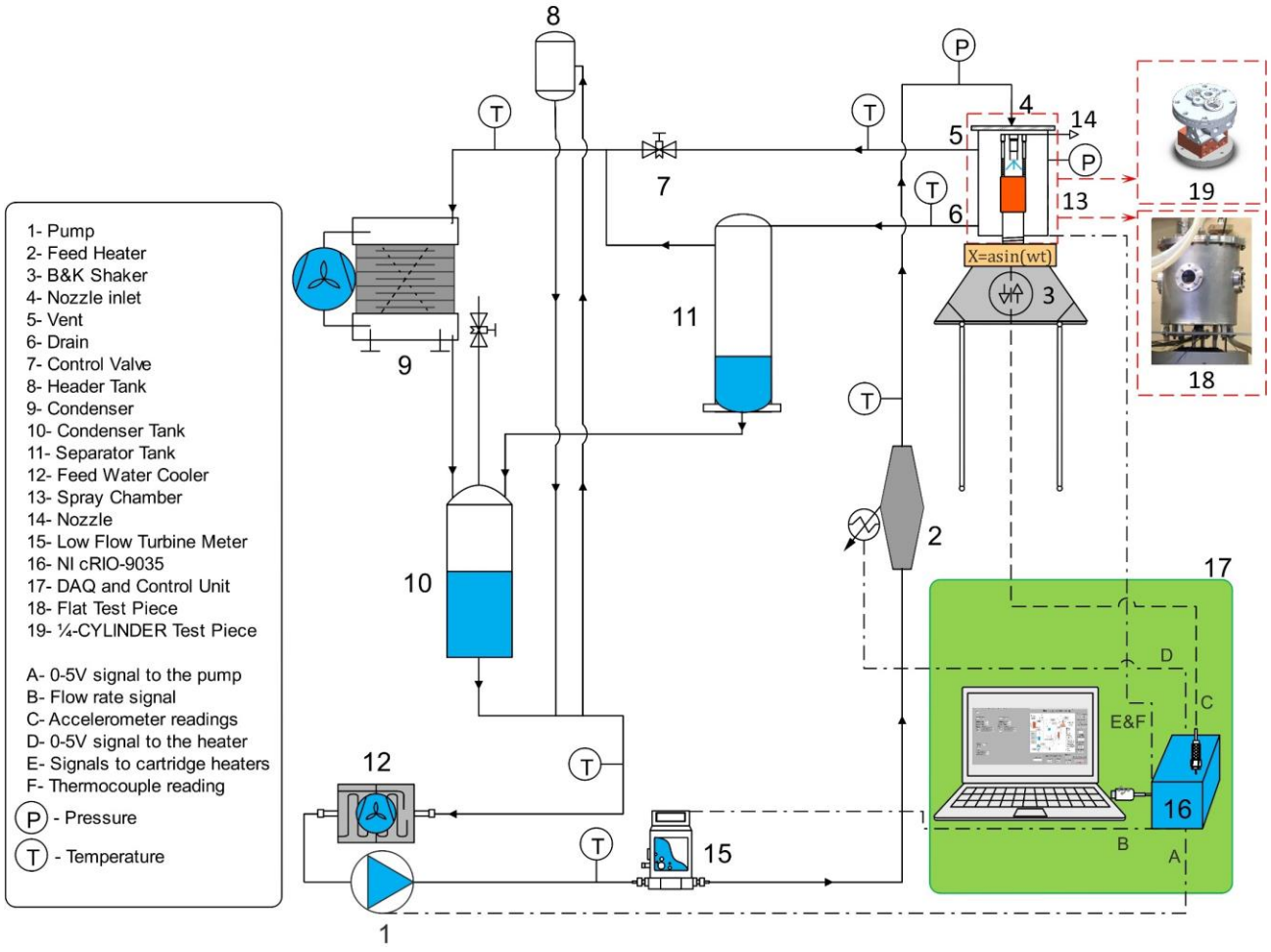

Fig. 3-1. Schematic view of the test rig with test pieces and DAQ and control unit system

Spray rig pipework

The cooling loop contains the following components: a system of pipework (1/8 to 1/2 inch stainless steel pipes and compression fittings), a condenser (Denso RDP 583), a heater module (Two 345 W band-heaters), a miniature heat exchanger, a pump (Micropumps MGD100P), K and T-Type thermocouples, two digital pressure transducers (Omega PXM309), a low-flow turbine meter (Omega FLR1009ST-D), and condenser and separator tanks. Starting from the pump (see Figure 3-1, number 1), this circulates the de-Ionized water within the piping system. The flow meter (number 15) reads the real-time flow rate measurements. The Feed Heater (2) heats the water supplied to the nozzle inlet (4) just before the

test unit. The flexible pipework that carries water to and from the test piece is made from silicone rubber. Vent (5) and drain (6) respectively route the evaporated and accumulated droplets in the test chamber (13) into the condenser (9) and the separator tank (11). Water (from the condenser and the tank) then flows down through the pipes into the condenser tank. A header tank (8) is fitted at the highest point in the circuit to remove air and provide a positive feed. To complete a cooling cycle, the feed water cooler (12) cools the condensate to below the maximum operating temperature of the pump (100 ˚C).

The Data acquisition (DAQ) and the control unit

The main components of the Data acquisition system provided by National Instruments are listed in Table 3-1. As shown in Figure 3-1, an NI cRIO-9035 (the main processor, number 16) is connected through its modules to the pump (A), the flow meter (B), an accelerometer (C), the pre-Heater (D), the cartridge heaters (E), the test-piece thermocouples (F) and a host computer via ethernet. In the host computer, an FPGA and the LabVIEW software are configured for DAQ and control purposes, and with a human-machine interface unit. The pump flow rate (in the Micropumps MGD100P controller), the cartridge heaters (Watlow 250W), and the band heaters, are operated using 0 to 5 V control signals. These control signals come from an NI9264 module in the CRIO-9035 National Instrument. The flow meter and pressure transducers signals are collected by NI 9205. There is a power supply to the pressure transducers, the flow meter, and the pump. The pre-heater has a PID temperature controller to account for the thermal inertia of the coolant feed. Therefore, the system is kept stable by the PID controller in staying within the evaporative phase even during rapid changes in pump speed (note that doubling the flow rate will only cause a temperature difference of ±5 ˚C). Two (EVR-25BF) power regulators are used to obtain the 0 to 5 V signals (from the NI 9264) and convert them to the required

power for the band and the cartridge heaters. Thus, for different control scenarios the test-piece receives constant and variable heat loads from the cartridge heater.

Table 3-1. Data Acquisition System.

Module	Description	Absolute accuracy
NI cRIO-9035	Main processor, Control algorithm	-
NI 9205	Analog inputs – 16 Bit – 32 Channels (Differential and Single-Ended)	4.9 mV
NI 9212	Thermocouple module – 24 Bit – 8 Channels	-
NI 9230	AI 24 Bit – 3 Channels	-
NI 9264	AO 16 Bit – 16 Channels	17 mV
NI 9472	DO 24 V – 8 Channels	-

The current configuration of the DAQ and control unit provides a high level of precision and flexibility - which is quantifiable by following NI procedures (for which the system accuracy relative to the input, is quantified to be 0.177%, with example results shown in Table 3-1). In addition, the control unit hosts the desired control algorithms. Temperature measurements from the thermocouples (located 1 mm under the coolant surfaces in either test-piece) are used as a state variable for the PID controller in the FPGA CRIO-9035 hardware to control the pump voltage. The amplitude and frequency of the shaker is controlled using a Feedback Instruments FG600 signal generator with a pure sine wave option. A Piezotronics PCB A 353B15 accelerometer (10.27 mV/g, 1 Hz - 10 kHz) is attached (for the flat-test-piece measurements), to the bottom of the drive shaft which is bolted to the shaker head. Whereas, for the ¼-cylinder test piece, the accelerometer is located on top of its test chamber. The corresponding acceleration signals are measured by the NI 9230 sound and vibration input module. A spectral analysis of vibration at the surface was done by LabVIEW (front panel and block diagram screenshots are available in Appendix 1). The signal from the accelerometer was then transformed from the time domain to the frequency domain using FFT (Fast Fourier Transform, available as a built-in function in LabVIEW). This enables surface temperature control of an actual spray evaporative cooling system in the presence of vibration to be obtained during experimentation.

Flat-surface and ¼-CYLINDER test pieces.

The test unit is positioned on top of a mechanical shaker (Bruel & Kjaer V555) and hosts two different test pieces: a flat-surface circular test-piece, and a ¼- cylinder test-piece. The flat-surface test piece (Figure 3-2) is to investigate nucleate boiling and CHF heat transfer characteristics as well as the capability of surface temperature control considering heat flux requirements without and with mechanical vibration.

Figure 3-2 shows the flat test-piece arrangement located in a cylindrical chamber, attached by a shaft to the mechanical shaker. The test-piece and nozzle inside the chamber (fixed together with two long bolts) can be simultaneously shaken at different amplitudes and frequencies. The test piece is heated by six cylindrical Watlow 250W cartridge heaters that are located vertically in designated cylindrical holes inside a copper heater block. This is designed to provide strongly one-dimensional heat conduction to the test piece. The test piece is made of copper with a smooth surface, and has a diameter of 20 mm, and a thermal conductivity of 385 Wm/K. Three T-Type thermocouples are used, the first of which is located 1 mm under the coolant surface of the test chamber, followed by two more thermocouples evenly located 5.5 mm below each other. This is to facilitate heat flux measurement capabilities. A shroud is also placed around the test piece disc to guide the liquid film to the bottom of the chamber for drainage. Spray nozzles can be located on top of the test chamber (via the nozzle fitting). All the joints and bolts are sealed with a copper paste which is intermittently able to stand a maximum temperature of 350˚C.

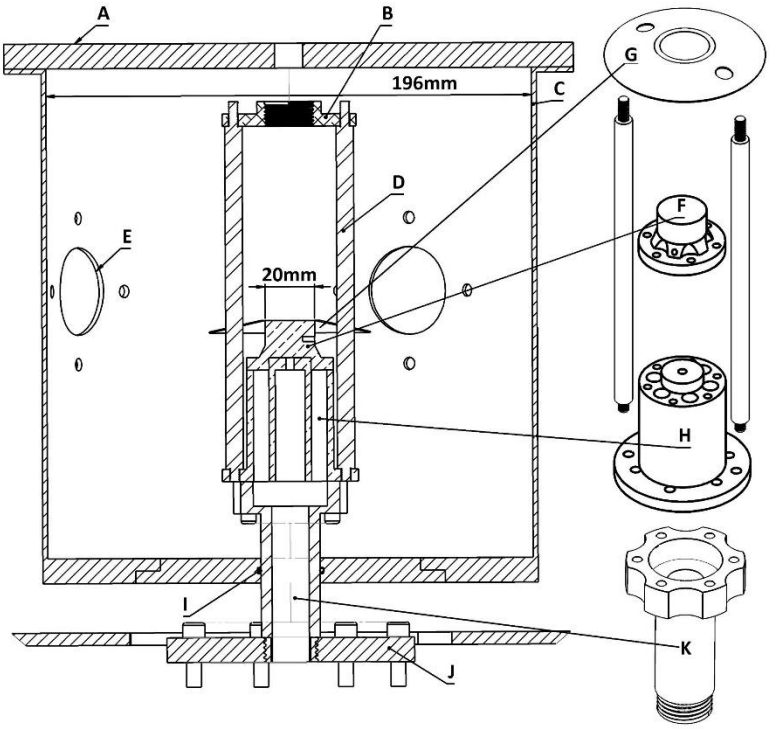

A- Chamber Lid	E- Window	I- O-ring
B- Nozzle Fitting	F- Flat Test Piece	J- Shaker Plate
C- Chamber	G- Shroud	K- Shaker Shaft
D- Bolt	H- Heater Block	

Fig. 3-2. Spray chamber cross-section view and exploded view of copper test piece and heater block

A ¼-cylinder test-piece is shown in Figure 3-3. This test-piece is intended to represent the thermal performance and management problem of an automotive component in a more realistic way (i.e. cooling on a three-dimensional surface). Therefore, the ¼-cylinder test-piece is designed to be part of a prototype cooling system for a highly-boosted IC engine. The ¼-cylinder test-piece has four times the projected cooling surface area of the flat test-piece. As shown in Figure 3-3a, the ¼-cylinder test-piece comprises a test chamber, a heater block and an insulated base. The test chamber is heated by eight Watlow 250W cartridge heaters. Six of these are located in the copper heater block underneath the test piece. The remaining two heaters are positioned at the top of the test chamber and located inside the castings to emulate an injector and valve guide bosses. A single Type K thermocouple is located 1

mm under the coolant surface of the test chamber. Attaching the heater block to the test-piece, is a dovetail joint between heater block and test piece (see Figure 3-3b). This is assembled with a predetermined cold clearance, but differential thermal expansion eliminates this clearance. At the operating point there is good thermal contact between the heater block and the test-piece. A finite element-based thermal-stress analysis was undertaken during the design process [143] to establish the suitability of attaching the heater block to the test-piece. It was found that a 0.05 mm clearance between the mating surfaces of the dovetail was required. Two Bete PJ8 atomising misting nozzles are located on the top of the test chamber.

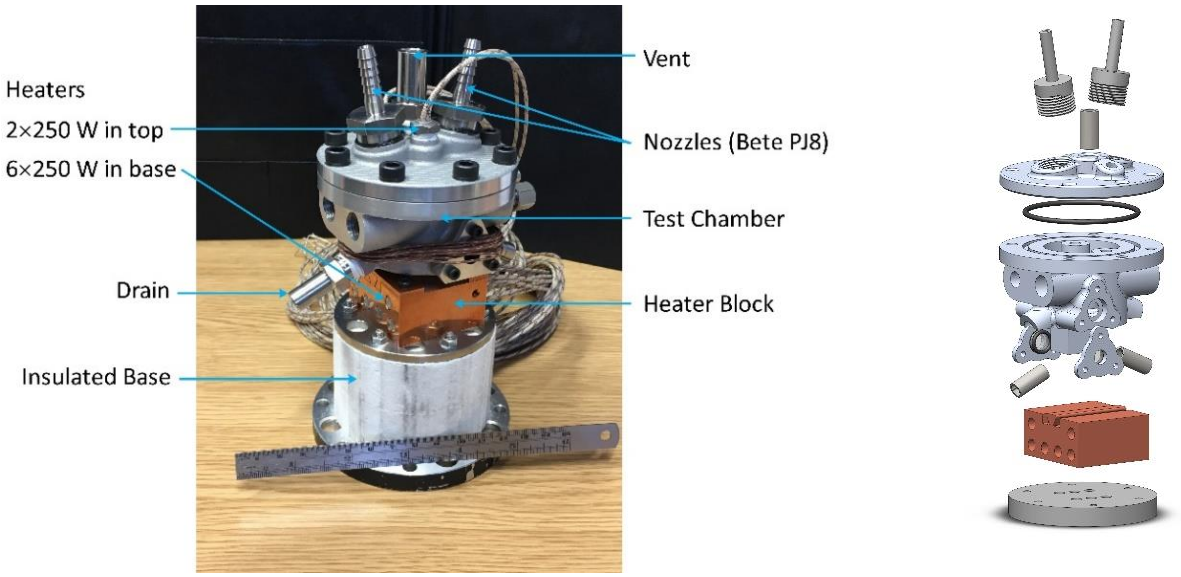

(a) (b)

Fig. 3-3. The ¼-CYLINDER test piece: (a) photo of manufactured assembly, (b) Exploded view of assembly (based on [144])

3.2. Experimental test procedures and data reduction

Based on the dimensional analysis and similitude, and the objectives of the study, three experimental measurement test plans were designed. The first two sets of experimental measurements were to study the heat transfer characteristics of spray evaporative cooling of vibrating surfaces in the nucleate boiling regime, and at CHF. The third set of experimental measurements were designed to address thermal management of the flat test-piece hardware in the form of temperature control. Following these three sets of test procedures, the measurements are themselves comprehensively explained in the following chapters. For the purpose of data collection at nucleate boiling and CHF, at the beginning of each test run (with or without vibration), the power was applied to the cartridge heaters to bring the cooling surface to a condition within the two-phase heat transfer mode. To make sure that the data collection was in the right spray cooling modes (as explained in chapter 1), different flow regimes of single-phase, incipient boiling, nucleate boiling, and transition boiling were observed and distinguished using two windows on the flat test piece spray chamber (see E in Figure 3-2). Figure 3-4 shows these regimes (photos only for PJ10 nozzle taken by a PROSILCA-GE allied-vision camera and with the required illumination). In the nucleate boiling, steady state was assumed when all temperature differences associated with all three thermocouples in time intervals of three minutes were less than 0.3 ℃ (as convergence criterion). Then, the power was gradually added until the CHF occurred.

As was explained in Chapter 2, the correlation models, were constructed using the Generalized Buckingham π-theorem [142]. To develop a functional form, key independent parameters (including surface roughness, subcooling degree, nozzle-to-surface distance etc.) identified for the static conditions in [23], were considered. However, the next step in using the Generalized Π-Theorem was to define invariant parameters relevant to the intended measurement test plan. In the current thesis, surface roughness, chamber pressure, the degree of subcooling (in the nucleate boiling regime), and

the nozzle-to-surface distance (at the CHF mode), are constant, and can therefore be treated as invariant parameters.

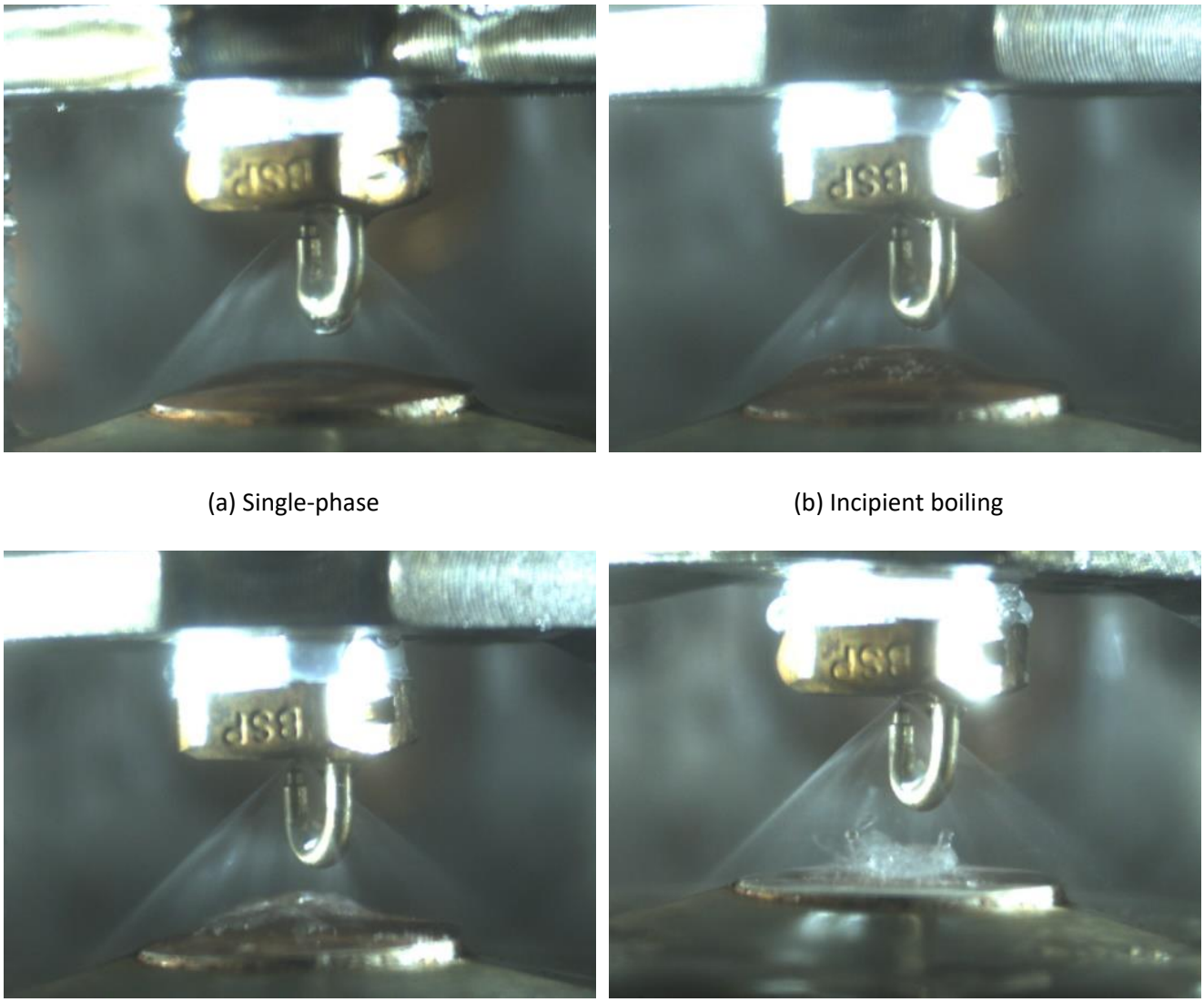

(a) Single-phase

(b) Incipient boiling

© Nucleate boiling

(d) Transition boiling

Fig. 3-4. Examples of observed spray cooling modes: (a) Single-phase, (b) Incipient boiling, (c) Nucleate boiling, and (d) Transition boiling

To collect the data in the 'nucleate boiling' region a total of 70 test runs were undertaken for both *static* conditions (without vibration) and *dynamic* conditions (with vibration at frequencies ranging from 1.9

to 400 Hz). The vibration test amplitude ranged from ± 0.02 to ± 12 mm. Table 3-2 gives the test data for this empirical study.

Table 3-2: Test plan and spray specification for the operating conditions of the UNIJET TG nozzle in the nucleate boiling.

$P_{chamber}$ (bar)	v (ml/min)	$T_{coolant}$ (°C)	H (mm)	Static	f(Hz) / a (mm)	1.9	3	6	10	60	100	200	400
1	140, 160, 180 and 200	Constant at 80±1.5℃	17 and 21	✓	0.02	-	-	-	-	-	✓	✓	✓
					0.1	-	-	-	✓	-	✓	-	-
					0.08	-	-	-	-	-	-	✓	-
					0.2	-	-	-	-	✓	-	-	-
					1	-	-	-	✓	✓	-	-	-
					2	-	✓	✓	-	-	-	-	-
					4	-	✓	✓	-	-	-	-	-
					8	-	✓	✓	-	-	-	-	-
					12	✓	-	-	-	-	-	-	-

UNIJET TG HYDRAULIC FULL CONE SPRAY SPECIFICATIONS

d_n (mm)	α (◦)	Covering d. (mm)	$\Delta P\ (bar)$	$u_m(\frac{m}{s})$	d_{05} (µm)	d_{32} (µm)
0.51	50-61	16-25	1.3-3	16.5-25	89-146	198-246

During each test-run, the data for any measured state was collected for a duration between 3 to 7 minutes (depending on the thermal inertia). This was achieved after changing the cartridge heater loads to make sure that the system reached steady state conditions (ensuring that a convergence criterion of 0.3 ℃ was also met).

For CHF measurements, the test plan operating conditions are shown in Table 3-3. The chamber pressure (1 bar), and surface-to-nozzle distance (12 mm), are kept constant. Three volumetric flow rates are tested for three nozzles of type: PJ8 (55 ml/min), PJ10 (75-100 ml/min) and MW145 (55 ml/min). For all test runs, two subcooling degrees of 10 ℃ and 45 ℃ are considered. The surface without vibration (i.e. the 'static' case), and the dynamic case with different vibration-amplitudes and -frequencies are tested. The dynamic cases with different combinations of amplitude and frequency are identified and labelled in the last column of Table 3-3 (and will be used for data analysis in Chapter 5).

In addition, the spray specifications associated with the operating conditions for these test runs are provided. A total of 64 test runs generate the required measured data.

Table 3-3: Test plan and spray specification for the operating conditions of the PJ and MW145 nozzles at CHF.

$P_{chamber}$ (bar)	v (ml/min)	ΔT_{sub} (°C)	H (mm)	Static	f(Hz) / a (mm)	2	4	8	50	50	100	200	Case
1	55, 75 and 100	10 and 45	12	✓	8	✓	-	-	-	-	-	-	D-1
					4	-	✓	-	-	-	-	-	D-2
					1	-	-	✓		-	-	-	D-3
					1	-	-	-	✓		-	-	D-4
					0.2	-	-	-	-	✓	-	-	D-5
					0.2	-	-	-	-	-	✓	-	D-6
					0.04	-	-	-	-	-	-	✓	D-7

NOZZLE SPRAY SPECIFICATIONS

Nozzle	d_n (mm)	α (◦)	Covering d. (mm)	$\Delta P\ (bar)$	$u_m(\frac{m}{s})$	d_{05} (μm)	d_{32} (μm)
PJ8	0.20	90	24	4.7	31.3	22	107
PJ10	0.25	90	24	2.9-5.2	24.6-32.9	26-33	117-137
MW145	0.41	70	17	7	38.2	47	141

For thermal management purposes, Table 3-4 gives the test plan and operating conditions for two test cases of flat-plate and ¼-cylinder. All the test runs were undertaken at atmospheric pressure. The test runs were undertaken for both *static* conditions (without vibration) and *dynamic* conditions (with vibration). For the flat-surface test-piece, two dynamic cases were considered: a high-frequency vibration with a frequency of f=400 Hz and amplitude of a=0.02 mm, and a large-amplitude vibration of f=1.9 Hz and a=12 mm. These two cases are based on the results of nucleate boiling experiments and have had the highest heat flux deviations from the *static* case results in steady-state conditions (see figures 4-7 and 4-8 in Chapter 4). A vibration amplitude of 12 mm is typical of vehicle-mounted hardware. However, the high mass of the ¼-cylinder test-piece only allows a maximum vibration amplitude of 3 mm to be reached with the shaker, rather than the derived 12 mm test amplitude of typical of vehicle-mounted hardware. It should be noted that the flow rate boundary conditions for

both test pieces are identified as part of a safety measure for the designed thermal management system (as explained in Section 5 of Chapter 6).

Table 3-4: Test plan and operating parameters during the thermal management experiments.

Test case	$P_{chamber}$ (bar)	v (ml/min)	$T_{coolant}$ (°C)	H (mm)	Static	f(Hz) / a (mm)	1.9	6	100	200	400
¼-cylinder	1	60-130	80	NA	✓	0.01	-	-	-	-	✓
						0.08	-	-	-	✓	-
						0.09	-	-	✓	-	-
						1	-	✓	-	-	-
						3	-	✓	-	-	-
Flat	1	120-225	80	17	✓	0.02	-	-	-	-	✓
						12	✓	-	-	-	-

Heat flux measurement

The heat flux for both nucleate boiling and CHF was calculated from the readings of the uniform temperature gradient between three thermocouples evenly spaced 5.5 mm apart. (During the experiments the linearity of temperature measurements was monitored so that the one-dimensional heat transfer is valid.) Therefore, the one-dimensional conduction equation:

$$q = -k\frac{dT}{dx} \tag{3-1}$$

is used where k, dT, and dx are the thermal conductivity, the temperature difference, and the distance between the top and bottom thermocouples located in the test-piece. The surface temperature was obtained by extrapolating the linear temperature distribution to the surface (as done by Mudawar and Valentine in [44]).

During the thermal management experiments, the transient heat flux was calculated using a numerical solution for the one-dimensional heat conduction equation:

$$\frac{\partial^2 T}{\partial x^2} = \frac{1}{\alpha}\frac{\partial T}{\partial t} \tag{3-2}$$

where T, x, $\alpha = \frac{k}{\rho C_p}$, and t are the temperature, position, thermal diffusivity, and time, respectively. For copper, density (ρ) and specific heat (C_p) are 8900 kg/m^3 and 395 J/kg K. A finite deference method has been used to approximate the temperature at different points across the thickness of the test piece by using discrete time steps. Therefore, the material needs to be spatially discretized into nodes. The spatial derivative on the LHS of equation (3-2), and the temporal derivative on the RHS can be approximated in the following form:

$$\frac{T_{(i+1)}^{(n)} - 2T_{(i)}^{(n)} + T_{(i-1)}^{(n)}}{(\delta x)^2} = \frac{T_{(i)}^{(n+1)} - T_{(i)}^{(n)}}{\alpha \delta T} \tag{3-3}$$

Subscript 'i' and superscript 'n' in equation (3-3) respectively stand for the current grid point, and the time step. 'i-1' and 'i+1' are the grid points before and after grid point 'i'. 'n+1' stands for the following time step. To obtain the temperature at the interior grid points, equation (3-3) can be rearranged as follows:

$$T_{(i)}^{(n+1)} = \delta Fo . T_{(i+1)}^{(n)} + (1 - 2\delta Fo) T_{(i)}^{(n)} + \delta Fo . T_{(i-1)}^{(n)} \tag{3-4}$$

where $\delta Fo = {\alpha \delta t}/{\delta x^2}$ is the Fourier Number in which δt is the time step size. δx is the distance between the grid points. Stability criteria has to be checked to achieve accurate results. The stability criteria are:

$$\delta Fo(1 + \delta Bi) < 0.5 \tag{3-5}$$

and

$$\delta t < \frac{0.5\, \delta x^2}{\alpha\left(1 + {\delta x h}/{k}\right)} \tag{3-6}$$

in which $\delta Bi = {\delta x h}/{k}$ is the Biot number. To meet the stability criteria, the distance between the first and third thermocouple is split into 22 nodes. Thus, the distance between the grid points δx is $5.24 \times 10^{-4}\, m$. The time step δt is set as $0.0004\, s$. The time step is much smaller than the sampling

rate, so the boundary temperatures (i.e. T1 and T3, the top and bottom thermocouples embedded in the flat test piece) had to be interpolated between the measured temperatures. To interpolate the measured temperatures, Piecewise Polynomials are used.

Finally, the surface temperature gradient $\nabla T = {}^{\partial T}/_{\partial x}$ needed for the transient heat flux calculation, can be obtained by a second-order backward difference scheme according to:

$$\frac{\partial T}{\partial x} \approx \frac{3T_i - 4T_{i-1} + T_{i-2}}{2\,\delta x} \tag{3-7}$$

For the ¼-cylinder, owing to the design of the test chamber, and the two-dimensional nature of the heat flux distribution, it was not possible to obtain quantitative estimates of the heat flux from differential temperature measurements involving embedded thermocouples. Instead, comparative estimates have been made from the rate of change of measured temperature (obtained from a thermocouple positioned 1 mm below the coolant-side surface) with time.

Uncertainty analysis

Table 3-5 gives the parameter uncertainties and measurement errors. To determine the uncertainty in the calculation of heat flux, a method by Moffat [99] has been used. This method starts with equation (3-1), where $K = 385\ W/mK$, $dT = 28.0193$ °C, and $dx = 0.0055$ m. (Note: dT was calculated from the maximum heat flux of 1.961351 MW/m^2 in the thermal management experiments). According to Moffat [99]:

$$\delta R = \left[\sum_{i=1}^{n} \left(\frac{\partial R}{\partial X_i}\delta X_i\right)^2\right]^{\frac{1}{2}} \tag{3-8}$$

Thus:

$$\delta R_q = \left[\left(\frac{\partial}{\partial \delta dT}\frac{k\delta dT}{dx}\delta dT\right)^2 + \left(\frac{\partial}{\partial dx}\frac{kdT}{dx}\delta dx\right)^2\right]^{1/2} \tag{3-9}$$

i.e.:

$$\delta R_q = \left[\left(\frac{k}{dx}\delta dT\right)^2 + \left(\frac{-kdT}{dx^2}\delta dx\right)^2\right]^{1/2} \quad (3\text{-}10)$$

Based on the test rig and measurement uncertainties in the table below:

Table 3-5. Uncertainties of the calculated and measured parameters.

Parameter	Uncertainty (%)	Units
Thermocouples	±0.4	℃
Volumetric flow rate	±0.6 (of full scale)	ml/min
Accelerometer frequency	±5	Hz
Pressure transducers	±0.25	bar
Diameter	±1	mm
Length	±1	mm
Heat flux	±2.97 (max.)	MW/m^2

it follows that $\delta dx = 0.00001$ m, $\delta T = 0.004 \times T$, $\delta T_1 = 0.004 \times 136.159 = 0.5446$, $\delta T_2 = 0.004 \times 164.178 = 0.6567$, and $\delta dT = [0.5446^2 + 0.6567^2]^{1/2} = 0.7279$. By substituting the uncertainties into the derived uncertainty for heat flux, from equation (3-10):

$$\delta R_{q:1961351\,W/m^2} = \left[\left(\frac{385}{0.0055} \times 0.7279\right)^2 + \left(\frac{-385\times 28.0193}{0.0055^2}0.00001\right)^2\right]^{1/2} = 51077.639 \quad (3\text{-}11)$$

and therefore the % uncertainty is:

$$100\delta R_{q:1961351\,W/m^2} = \frac{51077.639}{1961351} \times 100 = 2.604\,\% \sim 2.6\% \quad (3\text{-}12)$$

The highest expected uncertainty in the calculation of heat flux, at maximum experimentally-measured data point of 1.96 MW/m^2, is therefore 2.6%.

For nucleate boiling and CHF experiments, the same method was used. The results for nucleate boiling with the UNIJET nozzle show that the maximum uncertainty in the calculation of heat flux at the maximum measured data point of 3.23 MW/m^2, is estimated to be 2.97%. The highest expected uncertainty in the calculation of critical heat flux with the PJ and MW145 nozzles, at maximum experimentally-measured data point of 2.67 MW/m^2 is 2.57%. Therefore, the highest expected uncertainty of 2.97% is supplied in Table 3-5, to be used in the data analysis part of this study.

As can be seen in the fifth column of Table 1.1, for heat flux measurements, uncertainties between 1.05% and 10% are reported. The reason for such a range is different operating conditions in the studies. Hsieh et al. 2004 [54] reported an uncertainty of 1.05% for high heat fluxes. In another study, Hsieh et al. (2015) [93] reported uncertainty of less than 5% for slightly lower heat flux ranges. Pereira et al. (2013) [90] reported uncertainties between 1.3% and 1.7%. Tan et al. (2013) [97] obtained uncertainties between 3.3% and 5.1%.

Processing of measured data.

Since the current application requires high-speed streaming and obviously searchable data for the control algorithm, the data logging has been achieved using the NI TDMS file format which has a high-speed streaming performance with a small disk footprint. This enables the accelerometer data to be precisely tracked and stored. The low-level FPGA I/O functions have provided a high response control capability for the thermal management system. The performance of the processors in both cRIO-9035 and the host computer, sufficiently secure the required accuracy and sampling rates for the 'read' and 'write' operations of the states, as well as sending the required control signals.

Reproducibility

For the nucleate boiling experiments, a test-run for the case study involving *static* cooling surfaces with a flow rate of $180\ \mathrm{ml/min}$, was undertaken twice for the purpose of checking repeatability of the test facility.

Figure 3-5 shows the repeatability of the nucleate boiling data. As can be seen, the maximum difference is 2.98% which is close to the maximum estimated uncertainty in Table 3-5 (i.e. 2.97%). In general, the reproducibility of the data in the nucleate boiling regime using the designed test rig was good.

For CHF, great care was taken to identify key factors involved in the successful reproducibility of the data. A regular change of de-ionized water, and checking that the cooled disc had the same surface roughness using the same sandpaper grit (and therefore no copper oxidation), was found to be the two most important precautions required for conducting experiments on different days.

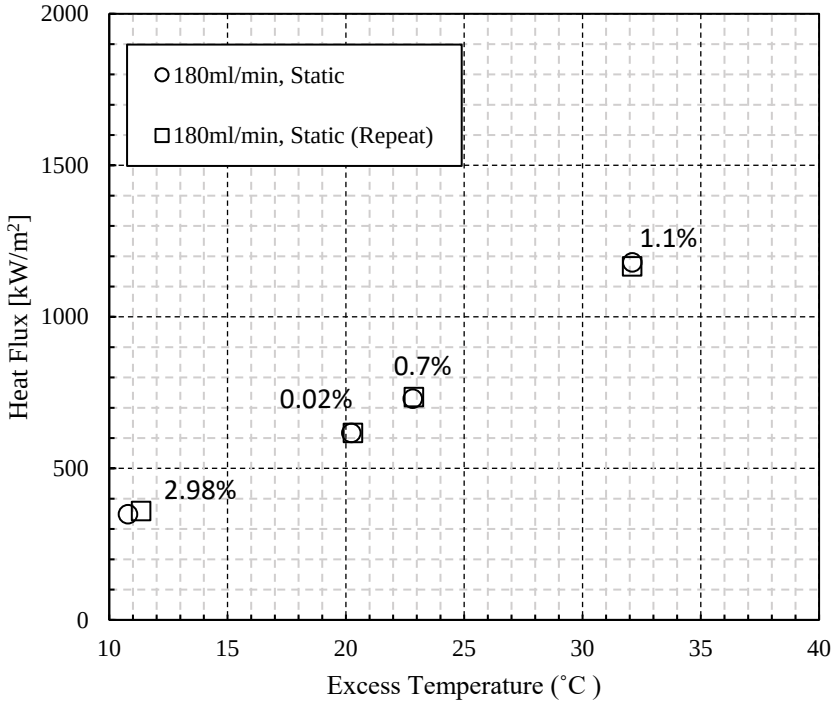

Fig. 3-5. Reproducibility of the nucleate boiling results showing percentage of heat flux deviations.

For the sake of maximum reliability in the reproducibility of the data, each case in Figure 3-6 was repeated twice on two different days, and only cases with the largest deviations are reported. At the beginning of each day, the de-ionized water was replaced, and the copper surface was polished with sandpaper. As can be seen, the maximum deviations for CHF are less than the estimates from the uncertainty analysis, except for MW145 (4%). For the excess temperature, the average deviation is higher than the thermocouple uncertainty. For that reason, the maximum deviations caused for CHF (only for MW145) and the excess temperature during repeatability analysis, has been taken into consideration for the interpretation of the data and trends in the results and discussion section.

However, it is noteworthy that all the test runs for each nozzle were taken on one day to minimise the effect of reproducibility and to maximise the reliability of the comparisons.

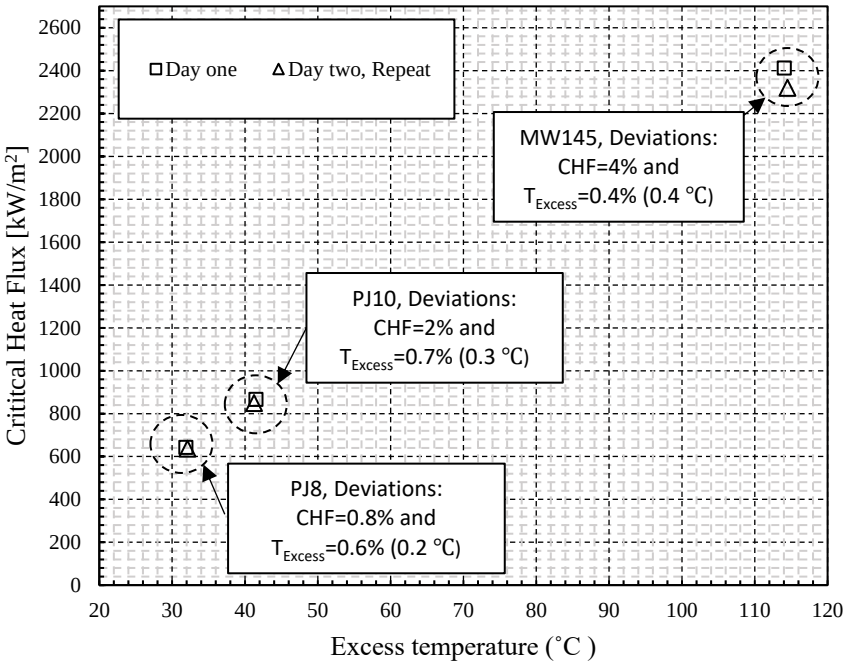

Fig. 3-6. Reproducibility of the results with CHF and excess temperature maximum deviations.

To check the level of uncertainty in the repeatability of the control scheme during the thermal management experiments (i.e. with disturbance), the same PID gains are attempted, and the results are available in Table 3-6. The 3 s difference in settling time, and only a temperature difference of 0.1 $^{\circ}C$ in overshoot, offers a high level of repeatability.

Table 3-6. The level of uncertainty in repeatability tests involving the control scheme for thermal management experiments.

#	P	I	D	Disturbance	$q\ (\frac{MW}{m^2})$	$T_w(^{\circ}C)$	Settling time (s)	Overshoot ($^{\circ}C$)
1	-2	0.7	0.002	Dynamic (a=0.02mm, f=400Hz)	0.2-1.8	110-135	70	0.6
2	-2	0.7	0.002	Dynamic (a=0.02mm, f=400Hz)	0.2-1.8	110-135	67	0.7

3.3. The Conclusions of Chapter 3

An experimental test facility and a control programme has been designed to help meet the three main objectives of the thesis. The first two objectives include data collection in the nucleate boiling regime and associated critical heat flux with and without vibrating surfaces to be used for correlation development in the static and dynamic conditions. The third objective is to undertake thermal management of an evaporative spray cooling test rig involving flat and three-dimensional surfaces under vibration. Two test-pieces are mounted on the dynamic test rig and controlled in an actual hardware. The flat test-piece is for heat flux exploration and correlation developments, whereas the ¼-cylinder emulates a cooling system of a highly boosted IC engine (with three-dimensional cooling surfaces). The dynamic test rig is equipped with a mechanical shaker to induce vibrations typical of vehicle-mounted hardware. The DAQ and control unit hosts the control algorithm and provides supervision through a human-machine interface. Experimental test plans and heat flux measurements have been discussed. The uncertainties associated with the measurement facilities have also been discussed and have been used to estimate the uncertainty in heat flux. The following conclusions can be drawn from this chapter:

- The maximum expected uncertainty in the calculation of heat flux is 2.97% in the nucleate boiling regime. The estimated uncertainty in the heat flux for the CHF and thermal management results are respectively 2.57% and 2.6%. Therefore, an uncertainty figure of 2.97% is used in the data interpretation and comparisons in the following chapters.
- The reproducibility of the data for all the measurement programmes was also studied to make sure the results are of high quality. For nucleate boiling, the maximum deviation in the repeated test runs is 2.98% which is close to the maximum estimated uncertainty.

- For CHF test plans, the maximum deviations in the repeated results on two different days were all less than the expected % uncertainty (except for the MW145 nozzle which is 4%). For the temperature associated with CHF, the deviations are higher than the uncertainty associated with the thermocouples. Thus, the maximum deviations for the CHF and its associated temperature during repeatability analysis has been examined and its meaning established for the next chapters.
- A set of repeatability tests for the tuned control scheme was also undertaken with a very reasonable reproducibility obtained in the temperature profile and the settling time.

In the chapters 4 and 5, the results from experimental test plans are given. Key parameters will be obtained from the fitted correlation models of Chapter 2.

4. HEAT FLUX CHARACTERISTICS IN SPRAY EVAPORATIVE COOLING OF VIBRATING SURFACES IN THE NUCLEATE BOILING REGION – FITTING PREDICTIVE CORRELATION MODELS.

In this chapter, the objective is to investigate (for the first time) the effect of vibration on spray evaporative nucleate boiling for a full-cone spray impinging on a (heated) flat circular copper test piece, driven by a shaker. Experimentally-measured spray evaporative cooling data is obtained from the rig discussed in Chapter 3 and used to both better understand the physics and also fit the corresponding empirical correlation models (developed in Chapter 2) using the Vibrational Reynolds Number and a dimensionless Acceleration Number which better correlate the influence of surface frequency and amplitude in the nucleate boiling regime. Different coolant flow-rates through a full-cone spray nozzle are used to cool a flat circular test-piece acting as a horizontal surface. The test-piece surface is excited by a shaker through a range of low and high vibration amplitudes and frequencies. The results show that surface dynamic effects certainly influence nucleate boiling, but they also show that surface vibration does not have the same effect for all excess temperatures - dynamic effects can either increase or decrease heat transfer depending on the heat transfer mechanism. The new predictive correlation models are important for thermal management in several areas, particularly involving batteries, power electronics, and electrical machines in automotive and aerospace applications.

The following sections present the results of the static and dynamic case studies, as well as the developed correlations. First, there is a comparison between the equivalent boiling curves (with and without mechanically-induced vibration) to assess the prospective influence of vibration on the heat flux. Next there is a discussion of the effects of low to high frequencies as well as small to large amplitudes to further understand the trend of vibration results compared with static results. The final section presents evidence of the efficiency of the fitted correlations (already derived by Dimensional

Analysis in Chapter 2). There is also a discussion of prediction error bands, which play a vital role in the development of a concise and reliable model for spray cooling under static and dynamic conditions.

4.1. Static surface results

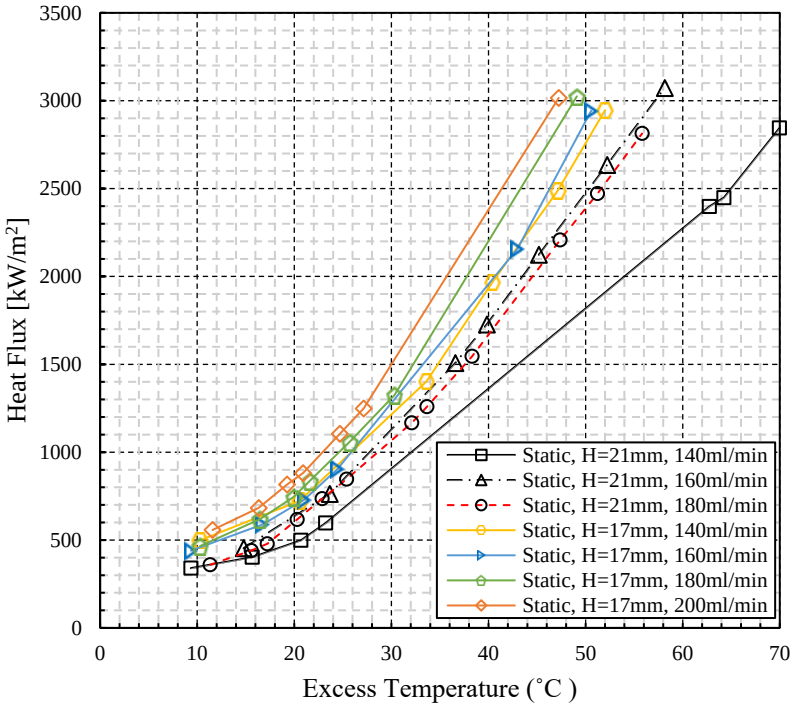

Fig. 4-1. Nucleate boiling curves for the case study involving static cooling surfaces.

Figure 4-1 shows the effect of volumetric flow rate and nozzle-to-surface distance on the measured heat flux over different excess temperatures. Two different nozzle-to-surface distances are chosen at 17 and 21 mm. The volumetric flow rate ranges from 140 and 200 $\mathrm{ml/min}$, the heat flux from 359.68 $\mathrm{kW/m^2}$ to 3072.5 $\mathrm{kW/m^2}$ and the excess temperature from 9.36 to 69.98 ˚C. Heat fluxes are at their lowest and highest values at flow rates of 180 $\mathrm{ml/min}$ and 160 $\mathrm{ml/min}$. An increase in the flow rate at most of the equivalent excess temperatures gives rise to an increase in heat flux. However, there are two important reverse trends. One occurred when the flow rate is increased from 160 to 180 $\mathrm{ml/min}$ for a nozzle height of 21 mm, where there is actually a slight reduction in the heat flux during all excess

temperatures (rather than an increase). The second occurred at an excess temperature of around 10 ˚C where there is a reverse trend in the heat flux for the flow rate of 140 $\mathrm{ml/min}$, which has a slightly greater value than those for 160 and 180 $\mathrm{ml/min}$.

It can be hypothesised that the first reverse trend is a result of an increased spray angle. In this case, a higher volumetric flow rate causes a higher pressure difference across the nozzle, i.e. here from 1.6 bar to 2.3 bar. It is stated on the (UNIJET® nozzle, TG tip Type) manufacturer's data sheet, that the spray angle varies from 50˚ to 61˚. This hypothesis is supported by two studies. In their research on the effect of spray angle on spray cooling performance, Schwarzkopf et al. [145] report a heat transfer deterioration when the spray angle exceeds 50˚. In this case, increased spray cone-angle at 180 ml/min means lower effective volumetric flow rate covering the test piece, providing less heat-transfer compared to that for a lower volumetric flow rate of 160 ml/min but with a higher effective flow rate. The same reverse trend has been observed by Zhang et al [60]. In support of this observation, the reader should refer to the results for the smaller nozzle-to-surface distance of 17 mm for 160 and 180 $\mathrm{ml/min}$ in Figure 4-1. Thus with an increase in flow rate, the spray is able to increase its volumetric flux. In general, the trend shows that the effect of reducing the surface-to-nozzle distance is beneficial to the heat transfer and therefore increases the heat flux during all of the excess temperature regions. It is possible to maintain the same volumetric flux even with a reduction in cone angle by reducing the height H. This is evident from the volumetric flux equation [50]:

$$\bar{\vec{v}} = \frac{v}{\pi(Htan\left(\frac{\alpha}{2}\right))^2} \tag{4-1}$$

where $\bar{\vec{v}}$ is the volumetric flux, v is volumetric flow rate, α represents spray cone angle, and H is nozzle-to-surface distance. Owing to the limited experimental conditions, it was impossible to find a precise threshold for the reduced volumetric flux caused by the cone angle alteration. Furthermore, a reduction in the nozzle-to-surface distance results in increased momentum, and droplet impact velocity, plus more droplet-liquid film interactions, which can also lead to heat transfer enhancement [146]. The droplet impact velocity, or droplet breakup velocity, can be obtained from a simple energy balance developed by Ghodbane and Holman [48], and further developed by Qiao and Chandra [70] to include gravitational potential energy which is formulated as follows:

$$u_m = \left(u_o^2 + \frac{2\Delta P}{\rho_l} - \frac{12\sigma}{\rho d_{05}} - 2gHsin(\alpha)\right)^{1/2} \tag{4-2}$$

where u_o, ΔP and d_{05} are respectively the mean velocity of water entering nozzle, the pressure drop across spray nozzle, and the mass median droplet diameter.

The second reverse trend (at an excess temperature of 10 ˚C) can be explained by a smaller droplet impact velocity onto the thin layer of water accumulated on the surface (for the data point at 140 $\mathrm{ml/min}$), owing to a lower pressure difference across the nozzle (i.e. 1.3 bar for 140 $\mathrm{ml/min}$ compared to 1.6 and 2.3 bar respectively for 160 and 180 $\mathrm{ml/min}$). Such a change makes a lower penetration impact lead to nucleation at a lower surface temperature, owing to less suppression force in front of bubble departure from nucleation sites. The conclusion then is that moving the nucleate boiling regime to a lower surface temperature, enhances the heat transfer coefficient at the same excess temperature.

The flow rate and nozzle specifications correspond to hybrid electric vehicle cooling systems and other high heat flux situations. These requirements are, on one hand, chosen to address thermal problems [34] such as controlling steady-state surface temperature for heat flux, i.e. between 0-2 MW/m^2. Meeting these thermal requirements is feasible in the nucleate boiling regime [23] which is the prime interest undertaking these experiments. On the other hand, the parameters and operating conditions are limited by the power of the pump (Micropumps MGD100P) not being able to provide the required flow rate for the current nozzle. This pump is chosen to provide Coefficients of Performance (Heat Flux/Pump Electrical Power) COP$>$5 which is typically the situation for cooling of high powered electrical systems used in hybrid and battery-powered electric vehicle cooling systems. Moreover, the UNIJET® nozzle (based on its manufacturer datasheet), does not have a full cone spray for lower flow rate than the current operating region (i.e. 140ml/min). The experimental findings are therefore limited to the operating conditions and parameters of the present study. Extending the operating conditions could indeed change the overall trend but this is beyond the scope of the current study.

4.2. Dynamic surface results

First, the influence of vibration on the heat transfer will be investigated in the middle range operating conditions. Then, the results of harsh dynamic conditions, including high frequency vibration with small amplitudes, and large amplitude vibration at low frequencies, will be thoroughly evaluated to cover a wide operating condition. In addition, the results associated with the effect of flow rate and nozzle-to-surface distance are compared for high frequency vibration and the relationship between them is explained (i.e. for two nozzle heights). This is because the trend showing the effect of vibration for different flow rates and nozzle heights may be different. In particular, having the information in the same figure provides an opportunity to study the influences of flow rate and nozzle height in the

presence of vibration. Large amplitude results represent typical dynamic operating conditions associated with real vehicle dynamics, a primary focus of the study.

The effect of varying flow rate on heat flux with and without surface vibration

Figure 4-2, Figure 4-3, and Figure 4-4 show the measured heat flux versus excess temperature for flow rates between 140 $\mathrm{ml/min}$ and 180 $\mathrm{ml/min}$ at a nozzle height of 21 mm for middle frequency range vibrations. Also shown on each figure (and on later figures) is the *effect ratio*. This is defined as the ratio of the dynamic-heat-flux/static-heat-flux which in all cases (except for Figure 4-2c) uses the dynamic case that produces the largest effect. First, to inspect the *static* and *dynamic* results for any amplitude influence on the heat flux, two fixed frequencies of 10 Hz and 60 Hz are considered together (respectively in subplots of (a) and (b) in figures 4-2, 4-3, and 4-4). To allow room for inspection, the vibration amplitude for all three flow rates change from 0.1 mm to 1 mm at 10 Hz, and from 0.2 mm to 1 mm at 60 Hz. By increasing the amplitude, the lower values of measured heat flux for the most data points indicate that the vibration amplitude itself impedes the heat transfer rate. It should be noted that the effect is more visible on lower excess temperatures (i.e. less than 30 ˚C) for flow rates of 140 $\mathrm{ml/min}$ and 160 $\mathrm{ml/min}$ at 10 Hz, which adversely affects the incipient nucleate boiling regime. To support this claim, are the reductions in the heat flux in Figure 4-2a (i.e.: -14.9% at 9.3 ˚C), and in Figure 4-3a (i.e. -18.1% at 14.7 ˚C), whereas there is only a subtle decrease in the heat flux of 180 $\mathrm{ml/min}$ in Figure 4-4a.

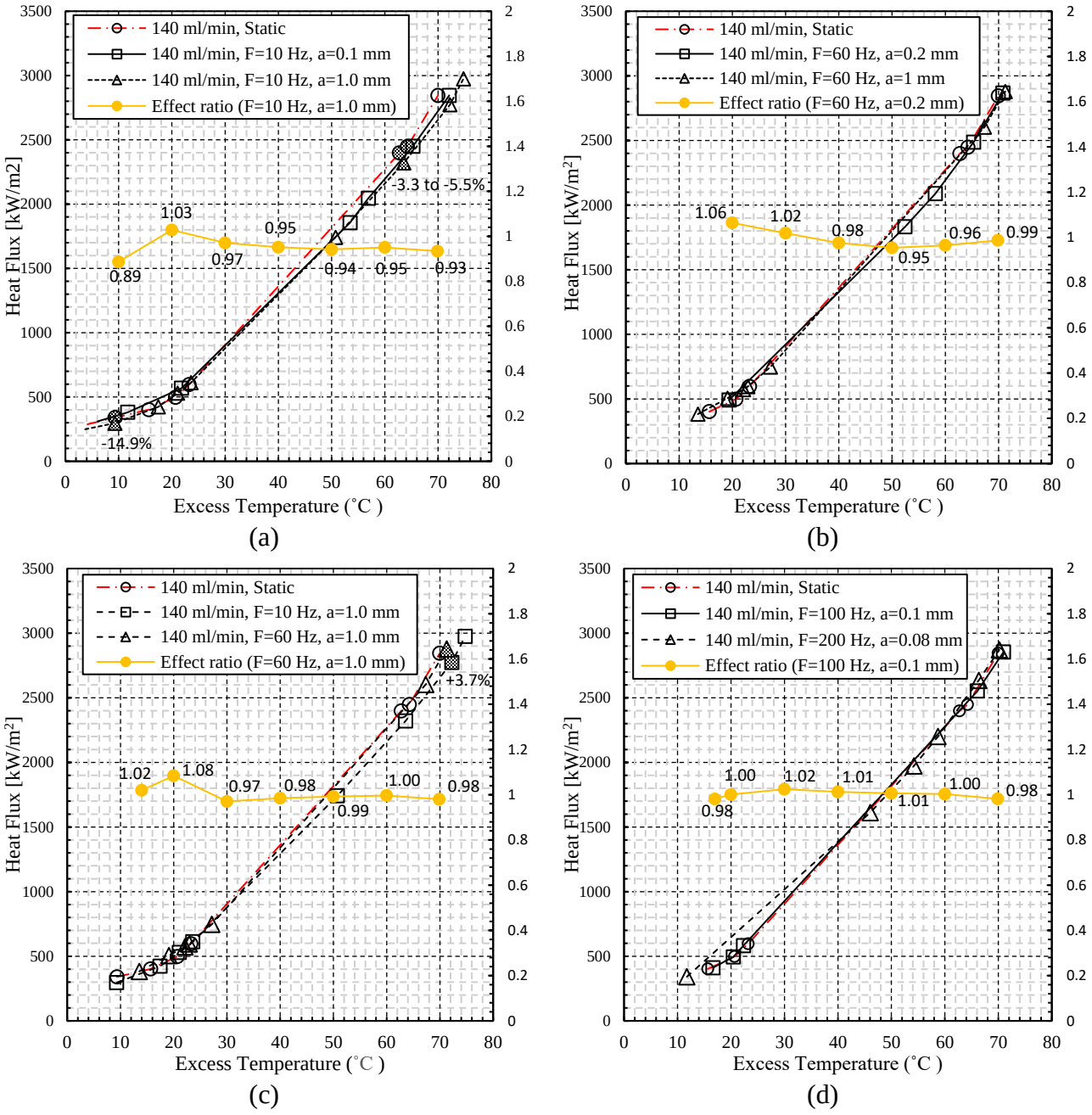

Fig. 4-2. Nucleate boiling curves with and without vibration for the flow rate of 140 ml/min.

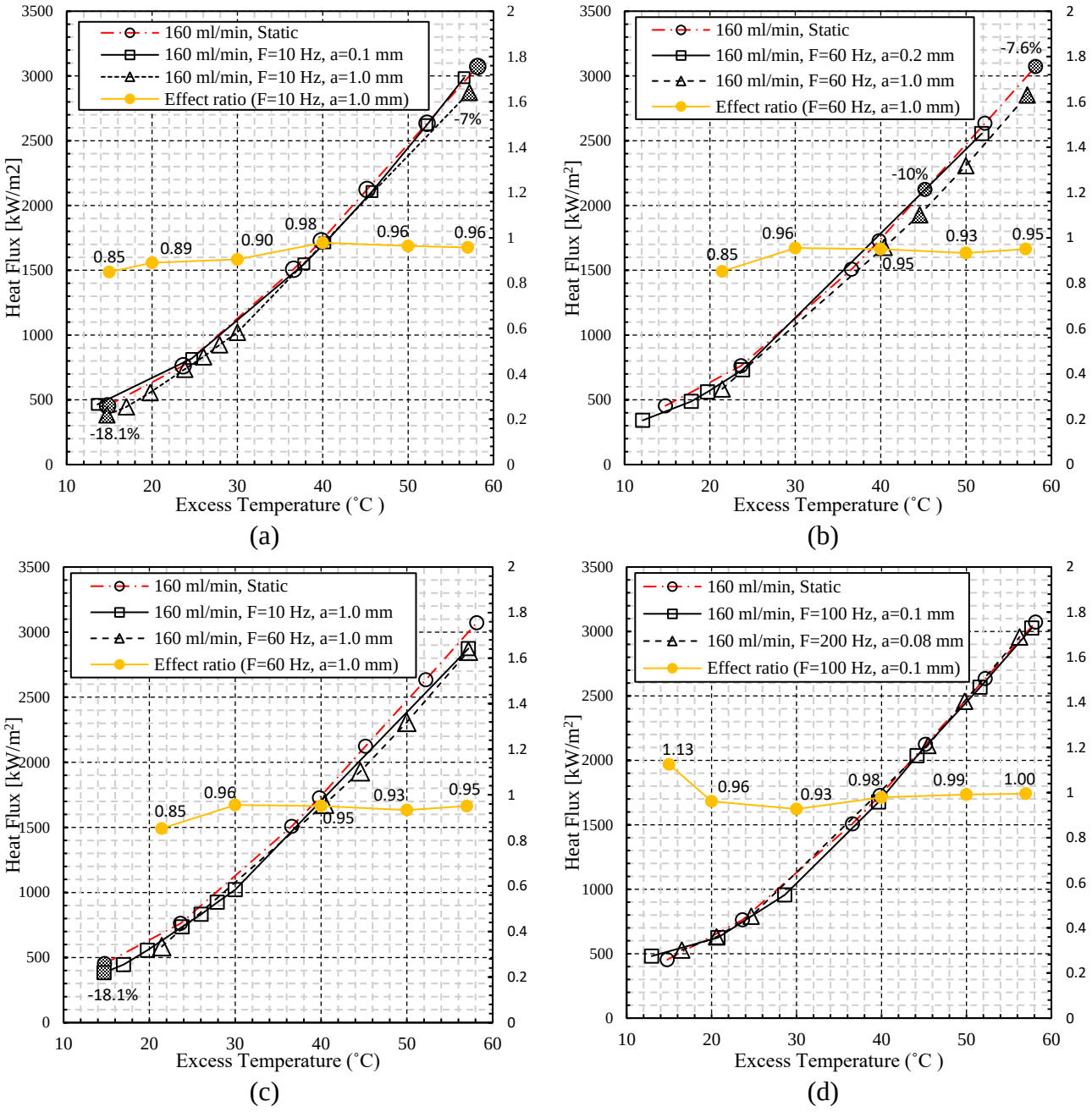

Fig. 4-3. Nucleate boiling curves with and without vibration for the flow rate of 160 ml/min.

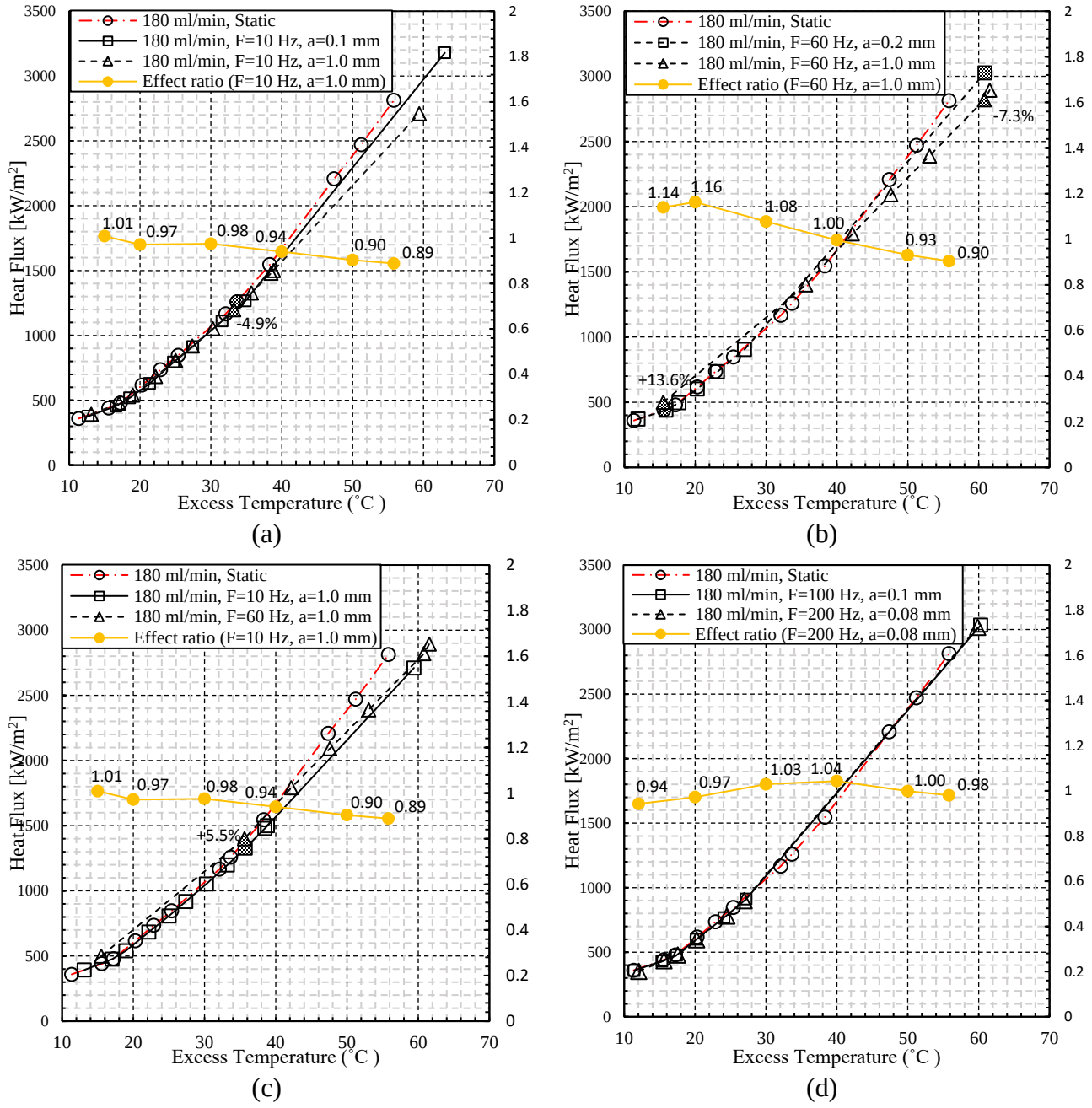

Fig. 4-4. Nucleate boiling curves with and without vibration for the flow rate of 180 ml/min.

By increasing the amplitude from 0.2 mm to 1 mm at the higher frequency of 60 Hz, there is a similar trend for the flow rate of 160 ml/min. At the low excess temperature of 15.9 ˚C for mass flow rate of 180 ml/min, the impact of vibration becomes positive. This reverse trend, with the noticeable heat transfer increase of +13.6% can be attributed to the faster periodic change in the target surface height

(with respect to the spray flow field), owing to the 1 mm vibration amplitude, which in turn, can result in a spray angle change. As was explained in the previous section, for the mass flow rate of 180 $\mathrm{ml/min}$ at nozzle height of 21 mm, there was a threshold adversely affecting the heat transfer rate that was attributed to the resultant change in the spray angle. To explain this, as can be seen in Figure 4-4a, compared to the trend of the boiling curves for the lower flow rates at 10 Hz, the effect of heat transfer deterioration owing to amplitude, has been weakened. In this particular case, therefore, this conjecture has credibility, in that at a higher frequency of 60 Hz, the faster change in amplitude (i.e. ±1 mm) and the shorter periods of impeding spray angle, enhance the average local heat flux.

By contrast, Figure 4-2c, Figure 4-2d, Figure 4-3c, Figure 4-3d, Figure 4-4c, and Figure 4-4d show the influence of frequency on the heat flux at fixed amplitudes of 0.08, 0.1, and 1 mm for step changes in frequency of 10 to 60 Hz, and 100 to 200 Hz. Considering the step change of 10 Hz to 60 Hz, there are only two visible enhancement effects in flow rates of 140 $\mathrm{ml/min}$ and 180 $\mathrm{ml/min}$. As can be seen in Figure 4-2c, at 140 $\mathrm{ml/min}$, the higher frequency of 60 Hz around an excess temperature of 72 ˚C, contributes to heat transfer augmentation (of 3.7%), compared to that for a lower frequency of 10 Hz. A heat transfer enhancement of 5.5% is observed at the flow rate of 180 $\mathrm{ml/min}$ around a 'superheat' of 35.5 ˚C. The reason for this increase in heat flux for a higher frequency (from 10 to 60 Hz) at a fixed amplitude, is due in part to the augmented vibrational Reynolds Number ($Re_V = \rho_l a \omega d_H / \mu_l$) promoting turbulence. Additionally, the resulting acceleration in the liquid film plays a prominent role in providing better liquid drainage [60], and a thinner layer on top of the surface, thereby reducing thermal insulation. This claim can be supported by the fact that the acceleration ($\omega^2 a/g$) is more affected by increased frequency owing to having a higher sensitivity to angular velocity (of the order, a power two).

Further inspection of Figure 4-2d, Figure 4-3d, and Figure 4-4d shows no visible change in the heat flux by the step change in higher range frequencies of 100 Hz to 200 Hz. This observation is not inconsistent with the previous conclusion because the effect of vibration in the presented range of amplitude and frequency is in general impeding. At this step change, for all flow rates, the trend shows a convergence to the results of the *static* cases. Therefore, in comparison with the results at low frequency vibration versus the *static* case, no change in the heat flux for the higher frequencies (over *static*), offers an improvement by the increased Reynolds Number and increased Acceleration Number.

The effect of high-frequency low-amplitude surface vibration on heat flux

To understand how frequency can affect the characteristics of the nucleate boiling, results with quite low amplitude of 0.02 mm, and three high frequencies of 100, 200, and 400 Hz, are shown in Figure 4-5, Figure 4-6, and Figure 4-7. The results for nozzle-to-surface distances of 17 mm and 21 mm are given. For the nozzle height of 21 mm, considering the lower flow rates of 140 $\mathrm{ml/min}$, results are given in Figure 4-5b, and for 160 $\mathrm{ml/min}$, the results are given in Figure 4-6b. Across all the excess temperature regions, the heat-flux does not follow the changes in frequency, although a small decrease in heat-flux from increasing frequency is evident in the results for the lower excess temperature regions (i.e. below 30 ˚C). By contrast, for excess temperature above 30 ˚C, by increasing frequency, the gradients of the curves in Figure 4-5b and 4-6b are identical to the heat transfer coefficient slopes at a higher angle. This effect becomes more marked with a higher flow-rate of $180\ \mathrm{ml/min}$ as shown in Figure 4-7b, as the gaps between the curves gradually expand by an increase in frequency and excess temperature (up to 8.2% in Figure 4-7b). This clearly indicates that there is a definite effect of frequency on the heat transfer, which can be either augmentation or deterioration, depending on the mechanism of nucleation.

Exploring the effect of high frequency vibrations on the trend for the lower nozzle height of 17 mm, Figure 4-5a, Figure 4-6a, Figure 4-7a and Figure 4-7c show that high frequency makes the deterioration effect more evident. During the lower excess temperatures in which nucleation is the primary mechanism, by increasing the frequency, it is evident that the greatest heat transfer deterioration of -30.1%, occurs for the lowest mass flow rate of 140 $\mathrm{ml/min}$ at the lowest excess temperature of 10 ˚C. This is because suppressed bubbles are generated on the surface within the liquid film by the high acceleration of 12.9 g which results from the high frequency vibration. Inducing such a force can delay the departure of the bubbles from the surface, and in turn, the trapped bubbles reduce the density of nucleate sites, which subsequently cause a significant heat flux reduction. Nevertheless, from the higher flow rates of 160 $\mathrm{ml/min}$ to 200 $\mathrm{ml/min}$, as shown in Figure 4-7c, this hindrance to the departure of bubbles has been weakened by a more powerful penetration impact of the droplets which were strengthened by a higher flow rate. Therefore, the impeding effect of high frequency vibration has disappeared from the trend. During the higher excess temperature regions, from the lowest flow rate to the maximum of 200 $\mathrm{ml/min}$, the gap between the curves (corresponding to cases with and without vibration) expands, giving rise to heat transfer rate reduction of -3.6% in Figure 4-6a. This is because of the impeding effect of high acceleration on the departure of the bubbles, which occurs when the penetration force of the high velocity droplets is no longer able to improve the density of the nucleate sites. The bubbles at higher surface temperatures start to accumulate and develop small slugs which adversely affect the heat transfer rate [22].

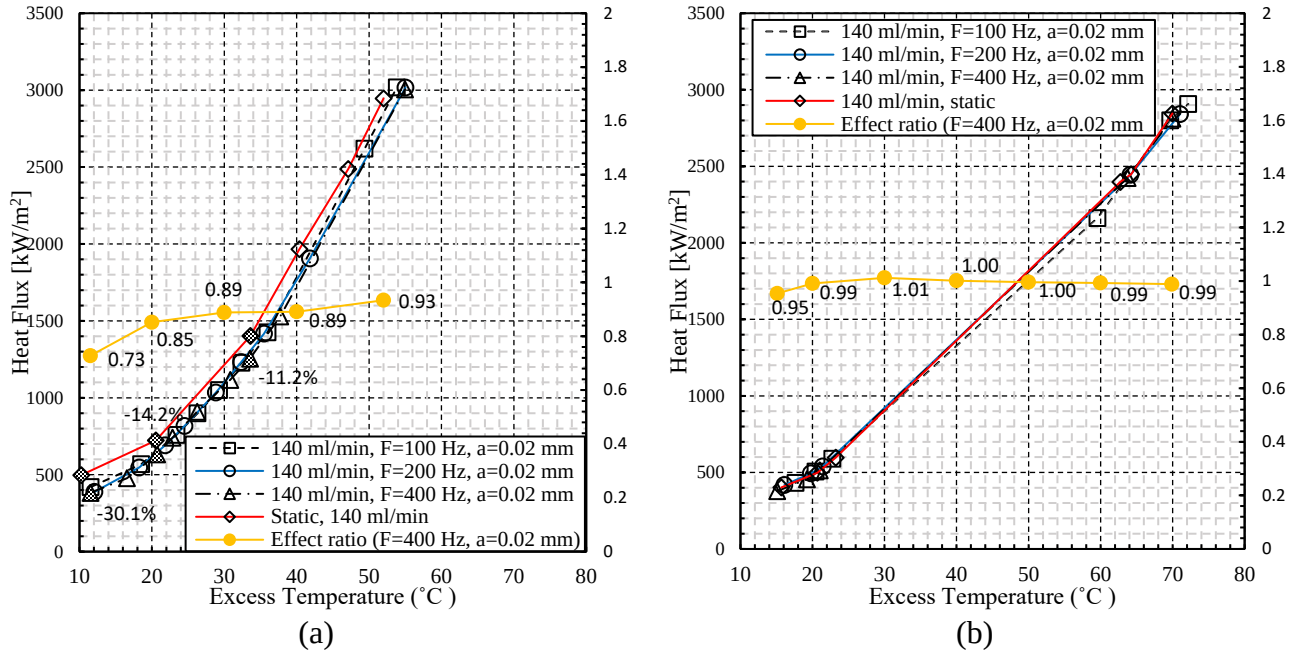

Fig. 4-5. Heat flux over the excess temperature for *static* and *Dynamic* test runs with the amplitude of 0.02 mm and frequencies up to 400 Hz for nozzle heights of: a) H =17 mm b) H =21 mm

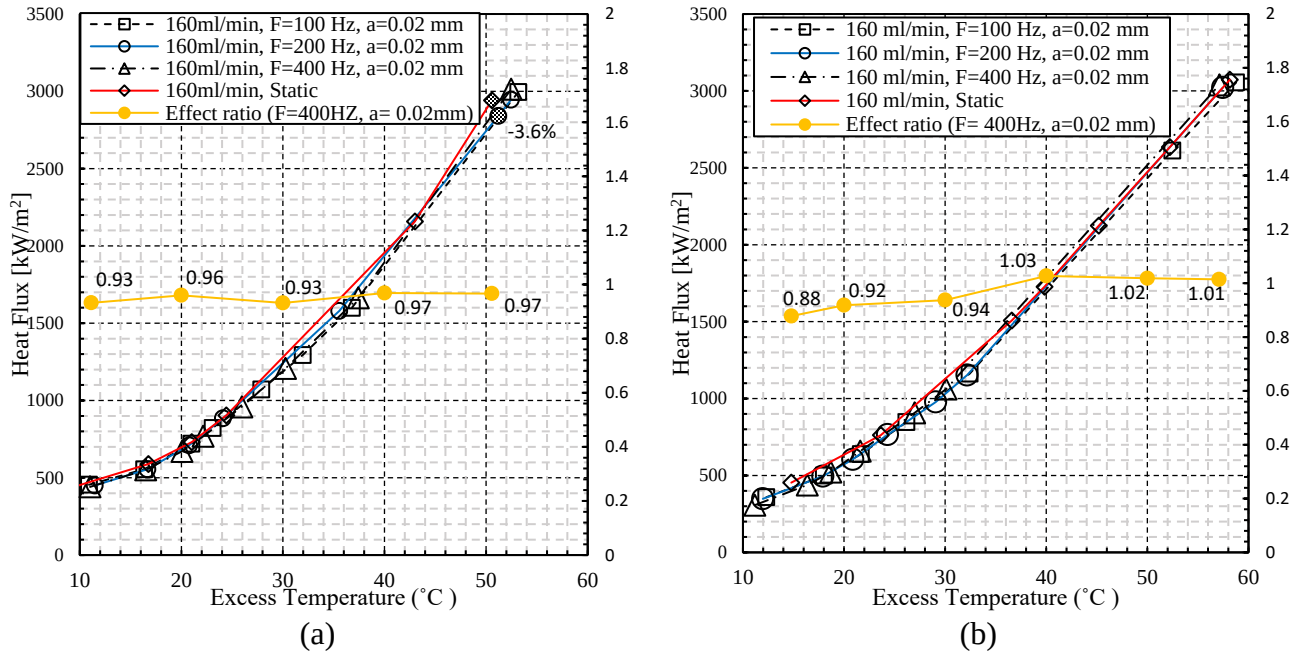

Fig. 4-6. Heat flux over excess temperature for *static* and *Dynamic* test runs with the amplitude 0.02 mm and frequencies up to 400 Hz: (a) v =160ml/min and H =17mm (b) v =160ml/min and H =21mm

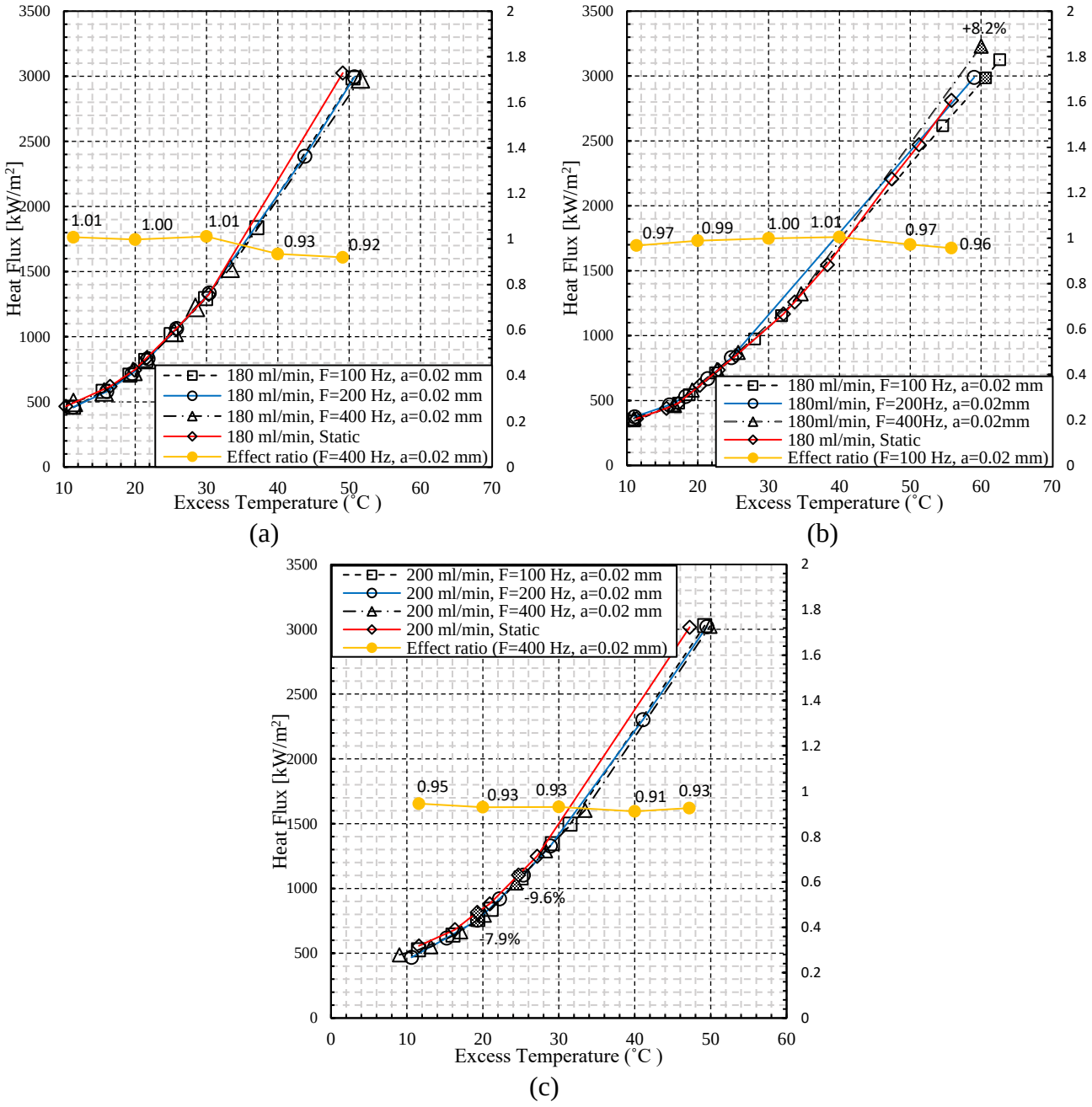

Fig. 4-7. Heat flux over excess temperature for *static* and *Dynamic* tests with an amplitude of 0.02 mm and frequencies up to 400 Hz: (a) v =180ml/min and H =17mm, (b) v =180ml/min and H =21mm, (c) v =200ml/min and H =17mm

The effect of low-frequency high-amplitude surface vibration on heat flux

The results so far have shown the effect of low amplitude vibration on spray cooling for middle range and high frequency test runs. The trend for each flow rate was found to be highly dependent on the complex relationship between frequency, amplitude, and excess temperature, since it is always either enhancing or deteriorating the impact in the lower and higher surface temperature regions. It would therefore be expected that there should be an optimum value of heat flux. Higher amplitudes are needed to assess the sensitivity of such an important parameter, which is important for design in application areas with dynamic conditions (e.g. thermal management of Electric Vehicle Range Extenders and power electronics in hybrid electric vehicles [34]). In this regard, 21 sets of measurements involving vibrations with the largest amplitude possible (i.e. up to 12 mm) corresponding to typical road test conditions, have been taken. The results are shown in Figure 4-8. By increasing the vibration amplitude, the trend shows interesting behaviour for different volumetric flow rates. During the high 'superheating' regions (i.e. above 40 ˚C), the gap between the curves associated with *dynamic* measurements (i.e. with vibration amplitudes up to 8 mm), and *static* measurements, gradually decreases by varying flow rate from 140 $\mathrm{ml/min}$ to 200 $\mathrm{ml/min}$. By contrast, a reverse trend is evident for the largest amplitude as the flow rate increases, when the heat flux is compared to the *static* case, as now explained in more detail.

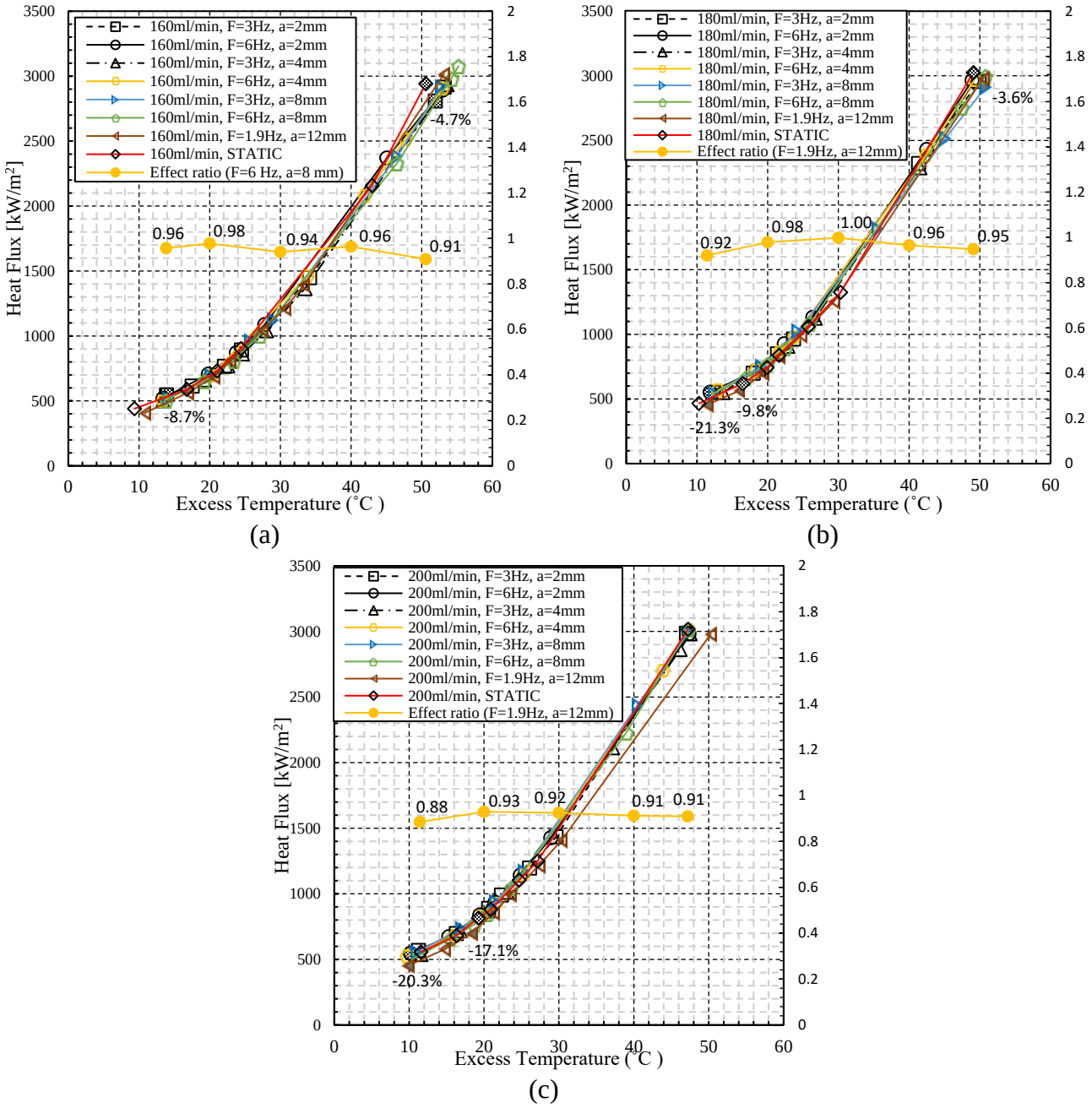

Fig. 4-8. Performance boiling curves for large amplitude vibrations at the nozzle height of 17mm

To explain the trend observed, the dimensionless Acceleration Number and the vibrational Reynolds Number for all the large amplitude vibration cases are given in Table 4-1 (each row represents the same case in the legend of the figures). By increasing the flow rate, the cases with a lower acceleration, and a Vibrational Reynolds Number up to 10252, follow the same behaviour; i.e. the gap between these

cases, and the *static* case, finally converge at a particular flow rate. There is obviously a trade-off between the deteriorating effect of vibration, and the enhancing influences of acceleration and flow rate. Considering case Number 5 in Table 4-1 with Vibrational Reynolds Number of 10252.81 but a lower Acceleration Number than case number 4, it is evident that the performance of Case Number 5 converges at a higher flow rate of 200 $\mathrm{ml/min}$. By contrast, the boiling curve for Case Number 4 (which has the same Reynolds Number) converges to the *static* performance curve at 180 $\mathrm{ml/min}$. Furthermore, for case 7, which has the largest amplitude case of 12 mm, but a smaller acceleration of 0.17 g, and a Vibrational Reynolds Number of 9740.167 (which is not very different from 10252), appears in comparison to cases 4 and 5, not to have yet converged at the flow rate of 200 $\mathrm{ml/min}$. Therefore, the reverse trend mentioned for the largest amplitude is now consistent with the conclusion. Deductions from the observed performances are used in the next section to evaluate how the fitted correlation data reliably emulate the effect of varying the key parameters.

Table 4-1. Acceleration and Vibrational Reynolds number for the large amplitude vibration test runs.

Test case	Frequency (Hz)	Amplitude (mm)	Acceleration (unit of g)	Vibrational Reynolds Number (-)
1	3	2	0.072	2563.202
2	6	2	0.289	5126.404
3	3	4	0.145	5126.404
4	6	4	0.579	10252.81
5	3	8	0.289	10252.81
6	6	8	1.159	20505.62
7	1.9	12	0.174	9740.167

4.3. Fitting the predictive correlation models

In choosing a reliable and applicable correlation model either for the purpose of design, or for thermal management of a hybrid electric vehicle cooling system, three issues are important. First it is important for the correlation to be valid in the range of the desired operational conditions. Second, the

reliability of the correlation model should be checked to establish the error band with which the correlation model is able to predict the experimental data (by comparison to the model accuracies shown in Table 1-1). Third, precision measuring instruments themselves add some uncertainty to the measured empirical data. The uncertainty of measured experimental data can be undertaken using the method proposed by Moffat [99]. All the available correlations in nucleate boiling regime are classified in Table 1-1, allowing different models to be chosen based on their operational conditions and experimental uncertainties, as well as modelling or data fitting errors. (Only the reported limitations are given in Table 1-1 since the operational conditions are reported with different hydrodynamic parameters).

For the specific aim of thermal management, owing to the undetectable variability in machining, the flow field of spray might differ, resulting in a sizeable error associated with using correlations. This may be the case even if the particular nozzle used, is consistent with information reported in the literature. Considering this, there are concerns about using spray flow data from one nozzle to predict the heat transfer characteristics of a different nozzle, even if they have the same geometry. Overall, the ideal solution is to use the same nozzle [44] to obtain both the hydrodynamic and heat transfer characteristics, and then try to use a fitting function, or any other modelling approach, to make a unique correlation for every nozzle.

Here the correlations developed by Dimensional Analysis and Similitude (Table 2-2) will be fitted to the measured data. The whole database associated with *Static* and *Dynamic* cases is considered in the data fitting process. The best root-mean-square error and average deviation for both *Static* and *Dynamic* cases is deemed an appropriate basis on which to fit the models. The model parameters are calculated using a nonlinear data fitting method via least square regression with an optimisation option of ‘bisquare’ for robustness, using the Levenberg-Marquardt algorithm all available in Matlab. Only the

results using this option are presented. In the current study, which has invariant parameters of chamber pressure and subcooling degree, the predictive model functions (for both cases) from Table 2-2, have been chosen.

For *static* results, Figure 4-9a shows the experimental results compared with the predicted data points using the chosen model function according to:

$$Bo = 3.9 \times 10^{-2} Ja^{1.557} \left(\frac{\rho_l^2 \sigma v}{{\mu_l}^3}\right)^{0.501} \quad (4\text{-}3)$$

where Bo is Boiling number ($qH/\mu_l h_{fg}$), and Ja is Jakob number ($Ja = C_l \Delta T / h_{fg}$), which considers both the convective and boiling heat transfer.

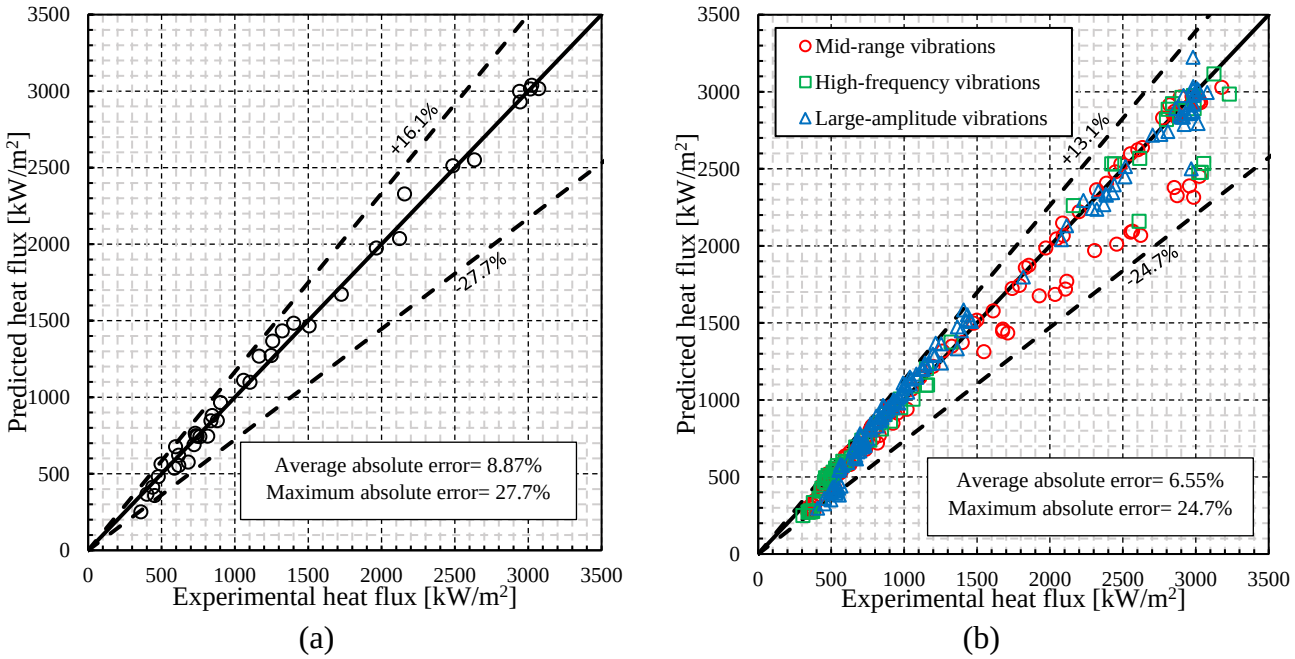

Fig. 4-9. Results predicted by correlations with the error windows: (a) *static* and (b) *Dynamic*.

For the measured *Dynamic* data, three ranges of high frequency, large amplitude, and mid-range frequency is designated to cover the entire operating region (Table 3-2).

Figure 4-9b shows the predicted results compared with the experimentally-measured data based on the fitted correlation model:

$$Bo = 1.2 \times 10^{-2} Ja^{1.392} \left(\frac{\rho_l^2 \sigma v}{{\mu_l}^3}\right)^{0.981} Re_V^{-0.987} \left(\frac{a}{H}\right)^{0.483} Ac^{0.499} \quad (4\text{-}4)$$

where $Re_V = \rho_l a \omega d_H / \mu_l$, the Vibrational Reynolds Number is used for the first time, which includes both the amplitude and frequency effects on the heat transfer rate, and where $Ac = \omega^2 a/g$, is the Dimensionless Acceleration Number.

Discussion of the fitted correlation models

For the *static* correlation model comparison, all the predicted results (of 42 data points) are shown between the error windows of -27.7% and +16.1%, with an average absolute error of 8.87%. The maximum absolute error occurred in the predicted data obtained for the data point with the lowest heat flux of 359.68 $\mathrm{kW/m^2}$at the flow rate of 180 ml/min (nozzle height of 17mm in Figure 4-1). As was mentioned previously, this flow rate had a reverse trend, which could be a reason for adversely affecting the prediction. Nonetheless, considering the low number of data points, and consequently low resolution in the *static* database, the correlation prediction quality comparing to the rest of the available models is of acceptable quality (with reference to the error bands in Table 1-1).

For the *dynamic* correlation model comparison, which is based on Vibrational Reynolds Number and Acceleration Number, this confirms reasonable prediction capability with average and maximum absolute errors of 6.55% and 24.7% respectively. The underestimation of -24.7% is mostly related to the mid-range vibrations for heat fluxes above 1500 $\mathrm{kW/m^2}$. For the large amplitude, low frequency vibration results (which are important for the thermal management in hybrid electric vehicles), most of the scatter (i.e. an underestimation and overestimation of +13.1%) is related to heat fluxes less than 1500 $\mathrm{kW/m^2}$. However, for most cooling systems, higher heat removal is important to keep surface

temperatures within a safe temperature range. Furthermore, since the correlation is concise and flexible enough to easily update its empirical coefficients (such as being needed to fit the model for use with other nozzles and operating conditions), the models fitted here potentially offer promising applications to future model-based spray evaporative cooling control systems [31, 147].

Further improvements can be obtained by allocating a dynamic model to every mechanical vibration range, i.e. Mid-range (a=0.08-1 mm, f=10-200 Hz), High-frequency (a=0.02 mm, f=100-400 Hz) and Large-amplitude (a=2-12 mm, f=1.9-6 Hz) vibrations. After nonlinear data fitting, new parameters associated with each range and resultant prediction errors are listed in Table 4-2. As can be seen, average absolute deviations and maximum absolute errors are all improved in comparison to the values for the whole range. As can be seen in Table 4.2, the parameters obtained for Mid-range vibrations are different from those obtained for High-frequency and Large-amplitude vibrations. This is because the trends of the data for High-frequency and Large-amplitude vibrations differ from the trend of data for Mid-range vibrations (as was explained in the previous sections). Figure 4-10 shows the predicted results compared with the experimentally-measured data for each range. The error windows are all improved in comparison with those for the whole range prediction.

Table 4-2. Dynamic correlation parameters and prediction errors for different vibration ranges.

Dynamic correlation model $Bo = a\,Ja^{\mathrm{b}}(\frac{\rho_l^2\sigma v}{\mu_l{}^3})^{\mathrm{c}}Re_V^{\mathrm{d}}\left(\frac{a}{H}\right)^{\mathrm{e}}Ac^{\mathrm{f}}$, Parameters: a, b, c, d, e, f

Vibration range	Parameters						Average absolute error (%)	Maximum absolute error (%)
	a	b	c	d	e	f		
Whole	0.012	1.392	0.981	-0.987	0.483	0.493	6.55	24.7
Mid	0.016	1.380	0.984	-1.035	0.504	0.525	2.4	22.4
High-frequency	0.001	1.382	1.058	-0.489	0.781	0.245	1	22.2
Large-amplitude	0.001	1.454	0.883	-0.454	0.204	0.238	3.06	23.2

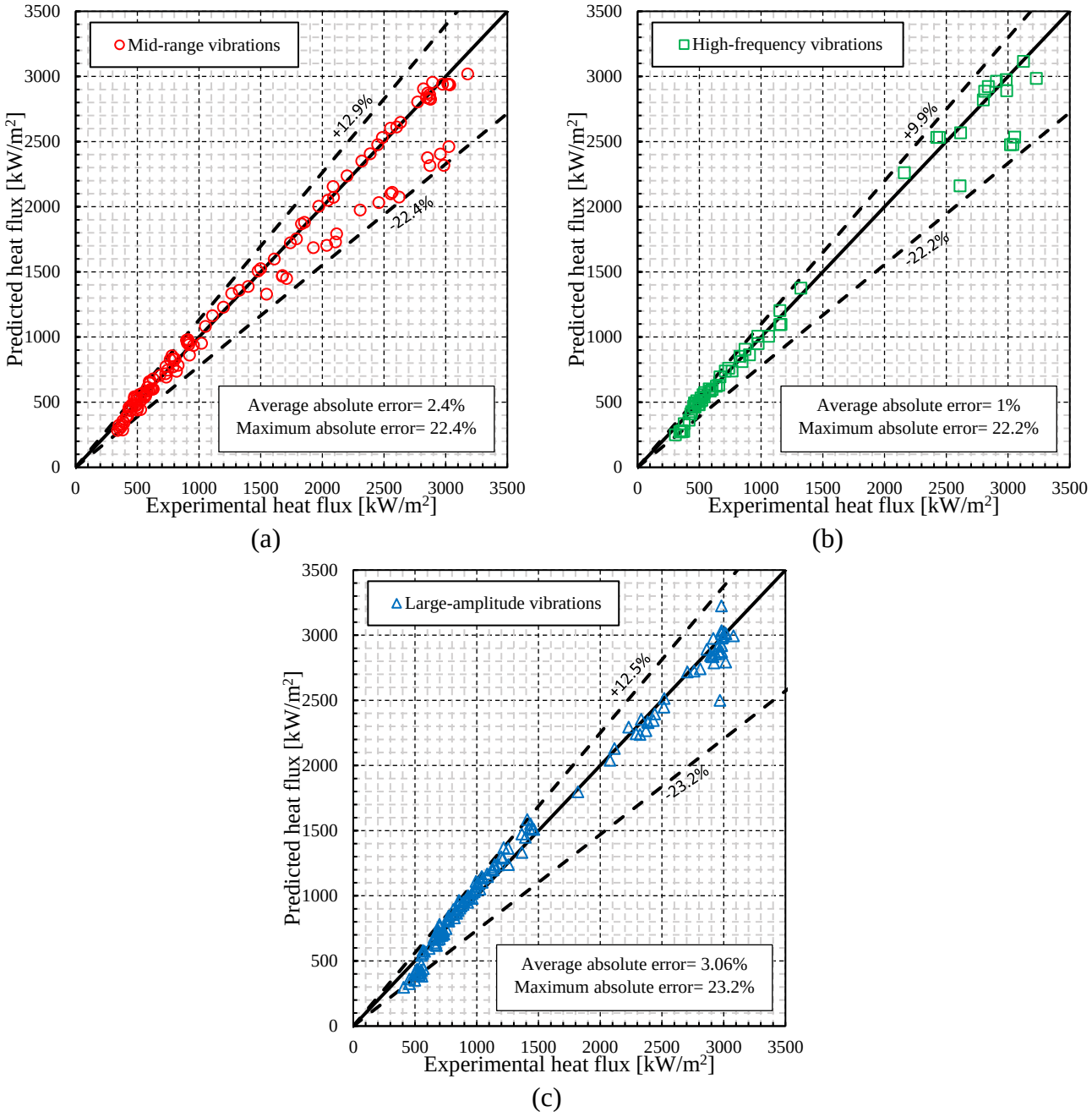

Fig. 4-10. Improved dynamic correlations for vibration ranges: (a) *Mid-range*, (b) *High-frequency* and (c) *Large-amplitude*.

The nucleate boiling results are based on a single nozzle from one manufacturer (i.e. UNIJET TG type). At the same volume flow rate, a nozzle with a different design can have very different spray characteristics. It is well-known that not only for a nozzle with different design, but also for a nominally identical nozzle from the same manufacturer, undetectable variability in machining, may cause the flow field of spray to differ across a population of nozzles. This variability can result in a significant error

associated with the use of correlations even if the nozzle is used consistently. Ideally, the best approach is to use the same nozzle [44] to obtain both the hydrodynamic and heat transfer characteristics, and then to try to use a fitting function or another modelling approach to construct a unique correlation for every nozzle. But in thermal management, a successfully-tuned robust controller can itself compensate for the errors associated with using a correlation model fitted to data for one nozzle. Being used as the plant model involving different nozzles. Evidence to support this hypothesis is published in [148], where the same correlation used in this study for a UNIJET nozzle (i.e. equation (4-4)), is used for the plant model with two PJ nozzles.

4.4. Conclusions of Chapter 4.

The effect of dynamic behaviour on the nucleate boiling regime of spray evaporative cooling of a horizontal flat test piece with, and without vibration, has been examined using measured data, and appropriate dynamic correlation models (developed in Chapter 2) have been adopted. The flat test-piece was excited by a shaker with water coolant supplied to the vibrating heated surface via a spray nozzle. Using a full-cone nozzle, four volumetric flow rates of 140 $\mathrm{ml/min}$, 160 $\mathrm{ml/min}$, 180 $\mathrm{ml/min}$ and 200 $\mathrm{ml/min}$ were tested. These flow rates are shown to be dependent on the range of vibrations, and the heights of the nozzles. Three sets of dynamic conditions have been investigated including a ‘mid-range’ frequency, a ‘high’ frequency, and large-amplitude vibrations at ‘low’ frequency. For the mid-range vibrations at frequencies from 10 Hz to 200 Hz, the amplitudes vary from 0.08 mm to 1 mm. Three high-frequency vibration test were undertaken at 100 Hz, 200 Hz, and 400 Hz, with a fixed amplitude of 0.02 mm, and varying flow rates of 140, 160, 180, and 200 $\mathrm{ml/min}$, at nozzle distances above the test piece of 17mm and 21mm. Large-amplitude vibration tests were undertaken at frequencies of 1.9 Hz, 3 Hz, and 6 Hz, with amplitudes

varying from 2 mm to 12 mm (emulating conditions associated with real vehicle dynamics) where the nozzle-to-surface distance was 17 mm, giving the highest effective flow rate. The main conclusions of Chapter 4 are:

- Any increase in volumetric flow-rate, under both *Static* and *Dynamic* conditions, was found to cause heat transfer coefficient augmentation, except for a flow rate of 180 $\mathrm{ml/min}$, at a nozzle height of 21 mm, where a reverse trend occurred. The reason for this reverse trend can be attributed to an increase in spray cone-angle with increasing flow-rate. Below a nozzle-specific cone angle threshold, heat flux increases with cone-angle. But when this threshold is exceeded, heat flux declines with further increase in cone-angle.
- For the mid-range vibration frequencies from 10 Hz to 200 Hz, the amplitude in general impedes the heat transfer rate, while the effect is more visible on the lower excess temperatures (less than 30 ˚C). Increasing frequency, augments the heat transfer by the increased Reynolds Number and Acceleration. However, the effect of vibration generally results in an attenuation in heat transfer compared with *static* cases. Several mechanisms have been identified as the reason depending on the vibration amplitude and frequency, flow rate, and excess temperature. At low amplitude, high frequency vibration, high surface acceleration causes bubble suppression which influences nucleate boiling, particularly for low flow rate. At high amplitude, low frequency vibration, there are two opposing effects associated with increasing dimensionless Acceleration Number which enhances heat transfer, and increasing Vibrational Reynolds Number, which suppresses heat transfer and proves to be more dominant.
- For high-frequency vibration, the heat transfer decline occurs more prominently for the lower nozzle height of 17 mm compared to the higher nozzle height of 21 mm. The maximum heat flux

reduction of -30.1% occurred for the lowest flow rate of 140 $\mathrm{ml/min}$ at the lowest level of 'superheating' of 10 ˚C. The reason appears to be that lower nozzle heights have greater sensitivity to bubble suppression, which influences nucleate boiling causing a reduction in heat transfer.

- A performance evaluation of large-amplitude vibrations demonstrated that there is a balance between the deteriorating effect of vibration and the enhancing influences of acceleration and flow rate.
- The results of the deriving and fitting new dynamic correlation models shows very reasonable prediction quality, which can be reliably used for future model-based thermal management applications.

5. CORRELATION MODELS OF CRITICAL HEAT FLUX AND ASSOCIATED TEMPERATURE FOR SPRAY EVAPORATIVE COOLING OF VIBRATING SURFACES

In this Chapter, the objective is to reveal the influences of vibration on the CHF and excess temperature, for vibration parameters relevant to the road transport sector. In addition, the correlation models of CHF (already constructed in Chapter 2) and corresponding excess temperature (described in this chapter) are fitted to experimentally-measured data. This objective will be achieved by a detailed examination of the effects of vibration on the CHF and excess temperature, culminating in the calibration of correlation models to provide a predictive capability for the observed physics. These empirical correlations cannot only be employed in the design process of spray evaporative cooling systems but also in the thermal management of such systems.

In the following sections, the influence of key parameters on the CHF and excess temperature are discussed. First, the effect of flow rate and degrees of subcooling with, and without vibration will be examined. This is to help understand the physics behind the trends in the data, which are useful for modelling. Second, the effect of vibration on the excess temperature at CHF will be investigated in detail. The maximum achievable temperature is a key parameter owing to its importance for thermal management applications, especially for safety reasons. Finally, correlation models discussed in Chapter 2, have been calibrated for prediction of CHF and maximum temperature.

5.1. Effect of nozzle flow parameters and degrees of subcooling for static surfaces

Flow rate and pressure drop are nozzle flow parameters. Figure 5-1.a shows the trend of the CHF data with three volumetric flow rates of 55 ml/min, 75 ml/min, and 100 ml/min for PJ8, PJ10, and MW145 nozzles. As can be seen for the PJ8 and PJ10 nozzles, CHF increases with flow rate, and this trend is valid for both degrees of subcooling (i.e. 10 and 45 ℃). Researchers such as Toda and Uchida [149], Hou et al. [150], Chow et al. [151], Moreno et al. [152], Estes and Mudawar [106] and Pais et al. [153] reported

that increasing flow rate increases CHF. However, CHF for MW145 has an almost three-fold increase in comparison with those for PJ nozzles, even though the flow rate for MW145 is 55 ml/min. It seems that CHF is not always increasing by volumetric flow rate. Chen et al. [154] and Tilton [155] suggested that the volumetric flow rate has only a subtle or no influence on CHF. The higher CHF for MW145 results stem from: i) a higher nozzle pressure drop (i.e. 7 bar, whereas the pressure drop is between 2.9 to 5.2 bar for PJ nozzles), and ii) different geometrical parameters (e.g. nozzle orifice and cone angle, see Table 3-3) which changes hydrodynamic parameters (such as mean droplet velocity).

In Figure 5-1b the same CHF results are shown as a function of average volumetric spray flux for each nozzle. Chen et al. [154], Estes and Mudawar [106], Pais et al. [153], Lin and Ponnappan [156], and Monde [157] have all suggested that CHF for different nozzles increases with volumetric flux without any reverse trends. Figure 5-1.b demonstrates the same behaviour for the PJ8 (0.77×10^{-3} m^3s^{-1}/m^2), PJ10 (1.05×10^{-3}-1.40×10^{-3} m^3s^{-1}/m^2), and the MW145 (9.03×10^{-3} m^3s^{-1}/m^2). The average volumetric flux, $\bar{\vec{v}}$, is proportional to volumetric flow rate, v, and can be calculated according to equation (5-1) [50]:

$$\bar{\vec{v}} = \frac{v}{\pi(Htan\left(\frac{\alpha}{2}\right))^2} \tag{5-1}$$

where H is nozzle-to-surface distance, and α is the spray cone angle.

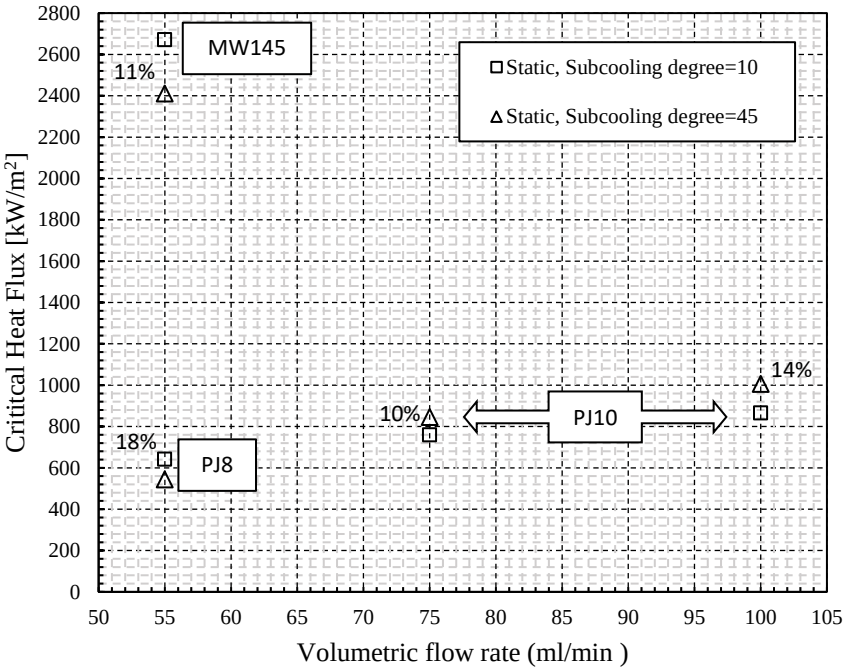

(a)

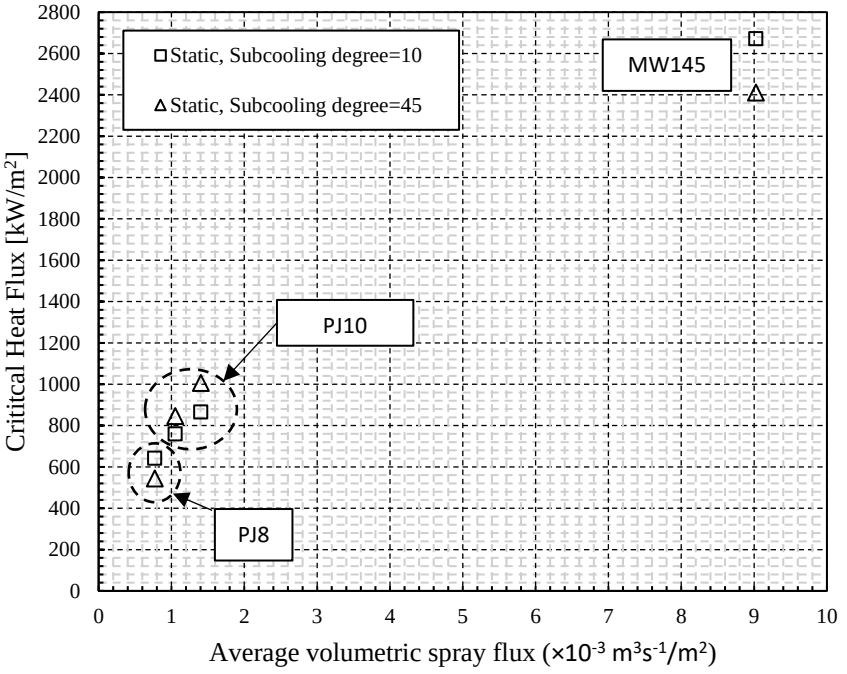

(b)

Fig. 5-1. CHF trend for static cooling surfaces based on nozzle flow parameters and degrees of subcooling.

Figure 5-1a also shows the subcooling effect on the CHF. For the PJ8 and MW145, with a lower flow rate of 55 ml/min, CHF values decrease by higher subcooled conditions at 45 ℃. As can be seen, the deviations for the PJ8 and MW145 are respectively 18 per cent and 11 per cent. This means that the

CHF acquires a higher value as soon as subcooling is closer to saturated conditions. Thiagarajan et al. [109] reported the same behaviour for the subcooling influence of low flow rate sprays. Conversely, for the PJ10 with higher flow rates of 75 and 100 ml/min, a higher subcooling degree of 45 ℃ enhances the CHF by 10 per cent and 14 per cent respectively. Visaria and Mudawar [158] found a similar trend in their data with subcooling degrees between 22 ℃ and 70 ℃. In their experiments, they noted that the CHF enhancement is more substantial when the subcooling degree exceeds 40 ℃. Overall, the trends of the CHF data for static surfaces are proven to be in good agreement with the literature. In the next section, the effects of the vibrating surfaces on the CHF as well as the excess temperature (also referred to as superheat) will be discussed.

5.2. Effect of vibrating surfaces on CHF and excess temperature

In this section the effects of vibration on CHF and excess temperature for all three nozzles of PJ8, PJ10 and MW145 are assessed. The CHF data points for static and dynamic cases are plotted against excess temperature, subcooling degrees, and volumetric flux to better investigate the combination of different effective parameters. An effect ratio has been defined as the ratio of the dynamic-CHF/static-CHF for subplots containing CHF versus excess temperature. For subplots containing two subcooling degrees and flow rates in which there are two comparable static cases, the effect ratio also includes corresponding static-CHF/static-CHF. Therefore, to make different effect ratios identifiable, three effect ratios are defined and used in corresponding subplots. First, a dynamic effect ratio θ_{Dyn} is defined as the ratio of the dynamic-CHF/static-CHF. Second, a volumetric flux effect ratio $\theta_{\dot{v}}$ includes both dynamic-CHF/static-CHF and corresponding static-CHF/static-CHF ratios. Third, a subcooling effect ratio θ_{SC}, includes both dynamic-CHF/static-CHF and corresponding static-CHF/static-CHF ratios. Data callouts on figures represent the effect ratio. Also legends in all the figures follow the same format to

facilitate inspection. In addition, to make room for inspection it is useful to define the vibration ranges considered. Large-amplitude vibrations include amplitudes from 1 to 8 mm, and frequencies up to 8Hz (the first three dynamic cases in the legends). High-frequency vibrations are the dynamic cases with frequencies above 50Hz, and amplitudes smaller than 1 mm (i.e. the last three dynamic cases in the legends). The dynamic case with a=1mm and f=50Hz corresponds to the highest Vibrational Reynolds Number of 21360, and the largest Acceleration Number of 10. (Vibrational Reynolds Number and dimensionless Acceleration Number are helpful in assessing the combined influence of surface amplitude and frequency at the CHF). These numbers for all the cases are supplied in Table 5-1 (each row is related to the same case as the legends of the figures).

Table 5-1. Static and dynamic cases with associated Acceleration and Vibrational Reynolds Numbers.

Test case	Amplitude (mm)	Frequency (Hz)	Vibrational Reynolds Number (-)	Acceleration (unit of g)
S	0	0	0	0
D-1	8	2	6835.2	0.13
D-2	4	4	6835.2	0.26
D-3	1	8	3417.6	0.26
D-4	1	50	21360	10.06
D-5	0.2	50	4272	2.01
D-6	0.2	100	8544	8.05
D-7	0.04	200	3417.6	6.44

Figures 5-2 and 5-3 show all the data points (CHF versus volumetric flux) for PJ8, PJ10 and MW145 nozzles respectively at two subcooling degrees of 10 and 45 ℃. Figures 5-2.b and 5-3.b show the results of PJ8 and PJ10 nozzles (as zoomed versions). This is to investigate the effect of volumetric flux and compare it with what was found for the static cases in the previous section. At first glance, the general trend in Figures 5-2a and 5-3a shows that CHF increases for dynamic cases with increasing volumetric flux. Considering the effect ratios on Figures 5-2 and 5-3, the enhancement for SC=45 ℃ is more appreciable. However, there are two exceptions in the zoomed-in Figures 5-2.b and 5-3.b including the results for PJ nozzles. These two exceptions are related to dynamic case D-7 with the highest frequency.

One is at SC=10 ℃ for PJ8 (Figure 5-2.b), for which the D-7 case (at $\bar{\vec{v}} = 0.77 \times 10^{-3}$m^{3}s^{-1}/m^2) has a greater CHF value compared to those for D-6, D-5 and D-4 cases of PJ10 with a greater volumetric flux of 1.05×10^{-3}m^{3}s^{-1}/m^2. The effect ratio of PJ8-D-7 is one percent greater than PJ10-D-6 and two percent greater than PJ10-D-5 and PJ10-D-4 cases. The second happened at SC=45 ℃ for D-7 case of PJ10 (Figure 5-3.b) at $\bar{\vec{v}} = 1.05 \times 10^{-3}$m^{3}s^{-1}/m^2, at which the CHF acquires a slightly greater value than D-4 at $\bar{\vec{v}} = 1.40 \times 10^{-3}$m^{3}s^{-1}/m^2 (Effect ratios for D-7 and D-4 at these volumetric fluxes are respectively 1.60 and 1.59). As was mentioned, D-4 has a larger amplitude and a lower frequency and has the highest Reynolds Number. The immediate reason for this reverse trend can be attributed to the enhancing effect of vibration for D-7 cases of PJ nozzles. However, further investigation is required to explain the effects of different elements of vibration such as amplitude and frequency, as well as the dependence on non-dimensional numbers of Acceleration and Reynolds Number. In the next subsections the influences of different key parameters are discussed.

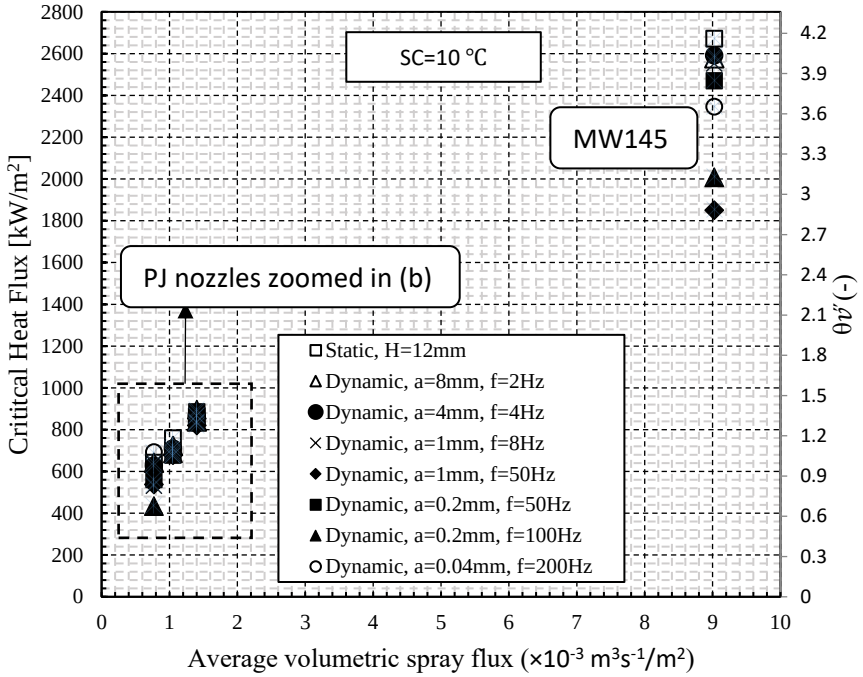

(a)

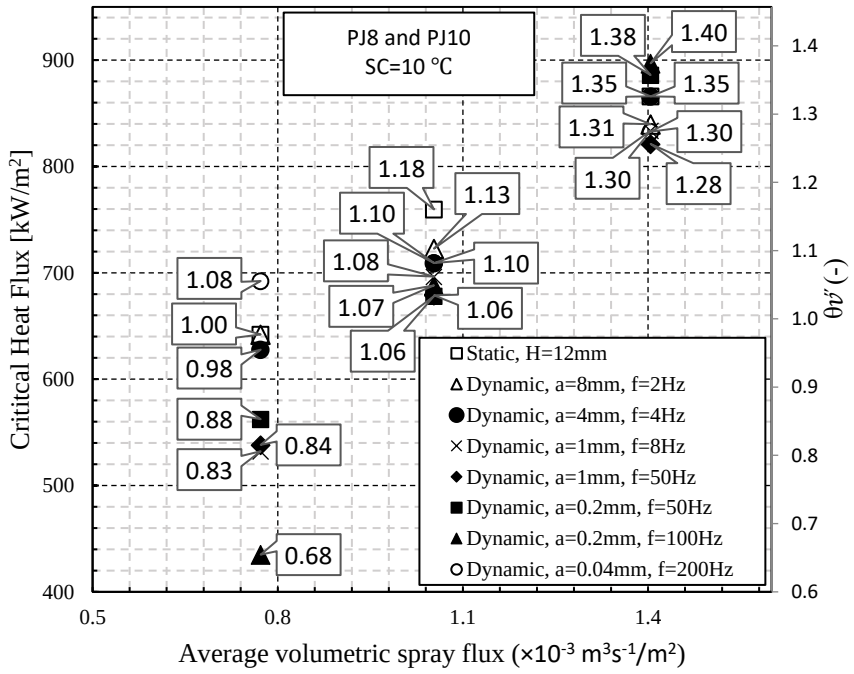

(b)

Fig. 5-2. CHF data points against volumetric flux at SC=10 ℃ : a) PJ and MW145 database b) zoomed version of PJ8 and PJ10 test cases.

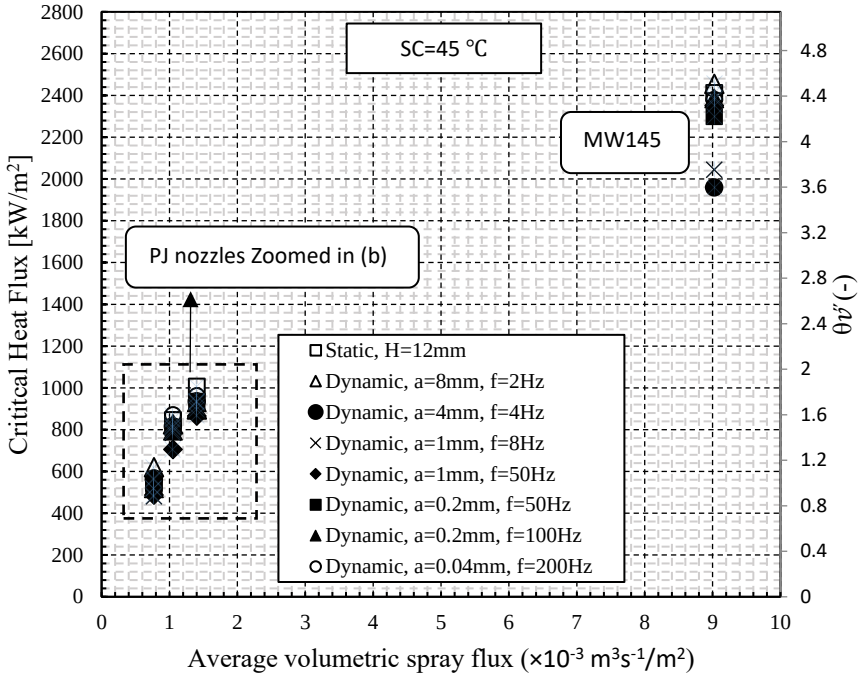

(a)

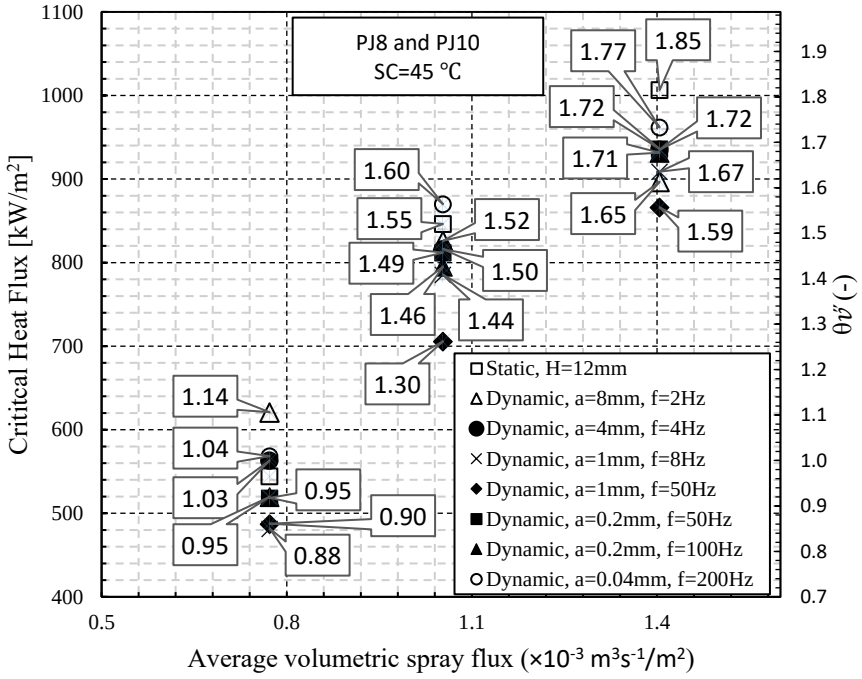

(b)

Fig. 5-3. CHF data points against volumetric flux at SC=45 ℃: a) PJ and MW145 database b) zoomed version of PJ8 and PJ10 test cases.

The largest deviation from the static CHF and the effects of Subcooling degrees

Figures 5-4 and 5-5 demonstrate all the data points for the PJ10 nozzle. Figures 5-6 and 5-7 contain the results of PJ8 and MW145 nozzles, respectively. As can be seen in Figures 5-4 to 5-7, CHF data points for the dynamic cases from the large-amplitude to high-frequency vibrations have resulted in a deviation from the corresponding static cases. For PJ10, as can be seen in Figures 5-4 and 5-5 (for both subcooling degrees in subplots a and b) the largest deviation from the static CHF belongs to the case D-4 with a=1 mm and f=50 Hz, and with the highest Reynolds number and largest Acceleration number (See effect ratios for each data point as shown by data callouts). For the flow rate of 75ml/min, at subcooling of 10 ℃ (Figure 5-4.a) the effect ratio for case D-4 is 89 percent, and at subcooling of 45 ℃ (Figure 5-4.b) the effect ratio is 83 per cent. It seems that the deterioration effect of vibration for the dynamic case D-4 (as shown by a diamond marker) becomes more appreciable by increasing the subcooling degree. The same behaviour for the same test case of D-4 can be seen for the flow rate of 100 ml/min. As can be seen in Figures 5-5.a and 5-5.b, at the subcooling of 10 ℃, the smallest effect ratio is 95 per cent which reduces to 86 per cent at the subcooling of 45 ℃.

For the PJ8, D-6 has the lowest effect ratio of 68% at SC=10 ℃ (Figure 5-6a). However, by increasing the subcooling to 45 ℃ the impeding effect of vibration reduces, and the D-6 datapoint has a 95% deviation. The same behaviour is valid for the MW145. The lowest effect ratio of 69% (for D-4 at 10 ℃ subcooling) increased to 98% at 45 ℃ of subcooling (Figure 5-7). This is opposite to what was found for the PJ10 with the lowest effect ratio to subcooling. The reason for this can be related to the reverse heat transfer trend (as was found in the previous section for static cases) stemming from the subcooling effect at low flow rate for the PJ8 and MW145 nozzles in comparison with the higher flow rate nozzle PJ10. To investigate this reverse trend, the subcooling influence is now discussed.

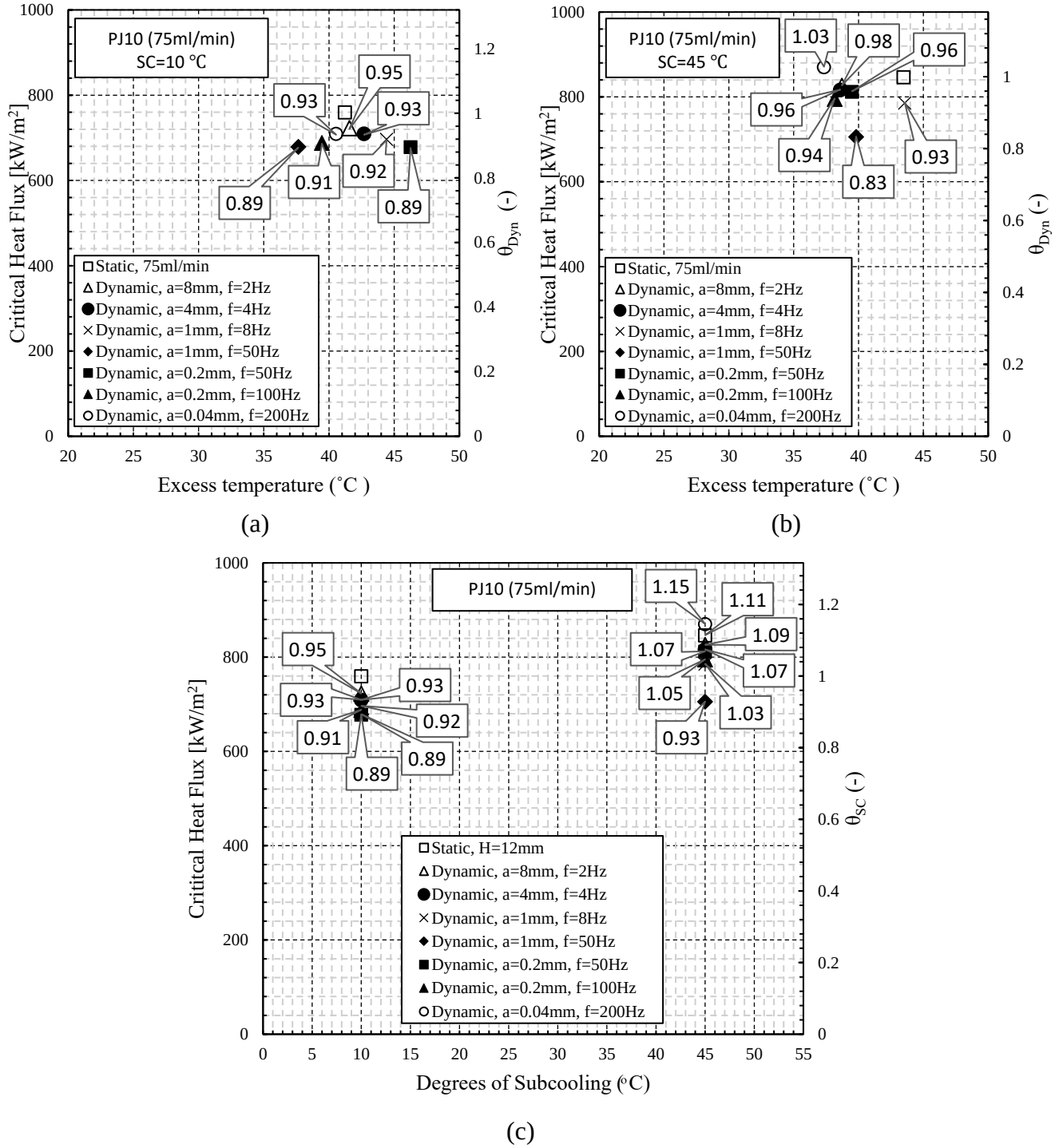

Fig. 5-4. CHF data points of PJ10 at 75 ml/min against excess temperature at $SC = 10$℃ (a) and $SC = 45$℃ (b), and the effect of subcooling on CHF (c) for the case studies involving static and dynamic cooling surfaces.

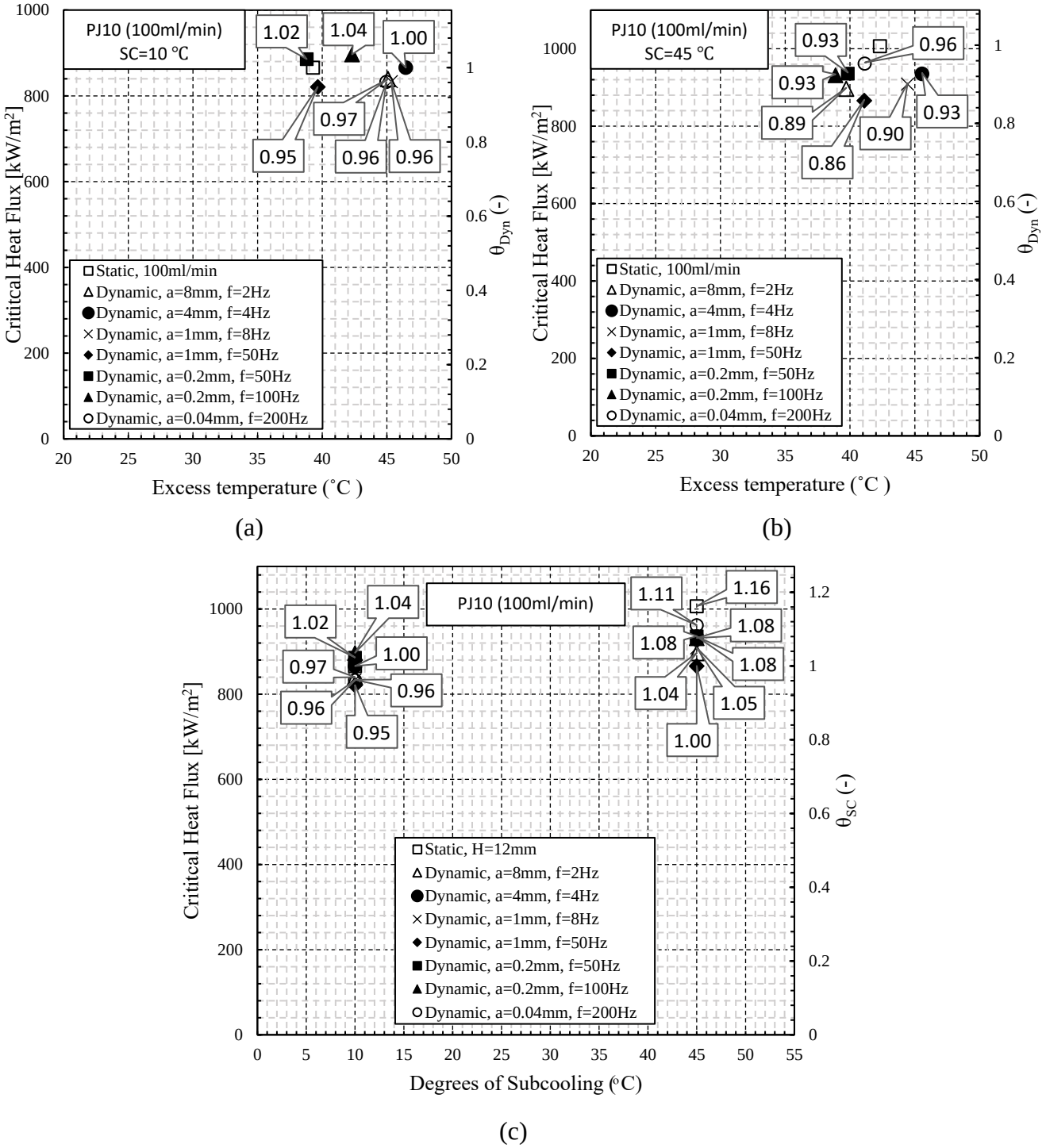

Fig. 5-5. CHF data points of PJ10 at 100 ml/min against excess temperature at $SC = 10$℃ (a) and $SC = 45$℃ (b), and the effect of subcooling on CHF (c) for the case studies involving static and dynamic cooling surfaces.

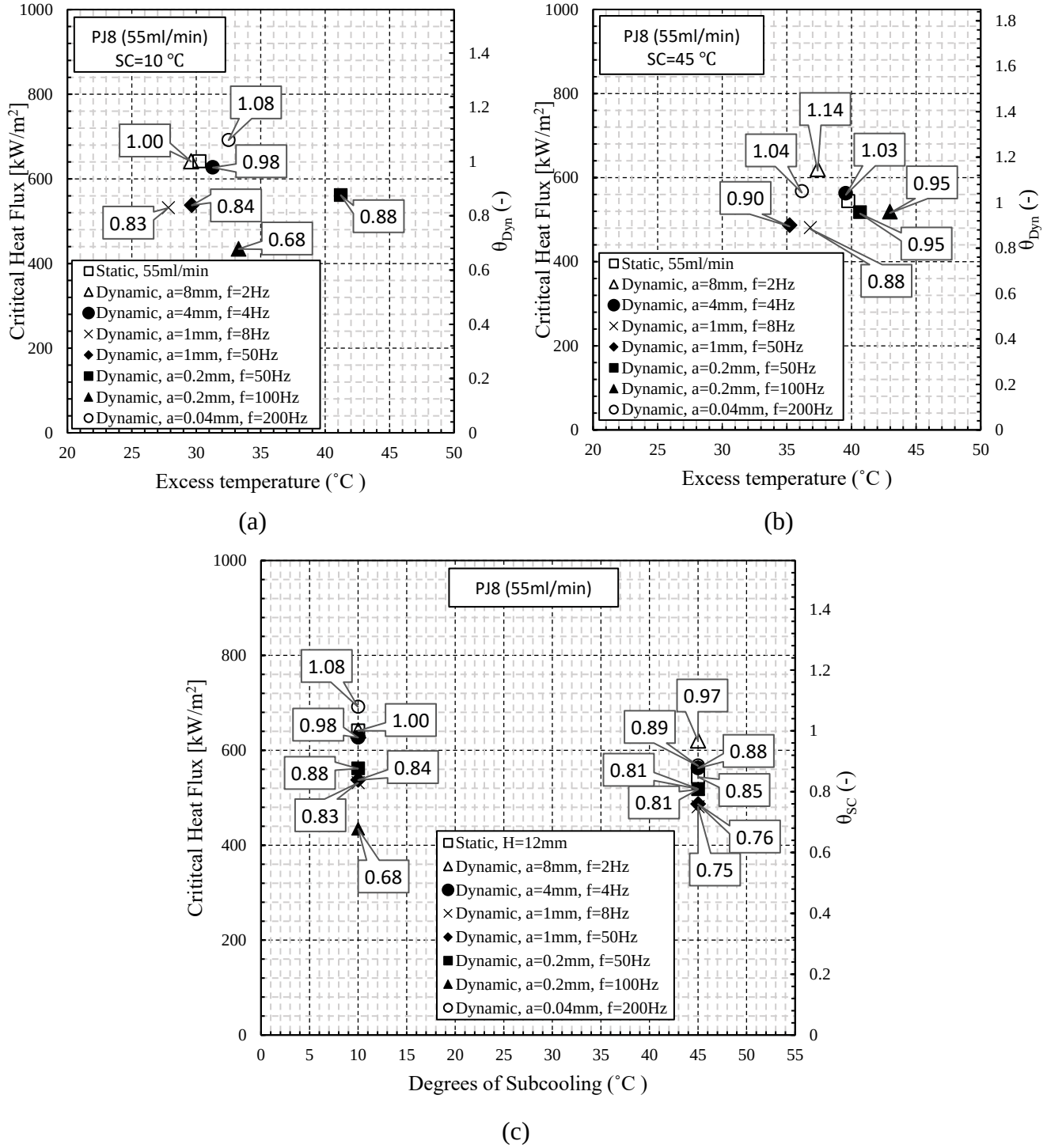

Fig. 5-6. CHF data points of PJ8 against excess temperature at $SC = 10$℃ (a) and $SC = 45$℃ (b), and the effect of subcooling on CHF (c) for the case studies involving static and dynamic cooling surfaces.

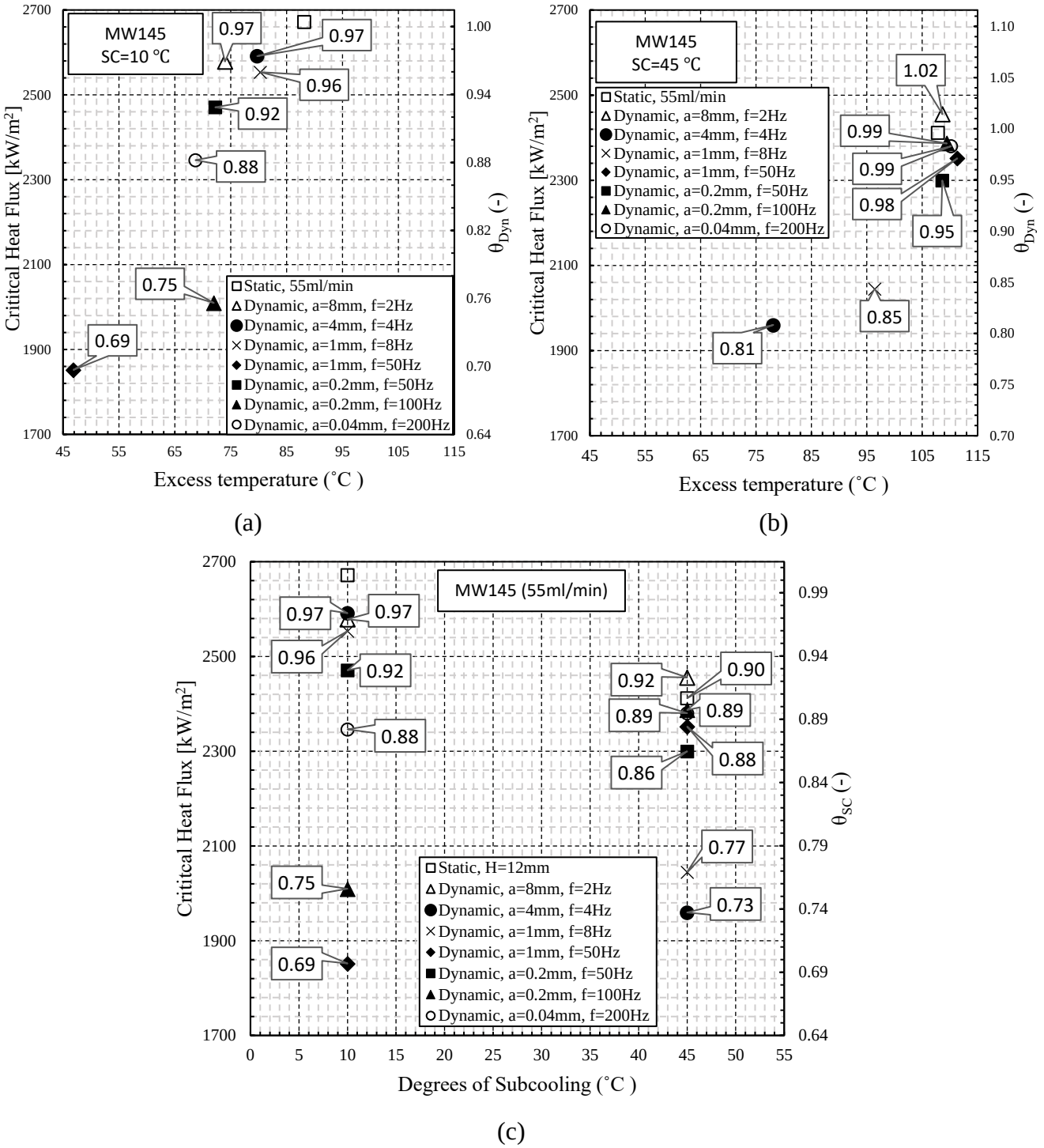

Fig. 5-7. CHF data points of MW145 nozzle against excess temperature at $SC = 10$℃ (a) and $SC = 45$℃ (b), and the effect of subcooling on CHF (c) for the case studies involving static and dynamic cooling surfaces.

To find out the influence of subcooling on dynamic-CHF data and compare that behaviour to what was found for the static cases in the previous section, subplots c of Figures 5-4 to 5-7 are shown. For the

PJ10 (at both flow rates in Figures 5-4.c and 5-5.c), the effect ratio for every dynamic case has been increased by increasing the subcooling degree. It is still following the same trend (as in the previous section). Therefore, increasing subcooling degrees for PJ10 increases CHF for its static and dynamic cases.

For the PJ8 and MW145, the behaviour is supposed to be opposite to PJ10 trend (as was found for the static cases). Inspecting the effect ratios in Figures 5-6c and 5-7c suggests that this trend is still valid apart from two cases of high-frequency vibrations of D-6 (for PJ8 and MW145) and D-4 (only for MW145). The CHF for case D-6 at SC=45 ℃ has higher values for both the PJ8 and MW145. The CHF for the D-4 case of MW145 nozzle acquires a higher value at the higher subcooling of 45 ℃. It clearly shows that the impact of vibrational elements such as surface amplitude and frequency can be responsible for the change in the trend. To reveal this further, the effect of vibration, in particular, the influence of amplitude and frequency, is now examined in more detail.

Effect of amplitude and frequency of vibrating surfaces

To establish whether the amplitude of vibrating surfaces has any effect on the dynamic-CHF, D-5 (a=0.2mm) and D-4 (a=1mm) cases, with a frequency of 50Hz, have been examined. D-5 and D-4 cases are respectively shown in Figures 5-4 to 5-7 (with square and diamond markers). For the PJ10, the vibration amplitude has a deteriorating effect on CHF (except for the case of flow rate 75 ml/min and subcooling of 10 ℃, which has no effect). The highest impeding effect of 13%, occurs for the flow rate of 75 ml/min at subcooling of 45 ℃ (noting that on Figure 5-4.b, D-5 and D-4 effect ratios are 0.96 and 0.83). At the flow rate of 100 ml/min (Figure 5-5), this deterioration effect for both subcooling degrees is 7%. Results for PJ8 (Figure 5-6) support the impeding effect of vibration amplitude on CHF. For subcooling degrees of 10 and 45 ℃, the impeding effects are respectively 4% and 5%, therefore, the

subcooling influence is only 1%. However, for MW145, at subcooling of 45 ℃ (Figure 5-7b), amplitude shows an enhancing influence. To address this reverse trend, the influence if the frequency of vibration should be examined.

To assess the effect of frequency of vibrating surfaces D-3 (f=8Hz) and D-4 (f=50Hz), cases with an amplitude of a=1mm are examined. The data associated with cases D-3 and D-4 are respectively shown by cross and diamond markers. Examination of these two cases for MW145 at SC=45 ℃ (Figure 5-7b), the frequency caused 13% enhancement (For D-3 the effect ratio is 0.85, and for D-4 it is 0.98). Whereas for SC=10 ℃ (Figure 5-7a), the frequency gives rise to 27% deterioration. Comparing the effects of amplitude and frequency for the MW145 offers the supposition that vibration frequency plays a dominant role. Small heat transfer enhancements are also seen in Figures 5-6a (1% increase at SC=10 ℃) and 5-6b (2% enhancement at SC=45 ℃) for the PJ8. For the PJ10 (Figures 5-4 and 5-5), for all the flow rates and subcooling degrees frequency has a deteriorating effect on the dynamic-CHF. The differences between these two cases in Figures 5-4a (SC=10 ℃), 5-4b (SC=45 ℃), 5-5a (SC=10 ℃), and 5-5b (SC=45 ℃) are respectively 3%, 10%, 1% and 4%. The impeding effect is more considerable for higher subcooling degrees of 45 ℃. It seems that by increasing the flow rate the deterioration influence decreases. In summary, frequency and amplitude is found to be a strong influence which suggests that non dimensional parameters considering the effect of both vibrational elements may explain such contradictory behaviour and give rise to better understanding. The next section, examines the effect of vibration specifically in terms of Vibrational Reynolds Number and Acceleration Number.

Impact of vibrational Reynolds and Acceleration numbers

Vibrational Reynolds and Acceleration numbers are useful in representing the dynamic nature of a spray field on a vibrating surface, such as the effect of vibration on droplet rebound, splash and liquid film

thinning. These dimensionless parameters are employed to investigate the complex influence of vibration on heat transfer. To assess this influence, cases D-3 (Re=3417.6) and D-2 (Re=6835.2) with the same Acceleration Number of 0.26 are considered. A comparison of all data points of D-3 and D-2 in Figures 5-4 and 5-5, reveals that for both flow rates and subcooling degrees of PJ10 nozzle, increasing Reynolds Number from 3417.6 to 6835.2 enhances the CHF but then impedes the CHF for the highest Reynolds Number (Re=21360, D-4). To support this claim, all the associated effect ratios are supplied in Table 5-2. For all data points in Table 5-2, the associated CHF values against Reynolds and Acceleration Numbers are shown in Figure 5-8 to facilitate the interpretation of the trends. For flow rate of 75ml/min, at SC=10 ℃ (Figure 5-4a), the effect ratio of D-3, D-2 and D-4 are respectively 0.92, 0.93, 0.89. For the same flow rate, at SC=45 ℃ (Figure 5-4b), the effect ratios of D-3, D-2 and D-4 are 0.93, 0.96, 0.83. As can be interpreted from Table 5-2, PJ nozzles follow the above mentioned behaviour for all the flow rates and subcooling degrees (as can also be seen in Figure 5-8a). The only exception is MW145 at SC=45 ℃ for which the effect ratio is first reduced through an increase in Reynolds Number (from 3417.6 to 6835.2) and then increased for the highest Reynolds Number. This is a converse trend in comparison to the other cases, which for the MW145 can be explained by its high dependency on the subcooling effect. The spray field for MW145 is a light fog resulting in a thinner liquid film on top of the cooling disc, whereas the PJ nozzles are misting nozzles which, from experimental observation, have a relatively thicker liquid film. For that reason, it appears that the MW145 is less dependent on the effect of Reynolds Number and Acceleration Number.

To explore the Acceleration effect, the results for the test cases of D-3 (Ac=0.26) and D-7 (Ac=6.44) with a Reynolds Number of 3417.6 are compared in Table 5-1 (as also shown in Figure 5-8.b). For PJ nozzles, CHF associated to D-7 are all enhanced by the larger acceleration except for flow rate 100ml/min at subcooling of 10 ℃ which acceleration does not have any influence on CHF. The enhancing effect of

acceleration is consistent with the results of Michalak et al. [118] for the acceleration range of $0.15g < Ac < 1.80g$. However, other studies, such as works done by Zhang et al. [159, 160] and Conrad et al. [161], suggest that the acceleration enhancement is limited to the operating conditions – other parameters have greater influence over heat flux. For the MW145, at SC=10 ℃, there is a decrease in the effect ratio for D-3 and D-7 which shows that other key parameters determine this impeding effect. As was confirmed for the MW145 at SC=10 ℃ (in the previous section), frequency has a noticeable deteriorating effect, in fact switching the frequency from 8Hz (D-3) to 200Hz for case D-7 supports the independence of MW145 results to Acceleration. Another key parameter responsible for this reverse behaviour for Reynolds Number can be the considerable effects of subcooling. In the next section, the complex effects of vibration and subcooling degrees on the maximum temperature (at which CHF occurs) are investigated.

Table 5-2. Effect ratios for the chosen dynamic cases to explore the Acceleration and Vibrational Reynolds effects.

	PJ10				PJ8		MW145		Re_V	Ac
Flow rate (ml/min)	75		100		55		55			
Subcooling (℃)	10	45	10	45	10	45	10	45		
D-3	0.92	0.93	0.96	0.90	0.83	0.88	0.96	0.85	3417.6	0.26
D-2	0.93	0.96	1	0.93	0.98	1.03	0.97	0.81	6835.2	0.26
D-4	0.89	0.83	0.95	0.86	0.83	0.90	0.69	0.98	21360	10.06
D-7	0.93	1.03	0.96	0.96	1.08	1.04	0.88	0.99	3417.6	6.44

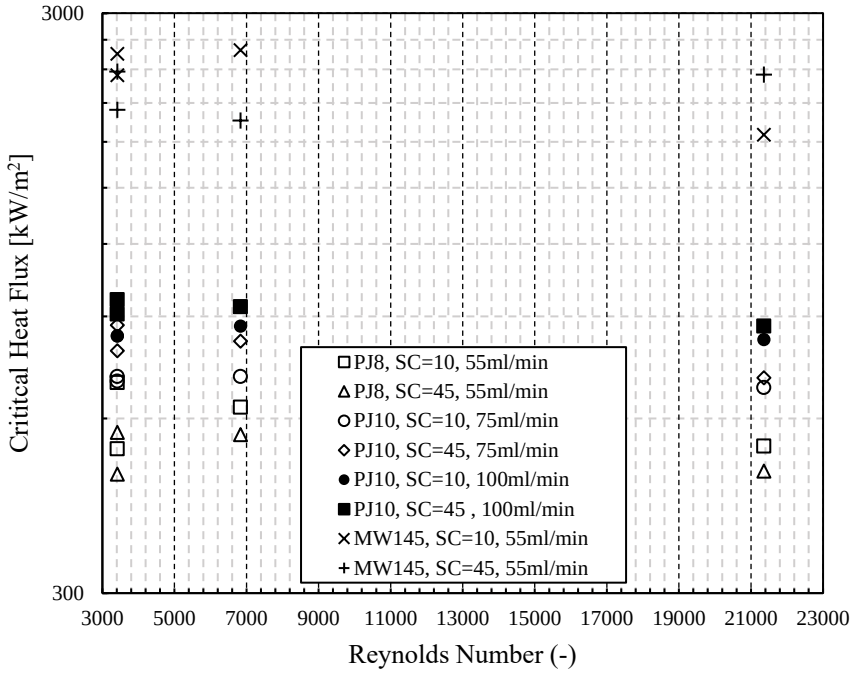

(a)

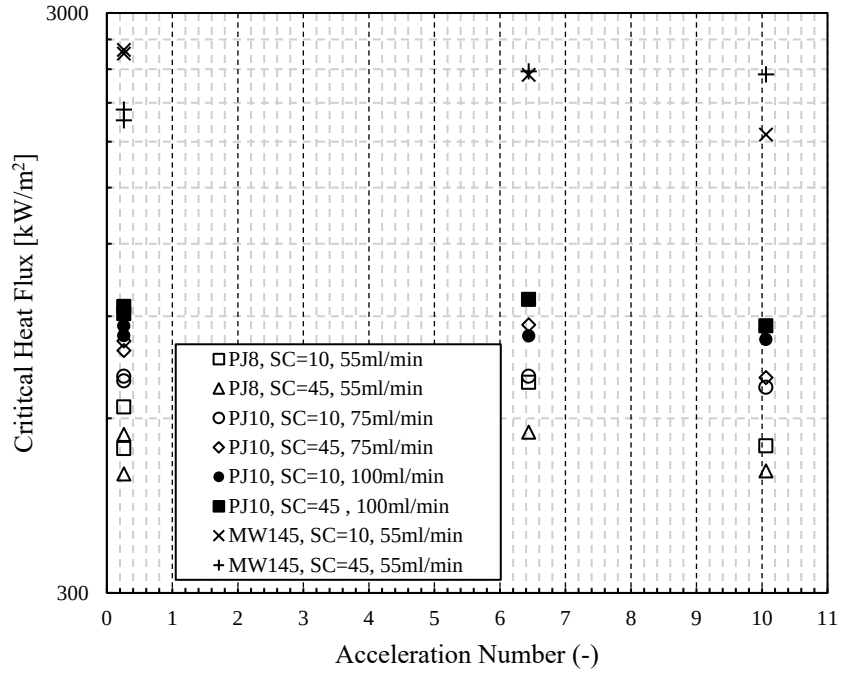

(b)

Fig. 5-8. Vibrational Reynolds Number effect (a), and Acceleration Number effect (b), for the chosen dynamic cases in Table 5-2

Effect of vibration on excess temperature

By further inspection of Figures 5-4a, 5-4b, 5-5a, 5-5b, 5-6a, 5-6b, and Figure 5-7, it is observed that vibration changes the excess temperature at which the Static-CHF occurs. It is evident that, Acceleration and Reynolds Numbers affect the dynamic behaviour of the spray field and consequently the heat transfer mechanisms. For instance, vibrating surfaces with different amplitude and frequencies can be responsible for both thinning and thickening of the liquid film. These effects can either lead or delay the transition from nucleate boiling to transition boiling (where the maximum temperature and CHF occurs). Thinning and thickening of the liquid film (which has a two-phase nature) can influence the chance of slug propagation, therefore leading or lagging the CHF occurrence. In addition, the fluctuating relative speeds of vibrating surfaces changes the intensity of drop rebounding and splashing in the flow field. All the mechanisms mentioned are important for spray cooling. Table 5-3 gives the temperature differences between the dynamic and corresponding static cases for each nozzle and associated operating conditions.

Table 5-3. Temperature difference (℃) from static cases to inspect any effects of vibration on excess temperature.

	PJ10				PJ8		MW145	
Flow rate (ml/min)	75		100		55		55	
$\overline{\vec{v}}$ ($\times 10^{-3}$m^{3}s^{-1}/m^2)	1.05		1.40		0.77		9.03	
Subcooling (℃)	10	45	10	45	10	45	10	45
D-1	0.3	-4.8	5.8	-2.6	-0.6	-2.4	-14.2	0.8
D-2	1.5	-4.9	7.2	3.3	1.0	-0.2	-8.4	-29.7
D-3	3.2	0	6.0	2.1	-2.4	-2.9	-7.8	-11.4
D-4	-3.6	-3.7	0.4	-1.2	-0.6	-4.5	-41.3	3.5
D-5	5	-4	-0.5	-2.5	11	0.9	-15.9	0.8
D-6	-1.8	-5.3	3	-3.4	3	3.2	-16.2	1.6
D-7	-0.7	-6.1	5.7	-1.2	2.3	-3.6	-19.5	2.4

The largest difference in the excess temperature of dynamic cases from those for static cases for PJ8 and PJ10 belong to cases with high-frequency vibrations with the exceptional case of PJ10 at 100 ml/min and SC=10 ℃. For MW145, the largest difference in the excess temperature happened for cases

in high-frequency vibrations at SC=10 ℃ while at SC= 45℃ the largest deviations are in the large-amplitude vibration range. For the PJ10 at 75 ml/min and SC=10 ℃ (Figure 5-4a), this difference is -3.6 ℃ for case D-4 and 5 ℃ for case D-5. At the subcooling of 45 ℃ (Figure 5-4b), the excess temperature difference for case D-6 and D-7 are respectively -5.3 ℃ and -6.1 ℃. Test cases of D-4, D-5, D-6 and D-7 all have accelerations above 2g (see Table 5-1). Considering these test cases, for both subcooling degrees, when the Acceleration and Vibrational Reynolds numbers are decreased (from D-4 to D-5 and D-6 to D-7), the temperature difference has increased. At 100 ml/min and subcooling of 45 ℃ (Figure 5-5b) the largest temperature difference also occurred for the case D-6 (3.4 ℃) which is within the region of high-frequency vibrations. By contrast, at 100ml/min and subcooling of 10 ℃ (Figure 5-5.a), the large-amplitude vibrations on average caused the largest temperature deviation from that for the static case. The test case of D-2 has a temperature difference of 7.2 ℃, and test cases of D-1 and D-3 have temperature differences of 5.8 ℃ and 6.0 ℃. Reference to Table 5-1 for the Acceleration and vibrational Reynolds numbers for these cases confirms that it is still valid to claim that decreasing these two dimensionless numbers the temperature difference increases. D-1 in comparison with D-2 has a smaller Acceleration but a fixed Re=6835, and D-3 has a lower Reynolds number in comparison with those for D-2 (while Ac=0.26). This indicates the effect of vibration on excess temperature. In the following, the effects of Acceleration and Reynolds numbers, as well as frequency and amplitude, are evaluated separately.

To see the effect of Acceleration on the excess temperature, cases D-1 (Ac=0.13) and D-2 (Ac=0.26) with a Re=6835, and D-3 (Ac=0.26) and D-7 (Ac=6.44) with a Re=3417 are considered. At Re=6835, acceleration has contributed to increasing the excess temperature deviations except for PJ8 at SC=45 ℃ and MW145 at SC=10 ℃. At the lower Reynolds of 3417, however, acceleration has a decreasing effect on the excess temperature deviations except, for one PJ10 case at $v = 75\ ml/min$ and SC=45℃,

one PJ8 data at SC=45 ℃, and one case of MW145 at SC= 10 ℃. This means at Re=6835 the increasing effect of acceleration on the excess temperature deviations is valid for 75% of dynamic cases, whereas for Re=3417 acceleration has a lessening effect on the temperature differences for 63% of data cases. It seems that the temperature differences with acceleration follow a nonlinear trend and therefore other parameters are needed to facilitate understanding of vibrational effects on excess temperature.

To study the Reynolds Number effect, D-2 (Re=6835) and D-3 (Re=3417) cases are compared. As can be seen in Table 5-3 for the PJ8, by increasing the Reynolds Number the deviations for both subcooling degrees are decreased while the temperature differences for MW145 are all increased. From this, it can be deduced that at the highest volumetric spray flux (9.03×10^{-3} m^3s^{-1}/m^2 for MW145), Reynolds Number increases the temperature deviations (an undesirable aspect for thermal management purposes), and at the lowest volumetric flux of 0.77×10^{-3} m^3s^{-1}/m^2 for the PJ8, increasing Reynolds decreases these temperature deviations (which is desirable for thermal management systems). The PJ10 nozzle (which has volumetric fluxes of 1.05×10^{-3} and 1.40×10^{-3} m^3s^{-1}/m^2 respectively for 75ml/min and 100ml/min) appears to be at the transition between these two increasing and decreasing effects of Reynolds number. For the lower volumetric flux of 1.05×10^{-3} m^3s^{-1}/m^2, which is closer to that for the PJ8, (the decreasing effect of Reynolds is only recognised for PJ10 at SC=10 ℃). For the volumetric flux of 1.40×10^{-3} m^3s^{-1}/m^2 (which is about twice that of the PJ8, and therefore closer to the MW145 volumetric flux), the increasing effect of Reynolds number on the temperature differences is detectable at both subcooling degrees (as given in Table 5-3), an effect mentioned earlier for the MW145 nozzle. The only exception is for PJ10 at the lower volumetric flux of 1.05×10^{-3} m^3s^{-1}/m^2 (i.e. 75 ml/min in Table 5-3) and SC=45 ℃ which stems from the dominant effect of subcooling on different heat transfer mechanisms of spray cooling.

To investigate the effect of vibration amplitude cases, D-4 (a=1mm) and D-5 (a=0.2mm) both with a frequency of 50Hz, are examined. For PJ nozzles, all temperature differences, except for PJ8 at SC=45 ℃, have been decreased by increasing the amplitude. For the MW145 and PJ8 at SC=45 ℃ this behaviour is opposite (i.e. temperature differences have been increased by increasing amplitude). For frequency influence cases, D-5 (50Hz) and D-6 (100Hz) are good candidates with the same amplitude of 0.2 mm. For all nozzles at SC=45 ℃, doubling the frequency increases the maximum temperature differences. For SC=10 ℃ it appears that volumetric flux again has the governing effect on the excess temperature deviations. Starting with the PJ8 ($\bar{\vec{v}}$ =0.77× 10^{-3}m^{3}s^{-1}/m^2) and PJ10 ($\bar{\vec{v}}$ =1.05× 10^{-3}m^{3}s^{-1}/m^2) doubling the frequency decreases the temperature deviations, while from $\bar{\vec{v}}$ =1.40× 10^{-3}m^{3}s^{-1}/m^2 (for the PJ10), appears to be a transition point above which, doubling the frequency starts to increase the temperature difference. The increasing the effect of frequency on maximum temperature also remains valid with a lower intensity for the MW145 with $\bar{\vec{v}}$ =9.03× 10^{-3}m^{3}s^{-1}/m^2.

Observing all these nonlinearities in the trends of the data motivates the development of correlation models with promising prediction capabilities, which is addressed in the next section.

5.3. Calibrating a dynamic correlation model for CHF and associated temperature prediction

To calibrate an appropriate dynamic correlation model in Table 2-3 for CHF and associated temperature prediction, a nonlinear least square regression is used. This fitting process is also used to calibrate 'static' correlations from Table 2-3, which are used for comparative purposes. The Matlab Levenberg-Marquardt optimisation algorithm is used (with the method option set to 'bisquare' for robustness). Functional forms in Table 2-3 should be also chosen based on considerations about the measurements (i.e. sensors available in a thermal management system), the system identification method, inferences from measurements, the trends of different key parameters, and information in the literature. Based on the literature review by Liang et al. [23], there is contradictory information regarding the spray

specifications effects on the CHF. There are also suggestions regarding modelling approaches. Chen et al. [162] found that CHF is independent of Sauter mean diameter. Using mean droplet velocity is generally not recommended for correlating CHF data [106] owing to failure to account for the cumulative effect of multi-droplet impact. For mist cooling, Toda [163, 164] showed that the CHF for water sprays is insensitive to droplet velocity (the nozzles in this study all have misting flow). Therefore, based on the objectives of the CHF modelling (for the specific purpose of thermal management) and the trends of key parameters, functional forms with *'flow rate'* for both static and dynamic cases have been chosen as:

$$Bo = a\,Ja^{\mathrm{b}}\left(\frac{\rho_l^2\sigma v}{{\mu_l}^3}\right)^{\mathrm{c}}\text{, Static} \tag{5-3}$$

and

$$Bo = a\,Ja^{\mathrm{b}}\left(\frac{\rho_l^2\sigma v}{{\mu_l}^3}\right)^{\mathrm{c}} Re_V^{\mathrm{d}}\left(\frac{a}{H}\right)^{\mathrm{e}} Ac^{\mathrm{f}}\text{, Dynamic} \tag{5-4}$$

The data for the PJ8 and PJ10 nozzles which showed similar trends are considered for fitting the associated static and dynamic functional forms. The entire dataset associated with the static and dynamic cases for MW145 is separately fitted to the related functional forms. Table 5-4 shows the parameters obtained after fitting and optimisations. These parameters for each correlation result have the best root-mean-square errors and average deviations for both *Static* and *Dynamic* cases of PJ and MW145 nozzles. The parameter values themselves obtained for the calibrated models shown in Table 5-4 qualitatively support the finding discussed in Sections 5-1 and 5-2 for each nozzle. For instance, parameter 'a' for the MW145 is greater than those for PJ nozzles in both dynamic and static cases indicating that MW145 correlation obtains higher CHF results. Negative values for parameter 'b' also support the inverse trend of MW145 in response to subcooling degrees.

Table 5-4. Dynamic and static correlation parameters for PJ and MW145 nozzles.

Dynamic correlation model $Bo = a\,Ja^{b}(\frac{\rho_l^2\sigma v}{{\mu_l}^3})^{c}Re_V^{d}\left(\frac{a}{H}\right)^{e}Ac^{f}$, Parameters: a, b, c, d, e, f **Static correlation model $Bo = a\,Ja^{b}(\frac{\rho_l^2\sigma v}{{\mu_l}^3})^{c}$, Parameters: a, b, c**							
Correlation	Nozzles	Parameters					
		a	b	c	d	e	f
Dynamic	PJ8 and PJ10	2.46E-04	0.0497	0.7348	-0.4958	0.2357	0.2329
	MW145	3.43E-04	-0.0317	0.7512	-0.4535	0.2065	0.1886
Static	PJ8 and PJ10	1.71E-06	0.0507	0.7383			
	MW145	2.81E-05	-0.0681	0.6565			

Figure 5-9 shows the experimental results for CHF over the predicted data points with error bands as well as average and maximum absolute errors. As can be seen, the static correlation (Figure 5-9a) is predicting the data (8 data points) with an average absolute error of 5% and maximum absolute error of 16.7%. The predicted CHF results are in the -8.3% and +16.7% error windows. Comparing these error bands with those for other static models in the literature (See Table 1-6) the correlation prediction is of good quality. The dynamic model prediction quality is demonstrated in Figure 5-9b. The average and maximum absolute deviations are respectively 12.6% and 18.8% which is promising based on what is the common acceptance criteria for empirical correlations. (The predicted CHF results of all nozzles are within the error bands of -18.8% and +18.5%.) As can be seen, the correlation models represent the best prediction quality for PJ10 nozzles. By contrast, the maximum absolute errors for both static and dynamic models occurred for PJ8 static case with the SC=45 ℃ and dynamic case of D-7 which is a high

frequency vibration. This is due to the higher number of PJ10 data points (i.e. 28 for PJ10, 14 for MW145, and 12 for PJ8), and consequently the higher resolution for the PJ10 dataset.

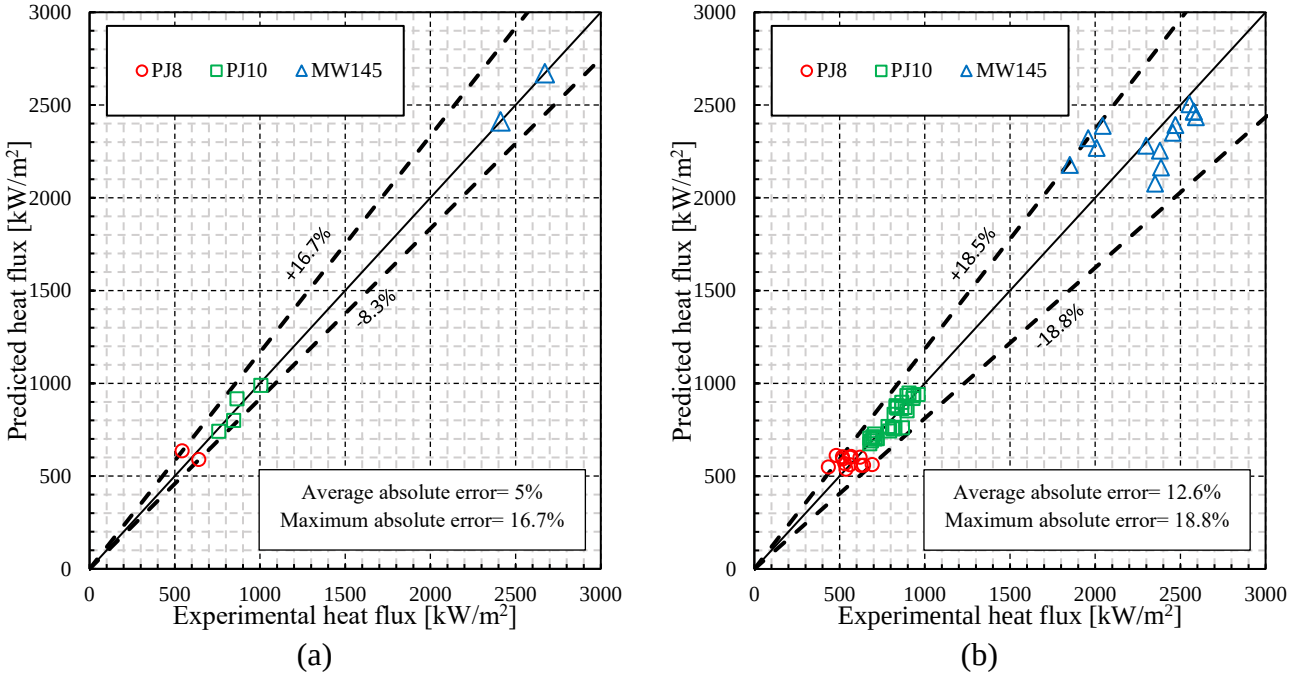

Fig. 5-9. CHF results predicted by correlations with the error bands: (a) *static* and (b) *Dynamic*.

Excess temperature correlation model

For the specific purpose of thermal management, there is also a need to use a correlation model that is capable of predicting the excess temperature at which CHF occurs (which is also known as maximum controllable surface temperature or stable CHF temperature). In this regard, the same method as the work of Mudawar and Valentine [44] has been employed. In their study, T_{max} was determined by combining a CHF model with a different functional form which included the excess temperature ($\Delta T_{excess} = T_{w,max} - T_{sat}$) and then solving for the surface temperature. The functional form containing excess temperature when based on generalized Π–Theorem (Chapter 2) is according to:

$$\frac{\Delta T_{excess}}{\Delta T_{Sub}} = a \left(\frac{q_{CH} H}{\mu_l h_{fg}}\right)^b \left(\frac{\rho_l^2 \sigma v}{{\mu_l}^3}\right)^c Re_V^d \left(\frac{a}{H}\right)^e Ac^f \qquad (5\text{-}5)$$

where the critical heat flux, q_{CH}, in equation (5-5) is obtained from fitted dynamic correlations in Table 5-4. This requires equation (5-5) to be used with the previously fitted correlation model for CHF. Therefore equation (5-5) is separately fitted to measured CHF and excess temperature data points associated with both the PJ and MW145 nozzles. In equation (5-5), a dimensionless surface temperature ($T_{CHF} = \Delta T_{excess}/\Delta T_{Sub}$) is defined similar to the CHF studies of Dou et al [89] and Abbasi and Kim [114]. To achieve high accuracy in fitting equation (5-5), the data is split into two different subcooling degrees. The reason for this is the high dependency of the excess temperature on subcooling degrees (as indicated by the trends identified earlier). The optimised parameters resulting in the least root mean square errors are provided in Table 5-5. Figure 5-10 illustrates the predicted excess temperature versus the experimentally measured values for two different subcooling degrees of 10 ℃ (Figure 5-10a) and 45 ℃ (Figure 5-10b). The error bands for SC=10 ℃ have a wider range (-15.5% and +15.9%) than those for SC=45 ℃ (-9.8% and +10.3%) indicating the effect of subcooling on the excess temperature. As was expected, at SC=10 ℃, the PJ10 results deviate more from PJ8 excess temperature as compared with what can be seen for the PJ10 and PJ8 data points at SC=45 ℃. Overall, the model prediction quality is promising for both subcooling degrees (considering the under- and over-estimations not more than 15.9%). This level of accuracy is important for an evaporative spray cooling thermal management system at the safety phase, which requires accurate prediction of the maximum controllable temperature to safely set the boundaries for controllers. The work is limited to the operating parameter range of the experimental test programme which is now given in Table 5.6.

Table 5-5. Excess temperature correlation parameters for PJ and MW145 nozzles at two subcooling degrees.

Excess temperature correlation model $\frac{\Delta T_{excess}}{\Delta T_{Sub}} = a\left(\frac{q_{CH}H}{\mu_l h_{fg}}\right)^b \left(\frac{\rho_l^2 \sigma v}{\mu_l^3}\right)^c Re_V^d \left(\frac{a}{H}\right)^e Ac^f$ Parameters: a, b, c, d, e, f							
Subcooling (°C)	Nozzles	Parameters					
		a	b	c	d	e	f
10	PJ8 and PJ10	1.22E-05	-0.2879	0.6472	-0.0783	0.0074	-0.0011
	MW145	1.26E-05	0.1644	0.6112	-0.0738	-0.0479	-0.0664
45	PJ8 and PJ10	1.28E-04	-0.2393	0.3228	0.2411	-0.1228	-0.1302
	MW145	3.46E-05	1.1914	0.2584	0.1030	-0.0607	-0.0466

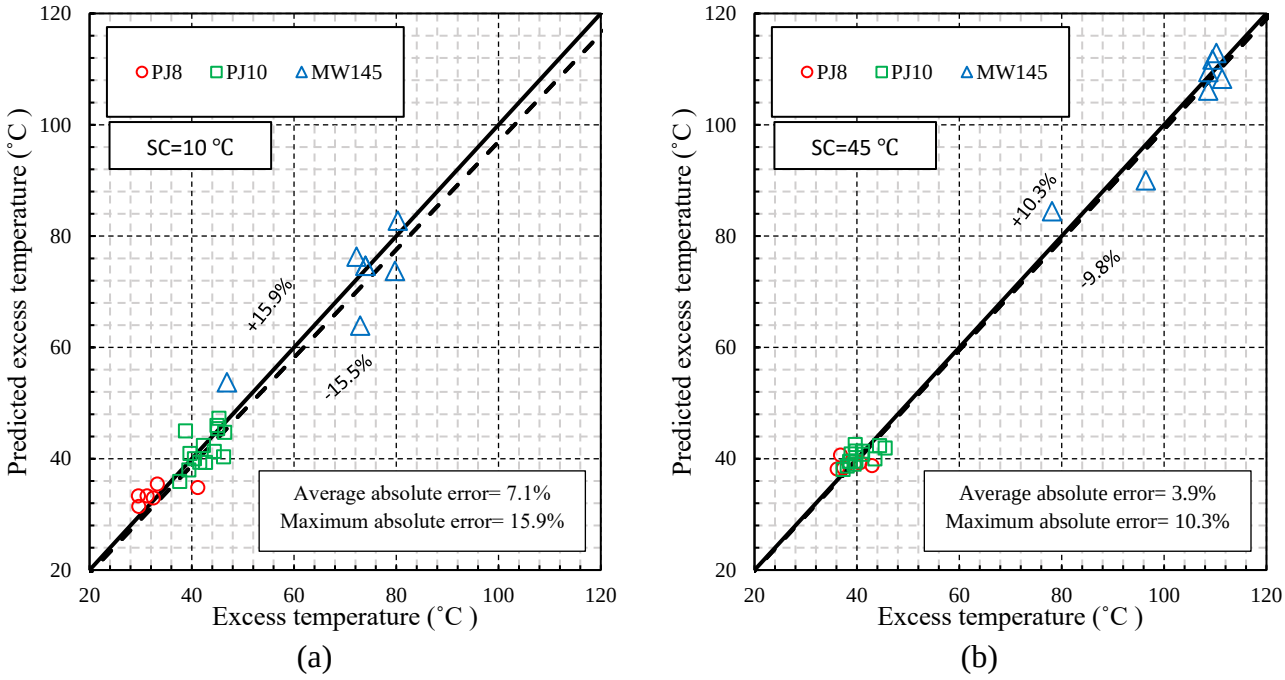

Fig. 5-10. Excess temperature results predicted by correlations with the error bands: (a) SC=10 ℃ and (b) SC=45 ℃.

Table 5-6. The range of applicability of CHF correlations.

P_{ch} (bar)	v (ml/min)	Subcooling (°C)	H (mm)	$Static$ (without vibration)	$Dynamic$ (with vibration)	
					Frequency (Hz)	Amplitude (mm)
1	55-100	10-45	12	Yes	2-200	0.04-8

5.4. Conclusions of Chapter 5.

Experiments have been undertaken to investigate the effect of vibrational surfaces on the critical heat flux (CHF) in spray evaporative cooling, and to assess the effectiveness of calibrated prediction models. In this regard, a flat copper test-piece located inside a spray chamber has been mounted on top of a shaker while being heated by a heater block using cartridge heaters. A wide range of vibrations (namely 'large-amplitude' and 'high-frequency') have driven the test piece during spray cooling with three different nozzles of PJ8 (55 ml/min), PJ10 (75 and 100 ml/min) and MW145 (55 ml/min). The CHF data points, and their corresponding excess temperatures, for two subcooling degrees of 10 ℃ and 45 ℃, have been collected using DAQ and human-machine interface. Data analysis and comparisons have been undertaken to comprehensively investigate all the vibrational key parameters both individually and in a combined relation using non dimensional numbers.

For experiments without vibration (static), the influence of flow rate, volumetric flux, and subcooling have been compared with the results of previously undertaken studies in the literature. The trend of the CHF data with spray volumetric flux was in agreement with the literature. The subcooling effect for nozzles PJ8 and MW145 with the lowest flow rate of 55 ml/min, was found to be deteriorating (18% and 11%) while for PJ10 with higher flow rates of 75 ml/min and 100 ml/min the subcooling influence was enhancing (10% and 14%). Both impeding and enhancing behaviours for the low flow rate nozzles

(PJ8 and MW145) and higher flow rate nozzle of PJ10 are in accordance with the trends found for similar flow rates in the literature.

For the dynamic results (CHF for vibrating surfaces), first, the effect of volumetric flux was assessed. In general, CHF enhances with increasing volumetric flux. Second, the largest deviations from the static CHF for all nozzles have been identified as for the effect of vibration. For the PJ10, the dynamic case with a=1 mm and f=50 Hz, and with the highest Reynolds number and largest Acceleration number was found to have the largest deviation for both flow rates and subcooling degrees. It was found that the deterioration effect of vibration became more noticeable by increasing the subcooling degree (for 75 ml/min, 11% at SC=10 ℃, and 17% at SC=45 ℃, and for 100 ml/min, 5% at SC=10 ℃, and 14% at SC=45 ℃.) By contrast, for the low flow rate nozzles of PJ8 and MW145, the impeding effect of vibration reduces by increasing subcooling. For the PJ8, the deterioration was 32% at SC=10 ℃ and 5% at SC=45 ℃. For the MW145, it was 31% at SC=10 ℃ and 2% at SC=45 ℃.

The influence of subcooling on dynamic-CHF data has also been discussed. For the PJ10 (at both flow rates), it followed the same trend as static cases. That is, subcooling for PJ10 augments CHF for its static and dynamic cases. For the PJ8 and MW145, the impeding trend (as for static) was also valid for most of the data, apart from only two high-frequency vibrations of 50Hz (D-4) and 100 Hz (D-6). The CHF for these cases acquired a higher value at the higher subcooling of 45 ℃.

Evaluation of frequency and amplitude effects encouraged the use of non-dimensional analysis using the Vibrational Reynolds and Acceleration numbers. For both flow rates and subcooling degrees of PJ nozzles, increasing Reynolds Number from 3417.6 to 6835.2 enhances the CHF but then impedes the CHF for the highest Reynolds Number of 21360. The same behaviour was observed for the MW145 at SC=10 ℃, however, the trend for MW145 at SC=45 ℃ was opposite to the others. This opposite behaviour stemmed from the high dependency of MW145 to the subcooling effect. For PJ nozzles,

acceleration had an enhancing effect which was in agreement with published experimental results. Further investigation revealed the independency of MW145 results to acceleration.

The effect of vibration on excess temperature was also studied in detail. For all nozzles in general, cases with high-frequency vibration gave rise to the greatest deviations in the excess temperature (except for MW145 at SC= 45℃ that the greatest deviations happened by the large-amplitude vibrations). At Re=6835, acceleration had an increasing effect on the excess temperature deviations which was valid for 75% of dynamic cases. At Re=3417, acceleration had a decreasing influence on the temperature differences for 63% of data cases. Volumetric flux was found to produce the greatest effect on excess temperature. At the highest volumetric spray flux (9.03×10^{-3} m^3s^{-1}/m^2 for MW145), Reynolds Number increased the temperature deviations and at the lowest volumetric flux of 0.77×10^{-3} m^3s^{-1}/m^2 for PJ8, increasing Reynolds Number decreased the temperature deviations.

Predictions of CHF, and associated excess temperature, using calibrated correlation models for the dynamic conditions, were very reasonable, with maximum absolute errors of 18.8% and 15.9%, respectively. These calibrated correlation models are of potential value for safe operation of thermal management systems using spray evaporative cooling.

6. TEMPERATURE CONTROL OF HEAT-GENERATING HARDWARE EXPOSED TO VIBRATION

Based on the findings in previous Chapters, the potential exists therefore, for spray evaporative cooling to achieve high heat transfer rates with low mass flows. However, there are significant concerns remaining about the ability of actual hardware to achieve stable control of a spray evaporative cooling system at the required heat flux and temperatures. To date, there has been no published evidence of successful thermal management and control of hardware involving two-phase spray evaporative cooling of vibrating surfaces. In this Chapter, the design and performance of an experimental spray evaporative cooling control system is reported. In particular, the effects of different controller gains on the controller performance and its implications for future thermal management is examined. In addition, the steady-state error is examined to assess the safety of the proposed system.

The objective of the study is to establish the efficacy of a particular control strategy for evaporative spray cooling of vibrating surfaces in terms of being able operate successfully at target temperature setpoints needed for high-heat-flux cooling of the flat test-piece (explained in Chapter 3). Moreover, no one has so far attempted to control the curved surface temperature of an actual spray evaporative cooling system in the presence of vibration. To address this need, the ¼-Cylinder test-piece (shown in Chapter 3) has been tested on the same test rig and control architecture as the flat test-piece. This is also to address the question of whether the system has adequate precision, flexibility, and viability in investigating surface-temperature control using flow-rate control (via pump speed control). The next sections discuss the proposed thermal management system, correlation model of the plant, optimum linearization of the correlation model, stability analysis, control architecture design, and finally, temperature control results for both test pieces.

6.1. Proposed thermal management system

The proposed thermal management system involves a 'plant' which here represents an evaporatively cooled test-piece (exposed to vibration) whose temperature is regulated by feedback control. Figure 6-1 shows a high-level representation of the closed-loop feedback control system for temperature control of the hardware. As can be seen, a test-piece is in contact with the heating source and is aimed to be cooled using evaporative spray cooling. The objective of the controller is to keep the cooling process in the nucleate boiling regime to benefit from the heat removal achievable in the form of latent heat. In this regard, a PID controller has been designed to control the coolant pump flow rate to maintain the coolant side temperature of the test piece (exposed to displacement vibration) at a target value. There are two circuits in Figure 6-1. The first circuit (in blue) shows the coolant flow starting from the coolant pump to the full cone nozzle on top of the test piece (v is the volumetric flow rate). The saturated water breaks up into droplets and impinges on the test-piece surface in order to cool down the heat generated by the hardware. Then, the vapour and accumulated droplets are drained into the vapour chamber and condenser tank, respectively. Finally, the condensed water reaches the suction side of the coolant pump to complete the circuit. The second circuit (in black) is the feedback signal from the cool-metal surface temperature. This state is compared with the desired surface temperature (as a reference signal) to generate the error required to be used as an input signal to the PID controller. The control signal to the coolant pump completes this circuit.

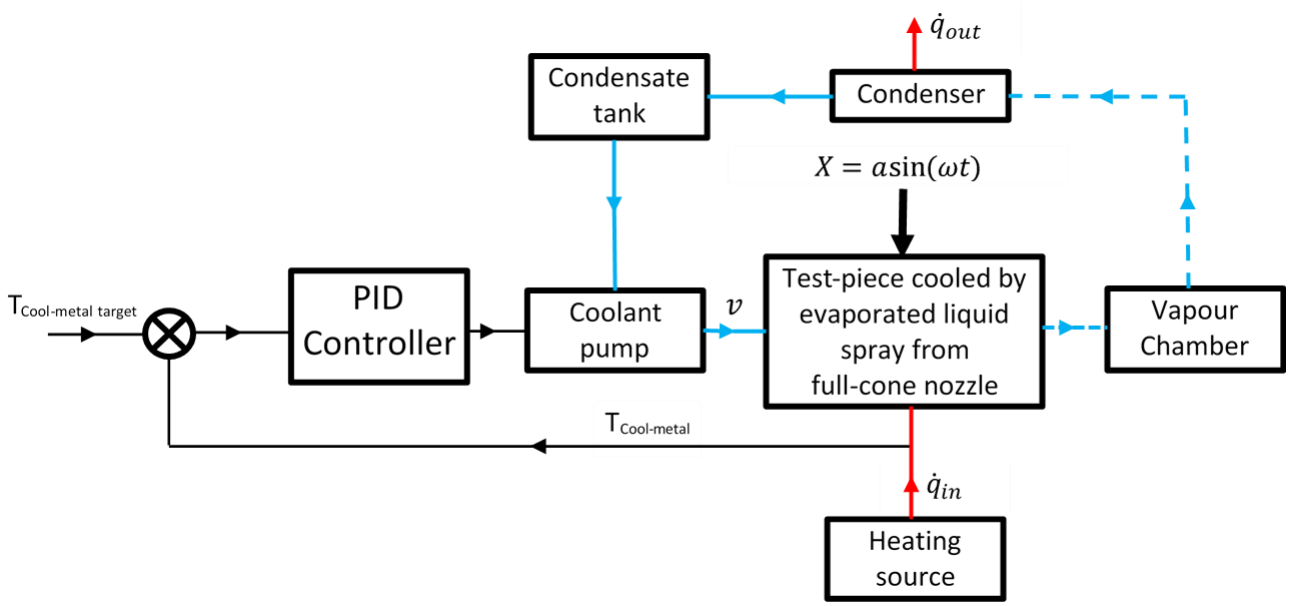

Fig. 6-1. PID temperature controller for spray evaporative cooling of hardware (showing a disturbance from displacement vibration $X = a\sin(\omega t)$)

6.2. Correlation model of the 'plant'

To undertake performance assessment and tuning of the thermal management system in Figure 6-1, a closed-loop feedback control system model is constructed to accurately model the entire physics during the cooling process (i.e. when the heat-generating hardware exposed to the vibration is cooled via spray evaporative cooling in the nucleate boiling region). To describe the physics of the evaporative spray cooling needed for the 'plant' model, the following empirical correlation model has been constructed in [27] (using the Generalised Buckingham Pi method [142]) to represent spray evaporative heat transfer characteristics for the test piece under vibration in the nucleate boiling region:

$$Bo = 1.24 \times 10^{-2} Ja^{1.3920} \left(\frac{\rho_l^2 \sigma v}{{\mu_l}^3}\right)^{0.9809} Re_V^{-0.9869} \left(\frac{a}{H}\right)^{0.4825} Ac^{0.4998} \quad (6\text{-}1)$$

where Bo is Boiling number ($qH/\mu_l h_{fg}$) which includes heat flux q, nozzle-to-surface distance H, viscosity μ_l and specific enthalpy h_{fg}. $Re_V = \rho_l a \omega d_H / \mu_l$ is the Vibrational Reynolds Number. The Vibrational Reynolds Number term contains angular frequency ($\omega = 2\pi f$) and the amplitude (a)

representing the dynamic behavior of the plant. $Ac = \omega^2 a/g$, is the Dimensionless Acceleration Number. Ja is Jakob number ($Ja = C_l \Delta T/h_{fg}$), which is the ratio of sensible heat to latent heat.

To construct the plant model a simple heat balance for the heat-generating hardware has been used to model the temperature control. A similar approach, adopted by Setlur et al. [165], Eberth et al. [166], Wagner et al. [167-169], and Henry et al. [170], results in a heat balance equation as follows:

$$mC\dot{T} = \dot{Q}_{in} - \dot{Q}_{out} \tag{6-2}$$

where $m = 404.4\ g$ is the test-piece mass, C is the specific heat capacity of the cooled test-piece (in this case cooper), $\dot{T}$ is time-varying temperature of the test piece, $\dot{Q}_{in}$ is the rate of heat release of the source, $\dot{Q}_{out}$ is the rate of heat removal of the proposed cooling system. To obtain the coolant side temperature, equation (6-1) is substituted into equation (6-2), and by setting $\dot{Q}_{out} = qA$, this gives a first-order (nonlinear) differential equation model for the test-piece temperature T_{w} which will shortly be linearized, a necessary step to ultimately undertake practical stability analysis. For these parameters, the first-order (nonlinear) differential equation model takes the form:

$$mC\dot{T}_w = \dot{Q}_{in} - 1.24 \times 10^{-2} A\left(\frac{\mu_l h_{fg}}{H}\right)\left(\frac{C_l \Delta T}{h_{fg}}\right)^{1.3920}\left(\frac{\rho_l^2 \sigma v}{{\mu_l}^3}\right)^{0.9809} Re_V^{-0.9869}\left(\frac{a}{H}\right)^{0.4825} Ac^{0.4998} \tag{6-3}$$

where ΔT is the excess temperature (in the term $Ja = C_l \Delta T/h_{fg}$) which is the difference between the test-piece surface temperature (T_w, a state in the plant) and the saturation temperature (constant at 1 bar i.e. $T_{sat} = 99.6\,^{\circ}C$). Equation (3) represents the model for a single-input single-output (SISO) system, the input being v, and the output being the time-varying wall temperature T_w.

Linearisation of the plant model.

The correlation model for the plant given by equation (6-3) can be linearised in a number of ways. The experimental facilities are described in Chapter 3 but for the linearization process, it is appropriate here

to state numerical values for the flat circular test-piece. The mass $m = 404.4\ g$, the diameter of $d_H = 20mm$, and specific heat capacity (for copper) $C = 385\ {}^{j}/_{kgK}$. The correlation model of the plant then can be considered at a fixed operating point within the operating condition of the current study which is: nucleate boiling at 1 bar, nozzle-to-surface distance of $H = 17\ mm$, $\omega = 2\pi \times 1.9\ Hz$, $a = 12mm$ and a pump flow rate of 200 ml/min ($v = 0.00333\ m^3 s^{-1}$). The constants (set at the operating point) are: $\dot{Q}_{in} = A \times 1200000 W/m^2$, $\mu_l = 0.00028$ Kg/m s, $h_{fg} = 2257$ kJ/kg, $C_l = 4.219$ kJ/kg k and $\rho_l = 958$ kg/m^3 and $\sigma = 0.0589$ N/m. A is the area of the circular test piece with a diameter of $d_H = 20mm$. Substituting these values in equation 6-3 gives the first order differential equation with a simpler appearance as:

$$\dot{T}_w(t) = \frac{A}{mC}(1200000 - 3.7348 \times 10^6\ (T_w - 99.6\ )^{1.3920} v^{0.9809}) \quad (6\text{-}4)$$

when with $\frac{A}{mC} = 2.0177 \times 10^{-6}$, the model simplifies further to:

$$\dot{T}_w(t) = 2.4213 - 7.5357\ (T_w - 99.6\ )^{1.3920} v^{0.9809} \quad (6\text{-}5)$$

There is no closed-form solution to Equation (6-5) but it can be linearised in a number of ways and an exact solution is then trivial. The simplest way to linearize equation (6-5) is to expand the nonlinearity in a Taylor series about an operating point then truncate, retaining only the linear term. For example, when the initial (temperature) condition $T_w = 110$ ℃ is chosen as the expansion point, using the MATLAB Control System Toolbox, the resulting linearised state-space equation which is a first-order truncated Taylor series approximation for the system is given as:

$$\dot{T}_w(t) = -0.166\ T_w(t) - 1419\ v(t) \quad (6\text{-}6)$$

However, solving Equation 6-5 numerically (using the ODE45 Solver), and also the linearized Equation 6-6 analytically at the point about which the solution is linearised, shows that linearisation about the initial condition gives a solution that deviates significantly from the full nonlinear solution. Therefore,

an alternative (better) linearisation approach is to construct a linear model based on a least-square solution [171] (over the entire time range). This is an iterative process involving numerical solution of equation (6-5) using a known initial condition, corresponding for example, to the response to a step input, or a free decay response. When an initial condition of 110 ℃ is used in the numerical solution (corresponding to a step input of 135 ℃), the least-square-error linear model obtained is:

$$\dot{T}_w(t) = -0.14166T_w(t) + 5755.6\ v(t) \tag{6-7}$$

By contrast, when the initial condition of 140 ℃ is used (corresponding to a free decay response), the least-square-error linear model obtained is:

$$\dot{T}_w(t) = -0.14654T_w(t) + 5469.2\ v(t) \tag{6-8}$$

Figure 6-2a and figure 6-2b show a comparison of the responses obtained by the numerical solution of equation (6-5) and the linearized model equation (6-7) for the step-input, and equation (6-8) for the free-decay response. It can be seen from figures 6-2a and 6-2b, that the least-square error linearized model responses are in excellent agreement in predicting the responses of the nonlinear model with the same initial conditions. However, when the equivalent linear models are switched, the predicted results are very poor (not shown). To attempt to overcome this deficiency, a single least-square-error linear model was constructed with the best overall performance for both the step input and free decay response. This model is:

$$\dot{T}_w(t) = -0.13363\ T_w(t) + \ 5129\ v(t) \tag{6-9}$$

Analytical solutions to Equation (6-9) with initial conditions of respectively 110 and 140 $^{\circ}C$, are:

$$T_w(t) = 127.8124 - 17.8124e^{-0.13363t} \tag{6-10}$$

and

$$T_w(t) = 12.1876e^{-0.13363t} + 127.8124 \quad (6\text{-}11)$$

where the transfer function obtained for the linearised plant model equation (6-9) is:

$$\frac{T_w(s)}{v(s)} = \frac{5129}{S+0.13363} \quad (6\text{-}12)$$

Figure 6-2c and 6-2d show respective comparisons between the step responses to equation (6-5) (with initial conditions of 110 and 140 $^{\circ}C$), and the corresponding responses obtained from equations (6-10) and (6-11).

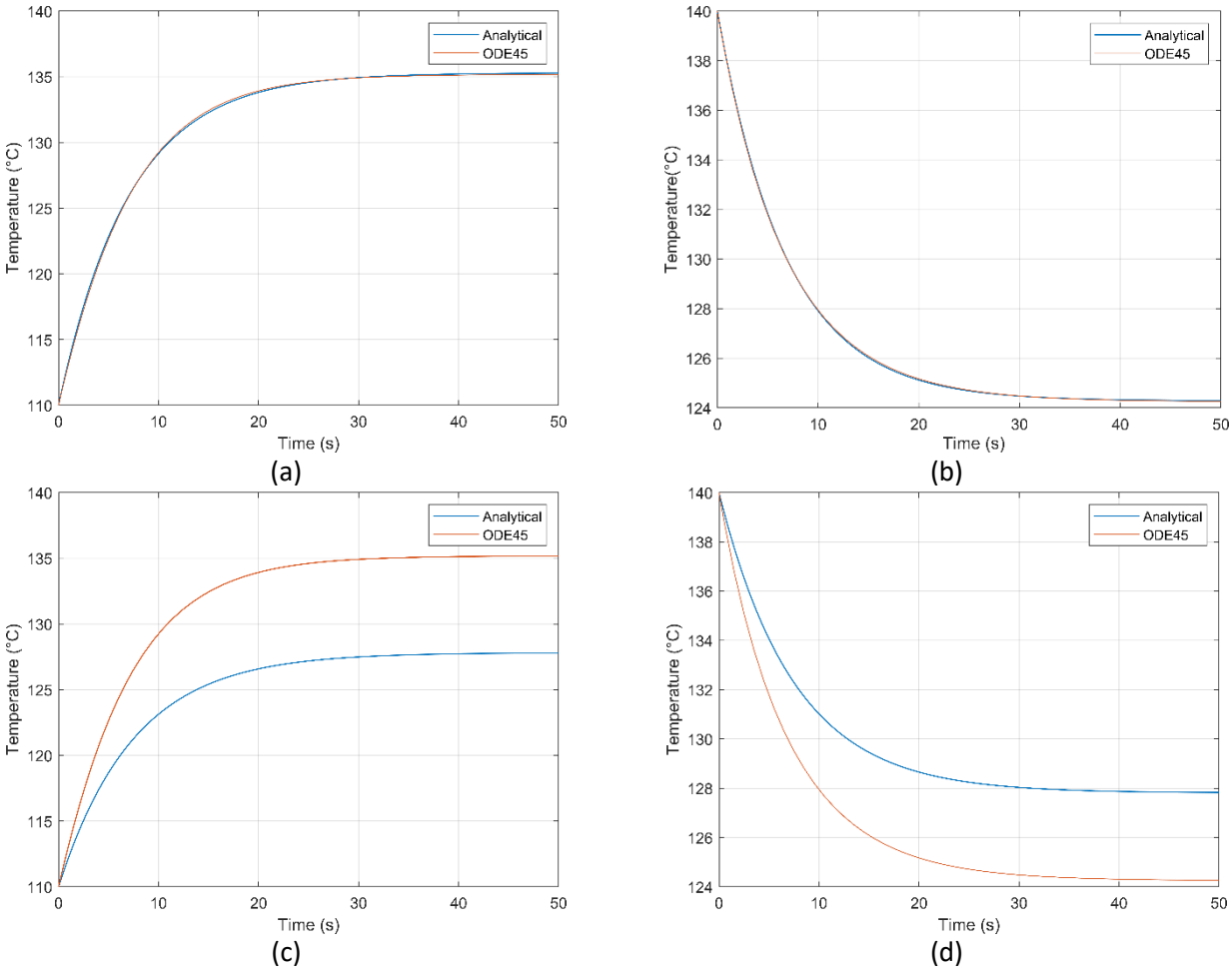

Fig. 6-2. Responses obtained by numerical solution of equation (6-5) and the linearized model: a) equation (6-7) for the step-input, and b) equation (6-8) for the free-decay response; c) and d) step responses to equation (6-5) (with respective initial conditions of 110 and 140 ℃), and the corresponding responses obtained from equations (6-10) and equation (6-11).

It is evident from Figure 6-2c and 6-2d, that the level of agreement between the linearised model and the numerical solution of the full nonlinear model equation (6-5) is still poor. A more rigorous linearization process therefore needs to be followed such as the use of the Wiener Hopf approach, as now explained.

Obtaining the optimal fixed-order linear model using the Wiener-Hopf approach

To obtain the optimal model to replace equation (6-4), the Wiener-Hopf approach is used to obtain the minimum mean square error fixed-order linear transfer function [172]. For the required input to a Finite Impulse Response (FIR) filter (i.e. the optimal filter weighting function), a random temperature history is generated by numerical simulation involving equation (6-3), with a white noise input. To generate the input temperature (as shown in Figure 6-3a), in the Matlab-Simulink model of the plant, the heat flux as the heat source in $\dot{Q}_{in} = qA$ and volumetric flow rate v, have respectively been randomly varied from 0 to $1.2 \times 10^6 W/m^2$, and from 0 to $0.00333\ m^3 s^{-1}$. This satisfies the assumptions associated with the Wiener filter theory namely that both signal and noise are random processes with known spectral characteristics. Here, to ensure the simplest closed-loop stability analysis, an optimal 1st-order linear model is chosen. The additive combination of randomly generated input-temperature and white noise (shown in Figure 6-3b (in red)) has been correlated using the FIR filter. Figure 6-3b, shows that the FIR filter is successful in modeling the temperature with noise (where the output signal is in blue). The Mean Square Error (MSE) between two signals in Figure 6-3 is 0.77. The transfer function of the optimal filter weighting function is as follows:

$$H_{FIR}(s) = \frac{0.5S+0.5}{S} \tag{6-13}$$

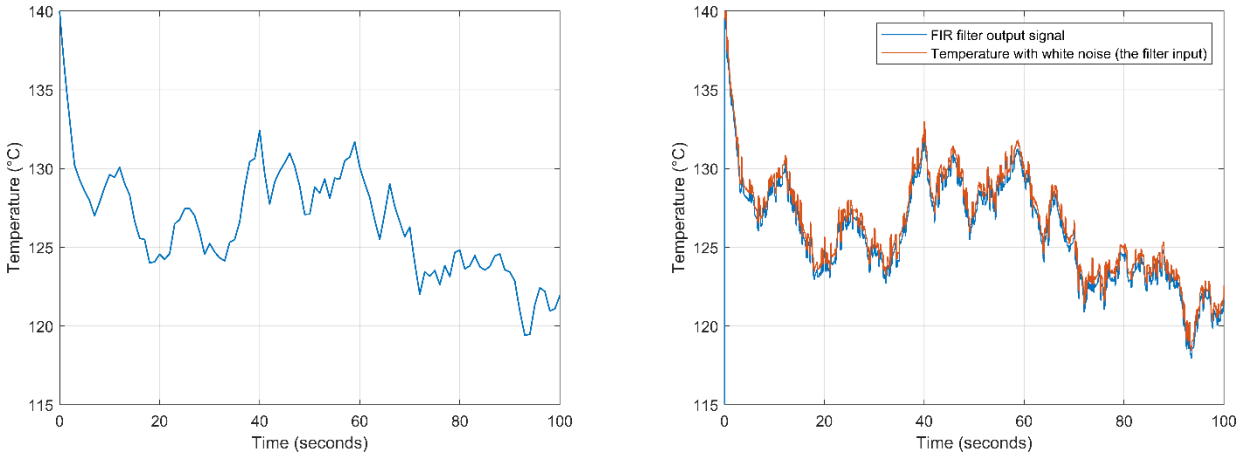

(a) (b)

Fig. 6-3. a) Numerically-generated temperature; b) the input signal to the Wiener-Hopf model; the temperature with additive white noise, and the FIR output signal.

6.3. Stability analysis of the closed-loop transfer function

To design a stable hardware controller, both the least square linearised transfer function using a step input and a free decaying condition, and the minimum least-square solution to the nonlinear ODE of the 'plant' model obtained by the Wiener-Hopf approach have been used to undertake a stability analysis. Stability of the closed-loop control transfer function is assessed iteratively using the root locus method (implemented using the Matlab Control System Toolbox). First, the root locus diagram is shown in Figure 6-4a for the open-loop linearised correlation model of the plant (equation (6-12)). The stability of the closed-loop transfer function is shown in Figure 6b with proportional gains from 0 to 2 (in increments of 0.5); integral gains are shown ranging from 0 to 0.08 (in increments of 0.02); and derivative gains from 0 to 0.004 (in increments of 0.001). As can be seen, the system is stable for all sets of PID gains. After finding the best integral gain to improve the steady-state error, as well as increasing the stability using small values of derivative gains, the most promising PID gains are: P=2.1, I=0.08, D=0.001. Since the transfer function for a PID controller is:

$$k_p + \frac{k_i}{S} + k_d S = \frac{k_d S^2 + k_p S + k_i}{S} \qquad (6\text{-}14)$$

the gain values thus found are chosen as starting gains for the hardware. Using the PID controller transfer function (equation (6-14)) and the chosen gains, the linearised closed-loop feedback control system transfer function is achieved in the form of equation (6-15) as follows:

$$G(s) = \frac{5.129\,S^2+10770\,S+410.3}{6.129\,S^2+10770\,S+410.3} \qquad (6\text{-}15)$$

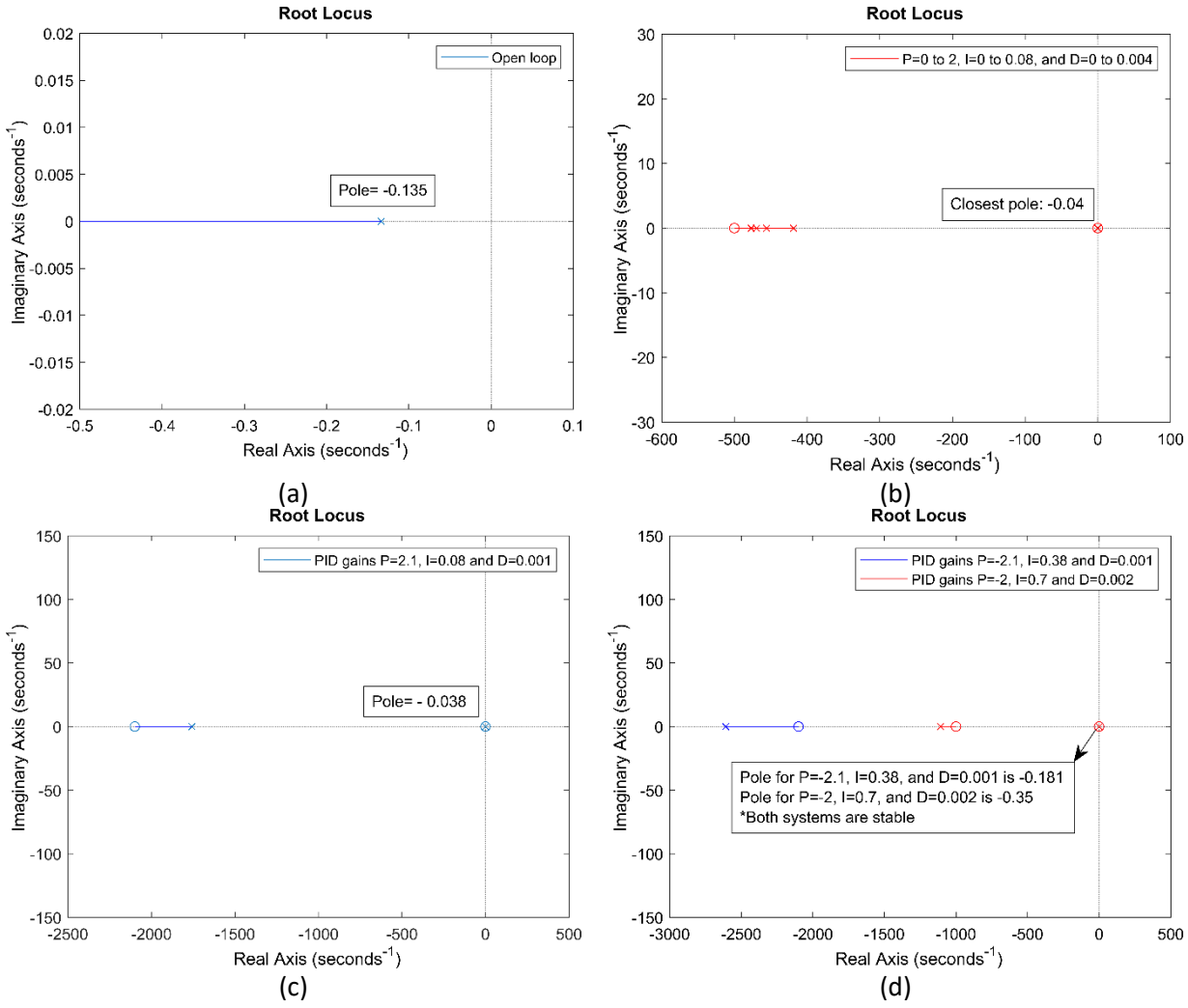

Fig. 6-4. *Root locus* diagrams: for (a) linearised open-loop correlation model of the plant, (b) linearised closed-loop feedback control with P=0 to 2, I=0 to 0.08 and D=0 to 0.004, (c) the designed controller with P=2.1, I=0.08 and D=0.001, and (d) closed-loop control system with negative proportional PID controllers; one with P=-2.1, I=0.38 and D=0.001 and another with P=-2.1, I=0.7 and D=0.002.

The root locus diagram for equation (6-15) shown in Figure 6c, gives stability information of a thermal management system using the PID controller. In a series of trial and error tests, both for the simulation

and for the experimental hardware, it becomes apparent that another set of PID controller gains (P=-2.1, I=0.38 and D=0.001) with a negative proportional gain of -2.1, can also make the system stable (as shown by the root locus diagram in Figure 6-4d). Increasing the integral gain (to I=0.7) and doubling the derivative gain (to D=0.002) results in better stability and robustness of the system (the poles for these two sets of PID gains are shown in Figure 6-4d, along with robustness information in Table 6-1).

Table 6-1. Summary of the robustness results for the actual closed-loop control system.

PID Controller No.	P	I	D	Disturbance	$q\ (\frac{MW}{m^2})$	$T_w(^{\circ}C)$	Settling time (s)	Overshoot ($^{\circ}C$)
1	2.1	0.08	0.001	No, Static	0.2-1.8	110-135	155	1.3
2	-2	0.7	0.002	No, Static	0.2-1.8	110-135	129	0
3	-2	0.7	0.002	Dynamic (a=12mm, f=1.9Hz)	0.2-1.8	110-135	61	0.5
4	-2	0.7	0.002	Dynamic (a=0.02mm, f=400Hz)	0.2-1.8	110-135	70	0.6
5	-2	0.7	0.002	Dynamic (a=0.02mm, f=400Hz)	0.2-1.8	110-135	67	0.7

The linearised closed-loop control system transfer function for this PID controller (i.e. with P=-2, I=0.7, D=0.002) is according to:

$$G(s) = \frac{10.26\,S^2+10258\,S+3590}{9.258\,S^2+10260\,S+3590} \tag{6-16}$$

As expected, during the tuning process of the PID controllers in the actual control hardware, these two sets of PID controller gains (i.e. one with a positive and another with a negative proportional gain) were found to be promising. As can be seen from the root locus plot in Figure 6-4c and d, each set has benefits and disadvantages. The pole for the positive proportional PID control system is closer to the imaginary axis (i.e. -0.038 for the PID with P=2.1, I=0.08 and D=0.001, and -0.35 for the PID with P=-2, I=0.7 and D=0.002.) Thus, the negative proportional PID controller can theoretically be more stable although it has a smaller range of stability for the PID with the larger integral and derivative gains (as shown in Figure 6-4d).

To further support this finding, the stability of the optimal model (obtained using the Wiener-Hopf approach) is also examined. The stability of both the open loop and closed-loop transfer functions with the same PID gains have been examined using a root locus diagram. As expected, the closest poles in both Figures 6-4b and 6-5b with the same ranges of P, I, and D gains are quite similar (0.040 for the step/free decay derived least-square solution to the nonlinear ODE of the 'plant' model, and 0.042 for the Wiener-Hopf derived model). The closest poles to the imaginary axis for PID gains of P=2.1, I=0.08 and D=0.001 on the root locus diagrams for both models are also very similar (-0.038 for the linearised model in Figure 6-4c, and -0.039 for Wiener-Hopf derived model in Figure 6-5c). Examining the poles in Figures 6-4d and 6-5d for the negative proportional PID controllers, suggests the same trend. Moreover, the root locus diagrams in Figure 6-5c and 6-5d still support the previous finding that the pole for the positive proportional PID control system is closer to the imaginary axis. Therefore, the closed-loop control system with positive gains is actually less stable in comparison to the system designed with a negative proportional PID gain. The only difference between the stability findings is related to the stability range of the PID controller with larger integral and derivative gains (P=-2.1, I=0.7 and D=0.002). In Figure 6-5d (corresponding to the Wiener-Hopf model) the s-domain for which the system is stable, has two complex conjugate poles of -0.37±36.7i. This difference however, does not make any change since complex conjugate poles contribute no net angle to the real axis. Therefore, this does not indicate any reduction in stability.

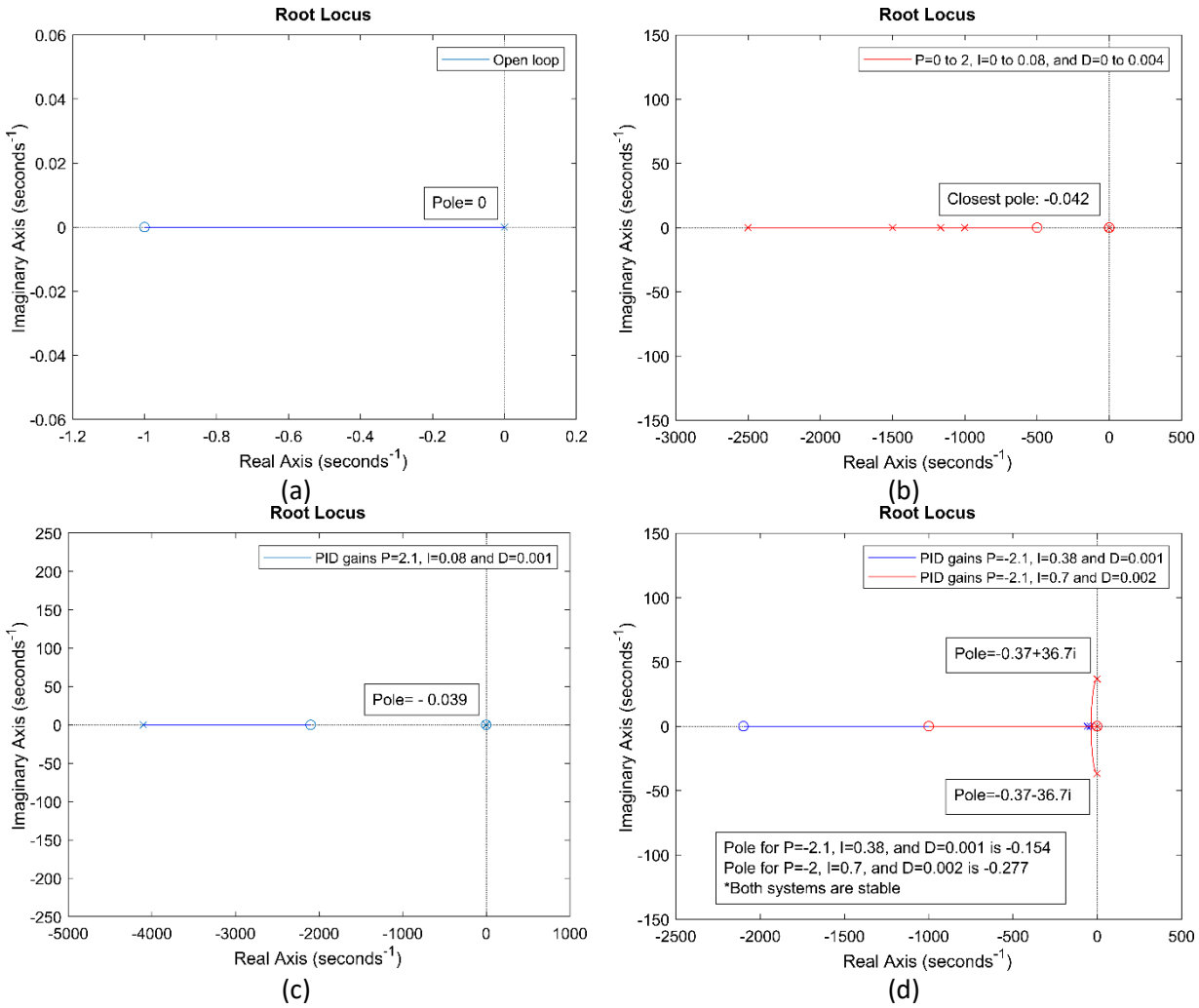

Fig. 6-5. *Root locus* diagrams for model obtained by Wiener-Hopf approach: for (a) open-loop correlation model of the plant, (b) closed-loop feedback control with P=0 t 2, I=0 to 0.08 and D=0 to 0.004, (c) the designed controller with P=2.1, I=0.08 and D=0.001, and (d) closed-loop control system with negative proportional PID controllers; one with P=-2.1, I=0.38 and D=0.001 and another with P=-2.1, I=0.7 and D=0.002.

Regarding the actual hardware, both the positive and negative proportional PID controllers have been implemented, and their effects on the robustness are summarized in Table 6-1 (which are derived from results that will be discussed in Section 6-5). PID Controllers Number 1 and 2 are used in tuning the actual hardware without vibrational disturbance (i.e. under static conditions), whereas for the PID Controllers Numbers 3, 4, and 5 the actual hardware was tested with vibrational disturbances. Comparing the settling time and overshoot, the results for PID Controllers Numbers 1, 2, 3, 4, and 5, confirm better stability for the negative proportional gain controller. There are evident reductions in

the settling time and overshoot for the PID controllers with negative proportional gains. Disturbance rejection for the responses in the dynamic cases is good. Moreover, to check the level of uncertainty in the repeatability of the control, the same PID gains are attempted and the results are available in rows 4 and 5 of Table 6-1. The 3 s difference in settling time, with a temperature difference of only 0.1 $^{\circ}C$ overshoot, offers an impressive level of repeatability which is further confirmation of the stability of the closed-loop control system.

Table 6-2 shows the proposed controller performance of published findings. This includes both simulation and experimentally measured results of temperature control and thermal management using spray cooling systems applied to electronic components and power plant (e.g. a superheater) - all without any vibrational disturbances. All of the cited literature noted the complexity of temperature control owing to nonlinearity, and the time-lag in the plant dynamics. Table 6-2 shows that all results have a higher settling time in comparison with the proposed control system (as given in Table 6-1) while the overshoot is similar. The performance of the proposed closed-loop control system, resulting from use of negative proportional gains in the PID controller, has improved the settling time (by 37%) and the Coefficient of Performance (by 10.5%, COP). Overall, the proposed control system is stable and robust.

Table 6-2. Studies on temperature control and thermal management with spray cooling systems.

Authors (Date)	Apply on	Coolant	Test Piece	Requirements		Control variable	Controller	Robustness	
				$q\ (\frac{MW}{m^2})$	$T(^{\circ}C)$			Settling /rise time (s)	Overshoot $(^{\circ}C)$/(%)
Wang et al. [15] (2013), S[1]	IGBT[2]	water	SPC[3] wick	4	153	Pump voltage	PID	868/-	2.1 $^{\circ}C$
							Fuzzy-PID	682/-	0.98 $^{\circ}C$
Ding et al. [16] (2014), E[4]	IGBT	water	IGBT	0.64-0.68	91	Pump voltage	PID	155/43	NA (small)
							Fuzzy-PID	-	smaller
Sai and Reddy [120] (2016), S&E	Power Plant	water	Superheater	-	540	Coolant temp	PID	450/55	1.64/21.84
							Fuzzy-PID	344/70	1.4/14.62

[1]Simulation, [2]Insulated gate bipolar transistor, [3]Sintered porous copper wick, [4]Experimental

6.4. Setting operating conditions and control architecture

Safety and efficacy are of prime importance in thermal management. The question is: are the operating parameters and control algorithm safe to implement in hardware? Some minor deviations from desired setpoints can be acceptable, but the control scheme must not cause any harm to the hardware. Efficacy measures how effective the thermal management is in fulfilling the setpoints for variable loads.

To secure the safety and test the efficacy, the thermal management system goes through two phases of trials. '*Phase one*' is the safety trial. Therefore, the previously fitted correlations, operating parameters, setpoints, and thermal requirements must be evaluated. Moreover, since the disturbances to the hardware are vibrations with different amplitudes and frequencies and resultant accelerations, a dynamic correlation containing vibrational parameters and acceleration must be considered in the thermal management system. In this regard, the following correlation models fitted to the UNIJET® nozzle data for *static* and *dynamic* cases (constructed in [27] using the Generalised Buckingham Pi method [142]) are introduced to the thermal management system:

$$Bo = 3.87 \times 10^{-2} Ja^{1.5573} \left(\frac{\rho_l^2 \sigma v}{{\mu_l}^3}\right)^{0.5008} \qquad \textit{Static} \qquad (6\text{-}17)$$

and

$$Bo = 1.24 \times 10^{-2} Ja^{1.3920} \left(\frac{\rho_l^2 \sigma v}{{\mu_l}^3}\right)^{0.9809} Re_V^{-0.9869} \left(\frac{a}{H}\right)^{0.4825} Ac^{0.4998} \qquad \textit{Dynamic} \qquad (6\text{-}18)$$

where Bo is Boiling number ($qH/\mu_l h_{fg}$). $Re_V = \rho_l a \omega d_H/\mu_l$ is the Vibrational Reynolds Number. $Ac = \omega^2 a/g$, is the Dimensionless Acceleration Number. Ja is Jacob number ($Ja = C_l \Delta T/h_{fg}$), which considers both the convective and boiling heat transfer.

The thermal management system exploits a step-by-step algorithm shown in Figure 6-6. First, the initial operating conditions (fixed during the experiments) are set by the operator in a human-machine interface (HMI). A graphical user interface (GUI) is programmed in LabVIEW, hosted by a Windows computer. Then, the iterative part using the correlations examines the boundaries, considering the applicability of the spray system in maintaining conditions within the desired regime of nucleate boiling. (Nucleate boiling during all operating conditions must be capable of providing sufficient heat removal as required).

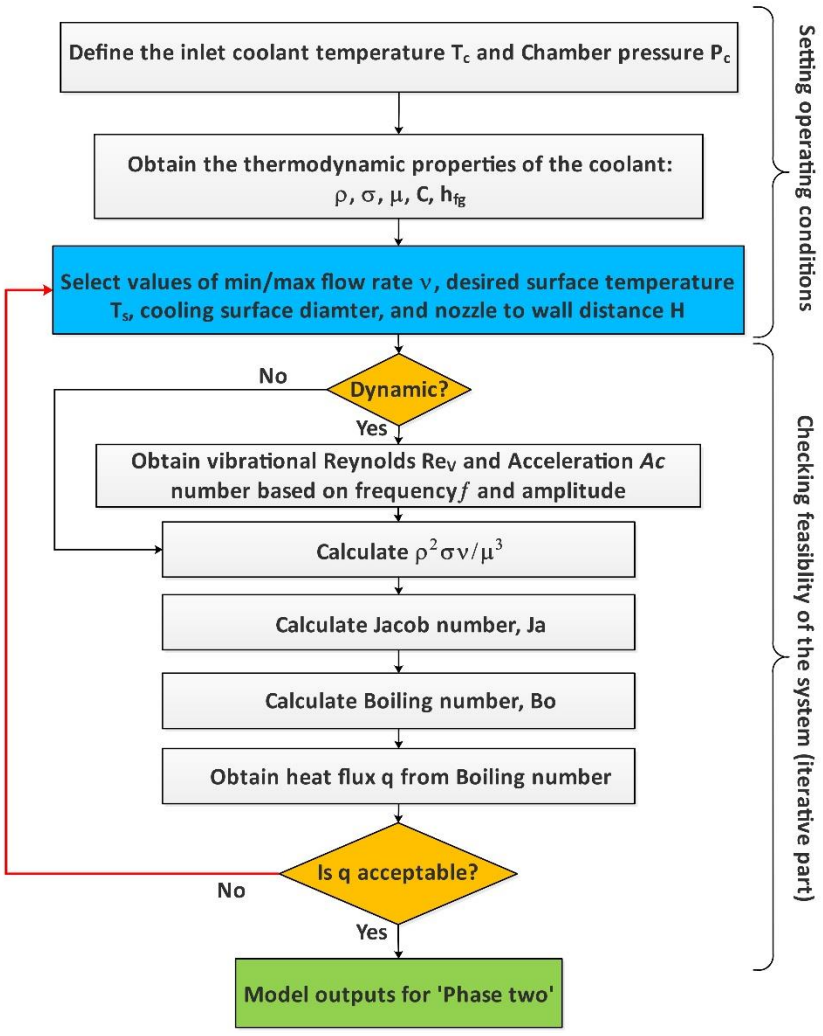

Fig. 6-6. Procedure of setting the operating conditions (Phase one: Safety test)

Choosing suitable setpoints for the spray cooling system is as important and challenging as the control task [147]. The desired parameters (such as surface temperature and flow rate) and requirements (e.g. heat flux) are complexly dependent on each other. In addition, several *dynamic* cases have substantial deviations from *static* results (heat flux and excess temperature). Therefore, the flow rates and spray patterns which result in an effective cooling at the same setpoints are different. In the present study, the trade-off between setpoints, boundaries, spray specifications and the requirements have been determined from plant trial and error and previous experience [27].

Once the desired operating parameters and suitable boundaries are successfully fixed, the thermal management system moves onto phase two. '*Phase two'* is the efficacy trial which demonstrates how well the control scheme works in tracking the trajectories induced by variable heat loads. This is done by an automatic control loop and a variable heat load generator. Figure 6-7 shows the sensor-based control diagram containing two closed-loop PID controllers, a setpoint generator, the HMI, the test section and the CompactRIO (NI cRIO-9035) with the FPGA containing I/O modules.

As can be seen in Figure 6-7, the flat test-piece is exposed to displacement vibration of the form $X = a\sin(\omega t)$ generated by the shaker. The tuning process of the PID controllers is a manual activity which will be explained in the next section. With a real-time processor, the FPGA in CompactRIO sends the control signals through a PCI bus, and receives sensor data. This data requires high-speed logic and precise timing (e.g. the control signals to the power regulators for the cartridge heaters, feed heaters, and the pump). Simultaneously, the human-machine interface (with a GUI) runs on the host computer screen to allow monitoring of the system state and for setting the operating parameters. The PID function chosen in the block diagram of LabVIEW also has an output range (filter) for the output voltage to the pump, which controls the pump speed and therefore the volumetric flow rate (read by the flowmeter). In practice, outputs from controllers are filtered to prevent damage to the actuators (in

our case, the pump). And second, to eliminate the risk of pump speed saturation which is harmful to the entire control strategy.

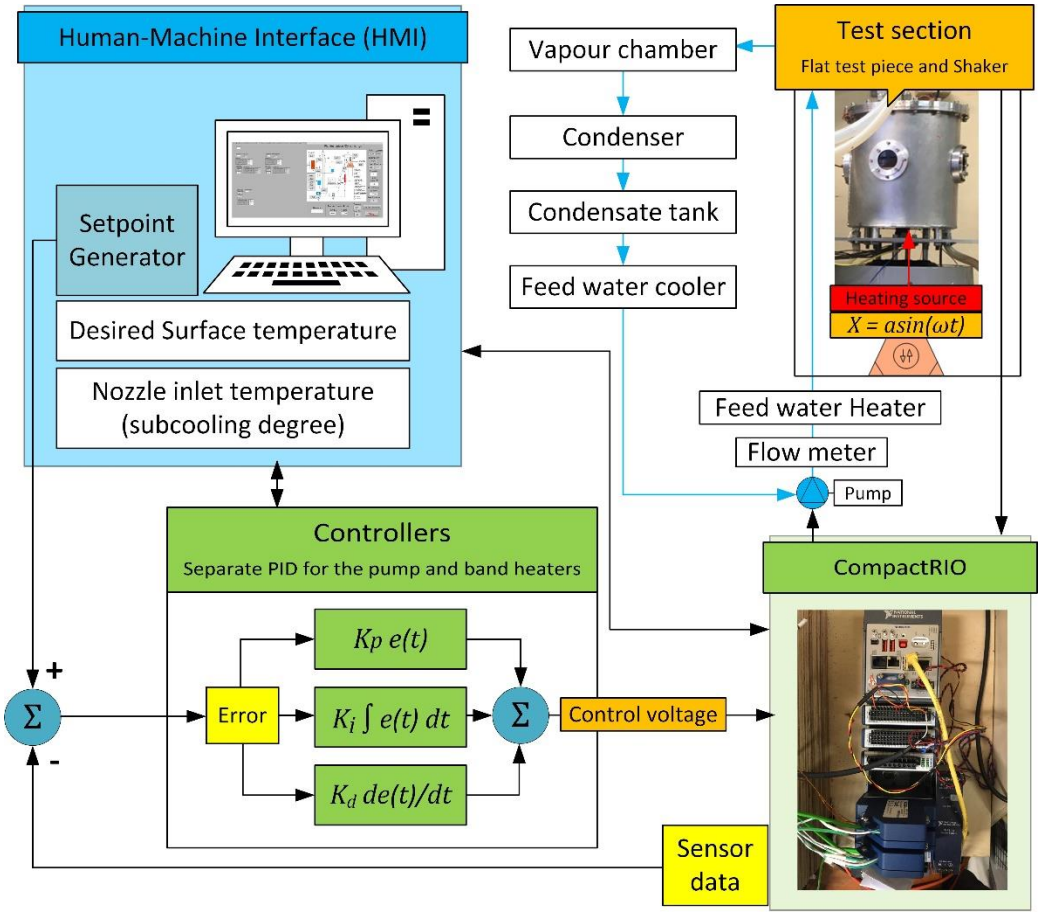

Fig. 6-7. Sensor-based control system diagram

6.5. Flat test-piece – Controller tuning and thermal management effectiveness in static and dynamic cases

The results for the flat test piece are given in the following three subsections. First, the manual tuning process of the surface temperature controller under *static* condition, are assessed, allowing with the efficacy and robustness of the tuned controller. Second, the impact of different controller gains on the control and thermal performance are discussed. In addition, the effectiveness of the thermal management system in energy saving for the pump is assessed in terms of coefficient of performance

(COP). Finally, the statically-tuned controller is used for *dynamic* conditions. The thermal management system is tested in dynamic cases with the highest change from static results in order to check the efficacy and suitability of the proposed thermal management system.

Control system tuning and thermal management

The tuning process of the surface temperature is a manual process. This has been achieved by trial-and-error with a closed-loop (feedback) control system plant in the hardware (explained in section 3.2), as well as the previous experience of the correlation model developments [27]. Figure 6-8 shows the temperature tracking and pump response to the applied setpoints and induced heat fluxes. The temperature setpoints are typical requirements and operating ranges chosen based on the thermal management needs of range extended hybrid electric vehicles [34], or electric vehicle cooling systems as well as electronic components (i.e. 110˚C to 135˚C and vice versa with heat flux changing between 0.2 to 1.96 MW/m^2). After several trial-and-error tests with a negative feedback PID controller, the most acceptable gains which sufficiently minimised the overshoot and undershoot (and gave rise to a reasonably quick settling time during the same trajectories) were found to be P=2.1, I=0.08, and D=0.001 respectively. Settling time plays a vital role in thermal performance and energy efficiency of the internal combustion engine (ICE) [31] in range extended hybrid vehicles. Also the thermal management system required for most of electronic components needs to have a fast response (less than 100 seconds). The ¼-cylinder test-rig and pipework designed and used in the present study resulted however, in a larger thermal inertia than acceptable. For this reason the settling time for a change in temperature from two setpoints of 110˚C to 135˚C in Figure 6-8a was an overly long 155 seconds. Test rigs of miniature scale are therefore suitable for the investigation of electronic component cooling.

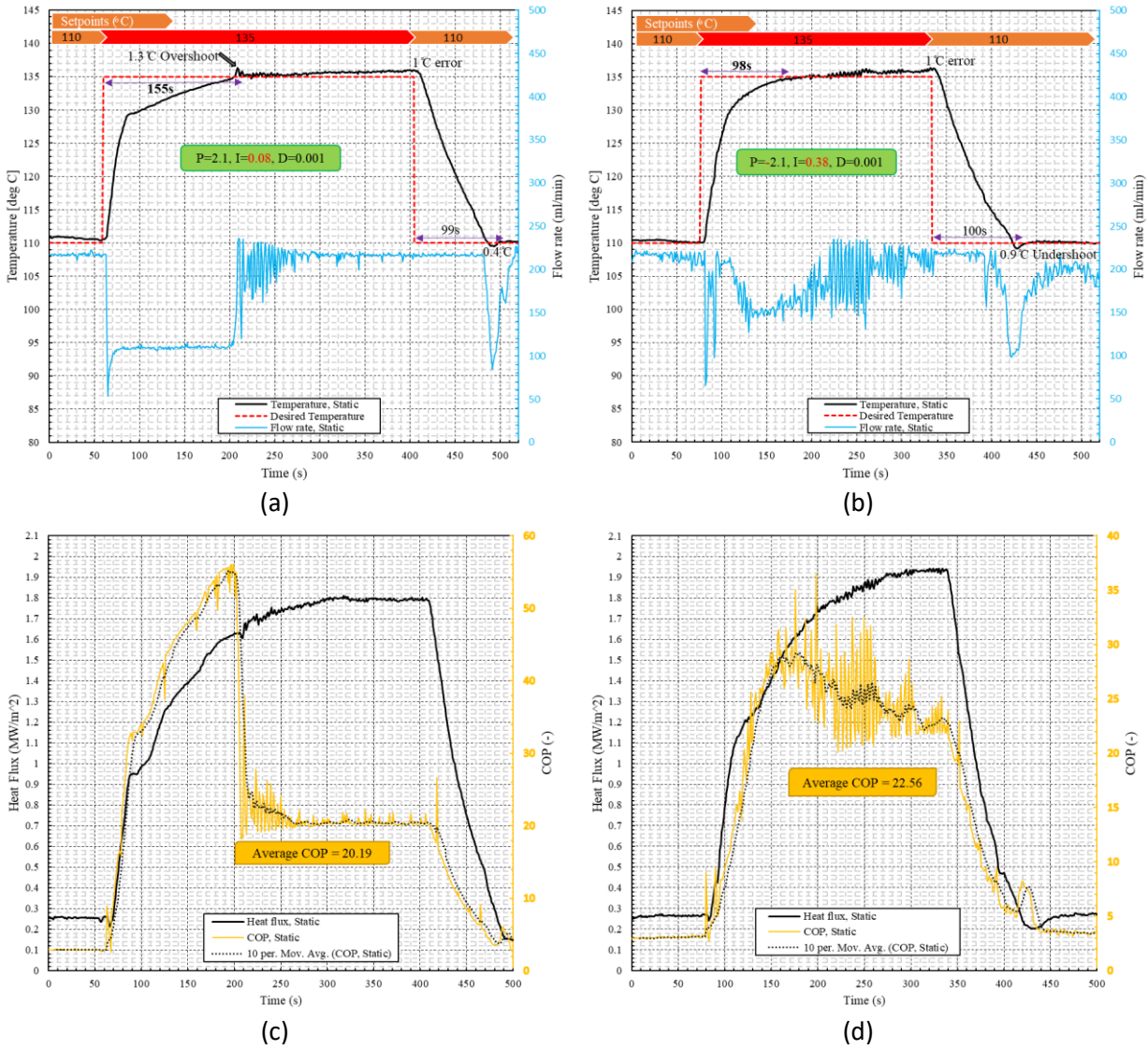

Fig. 6-8. *Static* case temperature tracking and the pump response to the applied setpoints: for (a) a positive proportional gain of P=2.1 with I=0.08 and D=0.001, (b) a negative proportional P=-2.1 with a large integral gain of I=0.38 and D=0.001; (c) and (d) Associated heat fluxes and COP measurements.

Although the current dissertation is mainly about testing the safety and efficacy of a spray thermal management system, several modifications considered to be practical in reducing the settling time were examined in another trial-and-error phase. The most successful was found to use a negative proportional gain (P=-2.1 in Figure 6-8b). It also used a larger integral gain (comparing to Figure 6-8a) and the same derivative gain (in Figure 6-8a), each with 'normal' positive signs. The negative proportional control would act to make the error worse during the rise time, but, after some time

(during the settling time) the integral control would dominate and correct the system. This has effectively worked to reduce the settling time (from 155 s to 98 s - a significant 37% improvement) with a negligible 1 s increase in settling time in cooling setpoints from 135 ˚C to 110 ˚C. In the current configuration, having a larger integral gain (i.e. 0.38 in comparison to 0.08 in Figure 6-8a) finally adjusts the controller to maintain a negative feedback loop. A negative proportional controller is generally unusual in and can suffer from a diminished phase margin or more severe overshoot, but it can work well in certain circumstances. Based on the desirable cost-benefit in the current thermal management system, it has been shown to be even more superior to a 'normal' set of PID gains.

An explanation of how and why this type of controller is workable is in the pump response in Figure 6-8. For the regular PID controller (Figure 6-8a), the pump works at a low speed and provides a flow rate of around 110 ml/min during the rise time. As soon as the error becomes positive, the flow rate surges to the highest possible (around 230 ml/min), trying to tackle the overshoot. Conversely, the flow rate for the negative proportional PID (Figure 6-8b) peaks at around 220 ml/min during the rise time, then gradually drops to around 160 ml/min to reach the setpoint (135˚C). Based on previous experience in developing the correlations [27], it was noticed that there is a reverse trend from a threshold when the covering diameter of the spray cone exceeds the area of the surface target. From that specific flow rate (threshold) the volumetric flux (a measure for effective volumetric flow rate) reduces. Therefore, the heat transfer rate reduces accordingly. (Note that it is stated on the UNIJET® nozzle manufacturer's data sheet, that the spray angle varies from 50˚ to 61˚). This hypothesis is therefore supported by Schwarzkopf et al. [145]. This means from a threshold, the trend of heat transfer is the opposite; the higher the flow rate is, the lower the heat transfer rate will be (with the current configuration, it is conjectured to be above 200 ml/min). The same reverse trend has been observed by Zhang et al [60]. Thus, for the negative proportional PID controller, it is concluded that the shift between two trends of

heat transfer during rise time between 90 to 110 seconds (20 seconds of reverse trend) could have resulted in a further increase in the surface temperature and therefore a reduced settling time. (The equivalent results in Figure 6-8 subplots can be compared.) This reverse trend above 200 ml/min could be supported by Figure 6-8b when the steady-state error of 1 ˚C has occurred but only after passing 200 ml/min. It should be noted that the differences between heat transfer rates before and after this threshold are subtle. However, the difference is apparently practical enough to be used for the purpose of adjusting the settling time to approach a more realistic time constant.

The proposed controller initially raises several important questions. The first question concerns why a lower flow-rate has not been considered by setting a minimum margin in order to have a smaller heat transfer rate to do the same task (i.e. a reduced settling time). The answer is: because the UNIJET nozzle is not able to produce a full cone spray at low mass flow rate, owing to lower nozzle pressure differences. But imperfections in the spray flow field could change the expected trends in the cooling regimes. For example, a very low flow rate may not be able to maintain the nucleate boiling regime for the required high heat fluxes and would therefore endanger the safety. For this reason, it has not been tested. In addition, a low flow rate (e.g. 50 ml/min, see figure 6-8c at around 65 seconds) cannot secure the required high heat fluxes. Moreover, a negative proportional PID gain which results in having a higher volumetric flow rate during the rise time would suppress the effect of vibration frequency as a result of a higher droplet velocity, which is consistent with the experimental results in [173]. This means that during the rise time the negative-proportional PID controller could in theory be more reliable and adaptive to the dynamic conditions including high-frequency cases. The dynamic results discussed shortly will support the hypothesis.

The second question concerns other possible control solutions such as controlling the nozzle-to-surface distance, changing the degree of subcooling [158], introducing a pulsating spray flow field [128,

174], calculating volumetric flux to reflect a proper trend of the effective spray flow-rate. Control of the nozzle-to-surface distance cannot be made fast enough owing to the need for a mechanical mechanism in the form of a micro positioning slide [173]. The inertia of the feed-heaters does not allow a rapid change in the inlet temperature required to control the degree of subcooling. Also, the calculation of volumetric flux, to reflect a proper trend of the effective spray flow-rate, impinged on the target surface, is not feasible in a design of a cooling system in which a minimum number of sensors is required. Even using existing empirical correlations for volumetric flux [50] such as given by:

$$\bar{\vec{v}} = \frac{v}{\pi(Htan(\frac{\vartheta}{2}))^2} \tag{6-19}$$

needs a real time spray angle (ϑ) measurement which adds uncertainty to the plant. These issues leave room for future investigation although they incorporate many complexities into the design of the test pieces. For instance, a pulsating spray cooling module in the current thermal management system requires a fast response solenoid valve and an electronic circuit. Furthermore, the correlations must be updated through dimensional analysis and involve the effect of pulsed spray flow field expressed in terms of Strouhal Number ($St = \frac{fd}{v}$). Therefore, the best solution for the current design and configuration is using a variable speed pump module. Overall, using a negative-proportional PID controller, is workable and fulfills the aims of the study. The efficacy and robustness of a PID controller with negative-proportional gain, both with and without vibration is now examined.

The effect of PID controller gain changes without test-piece vibration: static cases

To better understand the effects of PID gain changes on the thermal performance and energy efficiency, a coefficient of performance (COP) has been defined and included in figure 6-8c and 6-8d. The COP is defined as the ratio of the heat removal to the required pumping power given as:

$$COP = \frac{Q=q\pi d^2/4}{VI} \quad (6\text{-}20)$$

where, Q, V, and I are respectively: the heat removal provided by the spray cooling, the voltage, and the current supplied to the pump. To smooth out noisy fluctuations in the COP, a 10-sample moving average is used. As can be seen in Figure 6-8d, using a negative proportional not only achieves a higher heat transfer rate, but also gives an average COP=22.56, which is a 10.5% increase in the performance compared with use of the regular PID controller (Figure 6-8c).

Figure 6-9 shows the results for two more data sets during the tuning process. First, up to 450 s, with a slightly larger integral gain (I=0.48) and after 450 s with a smaller proportional gain (P=-2). A further decrease in the settling time was observed with a higher integral gain of I=0.48. This was because the integral gain counteracted the negative proportional gain after a longer time. Consequently, the spray flow rate has been maintained in the reverse trend for a longer period. As already explained, this is a reason for a faster settling time. The lower heat transfer rate could be supported by the 1 ˚C steady-state error (in Figure 6-9 at around 130 s) while the pump was operating at approximately 215 ml/min. A disadvantage of this, is that after the integral gain was compensated for, the effect of a negative proportional gain, resulted in the thermal management system being unstable and fluctuating between two trends (at 170 s in Figure 8a). This resulted in a 'bouncing' response, although a derivative gain twice the previous magnitude (i.e. D=0.002), was able to stabilize these fluctuations. The result for a smaller proportional gain (P=-2) is also consistent. Since the integral gain is then dominant, the fluctuations occur earlier producing a longer settling time (but still faster than a positive proportional gain). But these settings are not recommended because the COP values of 22.25 and 22.52 in Figure 6-9b are less than the previous COP=22.56.

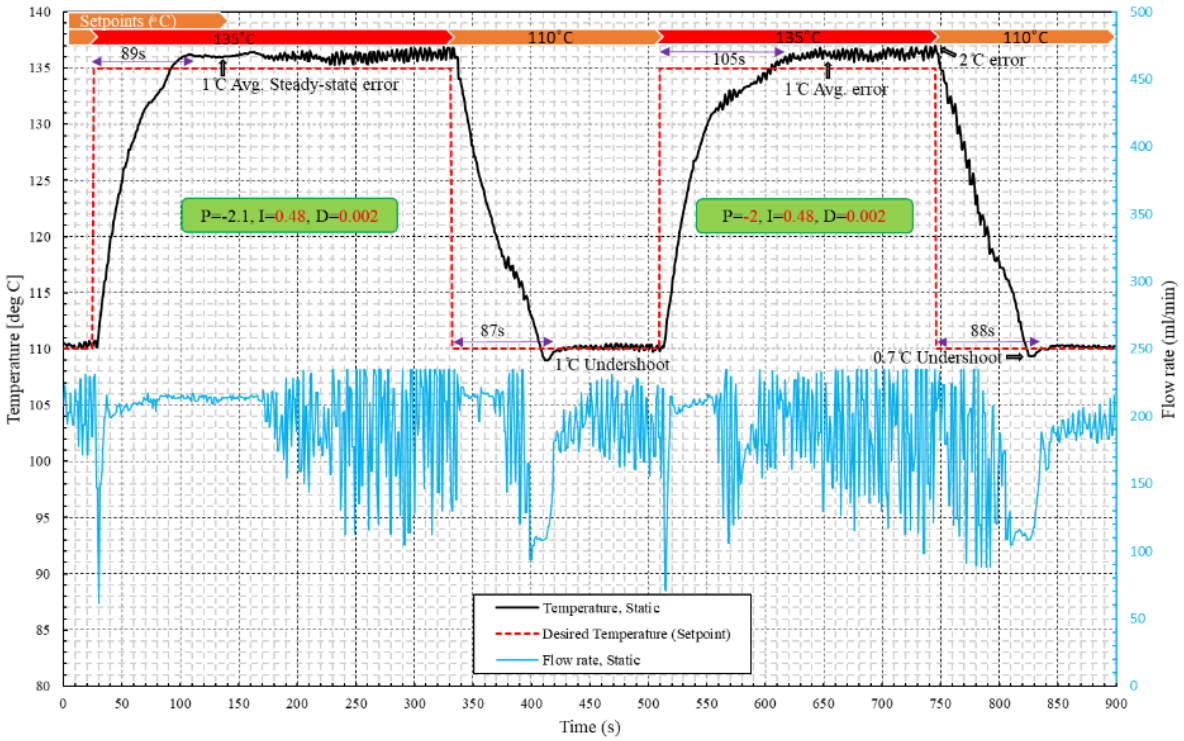

(a)

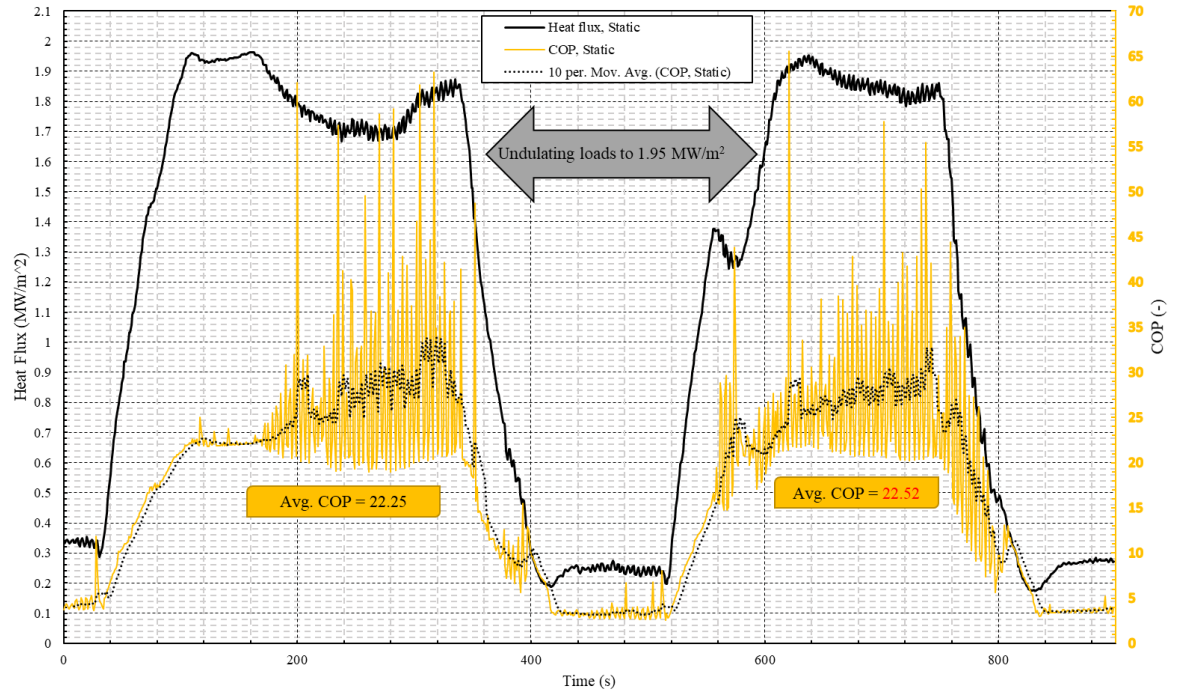

(b)

Fig. 6-9. *Static* case temperature response to the applied setpoints (between 110 and 135˚C) and load steps between 0.2 and 1.95 MW/m^2: (a) Temperature tracking and the pump response for proportional gains of -2.1 and -2 with I=0.48 and D=0.002, (b) Associated heat flux and COP measurements

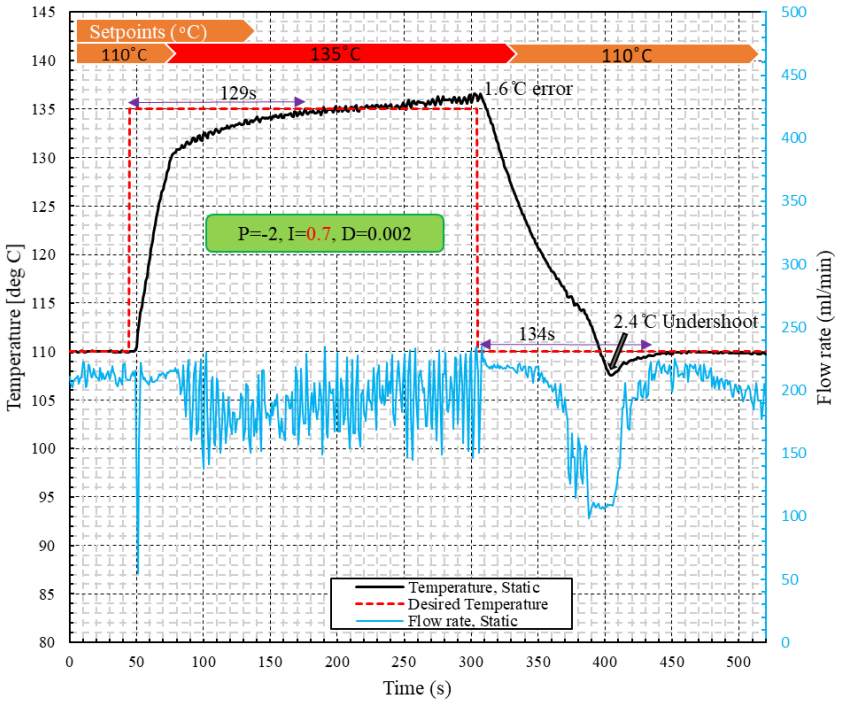

(a)

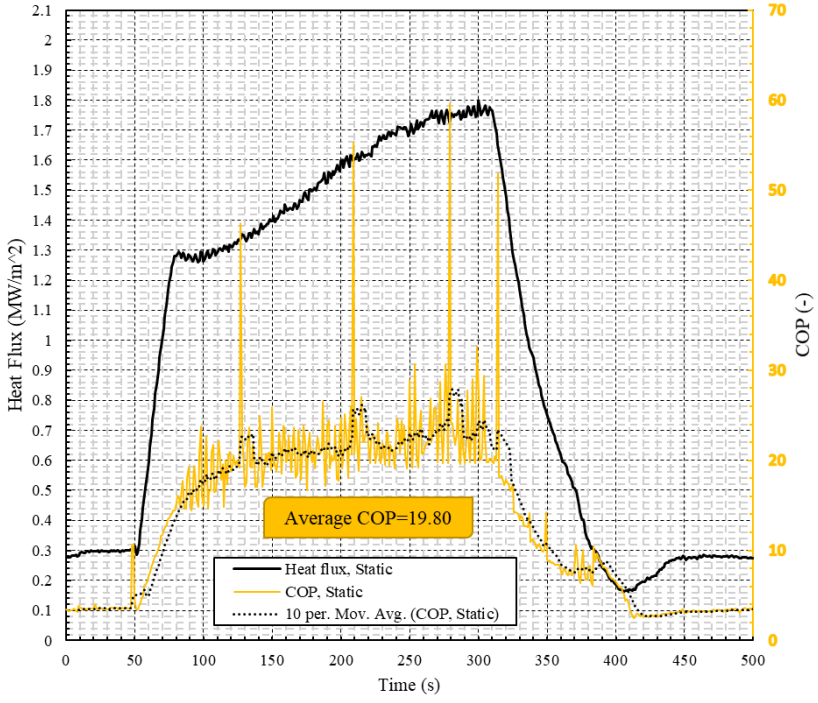

(b)

Fig. 6-10. *Static* case temperature response to the applied setpoints (between 110 and 135˚C) and load steps between 0.2 and 1.8 MW/m^2: (a) Temperature tracking and the pump response for a larger integral gain of 0.7, (b) Associated heat flux and COP measurements

Figure 6-10 shows the effect of changing the integral gain in another trial and error experiment. The PID has the larger integral gain value of 0.7 but the same gains as Figure 6-9a. This was to reduce the fluctuations in the pump response to changes in temperature. In comparison to Figure 6-9a, the oscillations in the flow rate are reduced. The settling time increases since on average during the rise time the flow rate was in the reverse trend (i.e. above 200 ml/min) for a shorter time. The overshoot was slightly better, but the undershoot was worse (at 2.4˚C). A disadvantage of using a larger integral gain is the average COP, as is shown in Figure 6-10b, is less than those using a smaller integral gain of 0.48. As soon as the influences of the PID gains were discovered through the tuning process, the thermal management system was challenged for *dynamic* cases. The next section examines these results further.

The effects of PID controller gain changes with test-piece vibration: dynamic cases

Experimental evidence shows that vibration generally lead to an attenuation of convective heat transfer rate. As a consequence, when the test-piece is made to vibrate, the controller instructs the pump to compensate for the deterioration in the rate of heat transfer. This consumes more power and thus reduces the COP for the dynamic cases below those of static conditions. This section investigates the performance of the controller with vibration, in particular, the effect that different gains have on heat flux.

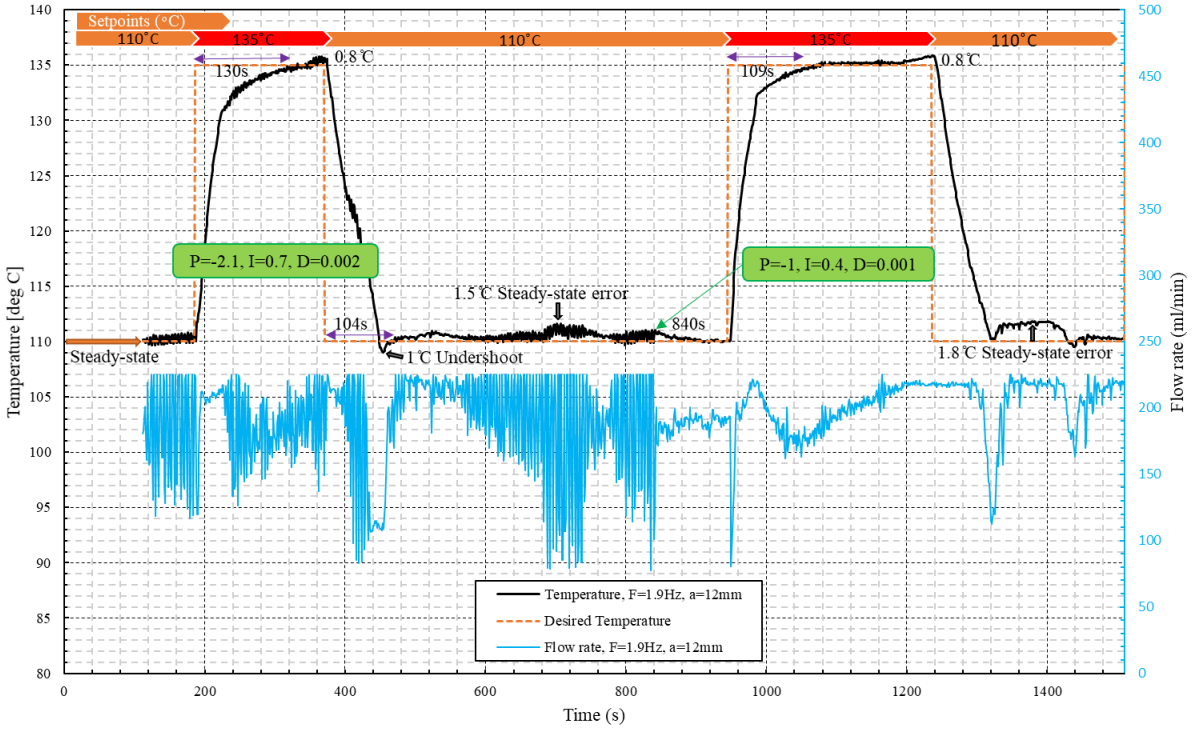

(a)

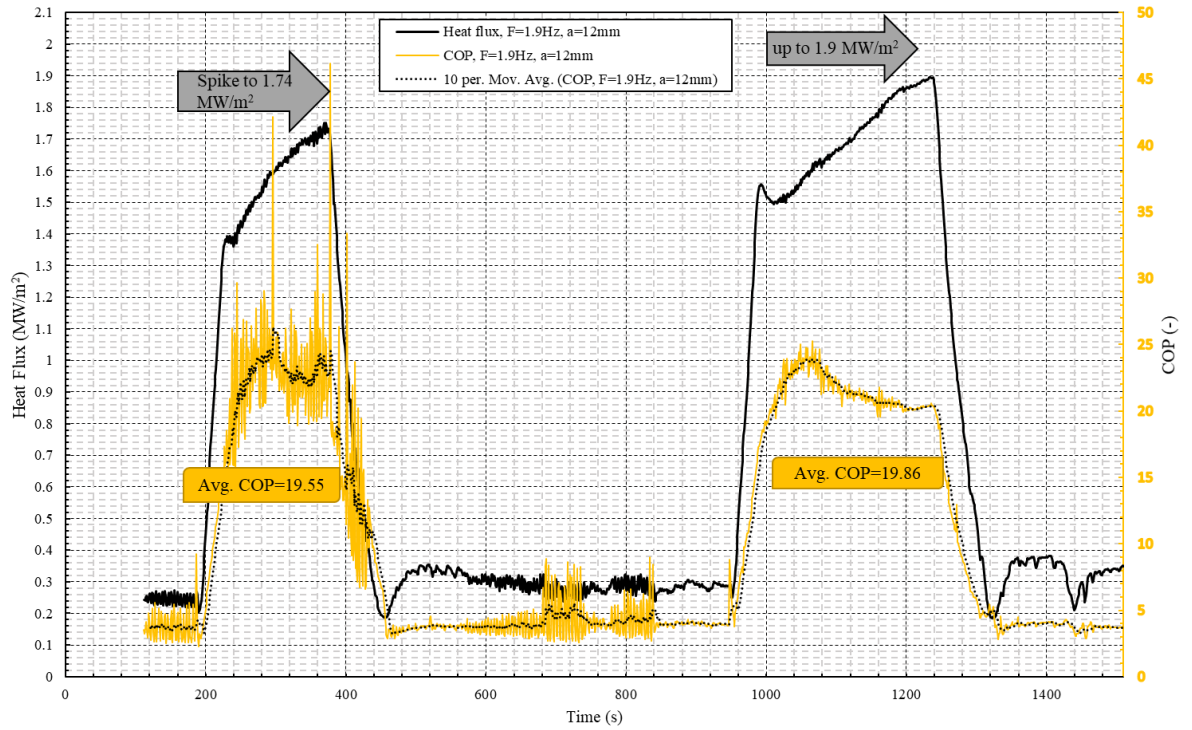

(b)

Fig. 6-11. Temperature trajectories induced by applying temperature setpoints and load steps for large-amplitude vibration of 12mm: (a) Temperature tracking and pump response for a PID with large gains following by a smaller gain PID, (b) Heat flux disturbances and real-time COP measurements

Figure 6-11 shows a data set during the tuning process of a large amplitude vibration case with a=12 mm at a frequency of f=1.9 Hz. On the left-hand side of Figure 6-11 for a duration up to 840 seconds, a trial of an unsuccessful PID controller (with large gains) is shown. From 840 seconds, a PID controller with considerably smaller gains was considered to allow inspection. Oscillations in temperature history and the undulating pump response, for higher gains, clearly indicates the profound influence of having different gains. As can be seen, the smaller gains of P=-1, I=0.4, and D=0.001 smooth the pump response and consequently also smooth the undulating temperature tracking. Furthermore, the settling time is also improved. The problem with small gains is that a steady-state error of 1.8°C produced, which also leads to a longer return time.

Taking into consideration the deteriorating consequences in the dynamic cases, plus the need to test the adaptive capability of a PID controller tuned for the static cases, a PID controller with gain values: P=-2, I=0.7, and D=0.002 was chosen to produce the results in Figure 6-12. These gains were the same as those that were attempted for the static case in Figure 6-10. As expected, the rise time is improved compared with the static case owing to the impeding effect of vibration. Moreover, the lower average COP value of 18.06 in Figure 6-12b (compared to 19.80 for the static case) indicates increased power consumption for the same heat flux (up to 1.8 MW/m^2).

Beyond 400 seconds, a PI controller with gains: P=-2, I=0.7, D=0 (rather than D=0.002) is tested to establish whether the derivative gain is genuinely having any influence. A broadly accurate guide in the tuning process of a PID controller is to add derivative control to reduce the overshoot. It is evident that the differences between overshoot and undershoot, with and without the derivative gain, actually justifies derivative control. Furthermore, the subtle difference in COP, being smaller for the PID, suggests the pump is managed by the derivative gain.

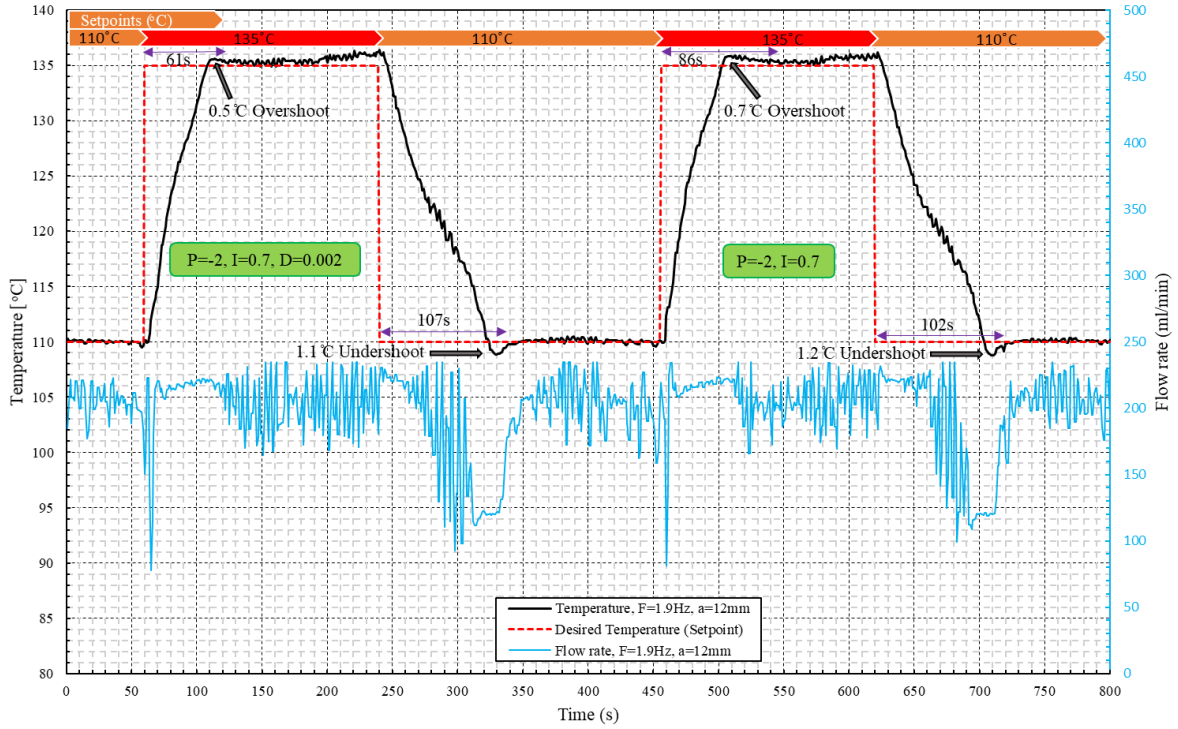

(a)

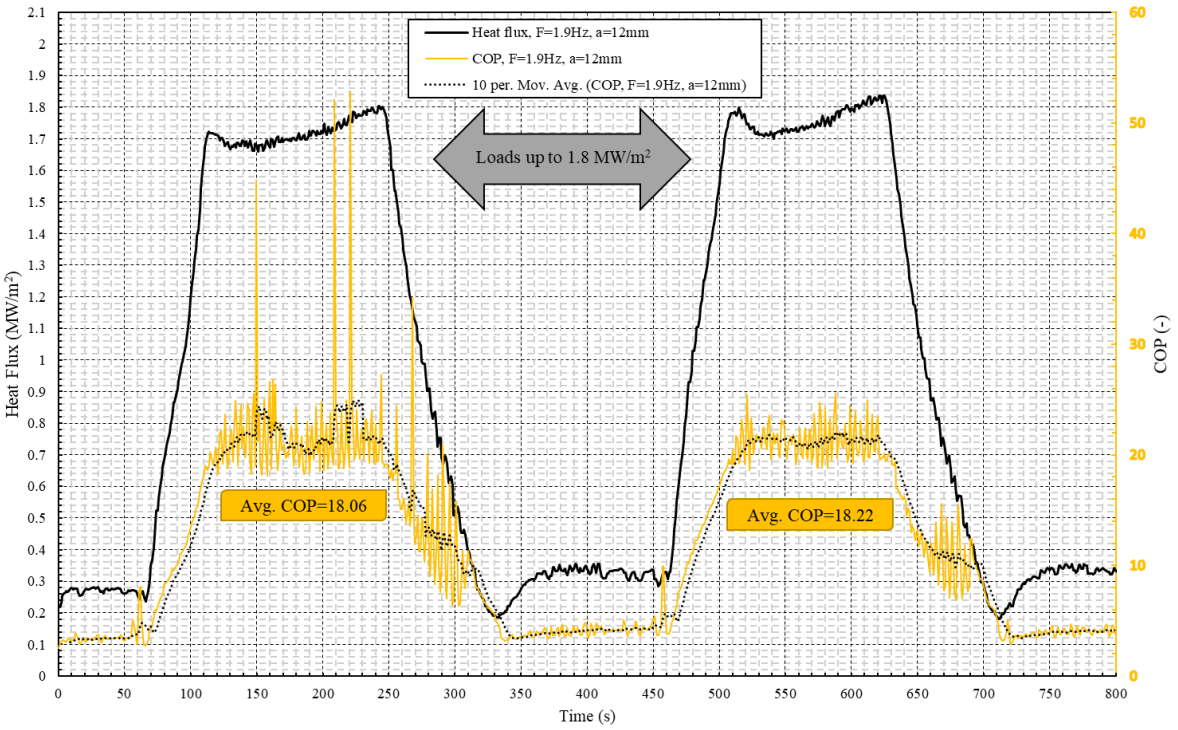

(b)

Fig. 6-12. Temperature trajectories induced by applying setpoints (between 110 and 135˚C) and load steps (up to 1.8 MW/m^2) for large-amplitude vibration of 12mm: (a) Temperature tracking and pump response for a PID and a PI controller, (b) Heat flux disturbances and real-time COP measurements

Figure 6-13 shows results for another important dynamic case of high frequency vibrations. The test piece during this experiment was shaken with a frequency of f =400 Hz and an amplitude of a=0.02 mm. The same PI and PID controllers for the large amplitude case managed the variable speed pump for the role of surface temperature tracking. The results in Figure 6-13 show a reasonable rise time, overshoot and undershoot, and that successful thermal management was achieved for loads between 0.2 MW/m^2 to 1.8 MW/m^2. Also, the effect of derivative gain was consistent with the previous explanation (i.e. error reduction and less settling time for PID controller). Similarly for the PI controller in comparison with the PID controllers in Figure 6-13a, there is an increase in overshoot, undershoot, and settling time of 0.3 - 0.4°C, 0.4 - 0.5°C and 16 - 20s, respectively (note that there is a repeat for the PID controller). As expected, the COPs for the PID controllers shown in Figure 6-13b, were lower than for the PI controller.

The repeatability of the results is finally examined with an extra step-load for the PID controller. The resulting temperature differences were 0.1°C for overshoot and undershoot, and a 3 second difference in the rise and settling times. The coolant flow rate during the repeatability test was similar to the previous load step, suggesting that overall, the experimental measurements were repeatable.

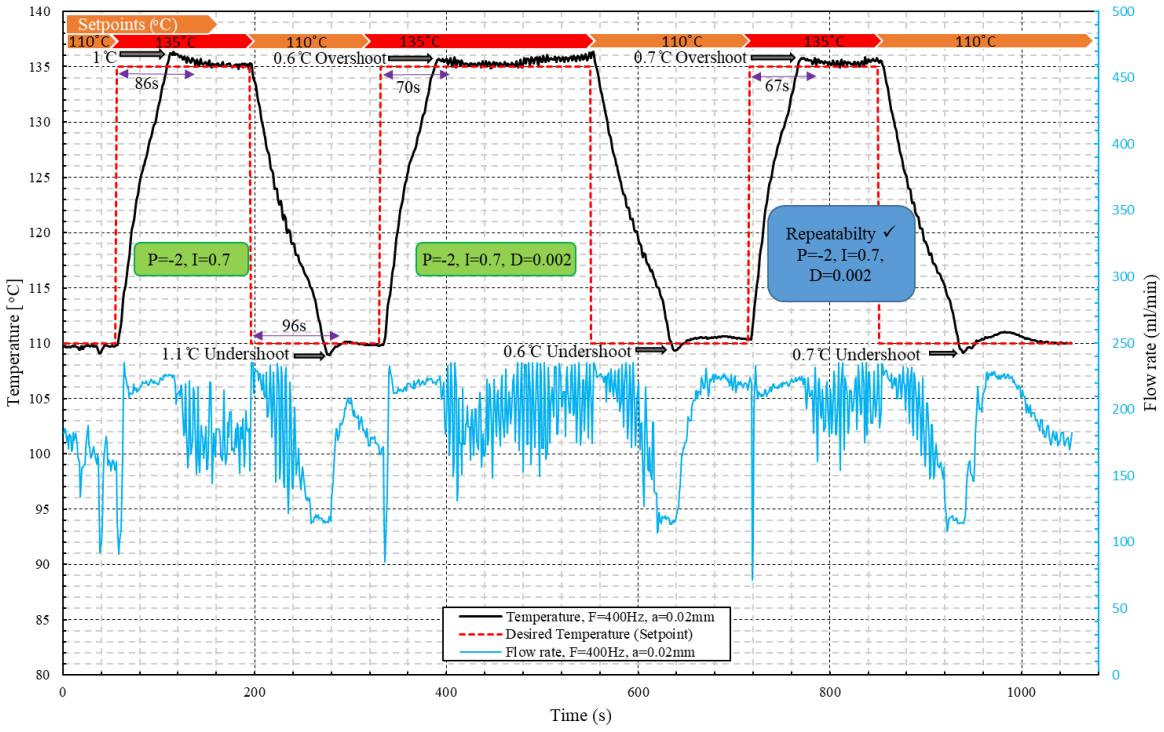

(a)

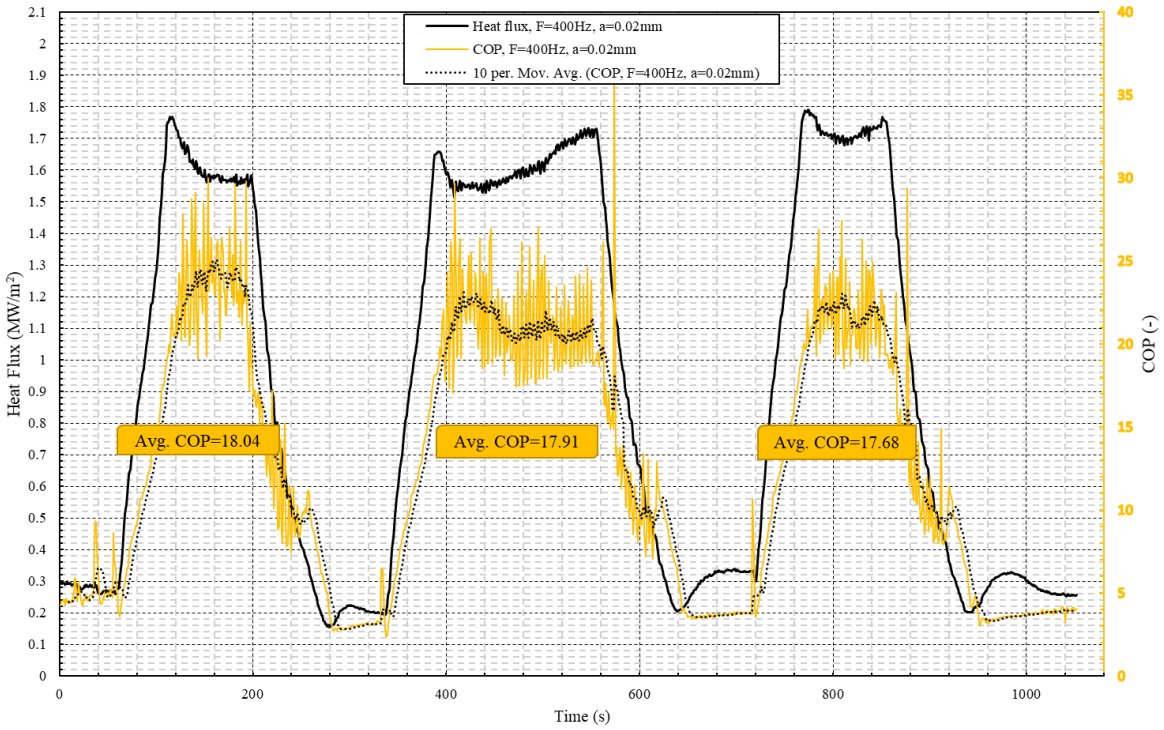

(b)

Fig. 6-13. Temperature trajectories induced by applying setpoints (between 110 and 135˚C) and load steps for high-frequency vibration of 400Hz: (a) Temperature tracking and pump response for PI and PID controllers, (b) Heat flux disturbances and real-time COP measurements

6.6. Spray evaporative heat transfer assessment for curved vibrating surfaces using temperature ratio, and tuning the hardware control system for use with the ¼-Cylinder test-piece

Before attempting to show the temperature control results of the ¼-cylinder test-piece, some preliminary explanation is needed of the measures taken to get the hardware control system shown in Figure 6-7 to function as intended. To put this need into an application context, Mudawar et al. [34] reported that feasible thermal management applications for hybrid electric vehicles should have the potential to dissipate heat within the range of flux 1.5 - 2 MW/m^2. In this respect, spray evaporative cooling indicates that such heat removal requirement is achievable. There is however no published evidence yet, of successful surface temperature control of an actual spray evaporative cooling system in the presence of vibration. To address this need, the ¼-Cylinder test-piece has been used to establish whether the temperature control system in Figure 6-7 has adequate precision, flexibility, and viability to control surface temperature mainly using coolant flow-rate control (using varying pump speed). In the next section, the effect of mechanical vibration on spray evaporative cooling of curved surfaces is now addressed.

Effect of vibration on the heat transfer of three-dimensional surfaces – temperature ratio and time constant during free response conditions.

The test results presented here aim to examine the effect of mechanical vibration on the heat transfer of three-dimensional surfaces. The heat flux distribution in the ¼-Cylinder has a two-dimensional nature. This stems from the design of the test chamber. Therefore, it has not been possible to obtain quantitative estimates of the heat flux from differential temperature measurements involving embedded thermocouples. Instead, comparative estimates have been made from the rate of change of measured temperature (obtained from a thermocouple positioned 1mm below the coolant-side surface) with time. Thus, it is useful to define a temperature ratio, θ, where:

$$\theta = \frac{T_t - T_{ref}}{T_{t=0} - T_{ref}} \quad (6\text{-}21)$$

And where T_t is the measured temperature at time t, $T_{t=0}$ is the measured temperature when the heaters are turned off, and T_{ref} is some reference temperature (taken as $T_{ref} = 110\,^{\circ}C$).

The variation of this temperature ratio with time is shown in Figure 6-14 for all the tests undertaken with and without vibration (with a=0.01 to 3 mm for f=6 to 400 Hz), and with constant electrical power (1 kW) and mass flow of 110 ml/min (two nozzles i.e. 2×55 ml/min). The maximum temperature (recorded 1 mm below the coolant-side surface) was achieved in around 10 minutes. The location of this thermocouple was chosen based on a transient thermal FEA model where the maximum temperature occurred. After about two minutes at a thermal steady-state, the heaters were switched off, and the test piece allowed to cool down.

Inspection of Figure 6-14 suggests that there is a definite effect of mechanical vibration on the heat transfer. This is supported by the time it takes for each cooling response to decrease to 37% of the initial value (i.e. time constant). Since the cooling follows from turning-off the heaters, the results in Figure 6-14 can be considered as the system free response. Therefore, as can be seen from Figure 6-14b (a zoomed-plot of Figure 6-14a), the time constant for the static case results is shorter (at 122 s) than those cases with vibration (greater equal than 129 s). This is consistent with the flat test-piece results that the vibration in general impedes the heat transfer. However, at the beginning (between 0 to 40 s), the local heat transfer rate for some of the dynamic cases is slightly higher, but this could be the effect of uncertainty. But the level of confidence in this result is demonstrated through two sets of repeat tests (shown in Figure 6-15). The higher heat transfer for the static case, however, is evident after t=80 s in Figure 6-14a. This higher rate allows the test piece to be cooled down to 110 ℃ between 26 and 38 seconds faster than for dynamic cases.

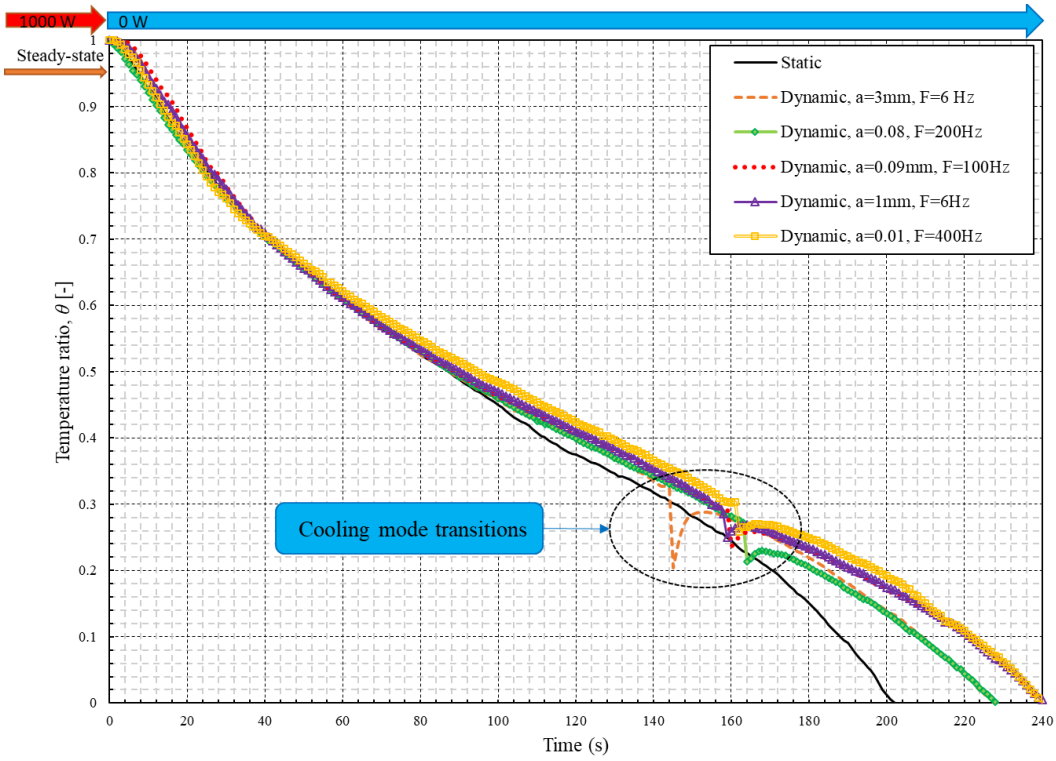

(a)

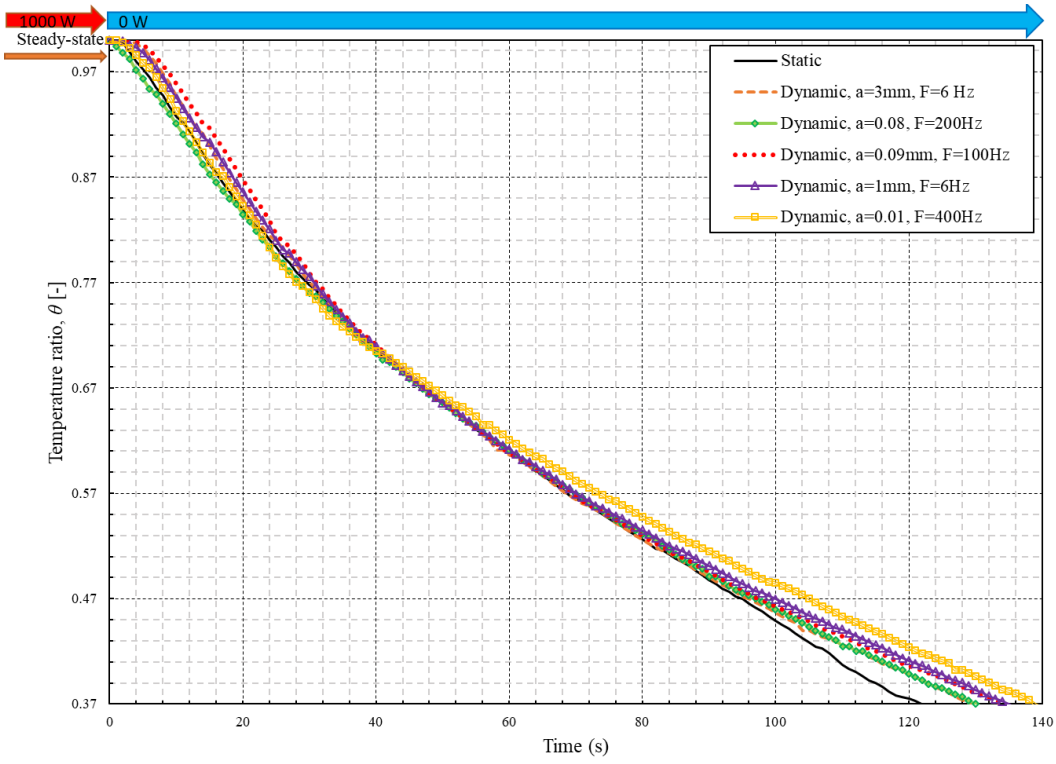

(b)

Fig. 6-14. ¼-Cylinder free response results: a) temperature ratio, θ, for static vs dynamic results, and b) time constant results (from 100% to 37% of the initial value)

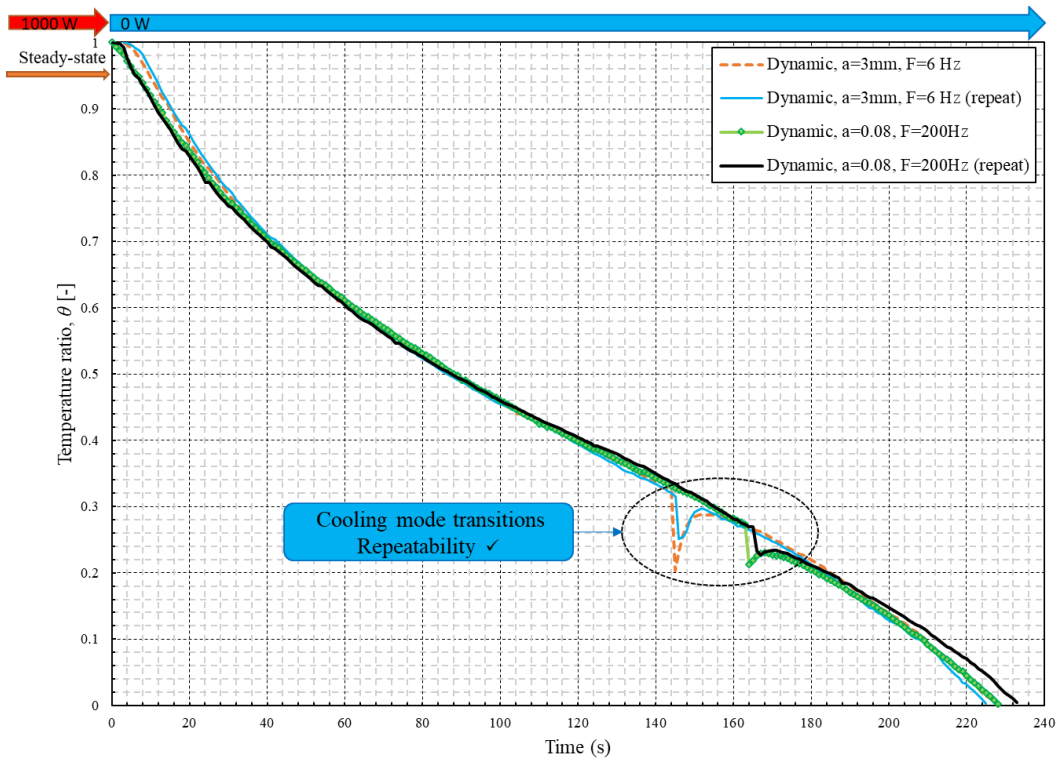

Fig. 6-15. Repeatability of the temperature ratio results for the ¼-cylinder test piece

It should be mentioned that, there is a change in slope of the variation of metal temperature with time. The time of this change for each case is different. For the dynamic cases, this change occurs with a sudden plunge in temperature between 144 s and 148 (signified with an ellipse in Figure 6-14a). These temperatures are equivalent to the surface temperatures of between 114 and 116 ℃. This occurred in all the dynamic cases and is consistent with the surface temperature itself reaching the temperature at which nucleate boiling begins to take place. It is conjectured that for the results with vibration, an earlier transition from two-phase to single-phase cooling modes is the reason for slower cooling in comparison to the static case. In other words, the contribution to the total heat transfer by latent heat is higher for the static case, therefore proving that the vibration impedes the heat transfer. This hypothesis is consistent in the remaining experimental measurements reported in the next section (i.e. temperature control results). Furthermore, the repeatability of the cooling mode transitions is also examined in Figure 6-15, which shows very reasonable quality.

Control performance results: Static Vs Dynamic

Hot-metal temperature control of actual ¼-cylinder test piece hardware is discussed in this section. A total of three PID controllers (all implemented using NI LabVIEW) have been adapted to achieve coolant-side metal temperature control and verification: one PID controller acts as the temperature controller, another controls the coolant pump speed, and a third controls feed-water temperature. The temperature PID controller is actually PI (since the PID gains are: P=2, I=0.6, D=0). It is used to follow the desired cooled-metal surface temperature during variable thermal load-steps, with temperature measured using a single embedded thermocouple 1 mm beneath the surface inside the test chamber. The PID controller, used for flow-rate control, has gains P=0.003, I=0.008, and D=0.05. This achieved flow stability which was important to avoid sudden on-off switching of the pump should the surface temperature PID controller be suddenly switched-off. The third PID controller (with gains P=3, I=0.78, D=0.09) maintains the feed-water temperature at the desired set-point to maintain constant degrees of sub-cooling at the inlet. This is achieved with a 0 to 5 V controllable power regulator (United Automation, EVR-25BF, AC Burst Fire Controller). All of the PID controllers are implemented via the NI LabVIEW software (the same as for the flat test-piece control architecture).

Figure 6-16 shows the controlled surface temperatures during different set points and thermal loads for two sets of test runs with vibration (at F=6 Hz, and a=3 mm), and without vibration. The equivalent results are plotted against each other to better compare the effect of vibration on the control scheme. The secondary axis shows the flow rate, or in other words, the response of the pump during the load steps and set points. This is done by first conducting the static test runs and obtaining the best control performance by trial and error in the tuning process of PID controllers (i.e. the least steady-state error and settling time). Then, the dynamic test runs were performed to establish that the controller can adapt to the dynamic environment created by the shaker, and also to show the effect that vibration has

on the control of temperature. The arrows on Figure 6-16, show variable thermal load fluctuations of between ± 35 – 40 W, which are superposed at the end of each of the step changes when a steady-state temperature has been reached and the steady-state control error is zero.

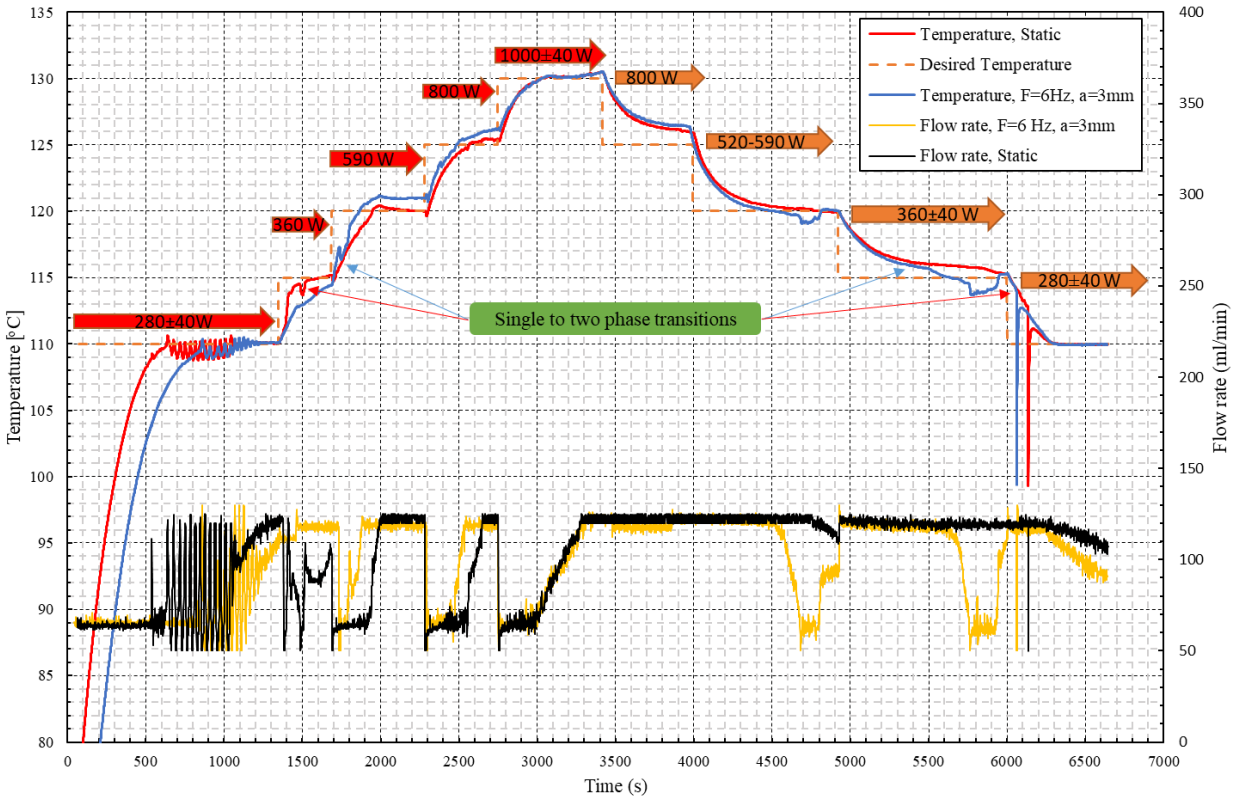

Fig. 6-16. Coolant surface temperature control of the ¼-cylinder test piece; whole range

The results in Figure 6-16 clearly show that the controller during the heating mode is successfully adapting to the dynamic condition with only a steady-state error of around 1 ˚C at setpoints of 120 ˚C and 125 ˚C. During the cooling mode (involving steps from higher loads to lower thermal loads, i.e. after 3400 s) where there is one step from 130 ˚C to 125 ˚C, the steady state error is also about 1 ˚C. This steady-state error is present for both of static and dynamic cases. The reason for this is evident from the flow-rate where the pump-speed has reached maximum before the end of the cooling step and not able to provide higher flow-rate of above 130 ml/min needed for PJ8 nozzles.

To confirm this, and to show that when maximum speed is not reached, temperature control is robust, two consecutive thermal load changes were made, from the minimum of 280 W to a maximum of 800 W, and back to 280 W, with the desired surface temperatures ranging between 110 ˚C and 125 ˚C. The results are shown in Figure 6-17. As can be seen, the flow-rate range is now sufficient to manage this extreme scenario. Control has been achieved without any steady-state error for both dynamic and static cases.

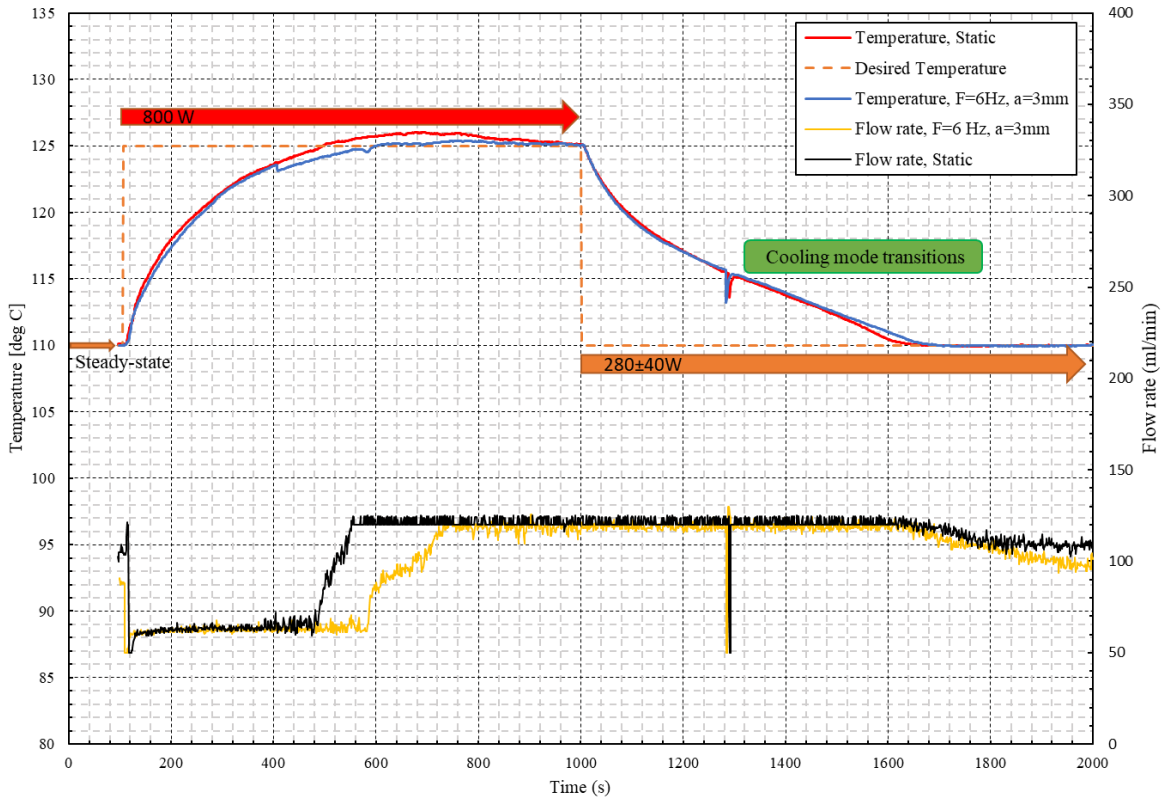

Fig. 6-17. Coolant surface temperature control of the ¼-cylinder test piece; high-low and low-high load steps

Single to two-phase transitions are also demonstrated in Figure 6-16 which play a prominent role in the control of spray evaporative cooling. For the spray cooling during heating and cooling the test piece (i.e. above approximately 114˚C for static and 116˚C for dynamic) vibration appears to reduce the two-phase spray cooling-rate, showing that the controller works better in the static case. By contrast, during the single-phase regime (i.e. less than about 114˚C for static and 116˚C for the dynamic case), vibration

has an enhancing effect on the surface temperature and therefore the controller uses lower flow-rate variations in comparison to the static case. The flow rate however, is not an appropriate measure for the comparison (as was mentioned for the UNIJET nozzle in the flat test piece results) because it is also stated in the manufacturer's data sheet for PJ8 nozzles that the spray angle performance varies with pressure. For the single-phase, the results are consistent with the enhancing effect of vibration to the heat transfer as mentioned in the work of Sathyabhama et al. [10].

6.7. Conclusions of Chapter 6.

A thermal management system, using spray evaporative cooling, has been designed, built, and experimentally-tested to assess its ability to control the temperature of two particular instrumented and electrically-heated test-pieces exposed to vibration from a shaker. These component parts represent a flat test-piece and a ¼-cylinder test-piece. To model the system, an experimentally calibrated dynamic correlation model has been used to represent the physics of spray evaporative cooling of a flat test-piece exposed to vibration. To enable stability analysis of the thermal management system using a PID controller, the nonlinear correlation model has been replaced by an optimum 1^{st}-order linear model obtained by solving an appropriate Wiener-Hopf equation. This allows practical stability assessment of closed-loop temperature control for particular choices of PID controller gains. To verify the predicted control system performance via simulation, experimental measurements appropriate to automotive vehicle component applications, includes large-amplitude, low frequency vibration, at 12 mm and 1.9 Hz, and at low amplitude, high-frequency vibration, at 0.02 mm and 400 Hz. The effects of different PID controller gains on the thermal management system performance under static and dynamic conditions, has been assessed using a coefficient of performance (COP), defined as

the ratio of heat power removal to the required pumping power. The main conclusions of Chapter 6 are:

- The tuning process of the actual control system implemented in hardware is a manual approach. A set of trial-and-error tests has been undertaken involving experiments without vibration to obtain the best PID gains for a closed-loop (negative feedback) control system. Gains with a very reasonable overshoot (1.3 °C) and settling time (155 s) were found to be P=2.1, I=0.08, and D=0.001.
- The thermal inertia of the test rig, however, does not represent a realistic hardware for cooling electronic components (time constants need to be less than 100 seconds). To achieve a reduction in the settling time and increase the rise time, a negative proportional PID controller (P=-2.1, I=0.38, and D=0.001) showed promising results after more trial-and-error tests and using previous experience. The settling time was improved substantially by 37% (i.e. 155 to 98 s).
- The negative proportional PID controller with 'normal' integral and derivative gains (i.e. positive) proved to be superior to a normal set of PID gains. It was observed that the negative proportional gain at first (during the rise time) made the error worse, however, the integral gain (during the settling time) dominated later, and adjusted the controller to maintain a negative feedback.
- A coefficient of performance (the ratio of the heat removal to the required pumping power) was introduced to the thermal management system to evaluate the effects of different PID gains on the thermal performance of the cooling system and its contribution to energy efficiency. A maximum COP of 22.56 was obtained by the negative proportional PID gain. This is a 10.5% increase in the performance in comparison with those for the regular PID controller.

- For the flat test-piece exposed to vibration, two sets of test runs including large-amplitude (a=12 mm and f=1.9 Hz) and high-frequency (f=400 Hz and a=0.02) were undertaken. The same negative proportional PID controller for the *static* case with P=-2, I=0.7, and D=0.002, showed the best results, proving the adaptability of the controller.
- COP results were decreased owing to a lower heat transfer rate in spray cooling with vibration (as was expected). Owing to the impeding effect of vibration, more realistic time constants of 61 s (for the large-amplitude case) and 70 s (for the high-frequency test) were achieved.
- A set of repeatability tests for the tuned control scheme was also examined with a very reasonable reproducibility observed in the temperature history, heat flux, COP and pumping response.
- The spray evaporative cooling thermal performance for vibrating three-dimensional surfaces has also been investigated for the first time. In this regard, comparative estimates for the ¼-cylinder test piece have been made from the rate of change of measured temperature. Time constants for different dynamic cases (ranging from a=0.01 to 3 mm and f=6 to 400 Hz) were compared against the static condition result. The deteriorating effect of vibration was consistent with the results of the flat test-piece. The cooling mode transitions (i.e. of incipient boiling) have also been identified for the dynamic cases (around 116 $^{\circ}$C). Repeatability tests for these transitions were also very promising.
- An updated version of the actual control system (with slightly different PID gains) for the flat test-piece has been implemented in hardware to thermally-manage the ¼-cylinder test-piece. Temperature control results have been obtained under dynamic and static conditions. The study shows that within the thermal inertia and mass limitations of the ¼-cylinder test-piece, temperature control is indeed achievable in practice.

7. CONCLUSIONS AND FUTURE WORK

This dissertation has involved heat transfer modeling and temperature control of evaporative spray cooling systems exposed to vibration for applications to cooling of electronic components and internal combustion engines with particular focus on hybrid and electric vehicles. Evaporative spray cooling is a promising technology, which offers the potential to reduce CO_2 emissions in hybrid electric vehicles, and to extend the range of battery electric vehicles. The literature review in Chapter 1 shows that, evaporative spray cooling in the nucleate boiling regime offers temperature stability and high heat transfer rates within the required excess temperature range and was therefore chosen as the focus of study in this thesis. In addition, it was found that the effects of vibration on nucleate boiling regime, CHF and its associated temperature had not been investigated. In particular, there were no published numerical and experimental studies which have constructed prediction models required for the thermal management purposes. As a consequence, key research questions were identified, culminating in three main objectives to address them. The first two objectives include data collection in the nucleate boiling regime and associated critical heat flux with, and without, vibrating surfaces, to be used for correlation development in static and dynamic conditions. The third objective is to undertake thermal management of an evaporative spray cooling test rig involving both flat and three-dimensional surfaces exposed to vibration.

To be specific, the objectives of the study were:

1) To investigate the effect of vibration on spray evaporative nucleate boiling for full-cone spray impinging on a (heated) flat circular copper test piece, driven by a shaker. To obtain experimentally-measured data in the nucleate boiling regime, and to develop corresponding empirical correlation models.

2) To reveal the influences of vibration, its frequency and amplitude (emulating the range present in the transportation sector), as well as acceleration on CHF and excess temperature. To obtain experimentally-measured data at CHF and associated excess temperature, and to develop the correlation models with CHF and excess temperature prediction capabilities.
3) To create a spray-evaporative-cooling-based thermal management system, and to experimentally verify its controllability. This was to address the concerns surrounding the temperature control of a system exposed to vibration that can operate near the required heat flux and yet remain stable. Furthermore, to address the lack of experimental data for heat transfer characteristics of three-dimensional vibrating surfaces and investigate the design and implementation in hardware of an appropriate spray evaporative cooling control system.

To address the modelling requirements of the thesis, in Chapter 2, new empirical correlation models are constructed to characterise heat transfer associated with spray evaporative cooling of vibrating surfaces - a process involving complex two-phase physics well beyond current numerical simulation capabilities. The proposed correlation models, which account for dynamic, rather than just static surface conditions (as in the prior models), are constructed using dimensional analysis involving the Generalized Buckingham Π-Theorem. Two nondimensional parameters are introduced in the form of Acceleration Number and Vibrational Reynolds Number to account for dynamic effects in the models which accommodate the combined effects of vibration amplitude and frequency.

Appropriate static and dynamic correlation models (developed in Chapter 2) can be chosen based on different experimental measurement conditions involving static and dynamic conditions. Experimental measurement conditions and heat flux measurements have been discussed in Chapter 3. The measurement conditions are used to design a suitable experimental test facility and a control

programme. Two test-pieces are mounted on a dynamic test rig and controlled in actual hardware. The flat test-piece is for heat flux exploration and correlation developments, whereas the ¼-cylinder test-piece emulates a cooling system of a highly boosted IC engine (with three-dimensional cooling surfaces). The dynamic test rig is driven by a mechanical shaker to induce vibrations typical of vehicle-mounted hardware. The DAQ and control unit hosts the control algorithm and provides supervision through a human-machine interface.

The uncertainties associated with the measurement facilities have also been discussed in Chapter 3, and have been used to estimate the uncertainty in heat flux. An uncertainty figure of 2.97% is used in the data interpretation and comparisons in chapters 4, 5 and 6. The reproducibility of the data for all the measurement programmes has also been studied in Chapter 3, to ensure that the results are of high quality. For nucleate boiling, the maximum deviation in the repeated measurement programme is 2.98% which is close to the maximum estimated uncertainty. The maximum deviations for the CHF and its associated temperature during repeatability analysis has been examined and its meaning established for Chapter 5 (where the CHF results are analysed). A set of repeatability tests for the tuned control system was also undertaken with very reasonable reproducibility obtained in the temperature profile and the settling time.

In chapters 4 and 5, to respectively address the first and second objectives of the thesis, the results from experimental measurement programme are given. In Chapter 4, the effect of dynamic behaviour on the nucleate boiling regime of spray evaporative cooling of a horizontal flat test-piece with, and without vibration, has been examined using measured data, and appropriate dynamic correlation models (developed in Chapter 2) have been adopted (i.e. to address objective one). The flat test-piece was excited by the shaker with water coolant supplied to the vibrating heated surface via a spray nozzle. Using a full-cone nozzle, four volumetric flow rates of 140 $\mathrm{ml/min}$, 160 $\mathrm{ml/min}$, 180 $\mathrm{ml/min}$ and 200

$\mathrm{ml/min}$ were tested. Three sets of dynamic conditions have been investigated including a 'mid-range' frequency, a 'high' frequency, and large-amplitude vibrations at 'low' frequency. For the mid-range vibrations at frequencies from 10 Hz to 200 Hz, the amplitudes vary from 0.08 mm to 1 mm. Three high-frequency vibration test were undertaken at 100 Hz, 200 Hz, and 400 Hz, with a fixed amplitude of 0.02 mm, and varying flow rates of 140, 160, 180, and 200 $\mathrm{ml/min}$, at nozzle distances above the test piece of 17mm and 21mm. Large-amplitude vibration tests were undertaken at frequencies of 1.9 Hz, 3 Hz, and 6 Hz, with amplitudes varying from 2 mm to 12 mm (emulating conditions associated with real vehicle dynamics) where the nozzle-to-surface distance was 17 mm, giving the highest effective flow rate. The main conclusions of Chapter 4 are listed at the end of Chapter 4.

In Chapter 5, to address the second objective of the thesis, experiments have been undertaken to investigate the effect of surface vibration on the critical heat flux (CHF) in spray evaporative cooling, and to assess the effectiveness of calibrated prediction models. In this regard, a wide range of vibration conditions (namely 'large-amplitude' and 'high-frequency') have driven the test piece during spray cooling with three different nozzle types i.e. the PJ8 (55 ml/min), PJ10 (75 and 100 ml/min) and MW145 (55 ml/min). The CHF data points, and their corresponding excess temperatures, for two subcooling degrees of 10 ℃ and 45 ℃, were captured using the DAQ system and the human-machine interface. Data analysis and comparisons have been undertaken to comprehensively investigate all the key vibrational parameters, both individually and in a combined relation using dimensionless numbers. The main conclusions of Chapter 5 are stated at the end of Chapter 5.

In Chapter 6, to address the third objective of the thesis, a thermal management system, using spray evaporative cooling, has been designed, and experimentally-tested to assess its ability to control the temperature of two particular instrumented and electrically-heated test-pieces exposed to vibration (i.e. the flat test-piece and the ¼-cylinder test-piece). To model the system, the experimentally

calibrated dynamic correlation model (in Chapter 4) has been used to represent the physics of spray evaporative cooling of a flat test-piece exposed to vibration. To enable stability analysis of the thermal management system using a PID controller, the nonlinear correlation model has been replaced by an optimum 1st-order linear model obtained by solving an appropriate Wiener-Hopf equation. This allows practical stability assessment of closed-loop temperature control for particular choices of PID controller gains. To verify the predicted control system performance via simulation, experimental measurements appropriate to automotive vehicle component applications, includes large-amplitude, low frequency vibration, at 12 mm and 1.9 Hz, and at low amplitude, high-frequency vibration, at 0.02 mm and 400 Hz. The effects of different PID controller gains on the thermal management system performance under static and dynamic conditions, has been assessed using a coefficient of performance (COP), defined as the ratio of heat power removal to the required pumping power. The main conclusions of Chapter 6 are given at the end of Chapter 6.

The overall conclusions considering the objectives of the thesis are:

- Any increase in volumetric flux, under both *Static* and *Dynamic* conditions, was found to cause heat transfer coefficient augmentation in both nucleate boiling regime and at CHF occurrence.
- Depending on the mechanism, combinations of vibration amplitude and frequency can either increase or decrease the heat transfer coefficient compared with the static cooling surface.

Conclusions about **objective 1** are:

- In the nucleate boiling regime, the effect of vibration generally results in an attenuation in heat transfer compared with *static* cases. At high amplitude, low frequency vibration however, increasing dimensionless Acceleration Number enhances heat transfer.

- The results of the deriving and fitting new dynamic correlation models show very reasonable prediction quality in the nucleate boiling region, which can be reliably used for future model-based thermal management applications. This completed the **objective 1**.

Conclusions associated with **objective 2** are:

- The effect of vibration on CHF was generally deteriorating. The largest deviations from the static CHF for all nozzles have been identified as for the effect of vibration. For the PJ10, it was found that the deterioration effect of vibration became more noticeable by increasing the subcooling degree. By contrast, for the low flow rate nozzles of PJ8 and MW145, the impeding effect of vibration reduces by increasing subcooling.
- The effect of vibration on excess temperature was also studied in detail. For all nozzles in general, cases with high-frequency vibration gave rise to the greatest deviations in the excess temperature.
- Predictions of CHF, and associated excess temperature, using calibrated correlation models for the dynamic conditions, were very reasonable. These calibrated correlation models are of potential value for safe operation of thermal management systems using spray evaporative cooling. The **objective 2** was achieved.

Conclusions addressing **objective 3** are:

- The actual control system has been implemented in hardware to thermally-manage the flat test-piece. The tuning process was undertaken by a set of trial-and-error tests involving experiments without vibration. To achieve a reduction in the settling time and increase the rise time, a set of negative gain proportional PID controllers showed promising results after more trial-and-error tests. For the flat test-piece exposed to vibration, two sets of test runs including large-amplitude

and high-frequency were undertaken. The same negative proportional PID controller for the *static* case showed the best results, proving the adaptability of the controller.

- The spray evaporative cooling thermal performance for vibrating three-dimensional surfaces has also been investigated using temperature ratio. The deteriorating effect of vibration was consistent to the results of the flat test-piece.

- An updated version of the actual control system for the flat test-piece has been implemented in hardware to thermally-manage the ¼-cylinder test-piece. The study shows that within the thermal inertia and mass limitations of the ¼-cylinder test-piece, temperature control is indeed achievable in practice. This completed the **objective 3** of this thesis.

7.1. Contributions of this dissertation

The particular areas where this thesis has made contribution to the research is on experimental data collection, construction of very novel dynamic correlation models, implementation and testing in hardware of a robust spray evaporative cooling control system, and development by simulation of a robust spray evaporative cooling control system [144]. In particular, very novel experimental dynamic spray evaporative cooling data has been obtained for the nucleate boiling regime and its associated critical heat flux. These data have been comprehensively analysed and key parameters identified. Two non-dimensional numbers namely Acceleration Number and Reynolds Number are used to better understand the physics, and explain the trends. In addition, necessary archival correlations models have (for the first time) been constructed that are useful for thermal modelling and controller design purposes. Two journal papers have been written which include the correlation models – one has already been published [27] (the other can be found in Appendix 3). In addition, a control strategy has been developed by simulation, and implemented and tested in hardware, and the results show that it can

fully meet the requirements for a variety of control application under dynamic conditions, particularly for cooling automotive electrical and electronic powertrain components. (The thermal management results of the hardware, and the temperature control by simulation, have been used to produce two more journal papers [144], the other in Appendix 3).

The results will in general be of direct benefit to the academic community since it has generated new fundamental knowledge of dynamic spray evaporative cooling, of particular interest to hybrid electric and electric vehicle research. Existing cooling systems are nearing their thermal limits because they use forced convection-based heat transfer. This limit restricts the performance of spark ignition (SI) engines in hybrid electric vehicles, and the range of hybrid electric vehicles. Evaporative cooling is of considerable interest to automotive and aerospace vehicle manufacturers. Because many see the great potential of evaporative cooling over conventional convective systems, to achieve improved IC engine fuel economy, reduced CO_2 emissions, and extended range for Electric Vehicles.

7.2. Further work

The current findings of this thesis with the control architecture have been helpful in gaining experience in assessing the feasibility of the control. However, it has become apparent that the ¼-cylinder test-piece has several limitations. First, as was mentioned, PJ-8 nozzles are not able to provide the same flow-rate as the UNIJET® nozzle that has been used on the flat test-piece. The UNIJET® nozzle has a higher flow-rate range for the same pressure difference provided by the pump. Therefore, with the same work of the pump, UNIJET® nozzles would offer higher control flexibility (if it were possible to fit them into the ¼-cylinder test-piece). Second, owing to the ¼-cylinder test-piece geometry, and heater block design, the thermal inertia does not allow the cartridge heaters to provide high response temperature changes on the coolant-side that is close to the real system behaviour. The current results

in Chapter 6 were undertaken over time spans of 116 minutes 40 seconds (i.e. 7000 s). It was for this reason that the simulation approach (in Appendix 2) was developed to use the empirical dynamic correlation with a UNIJET® nozzle to be able to assess the thermal management of the proposed cooling system with a more realistic time scale (i.e. less than 20 seconds). For future work therefore, the ¼-cylinder test-piece geometry, and its heater block design needs to be improved to enable implementation and testing in hardware of the proposed cooling control system with a practical time scale. A solution to this problem could involve using embedded flexible heaters and flexible heat flux sensors.

A second control issue can be identified from the current study, which focused on continuous spray flow control and thermal management of an evaporative spray cooling system exposed to vibration. The literature reviewed in Chapter 1, suggests that pulsed- (or intermittent-) spray flow is a very active field of research. Intermittent spray cooling compared with continuous spray cooling experimental results, are predicted to offer liquid savings of 10–90% for the same energetic efficiencies [174]. In fact, a recent publication [173], gives comparisons between intermittent (pulsate) and continuous spray in terms of the specific heat flux (heat dissipated per kilogram of the water). Enhancements up to more than 100% are reported. But to date, the effect of vibration on pulsed-spray evaporative cooling and its temperature control stability have yet to be investigated. A high response speed solenoid valve would make a pulsating spray cooling module possible. The empirical correlations could also be updated using Strouhal Number ($St = fd/v$), to include the effect of a pulsed-spray flow field. A modified version of the control strategy in this dissertation, and an improved version of the proposed thermal management system, could be then examined for efficacy and safety involving pulsed-spray evaporative cooling system exposed to vibration.

Longer term, another important body of work will be to create a computational capability to predict the spray evaporative cooling characteristics on the curved geometries of vibrating surfaces. This capability would be of great value to augment the correlation models, and ultimately, to avoid needing to use them. The real benefit of fundamental physics-based computer models will be in design of both cooling systems but also in characterisation of nozzle sprays. The computational challenge however, is very significant. Since at present, even high performance computing power is still orders of magnitude too slow to simulate fully evaporative 2-phase spray cooling.

References

[1] J. Kim, J. Oh, H. Lee, Review on battery thermal management system for electric vehicles, Applied Thermal Engineering, 149 (2019) 192-212.
[2] S. Jafari, T.J.A.S. Nikolaidis, Thermal Management Systems for Civil Aircraft Engines: Review, Challenges and Exploring the Future, 8 (2018) 2044.
[3] J. Doty, K. Yerkes, L. Byrd, J. Murthy, A. Alleyne, M. Wolff, S. Heister, T.J.J.o.T. Fisher, H. Transfer, Dynamic thermal management for aerospace technology: review and outlook, 31 (2017) 86-98.
[4] Z. Mera, N. Fonseca, J.-M. López, J. Casanova, Analysis of the high instantaneous NOx emissions from Euro 6 diesel passenger cars under real driving conditions, Applied energy, 242 (2019) 1074-1089.
[5] J. Benajes, A. García, J. Monsalve-Serrano, S. Martínez-Boggio, Emissions reduction from passenger cars with RCCI plug-in hybrid electric vehicle technology, Applied Thermal Engineering, 164 (2020) 114430.
[6] S. Tsiakmakis, G. Fontaras, J. Dornoff, V. Valverde, D. Komnos, B. Ciuffo, P. Mock, Z. Samaras, From lab-to-road & vice-versa: Using a simulation-based approach for predicting real-world CO2 emissions, Energy, 169 (2019) 1153-1165.
[7] K. Ranasinghe, K. Guan, A. Gardi, R.J.E. Sabatini, Review of advanced low-emission technologies for sustainable aviation, 188 (2019) 115945.
[8] D.C. Deisenroth, M.J.E. Ohadi, Thermal Management of High-Power Density Electric Motors for Electrification of Aviation and Beyond, 12 (2019) 3594.
[9] B.J. Brelje, J.R.J.P.i.A.S. Martins, Electric, hybrid, and turboelectric fixed-wing aircraft: A review of concepts, models, and design approaches, Progress in Aerospace Sciences, 104 (2019) 1-19.
[10] S. Jafari, J.F. Dunne, M. Langari, Z. Yang, J.-P. Pirault, C.A. Long, J. Thalackottore Jose, A review of evaporative cooling system concepts for engine thermal management in motor vehicles, Proceedings of the Institution of Mechanical Engineers, Part D: Journal of Automobile Engineering, 231 (2017) 1126-1143.
[11] J.T. Jose, J.F. Dunne, J.-P. Pirault, C.A. Long, Spray Evaporative Cooling System Design for Automotive Internal Combustion Engines, in: ASME 2018 Internal Combustion Engine Division Fall Technical Conference, American Society of Mechanical Engineers, 2018, pp. V002T007A008-V002T007A008.
[12] Y. Ding, Z.P. Cano, A. Yu, J. Lu, Z. Chen, Automotive Li-ion batteries: current status and future perspectives, Electrochemical Energy Reviews, 2 (2019) 1-28.
[13] Q. Yue, C. He, H. Jiang, M. Wu, T. Zhao, A hybrid battery thermal management system for electric vehicles under dynamic working conditions, International Journal of Heat and Mass Transfer, 164 (2021) 120528.
[14] S. Khandekar, G. Sahu, K. Muralidhar, E.Y. Gatapova, O.A. Kabov, R. Hu, X. Luo, L. Zhao, Cooling of High-Power LEDs by Liquid Sprays: Challenges and Prospects, Applied Thermal Engineering, (2020) 115640.
[15] J. Wang, Y. Li, J. Wang, Transient performance and intelligent combination control of a novel spray cooling loop system, Chinese Journal of Aeronautics, 26 (2013) 1173-1181.

[16] Y. Ding, Y. Li, Y. Li, W. Chen, H. Zhang, D. Li, Intensive cooling method for power electronic component with high heat flux, in: 2014 13th International Conference on Control Automation Robotics & Vision (ICARCV), IEEE, 2014, pp. 163-168.
[17] J.-X. Wang, W. Guo, K. Xiong, S.-N. Wang, Review of aerospace-oriented spray cooling technology, Progress in Aerospace Sciences, 116 (2020) 100635.
[18] Y. Yang, L. Yang, X. Du, Y.J.A.T.E. Yang, Pre-cooling of air by water spray evaporation to improve thermal performance of lithium battery pack, 163 (2019) 114401.
[19] S. Lei, Y. Shi, G. Chen, Heat-pipe based spray-cooling thermal management system for lithium-ion battery: Experimental study and optimization, International Journal of Heat and Mass Transfer, 163 (2020) 120494.
[20] J. Zhang, T.S. Fisher, P.V. Ramachandran, J.P. Gore, I. Mudawar, A review of heat transfer issues in hydrogen storage technologies, JOURNAL OF HEAT TRANSFER, ASME, (2005).
[21] O.V. Kartuzova, M. Kassemi, J.P. Moder, J.H. Agui, Self-pressurization and spray cooling simulations of the multipurpose hydrogen test bed (MHTB) ground-based experiment, in: 50th AIAA/ASME/SAE/ASEE Joint Propulsion Conference, 2014, pp. 3578.
[22] J. Breitenbach, I.V. Roisman, C. Tropea, From drop impact physics to spray cooling models: a critical review, Experiments in Fluids, 59 (2018) 55.
[23] G. Liang, I. Mudawar, Review of spray cooling–Part 1: Single-phase and nucleate boiling regimes, and critical heat flux, International Journal of Heat and Mass Transfer, 115 (2017) 1174-1205.
[24] G. Liang, I. Mudawar, Review of spray cooling–Part 2: High temperature boiling regimes and quenching applications, International Journal of Heat and Mass Transfer, 115 (2017) 1206-1222.
[25] C. Cai, H. Liu, M. Jia, H. Yin, R. Xie, P.J.I.J.o.T.S. Yan, Numerical investigation on heat transfer of water spray cooling from single-phase to nucleate boiling region, 151 (2020) 106258.
[26] M. Langari, Z. Yang, J.F. Dunne, S. Jafari, J.-P. Pirault, C.A. Long, J.T.J.T.J.o.C.M.F. Jose, Multiphase computational fluid dynamics–conjugate heat transfer for spray cooling in the non-boiling regime, 10 (2018) 33-42.
[27] A. Sarmadian, J. Dunne, C. Long, J.T. Jose, J.-P. Pirault, C. Rouaud, Heat flux correlation models for spray evaporative cooling of vibrating surfaces in the nucleate boiling region, International Journal of Heat Mass Transfer, 160 (2020) 120159.
[28] C.A. Long, Essential heat transfer, Longman, 1999.
[29] C. French, Taking the heat off the highly boosted diesel, SAE Transactions, (1969) 1700-1716.
[30] I. Finlay, R. Boyle, J. Pirault, T. Biddulph, Nucleate and film boiling of engine coolants flowing in a uniformly heated duct of small cross section, in, SAE Technical Paper, 1987.
[31] S. Jafari, J.F. Dunne, M. Langari, Z. Yang, J.-P. Pirault, C.A. Long, J.T.J.J.o.T.S. Jose, E. Applications, Control of Spray Evaporative Cooling in Automotive Internal Combustion Engines, 10 (2018) 041011.
[32] M.R. Panão, A.L. Moreira, Intermittent spray cooling: a new technology for controlling surface temperature, International Journal of Heat and Fluid Flow, 30 (2009) 117-130.
[33] H. Bostanci, S. Altalidi, S. Nasrazadani, Two-phase spray cooling with HFC-134a and HFO-1234yf on practical enhanced surfaces, Applied thermal engineering, 131 (2018) 150-158.
[34] I. Mudawar, D. Bharathan, K. Kelly, S. Narumanchi, Two-phase spray cooling of hybrid vehicle electronics, IEEE Transactions on Components and Packaging Technologies, 32 (2009) 501-512.

[35] X. Zhao, Z. Yin, B. Zhang, Z. Yang, Experimental investigation of surface temperature non-uniformity in spray cooling, 146 (2020) 118819.
[36] S. Lei, Y. Shi, G.J.A.T.E. Chen, A lithium-ion battery-thermal-management design based on phase-change-material thermal storage and spray cooling, 168 (2020) 114792.
[37] X. Feng, S. Zheng, D. Ren, X. He, L. Wang, X. Liu, M. Li, M. Ouyang, Key characteristics for thermal runaway of li-ion batteries, Energy Procedia, 158 (2019) 4684-4689.
[38] Y. Xie, X.-j. He, X.-s. Hu, W. Li, Y.-j. Zhang, B. Liu, Y.-t. Sun, An improved resistance-based thermal model for a pouch lithium-ion battery considering heat generation of posts, Applied Thermal Engineering, 164 (2020) 114455.
[39] J. Du, Y. Liu, X. Mo, Y. Li, J. Li, X. Wu, M. Ouyang, Impact of high-power charging on the durability and safety of lithium batteries used in long-range battery electric vehicles, Applied energy, 255 (2019) 113793.
[40] M. Varini, P.E. Campana, G. Lindbergh, A semi-empirical, electrochemistry-based model for Li-ion battery performance prediction over lifetime, Journal of Energy Storage, 25 (2019) 100819.
[41] S. Jafari, J.F. Dunne, M. Langari, Z. Yang, J.-P. Pirault, C.A. Long, J.T. Jose, Control of Spray Evaporative Cooling in Automotive Internal Combustion Engines, Journal of Thermal Science and Engineering Applications, 10 (2018) 041011.
[42] W.-L. Cheng, W.-W. Zhang, H. Chen, L. Hu, Spray cooling and flash evaporation cooling: the current development and application, Renewable and Sustainable Energy Reviews, 55 (2016) 614-628.
[43] J. Yang, L. Chow, M. Pais, Nucleate boiling heat transfer in spray cooling, Journal of Heat Transfer, 118 (1996) 668-671.
[44] I. Mudawar, W. Valentine, Determination of the local quench curve for spray-cooled metallic surfaces, Journal of Heat Treating, 7 (1989) 107-121.
[45] E. Cabrera, Heat flux correlation for spray cooling in the nucleate boiling regime, Experimental heat transfer, 16 (2003) 19-44.
[46] J.R. Rybicki, I. Mudawar, Single-phase and two-phase cooling characteristics of upward-facing and downward-facing sprays, International Journal of Heat and Mass Transfer, 49 (2006) 5-16.
[47] S.-S. Hsieh, T.-C. Fan, H.-H.J.I.J.o.H. Tsai, M. Transfer, Spray cooling characteristics of water and R-134a. Part I: nucleate boiling, 47 (2004) 5703-5712.
[48] M. Ghodbane, J.J.I.J.o.H. Holman, M. Transfer, Experimental study of spray cooling with Freon-113, 34 (1991) 1163-1174.
[49] K.A. Estes, I.J.I.J.o.H. Mudawar, M. Transfer, Correlation of Sauter mean diameter and critical heat flux for spray cooling of small surfaces, 38 (1995) 2985-2996.
[50] I. Mudawar, K. Estes, Optimizing and predicting CHF in spray cooling of a square surface, Journal of Heat Transfer, 118 (1996) 672-679.
[51] M. Visaria, I.J.I.j.o.h. Mudawar, m. transfer, Theoretical and experimental study of the effects of spray inclination on two-phase spray cooling and critical heat flux, 51 (2008) 2398-2410.
[52] M. Visaria, I.J.I.j.o.h. Mudawar, m. transfer, Effects of high subcooling on two-phase spray cooling and critical heat flux, 51 (2008) 5269-5278.
[53] W. Klinzing, J. Rozzi, I. Mudawar, Film and transition boiling correlations for quenching of hot surfaces with water sprays, Journal of Heat Treating, 9 (1992) 91-103.

[54] S.-S. Hsieh, T.-C. Fan, H.-H. Tsai, Spray cooling characteristics of water and R-134a. Part II: transient cooling, International Journal of Heat and Mass Transfer, 47 (2004) 5713-5724.
[55] J. Wendelstorf, K.-H. Spitzer, R. Wendelstorf, Spray water cooling heat transfer at high temperatures and liquid mass fluxes, International Journal of Heat and Mass Transfer, 51 (2008) 4902-4910.
[56] S.K. Mishra, A. Arora, H. Chandra, Application of Vibration on Heat Transfer-A Review, i-Manager's Journal on Future Engineering and Technology, 15 (2019) 72.
[57] A. Sathyabhama, S. Prashanth, Enhancement of boiling heat transfer using surface vibration, Heat Transfer—Asian Research, 46 (2017) 49-60.
[58] H. Atashi, A. Alaei, M. Kafshgari, R. Aeinehvand, S. Rahimi, New Pool Boiling Heat Transfer in the Presence of Low-Frequency Vibrations Into a Vertical Cylindrical Heat Source, Experimental heat transfer, 27 (2014) 428-437.
[59] Z. Wang, Y. Xing, X. Liu, L. Zhao, Y.J.A.T.E. Ji, Computer modeling of droplets impact on heat transfer during spray cooling under vibration environment, 107 (2016) 453-462.
[60] Y. Zhang, L. Pang, M. Liu, Y. Xie, Investigation of spray cooling: Effect of different heater surfaces under acceleration, International Communications in Heat and Mass Transfer, 75 (2016) 223-231.
[61] K.-i. Yoshida, Y. Abe, T. Oka, Y.H. Mori, A. Nagashima, Spray cooling under reduced gravity condition, Journal of Heat Transfer, 123 (2001) 309-318.
[62] K. Baysinger, K. Yerkes, R. Harris, T. Michalak, J. McQuillen, Design of a microgravity spray cooling experiment, in: 42nd AIAA Aerospace Sciences Meeting and Exhibit, 2004, pp. 966.
[63] K. Sone, K. Yoshida, T. Oka, Y. Abe, Y. Miri, A. Nagashima, Spray cooling characteristics of water and FC-72 under reduced and elevated gravity for space application, in: IECEC 96. Proceedings of the 31st Intersociety Energy Conversion Engineering Conference, Vol. 2, IEEE, 1996, pp. 1500-1505.
[64] G.E. Cossali, M. Marengo, M. Santini, Single-drop empirical models for spray impact on solid walls: a review, Atomization and Sprays, 15 (2005).
[65] C. Tropea, I.V. Roisman, Modeling of spray impact on solid surfaces, Atomization and Sprays, 10 (2000).
[66] H. Liu, C. Cai, M. Jia, J. Gao, H. Yin, H. Chen, Experimental investigation on spray cooling with low-alcohol additives, Applied Thermal Engineering, 146 (2019) 921-930.
[67] J.D. Bernardin, C.J. Stebbins, I. Mudawar, Mapping of impact and heat transfer regimes of water drops impinging on a polished surface, International Journal of Heat and Mass Transfer, 40 (1997) 247-267.
[68] I. Roisman, J. Breitenbach, C. Tropea, Thermal atomisation of a liquid drop after impact onto a hot substrate, Journal of Fluid Mechanics, 842 (2018) 87-101.
[69] A. Moreira, A. Moita, M. Panao, Advances and challenges in explaining fuel spray impingement: How much of single droplet impact research is useful?, Progress in energy and combustion science, 36 (2010) 554-580.
[70] Y. Qiao, S.J.J.o.H.T. Chandra, Spray cooling enhancement by addition of a surfactant, 120 (1998) 92-98.
[71] N. Vargaftik, B. Volkov, L.J.J.o.P. Voljak, C.R. Data, International tables of the surface tension of water, 12 (1983) 817-820.

[72] T. Petrova, R.J.P.o.t.I.A.f.t.P.o.W. Dooley, M. Steam, Russia, Revised release on surface tension of ordinary water substance, (2014) 23-27.
[73] J.R. Rybicki, I.J.I.J.o.H. Mudawar, M. Transfer, Single-phase and two-phase cooling characteristics of upward-facing and downward-facing sprays, 49 (2006) 5-16.
[74] H. Xu, C. Si, S. Shao, C. Tian, Experimental investigation on heat transfer of spray cooling with isobutane (R600a), International journal of thermal sciences, 86 (2014) 21-27.
[75] J. Liu, R. Xue, L. Chen, X. Liu, Y. Hou, Influence of chamber pressure on heat transfer characteristics of a closed loop R134-a spray cooling, Experimental thermal and fluid science, 75 (2016) 89-95.
[76] M. Pais, L. Chow, E.J.J.o.H.T. Mahefkey, Surface roughness and its effects on the heat transfer mechanism in spray cooling, 114 (1992) 211-219.
[77] A. Morgan, L. Bromley, C.J.I. Wilke, E. Chemistry, Effect of surface tension on heat transfer in boiling, 41 (1949) 2767-2769.
[78] A. Lowery, J.J.I. Westwater, E. Chemistry, Heat Transfer to Boiling Methanol Effect of Added Agents, 49 (1957) 1445-1448.
[79] P. Jontz, J.J.A.J. Myers, The effect of dynamic surface tension on nucleate boiling coefficients, 6 (1960) 34-38.
[80] S. Shibayama, M. Katsuta, K. Suzuki, T. Kurose, Y.J.H.T. Hatano, A study on boiling heat transfer in a thin liquid film, 9 (1980) 12-40.
[81] T. Dunskus, J. Westwater, The effect of trace additives on the heat transfer to boiling isopropanol, in: Chemical Engineering Progress Symposium Series, Vol. 57, 1961, pp. 173-181.
[82] Y.M. Yang, J.R.J.J.o.H.T. Maa, Pool boiling of dilute surfactant solutions, 105 (1983) 190-192.
[83] Y.L. Tzan, Y.M.J.J.o.h.t. Yang, Experimental study of surfactant effects on pool boiling heat transfer, 112 (1990) 207-212.
[84] Y.M.J.I.c.i.h. Yang, m. transfer, Dynamic surface effect on boiling of aqueous surfactant solutions, 17 (1990) 711-727.
[85] W. Frost, C.J.J.I.J.o.H. Kippenhan, M. Transfer, Bubble growth and heat-transfer mechanisms in the forced convection boiling of water containing a surface active agent, 10 (1967) 931-949.
[86] C. Ammerman, S.J.J.o.H.T. You, Determination of the boiling enhancement mechanism caused by surfactant addition to water, 118 (1996) 429-435.
[87] S.R. Chowdhury, R.J.I.J.o.H. Winterton, M. Transfer, Surface effects in pool boiling, 28 (1985) 1881-1889.
[88] Y. Qiao, S. Chandra, Experiments on adding a surfactant to water drops boiling on a hot surface, in: Proceedings of the Royal Society of London A: Mathematical, Physical and Engineering Sciences, Vol. 453, The Royal Society, 1997, pp. 673-689.
[89] R. Dou, Z. Wen, G. Zhou, Heat transfer characteristics of water spray impinging on high temperature stainless steel plate with finite thickness, International Journal of Heat and Mass Transfer, 90 (2015) 376-387.
[90] R.H. Pereira, E.P.B. Filho, S.L. Braga, J.A.R. Parise, Nucleate boiling in large arrays of impinging water sprays, Heat Transfer Engineering, 34 (2013) 479-491.
[91] J. Holman, C.J.I.j.o.h. Kendall, m. transfer, Extended studies of spray cooling with Freon-113, 36 (1993) 2239-2241.

[92] M. Visaria, I. Mudawar, Application of two-phase spray cooling for thermal management of electronic devices, IEEE Transactions on Components and Packaging Technologies, 32 (2009) 784-793.
[93] S.-S. Hsieh, G.-W. Chen, Y.-F. Yeh, Optical flow and thermal measurements for spray cooling, International Journal of Heat and Mass Transfer, 87 (2015) 248-253.
[94] M.S. Sehmbey, L.C. Chow, O.J. Hahn, M.R. Pais, Effect of spray characteristics on spray cooling with liquid nitrogen, Journal of Thermophysics and heat Transfer, 9 (1995) 757-765.
[95] M.S. Sehmbey, L.C. Chow, O.J. Hahn, M.R. Pais, Spray cooling of power electronics at cryogenic temperatures, Journal of Thermophysics and heat Transfer, 9 (1995) 123-128.
[96] L. Ortiz, J.E. Gonzalez, Experiments on steady-state high heat fluxes using spray cooling, Experimental heat transfer, 12 (1999) 215-233.
[97] Y. Tan, J. Xie, F. Duan, T. Wong, K. Toh, K. Choo, P. Chan, Y. Chua, Multi-nozzle spray cooling for high heat flux applications in a closed loop system, Applied Thermal Engineering, 54 (2013) 372-379.
[98] E.J.E.h.t. Cabrera, Heat flux correlation for spray cooling in the nucleate boiling regime, 16 (2003) 19-44.
[99] R.J. Moffat, Describing the uncertainties in experimental results, Experimental thermal and Fluid Science, 1 (1988) 3-17.
[100] Y. Qiao, S. Chandra, Spray cooling enhancement by addition of a surfactant, Journal of Heat Transfer, 120 (1998) 92-98.
[101] S.K. Mishra, A. Arora, H. Chandra, Application of Vibration on Heat Transfer-A Review, J i-Manager's Journal on Future Engineering Technology, 15 (2019) 72.
[102] S. Jafari, T. Nikolaidis, Thermal management systems for civil aircraft engines: Review, challenges and exploring the future, Applied Sciences, 8 (2018) 2044.
[103] J. Doty, K. Yerkes, L. Byrd, J. Murthy, A. Alleyne, M. Wolff, S. Heister, T. Fisher, Dynamic thermal management for aerospace technology: review and outlook, Journal of Thermophysics Heat Transfer, 31 (2017) 86-98.
[104] J.T. Jose, J. Dunne, Numerical Simulation of Single-Droplet Dynamics, Vaporization, and Heat Transfer from Impingement onto Static and Vibrating Surfaces, J Fluids, 5 (2020) 188.
[105] Z. Wang, Y. Xing, X. Liu, L. Zhao, Y. Ji, Computer modeling of droplets impact on heat transfer during spray cooling under vibration environment, Applied Thermal Engineering, 107 (2016) 453-462.
[106] K.A. Estes, I. Mudawar, Correlation of Sauter mean diameter and critical heat flux for spray cooling of small surfaces, International Journal of Heat and Mass Transfer, 38 (1995) 2985-2996.
[107] I. Mudawar, K. Estes, Optimizing and predicting CHF in spray cooling of a square surface, Journal of Heat Transfer, 118 (1996) 672-679.
[108] S. Jiang, V.K. Dhir, Spray cooling in a closed system with different fractions of non-condensibles in the environment, International Journal of Heat and Mass Transfer, 47 (2004) 5391-5406.
[109] S.J. Thiagarajan, S. Narumanchi, R. Yang, Effect of flow rate and subcooling on spray heat transfer on microporous copper surfaces, International Journal of Heat and Mass Transfer, 69 (2014) 493-505.
[110] M. Visaria, I. Mudawar, Effects of high subcooling on two-phase spray cooling and critical heat flux, International Journal of Heat and Mass Transfer, 51 (2008) 5269-5278.

[111] L. Chow, M. Sehmbey, M. Pais, Critical heat flux in spray cooling, in: 34th Aerospace Sciences Meeting and Exhibit, 1996, pp. 727.
[112] M. Sawyer, S. Jeter, S. Abdel-Khalik, A critical heat flux correlation for droplet impact cooling, International Journal of Heat and Mass Transfer, 40 (1997) 2123-2131.
[113] E.A. Silk, J. Kim, K. Kiger, Energy conservation based spray cooling CHF correlation for flat surface small area heaters, in: ASME/JSME 2007 Thermal Engineering Heat Transfer Summer Conference collocated with the ASME 2007 InterPACK Conference, American Society of Mechanical Engineers, 2007, pp. 805-813.
[114] B. Abbasi, J. Kim, Prediction of PF-5060 spray cooling heat transfer and critical heat flux, Journal of heat transfer, 133 (2011) 101504.
[115] X. Zhao, B. Zhang, X. Xi, Z. Yin, Analysis and prediction of single-phase and two-phase cooling characteristics of intermittent sprays, International Journal of Heat and Mass Transfer, 133 (2019) 619-630.
[116] L. Elston, K. Yerkes, S. Thomas, J. McQuillen, Effect of Variable Gravity on the Cooling Performance of a 16-Nozzle Spray Array, in: 47th AIAA Aerospace Sciences Meeting Including The New Horizons Forum and Aerospace Exposition, 2009, pp. 1025.
[117] L.J. Elston, K.L. Yerkes, S.K. Thomas, J. McQuillen, Cooling performance of a 16-nozzle array in variable gravity, Journal of Thermophysics Heat Transfer, 23 (2009) 571-581.
[118] T.E. Michalak, K.L. Yerkes, S.K. Thomas, J.B. McQuillen, Acceleration effects on the cooling performance of a partially confined FC-72 spray, Journal of Thermophysics Heat Transfer, 24 (2010) 463-479.
[119] J. Breitenbach, I.V. Roisman, C.J.E.i.F. Tropea, From drop impact physics to spray cooling models: a critical review, 59 (2018) 55.
[120] T. Sai, K. Reddy, Design of fuzzy gain scheduler for superheater temperature control in power plant, in: 2016 2nd International Conference on Control, Instrumentation, Energy & Communication (CIEC), IEEE, 2016, pp. 521-525.
[121] M. Panão, A. Moreira, Thermo-and fluid dynamics characterization of spray cooling with pulsed sprays, Experimental thermal and fluid science, 30 (2005) 79-96.
[122] A. Moreira, M. Panao, Heat transfer at multiple-intermittent impacts of a hollow cone spray, International Journal of Heat and Mass Transfer, 49 (2006) 4132-4151.
[123] M.R. Panão, A.L. Moreira, Two-phase cooling characteristics of a multiple-intermittent spray, in: 13th International Symposium on Applications of Laser Techniques to Fluid Mechanics, 26th-29th June, Citeseer, 2006.
[124] A.L. Moreira, J. Carvalho, M.R. Panao, An experimental methodology to quantify the spray cooling event at intermittent spray impact, International Journal of Heat and Fluid Flow, 28 (2007) 191-202.
[125] M.R. Panão, A.M. Correia, A.L. Moreira, High-power electronics thermal management with intermittent multijet sprays, Applied thermal engineering, 37 (2012) 293-301.
[126] S. Somasundaram, A.A. Tay, Intermittent spray cooling—Solution to optimize spray cooling, in: 2012 IEEE 14th Electronics Packaging Technology Conference (EPTC), IEEE, 2012, pp. 588-593.
[127] B. Majaron, L.O. Svaasand, G. Aguilar, J.S. Nelson, Intermittent cryogen spray cooling for optimal heat extraction during dermatologic laser treatment, Physics in Medicine & Biology, 47 (2002) 3275.

[128] S. Somasundaram, A.A. Tay, An experimental study of closed loop intermittent spray cooling of ICs, Applied Thermal Engineering, 31 (2011) 2321-2331.
[129] G. Liang, I. Mudawar, Review of spray cooling–Part 2: High temperature boiling regimes and quenching applications, International Journal of Heat Mass Transfer, 115 (2017) 1206-1222.
[130] R.B. Biniwale, N. Kariya, H. Yamashiro, M. Ichikawa, Heat transfer and thermographic analysis of catalyst surface during multiphase phenomena under spray-pulsed conditions for dehydrogenation of cyclohexane over Pt catalysts, The Journal of Physical Chemistry B, 110 (2006) 3189-3196.
[131] J. Gibbins, H. Chalmers, Carbon capture and storage, Energy policy, 36 (2008) 4317-4322.
[132] The ten point plan for a green industrial revolution, in: E.I.S. Department for Business, Prime Minister's Office, 10 Downing Street, The Rt Hon Alok Sharma MP, and The Rt Hon Boris Johnson MP (ed.), https://www.gov.uk/government/publications/the-ten-point-plan-for-a-green-industrial-revolution, 2020.
[133] L.J. Turek, D.P. Rini, B.A. Saarloos, L.C. Chow, Evaporative spray cooling of power electronics using high temperature coolant, in: 2008 11th Intersociety Conference on Thermal and Thermomechanical Phenomena in Electronic Systems, IEEE, 2008, pp. 346-351.
[134] L.J. Turek, D.P. Rini, B.A. Saarloos, L.C. Chow, Enabling much higher power densities in aerospace power electronics with high temperature evaporative spray cooling, in, SAE Technical Paper, 2008.
[135] H. Bostanci, D. Van Ee, B.A. Saarloos, D.P. Rini, L.C. Chow, Thermal management of power inverter modules at high fluxes via two-phase spray cooling, IEEE Transactions on Components, Packaging and Manufacturing Technology, 2 (2012) 1480-1485.
[136] K. Kelly, T. Abraham, K. Bennion, D. Bharathan, S. Narumanchi, M. O'Keefe, Assessment of thermal control technologies for cooling electric vehicle power electronics, in, National Renewable Energy Lab.(NREL), Golden, CO (United States), 2008.
[137] K.J. Åström, T. Hägglund, The future of PID control, Control Engineering Practice, 9 (2001) 1163-1175.
[138] G. Bluman, Dimensional analysis, modelling and symmetry, International Journal of Mathematical Education in Science and Technology, 14 (1983) 259-272.
[139] E. Buckingham, Model experiments and the forms of empirical equations, Verlag nicht ermittelbar, 1915.
[140] E. Buckingham, On physically similar systems; illustrations of the use of dimensional equations, Physical review, 4 (1914) 345.
[141] A. Flaga, Basic principles and theorems of dimensional analysis and the theory of model similarity of physical phenomena, Czasopismo Techniczne, (2015).
[142] A.A. Sonin, A generalization of the Π-theorem and dimensional analysis, Proceedings of the National Academy of Sciences, 101 (2004) 8525-8526.
[143] J.T. Jose, Spray Evaporative Cooling of Vibrating Surfaces with Application to Automotive Combustion Engines, in: Department of Engineering and Design, Vol. PhD, University of Sussex, 2020.
[144] J.T. Jose, A. Sarmadian, J. Dunne, C. Long, J.-P. Pirault, C. Rouaud, An experimentally-verified temperature control simulation model for spray evaporative cooling of vibrating powertrain parts, International Journal of Heat and Mass Transfer, 170 (2021) 121041.

[145] J. Schwarzkopf, T. Cader, K. Okamoto, B. Li, B. Ramaprian, Effect of spray angle in spray cooling thermal management of electronics, in: ASME 2004 Heat Transfer/Fluids Engineering Summer Conference, American Society of Mechanical Engineers Digital Collection, 2004, pp. 423-431.
[146] R.-H. Chen, L.C. Chow, J.E. Navedo, Optimal spray characteristics in water spray cooling, International Journal of Heat and Mass Transfer, 47 (2004) 5095-5099.
[147] B. Petrus, K. Zheng, X. Zhou, B.G. Thomas, J. Bentsman, Real-time, model-based spray-cooling control system for steel continuous casting, Metallurgical and materials transactions 42 (2011) 87-103.
[148] J.T. Jose, A. Sarmadian, J. Dunne, C. Long, J.-P. Pirault, C. Rouaud, An experimentally-verified temperature control simulation model for spray evaporative cooling of vibrating powertrain parts, International Journal of Heat Mass Transfer, 170 (2021) 121041.
[149] S. Toda, H. Uchida, Study of liquid film cooling with evaporation and boiling, J Trans. JSME, 2 (1973) 44-62.
[150] Y. Hou, J. Liu, X. Su, Y. Qian, L. Liu, X. Liu, Experimental study on the characteristics of a closed loop R134-a spray cooling, Experimental thermal and Fluid Science, 61 (2015) 194-200.
[151] L.C. Chow, M.S. Sehmbey, M.R. Pais, High heat flux spray cooling, Annual Review of Heat Transfer, 8 (1997).
[152] G. Moreno Jr, S.M. You, E. Steinthorsson, Spray cooling performance of single and multi-jet spray nozzles using subcooled FC-72, in: Heat Transfer Summer Conference, Vol. 42746, 2007, pp. 783-790.
[153] M. Pais, L. Chow, E. Mahefkey, Surface roughness and its effects on the heat transfer mechanism in spray cooling, J. Heat Transf. – Trans. ASME, 114 (1992) 211-219.
[154] R.-H. Chen, L.C. Chow, J.E. Navedo, Effects of spray characteristics on critical heat flux in subcooled water spray cooling, International Journal of Heat and Mass Transfer, 45 (2002) 4033-4043.
[155] D.E. Tilton, Spray cooling PhD Dissertation, in, Vol. PhD, University of Kentucky, Lexington, USA, 1989.
[156] L. Lin, R. Ponnappan, Critical heat flux of multi-nozzle spray cooling, J. Heat Transfer - Trans. ASME, 126 (2004) 482-485.
[157] M. Monde, Critical heat flux in the saturated forced convection boiling on a heated disk with impinging droplets, in: Trans. JSME, Vol. 45, 1980, pp. 849-858.
[158] M. Visaria, I. Mudawar, Effects of high subcooling on two-phase spray cooling and critical heat flux, International Journal of Heat Mass Transfer, 51 (2008) 5269-5278.
[159] Y. Zhang, L. Pang, Y. Xie, S. Jin, M. Liu, Y. Ji, Experimental investigation of spray cooling heat transfer on straight fin surface under acceleration conditions, Experimental Heat Transfer, 28 (2015) 564-579.
[160] Y. Zhang, L. Pang, M. Liu, Y. Xie, Investigation of spray cooling: Effect of different heater surfaces under acceleration, International Communications in Heat Mass Transfer, 75 (2016) 223-231.
[161] B.L. Conrad, J.C. Springmann, L.A. McGill, T.A. Shedd, Effectiveness of linear spray cooling in microgravity, in: AIP Conference Proceedings, Vol. 1103, American Institute of Physics, 2009, pp. 67-72.

[162] R.-H. Chen, L.C. Chow, J.E. Navedo, Optimal spray characteristics in water spray cooling, International Journal of Heat Mass Transfer, 47 (2004) 5095-5099.
[163] S. Toda, A study of mist cooling (1st report, investigation of mist cooling), J Kikaigakkai Ronbunshu, 38 (1972) 581-588.
[164] S. Toda, A study of mist cooling (2nd report: theory of mist cooling and its fundamental experiments), Heat Transf.-Jap. Res, 3 (1974) 1-44.
[165] P. Setlur, J.R. Wagner, D.M. Dawson, E. Marotta, An advanced engine thermal management system: Nonlinear control and test, IEEE/ASME transactions on mechatronics, 10 (2005) 210-220.
[166] J.F. Eberth, J.R. Wagner, B.A. Afshar, R.C. Foster, Modeling and validation of automotive "Smart" thermal management system architectures, in, SAE Technical Paper, 2004.
[167] J.R. Wagner, V. Srinivasan, D.M. Dawson, E.E. Marotta, Smart thermostat and coolant pump control for engine thermal management systems, in, SAE Technical Paper, 2003.
[168] J.R. Wagner, M.C. Ghone, D.W. Dawson, E.E. Marotta, Coolant flow control strategies for automotive thermal management systems, in, SAE Technical Paper, 2002.
[169] J. Wagner, E. Marotta, I. Paradis, Thermal modeling of engine components for temperature prediction and fluid flow regulation, in, SAE Technical Paper, 2001.
[170] R.R. Henry, J. Koo, C. Richter, Model development, simulation and validation, of power train cooling system for a truck application, in, SAE technical paper, 2001.
[171] D. Mortari, H.R. Johnston, L.I. Smith, Least-squares solutions of nonlinear differential equations, in: 2018 Space Flight Mechanics Meeting, 2018, pp. 0959.
[172] A.D. Poularikas, Adaptive filtering: Fundamentals of least mean squares with MATLAB®, CRC Press, 2017.
[173] X. Zhao, B. Zhang, X. Xi, Z. Yin, Analysis and prediction of single-phase and two-phase cooling characteristics of intermittent sprays, International Journal of Heat Mass Transfer, 133 (2019) 619-630.
[174] M.R. Panão, A.L. Moreira, Intermittent spray cooling: a new technology for controlling surface temperature, International Journal of Heat Fluid Flow, 30 (2009) 117-130.

Appendix 1

LabVIEW and SIMULINK diagrams

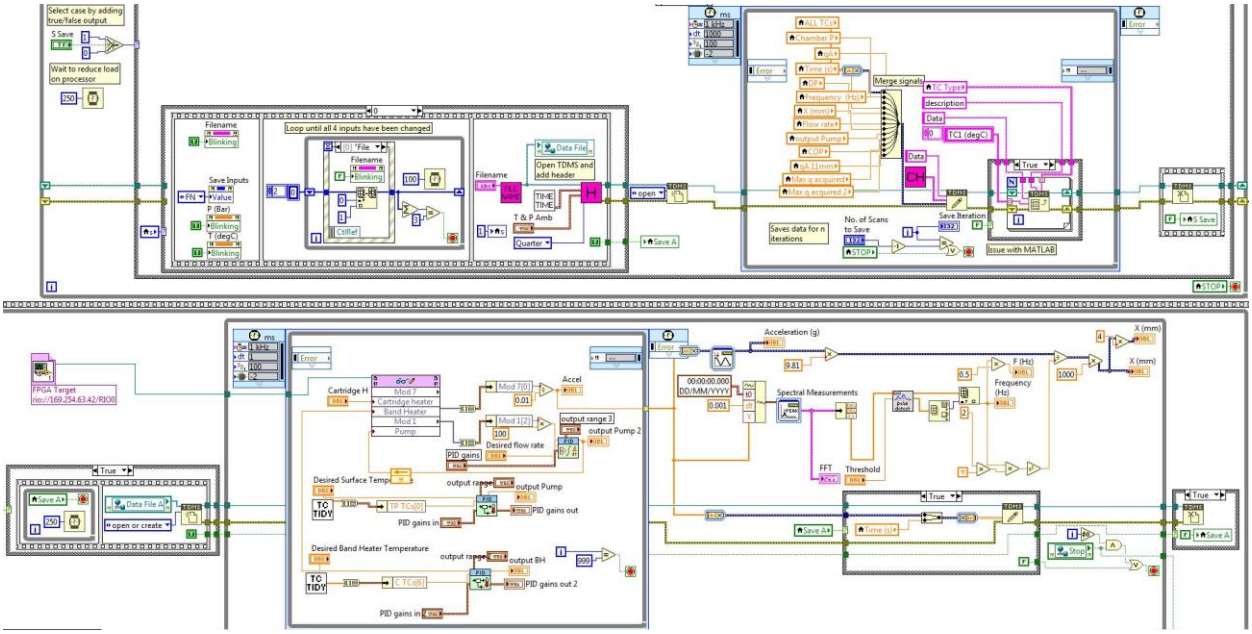

Fig A1-1. LabVIEW block diagram of DAQ and Control unit.

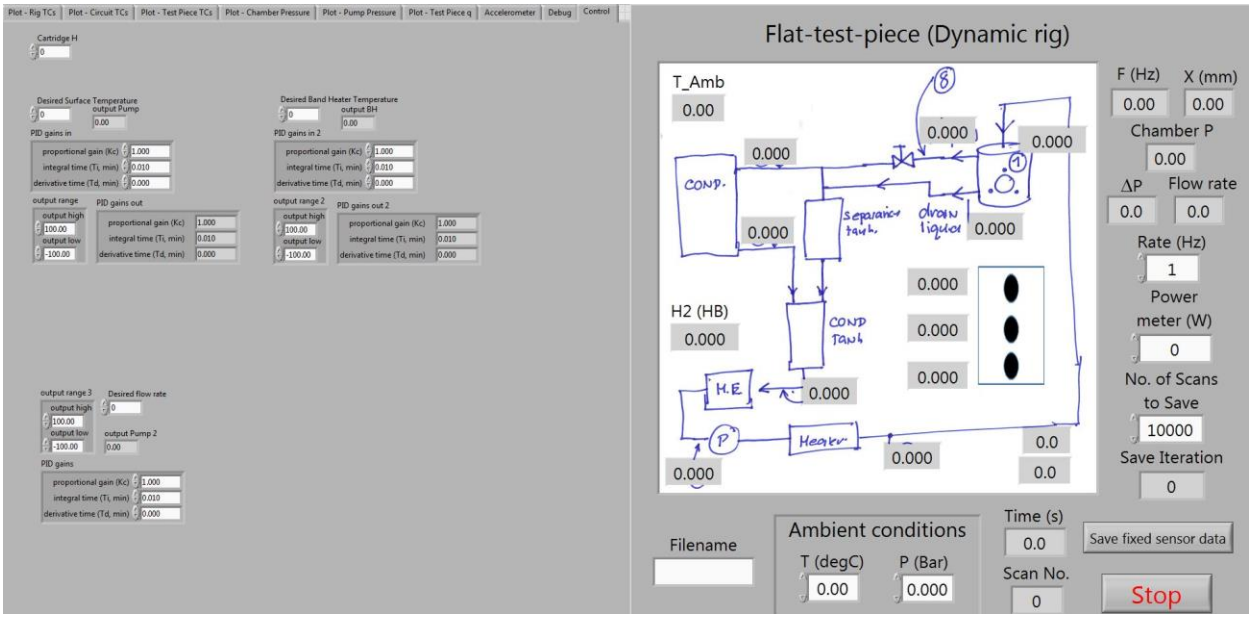

Fig A1-2. LabVIEW front panel of Control unit tab.

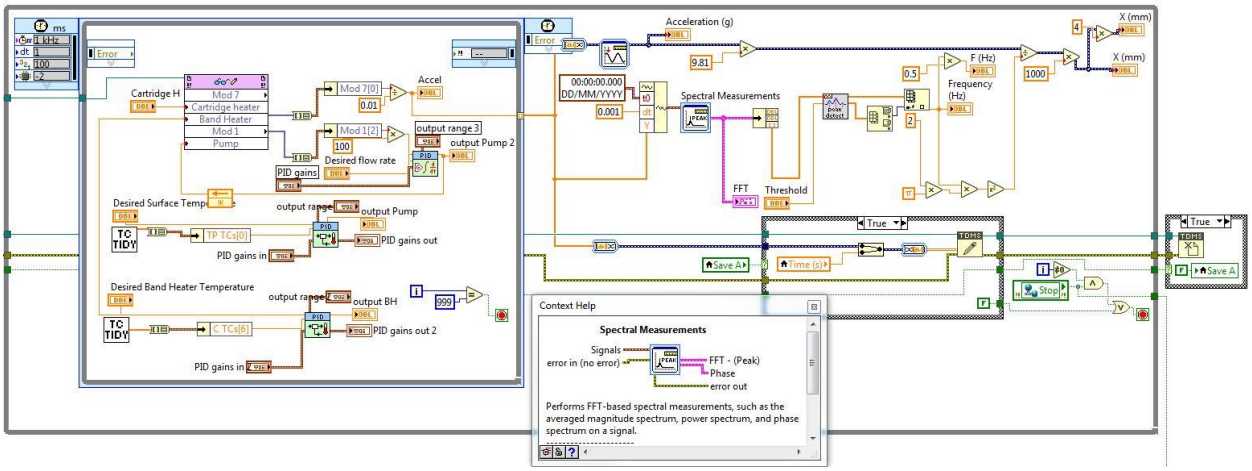

Fig A1-3. LabVIEW block diagram of PIDs and vibration spectral measurements.

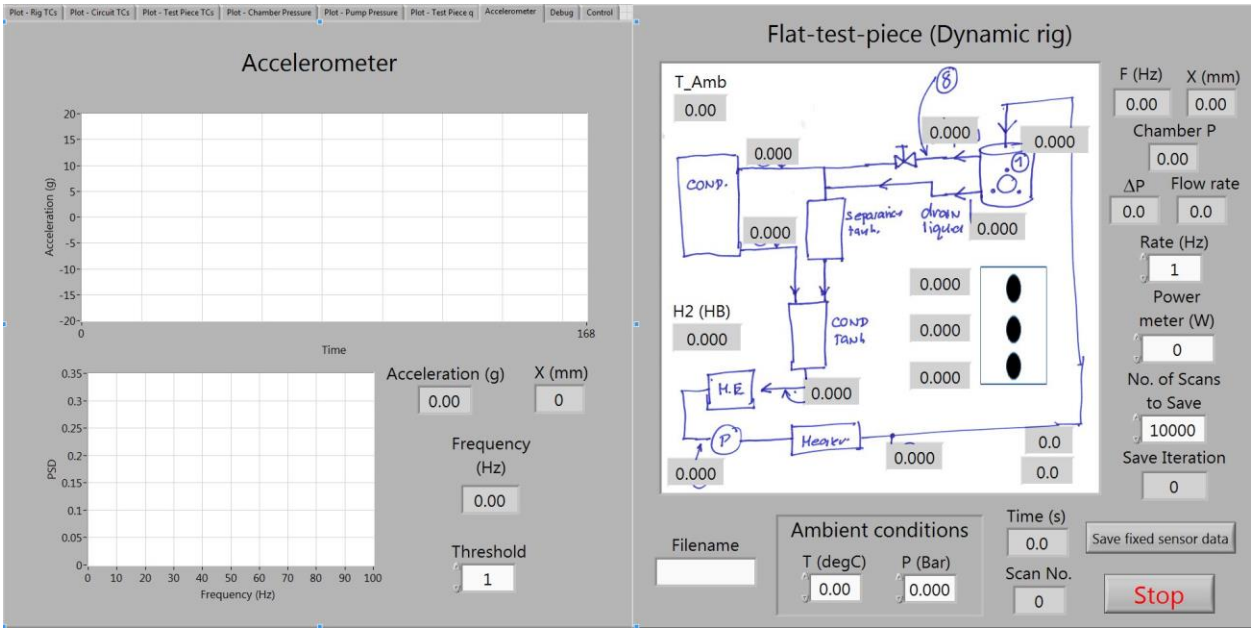

Fig A1-4. LabVIEW front panel of vibration spectral measurements tab.

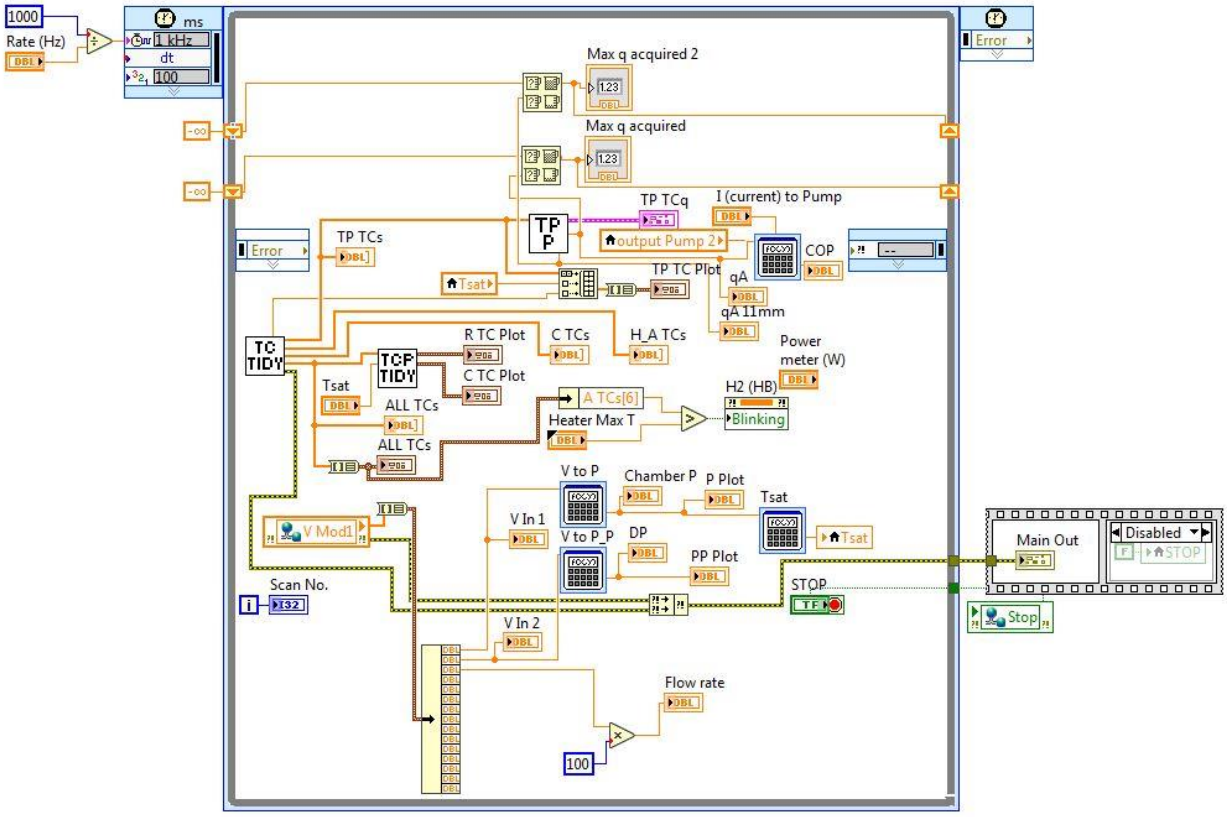

Fig A1-5. LabVIEW block diagram of heat flux and COP measurements.

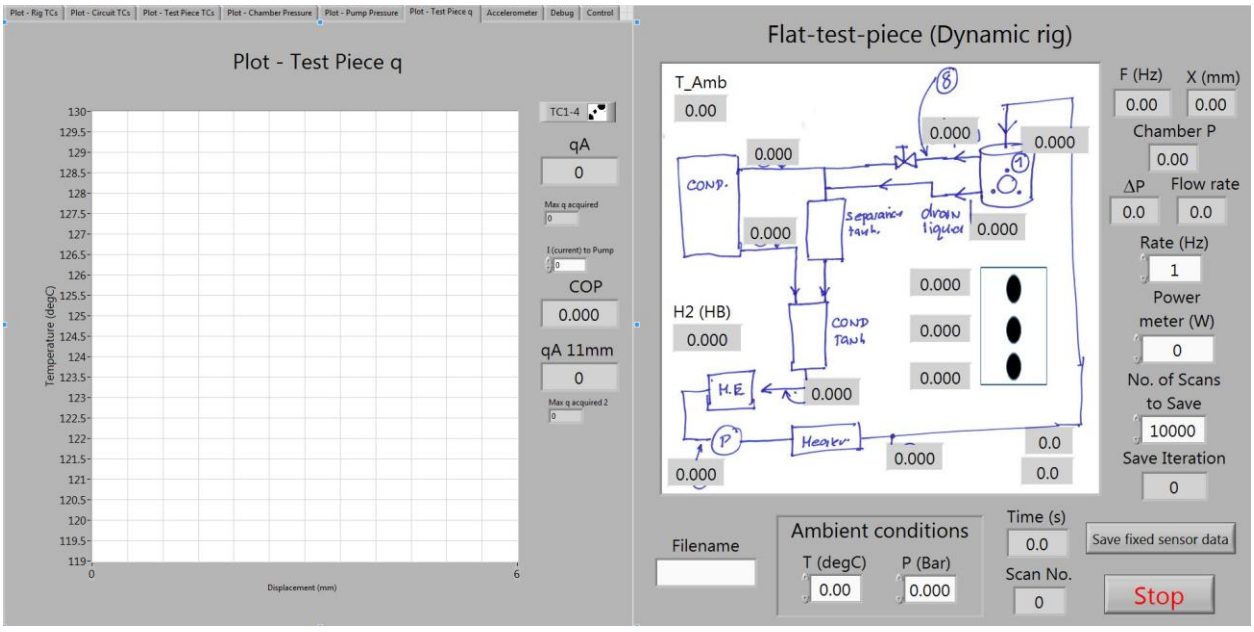

Fig A1-6. LabVIEW front panel of heat flux and COP measurements tab.

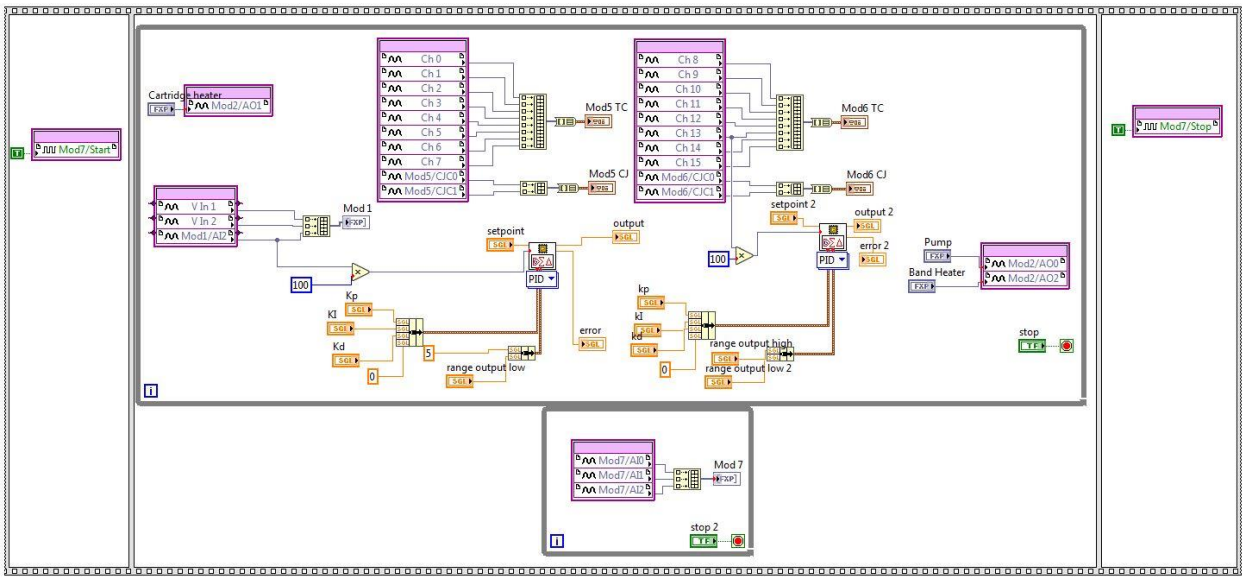

Fig A1-7. LabVIEW FPGA setup.

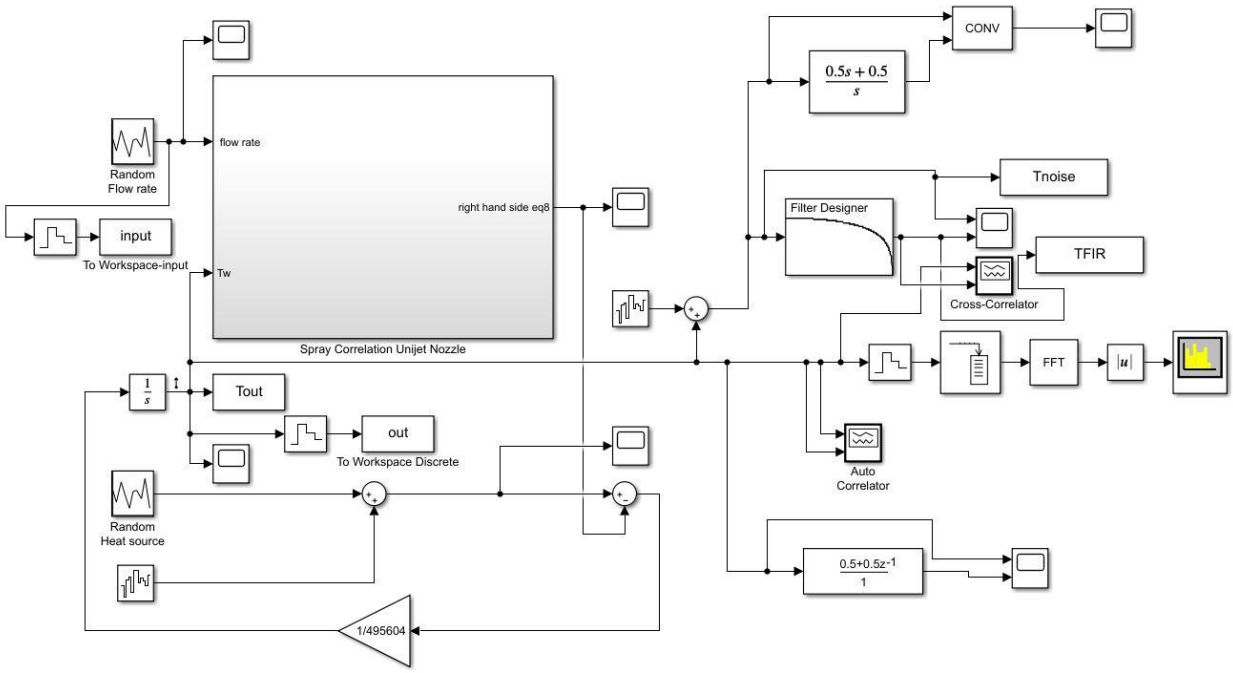

Fig A1-8. SIMULINK diagram of correlation models and Wiener-Hopf approach.

Appendix 2

The author's publications

Relevant to this thesis

- Jose, J.T., Sarmadian, A., Dunne, J.F., Long, C.A., Pirault, J.P. and Rouaud, C., 2021. An experimentally-verified temperature control simulation model for spray evaporative cooling of vibrating powertrain parts. *International Journal of Heat and Mass Transfer*, *170*, p.121041.
- Sarmadian, A., Dunne, J.F., Long, C.A., Jose, J.T., Pirault, J.P. and Rouaud, C., 2020. Heat flux correlation models for spray evaporative cooling of vibrating surfaces in the nucleate boiling region. *International Journal of Heat and Mass Transfer*, *160*, p.120159.

Relevant to other work

- Sarmadian, A., Moghaddam, H.A., Asnaashari, A., Joushani, H.A.N., Moosavi, M., Islam, M.S., Saha, S.C. and Shafaee, M., 2020. Flow boiling heat transfer and pressure drop characteristics of Isobutane in horizontal channels with twisted tapes. *International Journal of Heat and Mass Transfer*, *162*, p.120345.
- Moghaddam, H.A., Sarmadian, A., Asnaashari, A., Joushani, H.A.N., Islam, M.S., Saha, S.C., Ghasemi, G. and Shafaee, M., 2020. Condensation heat transfer and pressure drop characteristics of Isobutane in horizontal channels with twisted tape inserts. *International Journal of Refrigeration*, *118*, pp.31-40.
- Moghaddam, H.A., Sarmadian, A., Shafaee, M. and Enayatollahi, H., 2020. Flow pattern maps, pressure drop and performance assessment of horizontal tubes with coiled wire inserts during condensation of R-600a. *International Journal of Heat and Mass Transfer*, *148*, p.119062.
- Alimardani, F., Moghaddam, H.A., Sarmadian, A. and Shafaee, M., 2019. Pressure loss and performance assessment of horizontal spiral coil inserted pipes during forced convective evaporation of R-600a. *International Journal of Refrigeration*, *107*, pp.20-30.
- Moghaddam, H.A., Sarmadian, A. and Shafaee, M., 2019. An experimental study on condensation heat transfer characteristics of R-600a in tubes with coiled wire inserts. *Applied Thermal Engineering*, *159*, p.113889.
- Mashouf, H., Shafaee, M., Sarmadian, A. and Mohseni, S.G., 2017. Visual study of flow patterns during evaporation and condensation of R-600a inside horizontal smooth and helically dimpled tubes. *Applied Thermal Engineering*, *124*, pp.1392-1400.
- Sarmadian, A., Shafaee, M., Mashouf, H. and Mohseni, S.G., 2017. Condensation heat transfer and pressure drop characteristics of R-600a in horizontal smooth and helically dimpled tubes. *Experimental Thermal and Fluid Science*, *86*, pp.54-62.
- Shafaee, M., Mashouf, H., Sarmadian, A. and Mohseni, S.G., 2016. Evaporation heat transfer and pressure drop characteristics of R-600a in horizontal smooth and helically dimpled tubes. *Applied Thermal Engineering*, *107*, pp.28-36.

Appendix 3

Co-authored publications submitted to journals and conferences but either not yet published or accepted.

The manuscripts:

Correlation models of critical heat flux and associated temperature for spray evaporative cooling of vibrating surfaces by A Sarmadian, J.F. Dunne, J. Thalackottore Jose, C.A. Long, and J-P Pirault. Submitted to the Elsevier *International Journal of Heat and Mass Transfer*. (A2-1)

Temperature control of vibrating heat-generating hardware using spray evaporative cooling in the nucleate boiling region by A Sarmadian, J.F. Dunne*, J. Thalackottore Jose, C.A. Long, and J-P Pirault. Submitted to the Elsevier *International Journal of Heat and Mass Transfer*. (A2-38)

The effect of surface vibration on spray evaporative cooling by A Sarmadian, J. F. Dunne, C. A. Long, J-P Pirault, J. Thalackottore-Jose, and Cedric Rouaud. Submitted to Proceedings of *the 8th International Conference on Fluid Flow, Heat and Mass Transfer*. (A2-75)

The effect of surface-to-nozzle distance on the critical heat flux of spray evaporative cooling applied to vibrating surfaces by A Sarmadian, J. Thalackottore-Jose, J. F. Dunne, C. A. Long, J-P Pirault, and Cedric Rouaud. Submitted to *the 15th International Conference on Heat Transfer, Fluid Mechanics and Thermodynamics (HEFAT)* and Editorial Board of Elsevier *Applied Thermal Engineering* (ATE). (A2-82)

Correlation models of critical heat flux and associated temperature for spray evaporative cooling of vibrating surfaces

by

A Sarmadian, J.F. Dunne*, J. Thalackottore Jose, C.A. Long, and J-P Pirault

Department of Engineering and Design
School of Engineering and Informatics
University of Sussex, Falmer, Brighton, BN1 9QT, UK.
*Corresponding author: E-mail: j.f.dunne@sussex.ac.uk

ABSTRACT

Prediction models have been constructed to investigate the effect of vibrating surfaces on the critical heat flux (CHF) and its associated temperature in spray evaporative cooling. Dimensional analysis has been used to construct the models to account for the influence of key dynamic parameters. Experimental measurements have been obtained from a flat, electrically-heated, copper test-piece, located inside a spray-chamber mounted on top of a shaker. A wide range of large-amplitude and high-frequency measurements have been obtained which correspond to test conditions for a piece of hardware mounted on board a light-duty automotive vehicle with vibration amplitudes ranging from 0 to 8 mm and frequencies from 0 to 200 Hz. Three nozzle types have been fed with distilled water at flow rates ranging from 55 to 100 ml/min being used to cool with subcooling degrees ΔT_{sub} ranging from 10℃ to 45℃. Measured data for both static and dynamic cases have been used to explore the influence on the CHF and the surface-to-fluid saturation temperature at which this occurs, of subcooling degrees, surface vibration amplitude and frequency, vibrational Reynolds Number and vibrational Acceleration Number. The measured data has also subsequently been used to calibrate the predictive models for use in thermal management systems. Static measurements (without vibration) show that the influence of flow rate, volumetric flux, and subcooling are largely in agreement with published literature. For dynamic cases, the influence of vibration is best explained in terms of the nondimensional parameters: Vibration Reynolds Number and Acceleration Number. The effect of vibration on CHF and associated temperature is assessed in detail for the three nozzle types at different flow rates and degrees of subcooling. Predictions of CHF and associated excess temperature, using the calibrated correlation models for the dynamic conditions, are very reasonable, and suitable for the intended purpose of ensuring safe operation of thermal management systems using spray evaporative cooling.

1. Introduction

Spray cooling is receiving considerable attention for advanced thermal management systems. The reason is that spray heat transfer characteristics are especially good in terms of achieving high Coefficient of Performance (COP) [1], high-heat flux, and high-temperature heat removal [2]. Spray cooling applications can be found in numerous areas. In the automotive sector for example, they include both battery electric [3], and hybrid electric vehicles [4]. In power electronics they include high-power LEDs [5], IGBTs [6] and associated IGBT heat sinks [7]. In aerospace, spray cooling applications are found in micro-electro-mechanical systems [8], and high performance lithium-ion batteries [9][10]. And in power generation, for thermal management of superheaters [11], hydrogen-based systems [12], storage tanks[13], and surface temperature control of hydrogen fuel cell catalysts [14]. Elsewhere, in carbon capture, water spray cooling for the CO_2 separation proves most cost-effective for gasifier design [15]. These applications conform to the UK government 10-point green industrial revolution plan [16]. But with the goal of achieving net zero carbon emissions by 2050, increasingly efficient and safe thermal management systems will be essential. Spray *evaporative* cooling has a role to play in achieving that goal because it offers even better characteristics than single-phase spray cooling.

In general, thermal management systems require two attributes: efficacy and safety. For evaporative spray cooling, efficacy requires a thorough understanding of the dynamic and heat transfer mechanisms involved. Spray dynamics involve many complex relations, from droplet impingement to rebound and splashing, followed by bubble generation during nucleation within the liquid film [17]. The heat transfer mechanisms comprise such complexities as impinged drop convection, liquid film evaporation, film-flow convection, surface and secondary nucleate boiling [18]. To better understand how these mechanisms combine, researchers have separated different modes of spray cooling based on achievable excess temperature and heat flux (where the excess temperature is the difference between the cooled surface temperature and the fluid saturation temperature). Spray cooling modes start from single-phase (similar to pool boiling), with high degrees of subcooling appropriate for low heat-flux and low-temperature requirements. The next mode is nucleate boiling with high heat transfer rates and high surface temperature capabilities ideal for cooling systems with extreme thermal requirements [19]. Following the so called ‘critical heat flux’, transition boiling occurs. In the transition boiling mode, bubbles merge forming small slugs in the liquid film resulting in partial contact of a thin surface layer. The Leidenfrost point occurs when the heat transfer mode changes from transition boiling to film boiling, where a thermally-insulated layer forms between the hot surface and the impinging spray droplets. Film boiling therefore gives poor heat transfer.

For design of safe thermal management systems, the prediction of critical heat flux immediately after nucleate boiling plays an important role. This is because nucleate boiling is the desired two-phase spray mode. Remaining within this regime requires accurate prediction of the transition to CHF. Mudawar and Valentine [20] reported that prediction of steady-state temperature is difficult in the transition to film boiling which occurs just after the CHF point (caused by low heat flux and surface oxidation). This means to achieve robust temperature control in a thermal management system, models are required to predict both the critical heat flux and the excess temperature at which CHF occurs. Owing to the complexity of these heat transfer mechanisms and the need for efficient prediction of CHF, zero

dimensional models are often adopted. These models, and their range of valid operation, are listed in Table 1. Owing to uncertainty in measured data, and in the model fitting process, error analysis in both phases of thermal management and controller design, is important. But predictive models of the excess temperature at which CHF occurs are rare, stemming mainly from contradictory issues associated with the dynamics of the heat transfer mechanisms, and the key parameters. Examples include the empirical surface temperature models at CHF by Mudawar and Valentine [20] and Dou et al. [21], also the analytical model for aerospace applications by Baysinger et al. [22]. But to include dynamic effects such as vibration, more experimental evidence is needed.

The literature shows that vibration affects heat transfer involving Newtonian and non-Newtonian fluids, also nano-fluids [23]. Vibration velocity and acceleration are important parameters and need to be considered in the thermal management of systems exposed to dynamic agitation such as automotive vehicles [24] and aircraft [25, 26]. The effects of vibration on spray cooling in single-phase [27], incipient boiling [28, 29], and nucleate boiling [30] modes have recently been investigated. Reynolds numbers and nondimensional Acceleration Number have been used to address the effects of vibration with a reliance on either empirical or theoretical modelling. The Vibrational Reynolds Number is a representation of the turbulence caused by vibrating surfaces [31]. It can be used in modelling to establish how vibration induced turbulence affects the heat transfer. The Acceleration Number can explain the effects of experimentally-measured acceleration on spray cooling heat transfer. Elston et al. [32, 33] studied the effect of acceleration on the cooling performance of spray arrays on NASA's C-9 aircraft exposed to acceleration levels of 0.02g to 2.02g, reporting that acceleration impedes spray heat transfer in nucleate boiling. By contrast, Michalak et al. [34] claimed that accelerations between 0.15g and 1.8g, increasingly enhances spray heat transfer. There are however no studies published examining the effect of vibration on CHF, and how it influences the corresponding CHF excess temperature. In this study, the objective is to reveal the influences of vibration on CHF and excess temperature, for vibration parameters relevant to the road transport sector. Correlation models of CHF and corresponding excess temperature are developed and calibrated. These empirical correlations can be used for design of spray evaporative cooling systems and in their subsequent thermal management. Construction of correlation models is first described, followed by a detailed examination of the effects of vibration on CHF and excess temperature, culminating in the calibration of correlation models to provide a predictive capability for the observed physics.

1. A correlation modelling approach for CHF and corresponding temperature predictions

This section outlines a modelling approach to obtain CHF and excess temperature both with, and without vibration. This is based on dimensional analysis [63] in the form of the generalized Π-Theorem proposed by Sonin [64] - a developed form of the well-known Buckingham Π-Theorem [65, 66]. The method has been widely used in developing the empirical correlations, in particular, for spray cooling. For prediction of critical heat flux q_{CHF} with static surfaces, it can be established from Table 2, that the heat flux, as a dependent variable, can be completely determined from the fluid properties, geometry, forcing, and spray specifications as provided in the functional relationship according to:

$$q_{Static-CHF} = \varphi(\rho_l, \rho_v, h_{fg}, \mu_l, C_l, \sigma, T_c, P_n, P_{ch}, \Delta T_{sub}, P_{at}, u_d \text{ or } u_m, \dot{m} \text{ or } v \text{ or } \bar{\vec{v}}, d_{32} \text{ or } d_{05}, H) \quad (1)$$

where the dimensions and description of the different parameters are provided in Table 2.

Table 1. Studies on the prediction of Critical Heat Flux (CHF).

Authors	Working fluid	Test conditions: (as reported in referenced publication)	Error range of the correlations (%)	Experimental uncertainty of measured heat flux (%)	Derived experimental correlations*
Mudawar and Valentine (1989) [20]	**Water**	$T_c = 23 - 80\ ^\circ C$, $v^{"} = 0.6 \times 10^{-3} - 9.96 \times 10^{-3} m^3 s^{-1}/m^2$ $d_{0.5}$ = 0.434-2.005 mm, u_m =10.6-26.5 m/s	±20	-	(C1)
Estes and Mudawar (1995) [35]	**Water, FC-72, FC87**	$v = 2.52 \times 10^{-6} - 3.15 \times 10^{-5}\ m^3 s^{-1}$, $\Delta T_{sub} = 13 - 33^\circ C$	±25	-	(C2)
Mudawar and Estes (1995) [36]	**FC-72, FC87**	$v^{"} = 16.6 \times 10^{-3} - 216 \times 10^{-3} m^3 s^{-1}/m^2$, $\Delta T_{sub} = 13 - 33\ ^\circ C$	±30	-	(C3)
Jian and Dhir (2004) [37]	**Water**	$v^{"} = 2.9 \times 10^{-3} - 5.1 \times 10^{-3} m^3 s^{-1}/m^2$, $T_c = 23 - 70\ ^\circ C$	±23	±4.3	(C4)
Thiagarajan et al.(2013) [38]	**HFE-7100**	$v = 1.1 \times 10^{-6} - 15.8 \times 10^{-6}\ m^3 s^{-1}$, $\Delta T_{sub} = 0 - 30^\circ C$	±30	±6	(C5)
Thiagarajan et al. (2013) [38]	**HFE-7100**	A microporous surface: 100 μm coating, porosity of 57%.	±30	±6	(C6)
Dou et al. (2015) [21]	**Water**	$G = 6.2 - 12.4$ kg/m^{2}s, $\Delta P = 2 - 7 bar$	±20	±6.3	(C7)
Visaria and Mudawar (2008) [39]	**FC-77**	$\Delta T_{sub} = 22 - 70\ ^\circ C$, $v = 3.33 - 20.4\ cm^3 s^{-1}$	±30	-	(C8)
Sehmbey et al. (1995) [40]	**Liquid nitrogen**	$d_{32} = 14 - 29\ \mu m$, $G = 16.9 - 88.9$ kg/m^{2}s, $P_n = 2.8 - 8.3\ bar$	±30	±8	(C9)
Chow et al. (1996) [41]	**Water Liquid nitrogen Air-water R-113**	$\Delta T_{sub} = 0 - 50\ ^\circ C$, $u_m = 10 - 50\ m/s$, $G = 1.12 - 6.75$ kg/m^{2}s	±30	-	(C10)
Sawyer et al. (1996) [42]	**Water**	$u_m = 2.4 - 4.6\ m/s$, $We = 175 - 730$	±22	±5	(C11)
Silk et al. (2007) [43]	**Water Methanol Perfluorocarbons**	$Pr = 0.33$, $T_{sat} = 31 - 80$ ℃	±30	-	(C12)
Cabrera and Gonzalez (2003) [44]	**Water**	$\Delta T_{sub} = 25 - 78\ ^\circ C$, $P_n = 1 - 1.8\ bar$, $R_t = 5 - 79 \mu m$, $G = 340 - 750$ kg/m^{2}s	±15	±10	(C13)
Abbasi and Kim (2011) [45]	**PF-5060**	$\Delta T_{sub} = 11 - 31\ ^\circ C$, $P_n = 2 - 6.9\ bar$, $H = 3, 5,$ and 7 mm	±25	±6.3	(C14)
Zhao et al. (2019) [46]	**Water**	$\Delta T_{sub} = 61.3\ ^\circ C$, $\bar{v} = 2.42 - 8.04$ m^{3}s^{-1}/m^2	±12.31	±4.6	(C15)

Table 1. Continued:

*Developed correlations associated with Refs. [18][20-31] identified by Equations C1 to C15 as appropriate:

$$q_{CHF} = 122.4 \rho_g h_{fg} v^{"} \left[1 + 0.0118 \left(\frac{\rho_g}{\rho_f}\right)^{1/4} \left(\frac{\rho_f C_{p,f} \Delta T_{sub}}{\rho_g h_{fg}}\right)\right] \left(\frac{\sigma}{\rho_f v^{"2} d_{32}}\right)^{0.198} \quad \text{(C1)}$$

$$q_{CHF} = 134.3 \rho_g h_{fg} v^{"} \left[1 + 0.0118 \left(\frac{\rho_g}{\rho_f}\right)^{1/4} \left(\frac{\rho_f C_{p,f} \Delta T_{sub}}{\rho_g h_{fg}}\right)\right] \left(\frac{\sigma}{\rho_f v^{"2} d_{0.5}}\right)^{0.192} \quad \text{(C1)}$$

$$q_{CHF,p} = 2.3 \rho_g h_{fg} v^{"} \left(\frac{\rho_f}{\rho_g}\right)^{0.3} \left(\frac{\rho_f v^{"2} d_{32}}{\sigma}\right)^{-0.35} \left[1 + 0.0019 \left(\frac{\rho_f C_{p,f} \Delta T_{sub}}{\rho_g h_{fg}}\right)\right] \quad \text{(C2-a)}$$

$$q_{CHF,p} = \frac{q_{CHF} L^2}{L^2 (\pi/4)} = \frac{4}{\pi} q_{CHF} \quad \text{(C2-b)}$$

$$v^{"} = \frac{2v}{\pi L^2} \left[(1 + \cos(\frac{\theta}{2})) \cos(\frac{\theta}{2})\right] \quad \text{(C2-c)}$$

$$q_{CHF} = 1.467 \rho_g h_{fg} \bar{v}^{"} \left[(1 + \cos(\frac{\theta}{2})) \cos(\frac{\theta}{2})\right]^{0.3} \left(\frac{\rho_f}{\rho_g}\right)^{0.3} \left[\frac{\rho_f \bar{v}^{"2} d_{32}}{\sigma}\right]^{-0.35} \left[1 + 0.0019 \left(\frac{\rho_f C_{p,f} \Delta T_{sub}}{\rho_g h_{fg}}\right)\right] \quad \text{(C3)}$$

$$q_{CHF} = 2.3\rho_g h_{fg} \bar{v}^{"} \left(\frac{\rho_f}{\rho_g}\right)^{0.5} \left(\frac{\rho_f \bar{v}^{"2} d_o}{\sigma}\right)^{-0.2} \left[1 + 0.0019\left(\frac{\rho_f C_{p,f} \Delta T_{sub}}{\rho_g h_{fg}}\right)\right] \quad \text{(C4)}$$

$$q_{CHF} = 1.449\rho_g h_{fg} \bar{v}^{"} \left(\frac{\rho_f}{\rho_g}\right)^{0.3} \left[\frac{\rho_f \bar{v}^{"2} d_{32}}{\sigma}\right]^{-0.3371} \left[1 + 0.0058\left(\frac{\rho_f C_{p,f} \Delta T_{sub}}{\rho_g h_{fg}}\right)\right] \quad \text{(C5)}$$

$$q_{CHF} = 2.14\rho_g h_{fg} \bar{v}^{"} \left(\frac{\rho_f}{\rho_g}\right)^{0.3} \left[\frac{\rho_f \bar{v}^{"2} d_{32}}{\sigma}\right]^{-0.363} \left[1 + 0.0058\left(\frac{\rho_f C_{p,f} \Delta T_{sub}}{\rho_g h_{fg}}\right)\right] \quad \text{(C6)}$$

$$q_{CHF,p} = 2.52 \times 10^{-3} \rho_g h_{fg} v^{"} \left(\frac{\rho_f \bar{v}^{"2} d_{32}}{\sigma}\right)^{-0.4255} \left[1 + 0.013\left(\frac{\rho_f}{\rho_g}\right)^{-0.25} \left(\frac{\rho_f C_{p,f} \Delta T_{sub}}{\rho_g h_{fg}}\right)\right] \quad \text{(C7)}$$

$$q_{CHF,p} = 2.3\rho_g h_{fg} v^{"} \left(\frac{\rho_f}{\rho_g}\right)^{0.3} \left(\frac{\rho_f v^{"2} d_{32}}{\sigma}\right)^{-0.35} \left[1 + 0.005\left(\frac{\rho_f C_{p,f} \Delta T_{sub}}{\rho_g h_{fg}}\right)\right] \quad \text{(C8)}$$

$$q_{CHF} = 0.31\rho_g h_{fg} \left(\frac{\rho_f}{\rho_g}\right)^{0.5} \left(\frac{6\bar{v}^{"}\sigma}{\pi\rho_f d_{32}}\right)^{1/3} \quad \text{(C9)}$$

$$q_{CHF} = 0.38\rho_g h_{fg} u_m \left(\frac{\rho_f {u_m}^2 d_{32}}{\sigma}\right)^{-1/3} \left(\frac{\rho_f}{\rho_g}\right)^{-0.5} \left(\frac{P_a}{P_s}\right)^{-0.25} \quad \text{(C10)}$$

$$q_{CHF} = 0.166\rho_f h_{fg} u_d \left(\frac{\rho_f u_d^2 d_d}{\sigma}\right)^{-0.4138} \left(\frac{f d_d}{u_d}\right)^{0.8906} \quad \text{(C11)}$$

$$q_{CHF} = 5.3 Re_d^{0.55} Pr_f^{0.33} \left[\frac{1+0.8\left(C_{p,f}\Delta T_{sub}/h_{fg}\right)}{\left(\frac{\rho_f}{\rho_g}\right)^{0.4}}\right] \left(\frac{\pi N^{+} d_{32}^3}{6}\right)^{0.09} \left(\frac{k_f}{L}\right) \left(\frac{h_{fg}}{c_{p,f}}\right) \quad \text{(C12)}$$

$$q_{CHF} = 1.623(We)^{-0.315}(S_t)^{0.0465} = 1.623 G h_{fg} \left(\frac{\rho_f u_d^2 d_d}{\sigma}\right)^{-0.315} \left(\frac{R_t}{R_d}\right)^{0.0465} \quad \text{(C13)}$$

$$q_{CHF}^{"} = 9.15 * 10^4 P^{0.4} \left(1 + 2.42\left(\frac{C_{p,f}\Delta T_{sub}}{h_{fg}}\right)\right)^{0.52} \quad \text{(C14)}$$

$$q_{CHF} = 58.0628\rho_g h_{fg} \bar{v}^{"} \left[1 + 0.00118\left(\frac{\rho_f}{\rho_g}\right)^{-0.25} \left(\frac{\rho_f C_{p,f} \Delta T_{sub}}{\rho_g h_{fg}}\right)\right] We^{-0.2054} St^{0.4462} \quad \text{(C15)}$$

Table 2. Parameters with dimensions in SI and MLT systems.

		Dimensions	
Quantity	Symbol	SI	MLT
q_{ch}	Heat Flux	W/m^2	MT^{-3}
ρ_1	Density	kg/m^3	ML^{-3}
h_{fg}	Latent heat	J/kg	L^{2}T^{-2}
μ	Dynamic viscosity	Kg/m s	ML^{-1}T^{-1}
C_l	Specific heat	J/kg k	L^{2}T^{-2}θ^{-1}
σ	Surface tension	N/m	MT^{-2}
T	Coolant temperature	K	θ
P_2	Pressure	Pa	ML^{-1}T^{-2}
ΔT_{sub}	Subcooling degree	K	θ
u_3	velocity (u_d and $u_m^2 = \frac{2\Delta P}{\rho}$ based on [67])	m/s	LT^{-1}
$\dot{m}$	Mass flow rate	kg/s	MT^{-1}
v	Volumetric flow rate	m^3/s	L^3 T^{-1}
$\bar{\vec{v}}$	Average volumetric spray flux	m^{3}s^{-1}/m^2	LT^{-1}
d_{32}	Sauter mean diameter (correlated in [68])	m	L
d_{05}	mass or volume median diameter (correlated in [69])	m	L
d_H	Hydraulic diameter of the heating surface	m	L
H	Nozzle to surface distance	m	L
a	Amplitude	m	L
ω	Angular frequency	1/s	T^{-1}
g	Acceleration of gravity	m/s^2	LT^{-2}

[1]subscripts v and l are respectively vapour and liquid phases.
[2]subscripts n, ch, and at represent nozzle, chamber, and atmosphere, respectively.
[3]subscripts d and m are respectively droplet and mean droplet breakup velocities
For model fitting, heat flux, latent heat, specific heat, and pressure, are respectively in kW/m^2, kJ/kg, kJ/kg k, and kPa.

For vibrating surfaces producing a dynamic-CHF, there are no published studies which have employed dimensional analysis. Therefore, there is no correlation available to predict critical heat flux (See Table 1). To develop a functional relationship, fluid dynamics suggests that the heat flux should depend not only on the static condition parameters but also the vibration amplitude (a) and angular frequency ($\omega = 2\pi f$). To achieve this, the proposed functional form is:

$$q_{Dynamic-CHF} = \varphi(\rho_l, \rho_v, h_{fg}, \mu_l, C_l, \sigma, T_c, P_n, P_{ch}, \Delta T_{sub}, P_{at}, u_d \text{ or } u_m, \dot{m} \text{ or } v \text{ or } \bar{\bar{v}}, d_{32} \text{ or } d_{05}, d_H, H, a, \omega, g) \quad (2)$$

where d_H is the hydraulic diameter of the heating surface, and g is gravitational acceleration. After defining independent variables (key parameters) through dimensional analysis, using the generalized Π-Theorem, invariant parameters for different cases can be identified. Invariant parameters (such as Chamber Pressure) can be identified in the test procedure. For example, when experiments are only undertaken at atmospheric pressure, then those dimensionless Π-parameters that comprise entirely invariant quantities, can be neglected, which results in simplification. All the derived functional forms corresponding to the different test plans for both dynamic and static conditions are provided in Table 3.

Table 3. Dimensional analysis for CHF prediction.

Surface condition	Invariant Parameter	Number of Π-terms	Measurements needed	Functional form
Static (No vibration)	None	4	Spray spec.[3]	$\frac{qH}{\mu_l h_{fg}} = f\left(\frac{C_l \Delta T_{sub}}{h_{fg}}, \frac{\rho_l (u_m^2 or \bar{\bar{v}}^2) d_{32}}{\sigma}, \frac{P_{ch}}{P_{at}}, \frac{\rho_l}{\rho_v}\right)$
			Flow rate	$\frac{qH}{\mu_l h_{fg}} = f\left(\frac{C_l \Delta T_{sub}}{h_{fg}}, \frac{\rho_l \sigma \dot{m}}{{\mu_l}^3} or \frac{{\rho_l}^2 \sigma v}{{\mu_l}^3}, \frac{P_{ch}}{P_{at}}, \frac{\rho_l}{\rho_v}\right)$
	P_{ch}	2	Spray spec.	$\frac{qH}{\mu_l h_{fg}} = f\left(\frac{C_l \Delta T_{sub}}{h_{fg}}, \frac{\rho_l (u_m^2 or \bar{\bar{v}}^2) d_{32}}{\sigma}\right)$
			Flow rate	$\frac{qH}{\mu_l h_{fg}} = f\left(\frac{C_l \Delta T_{sub}}{h_{fg}}, \frac{\rho_l \sigma \dot{m}}{{\mu_l}^3} or \frac{{\rho_l}^2 \sigma v}{{\mu_l}^3}\right)$
	$P_{ch}, \Delta T_{sub}$	1	Spray spec.	$\frac{qH}{\mu_l h_{fg}} = f\left(\frac{\rho_l (u_m^2 or \bar{\bar{v}}^2) d_{32}}{\sigma}\right)$
			Flow rate	$\frac{qH}{\mu_l h_{fg}} = f\left(\frac{\rho_l \sigma \dot{m}}{{\mu_l}^3} or \frac{{\rho_l}^2 \sigma v}{{\mu_l}^3}\right)$
Dynamic (Vibration)	None	7	Spray spec.	$\frac{qH}{\mu_l h_{fg}} = f\left(\frac{C_l \Delta T_{sub}}{h_{fg}}, \frac{\rho_l (u_m^2 or \bar{\bar{v}}^2) d_{32}}{\sigma}, \frac{P_{ch}}{P_{at}}, \frac{\rho_l}{\rho_v}, \frac{a}{H}, \frac{\omega^2 a}{g}, \frac{\omega a}{u_d}\right)$
			Flow rate	$\frac{qH}{\mu_l h_{fg}} = f\left(\frac{C_l \Delta T_{sub}}{h_{fg}}, \frac{\rho_l \sigma \dot{m}}{{\mu_l}^3} or \frac{{\rho_l}^2 \sigma v}{{\mu_l}^3}, \frac{\rho_l a \omega d_H}{\mu_l}, \frac{P_{ch}}{P_{at}}, \frac{\rho_l}{\rho_v}, \frac{a}{H}, \frac{\omega^2 a}{g}\right)$
	P_{ch}	5	Spray spec.	$\frac{qH}{\mu_l h_{fg}} = f\left(\frac{C_l \Delta T_{sub}}{h_{fg}}, \frac{\rho_l (u_m^2 or \bar{\bar{v}}^2) d_{32}}{\sigma}, \frac{a}{H}, \frac{\omega^2 a}{g}, \frac{\omega a}{u_d}\right)$
			Flow rate	$\frac{qH}{\mu_l h_{fg}} = f\left(\frac{C_l \Delta T_{sub}}{h_{fg}}, \frac{\rho_l \sigma \dot{m}}{{\mu_l}^3} or \frac{{\rho_l}^2 \sigma v}{{\mu_l}^3}, \frac{\rho_l a \omega d_H}{\mu_l}, \frac{a}{H}, \frac{\omega^2 a}{g}\right)$
	$P_{ch}, \Delta T_{sub}$	4	Spray spec.	$\frac{qH}{\mu_l h_{fg}} = f\left(\frac{\rho_l (u_m^2 or \bar{\bar{v}}^2) d_{32}}{\sigma}, \frac{a}{H}, \frac{\omega^2 a}{g}, \frac{\omega a}{u_d}\right)$
			Flow rate	$\frac{qH}{\mu_l h_{fg}} = f\left(\frac{\rho_l \sigma \dot{m}}{{\mu_l}^3} or \frac{{\rho_l}^2 \sigma v}{{\mu_l}^3}, \frac{\rho_l a \omega d_H}{\mu_l}, \frac{a}{H}, \frac{\omega^2 a}{g}\right)$
[1]Chamber pressure is constant, [2]Chamber pressure and degrees of subcooling are constant, [3]Spray specifications				

Based on invariant parameters, three different test procedures are considered, either for static or dynamic environments: i) with variable pressure, and degree of subcooling is indicated as '*None'* for 'Invariant Parameter' in Table 3; ii) under constant pressure (with invariant P_{ch} in the second column of Table 3); and iii) constant pressure and degrees of subcooling (P_{ch}, ΔT_{sub}). In this study, the functional forms with invariant P_{ch} are used. And as provided on the third column of table 3, the

number of Π-terms correspond to those for fixed P_{ch} and ΔT_{sub} which is resulted by Generalized Π–Theorem algorithm.

Dimensionless functional forms can be derived based on model requirements. Here '*spray specifications*' and '*flow rate*' are relevant (as in the fourth column of Table 3). Whether, this is for design purposes (in which spray specifications are important), or for a special control approach (where the pumping flow rate plays an important role on the wall temperature control) different dimensionless Π–terms can be obtained (as in the last column of Table 3). Also shown in Table 3, are three dimensionless numbers (common in spray fluid mechanics). These are Boiling Number ($Bo = \frac{qH}{\mu_l h_{fg}}$), Jacob Number ($Ja = \frac{C_l \Delta T_{sub}}{h_{fg}}$), and Weber Number ($We = \frac{\rho_l (u_m^2 or \bar{v}^2) d_{32}}{\sigma}$). Owing to the high dependency of CHF on the 'subcooling' temperature, $\Delta T_{sub} = T_{sat} - T_c$ is used in Jacob number. In the functional forms corresponding to '*flow rate*' measurements, $\frac{\rho_l \sigma \dot{m}}{{\mu_l}^3}$ is substituted for Weber number, which has spray specifications of $u_m \; or \; \bar{v}$ and d_{32}. For functional forms with invariant parameters of P_{ch} and ΔT_{sub}, the Jacob number $Ja = \frac{C_l \Delta T_{sub}}{h_{fg}}$ also stays invariant and therefore is eliminated according to the Generalized Π–Theorem. For dynamic conditions, the Vibrational Reynolds Number $Re_V = \frac{\rho_l a \omega d_H}{\mu_l}$, and the dimensionless Acceleration Number $\frac{\omega^2 a}{g}$ have also been derived.

The Functional forms should also be chosen to take measurement factors into consideration (i.e. which sensors are being used for system identification, and subsequently for the thermal management. There are however conflicting findings as pointed out by Liang et al. [19], in respect of spray effects on the CHF, and Chen et al. [70] who found that CHF is independent of Sauter mean diameter. Furthermore, the use of mean droplet velocity is not recommended for correlating CHF data [35] owing to its failure to account for the cumulative effect of multi-droplet impact. A view supported by Toda [71, 72], who showed that for mist cooling, CHF for water sprays is insensitive to droplet velocity. For this reason, for the purposes of gaining an understanding on the dependence of CHF on key parameters, and subsequently for thermal management, the CHF modelling approach adopted here, makes use of functional forms involving '*flow rate*' for both static and dynamic cases as follows:

$$Bo = a\, Ja^{\mathrm{b}} \left(\frac{\rho_l^2 \sigma v}{{\mu_l}^3}\right)^{\mathrm{c}} \qquad \text{(Static)} \tag{3}$$

$$Bo = a\, Ja^{\mathrm{b}} \left(\frac{\rho_l^2 \sigma v}{{\mu_l}^3}\right)^{\mathrm{c}} Re_V^{\mathrm{d}} \left(\frac{a}{H}\right)^{\mathrm{e}} Ac^{\mathrm{f}} \quad \text{(Dynamic)} \tag{4}$$

2. Experimental facilities

Since getting an understanding of the dependence of CHF on key parameters, and calibration of the correlation modelling approach described in Section 1, requires measured experimental data, this section describes the facilities used. Figure 1 shows both the experimental test rig used and the data acquisition system. The test rig comprised a spray chamber containing the test piece and a flow loop. The flow loop delivers de-ionised water at the desired operating conditions through stainless-steel piping to the spray nozzle inlet (No. 4). Three misting nozzles (of Type PJ8, PJ10, and MW145) are used

(whose spray specifications are described in Section 3). During spray cooling, the accumulated water at the bottom of the spray chamber (No. 13) drained (No. 6) into the separator tank (No. 11), and the vapour in the chamber vented (No. 5) into an air-cooled condenser (Denso RDP 583, No. 9). Finally, the condensed water is cooled by a miniature heat exchanger (No. 12) to a temperature of less than 55 ℃ before entering the pump. There is also a header tank (No. 8) that removes any air from the system. This completes the flow loop.

The operating conditions are set using the gear pump (Micropumps MGD100P, No. 1) and pre-heaters (No. 2) through the DAQ system and its control unit. Both pump and band heaters are connected to the controllers in order to satisfy: flow rate, nozzle pressure drop, and the inlet temperature control to set different subcooling degrees. The DAQ system comprises the main processor (NI cRIO-9035, No. 15) and C series modules which control the signals to the pump (A), 6 x 250 W cartridge heaters (E) and 2 x 345 W pre-heaters (D) using two (EVR-25BF) power regulators. The NI Compact Rio system, in conjunction with the Human-Machine interface (LabVIEW on Windows desktop), monitors the signals from flow meter (B), accelerometer (C), and test piece thermocouples (F). The flow meter (No. 14) is a low-flow turbine meter (Omega FLR1009ST-D). There are two pressure transducers (Omega PXM309), i.e. one just before the nozzle inlet, and one connected to the chamber to capture the nozzle inlet (No. 4) pressure, the nozzle pressure-drop, and the spray chamber pressure (No. 13).

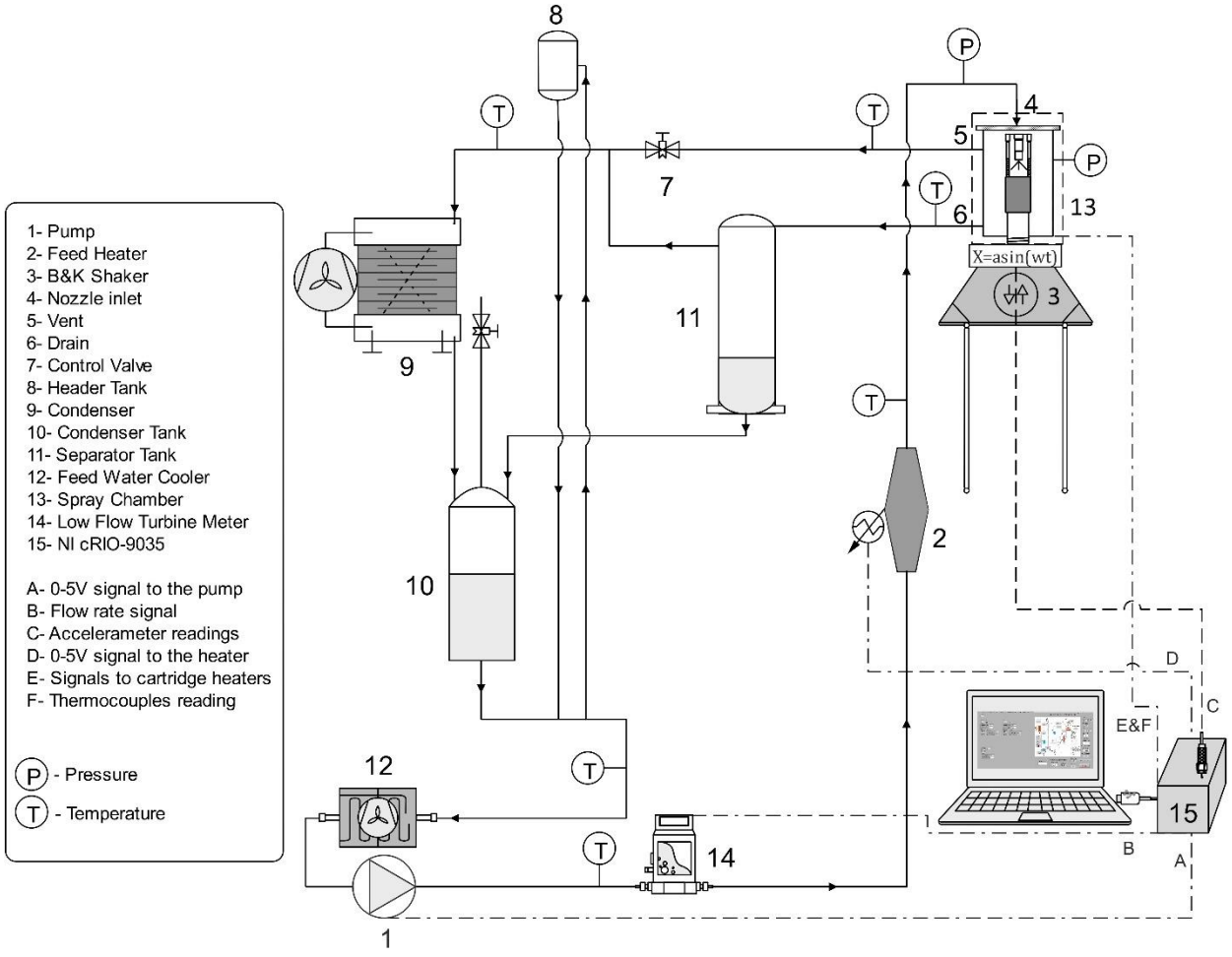

Fig. 1. Layout of the experimental hardware and the DAQ system

A more detailed view of the test-piece located in the spray chamber of figure 1, is shown in figure 2. Different spray nozzles are fitted on the top of the flat test-piece via nozzle fitting (B) and two long bolts (D). A shroud (G) is fitted around the test-piece to prevent spray impingement on the heater block to ensure one-dimensional heat transfer. The nozzle, two bolts, the shroud, the test piece, and the heater block, are shown located on top of a Bruel & Kjaer V555 mechanical shaker using a shaker shaft (K). The shaker (which drives the shaft through a joint in the shaker plate (J)) simulates vibration at appropriate amplitudes and frequencies chosen using a Feedback Instruments FG600 signal generator. A Piezotronics PCB A 353B15 accelerometer is also attached, to the bottom of the shaker plate.

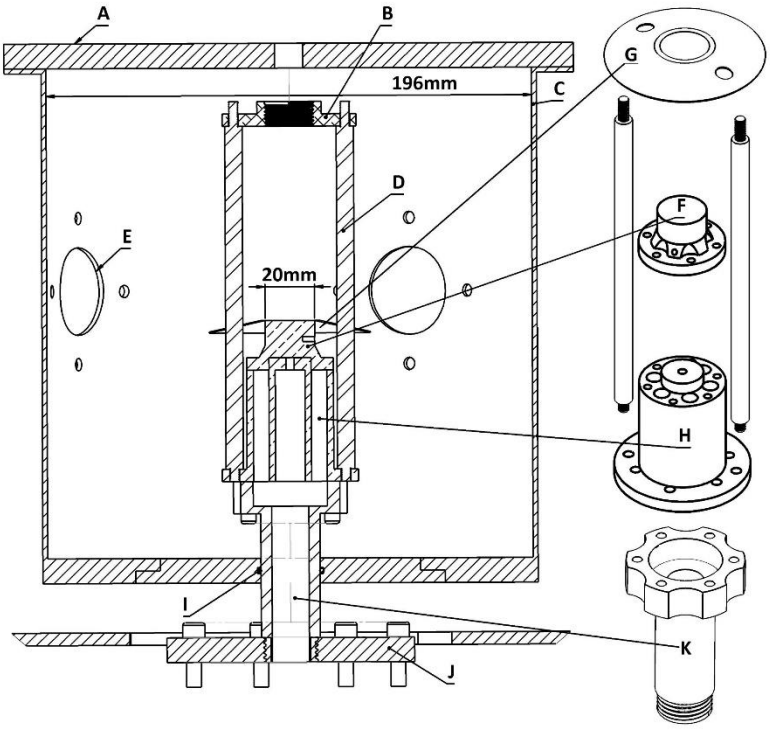

A- Chamber Lid	E- Window	I- O-ring
B- Nozzle Fitting	F- Flat Test Piece	J- Shaker Plate
C- Chamber	G- Shroud	K- Shaker Shaft
D- Bolt	H- Heater Block	

Fig. 2. Spray chamber cross-sectional view showing exploded view of copper test piece and heater block

Choosing an appropriate type of metal for the flat test-piece and heater-block is important in order to be able to accurately measure critical heat flux. Mudawar and Valentine [20] reported that using aluminium for the heater-block led to uncertainty in the repeatability of measurements owing to the high oxidation rate of aluminium (leading to their choice of copper based on the findings of Baumeister and Simon [47] who actually suggested similar results between copper and aluminium owing to their high thermal conductivity and near isothermal surface conditions. For this reason, high-purity copper

was chosen for the test-piece and heater-block, with a thermal conductivity of 390 W/m^2K which has a near-constant value over the experimental test range.

3. Experimental test procedure and data reduction

The experimental test procedure to generate the required data to meet the objectives are shown in Table 4 along with the operating conditions. A chamber pressure of 1 bar, and a surface-to-nozzle distance of 12 mm, are kept constant. Three different nozzles are studied with their respective volumetric flow rates given in parenthesis namely for a type PJ8 (55 ml/min), a PJ10 (75-100 ml/min), and an MW145 (55 ml/min). For all tests, two subcooling temperatures are considered at 10 ℃ and 45 ℃. Testing involving a total of 64 cases included the cooling surface having no vibration, referred to as 'static', plus dynamic cases with different vibration amplitudes and frequencies labelled in the last column of Table 4. The spray specifications associated with the operating conditions are also shown in Table 4.

Table 4. Test plan and spray specification for the operating conditions of the PJ and MW145 nozzles.

$P_{chamber}$ (bar)	v (ml/min)	ΔT_{sub} (℃)	H (mm)	Static	f(Hz) / a (mm)	2	4	8	50	50	100	200	Case
1	55, 75 and 100	10 and 45	12	✓	8	✓	-	-	-	-	-	-	D-1
					4	-	✓	-	-	-	-	-	D-2
					1	-	-	✓		-	-	-	D-3
					1	-	-	-	✓		-	-	D-4
					0.2	-	-	-	-	✓	-	-	D-5
					0.2	-	-	-	-	-	✓	-	D-6
					0.04	-	-	-	-	-	-	✓	D-7

NOZZLE SPRAY SPECIFICATIONS

Nozzle	d_n (mm)	α (◦)	Covering d. (mm)	$\Delta P\ (bar)$	$u_m(\frac{m}{s})$	d_{05} (μm)	d_{32} (μm)
PJ8	0.20	90	24	4.7	31.3	22	107
PJ10	0.25	90	24	2.9-5.2	24.6-32.9	26-33	117-137
MW145	0.41	70	17	7	38.2	47	141

At the beginning of each test (with or without vibration), the power was supplied to the cartridge heaters to bring the cooling surface to a condition within the two-phase heat transfer mode. Steady-state was assumed to occur when all temperature differences associated with all three thermocouples (in time intervals of three minutes) were less than 0.3 ℃ (as convergence criterion). The power was then gradually increased until the CHF occurred. The heat flux was calculated from the readings of the uniform temperature gradient between three thermocouples evenly spaced 5.5 millimetre apart. During the experiments, linearity of temperature measurements was monitored to ensure one-dimensional heat transfer. This measure justifies a predictive solution using the one-dimensional conduction equation:

$$q = -K\frac{dT}{dx} \tag{5}$$

where K, dT, and dx are the thermal conductivity, the temperature difference, and the distance between the top and bottom thermocouples located in the test-piece. The surface temperature was obtained by extrapolating the linear temperature distribution to the surface (as done by Mudawar and Valentine in [20]).

Uncertainty analysis using Moffat's method [48] was undertaken. Results show that the maximum uncertainty in the calculation of heat flux at the maximum measured data point of 2.67 MW/m^2 is predicted to be 2.57%. Table 5 shows the measurement errors and calculated parameter uncertainties.

Table 5. Uncertainties in the calculated and measured parameters.

Parameter	Uncertainty (%)	Units
Thermocouples	±0.4	℃
Volumetric flow rate	±0.6 (of full scale)	ml/min
Accelerometer frequency	±5	Hz
Length	±1	mm
Heat flux	±2.57	MW/m^2

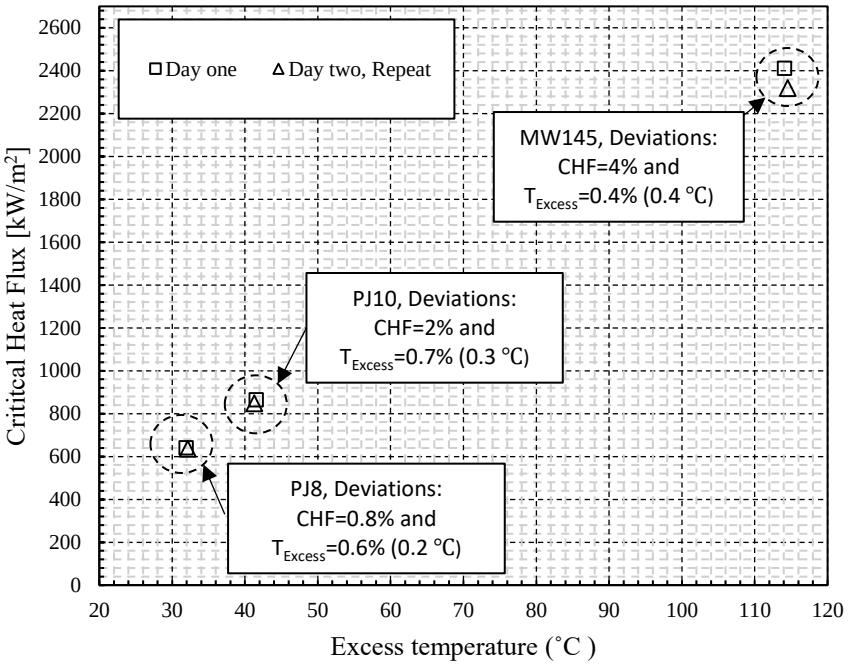

Fig. 3. CHF and excess temperature maximum deviations to reproducibility of the results.

Considerable care has been taken to identify the key factors involved in successful reproducibility of the data. A regular change of de-ionized water, and checking that the cooled disc has the same surface roughness using the same abrasive paper (and therefore ensuring no copper oxidation), was found to be the most important precautions required to be able to undertake experiments on different days.

For the sake of maximum reliability in the reproducibility of the data, each case in Figure 3 has been repeated twice on two different days - only cases with the largest deviation are reported. At the start of each day, the de-ionized water was replaced, and the copper surface was polished with a wet-dry paper. As can be seen, the maximum deviations for CHF are less than predicted by uncertainty analysis, except for MW145 (4%). For the excess temperature, the average deviation is higher than the thermocouples uncertainty. For that reason, the maximum deviations caused to CHF (for MW145), and the excess-temperature-during-repeatability analysis, has been taken into consideration to interpret the data, and the trends in the results. It should be noted however, that test runs for each nozzle, were actually taken on the same day to minimise the effect of reproducibility and to maximise the reliability in the comparisons.

4. Results and Discussion

In this section, the influence of surface vibration on the CHF and excess temperature are discussed. First, the effect of flow rate and degrees of subcooling with, and without vibration has been examined. This is to help understand the physics behind the trends in the data, which are useful for modelling. Second, the effect of vibration on the excess temperature at CHF has been investigated in detail. The maximum achievable temperature is a key parameter due to its importance for thermal management applications, especially in the safety mode. Finally, correlation models discussed in Section 2, have been calibrated for prediction of CHF and maximum temperature.

4.1. Effect of nozzle flow parameters and degrees of subcooling for static surfaces

Flow rate and pressure drop are nozzle flow parameters. Figure 4a shows the CHF variation with three volumetric flow rates of 55 ml/min, 75 ml/min and 100 ml/min for PJ8, PJ10, and MW145 nozzles. As can be seen for the PJ8 and PJ10 nozzles, CHF increases with flow rate, and this trend is valid for both degrees of subcooling (i.e. 10 and 45 °C). Toda and Uchida [49], Hou et al. [50], Chow et al. [51], Moreno et al. [52], Estes and Mudawar [35] and Pais et al. [53] all reported that increasing flow rate increases CHF. However, CHF for MW145 has an almost three-fold increase in comparison with those for PJ nozzles, even though the flow rate for MW145 is 55 ml/min, suggesting that the CHF does not always increase with volumetric flow rate. Chen et al. [54] and Tilton [55] suggested that the volumetric flow rate has only a subtle, or even no influence, on CHF. The higher CHF for the MW145 is a result of a higher nozzle pressure drop (i.e. 7 bar, in contrast to 2.9 to 5.2 bar for PJ nozzles), but also from different geometrical parameters (e.g. nozzle orifice and cone angle, see Table 4) which changes hydrodynamic parameters (such as mean droplet velocity).

Figure 4b shows the same CHF results plotted as a function of average volumetric spray flux for each nozzle. Chen et al. [54], Estes and Mudawar [35], Pais et al. [53], Lin and Ponnappan [56], and Monde [57] have all suggested that CHF for different nozzles, increases with volumetric flux with no reverse trends. Figure 4b shows the same behaviour for different nozzles namely: PJ8 (0.77×10^{-3} m^3s^{-1}/m^2), PJ10 (1.05×10^{-3}-1.40×10^{-3} m^3s^{-1}/m^2), and MW145 (9.03×10^{-3} m^3s^{-1}/m^2).

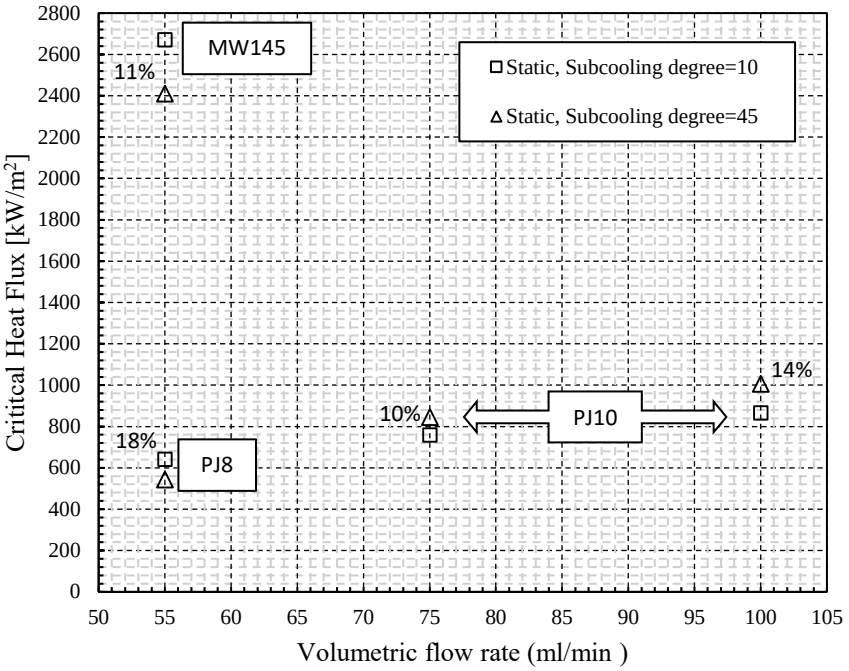

(a)

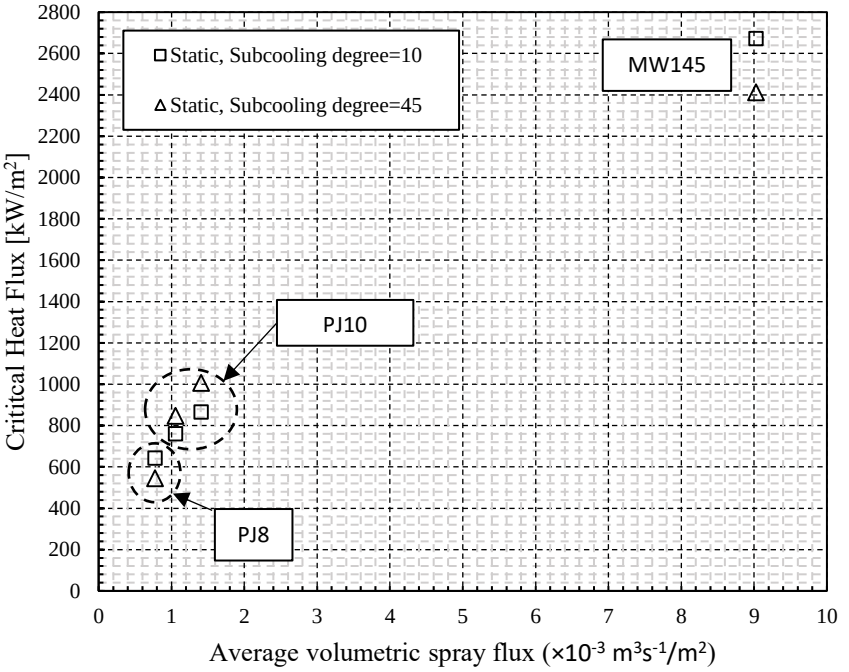

(b)

Fig. 4. CHF trend for static cooling surfaces based on nozzle flow parameters and degrees of subcooling.

The average volumetric flux, $\bar{v}$, is proportional to volumetric flow rate, v, and can be calculated according to equation (2) [58]:

$$\bar{v} = \frac{v}{\pi(Htan(\frac{\alpha}{2}))^2} \quad (6)$$

where H is nozzle-to-surface distance and α is the spray cone angle. Figure 4a also shows the subcooling impact on CHF. For the PJ8 and MW145 nozzles with a lower flow rate of 55 ml/min, CHF decreases by the higher subcooled conditions of 45 ℃. As can be seen, the deviations for the PJ8 and MW145 are respectively 18% and 11%. This means that the CHF acquires a higher value as soon as subcooling is closer to saturated conditions. Thiagarajan et al. [38] reported the same behaviour for the subcooling influence of low flow rate sprays. Conversely, for the PJ10 with higher flow rates of 75 and 100 ml/min, a higher subcooling degree of 45 ℃ enhances the CHF by 10% and 14% respectively. Visaria and Mudawar [59] found a similar trend in their data with subcooling degrees between 22 ℃ and 70 ℃. In the experiments in [59], it was noted that the CHF enhancement is more substantial when the subcooling degree exceeds 40 ℃. Overall, the trends in the CHF data for static surfaces are in good agreement with the literature. In the next section, the effects of the vibrating surfaces on the CHF as well as excess temperature will be discussed.

4.2. The effect of vibrating surfaces on CHF and excess temperature

In this section the effects of vibration on CHF and excess temperature for all three nozzles of PJ8, PJ10 and MW145 is assessed. The CHF data for static and dynamic cases are examined as a function of excess temperature, subcooling degrees, and volumetric flux to better understand the combined effect of different parameters. An 'effect ratio' is introduced, defined as the ratio of the dynamic-CHF/static-CHF which is shown versus excess temperature. For subplots containing two subcooling degrees and flow rates in which there are two comparable static cases, the effect ratio also includes corresponding static-CHF/static-CHF. Therefore, to make different effect ratios identifiable, three effect ratios are defined and used in corresponding subplots. First, a dynamic effect ratio θ_{Dyn} is defined as the ratio of the dynamic-CHF/static-CHF. Second, a volumetric flux effect ratio $\theta_{\vec{v}}$ includes both dynamic-CHF/static-CHF and corresponding static-CHF/static-CHF ratios. Third, a subcooling effect ratio θ_{SC} , includes both dynamic-CHF/static-CHF and corresponding static-CHF/static-CHF ratios. To make room for inspection it is useful to define considered vibrational ranges. Large-amplitude vibrations include data points with amplitudes from 1 to 8 mm and frequencies up to 8Hz (the first three dynamic cases). High-frequency vibrations are the dynamic cases with a frequency above 50Hz and amplitudes smaller than 1mm (the last three dynamic cases). The dynamic case with a=1mm and f=50Hz corresponds to the highest Vibrational Reynolds Number of 21360, and the largest Acceleration Number of 10. These numbers are supplied in Table 6 (each row is related to the same case in the legends of the figures).

Table 6. Static and dynamic cases with associated Acceleration and Vibrational Reynolds numbers.

Test case	Amplitude (mm)	Frequency (Hz)	Vibrational Reynolds Number (-)	Acceleration Number (unit of g)
S	0	0	0	0
D-1	8	2	6835.2	0.13
D-2	4	4	6835.2	0.26
D-3	1	8	3417.6	0.26
D-4	1	50	21360	10.06
D-5	0.2	50	4272	2.01
D-6	0.2	100	8544	8.05
D-7	0.04	200	3417.6	6.44

Vibrational Reynolds number and dimensionless Acceleration number are helpful in assessing the combined influence of surface amplitude and frequency at CHF. Figures 5 and 6 demonstrate all the data points (CHF versus volumetric flux) for PJ8, PJ10 and MW145 nozzles respectively at two subcooling degrees of 10 and 45 ℃.

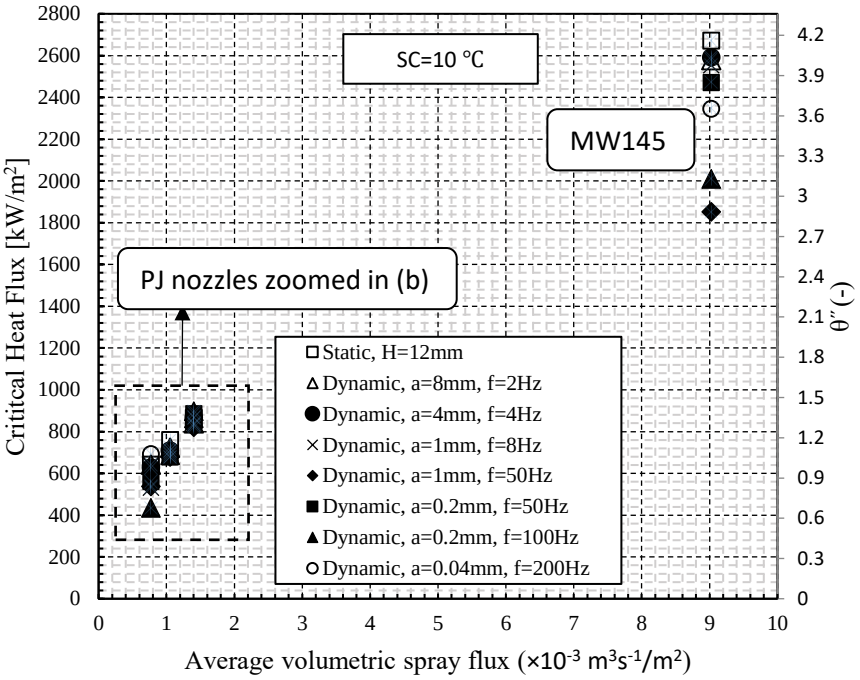

(a)

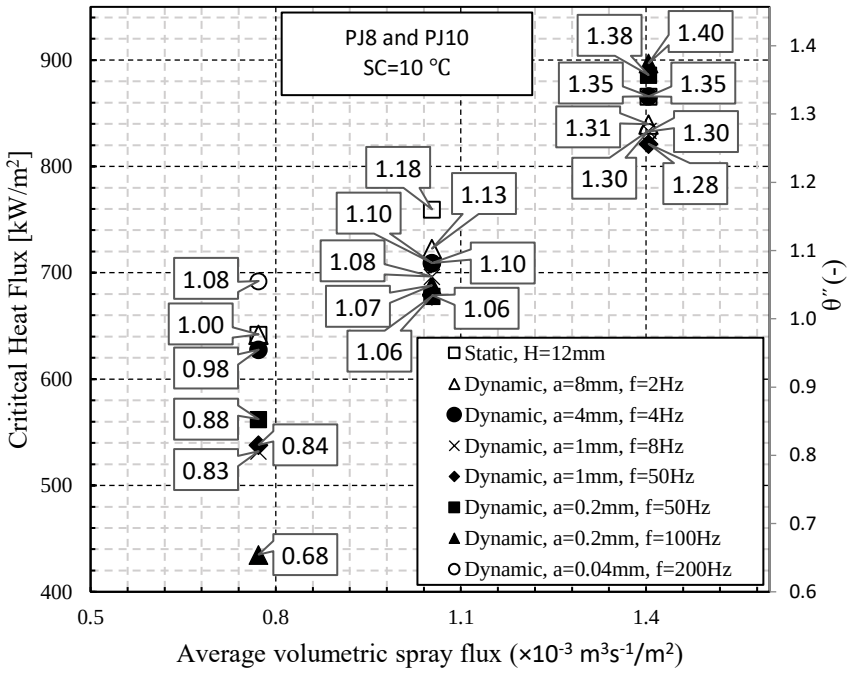

(b)

Fig. 5. Measured CHF versus volumetric flux at SC=10 ℃: a) PJ and MW145 database b) zoomed version of PJ8 and PJ10 test cases.

Figures 5b and 6b show the results of the PJ8 and PJ10 nozzles (as expanded versions). This is to investigate the effect of volumetric flux and compare it with what was found for the static cases in the previous section.

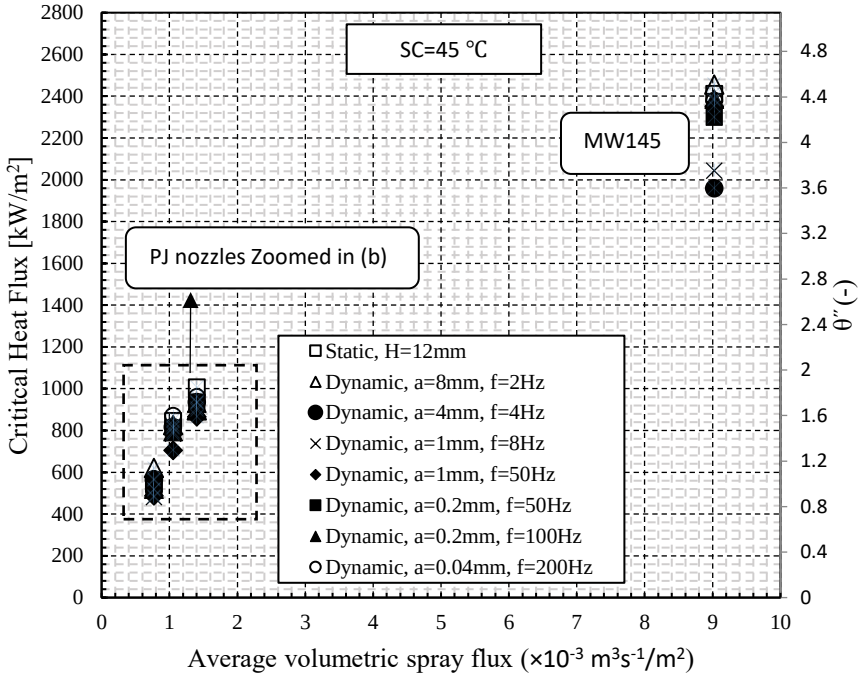

(a)

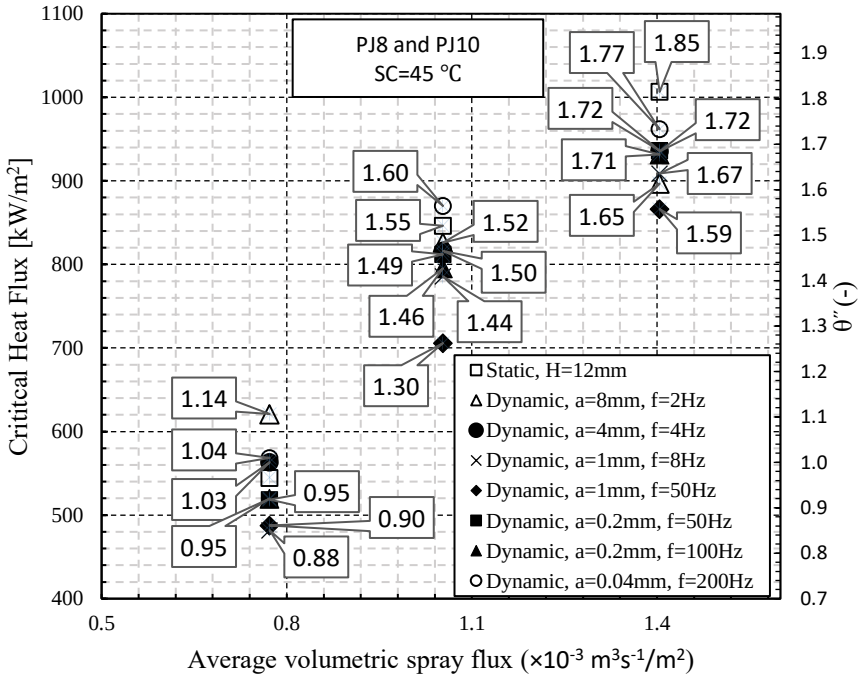

(b)

Fig. 6. Measured CHF versus volumetric flux at SC=45 ℃: a) PJ and MW145 database b) zoomed version of PJ8 and PJ10 test cases.

At first, the general trend in Figures 5a and 6a shows that CHF increases for dynamic cases with increasing volumetric flux. Considering the effect ratios on Figures 5 and 6, the enhancement for SC=45℃ is more appreciable. However, there are two exceptions in Figures 5b and 6b, including the results for PJ nozzles. These exceptions relate to the dynamic case D-7 with the highest frequency. One is at SC=10 ℃ for PJ8 (Figure 5b), for which the D-7 case (at $\bar{\vec{v}} = 0.77 \times 10^{-3}$m^{3}s^{-1}/m^2) has a greater CHF value compared to those for D-6, D-5 and D-4 cases of PJ10 with a greater volumetric flux of 1.05×10^{-3}m^{3}s^{-1}/m^2. The effect ratio of PJ8-D-7 is 1% greater than PJ10-D-6, and 2% greater than PJ10-D-5 and PJ10-D-4 cases. The second occurs at SC=45 ℃ for case D-7 of the PJ10 (Figure 6.b) at $\bar{\vec{v}} = 1.05 \times 10^{-3}$m^{3}s^{-1}/m^2, at which the CHF acquires a slightly greater value than D-4 at $\bar{\vec{v}} = 1.40 \times 10^{-3}$m^{3}s^{-1}/m^2 (where the effect ratios for D-7 and D-4 at these volumetric fluxes are 1.60 and 1.59 respectively). As mentioned, D-4 has a larger amplitude and a lower frequency and the highest Reynolds Number. The reason for this reverse trend can be attributed to the enhancing effect of vibration for the D-7 cases of PJ nozzles. However, further investigation is required to precisely explain the effects of different elements of vibration such as amplitude and frequency, as well as the effect of Acceleration and Reynolds Number. In the next subsections the influences of different key parameters are discussed.

4.2.1. The largest deviation from the static CHF and the effects of Subcooling degrees

Figures 7 and 8 show the results for the PJ10 nozzle at coolant flow rates of 75 ml/min and 100 ml/min respectively. Figures 9 and 10 show corresponding results for the PJ8 and MW145 nozzles. As can be seen from Figures 7 to 10, the CHF for the dynamic cases involving large-amplitude or high-frequency vibration result in a deviation from the corresponding static results. For the PJ10, as seen in Figures 7 and 8 (for both subcooling degrees in respective subplots a and b) the largest deviation from the static CHF belongs to the case D-4 with a=1 mm and f=50 Hz, and with the highest Reynolds Number and largest Acceleration Number (See the effect ratios in Figures 7 and 8, and for cases D-2, D-3, D-4, and D-7, in Table 7). For the flow rate of 75ml/min, at subcooling of 10 ℃ (Figure 7a) the effect ratio for case D-4 is 89 percent. And at subcooling of 45 ℃ (Figure 7b) the effect ratio is 83 per cent. It is evident that the deteriorating effect of vibration for the dynamic case D-4 (as shown by a diamond marker) becomes more appreciable by increasing the subcooling degree. The same behaviour for the same test case of D-4 can be seen in figure 8 for the flow rate of 100 ml/min. Figures 8a and 8b, at the subcooling of 10 ℃, show that the smallest effect ratio is 95 per cent which reduces to 86 per cent at the subcooling of 45 ℃.

Table 7. Dynamic effect ratios for the chosen dynamic cases to explore the Vibrational Reynolds and Acceleration effects.

	PJ10				PJ8		MW145		Re_V	Ac
Flow rate (ml/min)	75		100		55		55			
Subcooling (℃)	10	45	10	45	10	45	10	45		
D-3	0.92	0.93	0.96	0.90	0.83	0.88	0.96	0.85	3417.6	0.26
D-2	0.93	0.96	1	0.93	0.98	1.03	0.97	0.81	6835.2	0.26
D-4	0.89	0.83	0.95	0.86	0.83	0.90	0.69	0.98	21360	10.06
D-7	0.93	1.03	0.96	0.96	1.08	1.04	0.88	0.99	3417.6	6.44

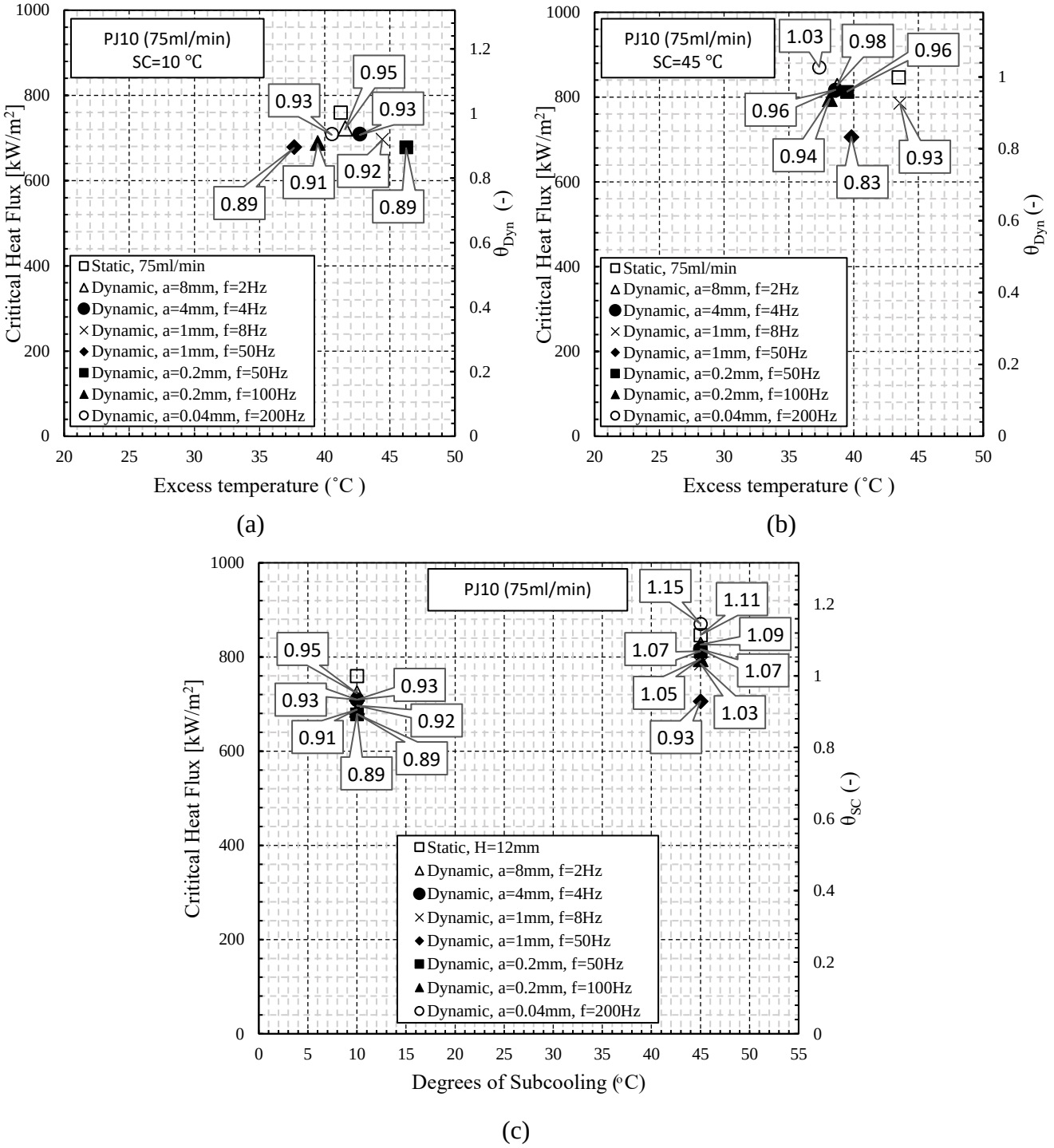

Fig. 7. Measured CHF for the PJ10 nozzle at 75 ml/min versus excess temperature at $SC = 10$℃ (a) and $SC = 45$℃ (b), and the effect of subcooling on CHF (c) for the case studies involving static and dynamic cooling surfaces.

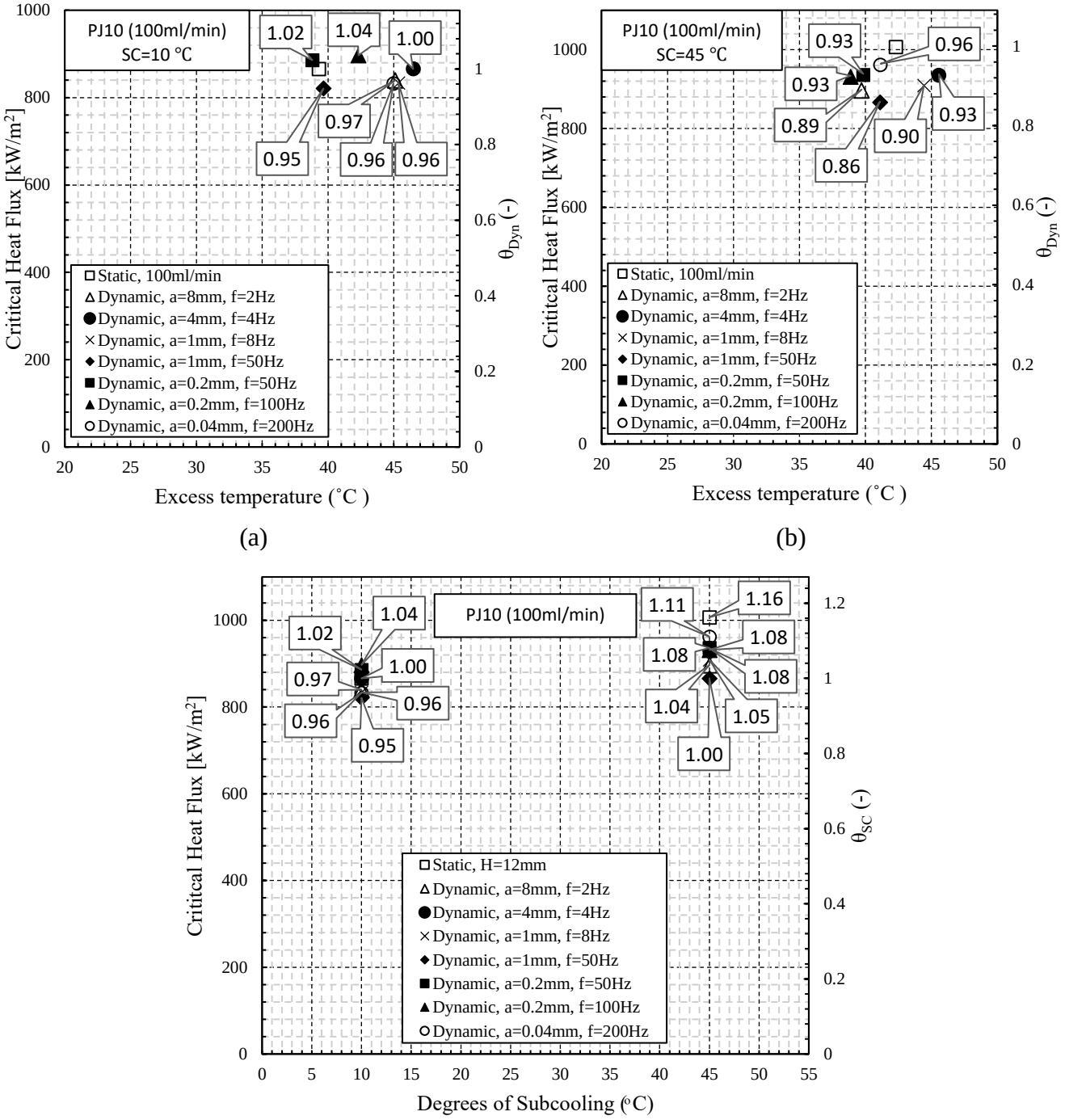

Fig. 8. Measured CHF for the PJ10 nozzle at 100 ml/min versus excess temperature at $SC = 10$℃ (a) and $SC = 45$℃ (b), and the effect of subcooling on CHF (c) for the case studies involving static and dynamic cooling surfaces.

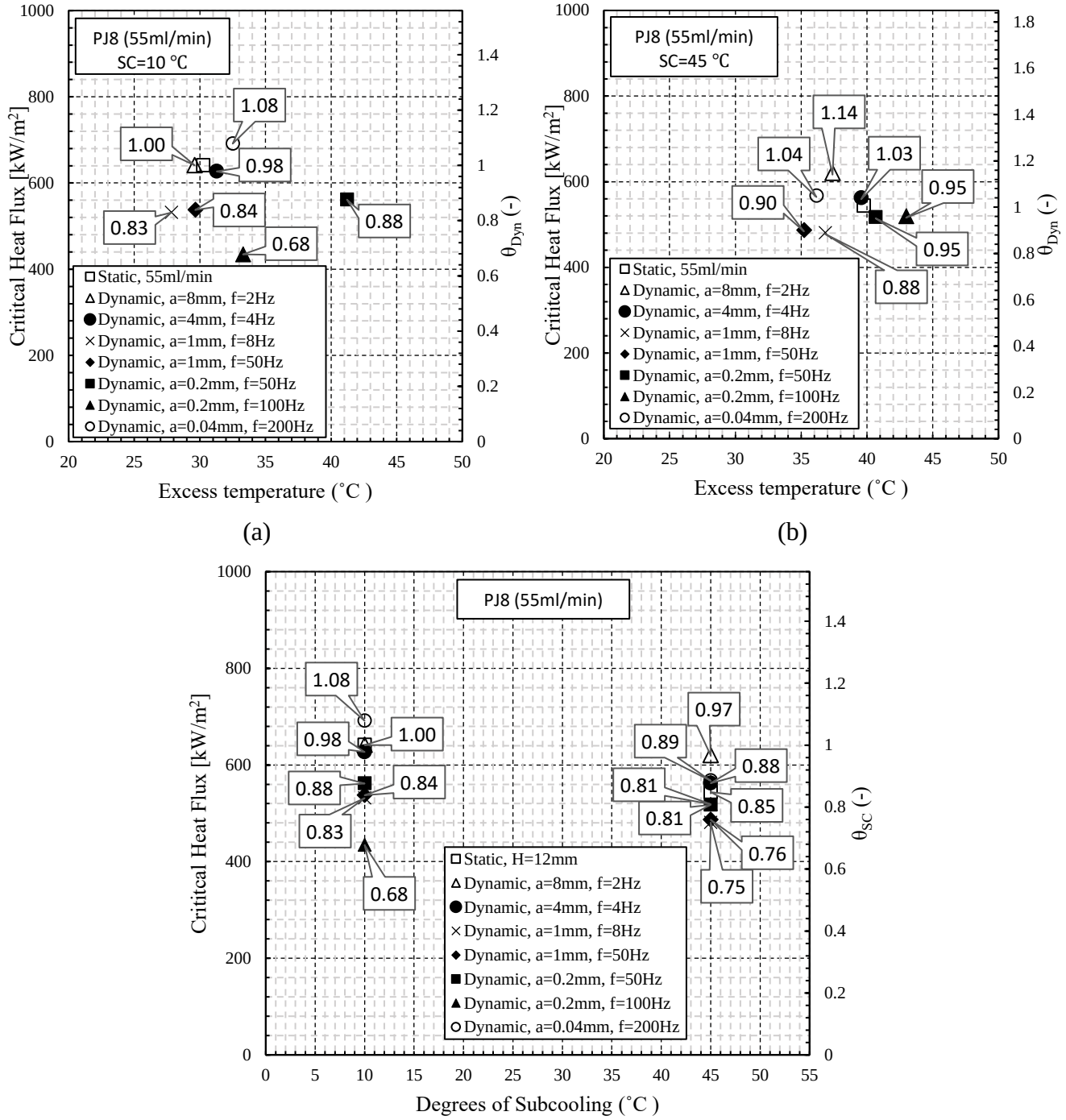

Fig. 9. Measured CHF for the PJ8 nozzle versus excess temperature at $SC = 10$℃ (a) and $SC = 45$℃ (b), and the effect of subcooling on CHF (c) for the case studies involving static and dynamic cooling surfaces.

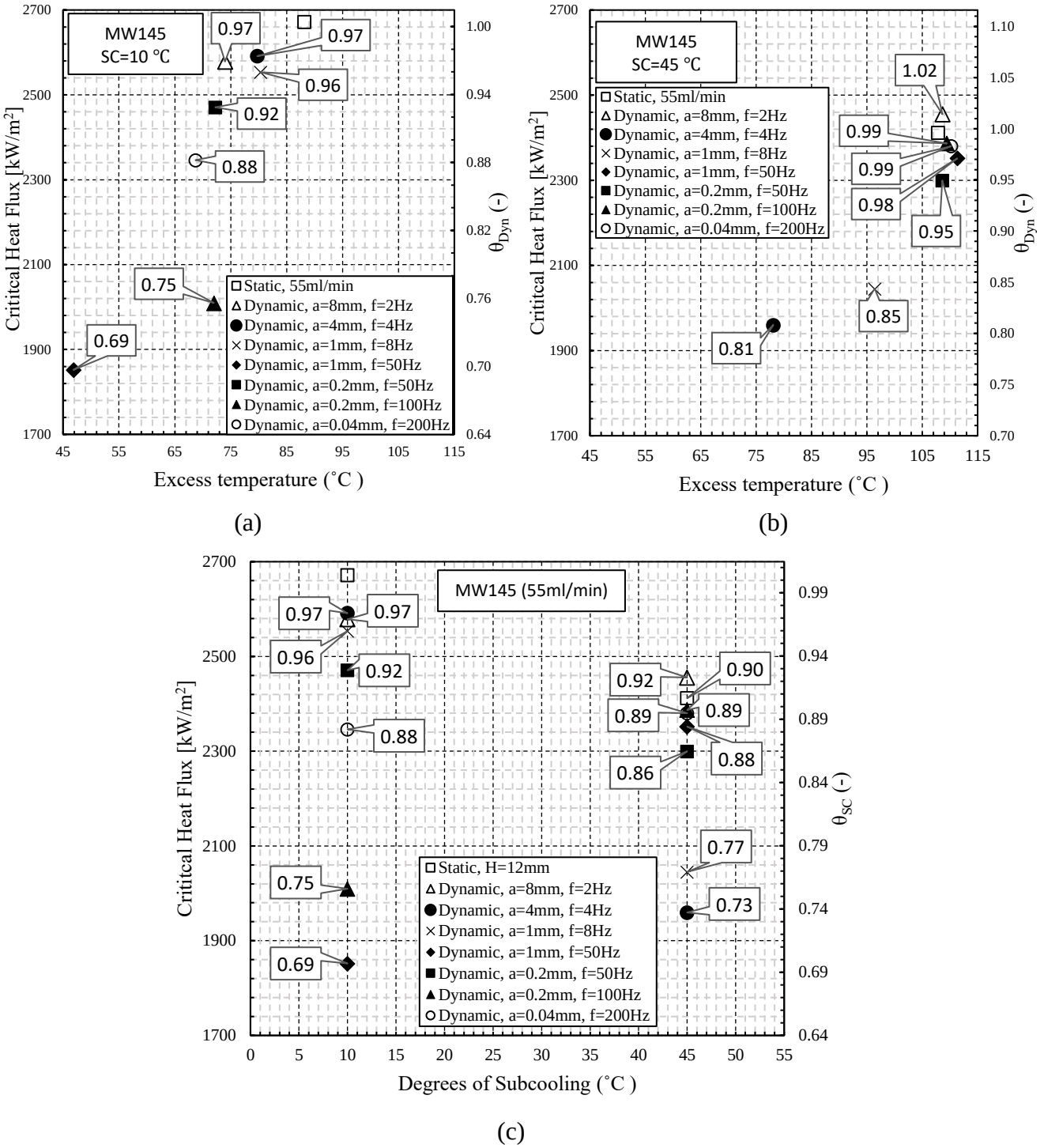

Fig. 10. Measured CHF for the MW145 nozzle versus excess temperature at $SC = 10$℃ (a) and $SC = 45$℃ (b), and the effect of subcooling on CHF (c) for the case studies involving static and dynamic cooling surfaces.

For the PJ8 nozzle, D-6 has the lowest effect ratio of 68% at SC=10 ℃ (Figure 9a). However, by increasing the subcooling to 45 ℃, the impeding effect of vibration reduces and the D-6 datapoint has a 95% deviation. The same behaviour is evident for the MW145. The lowest effect ratio of 69% (for D-4 at 10 ℃ subcooling) increased up to 98% at 45 ℃ of subcooling (Figure 10). This is the exact opposite to that

found for the PJ10 with the response of its lowest effect ratio to subcooling. The reason for this can be associated with the reverse heat transfer trend (as was found in the previous section for static cases) stemming from the subcooling effect at low flow rate for the PJ8 and MW145 nozzles in comparison to the higher flow rate of the PJ10 nozzle.

To investigate this reverse trend, the influence of subcooling on the dynamic-CHF data and a comparison of the behaviour with the static cases in the previous section is examined, particularly Subplots c in Figures 7 to 10. For the PJ10 nozzle (at both flow rates in Figures 7c and 8c), the effect ratio for every dynamic case has been increased by augmenting the subcooling degree. It is still following the same trend (as in the previous section). Therefore, increasing subcooling degrees for the PJ10 increases CHF for its static and dynamic cases. By contrast, for the PJ8 and MW145, the behaviour should be the exact opposite of the PJ10 trend (as was found for the static cases). But inspecting the effect ratios in Figures 9c and 10c suggests this trend is still valid apart from two high-frequency vibration cases: D-6 (for the PJ8 and MW145) and D-4 (for the MW145 only). The CHF for case D-6 at SC=45 ℃ have higher values for both the PJ-8 and MW145. The CHF for D-4 case of the MW145 nozzle reaches a higher value at the higher subcooling of 45 ℃. This clearly shows that surface vibration causes a change in the trend identified. To reveal this further, the effect of vibration, in particular the influence of amplitude and frequency, is now examined in more detail.

4.2.2. The effect of vibrating surface amplitude and frequency on CHF

To establish whether the amplitude of a vibrating surface has any impact on the dynamic-CHF, the cases D-5 (a=0.2mm) and D-4 (a=1mm) at a frequency of 50Hz are examined. The D-5 and D-4 cases are respectively shown in Figures 7 to 10 with square and diamond markers. For the PJ10 nozzle, the amplitude has a deteriorating effect on CHF (except for flow rate 75 ml/min and subcooling of 10 ℃, that amplitude has no effect). The highest impeding effect of 13 percent occurs for the flow rate of 75 ml/min at subcooling of 45 ℃ (on Figure 7b, D-5 and D-4 effect ratios are 0.96 and 0.83). At the flow rate of 100 ml/min (Figure 8), this deterioration effect, for both subcooling degrees, is 7 percent. The results for the PJ8 (Figure 9) support the argument suggesting the impeding effect of amplitude on CHF. For subcooling degrees of 10 and 45 ℃, the impeding effects are respectively 4 and 5 percent. Therefore, the subcooling influence is only 1 per cent. However, for MW145, at subcooling of 45 ℃ (Figure 10b), vibration amplitude shows an enhancing influence. To address this reverse trend, the frequency element of vibration is now examined.

To assess the effect of frequency of a vibrating surface, cases D-3 (f=8Hz) and D-4 (f=50Hz), with an amplitude of a=1mm are examined. The data associated with D-3 and D-4 cases are respectively shown by cross and diamond markers. For these two cases for the MW145 at SC=45 ℃ (Figure 10b), the frequency causes a 13 per cent enhancement (For D-3 the effect ratio is 0.85, and for D-4 it is 0.98). But for SC=10 ℃ (Figure 10a), vibration frequency causes a 27% deterioration. Comparing the effects of amplitude and frequency for the MW145 suggests that vibration frequency plays a dominant role. Small heat transfer enhancements are also evident in Figures 9a (1% increase at SC=10 ℃) and 9b (2% enhancement at SC=45 ℃) for the PJ8. For the PJ10 (Figures 7 and 8), for all the flow rates and levels of subcooling, vibration frequency has a deteriorating effect on the dynamic-CHF. The differences between these two cases in Figures 7a (SC=10 ℃), 7b (SC=45 ℃), 8a (SC=10 ℃), and 8b (SC=45 ℃) are

respectively 3%, 10%, 1% and 4%. The impeding effect is more considerable for higher subcooling degrees of 45 ℃. It is evident that by increasing the flow rate, the deteriorating influence decreases. Vibration frequency and amplitude are probably better understood in terms of non-dimensional vibration parameters whose examination should better explain such contradictory behaviour. The next section, examines the effect of vibration specifically in terms of Vibrational Reynolds Number and Acceleration Number.

4.2.3. The influence on CHF of vibrational Reynolds Number and Acceleration Number

Vibrational Reynolds Number and Acceleration Number are useful for representing the dynamic nature of the spray field on a vibrating surface, such as the effect on droplet rebound, splash and liquid film thinning. These dimensional parameters are used to investigate the complex effects of vibration on the heat transfer mechanisms. To assess the influence of Vibrational Reynolds Number, cases D-3 (Re=3417.6) and D-2 (Re=6835.2) with the same Acceleration Number of 0.26 are considered. Comparison of all data points of D-3 and D-2 in Figures 7 and 8, reveal that for both flow rates and subcooling degrees of the PJ10 nozzle, increasing Reynolds Number from 3417.6 to 6835.2, first enhances the CHF, but then impedes it for the highest Reynolds Number (Re=21360, D-4). To support this claim, all the associated effect ratios are supplied in Table 7 for ease of reading. For all data points in Table 7, the associated CHF values against Reynolds and Acceleration numbers are plotted in Figure 11 to facilitate the interpretation of the trends. For flow rate 75ml/min, at SC=10 ℃ (Figure 7a), the effect ratio of D-3, D-2 and D-4 are respectively: 0.92, 0.93, 0.89. For the same flow rate, at SC=45 ℃ (Figure 7b), the effect ratios of D-3, D-2 and D-4 are 0.93, 0.96, 0.83. As can be seen from Table 7, PJ nozzles follow the behaviour mentioned for all the flow rates and subcooling degrees (as can also be seen in Figure 11a). The only exception is the MW145 at SC=45 ℃ for which the effect ratio is first reduced through an increase in Reynolds Number (3417.6 to 6835.2), and then increased for the highest Reynolds Number. This is different from the trend of the other cases. For the MW145 nozzle, the opposite behaviour can be explained by its high dependency on the subcooling effect. The spray field for MW145 is a light fog resulting in a thinner liquid film on top of the cooling disc, whereas for the (misting) PJ nozzles it has a relatively thicker liquid film (observed) during the experiments. For this reason, it appears that the MW145 nozzle is less dependent on Reynolds Number and Acceleration Number.

To explore the effect of Acceleration, the results for test cases of D-3 (Ac=0.26) and D-7 (Ac=6.44) both cases with a Reynolds Number of 3417.6 are compared in Table 7 (as also shown in Figure 11b). For PJ nozzles, CHF associated to D-7 are all enhanced by the larger Acceleration Number except for a flow rate 100ml/min at subcooling of 10 ℃ which Acceleration Number does not have any influence on CHF. The enhancing effect of acceleration conform to the results of Michalak et al. [34] for the acceleration range of $0.15g < Ac < 1.80g$. However, there are other studies such as work of Zhang et al. [60, 61], and Conrad et al. [62], suggesting that the acceleration enhancement is limited to the operating conditions, and other parameters are the main determinant of the heat flux. For the MW145, at SC=10 ℃ there is a reduction in the effect ratio for D-3 and D-7 which shows that other key parameters determine this impeding effect. As was shown for the MW145 at SC=10 ℃ (in the previous section), the frequency has a noticeable deteriorating effect. Switching the frequency from 8Hz (D-3) to 200Hz for

case D-7 supports the independence to Acceleration of the MW145 results. Another key parameter responsible for this reverse behaviour for Reynolds Number, can be the considerable effects of subcooling. In the next section, the complex effects of vibration and subcooling on the maximum temperature (at which CHF can occur) are investigated.

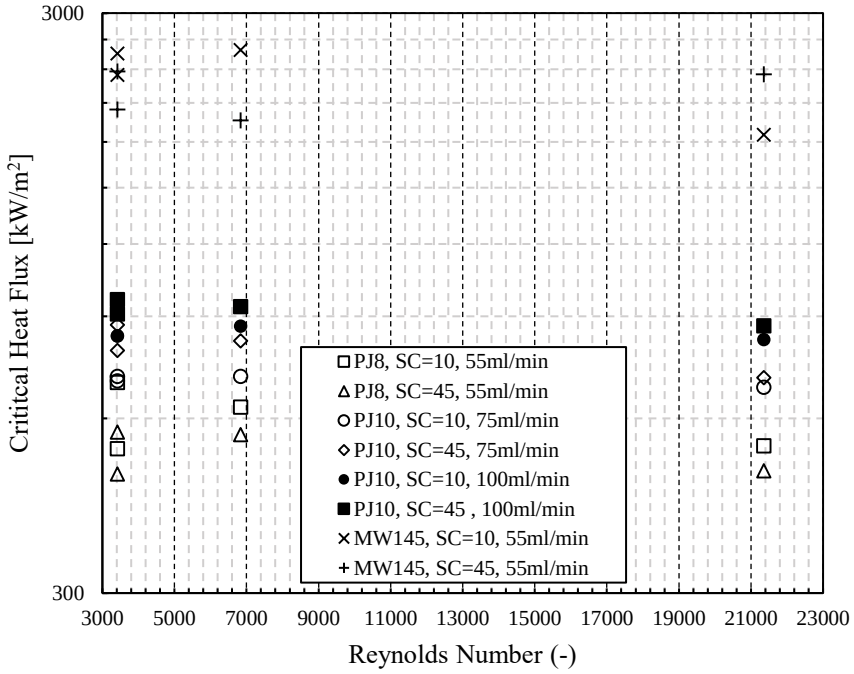

(a)

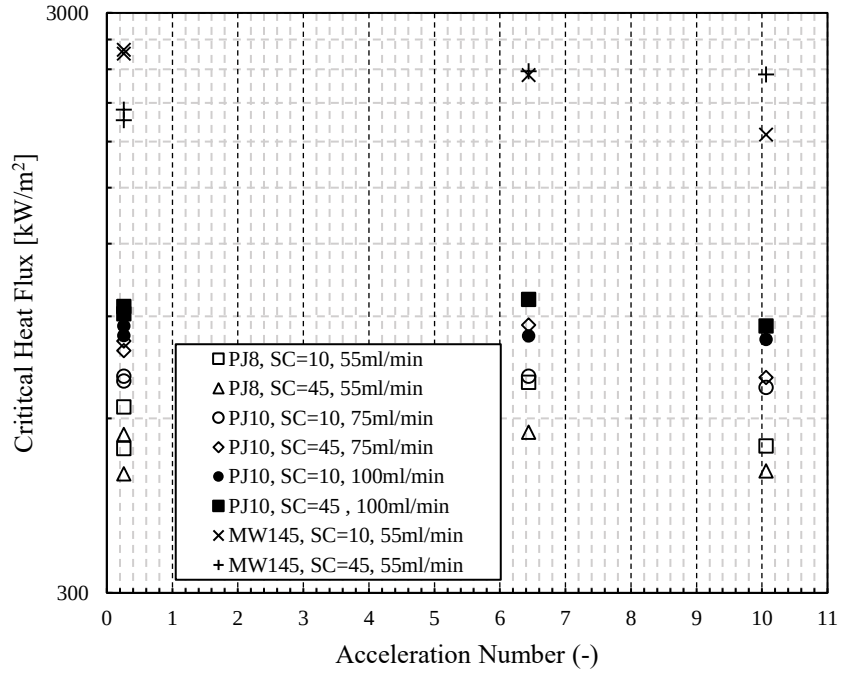

(b)

Fig. 11. Vibrational Reynolds Number effect (a), and Acceleration Number effect (b), for the chosen dynamic cases in Table 7.

4.2.4. The effect of vibration on excess temperature

Further inspection of the subplots of Figures 7a, 7b 8a, 8b, 9a, 9b, but also Figure 10, it is noticeable that vibration changes the excess temperature at which the Static-CHF occurs. To explain the reason for this, as mentioned before, Acceleration Number and Reynolds Number affect the dynamic behaviour of the spray field and consequently the heat transfer mechanisms. For instance, the vibration surfaces with different amplitude and frequencies can be responsible for thinning and thickening of the liquid film. These effects can either advance or delay the transition from nucleate boiling to transition boiling (where the maximum temperature and CHF occurs). In other words, thinning and thickening of the liquid film (which is two-phase in nature) can influence the chance of slug propagation and therefore promoting or delaying the incidence of the CHF. In addition, the fluctuating relative speeds due to the vibrating surfaces, changes the intensity of drop rebounding and splashing in the flow field. All the above mentioned are important in different heat transfer mechanisms involved in spray cooling. Table 8 shows the temperature differences between the dynamic and corresponding static cases for each nozzle and associated operating conditions.

Table 8. Temperature difference (℃) from static cases to inspect any effects of vibration on excess temperature.

	PJ10				PJ8		MW145	
Flow rate (ml/min)	75		100		55		55	
$\overline{\vartheta}$ ($\times 10^{-3}$m^{3}s^{-1}/m^2)	1.05		1.40		0.77		9.03	
Subcooling (℃)	10	45	10	45	10	45	10	45
D-1	0.3	-4.8	5.8	-2.6	-0.6	-2.4	-14.2	0.8
D-2	1.5	-4.9	7.2	3.3	1.0	-0.2	-8.4	-29.7
D-3	3.2	0	6.0	2.1	-2.4	-2.9	-7.8	-11.4
D-4	-3.6	-3.7	0.4	-1.2	-0.6	-4.5	-41.3	3.5
D-5	5	-4	-0.5	-2.5	11	0.9	-15.9	0.8
D-6	-1.8	-5.3	3	-3.4	3	3.2	-16.2	1.6
D-7	-0.7	-6.1	5.7	-1.2	2.3	-3.6	-19.5	2.4

The largest difference in the excess temperature of the dynamic cases from the static cases for PJ8 and PJ10 are for those with high-frequency vibrations with the exception of the PJ10 at 100 ml/min and SC=10 ℃. For the MW145, the largest difference in the excess temperature occurred for the cases in high-frequency vibrations at SC=10 ℃, while at SC= 45℃, the largest deviations are in the large-amplitude vibration range. For the PJ10 at 75 ml/min and SC=10 ℃ (Figure 7a), this difference is -3.6 ℃ for case D-4, and 5℃ for case D-5. At the subcooling of 45 ℃ (Figure 7b), the excess temperature difference for case D-6 and D-7 are respectively -5.3℃ and -6.1 ℃. Test cases of D-4, D-5, D-6 and D-7 all have accelerations above 2g (see Table 6). Considering these test cases, for both subcooling degrees, as soon as the Acceleration and Vibrational Reynolds numbers decreased (from D-4 to D-5 and D-6 to D-7) the temperature difference has increased. At 100 ml/min and subcooling of 45 ℃ (Figure 4b) the largest temperature difference also occurred for the case D-6 (3.4 ℃) which is within the range of high-frequency vibrations. By contrast, at 100ml/min and subcooling of 10 ℃ (Figure 4a), the large-amplitude vibrations on average caused the largest temperature deviation from that for the static case. The test

case of D-2 has a temperature difference of 7.2 ℃, and test cases of D-1 and D-3 have temperature differences of 5.8 ℃ and 6.0 ℃. Table 6, giving the Acceleration Number and the Vibrational Reynolds Number for these cases, confirms that it is still valid to claim that decreasing these two dimensionless numbers the temperature difference increases. Case D-1 in comparison to D-2 has a smaller Acceleration Number but a fixed Re=6835, and Case D-3 has a lower Reynolds Number in comparison to Case D-2 (while Ac=0.26). This shows the effect of vibration on effective excess temperature. The effect of Acceleration Number and Reynolds Number, in addition to frequency and amplitude, are now separately evaluated.

To establish the effect of Acceleration Number on the excess temperature, Cases D-1 (Ac=0.13), and D-2 (Ac=0.26) with a Re=6835, and Cases D-3 (Ac=0.26) and D-7 (Ac=6.44) with a Re=3417 are examined. At Re=6835, Acceleration Number has mainly contributed to an increase in excess temperature deviations except for PJ8 at SC=45 ℃ and MW145 at SC=10 ℃. At the lower Reynolds No of 3417, however, Acceleration Number has a decreasing effect on the excess temperature deviations except for Case PJ10 at $v = 75\ ml/min$ and SC=45℃, Case PJ8 data at SC=45 ℃, and Case MW145 at SC= 10℃. This means that at Re=6835, the increasing effect of Acceleration Number on the excess temperature deviations is valid for 75% of dynamic cases, whereas for Re=3417 Acceleration Number has less impact on the temperature differences for 63% of data cases. It appears that the temperature differences with Acceleration Number is nonlinear, and therefore, other parameters are needed to understand the effects of vibration on excess temperature.

To study the Reynolds Number effect, Cases D-2 (Re=6835) and D-3 (Re=3417) are compared. Table 8 for PJ8, shows that by increasing the Reynolds Number the deviations for both subcooling degrees are decreased while the temperature differences for MW145 are all increased. In other words, it can be deduced that at the highest volumetric spray flux (9.03×10^{-3} m^3s^{-1}/m^2 for MW145), Reynolds number increases the temperature deviations (which is a negative thing for thermal management purposes). And at the lowest volumetric flux of 0.77×10^{-3} m^3s^{-1}/m^2 for PJ8, increasing Reynolds Number decreases these temperature deviations (which is a positive thing for thermal management systems). The PJ10 nozzle (which has volumetric fluxes of 1.05×10^{-3} and 1.40×10^{-3} m^3s^{-1}/m^2 corresponding to 75ml/min and 100ml/min respectively) appears to be at the transition between these two increasing and decreasing effects of Reynolds Number. For the lower volumetric flux of 1.05×10^{-3} m^3s^{-1}/m^2 which is closer to that for the PJ8 (the decreasing effect of Reynolds Number is only recognised for the PJ10 at SC=10 ℃). For the volumetric flux of 1.40×10^{-3} m^3s^{-1}/m^2 (which is about twice that of the PJ8, and therefore closer to the MW145 volumetric flux) the increasing effect of Reynolds number on the temperature differences is detectable at both subcooling degrees (given in Table 8), an effect mentioned earlier for the MW145 nozzle. The only exception is for PJ10 nozzle at the lower volumetric flux of 1.05×10^{-3} m^3s^{-1}/m^2 (75 ml/min in Table 8) and SC=45 ℃ which stems from the dominant effect of subcooling on different heat transfer mechanisms of spray cooling.

To investigate the effect of amplitude, Cases D-4 (a=1mm) and D-5 (a=0.2mm), at a frequency of 50Hz, are examined. For PJ nozzles, all the temperature differences except for PJ8 at SC=45 ℃ have been decreased by augmenting the amplitude. For the MW145 and PJ8 at SC=45 ℃, this behaviour is the exact opposite from that previously observed. As far as establishing the influence of frequency, Cases

D-5 (50Hz) and D-6 (100Hz) with the same amplitude of 0.2 mm, are good candidates. For all nozzles at SC=45 ℃, doubling the frequency increases the maximum temperature differences. For SC=10 ℃, it seems that volumetric flux has again been the governing effect on the excess temperature deviations. Starting with the PJ8 nozzle ($\bar{v}$ =0.77× 10^{-3}m^{3}s^{-1}/m^2) and the PJ10 ($\bar{v}$ =1.05× 10^{-3}m^{3}s^{-1}/m^2), doubling the frequency decreases the temperature deviations, while $\bar{v}$ =1.40× 10^{-3}m^{3}s^{-1}/m^2 (for the PJ10), appears to be a transition point above which, doubling the frequency starts to increase the temperature difference. The increasing effect of frequency on maximum temperature also remains valid with a lower intensity for the MW145 nozzle with $\bar{v}$ =9.03× 10^{-3}m^{3}s^{-1}/m^2.

Having used the measured data obtained from the experimental test rig discussed in Section 3 to show the nonlinear dependence of the CHF and its associated temperature for different of nozzle types, it is now appropriate to consider the use of the correlation models discussed in Section 2 in creating a prediction capability. This is now a question of appropriately calibrating the dynamic correlation model equation (2) in the dynamic form given in Table 3 using the dynamic Boiling Number equation (4).

5. Calibrating a dynamic correlation model for CHF and associated temperature prediction

To calibrate an appropriate dynamic correlation model in Table 3 for CHF and associated temperature prediction, a nonlinear least square regression is used. This fitting process is also used to calibrate 'static' correlations from Table 3, which are used for comparative purposes. The Matlab Levenberg-Marquardt optimisation algorithm is used (with the method option set to 'bisquare' for robustness). The PJ8 and PJ10 nozzles are used to construct both static and dynamic functional correlational models.

Table 9. Dynamic and static correlation parameters for the PJ and MW145 nozzles.

Dynamic correlation model $Bo = a\,Ja^{b}(\frac{\rho_l^2\sigma v}{\mu_l{}^3})^{c}Re_V^{d}\left(\frac{a}{H}\right)^{e}Ac^{f}$, Parameters: a, b, c, d, e, f

Static correlation model $Bo = a\,Ja^{b}(\frac{\rho_l^2\sigma v}{\mu_l{}^3})^{c}$, Parameters: a, b, c

Correlation	Nozzles	Parameters					
		a	b	c	d	e	f
Dynamic	PJ8 and PJ10	2.46E-04	0.0497	0.7348	-0.4958	0.2357	0.2329
	MW145	3.43E-04	-0.0317	0.7512	-0.4535	0.2065	0.1886
Static	PJ8 and PJ10	1.71E-06	0.0507	0.7383			
	MW145	2.81E-05	-0.0681	0.6565			

Table 9 shows the parameters obtained in calibrating both the dynamic and static models which are those obtained which minimise the RMS errors between the prediction and measured data for the PJ and MW145 nozzles. The parameter values themselves obtained for the calibrated models shown in Table 9 qualitatively support the finding discussed in Section 4 for each nozzle. For example, the parameter 'a' for the MW145 nozzle is greater than those for PJ nozzles in both dynamic and static

cases indicating that MW145 correlation model will obtain a higher CHF prediction. Negative values for parameter b also support the inverse behaviour of MW145 in response to subcooling degrees.

Figure 12 shows a correlation diagram for PJ and MW145 nozzles giving the predicted CHF values using the dynamic and static models and parameters in Table 9 (vertical axis), compared to the experimentally-measured CHF values (using the horizontal axis). Model error bands are also shown plus numerical values of the average and maximum absolute errors. Figure 12a shows the static correlation results also showing error bands of 0%, -8.3%, and +16.7%. A total of 8 data points are predicted having an average absolute error of 5%, and a maximum absolute error of 16.7%. The accuracy of the predicted (static) CHF results are comparable with those for other static models in the literature (See Table 1) the quality of which is deemed to be good. The dynamic model prediction is shown in Figure 12b plus error bands of 0%, -18.8% and +18.5%. The average and maximum absolute deviations of the predictions are respectively 12.6% and 18.8%. The most accurate predictions are obtained for the PJ10 nozzle. By contrast, the maximum absolute errors are for the PJ8 nozzle for the static case with SC=45 ℃, and for dynamic case of D-7 (which is at high frequency vibration). This accuracy partly stems from the higher number of PJ10 data points (28 for PJ10, 14 for MW145, and 12 for PJ8), consequently better resolution from the PJ10 data.

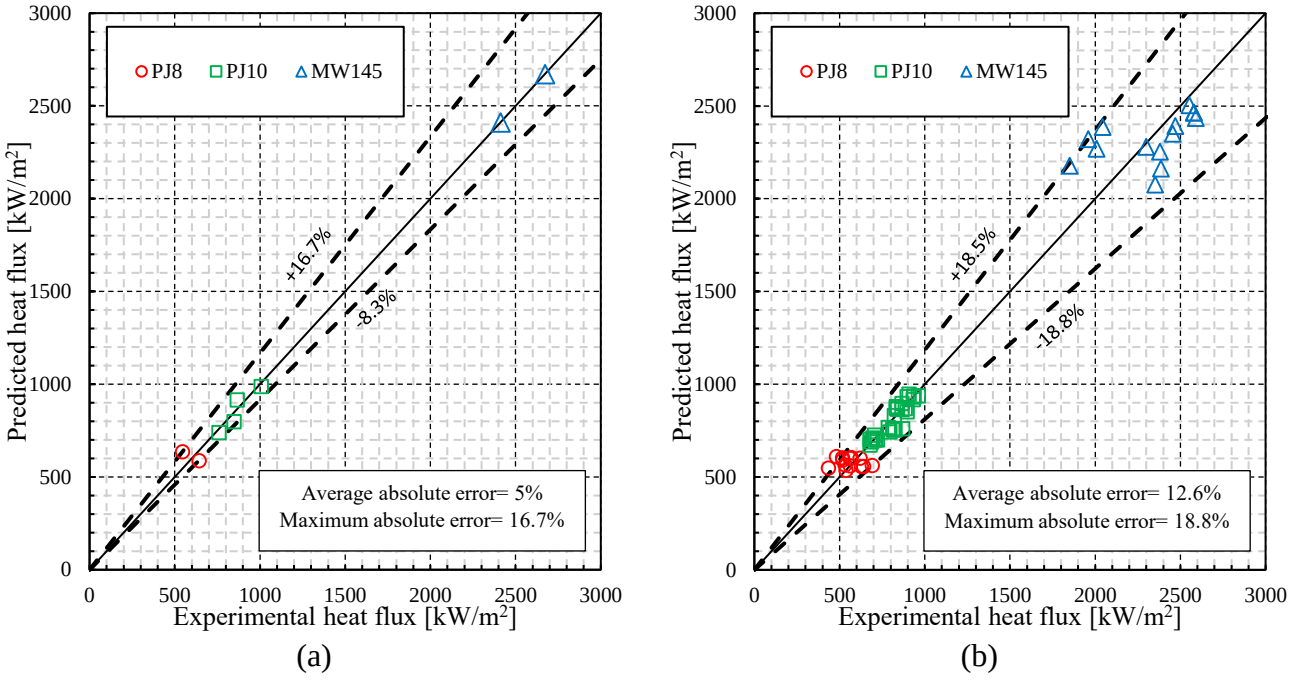

Fig. 12. Correlation of CHF predictions using the models in Table 9 versus experimental measurement showing error bands: (a) *static* and (b) *Dynamic*.

Excess temperature correlation model

For the purpose of thermal management, there is also a need to use a correlation model to predict the excess temperature at which CHF occurs (which is also known as maximum controllable surface temperature or stable CHF temperature). Mudawar and Valentine [20] determined T_{max} by combining a CHF model with a different functional form which included the excess temperature ($\Delta T_{excess} =$

$T_{w,max} - T_{sat}$) and then solving for the surface temperature. The functional form containing excess temperature when based on generalized Π–Theorem (Section 2) takes the form:

$$\frac{\Delta T_{excess}}{\Delta T_{Sub}} = a\left(\frac{q_{CH}H}{\mu_l h_{fg}}\right)^{b}\left(\frac{\rho_l^2 \sigma v}{{\mu_l}^3}\right)^{c} Re_V^{d}\left(\frac{a}{H}\right)^{e} Ac^{f} \quad (7)$$

where the critical heat flux, q_{CH}, in equation (7) is obtained from fitted dynamic correlation model in Table 9. This requires equation (7) to be used with the previously fitted correlation model for CHF. Therefore equation (7) is separately fitted to measured CHF and excess temperature data points associated with both the PJ and MW145 nozzles. In equation (7), a dimensionless surface temperature ($T_{CHF} = \Delta T_{excess}/\Delta T_{Sub}$) is defined similar to the CHF studies of Dou et al [21] and Abbasi and Kim [45].

To achieve high accuracy in fitting equation (7), the data is split into two different subcooling degrees. The reason for this is the high dependency of the excess temperature on subcooling degrees (as indicated by the trends identified earlier). The fitted parameters with the least rms errors are given in Table 10. Figure 13 shows the predicted excess temperature compared with the experimentally measured values for two different subcooling degrees of 10 ℃ (Figure 12a) and 45 ℃ (Figure 13b). The error bands for SC=10℃ have a wider range (-15.5% and +15.9%) than those for SC=45℃ (-9.8% and +10.3%) indicating the effect of subcooling on the excess temperature. As expected, at SC=10 ℃, the PJ10 nozzle results deviate more than the PJ8 excess temperature in comparison to what can be seen for the PJ10 and PJ8 data at SC=45 ℃. When an evaporative spray cooling thermal management system requires predicted maximum controllable temperature to safely set boundaries for controller operation, the model prediction quality is reasonable for both subcooling degrees.

Table 10. Excess temperature correlation parameters for PJ and MW145 nozzles at two subcooling degrees.

Excess temperature correlation model $\frac{\Delta T_{excess}}{\Delta T_{Sub}} = \alpha\left(\frac{q_{CH}H}{\mu_l h_{fg}}\right)^{\beta}\left(\frac{\rho_l^2 \sigma v}{{\mu_l}^3}\right)^{\gamma} Re_V^{\delta}\left(\frac{a}{H}\right)^{\varepsilon} Ac^{\epsilon}$ **Parameters:** $\alpha\ \beta\ \gamma\ \delta\ \varepsilon\ \epsilon$							
Subcooling (℃)	Nozzles	Parameters					
		α	β	γ	δ	ε	ϵ
10	PJ8 and PJ10	1.22E-05	-0.2879	0.6472	-0.0783	0.0074	-0.0011
	MW145	1.26E-05	0.1644	0.6112	-0.0738	-0.0479	-0.0664
45	PJ8 and PJ10	1.28E-04	-0.2393	0.3228	0.2411	-0.1228	-0.1302
	MW145	3.46E-05	1.1914	0.2584	0.1030	-0.0607	-0.0466

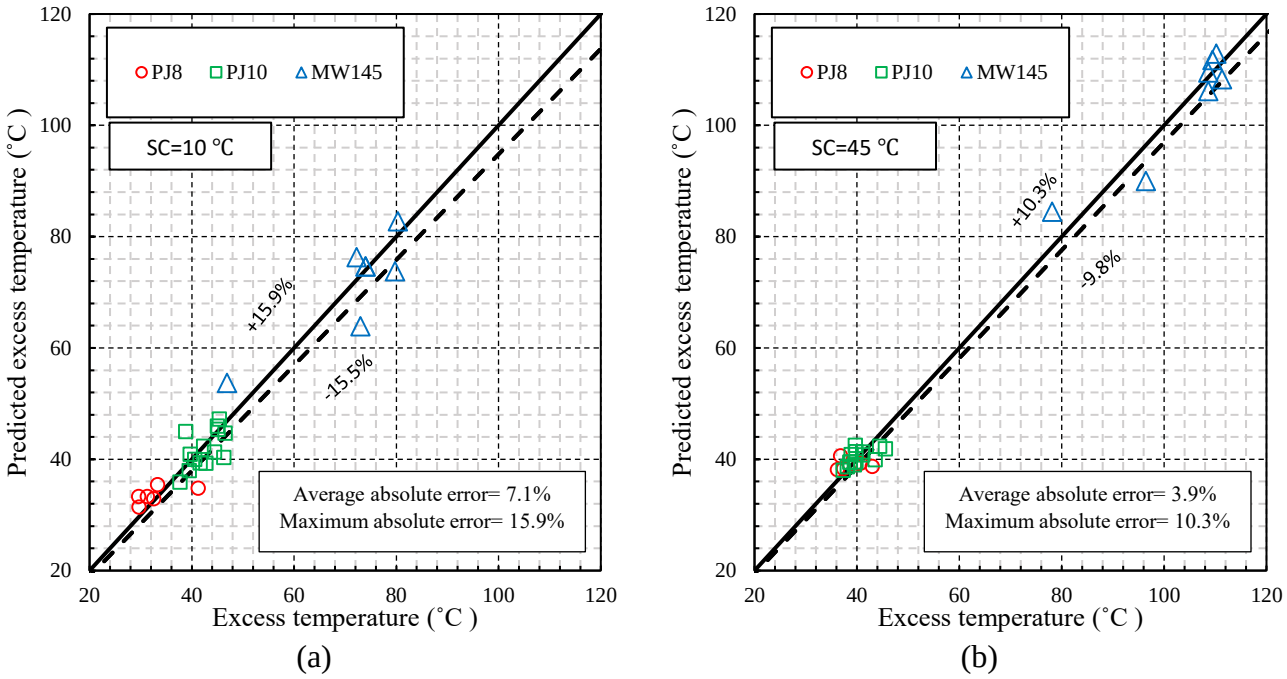

Fig. 13. Excess temperature predicted by the correlation model in Table 10 showing error bands: (a) SC=10 ℃ and (b) SC=45 ℃.

6. Conclusions

Experimental measurements have to obtained to investigate the effect of vibrating surfaces on the critical heat flux (CHF) in spray evaporative cooling and to assess the effectiveness of calibrated prediction models. Prediction models have been constructed using dimensional analysis, to take account of key dynamic parameters. Experimental hardware has been purpose-designed to electrically-heat a flat copper test-piece, located inside a spray-chamber mounted on top of a shaker, which has been used to generate data. A range of appropriately large-amplitude and high-frequency test-piece surface vibrations have been examined involving spray evaporative cooling. Three nozzle types, using distilled water have been examined, namely a PJ8, PJ10, and MW145 nozzle with respective flow rates of 75 ml/min, 100 ml/min, and 55 ml/min. CHF data points, and their corresponding excess temperatures, have been obtained for two 'subcooling degrees' of 10 ℃ and 45 ℃. All the key vibrational effects have also been expressed in terms of non-dimensional parameters.

For the static experiments, without vibration, the effect of flow rate, volumetric flux, and subcooling have been found to be largely in agreement with the published literature. For the dynamic cases, the effect of vibration is best explained in terms of nondimensional Vibrational Reynolds Number and Acceleration Number. With vibrating surfaces, increasing volumetric flux, is found to enhance CHF. For the PJ10 nozzle, Acceleration Number has the largest influence for both flow rate and subcooling degrees, where the deteriorating effect of vibration becomes evident for increasing subcooling degrees. By contrast, for the low flow-rate nozzles of the PJ8 and MW145, the impeding effect of vibration reduces with increasing subcooling. For both flow-rate and subcooling degrees of the PJ nozzles, increasing Reynolds Number initially enhances CHF but then impedes it. This is also found to be true for

the MW145 nozzle (at SC=10 ℃) but at SC=45 ℃ the opposite effect occurs owing to the high dependency of MW145 nozzle on the subcooling effect. For PJ nozzles, Acceleration had an enhancing effect.

The effect of vibration on excess temperature showed that for all nozzle types, high-frequency vibration produces significant deviations, although for the MW145 nozzle at SC= 45℃, vibration amplitude had more effect. In general, the volumetric flux was found to produce the greatest influence on excess temperature.

Predictions of CHF, and associated excess temperature, using calibrated correlation models for the dynamic conditions, were very reasonable, with maximum absolute errors of 18.8% and 15.9%, respectively. These calibrated correlation models are of potential value for safe operation of thermal management systems using spray evaporative cooling.

Acknowledgements

The authors acknowledge support for the development of the experimental facilities, in terms of funding from the EPSRC (under Contract Number: EP/M005755/1), and technical support from Ford Dunton UK, Ford Dearborn USA, Denso Italy, and the Ricardo Technical Centre Shoreham UK. The authors also wish to acknowledge additional financial and technical support from the Ricardo Shoreham Technical Centre, UK.

References

[1] S. Somasundaram, A.A. Tay, An experimental study of closed loop intermittent spray cooling of ICs, Applied thermal engineering, 31(14-15) (2011) 2321-2331.
[2] G. Liang, I. Mudawar, Review of spray cooling–Part 2: High temperature boiling regimes and quenching applications, International Journal of Heat Mass Transfer, 115 (2017) 1206-1222.
[3] Y. Ding, Z.P. Cano, A. Yu, J. Lu, Z. Chen, Automotive Li-ion batteries: current status and future perspectives, Electrochemical Energy Reviews, 2(1) (2019) 1-28.
[4] Q. Yue, C. He, H. Jiang, M. Wu, T. Zhao, A hybrid battery thermal management system for electric vehicles under dynamic working conditions, International Journal of Heat and Mass Transfer, 164 (2021) 120528.
[5] S. Khandekar, G. Sahu, K. Muralidhar, E.Y. Gatapova, O.A. Kabov, R. Hu, X. Luo, L. Zhao, Cooling of High-Power LEDs by Liquid Sprays: Challenges and Prospects, Applied Thermal Engineering, (2020) 115640.
[6] J. Wang, Y. Li, J. Wang, Transient performance and intelligent combination control of a novel spray cooling loop system, Chinese Journal of Aeronautics, 26(5) (2013) 1173-1181.
[7] Y. Ding, Y. Li, Y. Li, W. Chen, H. Zhang, D. Li, Intensive cooling method for power electronic component with high heat flux, in: 2014 13th International Conference on Control Automation Robotics & Vision (ICARCV), IEEE, 2014, pp. 163-168.
[8] J.-X. Wang, W. Guo, K. Xiong, S.-N. Wang, Review of aerospace-oriented spray cooling technology, Progress in Aerospace Sciences, 116 (2020) 100635.
[9] Y. Yang, L. Yang, X. Du, Y.J.A.T.E. Yang, Pre-cooling of air by water spray evaporation to improve thermal performance of lithium battery pack, 163 (2019) 114401.
[10] S. Lei, Y. Shi, G. Chen, Heat-pipe based spray-cooling thermal management system for lithium-ion battery: Experimental study and optimization, International Journal of Heat and Mass Transfer, 163 (2020) 120494.
[11] T. Sai, K. Reddy, Design of fuzzy gain scheduler for superheater temperature control in power plant, in: 2016 2nd International Conference on Control, Instrumentation, Energy & Communication (CIEC), IEEE, 2016, pp. 521-525.
[12] J. Zhang, T.S. Fisher, P.V. Ramachandran, J.P. Gore, I. Mudawar, A review of heat transfer issues in hydrogen storage technologies, Journal of heat transfer, ASME, (2005).
[13] O.V. Kartuzova, M. Kassemi, J.P. Moder, J.H. Agui, Self-pressurization and spray cooling simulations of the multipurpose hydrogen test bed (MHTB) ground-based experiment, in: 50th AIAA/ASME/SAE/ASEE Joint Propulsion Conference, 2014, pp. 3578.
[14] R.B. Biniwale, N. Kariya, H. Yamashiro, M. Ichikawa, Heat transfer and thermographic analysis of catalyst surface during multiphase phenomena under spray-pulsed conditions for dehydrogenation of cyclohexane over Pt catalysts, The Journal of Physical Chemistry B, 110(7) (2006) 3189-3196.
[15] J. Gibbins, H. Chalmers, Carbon capture and storage, Energy policy, 36(12) (2008) 4317-4322.
[16] The ten point plan for a green industrial revolution, in: E.I.S. Department for Business, Prime Minister's Office, 10 Downing Street, The Rt Hon Alok Sharma MP, and The Rt Hon Boris Johnson MP (Ed.), https://www.gov.uk/government/publications/the-ten-point-plan-for-a-green-industrial-revolution, 2020.
[17] J. Breitenbach, I.V. Roisman, C.J.E.i.F. Tropea, From drop impact physics to spray cooling models: a critical review, 59(3) (2018) 55.
[18] H. Liu, C. Cai, M. Jia, J. Gao, H. Yin, H. Chen, Experimental investigation on spray cooling with low-alcohol additives, Applied Thermal Engineering, 146 (2019) 921-930.
[19] G. Liang, I. Mudawar, Review of spray cooling–Part 1: Single-phase and nucleate boiling regimes, and critical heat flux, International Journal of Heat and Mass Transfer, 115 (2017) 1174-1205.
[20] I. Mudawar, W. Valentine, Determination of the local quench curve for spray-cooled metallic surfaces, Journal of Heat Treating, 7(2) (1989) 107-121.
[21] R. Dou, Z. Wen, G. Zhou, Heat transfer characteristics of water spray impinging on high temperature stainless steel plate with finite thickness, International Journal of Heat and Mass Transfer, 90 (2015) 376-387.
[22] K. Baysinger, K. Yerkes, R. Harris, T. Michalak, J. McQuillen, Design of a microgravity spray cooling experiment, in: 42nd AIAA Aerospace Sciences Meeting and Exhibit, 2004, pp. 966.
[23] S.K. Mishra, A. Arora, H. Chandra, Application of Vibration on Heat Transfer-A Review, J i-Manager's Journal on Future Engineering Technology, 15(1) (2019) 72.

[24] J. Kim, J. Oh, H. Lee, Review on battery thermal management system for electric vehicles, Applied thermal engineering, 149 (2019) 192-212.
[25] S. Jafari, T. Nikolaidis, Thermal management systems for civil aircraft engines: Review, challenges and exploring the future, Applied Sciences, 8(11) (2018) 2044.
[26] J. Doty, K. Yerkes, L. Byrd, J. Murthy, A. Alleyne, M. Wolff, S. Heister, T. Fisher, Dynamic thermal management for aerospace technology: review and outlook, Journal of Thermophysics Heat Transfer, 31(1) (2017) 86-98.
[27] H. Atashi, A. Alaei, M. Kafshgari, R. Aeinehvand, S. Rahimi, New Pool Boiling Heat Transfer in the Presence of Low-Frequency Vibrations Into a Vertical Cylindrical Heat Source, Experimental Heat Transfer, 27(5) (2014) 428-437.
[28] J.T. Jose, J. Dunne, Numerical Simulation of Single-Droplet Dynamics, Vaporization, and Heat Transfer from Impingement onto Static and Vibrating Surfaces, J Fluids, 5(4) (2020) 188.
[29] Z. Wang, Y. Xing, X. Liu, L. Zhao, Y. Ji, Computer modeling of droplets impact on heat transfer during spray cooling under vibration environment, Applied Thermal Engineering, 107 (2016) 453-462.
[30] A. Sarmadian, J. Dunne, C. Long, J.T. Jose, J.-P. Pirault, C. Rouaud, Heat flux correlation models for spray evaporative cooling of vibrating surfaces in the nucleate boiling region, International Journal of Heat Mass Transfer, 160 (2020) 120159.
[31] A. Sathyabhama, S. Prashanth, Enhancement of boiling heat transfer using surface vibration, Heat Transfer—Asian Research, 46(1) (2017) 49-60.
[32] L. Elston, K. Yerkes, S. Thomas, J. McQuillen, Effect of Variable Gravity on the Cooling Performance of a 16-Nozzle Spray Array, in: 47th AIAA Aerospace Sciences Meeting Including The New Horizons Forum and Aerospace Exposition, 2009, pp. 1025.
[33] L.J. Elston, K.L. Yerkes, S.K. Thomas, J. McQuillen, Cooling performance of a 16-nozzle array in variable gravity, Journal of thermophysics heat transfer, 23(3) (2009) 571-581.
[34] T.E. Michalak, K.L. Yerkes, S.K. Thomas, J.B. McQuillen, Acceleration effects on the cooling performance of a partially confined FC-72 spray, Journal of Thermophysics Heat Transfer, 24(3) (2010) 463-479.
[35] K.A. Estes, I. Mudawar, Correlation of Sauter mean diameter and critical heat flux for spray cooling of small surfaces, International Journal of Heat and Mass Transfer, 38(16) (1995) 2985-2996.
[36] I. Mudawar, K. Estes, Optimizing and predicting CHF in spray cooling of a square surface, Journal of Heat Transfer, 118 (1996) 672-679.
[37] S. Jiang, V.K. Dhir, Spray cooling in a closed system with different fractions of non-condensibles in the environment, International journal of heat and mass transfer, 47(25) (2004) 5391-5406.
[38] S.J. Thiagarajan, S. Narumanchi, R. Yang, Effect of flow rate and subcooling on spray heat transfer on microporous copper surfaces, International Journal of Heat and Mass Transfer, 69 (2014) 493-505.
[39] M. Visaria, I. Mudawar, Effects of high subcooling on two-phase spray cooling and critical heat flux, International journal of heat and mass transfer, 51(21-22) (2008) 5269-5278.
[40] M.S. Sehmbey, L.C. Chow, O.J. Hahn, M.R. Pais, Effect of spray characteristics on spray cooling with liquid nitrogen, Journal of Thermophysics and heat Transfer, 9(4) (1995) 757-765.
[41] L. Chow, M. Sehmbey, M. Pais, Critical heat flux in spray cooling, in: 34th Aerospace Sciences Meeting and Exhibit, 1996, pp. 727.
[42] M. Sawyer, S. Jeter, S. Abdel-Khalik, A critical heat flux correlation for droplet impact cooling, International Journal of Heat and Mass Transfer, 40(9) (1997) 2123-2131.
[43] E.A. Silk, J. Kim, K. Kiger, Energy conservation based spray cooling CHF correlation for flat surface small area heaters, in: ASME/JSME 2007 Thermal Engineering Heat Transfer Summer Conference collocated with the ASME 2007 InterPACK Conference, American Society of Mechanical Engineers, 2007, pp. 805-813.
[44] E. Cabrera, Heat flux correlation for spray cooling in the nucleate boiling regime, Experimental heat transfer, 16(1) (2003) 19-44.
[45] B. Abbasi, J. Kim, Prediction of PF-5060 spray cooling heat transfer and critical heat flux, Journal of heat transfer, 133(10) (2011) 101504.
[46] X. Zhao, B. Zhang, X. Xi, Z. Yin, Analysis and prediction of single-phase and two-phase cooling characteristics of intermittent sprays, International Journal of Heat and Mass Transfer, 133 (2019) 619-630.
[47] K. Baumeister, F. Simon, Leidenfrost temperature—its correlation for liquid metals, cryogens, hydrocarbons, and water, Transactions of ASME, Journal of Heat Transfer, (1973).

[48] R.J. Moffat, Describing the uncertainties in experimental results, Experimental thermal and fluid science, 1(1) (1988) 3-17.
[49] S. Toda, H. Uchida, Study of liquid film cooling with evaporation and boiling, J Trans. JSME, 2 (1973) 44-62.
[50] Y. Hou, J. Liu, X. Su, Y. Qian, L. Liu, X. Liu, Experimental study on the characteristics of a closed loop R134-a spray cooling, Experimental Thermal and Fluid Science, 61 (2015) 194-200.
[51] L.C. Chow, M.S. Sehmbey, M.R. Pais, High heat flux spray cooling, Annual Review of Heat Transfer, 8 (1997).
[52] G. Moreno Jr, S.M. You, E. Steinthorsson, Spray cooling performance of single and multi-jet spray nozzles using subcooled FC-72, in: Heat Transfer Summer Conference, 2007, pp. 783-790.
[53] M. Pais, L. Chow, E. Mahefkey, Surface roughness and its effects on the heat transfer mechanism in spray cooling, J. Heat Transf. – Trans. ASME, 114 (1992) 211-219.
[54] R.-H. Chen, L.C. Chow, J.E. Navedo, Effects of spray characteristics on critical heat flux in subcooled water spray cooling, International Journal of Heat and Mass Transfer, 45(19) (2002) 4033-4043.
[55] D.E. Tilton, Spray cooling PhD Dissertation, University of Kentucky, Lexington, USA, 1989.
[56] L. Lin, R. Ponnappan, Critical heat flux of multi-nozzle spray cooling, J. Heat Transfer - Trans. ASME, 126(3) (2004) 482-485.
[57] M. Monde, Critical heat flux in the saturated forced convection boiling on a heated disk with impinging droplets, in: Trans. JSME, 1980, pp. 849-858.
[58] I. Mudawar, K. Estes, Optimizing and predicting CHF in spray cooling of a square surface, Journal of Heat Transfer, 118(3) (1996) 672-679.
[59] M. Visaria, I. Mudawar, Effects of high subcooling on two-phase spray cooling and critical heat flux, International journal of heat mass transfer, 51(21-22) (2008) 5269-5278.
[60] Y. Zhang, L. Pang, Y. Xie, S. Jin, M. Liu, Y. Ji, Experimental investigation of spray cooling heat transfer on straight fin surface under acceleration conditions, Experimental Heat Transfer, 28(6) (2015) 564-579.
[61] Y. Zhang, L. Pang, M. Liu, Y. Xie, Investigation of spray cooling: Effect of different heater surfaces under acceleration, International Communications in Heat Mass Transfer, 75 (2016) 223-231.
[62] B.L. Conrad, J.C. Springmann, L.A. McGill, T.A. Shedd, Effectiveness of linear spray cooling in microgravity, in: AIP Conference Proceedings, American Institute of Physics, 2009, pp. 67-72.
[63] G. Bluman, Dimensional analysis, modelling and symmetry, International Journal of Mathematical Education in Science and Technology, 14(3) (1983) 259-272.
[64] A.A. Sonin, A generalization of the Π-theorem and dimensional analysis, Proceedings of the National Academy of Sciences, 101(23) (2004) 8525-8526.
[65] E. Buckingham, Model experiments and the forms of empirical equations, Verlag nicht ermittelbar, 1915.
[66] E. Buckingham, On physically similar systems; illustrations of the use of dimensional equations, Physical review, 4(4) (1914) 345.
[67] Y. Qiao, S.J.J.o.H.T. Chandra, Spray cooling enhancement by addition of a surfactant, 120(1) (1998) 92-98.
[68] K.A. Estes, I.J.I.J.o.H. Mudawar, M. Transfer, Correlation of Sauter mean diameter and critical heat flux for spray cooling of small surfaces, 38(16) (1995) 2985-2996.
[69] M. Ghodbane, J.J.I.J.o.H. Holman, M. Transfer, Experimental study of spray cooling with Freon-113, 34(4-5) (1991) 1163-1174.
[70] R.-H. Chen, L.C. Chow, J.E. Navedo, Optimal spray characteristics in water spray cooling, International Journal of Heat Mass Transfer, 47(23) (2004) 5095-5099.
[71] S. Toda, A study of mist cooling (1st report, investigation of mist cooling), J Kikaigakkai Ronbunshu, 38 (1972) 581-588.
[72] S. Toda, A study of mist cooling (2nd report: theory of mist cooling and its fundamental experiments), Heat Transf.-Jap. Res, 3 (1974) 1-44.

Nomenclature

$\dot{m}$	mass flow rate (kg/s)
$\vec{v}$	volumetric spray flux (m^3s^{-1}/m^2)
$\overline{\vec{v}}$	average volumetric spray flux (m^3s^{-1}/m^2)
A	surface area (m^2)
Ac	dimensionless acceleration (units of g)
a	Amplitude of vibration (m)
Bo	Boiling number (-)
C_p	specific heat (kJ/kg k)
d	diameter(mm)
d_{05}	mass or volume median diameter (m)
d_{32}	Sauter mean diameter (m)
f	Frequency (Hz)
G	mass velocity ($\mathrm{kg/m^2s}$)
h	specific enthalpy (kJ/kg)
H	height (m)
Ja	Jacob number
k	thermal conductivity (W/m K)
L	length (mm)
P	pressure (kPa)
Pr	Prandtl number, $C_p\mu/k$
v	volumetric flow rate (m^3/s) or (l/h)
q	heat flux ($\mathrm{kW/m^2}$)
Re	Reynolds number
R_t	mean roughness height (μm)
T	temperature (K)
u	velocity
We	Weber number

Greek symbols

μ	dynamic viscosity (Kg/m s)
Δp	pressure drop (kPa)
α	spray angle
ρ	density ($\mathrm{kg/m^3}$)
σ	surface tension (N/m)
ω	Angular velocity (Hz)
δ	liquid film thickness (m)

Subscripts

am	ambient
at	atmospheric
ch	chamber
CHF	Critical Heat Flux
c	coolant
d	droplet
f	liquid phase
v	vapor phase
V	vibration

g	gas side
h	heater
H	heater surface
i	inner
l	liquid
lat	latent
o	orifice
ref	refrigerant
s	surface
sat	saturation
sub	subcooling
w	Wall

List of figures

List of Tables

TEMPERATURE CONTROL OF VIBRATING HEAT-GENERATING HARDWARE USING SPRAY EVAPORATIVE COOLING IN THE NUCLEATE BOILING REGION

A Sarmadian, J.F. Dunne*, J. Thalackottore Jose, C.A. Long, and J-P Pirault.

Department of Engineering and Design, *School of Engineering and Informatics*,
University of Sussex, Falmer, Brighton, BN1 9QT, UK.
*Corresponding author

ABSTRACT

Thermal management of spray evaporative cooling of vibrating surfaces has been designed and verified experimentally in the nucleate boiling region. This is relevant to temperature control of heat-generating automotive vehicle components. By exploiting an experimentally calibrated dynamic correlation model to represent spray evaporative cooling of a flat test-piece, a PID controller has been adopted with emphasis focused on the choice of gain parameters to ensure both stability of temperature control, and favourable responses in terms of relevant performance measures. Optimum linearisation of the correlation model has been achieved by solving an appropriate Wiener-Hopf equation, mainly to undertake a practical stability assessment of the closed-loop temperature control system. To verify the predicted control system performance, experimental measurements have been obtained from an instrumented, and spray-evaporatively-cooled, flat test-piece exposed to displacement vibration from a shaker. Experimental testing, appropriate to automotive vehicle component applications, includes large-amplitude, low frequency vibration, at 12 mm and 1.9 Hz, and low amplitude, high-frequency vibration, at 0.02 mm and 400 Hz. To assess the effects of different PID controller gains on the thermal performance of the thermal management system, a coefficient of performance (COP) is used, defined as the ratio of heat power removal to the required pumping power. To achieve a reduction in the settling time and an increase the rise time of stable control, a PID controller with a negative proportional gain showed most promising results. A 10.5% increase in COP was achieved in comparison to a PID controller with positive gains. This information is useful for the design and optimization of a thermal management system using evaporative spray cooling.

1. Introduction

Thermal management plays a pivotal role in the electrification of both automotive vehicles [1] and aircraft [2, 3]. In these applications, high heat-flux levels > 1 MW/m^2 have increased the need for high energy conversion efficiency to meet stricter regulatory targets (such as those set by the EU for 2030 [4, 5]) to speed-up progress towards zero CO_2 emission transport systems [6]. This need has focused attention on electrification of vehicle powertrain and aircraft propulsion, with the aim of reducing their carbon footprint [7-9]. To meet the thermal management demand of high heat removal under controlled conditions, highly optimized cooling systems are needed. Addressing this need, Jafari et al. [10] reviewed state-of-the-art evaporative cooling systems for internal combustion engines, showing that there was considerable interest in spray evaporative cooling [11]).

There is a relatively large body of literature published on spray heat transfer characteristics. These include the review by Liang and Mudawar [12] on single-phase, nucleate boiling, critical heat flux; and the review on film boiling and quench curves [13]. Droplet impact and heat transfer correlation models has also been reviewed by Breitenbach et al. [14]. In the past two decades, a number of studies have

also revealed how key parameters affect the heat flux and surface temperature during cooling. These findings show how the regimes of heat transfer depend on spray characteristics, pressure, flow rate, and degree of subcooling. Figure 1a (based on [14]) shows the dynamic behaviour of a single droplet impinging onto a hot surface.

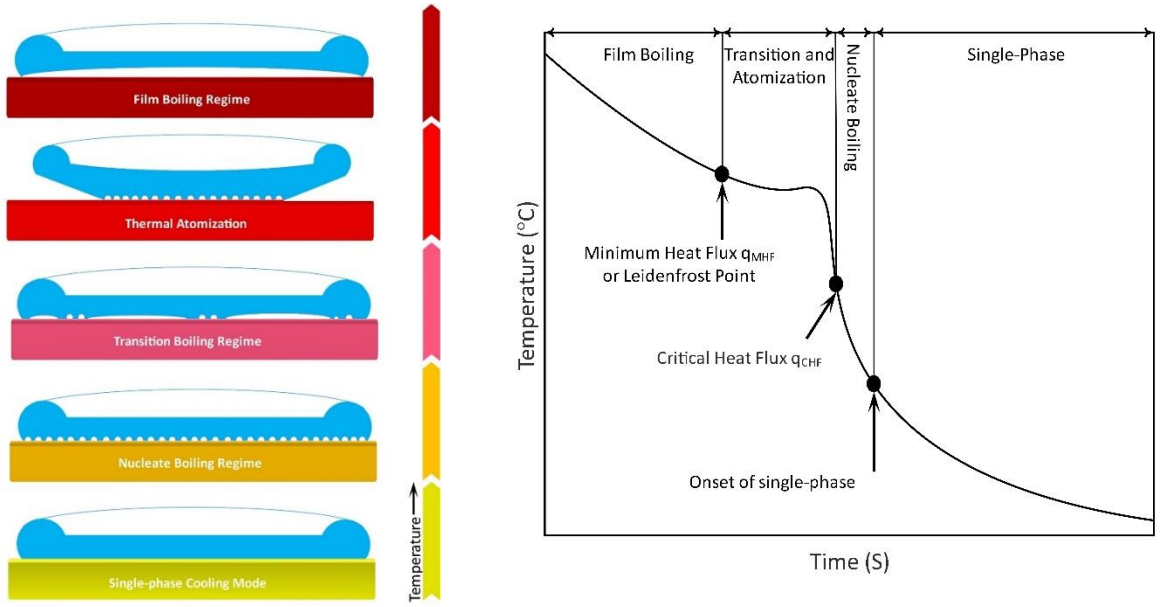

(a) (b)

Fig. 1. (a) Different flow regimes for surface impingement of a droplet for different heat loads; (b) Typical spray quench curve.

The relationship between excess temperature $\Delta T = T\text{wall} - T\text{sat}$ and the heat flux, varies notably between the different regimes. And this reflects the flow physics encountered in those regimes. In the single-phase regime, a complex liquid film covers the surface. At a higher value of ΔT nucleate boiling occurs where vapour bubbles are generated and promote the heat transfer rate. The heat flux increases rapidly with increasing excess temperature in this region up to the critical (or peak heat flux). Beyond this, transition boiling occurs, where a vapour partially covers the surface and acts as an insulator; further increases in ΔT lead to a decrease in q. At even higher values of ΔT, atomization of the film occurs and this is followed by a complete vapour film.

Spray evaporative cooling offers a significant increase in heat flux compared with single-phase convection [16, 17]. This is demonstrated in Figure 2a, which shows the variation of heat flux with excess temperature obtained from both single-phase convection with two different bulk velocities, and an evaporative spray of the type used in [18]. Also shown on Figure 2a is a pool boiling curve for water [19]. The single phase convection cooling curves [20, 21] in Figure 2, use a 50/50 water/glycol mix, whereas the other curves use pure water. Spray cooling, compared with flow boiling heat transfer, also offers significantly greater heat flux for a lower flow-rate [22, 23]. This evident from Figure 2b which shows, as a function of excess temperature, heat flux per unit mass-flow-rate (i.e. specific heat flux). Figure 2b shows that spray evaporative cooling has a specific heat flux several orders of magnitude greater than single-phase convection. Lower mass-flow rates are very advantageous because they result in a significant reduction in the required pumping power and mass of associated hardware [24].

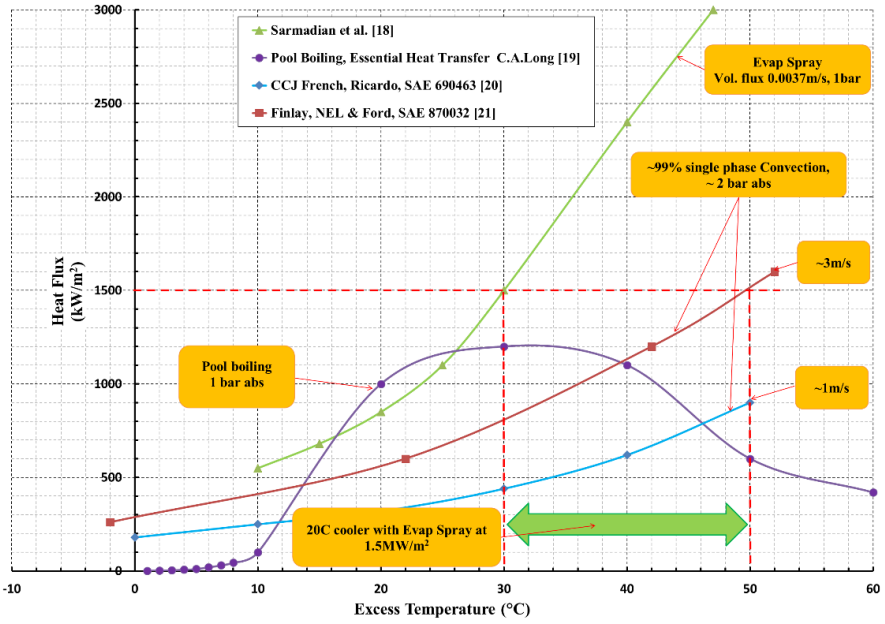

(a)

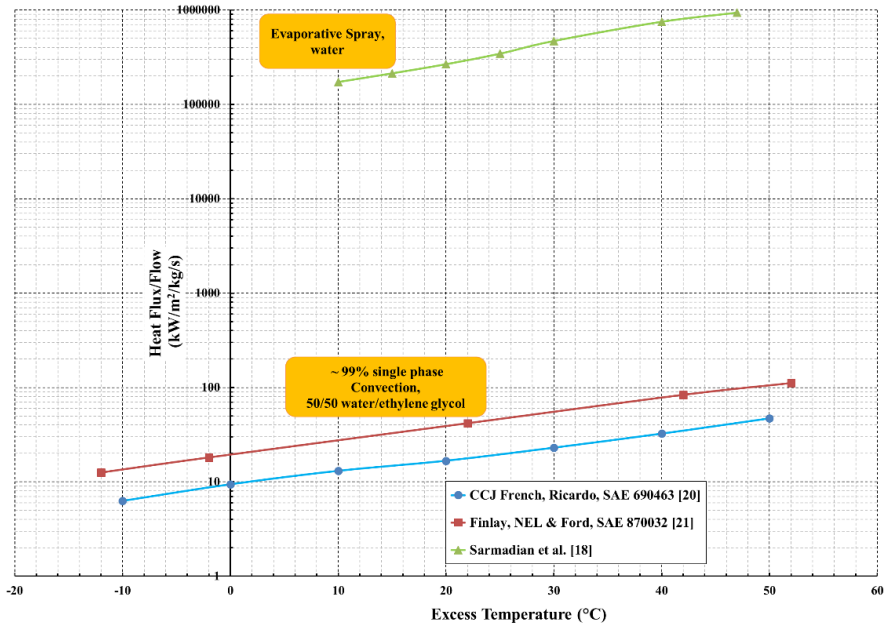

(b)

Fig. 2. Spray evaporative cooling (using pure water) compared with single-phase convection cooling [20, 21] (using 50/50 water/glycol): (a) variation of heat flux with excess temperature (T_{wall} - T_{sat}) including pool boiling; (b) specific heat flux (heat flux/mass-flow-rate) versus excess temperature.

Spray evaporative cooling meets all the extra heat removal requirements for downsized internal combustion engines (ICEs) for conventional vehicles [11], and as ICE range extenders in hybrid electric vehicles. Focusing on cooling of the electronic hardware in hybrid electric vehicles however, Mudawar et al. [25], reported that a feasible thermal management system should be able to dissipate heat in the

flux range 1.5 - 2 MW/m^2 while maintaining temperatures below 150 ˚C (i.e. the silicon-based transistors limit). Spray evaporative cooling should meet this challenge, moreover its two-phase flow helps eliminate hot spots, by providing a uniform temperature across all cooled surfaces [26]. Uniform temperature is vital in the thermal management of electronic hardware and Lithium-ion battery stacks [27], where there is risk of overheating [28, 29] and fires [30]. Further applications include indirect cooling, using pre-cooled air, which improves thermal performance of lithium battery packs [31]. Li-ion batteries have a narrow optimum working temperature range - exceeding the upper limit runs the risk of thermal runaway and fires; operating below the lower limit, reduces battery life. Operating at an optimal temperature maximizes power output, and also improves charging rate and longevity [32, 33].

Most potential applications of spray evaporative cooling in transport systems will be exposed to mechanical vibration, which can influence heat transfer [34]. This can be best seen in terms of two dimensionless parameters: the Vibrational Reynolds Number $Re_V = \rho_l a \omega d_H / \mu_l$, and the Acceleration Number $Ac = (\omega\text{^}2\ a)/g$, where a is the vibration amplitude and ω is frequency. The parameter Re_V is a measure of the increased turbulence that results from a vibrating surface [35] indicating how it can affect heat transfer. In fact, heat transfer changes resulting from vibration can be explained by turbulence changes to the boundary layer thickness, generated nucleation sites [36], and by changes to the wetting-angle [37]. The parameter Ac can be used to explain the influence of experimentally-measured acceleration on spray cooling heat transfer, which has been investigated in various dynamic conditions [18, 38-40]. It is still difficult however to draw general conclusions from such studies owing to the complexity of spray heat transfer mechanisms and from differences in the experimental conditions.

The potential exists therefore, for spray evaporative cooling to achieve high heat transfer rates with low mass flow rates. There are however significant concerns remaining about the ability of the actual hardware to achieve stable control of a spray evaporative cooling system at the required heat flux and temperature. There is currently no published evidence of successful thermal management and control of hardware involving two-phase spray evaporative cooling of vibrating surfaces. In this paper, the design and performance of an experimental cooling control system is examined to confirm, in the presence of vibration, effective thermal management of heat generating hardware using spray evaporative cooling. The effect of choosing different gain values on the controller performance is examined in detail The objective of the paper is to establish the efficacy of a particular control strategy for evaporative spray cooling of vibrating surfaces in terms of being able operate successfully at target temperatures needed for high-heat-flux cooling of a representative test piece.

2. Proposed thermal management system

The proposed thermal management system involves a ‘plant’ which here represents an evaporatively cooled test-piece (exposed to vibration) whose temperature is regulated by feedback control. Figure 3 shows a high-level representation of the closed-loop feedback control system for temperature control of the hardware. As can be seen, a test-piece, in contact with the heating source, is cooled using evaporative spray cooling. The objective of the controller is to keep the cooling process in the nucleate boiling regime to benefit from the heat removal in the form of latent heat to vapour. In this regard, a PID controller has been designed to control the coolant pump flow rate to maintain the coolant side temperature of the test piece (exposed to displacement vibration) at a target value. There

are two circuits in Figure 3. The first circuit (in blue) shows the coolant flow from the coolant pump to a full-cone nozzle on top of the test piece (where v is the volumetric flow rate). The saturated water, broken-up into droplets by the nozzle, impinges onto the test-piece surface, removing heat generated by the hardware. The vapour and accumulated droplets are drained into the vapour chamber, then the condenser tank. Finally, the condensed water reaches the suction side of the coolant pump to complete the circuit. The second circuit (in black) shows the temperature feedback signal from the cool-metal surface. This state is compared with the desired surface temperature (as a reference signal) to generate the error required to be used as an input signal for the PID controller. The control signal to the coolant pump completes this circuit.

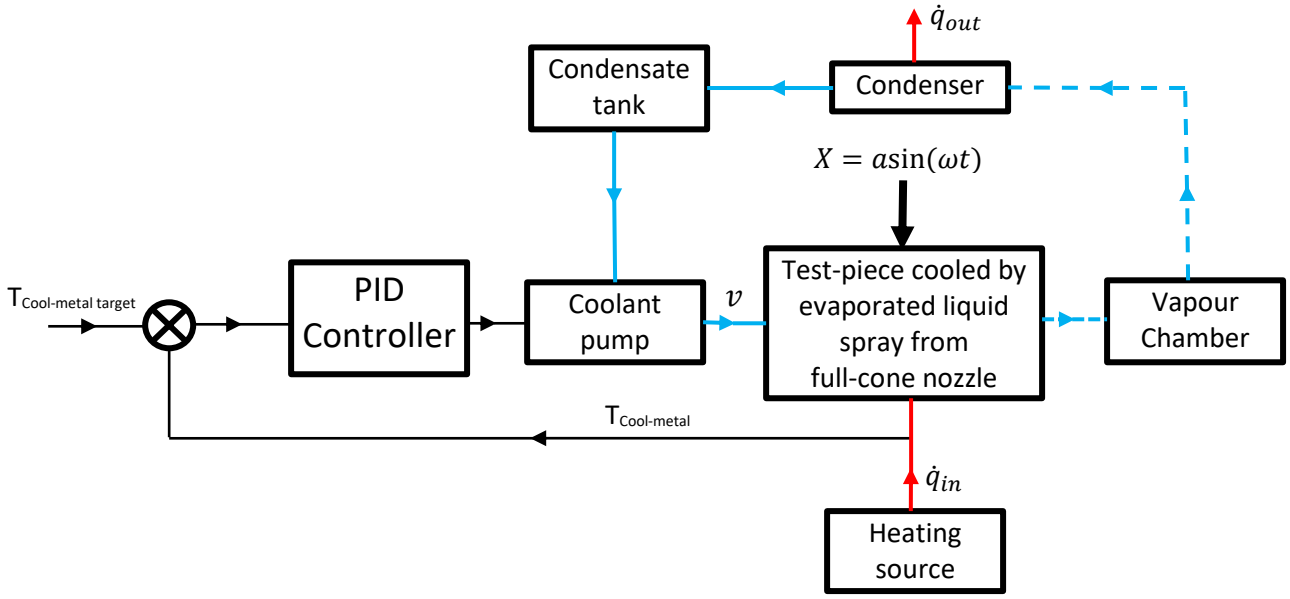

Fig. 3. PID temperature controller for spray evaporative cooling of hardware (showing a disturbance of the test-piece from displacement vibration $X = a\sin(\omega t)$).

2.1 Correlation model of the 'plant'.

To undertake performance assessment and tuning of the thermal management system in Figure 3, a closed-loop feedback control system model is constructed to accurately model the entire physics during the cooling process (i.e. when the heat-generating hardware exposed to the vibration is cooled using spray evaporative cooling in the nucleate boiling region). To describe the physics of the evaporative spray cooling needed for the 'plant' model, the following empirical correlation model has been constructed in [18] (using the Generalised Buckingham Pi method [41]) to represent spray evaporative heat transfer characteristics for the test piece under vibration in the nucleate boiling region:

$$Bo = 1.24 \times 10^{-2} Ja^{1.3920} \left(\frac{\rho_l^2 \sigma v}{{\mu_l}^3}\right)^{0.9809} Re_V^{-0.9869} \left(\frac{a}{H}\right)^{0.4825} Ac^{0.4998} \quad (1)$$

where Bo is Boiling number ($qH/\mu_l h_{fg}$) which includes heat flux q, nozzle-to-surface distance H, viscosity μ_l and specific enthalpy h_{fg}. Vibrational Reynolds Number $Re_V = \rho_l a \omega d_H / \mu_l$ involving

vibration amplitude a, and angular frequency ($\omega = 2\pi f$), Acceleration Number $Ac = \omega^2 a/g$, Ja is the Jakob Number ($Ja = C_l \Delta T/h_{fg}$), which is the ratio of sensible to latent heat.

To construct the plant model, a simple heat balance of the heat-generating hardware has been used to model the temperature control. A similar approach, adopted by Setlur et al. [42], Eberth et al. [43], Wagner et al. [44-46], and Henry et al. [47], results in a heat balance equation as follows:

$$mC\dot{T} = \dot{Q}_{in} - \dot{Q}_{out} \tag{2}$$

where m is the test-piece mass, C is the specific heat capacity of the cooled test-piece (in this case copper), $\dot{T}$ is time-varying temperature of the test piece, $\dot{Q}_{in}$ is the rate of heat release of the source, $\dot{Q}_{out}$ is the rate of heat removal of the proposed cooling system. To obtain the coolant side temperature, equation (1) is substituted into equation (2) and by setting $\dot{Q}_{out} = qA$ gives a first-order (nonlinear) differential equation model for the test-piece temperature T_w which will shortly be linearized, a necessary step to ultimately undertake practical stability analysis. The correlation model for the plant given by equation (3) can be linearised in a number of ways. The experimental facilities are described in Section 3 but for linearization, it is helpful to state the numerical values for the flat circular test-piece. The mass $m = 404.4$ gm, the diameter of $d_H = 20$ mm, and specific heat capacity (for copper) $C = 385\ {}^{J}/_{kgK}$. Parameters not assigned values, still appear as variables in the first-order (nonlinear) differential equation model, which takes the form:

$$mC\dot{T}_w = \dot{Q}_{in} - 1.24 \times 10^{-2} A \left(\frac{\mu_l h_{fg}}{H}\right) \left(\frac{C_l \Delta T}{h_{fg}}\right)^{1.3920} \left(\frac{\rho_l^2 \sigma v}{{\mu_l}^3}\right)^{0.9809} Re_V^{-0.9869} \left(\frac{a}{H}\right)^{0.4825} Ac^{0.4998} \tag{3}$$

where ΔT is the excess temperature in the term $Ja = C_l \Delta T/h_{fg}$ (with $T_{sat} = 99.6\,^{\circ}C$, assumed constant at 1 bar), A is the area of the circular test-piece. Equation (3) represents the model for a single-input single-output (SISO) system, the input being v, and the output being the time-varying wall temperature T_w.

By considering equation (3) at a fixed dynamic operating condition, for example corresponding to nucleate boiling at 1 bar, nozzle-to-surface distance of $H = 17$ mm, vibration amplitude $a = 12$ mm, frequency = $1.9\ Hz$, and a pump flow-rate of 200 ml/min, various 'constant' terms result in equation (3), namely $\dot{Q}_{in} = 1.2A \times 10^6\ W/m^2$, $\mu_l = 0.00028$ Kg/m s, $h_{fg} = 2257$ kJ/kg, $C_l = 4.219$ kJ/kg K, $\rho_l = 958$ kg/m^3, $\sigma = 0.0589$ N/m, and $\frac{A}{mC} = 2.0177 \times 10^{-6}$. Substitution into equation (3), with a simpler appearance:

$$\dot{T}_w(t) = 2.4213 - 7.5357\ (T_w - 99.6\ )^{1.3920} v^{0.9809} \tag{4}$$

Linearisation of the plant model.

There is no closed-form solution to Equation (4) but it can be linearised in a number of ways and an exact solution is then trivial. The simplest way to linearize is to expand the nonlinearity in a Taylor series about an operating point then truncate, retaining only the linear term. For example, when the initial (temperature) condition T_w= 110℃ is chosen as the expansion point, the linear model becomes.

$$\dot{T}_w(t) = -0.166\, T_w(t) - 1419\, v(t) \quad (5)$$

A comparison of the analytical solution of equation (5) with a numerical of equation (4) shows however a very significant difference, suggesting that linearization about the initial condition is not acceptable. An alternative linearization approach is to construct a least-square error solution [48] (over the entire time range). This is an iterative process involving numerical solution of equation (4) using a known initial condition, corresponding for example to the response to a step input, or a free decay response. When an initial condition of 110℃ is used in the numerical solution (corresponding to a step input of 135℃), the least-square-error linear model obtained is:

$$\dot{T}_w(t) = -\,0.14166 T_w(t) + 5755.6\, v(t) \quad (6)$$

By contrast when the initial condition of 140 ℃ is used (corresponding to a free decay response), the least-square-error linear model obtained is

$$\dot{T}_w(t) = -\,0.14654 T_w(t) + 5469.2\, v(t) \quad (7)$$

Figure 4a and figure 4b show a comparison of the responses obtained by the numerical solution of equation (4) and the linearized model equation (6) for the step-input, and equation (7) for the free-decay response. It can be seen from figures 4a and 4b, that the least-square error linearized model responses are in excellent agreement in predicting the responses of the nonlinear model with the same initial conditions. However, when the equivalent linear models are switched, the predicted results are very poor (not shown). To attempt to overcome this deficiency, a single least-square-error linear model was constructed with the best overall performance for both the step input and free decay response. This model is:

$$\dot{T}_w(t) = -0.13363\, T_w(t) + 5129\, v(t) \quad (8)$$

Analytical solutions to Equation (8), with initial conditions of respectively 110 and 140 $^{\circ}C$, (assuming constant $v = 0.00333\ m^3 s^{-1}$), are:

$$T_w(t) = 127.8124 - 17.8124 e^{-0.13363t} \quad (9)$$

and

$$T_w(t) = 12.1876 e^{-0.13363t} + 127.8124 \quad (10)$$

where the transfer function obtained for the linearised plant model equation (8) is:

$$\frac{T_w(s)}{v(s)} = \frac{5129}{S + 0.13363} \quad (11)$$

Figure 4c and 4d show respective comparisons between the numerical responses to equation (4) (with initial conditions of 110 and 140 $^{\circ}C$), and the corresponding responses obtained from equations (9) and (10).

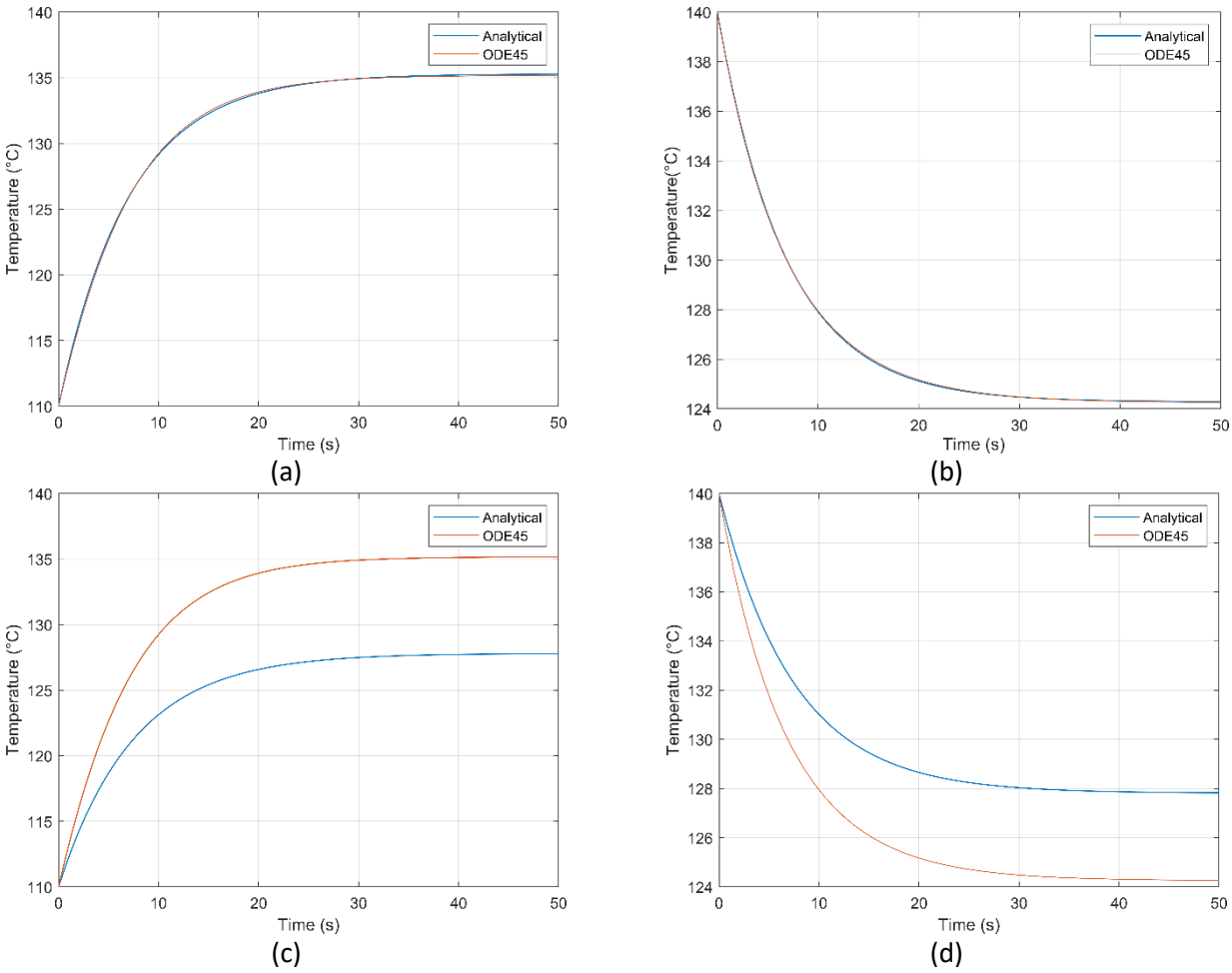

Fig. 4. Responses obtained by numerical solution of equation (4) and the linearized model: a) equation (6) for the step-input, and b) equation (7) for the free-decay response; c) and d) numerical responses to equation (4) (with respective initial conditions of 110 and 140 $^{\circ}C$), and the corresponding responses obtained from equations (9) and equation (10).

It is evident from Figure 4c and 4d, that the level of agreement between the linearised model and the numerical solution of the full nonlinear model equation (4) is still poor. A more rigorous linearization process therefore needs to be followed such as the Wiener Hopf approach, as now explained.

Obtaining the optimal fixed-order linear model using the Wiener Hopf approach

To obtain the optimal model to replace equation (4), the Wiener-Hopf approach is used to obtain a fixed-order linear transfer function [49]. For the required input to a Finite Impulse Response (FIR) filter (i.e. the optimal filter weighting function), a random temperature history is generated by numerical simulation involving equation (4), with a white noise input. To generate the input temperature (as shown for example in Figure 5a), as supplied to the Matlab-Simulink model of the plant, the heat flux

as the heat source in $\dot{Q}_{in} = qA$ and volumetric flow rate v, have respectively been randomly varied from 0 to $1.2 \times 10^6\ W/m^2$ and from 0 to $0.00333\ m^3 s^{-1}$. This satisfies the assumptions associated with the Wiener filter theory namely that both signal and noise are random processes with known spectral characteristics. Here, to ensure the simplest closed-loop stability analysis an optimal 1st-order linear model is chosen. The additive combination of randomly generated input-temperature and white noise (shown in Figure 5b (in red)) has been correlated using the FIR filter. Figure 5b, shows that the FIR filter is successful in modeling the temperature with noise (where the output signal is in blue). The Mean Square Error (MSE) between two signals in Figure 5 is 0.77, and the transfer function of the optimal filter weighting function is:

$$H_{FIR}(s) = \frac{0.5S+0.5}{S} \tag{12}$$

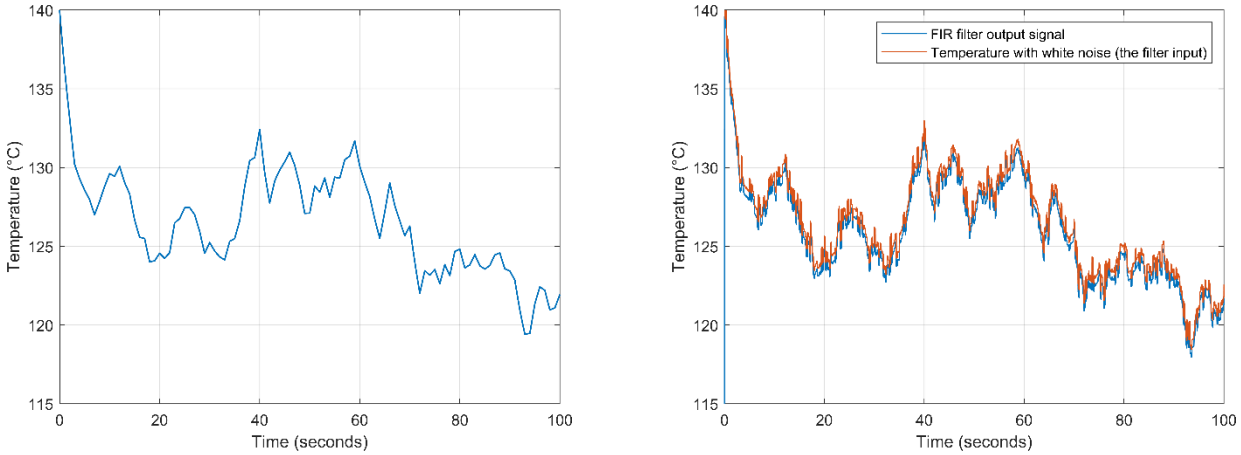

(a) (b)

Fig. 4. a) Numerically-generated temperature; b) the input signal to the Wiener-Hopf model; the temperature with additive white noise, and the FIR output signal.

2.2 Stability analysis of the closed-loop transfer function

The design of a stable hardware controller, now proceeds using the best least-square solution to the nonlinear 'plant' model obtained by the Wiener-Hopf approach. Stability of the closed-loop control transfer function, is assessed iteratively using the root locus method (implemented using the Matlab Control System Toolbox). First, the root locus diagram is shown in Figure 6a for the (original) linearised open-loop correlation model of the plant (equation (12)). The stability of the closed-loop transfer function is shown in Figure 6b with proportional gains from 0 to 2 (in increments of 0.5); integral gains ranging from 0 to 0.08 (in increments of 0.02); and derivative gains from 0 to 0.004 (in increments of 0.001). As can be seen, the system is stable for all sets of PID gains. After finding the best integral gain to improve the steady-state error, as well as increasing the stability using small values of derivative gains, the most promising PID gains are: P=2.1, I=0.08, D=0.001. Since the transfer function for a PID controller is:

$$k_p + \frac{k_i}{S} + k_d S = \frac{k_d S^2 + k_p S + k_i}{S} \tag{13}$$

the gain values thus found are chosen as starting gains for the hardware. Using the PID controller transfer function (equation (13)) with the starting gains, the linearised closed-loop feedback control system transfer function is given as follows:

$$G(s) = \frac{5.129\,S^2+10770\,S+410.3}{6.129\,S^2+10770\,S+410.3} \tag{14}$$

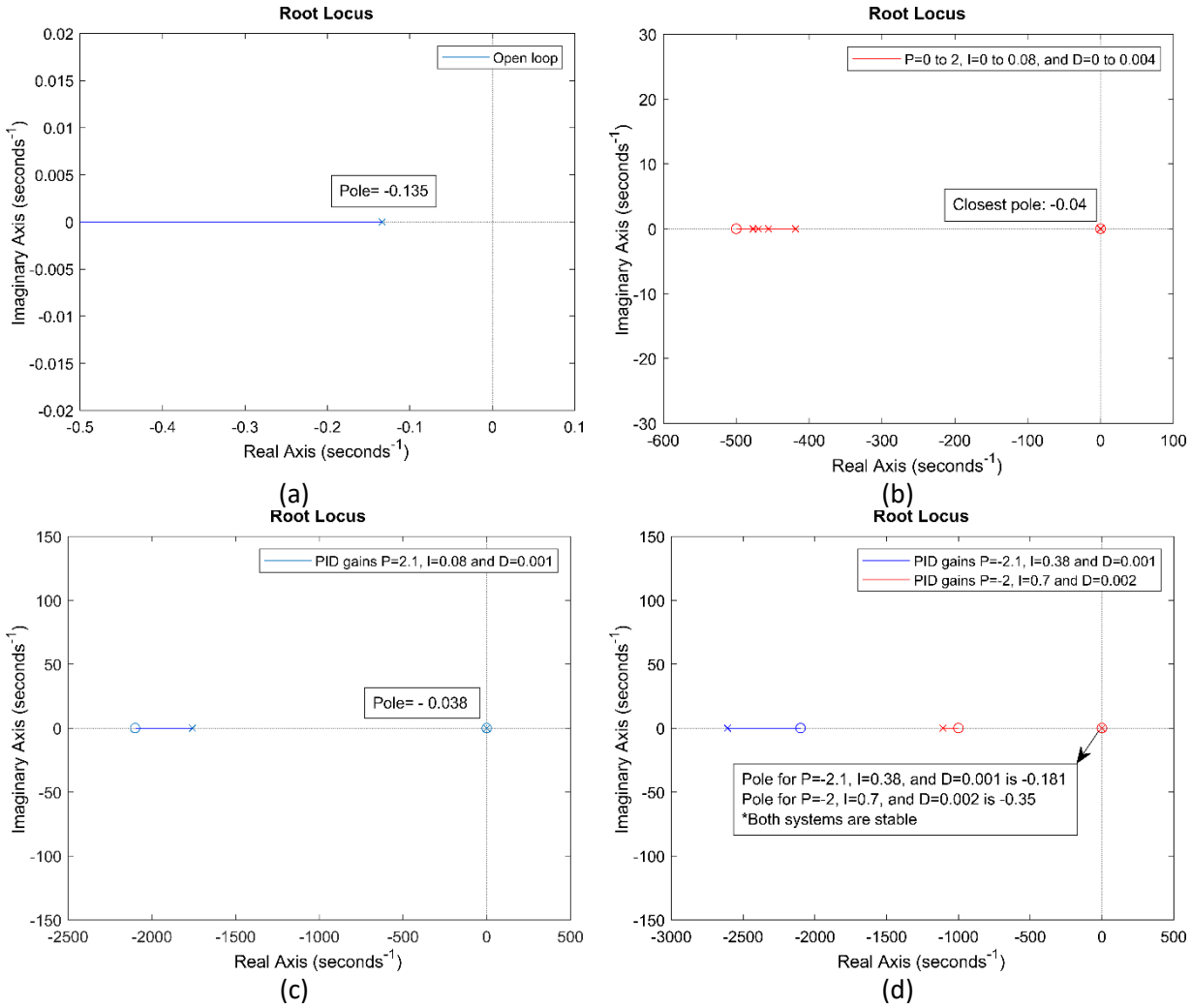

Fig. 5. *Root locus* diagrams: for (a) linearised open-loop correlation model of the plant, (b) linearised closed-loop feedback control with P=0 t 2, I=0 to 0.08 and D=0 to 0.004, (c) the designed controller with P=2.1, I=0.08 and D=0.001, and (d) closed-loop control system with negative proportional PID controllers; one with P=-2.1, I=0.38 and D=0.001 and another with P=-2.1, I=0.7 and D=0.002.

The root locus diagram for equation (14) shown in Figure 6c, gives stability information of a thermal management system using the PID controller. By a process of trial and error, both for the simulation and for the experimental hardware, it becomes apparent that another set of PID controller gains with a negative proportional gain of -2.1, namely P=-2.1, I=0.38, and D=0.001 can also make the system stable (as shown by the root locus diagram in Figure 6d). In fact, increasing the integral gain (to I=0.7)

and doubling the derivative gain (to D=0.002) actually results in better stability and robustness of the system. The poles for these two sets of PID gains are shown in Figure 6d, along with robustness information in Table 1.). The linearized closed-loop control system transfer function for this PID controller (i.e. with P=-2, I=0.7, D=0.002) is:

$$G(s) = \frac{10.26\,S^2+10258\,S+3590}{9.258\,S^2+10260\,S+3590} \tag{15}$$

As expected, during the tuning process of the PID controllers in the actual control hardware, these two sets of PID controller gains (i.e. one with a positive and another with a negative proportional gain) were found to be promising. As can be seen from the root locus plot in Figure 6.c and d, each set has its pros and cons. The pole for the positive proportional PID control system is closer to the imaginary axis. (It is -0.038 for the PID with P=2.1, I=0.08 and D=0.001, and -0.35 for the PID with P=-2, I=0.7 and D=0.002.) Thus, the negative proportional PID controller can theoretically be more stable although it has a smaller range of stability for the PID controller with the larger integral and derivative gains (as shown in Figure 4d).

To further support this finding, the stability of the optimal model (obtained using the Wiener-Hopf approach) is also examined. The stability of both the open loop and closed-loop transfer functions with the same PID gains have been examined using a root locus diagram. As expected, the closest poles in both Figures 6b and 7b with the same ranges of P, I, and D gains are quite similar (0.040 for the best least-square solution to the nonlinear ODE of the 'plant' model, and 0.042 for the Wiener-Hopf derived model). The closest poles to the imaginary axis for PID gains of P=2.1, I=0.08 and D=0.001 on the root locus diagrams for both models are also very similar (-0.038 for the linearised model in Figure 6c, and -0.039 for Wiener-Hopf derived model in Figure 7c). In fact, examining the poles in Figures 6d and 7d for the negative proportional PID controllers, suggests the same trend. Moreover, the root locus diagrams in Figure 7c and 7d still support the previous finding that the pole for the positive proportional PID control system is closer to the imaginary axis. Therefore, the closed-loop control system with positive gains is actually less stable in comparison to the system designed with a negative proportional PID gain. The only difference between the stability findings relates to the stability range of the PID controller with larger integral and derivative gains (P=-2.1, I=0.7 and D=0.002). In Figure 7d (corresponding to the Wiener-Hopf model) the s-domain for which the system is stable, has two complex conjugate poles of -0.37 ± 36.7i but this does not indicate any reduction in stability.

Regarding the actual hardware, both the positive and negative proportional PID controllers have been implemented - their effects on the robustness are summarized in Table 1 (which are derived from results that will be discussed in Section 5). PID Controllers Number 1 and 2 are used in tuning the actual hardware without vibrational disturbance (i.e. under static conditions), whereas for the PID Controllers Numbers 3, 4, and 5, the actual hardware was tested with vibrational disturbances. Comparing the settling time and overshoot, the results for PID controllers Numbers 1, and 2, 3, 4, and 5, confirm better stability for the negative proportional gain controller. In fact there are evident reductions in settling time and overshoot for the PID controllers with negative proportional gains. Disturbance rejection for the responses in the dynamic cases is good. Moreover, to check the level of uncertainty in the repeatability of the control, the same PID gains are attempted and the results are available in rows 4 and 5 in Table 1. The 3 s difference in settling time with a temperature difference of only 0.1 $^{\circ}C$

overshoot, offers an impressive level of repeatability which is further confirmation of the stability of the closed-loop control system.

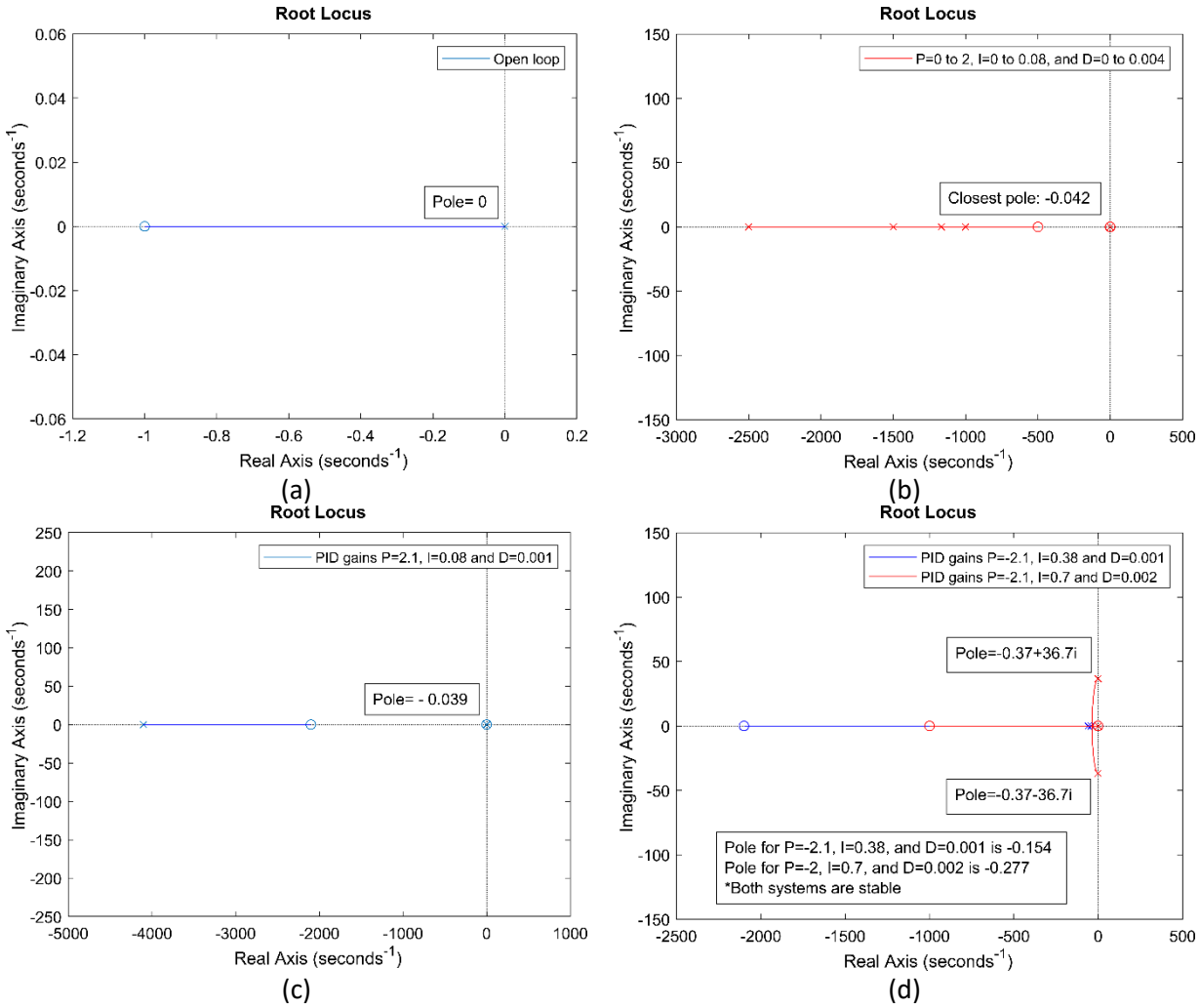

Fig. 6. *Root locus* diagrams for model obtained by Wiener-Hopf approach: for (a) open-loop correlation model of the plant, (b) closed-loop feedback control with P=0 t 2, I=0 to 0.08 and D=0 to 0.004, (c) the designed controller with P=2.1, I=0.08 and D=0.001, and (d) closed-loop control system with negative proportional PID controllers; one with P=-2.1, I=0.38 and D=0.001 and another with P=-2.1, I=0.7 and D=0.002.

Table 1. Summary of the robustness results for the hardware closed-loop control system.

PID Controller No.	P	I	D	Disturbance	$q\ (\frac{MW}{m^2})$	$T_w(^{\circ}C)$	Settling time (s)	Overshoot ($^{\circ}C$)
1	2.1	0.08	0.001	No, Static	0.2-1.8	110-135	155	1.3
2	-2	0.7	0.002	No, Static	0.2-1.8	110-135	129	0
3	-2	0.7	0.002	Dynamic (a=12mm, f=1.9Hz)	0.2-1.8	110-135	61	0.5
4	-2	0.7	0.002	Dynamic (a=0.02mm, f=400Hz)	0.2-1.8	110-135	70	0.6
5	-2	0.7	0.002	Dynamic (a=0.02mm, f=400Hz)	0.2-1.8	110-135	67	0.7

Table 2 shows the proposed controller performance compared with published findings. This comparison includes both simulation and experimentally measured results of temperature control and thermal management using spray cooling systems applied to electronic components and power plant (e.g. a superheater) - all without any vibrational disturbances. All of the cited literature noted the complexity of temperature control owing to nonlinearity, and the time-lag in the plant dynamics. Table 2 shows that all results have a higher settling time in comparison with the proposed control system while the overshoot is similar. The performance of the proposed closed-loop control system, resulting from use of negative proportional gains in the PID controller, has improved the settling time (by 37%) and the Coefficient of Performance (by 10.5%, COP). Overall, the proposed control system is stable and robust.

Table 2. Published temperature control and thermal management studies using spray cooling systems.

Authors (Date)	Apply on	Coolant	Test Piece	Requirements		Control variable	Controller	Robustness	
				$q\ (\frac{MW}{m^2})$	$T(^{\circ}C)$			Settling /rise time (s)	Overshoot $(^{\circ}C)$/(%)
Wang et al. [50] (2013), S[1]	IGBT[2]	water	SPC[3] wick	4	153	Pump voltage	PID	868/-	2.1 $^{\circ}C$
							Fuzzy-PID	682/-	0.98 $^{\circ}C$
Ding et al. [51] (2014), E[4]	IGBT	water	IGBT	0.64-0.68	91	Pump voltage	PID	155/43	NA (small)
							Fuzzy-PID	-	smaller
Sai and Reddy [52] (2016), S&E	Power Plant	water	Superheater	-	540	Coolant temp	PID	450/55	1.64/21.84
							Fuzzy-PID	344/70	1.4/14.62

[1]Simulation, [2]Insulated gate bipolar transistor, [3]Sintered porous copper wick, [4]Experimental

3. Experimental facilities

To generate measured data for the thermal management system shown in Figure 3, an experimental test rig has been used. The test rig comprises a 'plant', involving an instrumented test-piece, a shaker, a controller, and a data acquisition system (DAQ). The pipework, the plant, test-piece, control unit, and DAQ system, shown in Figure 8, are explained in the following subsections.

3.1. Spray rig pipework

The cooling loop in Figure 8 contains the following components: a system of pipework (1/8 to 1/2 inch stainless steel pipes and compression fittings), a condenser (Denso RDP 583), a heater module (2 x 345 W band-heaters), a miniature heat exchanger, a pump (Micropumps MGD100P), K and T-Type thermocouples, two digital pressure transducers (Omega PXM309), a low-flow turbine meter (Omega FLR1009ST-D), and a condenser and separator tank. Starting from the pump (No. 1 in Figure 3,), it circulates de-Ionized water within the piping system. The flow meter (No. 16) reads the real-time flow rate measurements. The 345 W feed heater (No. 2) heats the water supply to the nozzle inlet (No. 4) just before the test unit. Silicone rubber flexible pipework carries water to and from the test-piece. The vent (No. 5) and a drain (No. 6) respectively transfer evaporated and accumulated droplets inside the test chamber (No. 13), into the condenser (No. 9) and the separator tank (No. 11). Then, water (from condenser and the tank), flows down into the condenser tank. A header tank (No. 8) is fitted at the

highest point in the circuit to remove air and provide a positive feed. To complete the cooling cycle, the feed water cooler (No. 12) cools the condensate to a temperature below the operating maximum for the pump (100 ˚C).

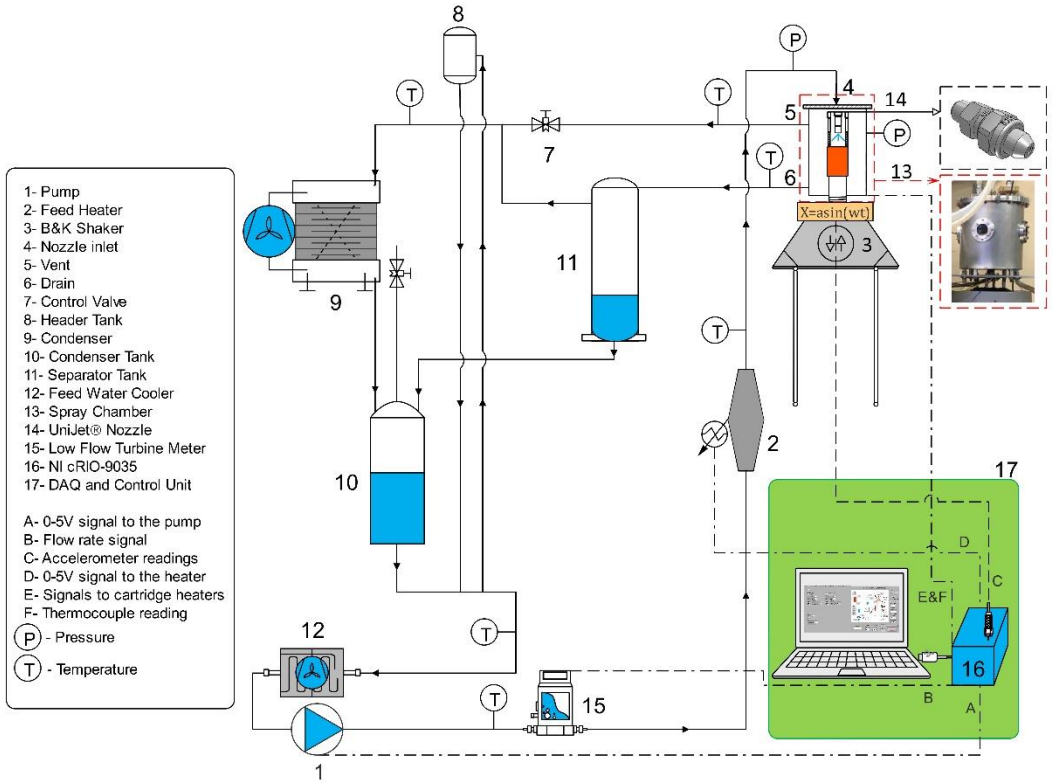

Fig. 8. Experimental test rig diagram with flat-surface test-piece, DAQ, and control unit.

3.2. A flat-surface test piece.

The test piece is positioned on top of a mechanical shaker (Bruel & Kjaer V555) flat-surface. The purpose of the flat-surface test piece shown in Figure 9 is to make it possible to investigate the capability of surface temperature control subject to heat flux requirements without, and with mechanical vibration.

Figure 9 shows the flat surface test-piece located in a cylindrical chamber, attached by a shaft, to the mechanical shaker. The test-piece and nozzle inside the chamber (fastened by two long bolts) can be shaken at different amplitudes and frequencies. The smooth copper test-piece, of 2 cm diameter, with thermal conductivity of 385 Wm/K, is heated electrically by six cylindrical Watlow 250W cartridge heaters vertically located in designated cylindrical holes inside the copper heater block. This is designed to provide strongly one-dimensional, heat conduction to the test-piece. Three T-Type thermocouples are used to measure temperature, the first of which is located 1 mm under the coolant surface of the test chamber, followed by two more thermocouples located evenly 5.5 mm below each other. These are to enable heat flux measurement. A shroud is also placed around the test-piece disc to guide the liquid film to the bottom of the chamber and out to drainage. A full-cone UNIJET® nozzle (TG tip Type) is located on top of the test chamber. All the joints and bolts are sealed with (LOCTITE® 5920™) copper paste able to intermittently stand a maximum temperature of 350˚C.

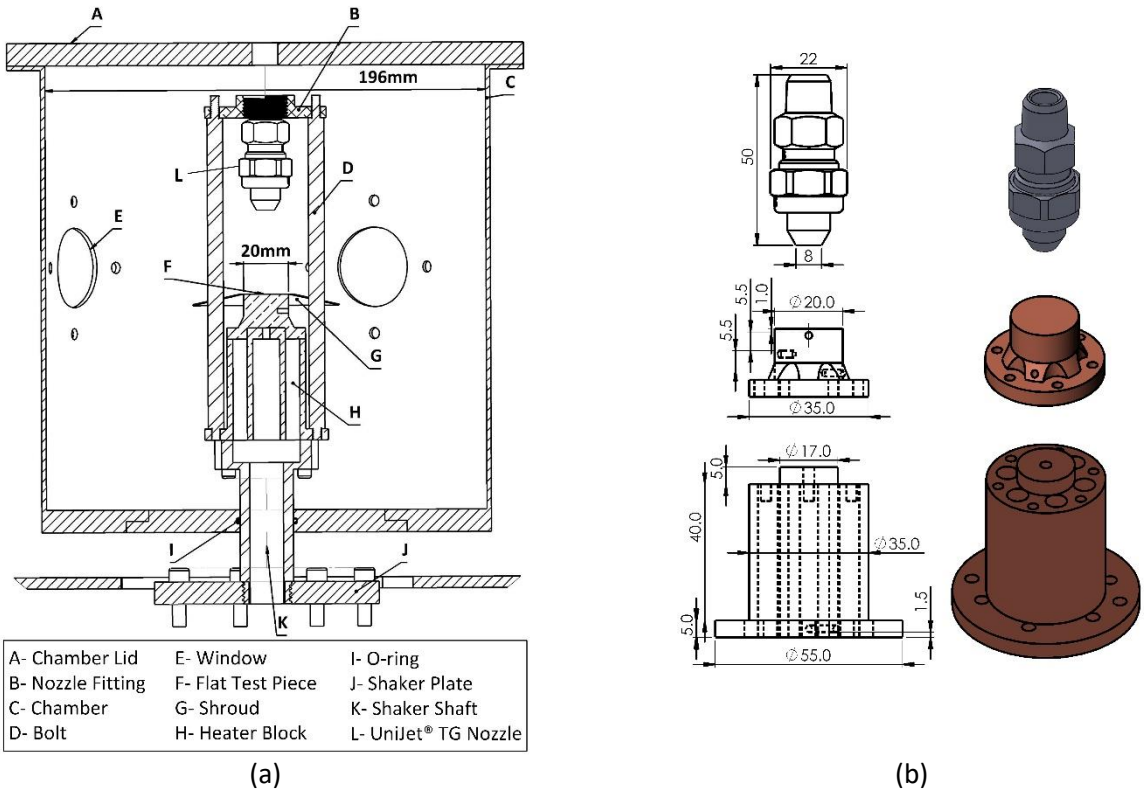

Fig. 9. Flat surface test-piece: (a) Chamber cross-section view, (b) From top to bottom, exploded view of UniJet® TG Nozzle, flat surface test piece and heater block (based on [18]).

3.3. Data acquisition system and control unit

The main components of the National Instruments data acquisition system are listed in Table 1. As shown in Figure 8, the main processor, an NI cRIO-9035 (No. 17), is connected through its modules to the pump (A), the flow meter (B), an accelerometer (C), the pre-Heater (D), cartridge heaters (E), test-piece thermocouples (F), and a host computer via ethernet. In the host computer, FPGA and LabVIEW programming are configured for DAQ and control purposes, and a human-machine interface unit. Pump flow-rate (in the Micropumps MGD100P controller), cartridge heaters (Watlow 250W), and the feed heaters are operated using 0 to 5 V control signals. These control signals are fed from an NI9264 module in the cRIO-9035 NI hardware. The flow meter, and pressure transducers signals, are collected by an NI 9205 unit. Separate power supplies are used for the pressure transducers, flow meter, and pump. Two (EVR-25BF) power regulators are used to obtain the 0 to 5 V signals (from an NI 9264) and convert them to the required power for the feed and the cartridge heaters. Thus, the test-piece receives constant and variable heat loads through the cartridge heater for different control scenarios. The feed heater has a PID temperature controller to tackle the thermal inertia of the coolant feed. Therefore, the PID controller keeps the system stable, in terms of staying within the evaporative phase, even during rapid changes in pump speed (e. g. doubling the flow rate will only cause a temperature difference of ±5 ˚C).

Table 3. Data Acquisition System details.

Module	Description	Absolute accuracy
NI cRIO-9035	Main processor, Control algorithm	-
NI 9205	Analog inputs – 16 Bit – 32 Channels (Differential and Single-Ended)	4.9 mV
NI 9212	Thermocouple module – 24 Bit – 8 Channels	-
NI 9230	AI 24 Bit – 3 Channels	-
NI 9264	AO 16 Bit – 16 Channels	17 mV
NI 9472	DO 24 V – 8 Channels	-

The DAQ and control system unit are configured to provide flexibility and high precision - which is quantifiable by following NI procedures (for which the system accuracy relative to the input, is quantified to be 0.177%, with example results shown in Table 3). In addition, the control unit hosts the desired control algorithms. Temperature measurements from the thermocouples (located 1 mm under the coolant surfaces in the test-piece) are used as a state variable for the PID controller in the FPGA CRIO-9035 hardware to control the pump voltage. The amplitude and frequency of the shaker is controlled using a Feedback Instruments FG600 signal generator with a pure sine wave option. A Piezotronics PCB A 353B15 accelerometer (10.27 mV/g, 1 Hz - 10 kHz) is attached to the bottom of the drive-shaft, bolted to the shaker head. Corresponding acceleration signals were measured by the NI 9230 sound and vibration input module. This enables surface temperature control of the actual spray evaporative cooling system to be achieved during experimentation in the presence of vibration.

4. Experimental test procedure and data reduction

Table 4 gives the test and operating conditions for the flat test-piece. All the tests were undertaken at atmospheric pressure for both *static* conditions (without vibration) and *dynamic* conditions (with vibration). Two harmonic dynamic cases have been considered: a low amplitude, high-frequency test at a=0.02 mm and f=400 Hz, and a high-amplitude, low frequency test at a=12 mm and f=1.9 Hz. These two cases are based on real vehicle test conditions [18], and had the highest heat flux deviations from the *static* case in steady-state conditions (a vibration amplitude of 12 mm is typical of vehicle-mounted hardware).

Table 4: Experimental test operating parameters.

$P_{chamber}$ (bar)	v (ml/min)	$T_{coolant}$ (°C)	H (mm)	Static	f (Hz) / a (mm)	1.9	400
1	120-225	80	17	✓	0.02	-	✓
					12	✓	-

4.1. Heat flux measurement

The Heat flux was estimated was calculated using a numerical solution of the one-dimensional transient heat conduction equation. The Fourier's one-dimensional transient conduction equation is as follows:

$$\frac{\partial^2 T}{\partial x^2} = \frac{1}{\alpha}\frac{\partial T}{\partial t} \tag{16}$$

where T, x, $\alpha = \frac{k}{\rho C_p}$, t are respectively the temperature, the position, the thermal diffusivity, and time. For copper, density ρ and specific heat C_p are 8900 kg/m^3 and 395 J/kg K. The finite deference method is to approximate the temperature at different points across the thickness of the test piece by using discrete time steps. To achieve this the material is discretized spatially into nodes. The spatial derivative on the LHS, and the temporal derivative on the RHS of equation (16) can be approximated by appropriate differences:

$$\frac{T_{(i+1)}^{(n)} - 2T_{(i)}^{(n)} + T_{(i-1)}^{(n)}}{\delta x^2} = \frac{T_{(i)}^{(n+1)} - T_{(i)}^{(n)}}{\alpha \delta T} \tag{17}$$

where subscript 'i' and superscript 'n' respectively refer to the current grid-point at time step. Grid points: 'i-1' and 'i+1' are those preceding and following grid-point 'i'. The time index 'n+1' stands for the following time step. To obtain the temperature at the interior grid points, equation (17) is rearranged as follows:

$$T_{(i)}^{(n+1)} = \delta Fo.T_{(i+1)}^{(n)} + (1 - 2\delta Fo)T_{(i)}^{(n)} + \delta Fo.T_{(i-1)}^{(n)} \tag{18}$$

where $\delta Fo = {\alpha \delta t}/{\delta x^2}$ is the Fourier number in which δt is the time step size, and δx is the distance between the grid points. Numerical stability criteria must be satisfied to achieve accurate results. The stability criteria are:

$$\delta Fo(1 + \delta Bi) < 0.5 \tag{19}$$

and

$$\delta t < \frac{0.5\ \delta x^2}{\alpha\left(1 + {\delta x h}/{k}\right)} \tag{20}$$

in which $\delta Bi = {\delta x h}/{k}$ is the Biot number. To meet the stability criteria, the distance between the first and third thermocouple is split into 22 nodes. Thus, the distance δx, between grid points, is $5.24 \times 10^{-4}\ m$. The time-step δt is set as $0.0004\ s$. The time-step is much smaller than the sampling rate, so the boundary temperatures (i.e. T1 and T3) must be interpolated between the measured temperatures. To interpolate the measured temperatures, piecewise polynomials are used.

Finally, the surface temperature gradient $\nabla T = {\partial T}/{\partial x}$, needed for the transient heat flux calculation, is obtained by a second-order backward difference scheme as follows:

$$\frac{\partial T}{\partial x} \approx \frac{3T_i - 4T_{i-1} + T_{i-2}}{2\ \delta x} \tag{21}$$

Table 5 gives the uncertainties in measured and derived quantities. To determine the uncertainty in the calculation of heat flux, a method by Moffat [53] has been used. The highest expected uncertainty in the calculation of heat flux, at maximum experimentally-measured data point of 1.96 MW/m^2 is found to be 2.6%.

Table 5. Uncertainties in the calculated and measured parameters.

Parameter	Uncertainty (%)	Units
Thermocouples	±0.4	℃
Volumetric flow rate	±0.6 (of full scale)	ml/min
Accelerometer frequency	±5	Hz
Pressure transducers	±0.25	bar
Diameter	±1	mm
Length	±1	mm
Heat flux	±2.6	MW/m^2

4.2. Setting operating conditions and control architecture

Safety and efficacy are of prime importance in thermal management. The question is whether the operating parameters and control algorithm is safe to implement in the hardware? Some minor deviations from desired setpoints can be acceptable, but the control scheme must not harm the hardware. Efficacy measures how effective the thermal management is in fulfilling the setpoints for variable loads.

To secure the safety and test the efficacy, the thermal management system is put through two phases of trials. '*Phase one*' is the safety trial. Using previously fitted correlations, operating parameters, setpoints, and thermal requirements, must be established. Moreover, since disturbances to the hardware take the form of vibrations of different amplitudes and frequencies (with resulting differences in acceleration), a dynamic correlation containing vibrational parameters and acceleration, must be considered in the thermal management system. In this regard, the following correlation models fitted to the UNIJET® nozzle data for *static* and *dynamic* cases (constructed in [18] using the Generalised Buckingham Pi method [41]) are used in the thermal management system i.e.:

$$Bo = 3.87 \times 10^{-2} Ja^{1.5573} \left(\frac{\rho_l^2 \sigma v}{{\mu_l}^3}\right)^{0.5008} \qquad \textit{Static} \qquad (22)$$

and

$$Bo = 1.24 \times 10^{-2} Ja^{1.3920} \left(\frac{\rho_l^2 \sigma v}{{\mu_l}^3}\right)^{0.9809} Re_V^{-0.9869} \left(\frac{a}{H}\right)^{0.4825} Ac^{0.4998} \qquad \textit{Dynamic} \qquad (23)$$

where Bo is Boiling number ($qH/\mu_l h_{fg}$). $Re_V = \rho_l a \omega d_H/\mu_l$ is the Vibrational Reynolds Number. $Ac = \omega^2 a/g$ is the Dimensionless Acceleration Number. Ja is Jacob number ($Ja = C_l \Delta T/h_{fg}$), which considers both convective and boiling heat transfer.

The thermal management system consults a step-by-step algorithm illustrated in Figure 10. First, the initial operating conditions to apply during each experiment, are set by the operator in a human-

machine interface (HMI). A graphical user interface (GUI) is configured in LabVIEW. The iterative part using the correlations, examines the boundaries, taking into consideration the applicability of the spray system in maintaining nucleate boiling.

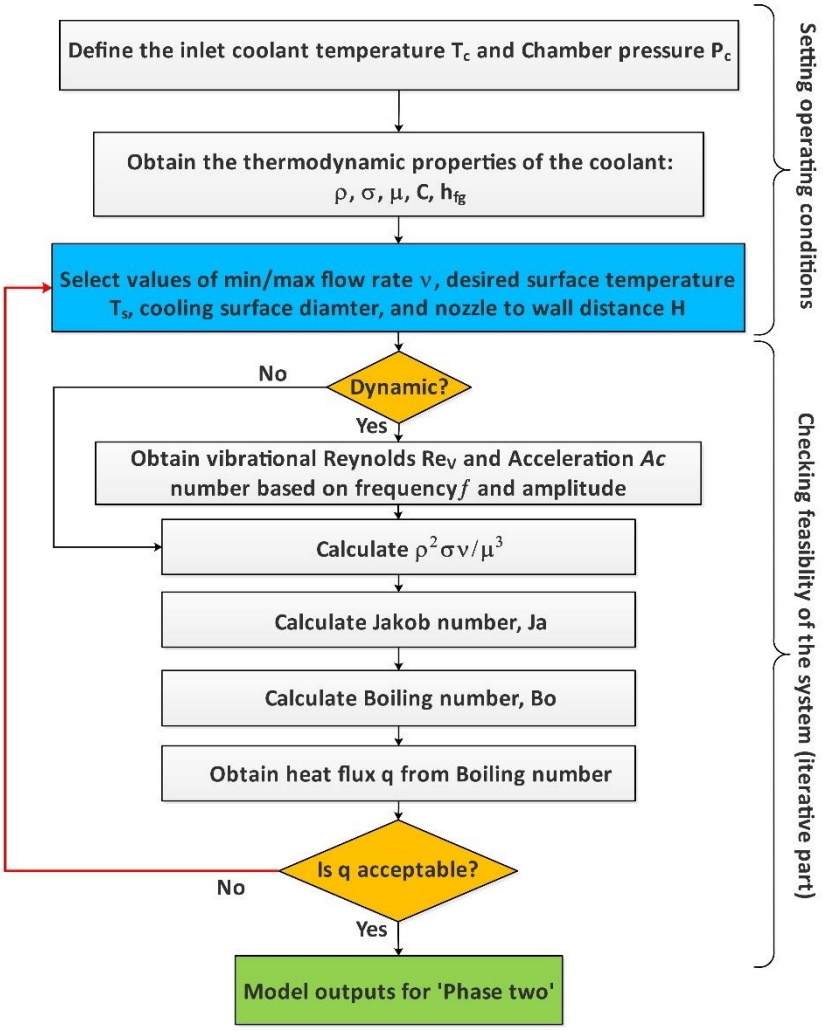

Fig. 10. Procedure for setting the operating conditions (Phase one: Safety test).

Choosing suitable 'setpoints' for the spray cooling system is as important and challenging as the control task [54]. The desired parameters (such as surface temperature and flow rate) and the requirements (e.g. heat flux), dependent on each other in a complex way. In addition, several *dynamic* cases produce substantially differences from the *static* results (heat flux and excess temperature). Therefore, the flow rates and spray patterns which result in effective cooling at the same setpoints are significantly different. The trade-off between setpoints, boundaries, spray specifications, and the specified requirements, have largely been determined by trial and error and prior experience [18].

Once the desired operating parameters and suitable boundaries are successfully fixed, the thermal management system moves to phase two. '*Phase two'* is the efficacy trial which demonstrates how well the control scheme works in tracking the trajectories induced by variable heat loads. This is done by an automatic control loop and a variable heat load generator. Figure 11 shows the sensor-based control

diagram containing two closed-loop PID controllers, a setpoint generator, the HMI, the test section, and the CompactRIO (NI cRIO-9035) with the FPGA containing I/O modules.

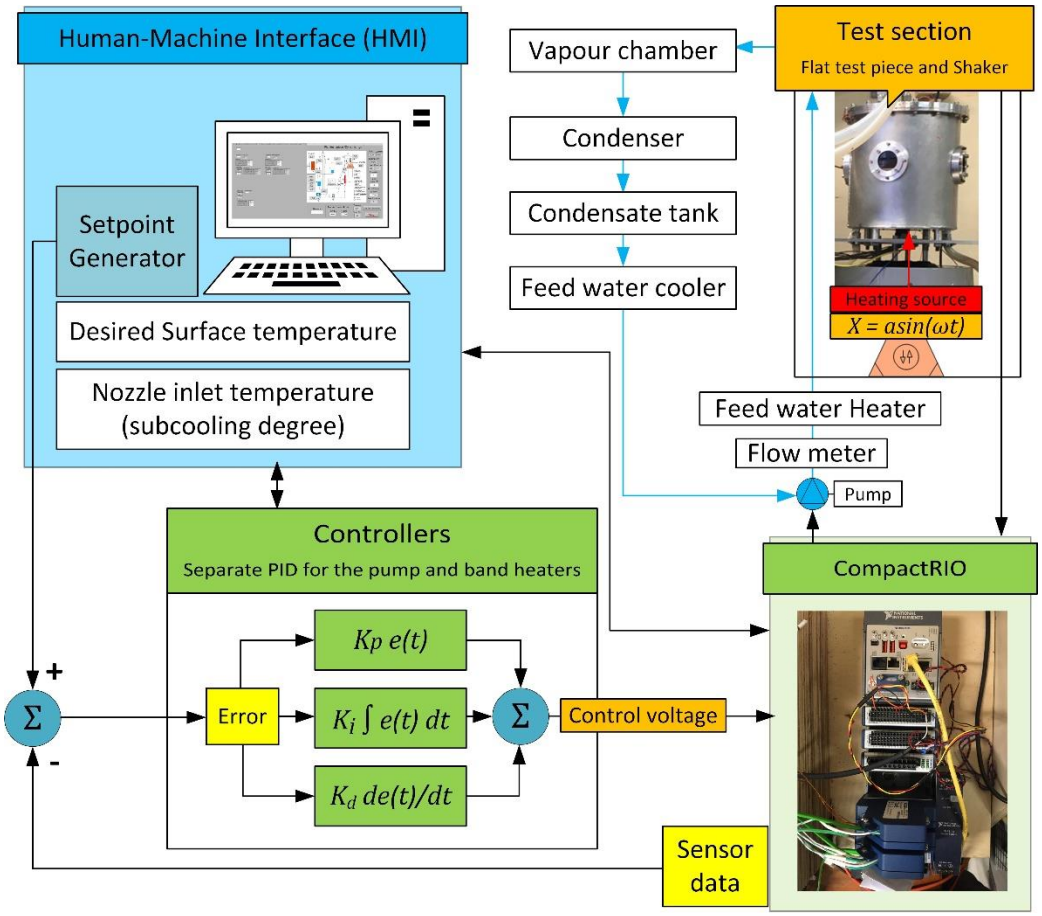

Fig. 11. Sensor-based control system diagram.

As can be seen in Figure 11, the flat test piece is exposed to displacement vibration of the form $X = \mathrm{asin}(\omega t)$ generated by the shaker. The PID controller tuning process is a manual activity which will be further explained in the results and discussion section. With a real-time processor, the FPGA in the CompactRIO sends the control signals through a PCI bus, and receives sensor data. This data requires high-speed logic and precise timing (e.g. the control signals to the power regulators for the cartridge heaters, band heaters, and the pump). Simultaneously, the human-machine interface (with a GUI) runs on the host computer to allow monitoring of the system state, and setting of the operating parameters.

5. Controller tuning and thermal management effectiveness in static and dynamic cases

The results for the flat test piece are given in the following three subsections. First, the manual tuning process of the surface temperature controller under *static* conditions, and the efficacy and robustness of the tuned controller, are assessed. Second, the impact of different controller gains on the control and thermal performance are discussed. In addition, the effectiveness of the thermal management system in energy savings for the pump is assessed in terms of coefficient of performance (COP). Finally,

the statically-tuned controller is used for *dynamic* conditions. The thermal management system has been tested in dynamic cases with the highest change from static results in order to check the efficacy and suitability of the proposed thermal management system.

5.1. Control system tuning and thermal management

Tuning of the surface temperature is a manual process. This has been achieved by trial-and-error using the closed-loop (feedback) control system plant hardware (explained in section 3.2). Figure 12 shows the temperature tracking and pump response to the applied setpoints, plus the induced heat flux. The temperature setpoints are typical requirements, and the operating ranges chosen are based on the thermal management needed for range-extended hybrid electric vehicle [25], or an all-electric vehicle cooling systems and electronic components (i.e. between 110˚C to 135˚C with the heat flux varying between 0.2 to 1.96 MW/m^2). After several trial-and-error attempts, with a negative feedback PID controller, the most acceptable gains which sufficiently minimised the overshoot and undershoot, and gave rise to a reasonably quick settling time during the same trajectories, were found to be P=2.1, I=0.08, and D=0.001 respectively. The settling time plays a vital role in thermal performance and energy efficiency of an internal combustion engine (ICE) [22] in range-extended hybrid electric vehicles. The thermal management systems required for most of the electronic components needs to have a high response (less than 100 seconds). The test rig and pipework used however, suffered from large thermal inertia. For this reason, the settling time for a change in temperature from the two setpoints of 110˚C to 135˚C in Figure 12a was 155 seconds. (Test rigs of miniature scale are suitable for the investigation of electronic component cooling).

Although the current focus is about testing the safety and efficacy of a spray-based thermal management system, several practical modifications that could be useful in reducing the settling time were examined in a further trial-and-error examination. It was found that the best option is to use a negative proportional gain (P=-2.1 in Figure 12b). It also found that a larger integral gain (comparing to Figure 12a) is beneficial keeping the same derivative gain. The negative proportional control gain would normally act to make the error worse (during the rise time). However, after some time (during the settling time), the integral action would dominate and correct the system. This effectively works to reduce the settling time from 155 s to 98 s (a very significant 37% improvement with a negligible 1 s increase in settling time in cooling during setpoints from 135˚C to 110˚C). Having a larger integral gain (0.38 compared to 0.08 in Figure 12a) finally adjusts the controller to maintain a negative feedback loop. Although a negative proportional controller is unusual since it can suffer from diminished phase-margin, and more severe overshoot, it can work well in certain circumstances. Based on the desirable cost benefit approach in developing the thermal management system proposed here, it has been demonstrated to be superior to a controller with a set of positive PID gains.

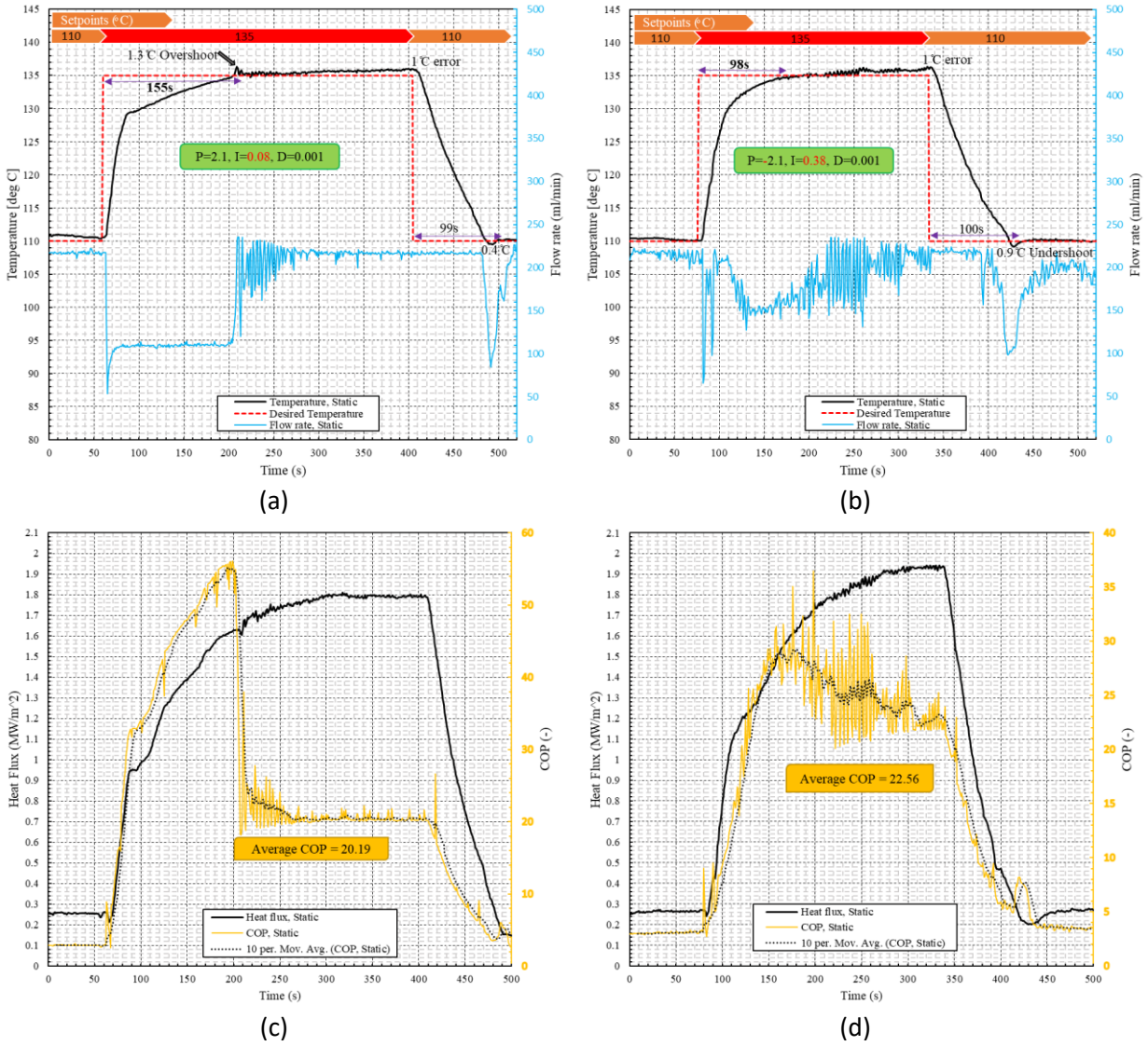

Fig. 12. *Static* case temperature tracking and the pump response to the applied setpoints: for (a) a positive proportional gain of P=2.1 with I=0.08 and D=0.001; (b) a negative proportional P=-2.1 with a large integral gain of I=0.38 and D=0.001; (c) and (d) Associated heat fluxes and COP measurements.

An explanation of why and how this type of controller is workable is evident from the pump response shown in Figure 12. For the regular PID controller (Figure 12a), the pump works at low speed and provides a flow rate of around 110 ml/min during the rise time. As soon as the error becomes positive, the flow-rate surges to its highest possible (around 230 ml/min), to address the overshoot. Conversely, for negative proportional PID gain (Figure 12b), the flow-rate peaks at around 220 ml/min during the rise time, then gradually drops to around 160 ml/min to reach the setpoint (135˚C). Based on previous experience in developing the correlations [18], it was noticed that there is a reverse trend when the splash diameter of the spray cone exceeds the area of the target surface. From that specific flow-rate (which can be deemed to be a 'threshold'), the volumetric flux reduces. Therefore, the heat transfer rate reduces accordingly - a hypothesis which is supported by Schwarzkopf et al. [55]. Note: it is actually stated on the UNIJET® nozzle manufacturer's data sheet, that the spray angle varies from 50˚ to 61˚, which means from the threshold, the heat transfer trend is the opposite: the higher the flow-rate, the

lower the heat transfer rate. The threshold flow-rate for the current experimental facility is around 200 ml/min. The same reverse trend has been observed by Zhang et al [38]. Thus, for the negative proportional PID controller, it was concluded that the shift between these two identified trends in heat transfer during the rise-time between 90 and 110 seconds (and 20 seconds of reverse trend) could have resulted in a further increase in the surface temperature and therefore a reduced settling time. This reverse trend above 200 ml/min is supported by Figure 12b when a steady-state error of 1 ˚C has occurred after passing the 200 ml/min. It should be noted that the differences between heat transfer rates before and after this threshold are subtle. However, the difference is of practical significance to be used for the purpose of adjusting the settling time to approach a more realistic time constant.

The proposed controller initially raised several important questions. The first question concerns why a lower flow-rate has not been considered by setting a minimum margin in order to have a smaller heat transfer rate to do the same task (i.e. a reduced settling time). The answer is: because the UNIJET nozzle is not able to produce a full cone spray at low mass flow rates, owing to the lower nozzle pressure differences. But imperfections in the spray flow field could change the expected trends in the cooling regimes. For example, a very low flow rate may not be able to maintain nucleate boiling for the required high heat fluxes and would therefore raise safety issues. For this reason, it has not been tested. In addition, a low flow-rate (e.g. around 50 ml/min, shown in figure 12c around 65 seconds) cannot achieve the required high heat fluxes. Moreover, a negative proportional PID gain which resulted in higher (rather than lower) volumetric flow rate during the rise time, would suppress the effects of vibration frequency owing to higher droplet velocity, which is consistent with the experimental results in [56]. This means during the rise time, that a negative-proportional gain PID controller could in theory be more reliable and adaptive in dynamic conditions including high-frequency cases. The dynamic results in section 4.3 will support the hypothesis.

The second question concerns other possible control solutions such as controlling the nozzle-to-surface distance, changing the degrees of subcooling [57], introducing a pulsating spray flow field [58, 59], to control either volumetric flux or flow-rate. Control of the nozzle-to-surface distance is not fast enough owing to the need for a mechanical mechanism in the form of a micro positioning slide [56]. The inertia of the feed heaters does not allow for rapid change in the inlet temperature required to control the degrees of subcooling. Also, the calculation of the volumetric flux to reflect a proper trend of the effective spray flow-rate impinged on the target surface, is not feasible in a design of a cooling system in which a minimum number of sensors is required. Even using existing empirical correlations for volumetric flux [60] such as given by:

$$\bar{\vartheta} = \frac{v}{\pi(Htan(\frac{\vartheta}{2}))^2} \tag{24}$$

needs a real time spray angle (ϑ) measurement which adds uncertainty to the plant. These issues leave room for improvement in the design of the test facility. For example, a high response speed solenoid valve would make possible a pulsating spray cooling module. The empirical correlations could be updated using Strouhal number ($St = \frac{fd}{v}$), to include the effect of a pulsed-spray flow field which would also benefit from a variable pump speed module. Overall, using a PID controller with a negative-proportional gain, although unusual, is still workable and fulfills the aims of this study. The efficacy and

robustness of a PID controller with negative-proportional gain, both without and with vibration is now examined.

5.2. The effect of PID controller gain changes without test-piece vibration: static cases

The effect of proportion gain changes

To better understand the effects of PID gain changes on the thermal performance and energy efficiency, a coefficient of performance (COP) has been included in figure 12c and 12d for the heat fluxes. The COP is the ratio of the heat removed to the pumping power given as:

$$COP = \frac{Q=q\pi d^2/4}{VI} \tag{25}$$

where, Q, V, and I are respectively: the heat removal by spray cooling, the voltage and the current supplied to the pump. To smooth out noisy fluctuations in the COP, a 10-sample moving average is used. As can be seen in Figure 12d, a negative proportional gain not only achieves a higher heat transfer rate, but also gives rise to an average COP=22.56 which is a 10.5% increase in the performance compared with a regular PID controller (Figure 12c).

Figure 13 shows results for two more sets of data obtained during the tuning process. First, up to 450 s, with a slightly larger integral gain (I=0.48), and after 450 s, with a smaller proportional gain (P=-2). A further decrease in the settling time was observed with the higher integral gain of I=0.48. This was caused by the integral gain counteracting the negative proportional gain after a longer time. Consequently, the spray flow-rate has been maintained in the reverse trend for a longer time. As was explained in Section 5.1, this is a reason for the faster settling time.

The lower heat transfer rate could be supported by the 1˚C steady-state error (at around 130 s) while the pump was operating at around 215 ml/min. A disadvantage of this, is that after the integral gain was compensated for, the effect of a negative proportional gain, the thermal management system was unstable and fluctuated between two trends (at 170 s in Figure 13a). This resulted in a 'bouncing' response, although a derivative gain twice the previous magnitude (i.e. D=0.002), was able to stabilize these fluctuations. The result for a smaller proportional gain (P=-2) is consistent. Since the integral gain is now dominant, the fluctuations occur earlier producing a longer settling time (but still faster than a positive proportional gain). But these PID settings are not recommended because the COP values of 22.25 and 22.52 in Figure 13b are not promising.

The effect of Integral gain changes

Figure 14 shows the effect of changing the integral gain in another trial and error experiment. The PID controller has the larger integral gain value of 0.7 but the same gains as Figure 13a. This was to reduce the fluctuations in the pump response to the temperature trajectory. In comparison to Figure 13a, the oscillations in the flow rate are reduced. The settling time increased since on average during the rise time the flow rate was in the reverse trend (i.e. above 200 ml/min) for a shorter time. The overshoot was slightly better, but the undershoot was worse (2.4˚C). A disadvantage to using a larger integral gain is the average COP, as is shown in Figure 9b, was less than those with a smaller integral gain of 0.48. As

soon as the influences of the PID gains were discovered through the tuning process, the thermal management system was challenged for *dynamic* cases. The next section delves into these results.

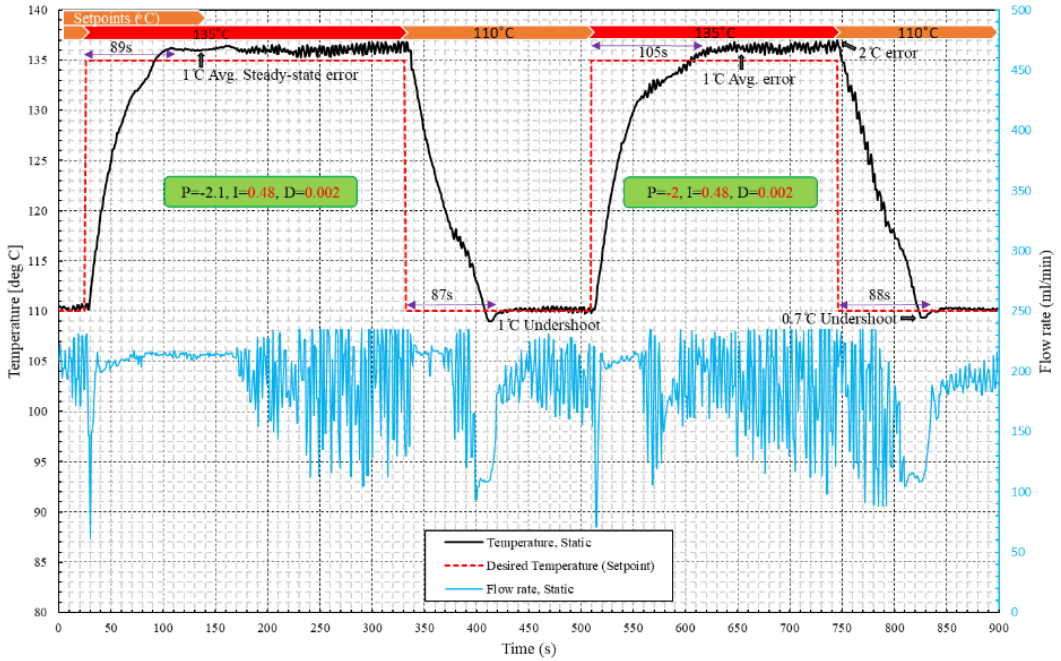

(a)

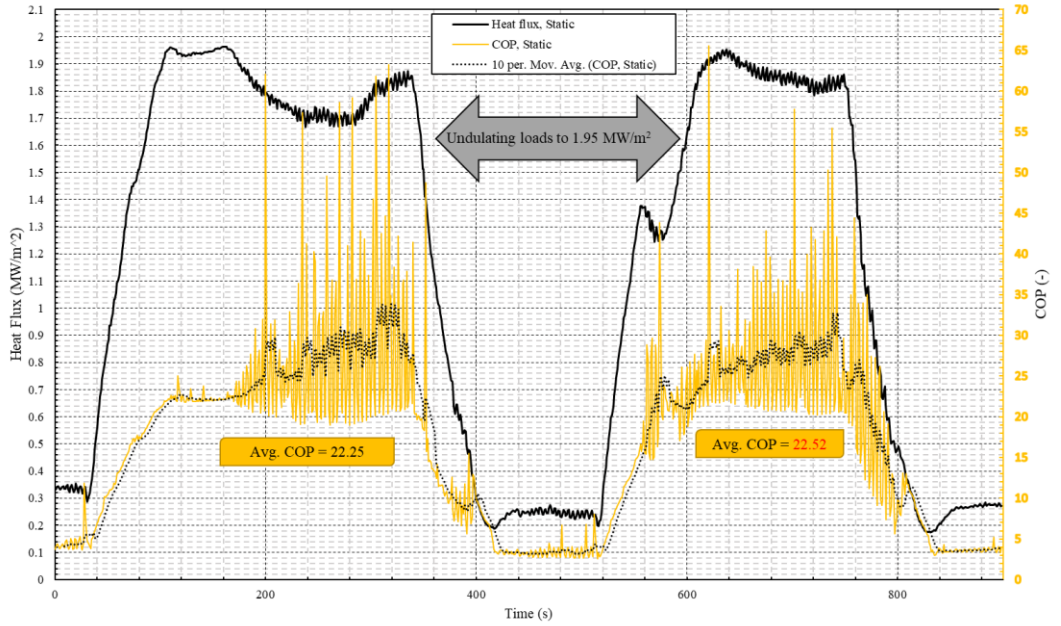

(b)

Fig. 13. *Static* case temperature response to the applied setpoints (between 110 and 135˚C) and load steps between 0.2 and 1.95 MW/m²: (a) Temperature tracking and the pump response for proportional gains of -2.1 and -2 with I=0.48 and D=0.002, (b) Associated heat flux and COP measurements.

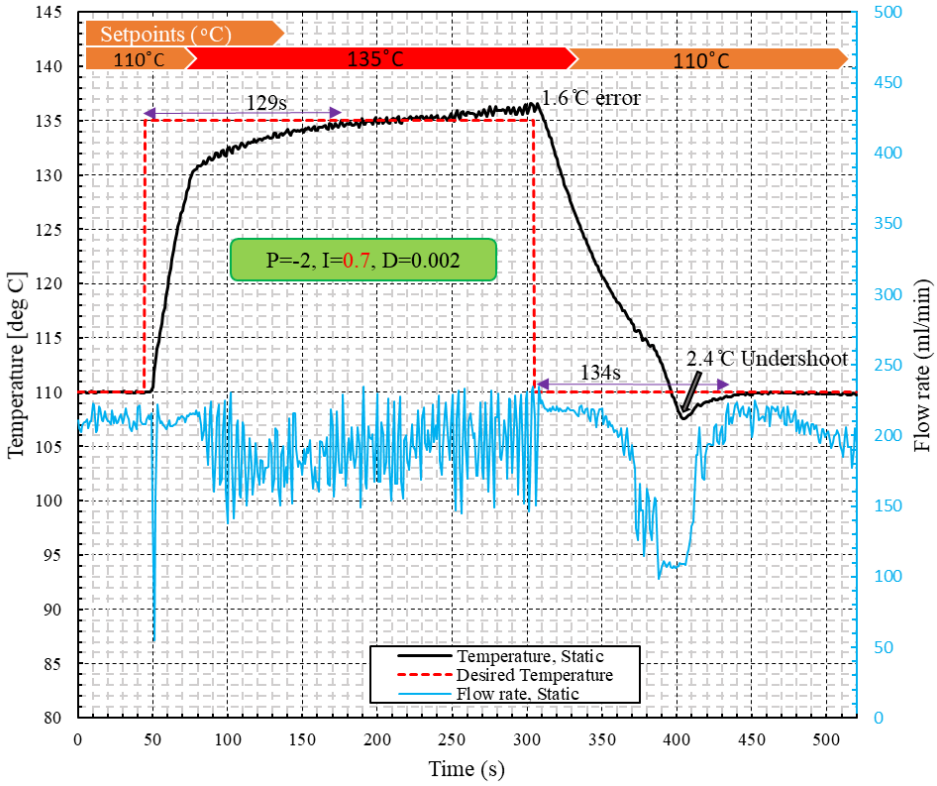

(a)

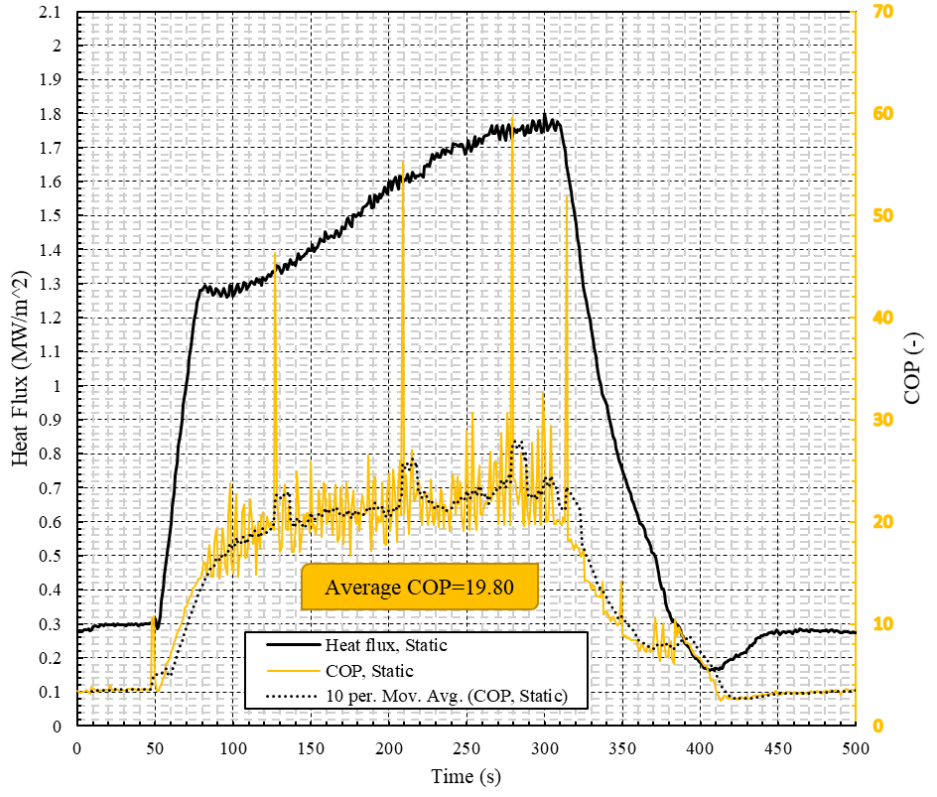

(b)

Fig. 14. *Static* case temperature response to the applied setpoints (between 110 and 135˚C) and load steps between 0.2 and 1.8 MW/m^2: (a) Temperature tracking and the pump response for a larger integral gain of 0.7; (b) Associated heat flux and COP measurements.

5.3. The effect of PID controller gain changes with test-piece vibration: dynamic cases

Experimental evidence shows that vibration generally lead to an attenuation of convective heat transfer rate. As a consequence, when the test-piece is made to vibrate, the controller instructs the pump to compensate for the deterioration in the rate of heat transfer. This consumes more power and thus reduces the COP for the *dynamic* cases below those of *static* conditions. This section investigates the performance of the controller with vibration, in particular, the effect different gains have on heat flux.

Figure 15 shows a data set during the tuning process for large amplitude vibration a=12 mm at a frequency f=1.9 Hz. On the left-hand side of Figure 15 up to 840 seconds, a trial involving an unsuccessful set of PID controller gains with is compared with a PID controller with larger gains. From 840 seconds onwards, a much smaller set of gains was also considered to allow comparison. It can be seen that there are oscillations in the temperature, also the undulating pump response for the higher gains clearly indicates the significant influence of different gains. Having the smaller PID controller gain values of P=-1, I=0.4, and D=0.001, smooths both the pump response and the undulating temperature. Furthermore, the settling time is also improved. The problem with small gains was the 1.8˚C steady-state error produced, also leads to a longer return time.

Taking into consideration the detrimental gain effect for dynamic cases, plus the need to test the adaptive capability of a PID controller tuned for static cases, a PID controller with gain values: P=-2, I=0.7, and D=0.002 was chosen for results in Figure 16. The gains in Figure 16 were the same for the static case in Figure 14. As expected, the rise time is improved compared with the static case owing to the impeding effect of vibration. Moreover, a lower average COP value of 18.06 in Figure 16b (compared to 19.80 for the static case) indicates increased power consumption for the same heat flux (up to 1.8 MW/m^2). Beyond t=400 s, a PI controller with gains: P=-2, I=0.7, D=0 (rather than D=0.002) is tested to establish whether the derivative gain is genuinely having any influence. Broadly speaking, derivative gain in a PID controller has the effect of reducing overshoot. It is evident that the differences between overshoot and undershoot, with and without the derivative gain, actually justifies derivative control. Furthermore, the subtle difference in COP, being smaller for the PID, suggests the pump is managed by the derivative gain.

Figure 17 shows a dynamic case at high frequency. The test piece was shaken at an amplitude of a=0.02 mm and frequency f=400 Hz. The same PI and PID controller gains for the large amplitude case appear to successfully manage the pump speed to enable it to achieve surface temperature tracking. The results in Figure 17 show a reasonable rise time, overshoot, and undershoot, and that successful thermal management for loads between 0.2 MW/m^2 to 1.8 MW/m^2 was achieved. Also, the effect of derivative gain was consistent with the previous explanation (i.e. error reduction and less settling time for PID controller). Similarly, there is a respective increase in overshoot, undershoot, and settling time of 0.3 - 0.4 ˚C, 0.4 - 0.5 ˚C and 16 - 20s, for the PI controller. As expected, the COP for the PID controller, shown in Figure 17b, were lower than for the PI controller. Finally repeatability of the results was examined by introducing an extra step load for the PID controller. The resulting temperature differences were 0.1˚C for overshoot and undershoot, and a 3 s difference in the rise and settling times. The coolant flow rate during the repeatability test was similar to the previous load step, suggesting that overall, the experimental measurements were repeatable.

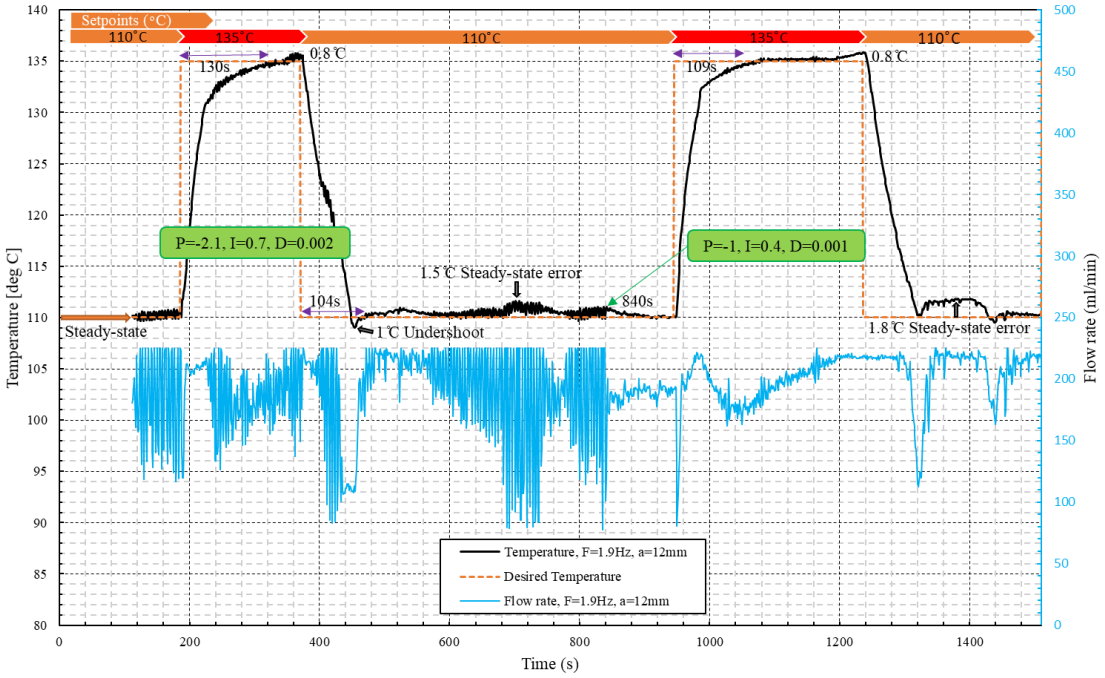

(a)

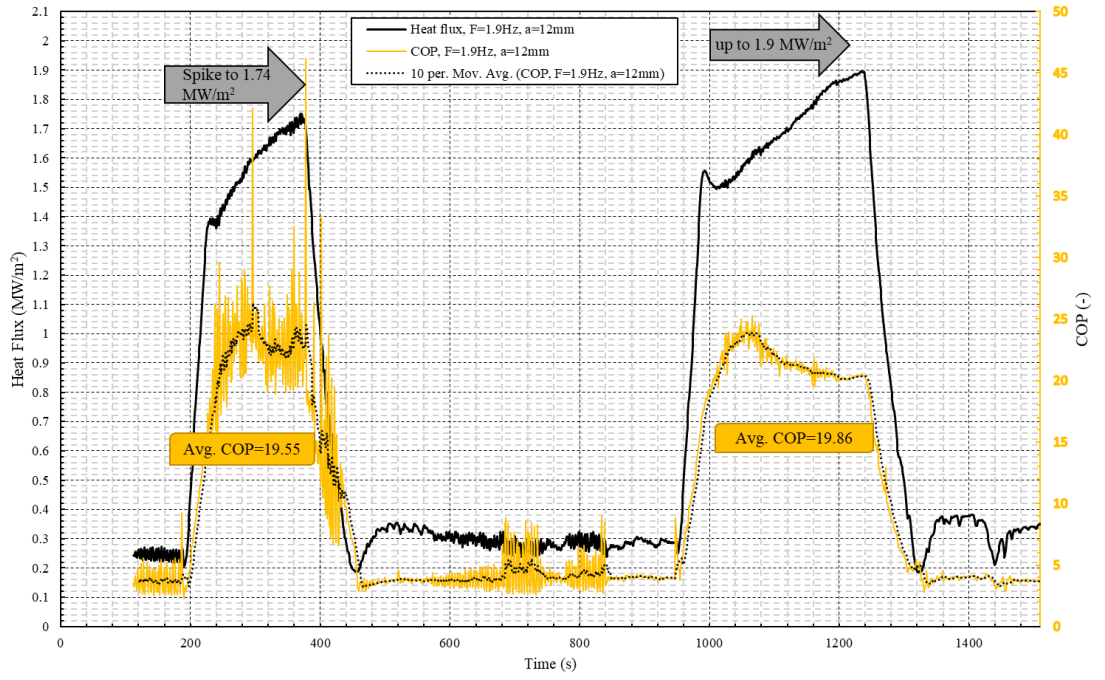

(b)

Fig. 15. Temperature response induced by applying temperature setpoints and load steps for large-amplitude vibration of 12mm: (a) Temperature tracking and pump response for a PID with large gains following by a smaller gain PID, (b) Heat flux disturbances and real-time COP measurements.

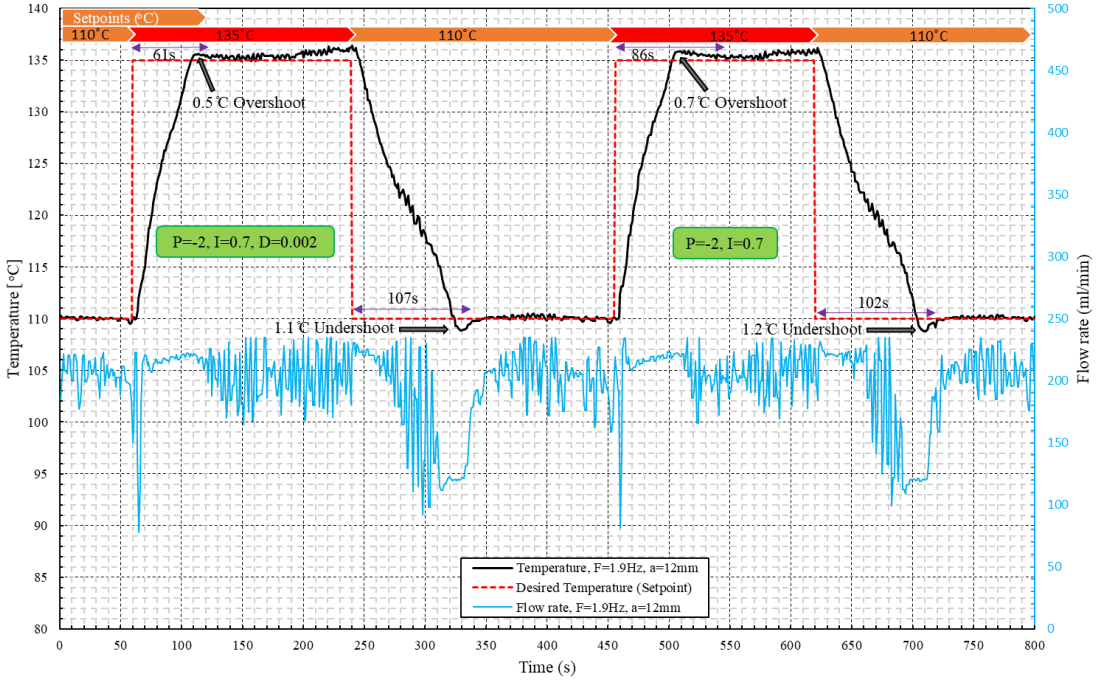

(a)

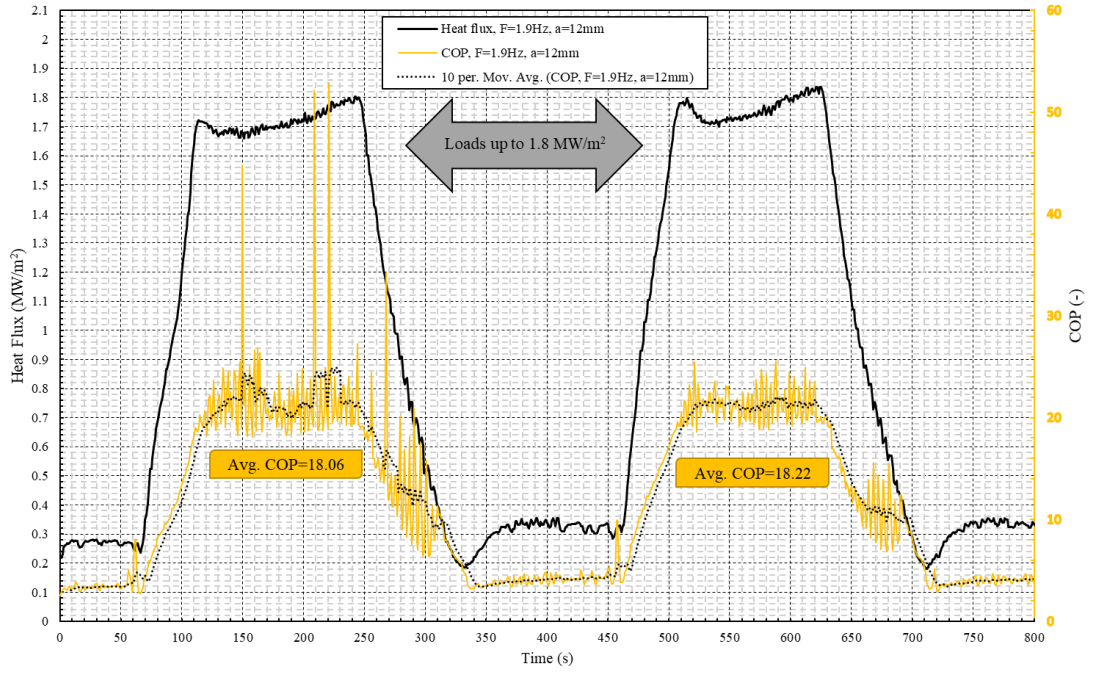

(b)

Fig. 16. Temperature response induced by applying setpoints (between 110 and 135˚C) and load steps (up to 1.8 MW/m²) for large-amplitude vibration of 12mm: (a) Temperature tracking and pump response for a PID and a PI controller, (b) Heat flux disturbances and real-time COP measurements.

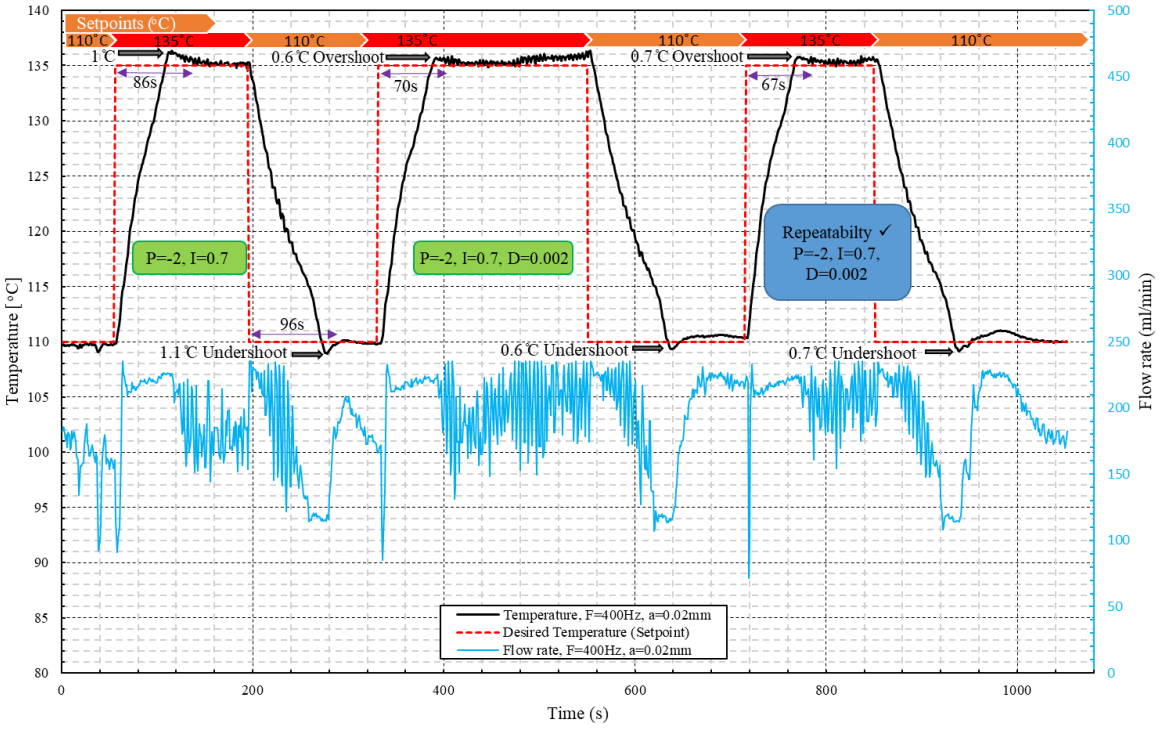

(a)

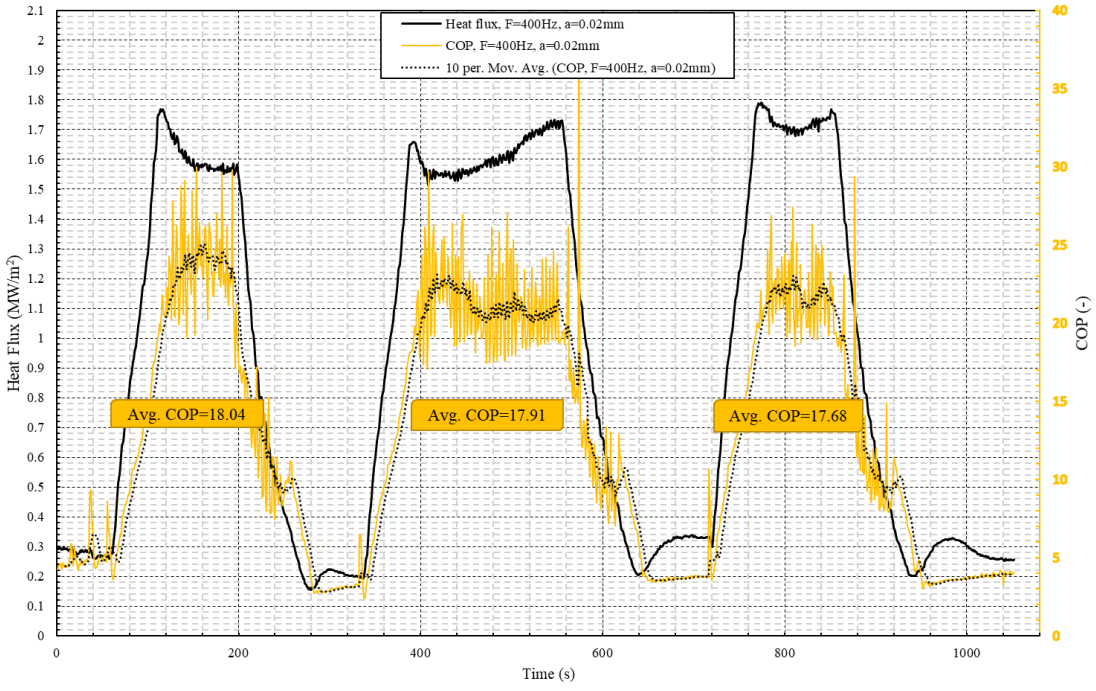

(b)

Fig. 17. Temperature response induced by applying setpoints (between 110 and 135˚C) and load steps for high-frequency vibration of 400Hz: (a) Temperature tracking and pump response for PI and PID controllers, (b) Heat flux disturbances and real-time COP measurements.

6. Conclusions

A thermal management system, using spray evaporative cooling, has been designed, built, and experimentally-tested to assess its ability to control the temperature of heat-generating hardware subject to heat flux requirements. To model the system, an experimentally calibrated dynamic correlation model has been used to represent the physics of spray evaporative cooling of a flat test-piece exposed to vibration. To enable stability analysis of the thermal management system using a PID controller, the nonlinear correlation model has been replaced by an optimum 1^{st}-order linear model obtained by solving an appropriate Wiener-Hopf equation. This allows practical stability assessment of closed-loop temperature control for particular choices of PID controller gains. To verify the predicted control system performance via simulation, experimental measurements appropriate to automotive vehicle component applications, includes large-amplitude, low frequency vibration, at 12 mm and 1.9 Hz, and at low amplitude, high-frequency vibration, at 0.02 mm and 400 Hz. The effects of different PID controller gains on the thermal management system performance under static and dynamic conditions, has been assessed using a coefficient of performance (COP), defined as the ratio of heat power removal to the required pumping power. The main conclusions of the study are:

1. Trial-and-error tuning of the hardware suggests that using the best PID gains for a closed-loop control system can give very reasonable thermal management performance in terms of temperature control, % overshoot, settling time, and coefficient of performance (COP).
2. A negative proportional-gain PID controller, with positive integral and derivative gains, was found to be stable, and proved to be superior in terms of performance, to a PID controller with all positive gains. In fact the use of this negative proportional-gain PID controller gave the largest coefficient of performance (COP) at 22.56, and a reduction of 37% in the settling time compared to a PID controller with positive gains.
3. The best negative proportional-gain PID controller for the *static* case also gave the best performance in *dynamic cases* confirming the robustness of the controller.

Acknowledgments

The authors acknowledge support for the development of the experimental facilities, in terms of funding from the EPSRC (under Contract Number: EP/M005755/1), and technical support from Ford Dunton UK, Ford Dearborn USA, Denso Italy, and the Ricardo Technical Centre Shoreham UK. The authors also wish to acknowledge additional financial and technical support from the Ricardo Shoreham Technical Centre, UK.

References

[1] J. Kim, J. Oh, H. Lee, Review on battery thermal management system for electric vehicles, Applied Thermal Engineering, 149 (2019) 192-212.
[2] S. Jafari, T.J.A.S. Nikolaidis, Thermal Management Systems for Civil Aircraft Engines: Review, Challenges and Exploring the Future, *Applied Sciences*, 8 (2018) 2044.
[3] J. Doty, K. Yerkes, L. Byrd, J. Murthy, A. Alleyne, M. Wolff, S. Heister, T.J.J.o.T. Fisher, H. Transfer, Dynamic thermal management for aerospace technology: review and outlook, 31 (2017) 86-98.
[4] Z. Mera, N. Fonseca, J.-M. López, J. Casanova, Analysis of the high instantaneous NOx emissions from Euro 6 diesel passenger cars under real driving conditions, Applied energy, 242 (2019) 1074-1089.
[5] J. Benajes, A. García, J. Monsalve-Serrano, S. Martínez-Boggio, Emissions reduction from passenger cars with RCCI plug-in hybrid electric vehicle technology, Applied Thermal Engineering, 164 (2020) 114430.
[6] S. Tsiakmakis, G. Fontaras, J. Dornoff, V. Valverde, D. Komnos, B. Ciuffo, P. Mock, Z. Samaras, From lab-to-road & vice-versa: Using a simulation-based approach for predicting real-world CO2 emissions, Energy, 169 (2019) 1153-1165.
[7] K. Ranasinghe, K. Guan, A. Gardi, R.J.E. Sabatini, Review of advanced low-emission technologies for sustainable aviation, 188 (2019) 115945.
[8] D.C. Deisenroth, M.J.E. Ohadi, Thermal Management of High-Power Density Electric Motors for Electrification of Aviation and Beyond, 12 (2019) 3594.
[9] B.J. Brelje, J.R.J.P.i.A.S. Martins, Electric, hybrid, and turboelectric fixed-wing aircraft: A review of concepts, models, and design approaches, Progress in Aerospace Sciences, 104 (2019) 1-19.
[10] S. Jafari, J.F. Dunne, M. Langari, Z. Yang, J.-P. Pirault, C.A. Long, J. Thalackottore Jose, A review of evaporative cooling system concepts for engine thermal management in motor vehicles, Proceedings of the Institution of Mechanical Engineers, Part D: Journal of Automobile Engineering, 231 (2017) 1126-1143.
[11] J.T. Jose, J.F. Dunne, J.-P. Pirault, C.A. Long, Spray Evaporative Cooling System Design for Automotive Internal Combustion Engines, in: ASME 2018 Internal Combustion Engine Division Fall Technical Conference, American Society of Mechanical Engineers, 2018, pp. V002T007A008-V002T007A008.
[12] G. Liang, I.J.I.J.o.H. Mudawar, M. Transfer, Review of spray cooling–Part 1: Single-phase and nucleate boiling regimes, and critical heat flux, 115 (2017) 1174-1205.
[13] G. Liang, I. Mudawar, Review of spray cooling–Part 2: High temperature boiling regimes and quenching applications, International Journal of Heat and Mass Transfer, 115 (2017) 1206-1222.
[14] J. Breitenbach, I.V. Roisman, C.J.E.i.F. Tropea, From drop impact physics to spray cooling models: a critical review, 59 (2018) 55.
[15] Y.-K. Lin, Z.-F. Zhou, Y. Fang, H.-L. Tang, B.J.A.T.E. Chen, Heat transfer performance and optimization of a close-loop R410A flash evaporation spray cooling, 159 (2019) 113966.
[16] C. Cai, H. Liu, M. Jia, H. Yin, R. Xie, P.J.I.J.o.T.S. Yan, Numerical investigation on heat transfer of water spray cooling from single-phase to nucleate boiling region, 151 (2020) 106258.
[17] M. Langari, Z. Yang, J.F. Dunne, S. Jafari, J.-P. Pirault, C.A. Long, J.T.J.T.J.o.C.M.F. Jose, Multiphase computational fluid dynamics–conjugate heat transfer for spray cooling in the non-boiling regime, 10 (2018) 33-42.
[18] A. Sarmadian, J. Dunne, C. Long, J.T. Jose, J.-P. Pirault, C. Rouaud, Heat flux correlation models for spray evaporative cooling of vibrating surfaces in the nucleate boiling region, International Journal of Heat Mass Transfer, 160 (2020) 120159.
[19] C.A. Long, Essential heat transfer, Longman, 1999.
[20] C. French, Taking the heat off the highly boosted diesel, SAE Transactions, (1969) 1700-1716.
[21] I. Finlay, R. Boyle, J. Pirault, T. Biddulph, Nucleate and film boiling of engine coolants flowing in a uniformly heated duct of small cross section, in, SAE Technical Paper, 1987.
[22] S. Jafari, J.F. Dunne, M. Langari, Z. Yang, J.-P. Pirault, C.A. Long, J.T.J.J.o.T.S. Jose, E. Applications, Control of Spray Evaporative Cooling in Automotive Internal Combustion Engines, 10 (2018) 041011.

[23] M.R. Panão, A.L. Moreira, Intermittent spray cooling: a new technology for controlling surface temperature, International Journal of Heat and Fluid Flow, 30 (2009) 117-130.
[24] H. Bostanci, S. Altalidi, S. Nasrazadani, Two-phase spray cooling with HFC-134a and HFO-1234yf on practical enhanced surfaces, Applied Thermal Engineering, 131 (2018) 150-158.
[25] I. Mudawar, D. Bharathan, K. Kelly, S. Narumanchi, Two-phase spray cooling of hybrid vehicle electronics, IEEE Transactions on Components and Packaging Technologies, 32 (2009) 501-512.
[26] X. Zhao, Z. Yin, B. Zhang, Z. Yang, Experimental investigation of surface temperature non-uniformity in spray cooling, 146 (2020) 118819.
[27] S. Lei, Y. Shi, G.J.A.T.E. Chen, A lithium-ion battery-thermal-management design based on phase-change-material thermal storage and spray cooling, 168 (2020) 114792.
[28] X. Feng, S. Zheng, D. Ren, X. He, L. Wang, X. Liu, M. Li, M. Ouyang, Key characteristics for thermal runaway of li-ion batteries, Energy Procedia, 158 (2019) 4684-4689.
[29] Y. Xie, X.-j. He, X.-s. Hu, W. Li, Y.-j. Zhang, B. Liu, Y.-t. Sun, An improved resistance-based thermal model for a pouch lithium-ion battery considering heat generation of posts, Applied Thermal Engineering, 164 (2020) 114455.
[30] J. Du, Y. Liu, X. Mo, Y. Li, J. Li, X. Wu, M. Ouyang, Impact of high-power charging on the durability and safety of lithium batteries used in long-range battery electric vehicles, Applied energy, 255 (2019) 113793.
[31] Y. Yang, L. Yang, X. Du, Y.J.A.T.E. Yang, Pre-cooling of air by water spray evaporation to improve thermal performance of lithium battery pack, 163 (2019) 114401.
[32] Y. Ding, Z.P. Cano, A. Yu, J. Lu, Z. Chen, Automotive Li-ion batteries: current status and future perspectives, Electrochemical Energy Reviews, 2 (2019) 1-28.
[33] M. Varini, P.E. Campana, G. Lindbergh, A semi-empirical, electrochemistry-based model for Li-ion battery performance prediction over lifetime, Journal of Energy Storage, 25 (2019) 100819.
[34] S.K. Mishra, A. Arora, H. Chandra, Application of Vibration on Heat Transfer-A Review, i-Manager's Journal on Future Engineering and Technology, 15 (2019) 72.
[35] A. Sathyabhama, S. Prashanth, Enhancement of boiling heat transfer using surface vibration, Heat Transfer—Asian Research, 46 (2017) 49-60.
[36] H. Atashi, A. Alaei, M. Kafshgari, R. Aeinehvand, S. Rahimi, New Pool Boiling Heat Transfer in the Presence of Low-Frequency Vibrations Into a Vertical Cylindrical Heat Source, Experimental heat transfer, 27 (2014) 428-437.
[37] Z. Wang, Y. Xing, X. Liu, L. Zhao, Y.J.A.T.E. Ji, Computer modeling of droplets impact on heat transfer during spray cooling under vibration environment, 107 (2016) 453-462.
[38] Y. Zhang, L. Pang, M. Liu, Y. Xie, Investigation of spray cooling: Effect of different heater surfaces under acceleration, International Communications in Heat and Mass Transfer, 75 (2016) 223-231.
[39] K. Sone, K. Yoshida, T. Oka, Y. Abe, Y. Miri, A. Nagashima, Spray cooling characteristics of water and FC-72 under reduced and elevated gravity for space application, in: IECEC 96. Proceedings of the 31st Intersociety Energy Conversion Engineering Conference, Vol. 2, IEEE, 1996, pp. 1500-1505.
[40] K. Baysinger, K. Yerkes, R. Harris, T. Michalak, J. McQuillen, Design of a microgravity spray cooling experiment, in: 42nd AIAA Aerospace Sciences Meeting and Exhibit, 2004, pp. 966.
[41] A.A. Sonin, A generalization of the Π-theorem and dimensional analysis, Proceedings of the National Academy of Sciences, 101 (2004) 8525-8526.
[42] P. Setlur, J.R. Wagner, D.M. Dawson, E. Marotta, An advanced engine thermal management system: Nonlinear control and test, IEEE/ASME transactions on mechatronics, 10 (2005) 210-220.
[43] J.F. Eberth, J.R. Wagner, B.A. Afshar, R.C. Foster, Modeling and validation of automotive “Smart” thermal management system architectures, in, SAE Technical Paper, 2004.
[44] J.R. Wagner, V. Srinivasan, D.M. Dawson, E.E. Marotta, Smart thermostat and coolant pump control for engine thermal management systems, in, SAE Technical Paper, 2003.
[45] J.R. Wagner, M.C. Ghone, D.W. Dawson, E.E. Marotta, Coolant flow control strategies for automotive thermal management systems, in, SAE Technical Paper, 2002.

[46] J. Wagner, E. Marotta, I. Paradis, Thermal modeling of engine components for temperature prediction and fluid flow regulation, in, SAE Technical Paper, 2001.
[47] R.R. Henry, J. Koo, C. Richter, Model development, simulation and validation, of power train cooling system for a truck application, in, SAE technical paper, 2001.
[48] D. Mortari, H.R. Johnston, L.I. Smith, Least-squares solutions of nonlinear differential equations, in: 2018 Space Flight Mechanics Meeting, 2018, pp. 0959.
[49] A.D. Poularikas, Adaptive filtering: Fundamentals of least mean squares with MATLAB®, CRC Press, 2017.
[50] J. Wang, Y. Li, J. Wang, Transient performance and intelligent combination control of a novel spray cooling loop system, Chinese Journal of Aeronautics, 26 (2013) 1173-1181.
[51] Y. Ding, Y. Li, Y. Li, W. Chen, H. Zhang, D. Li, Intensive cooling method for power electronic component with high heat flux, in: 2014 13th International Conference on Control Automation Robotics & Vision (ICARCV), IEEE, 2014, pp. 163-168.
[52] T. Sai, K. Reddy, Design of fuzzy gain scheduler for superheater temperature control in power plant, in: 2016 2nd International Conference on Control, Instrumentation, Energy & Communication (CIEC), IEEE, 2016, pp. 521-525.
[53] R.J. Moffat, Describing the uncertainties in experimental results, Experimental thermal and Fluid Science, 1 (1988) 3-17.
[54] B. Petrus, K. Zheng, X. Zhou, B.G. Thomas, J. Bentsman, Real-time, model-based spray-cooling control system for steel continuous casting, Metallurgical and materials transactions, 42 (2011) 87-103.
[55] J. Schwarzkopf, T. Cader, K. Okamoto, B. Li, B. Ramaprian, Effect of spray angle in spray cooling thermal management of electronics, in: ASME 2004 Heat Transfer/Fluids Engineering Summer Conference, American Society of Mechanical Engineers Digital Collection, 2004, pp. 423-431.
[56] X. Zhao, B. Zhang, X. Xi, Z. Yin, Analysis and prediction of single-phase and two-phase cooling characteristics of intermittent sprays, International Journal of Heat Mass Transfer, 133 (2019) 619-630.
[57] M. Visaria, I. Mudawar, Effects of high subcooling on two-phase spray cooling and critical heat flux, International Journal of Heat Mass Transfer, 51 (2008) 5269-5278.
[58] M.R. Panão, A.L. Moreira, Intermittent spray cooling: a new technology for controlling surface temperature, International Journal of Heat Fluid Flow, 30 (2009) 117-130.
[59] S. Somasundaram, A.A. Tay, An experimental study of closed loop intermittent spray cooling of ICs, Applied Thermal Engineering, 31 (2011) 2321-2331.
[60] I. Mudawar, K. Estes, Optimizing and predicting CHF in spray cooling of a square surface, Journal of Heat Transfer, 118 (1996) 672-679.

Nomenclature

$\bar{\vec{v}}$	average volumetric spray flux, $\bar{\vec{v}} = \frac{v}{\pi(Htan(\frac{\alpha}{2}))^2}$ (m^3s^{-1}/m^2)
A	surface area (m^2)
a	Amplitude of vibration (m)
Ac	dimensionless acceleration, $Ac = \omega^2 a/g$ (-)
Bo	Boiling number, $Bo = qH/\mu_l h_{fg}$ (-)
C	specific heat (kJ/kg k)
d	diameter(mm)
D	derivative gain
e	error
f	Frequency (Hz)
h	specific enthalpy (kJ/kg)
H	height (m)
I	Integral gain
Ja	Jakob number, $Ja = C_l \Delta T/h_{fg}$ (-)
k	thermal conductivity (W/m K)
P	pressure (kPa)
P	proportional gain
q	heat flux (kW/m^2)
Re	Reynolds number, $Re_V = \rho_l a \omega d_H/\mu_l$ (-)
St	Strouhal number, $St = \frac{fd}{v}$ (-)
T	temperature (K)
t	Time (s)
V	voltage
We	Weber number, $We = \rho_l(u_m^2 or \bar{\vec{v}}^2)d_{32}/\sigma$ (-)
I	current
Q	heat (kW)
x	position (m)
δBi	Biot number, $Bi = {xh}/{k}$ (-)

Greek symbols

ΔT	temperature difference (K)
v	volumetric flow rate (m^3/s)
α	thermal diffusivity $\alpha = \frac{k}{\rho C_p}$ (m^2/s)
θ	temperature ratio
μ	dynamic viscosity (Kg/m s)
ρ	density (kg/m^3)
σ	surface tension (N/m)
ω	angular velocity (Hz)
ϑ	spray cone angle

Subscripts/superscripts

at	atmospheric
c	coolant
ch	chamber
f	liquid phase
g	vapour phase and gravitational force
H	heating surface
i	grid point
l	liquid
n	time step
ref	reference temperature
s	surface
sat	saturation
sub	subcooling
V	vibration
w	Wall

Acronyms

CHF	critical heat flux
COP	coefficient of performance
FIR	finite impulse response
GUI	graphical user interface
HMI	human-machine interface
ICE	internal combustion engine
MSE	mean square error
PID	proportional integral derivative

List of Figures

List of Tables

Proceedings of the 7th International Conference on Fluid Flow, Heat and Mass Transfer (FFHMT'20)
Canada – June, 2020
Paper No. XXX (The number assigned by the OpenConf System)
DOI: TBA

The effect of surface vibration on spray evaporative cooling

A. Sarmadian[1], J. F. Dunne[1], C. A. Long[1], J-P Pirault[1], J. Thalackottore-Jose[1], Cedric Rouaud[2],

[1]Department of Engineering and Design/University of Sussex
BN1 9QT, Brighton, UK
a.sarmadian@sussex.ac.uk

[2]Ricardo plc
West Sussex BN43 5FG, Shoreham-by-Sea, UK

Abstract **–** An experimental investigation of the effect of surface vibration on spray evaporative cooling has been undertaken using a dynamic test rig. The horizontal circular test section involved a spray nozzle on top of a shaker being shaking at different frequencies and amplitudes to examine the effect of vibration on the nucleate boiling regime. The combination of the two-phase spray cooling and dynamic surface conditions has not previously been studied. The results clearly show that dynamic surface conditions influence nucleate boiling. In general, the evidence shows that vibration impedes heat transfer. The influence of amplitude and frequency are shown however not to have the same trend for all the excess temperatures. Depending on the mechanism, combinations of amplitude and frequency can either increase or decrease the heat transfer coefficient compared with the static cooling surface.

Keywords**:** Spray Cooling, Vibration, Frequency, Amplitude, Nucleate boiling, Heat transfer

1. Introduction

Spray cooling is fast becoming a promising method of cooling systems with high heat removal requirements such as electronic and electrical components. In recent years, there has been increasing interest in spray cooling mechanisms for different cooling purposes [1], including high-flux at low-temperature [2], and at high-temperature [3]. Spray evaporative cooling has several major advantages in comparison to the conventional forced-convection cooling. First, it benefits from higher heat transfer rates owing to the role of the latent heat transfer mechanism compared to the sensible heat transfer mechanism associated with conventional single-phase. Second, spray cooling requires much lower mass-flow rates. Therefore, spray evaporative cooling results in a substantial reduction in the required coolant mass, and additionally in a significant reduction in pumping power. Moreover, owing to the nature of two-phase flow, it provides a more uniform temperature across all cooling surfaces, therefore eliminating hot spots. This key aspect is vital in a number of cases including thermal management of electronic components and battery stacks in electric vehicles, where there is an essential requirement to protect against overheating and fires. Further possible applications can be found such as in cooling highly-boosted internal combustion engines in conventional vehicles (to improve the knock control), and for cooling range extender engines in hybrid electric vehicles, Jafari et al. [4].

A comprehensive understanding of the different flow regimes of spray cooling plays a vital role in thermal management for the design of future cooling systems. In general, the flow patterns associated with sprays impinging on a surface consists of a nucleate-boiling mode, a transition followed by critical heat flux (CHF), and a film-boiling regime [5]. **Fig. 1** shows a typical flow pattern map using the coordinates of heat flux and superheat temperature (i.e. the difference between the sprayed surface temperature and the saturation temperature). In fact, much of the current literature on spray cooling pays particular attention to the models and correlations that can predict such heat transfer mechanisms, which are important for design. By contrast, vibration is considered to have an impact on the heat transfer [6]. A recent study by Sathyabhama et al. [7] investigated the pool-boiling. (There are no published experimental studies in the literature addressing spray cooling involving nucleate boiling). The results of the study [7] concluded that at low frequencies (10Hz) and amplitudes (2.5 mm) vibration has a positive influence on heat transfer coefficient (by 26%) compared to when there is no vibration. At high frequencies and amplitudes, vibration however was shown to impede boiling. It would therefore be

expected that there is an intermediate optimum value. For spray cooling in two-phase flow nucleate boiling, the only investigation in the presence of surface vibration can be found in [8], involving a numerical study of single and multiple droplet impact on the surface performed by the volume of fluid (VOF) method [8]. Such a preliminary study considering only a number of droplets, cannot be used in modelling, thermal management, or system design of spray cooling systems especially under dynamic conditions (e.g. automotive). Therefore, there is a significant gap for further investigation. The objectives of the current study is, for the first time, to investigate the effect of vibration on nucleate boiling for a full-cone spray impinging on a flat circular copper test piece driven by a shaker.

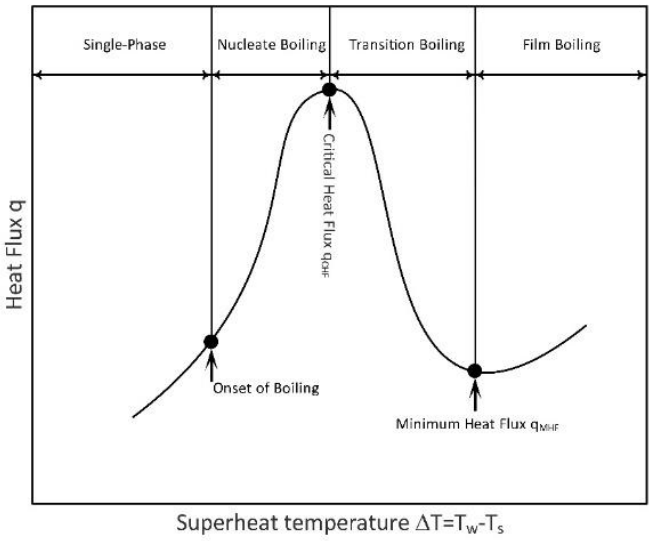

Fig. 1. Spray flow pattern map (boiling curve)

2. Experimental test rig and data collection

The test rig comprises the following components: a pump (Micropumps MGD100P) suppling de-ionised water to a full-cone UNIJET® nozzle (TG tip Type, ranging from 0.16 litres/min at 1.5 bar, to 0.39 litres/min at 10 bar) which is located on top of the test chamber. Second, a separation tank where vapour and liquid are separated and delivered to the condenser and condensate tank. Third, an air-cooled condenser (Denso RDP 583) where vapour from the test chamber is vented through a throttle valve; a miniature heat exchanger which is used to cool the condensate (at exit from the condenser) to below the maximum operating temperature of the pump (100 ˚C). Two 345W band-heaters (see the feed heater in **Fig. 2**) with a controllable 0 to 5 V power regulator (United Automation, EVR-25BF, AC Burst Fire Controller) used to heat the feed-water to the nozzle to obtain different degrees of sub-cooling (i.e. the difference between saturation and inlet temperatures) by a PID controller in CRIO-9035 National Instrument. Two digital pressure transducers (Omega PXM309) are linked to the data acquisition system to provide a constant record of the chamber pressure and the nozzle pressure difference. A low-flow turbine meter (Omega FLR1009ST-D) is installed just after the pump to measure the flow-rate, and is used as a state variable for the PID controller in FPGA CRIO-9035 to control the pumping voltage, in order to be able to have constant flow rates during experimentation. A header tank is also fitted at the highest point in the circuit to remove air and provide a positive feed. **Fig. 2** demonstrates the overall schematic view of the test rig.

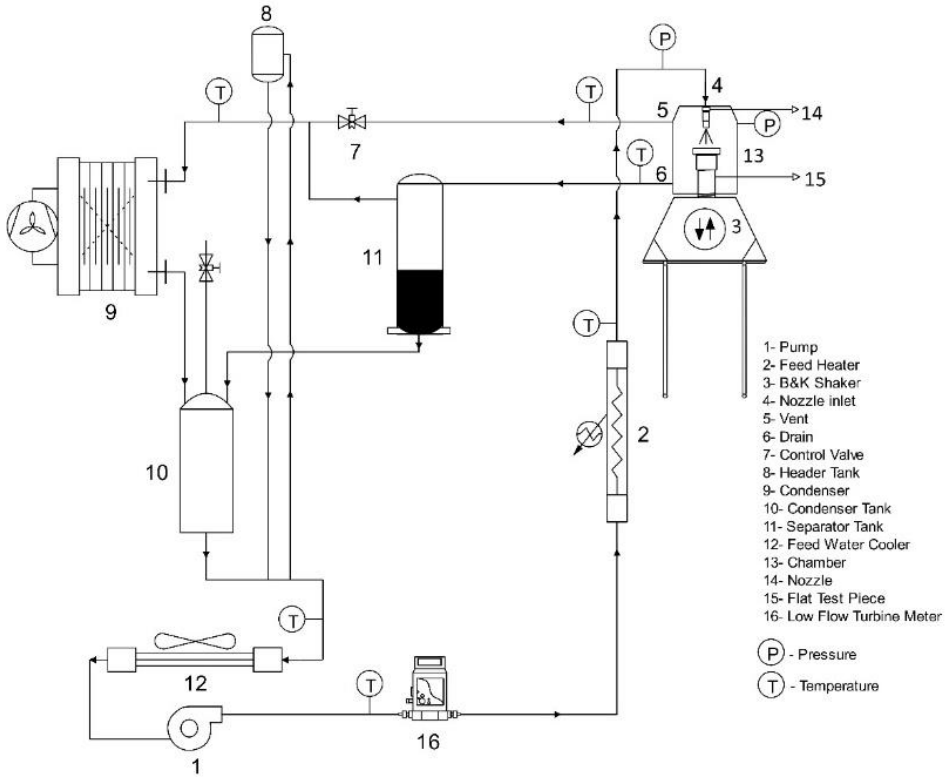

Fig. 2. Schematic view of the test setup

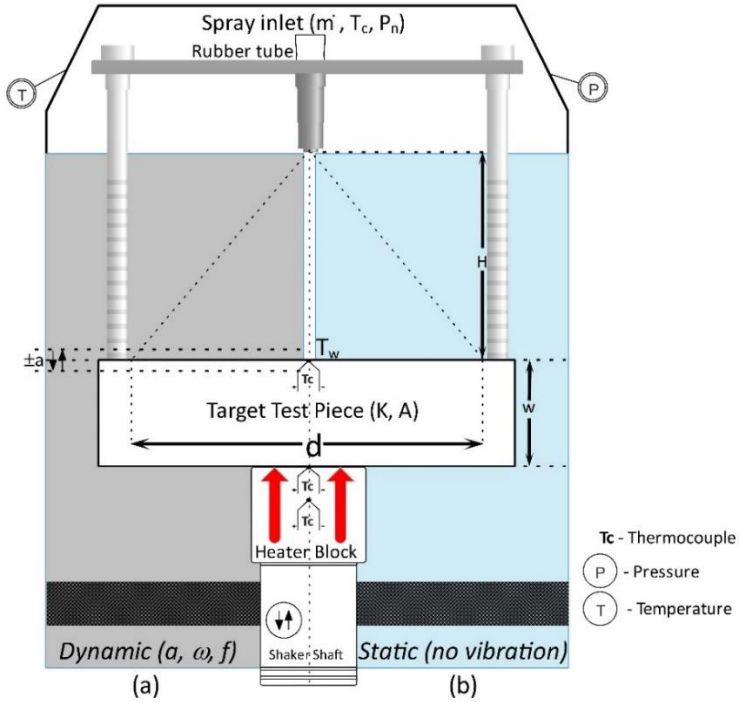

Fig. 3. Spray system configuration inside the chamber under: (a) dynamic and (b) static conditions. (Not to scale.)

As shown in Fig. 3, the test piece is located in a chamber mounted on a Bruel & Kjaer V555 mechanical shaker. Thus, the test piece and the nozzle inside the chamber can be simultaneously shaken at different frequencies (f) and amplitudes (a). A Piezotronics PCB A 353B15 accelerometer (10.27 mV/g, 1 Hz - 10 kHz) is attached to the bottom of the drive shaft attached to the shaker head. Corresponding acceleration signals were measured by a National Instruments data acquisition system. The amplitude and frequency of the shaker was controlled using a Feedback Instruments FG600 signal generator with pure sine wave option. The test chamber is heated by six Watlow 250W cartridge heaters controlled by 0 to 5 V signals from a NI9264 module and a power regulator (EVR-25BF). The test piece is a copper disc with a radius of 1 cm. It has a smooth surface and a thermal conductivity of 385 Wm/K. Three T Type thermocouples are used, the first of which is located 1 millimetre under the coolant surface of the test chamber followed by two more evenly located 5.5 millimetres underneath each other to facilitate the heat flux measurement capabilities.

3. Data Reduction

A test plan for this empirical study is supplied in **Table 1**. Overall, 18 test runs have been undertaken under *static* and *dynamic* conditions (respectively with and without vibration) at frequencies varying from 10 to 400 Hz, and with amplitude in the range from ±0.02 to ±01 mm.

Table 1: Test plan and operating parameters.

$P_{chamber}$ (bar)	v (ml/min)	$T_{coolant}$ (℃)	Static	f (Hz) / a (mm)	10	100	200	400
1	140, 160, and 180	Constant at 80±1.5°C	✓	0.02	-	✓	✓	✓
				0.1	✓	-	-	-
				1	✓	-	-	-

During each test-run the data for any new state was collected between 3 to 7 minutes (depending on the thermal inertia) after changing the cartridge heater loads to make sure that the system reached the steady state conditions. A test-run for the case study involving *static* cooling surfaces with a flow rate of 180 ml/min was conducted twice for the purposes of checking repeatability of the test facility. The heat flux was calculated using a solution for the one-dimensional conduction equation:

$$q = -K\frac{dT}{dx} \tag{1}$$

using measurements taken from thermocouples embedded in the test piece, where K, dT, and dx are the thermal conductivity, the temperature difference, and the distance between the top and the bottom thermocouples located in the test piece, respectively.

4. Results and discussion

In this section, the effect of volumetric flow rate on the heat flux, and the effect of frequency and amplitude of vibration will be separately investigated. Finally, the equivalent heat flux curves (with and without mechanically-induced vibration) will be compared to better understand the influence of vibration on the nucleate boiling regime.

4.1. Static – effect of volumetric flow rate and mass flux

Fig. 4 shows the results obtained for *static* test-runs representing the steady state data points of heat flux versus the excess temperature ($\Delta T_{excess} = T_{surface} - T_{saturation}$) at three different flow rates of 140, 160, and 180 ml/min. The highest and the lowest heat fluxes are 3072.5 kW/m^2 and 271.5 kW/m^2 at 160 and 180 ml/min. As the trend

shows, having higher flow-rate resulted in a higher heat-flux from 140 to 160 ml/min. However, it has a reverse trend after a threshold at around 180 ml/min where the equivalent heat fluxes are less than those for 160 ml/min. This effect is assumed to stem from the fact that after a higher mass-flow rate, and consequently a higher pressure difference around the nozzle (here from 1.6 to 2.3 bar), the angle of the spray cone increases. Increased spray cone-angle at 180 ml/min means lower mass-flux covering the test piece, and therefore it provides less heat-transfer compared to that for a lower volumetric flow rate of 160 ml/min. However, as can be seen from **Fig. 4** (b) (a zoomed-plot of **Fig. 4**) at the excess temperature of 4 ˚C, there is a reverse in the trend where the heat-flux of higher volumetric flow rate is noticeably higher. The reason for this trend can again be due to the effect of increased cone-angle, which changes the direction of droplet impact onto the thin liquid film on top of the surface. Such an incident makes a lower penetration impact lead to the advent of nucleation owing to less suppression force in front of bubble departure from nucleation sites. Leading the advent of the nucleate boiling regime to a lower surface temperature, enhances the heat transfer coefficient at the same excess temperature.

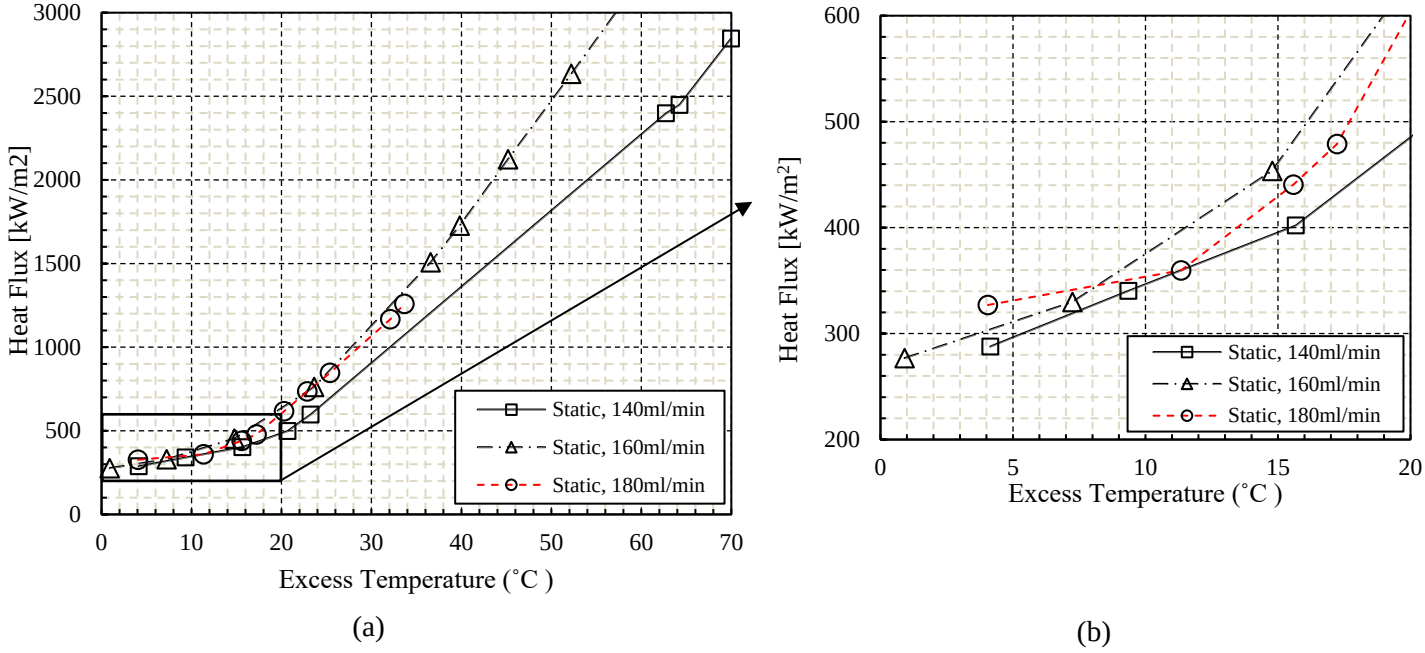

Fig. 4. The trend of heat flux changes with the change of excess temperature for *static* test runs.

4.2. Dynamics – the effect of frequency and amplitude

To understand how frequency can affect the trend of the nucleate boiling curve, results with quite a low amplitude of 0.02 mm, and three high frequencies of 100, 200, and 400 Hz, are shown in **Fig. 5**. Considering the lower excess temperature regions (i.e. from 0 to 30 ˚C) heat-flux does not follow the changes in frequency, although a small decrease in heat-flux from increasing frequency is evident in the results. On the other hand, for the excess temperature above 30 ˚C, the gradient of the curves is identical to the heat transfer coefficient slopes at a higher angle by increasing frequency. This effect gets more intense with a higher flow-rate of 180 ml/min as the gaps between the curves gradually expand by any increment in frequency and excess temperature. This clearly indicates that there is a definite effect of frequency on the heat transfer either augmentation or deterioration depending on the mechanism of nucleation.

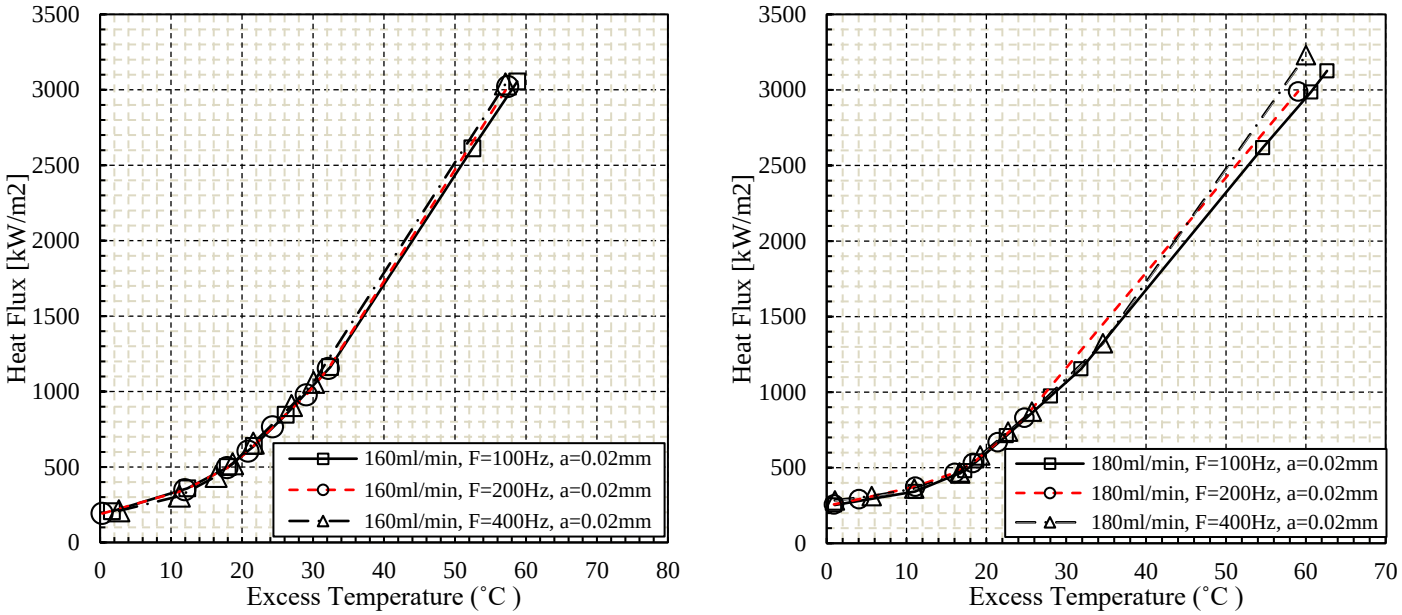

Fig. 5. Heat flux over the excess temperature for *Dynamic* test runs with the amplitude of 0.02 mm and frequencies up to 400 Hz.

To inspect the *static* and *dynamic* results for any amplitude influence on the heat flux, the low frequency data of 10 Hz, with amplitudes of 0.1 mm and 1 mm are shown on **Fig. 6**, with the equivalent heat-flux curves for static points. By adding to the amplitude, the represented lower values of the heat flux indicate that the amplitude itself impedes the heat transfer rate. It should be noticed that the effect is more visible on the lower excess temperatures (less than 30 ˚C) which adversely affects the incipient nucleate boiling regime, the exact opposite of the frequency's influence.

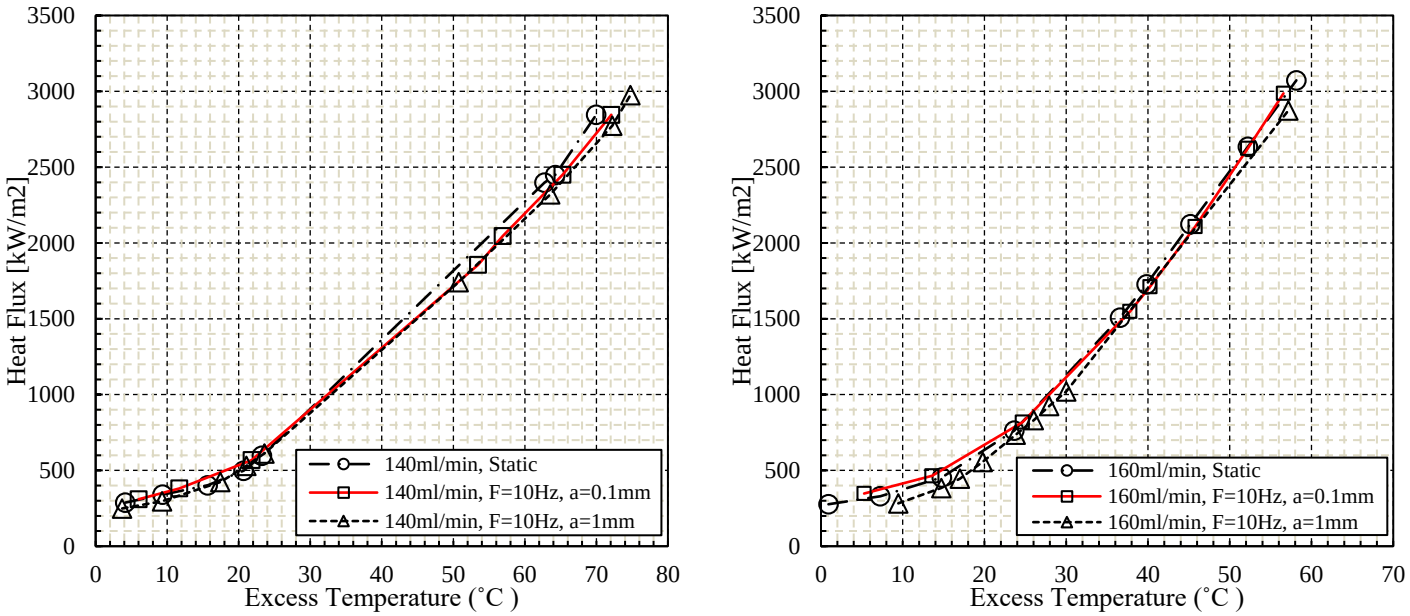

Fig. 6. Nucleate boiling curves with and without the vibration.

Fig. 6 also suggests that the effect of vibration in general is highly dependent on the complex relationship between frequency, amplitude, and excess temperature, since it is always either an enhancing or deteriorating the impact in the lower and higher surface temperature regions. However, it is only relevant to the amplitudes taken so far and there should definitely be an optimum value between. Higher amplitudes are needed to assess the sensitivity of such an important parameter, which is important to the design of the application areas under the dynamic condition e.g. thermal management of highly-boosted IC engines, and power electronics in electric vehicles.

4. Conclusions

An experimental investigation has been undertaken to examine the influence of dynamic behaviour on the nucleate boiling regime of a spray cooling system with and without vibration. The amplitudes and frequency have been varied between 0.02 mm and 1 mm, and from 10 Hz to 400 Hz for three volumetric flow rates of 140 ml/min, 160 ml/min and 180 ml/min. By exiting vibration from a shaker to the test piece, and with a spray nozzle supplying coolant to a heated surface, a definite effect of vibration on the heat flux over different excess temperatures was evident. The main conclusions are as follows:

- Any increase in volumetric flow-rate or mass-flux, under both Static and Dynamic conditions, causes heat transfer coefficient augmentation.
- During low excess or surface temperatures, the frequency and amplitude impedes heat transfer.
- In the higher excess temperature regions, vibration frequency enhances heat-flux. Vibration amplitude reduces the heat transfer coefficient.

Acknowledgements

The authors wish to acknowledge the financial and technical support in the study of the Ricardo Shoreham Technical Centre, UK.

References

[1] J. Breitenbach, I. V. Roisman, and C. Tropea, "From drop impact physics to spray cooling models: a critical review," *Experiments in Fluids,* vol. 59, no. 3, p. 55, 2018.

[2] G. Liang and I. Mudawar, "Review of spray cooling–Part 1: Single-phase and nucleate boiling regimes, and critical heat flux," *International Journal of Heat and Mass Transfer,* vol. 115, pp. 1174-1205, 2017.

[3] G. Liang and I. Mudawar, "Review of spray cooling–Part 2: High temperature boiling regimes and quenching applications," *International Journal of Heat and Mass Transfer,* vol. 115, pp. 1206-1222, 2017.

[4] S. Jafari *et al.*, "A review of evaporative cooling system concepts for engine thermal management in motor vehicles," *Proceedings of the Institution of Mechanical Engineers, Part D: Journal of Automobile Engineering,* vol. 231, no. 8, pp. 1126-1143, 2017.

[5] W.-L. Cheng, W.-W. Zhang, H. Chen, and L. Hu, "Spray cooling and flash evaporation cooling: the current development and application," *Renewable and Sustainable Energy Reviews,* vol. 55, pp. 614-628, 2016.

[6] S. K. Mishra, A. Arora, and H. Chandra, "Application of Vibration on Heat Transfer-A Review," *i-Manager's Journal on Future Engineering and Technology,* vol. 15, no. 1, p. 72, 2019.

[7] A. Sathyabhama and S. Prashanth, "Enhancement of boiling heat transfer using surface vibration," *Heat Transfer—Asian Research,* vol. 46, no. 1, pp. 49-60, 2017.

[8] Z. Wang, Y. Xing, X. Liu, L. Zhao, and Y. Ji, "Computer modeling of droplets impact on heat transfer during spray cooling under vibration environment," *Applied Thermal Engineering,* vol. 107, pp. 453-462, 2016.

THE EFFECT OF SURFACE-TO-NOZZLE DISTANCE ON THE CRITICAL HEAT FLUX OF SPRAY EVAPORATIVE COOLING APPLIED TO VIBRATING SURFACES.

by
A Sarmadian[a], J. Thalackottore Jose[a], J.F. Dunne[a*], C.A. Long[a], J-P Pirault[a], and C. Rouaud[b]

[a]Department of Engineering and Design
School of Engineering and Informatics
University of Sussex, Falmer, Brighton, BN1 9QT, UK.
* Corresponding Author
j.f.dunne@sussex.ac.uk

[b]Ricardo plc
West Sussex BN43 5FG, Shoreham-by-Sea, UK

ABSTRACT

This paper addresses for the first time, correlation model requirements for the combined influences of surface-to-nozzle distance and vibration on critical heat flux. A correlation model is constructed using dimensional analysis involving the Generalized Buckingham Π-Theorem. This correlation model is fitted to experimentally-measured spray evaporative cooling data, where a Vibrational Reynolds Number, an Acceleration Number, and a dimensionless surface-to-nozzle distance is introduced to better correlate the combined effects of frequency, amplitude, and surface-to-nozzle distance at critical heat flux. The experimental measurements involve different surface-to-nozzle distances, and coolant flow-rates through a misting spray nozzle which is used to cool a flat circular test-piece acting as a horizontal surface. This test-piece surface is excited by a shaker through a range of low and high frequencies of vibration, from small to large amplitudes.

The results show that surface-to-nozzle distance, in conjunction with dynamic effects, does indeed influence the critical heat flux but that vibration amplitudes and frequencies do not have the same effect for both surface-to-nozzle distances and flow rates. Depending on the vibration range, surface-to-nozzle distance can either increase or decrease the heat transfer. A calibrated correlation model can successfully predict the effect of surface-to-nozzle distance on the critical heat flux with an error range between -4.8% and +10.5%.

INTRODUCTION

The heat transfer characteristics of spray evaporative cooling applied to vibrating surfaces is important in several application areas. Applications including automotive transport (electric [1] and hybrid vehicles [2]), thermal management of highly-boosted IC engines [3], power electronics (e.g. cooling high-power LEDs [4], IGBTs [5], high-heat flux heat sinks for IGBTs [6], and MEMS [7]), batteries (for improving thermal performance [8], or to achieve optimised lifespan [9]), and hydrogen technologies [10] (cooling of storage tanks [11] in hydrogen-powered road vehicles and aircraft) are all significant.

Spray evaporative cooling, owing to its latent heat, offers a significant increase in heat flux compared with single-phase convection [12]. It also means that lower mass-flow rates are needed for cooling systems resulting in a substantial reduction in the required pumping power [13]. For the purpose of thermal management however, there are still concerns surrounding the control of a system that can operate near the required heat flux and yet remain stable. Moreover, most potential applications of spray evaporative cooling operate in environments where mechanically-induced vibration occurs. Vibration is considered to have an effect on the heat transfer characteristics [14]. This effect can be seen through Vibrational Reynolds Number and the dimensionless Acceleration Number. Vibrational Reynolds Number represents the effect of turbulence stemming from vibrating surfaces [15]. Acceleration Number is helpful in taking account any possible influences of acceleration.

Spray evaporative cooling, even with impingement on static surfaces, involves highly complex two-phase physics which is currently far beyond the capabilities of numerical simulation. For this reason, several empirical correlation models have been developed and calibrated for predicting the spray evaporative cooling characteristics of static surfaces [16]. For example, to predict the CHF, Mudawar and Valentine [17], Estes and Mudawar [18, 19], and Visaria and Mudawar [20, 21] have proposed correlations. No such correlation exists however to predict the effect of surface-to-nozzle distance on the critical heat flux (CHF) associated with spray evaporative cooling applied to vibrating surfaces.

In this paper, the objective is to study (for the first time) the combined effects of surface-to-nozzle distance and vibration on the spray evaporative CHF for a full-cone spray impinging on a (heated) flat circular copper test-piece, driven by a shaker. Experimentally-measured spray evaporative cooling data is obtained and used to fit the corresponding empirical correlation models (developed by Dimensional Analysis). In particular, use is made of Vibrational Reynolds Number, Acceleration Number, and a (dimensionless) Surface-to-Nozzle Distance which better correlate the influence of surface frequency and amplitude at the

incidence of CHF. These new models are important for design and thermal management of batteries, power electronics, and electrical machines in automotive and aerospace applications.

NOMENCLATURE

A	surface area (m^2)
Ac	dimensionless acceleration (units of g)
a	amplitude of vibration (m)
Bo	Boiling number (-)
C_p	specific heat (kJ/kg k)
d	diameter(mm)
d_{32}	Sauter Mean Diameter (SMD) (m)
DH	dimensionless surface-to-nozzle distance (-)
f	frequency (Hz)
h	specific enthalpy (kJ/kg)
H	surface-to-nozzle distance (m)
Ja	Jakob number
k	thermal conductivity (W/m K)
L	length (mm)
P	pressure (kPa)
Pr	Prandtl number
v	volumetric flow rate (m^3/s) or (ml/min)
q	heat flux (kW/m^2)
Re	Reynolds number
T	temperature (K)
u	velocity
We	Weber number

Greek symbols

μ	dynamic viscosity (Kg/m s)
Δp	pressure drop (kPa)
α	spray angle
ρ	density (kg/m^3)
σ	surface tension (N/m)
ω	angular velocity (Hz)
δ	liquid film thickness (m)

Subscripts

CHF	Critical Heat Flux
c	coolant
V	vibration
v	vapour
g	gas side
h	heater
H	heater surface
l	liquid
n	nozzle orifice
sat	saturation
sub	subcooling
w	wall

EXPERIMENTAL TEST RIG AND DATA COLLECTION

Figure 1 shows a schematic view of the overall test setup. The experimental test rig comprises the following components: a micropump (Micropumps MGD100P, number 1 in **Figure 1**) suppling de-ionised water to a PJ10 nozzle (Bete PJ nozzle, ranging from 75 ml/min at 2.9 bar, to 100 ml/min at 5.2 bar) which is located on top of the spray chamber (13). Second, a separation tank (11), where vapour and liquid are separated and delivered to the condenser and condensate tank (10). Third, an air-cooled condenser (Denso RDP 583, 9 in **Figure 1**) where vapour from the test chamber is vented through a throttle valve; a miniature heat exchanger (12) which is used to cool the condensate (at exit from the condenser) to below the maximum operating temperature of the pump (100 ˚C). Two 345W band-heaters (2) with a controllable 0 to 5 V power regulator (United Automation, EVR-25BF, AC Burst Fire Controller) used to heat the feed-water to the nozzle to maintain constant degrees of sub-cooling (i.e. the difference between saturation and inlet temperatures) by a PID controller in CRIO-9035 National Instrument. Two digital pressure transducers (Omega PXM309) are linked to the data acquisition system to provide a constant record of the chamber pressure and the nozzle pressure difference. A low-flow turbine meter (Omega FLR1009ST-D, 14) installed just after the pump to measure the flow-rate, and is used as a state variable (B) for the PID controller in the FPGA CRIO-9035 (15) to control the pumping voltage (A), in order to be able to achieve constant flow rates during measurement. A header tank (8) is also fitted at the highest point in the circuit to remove air and provide a positive feed.

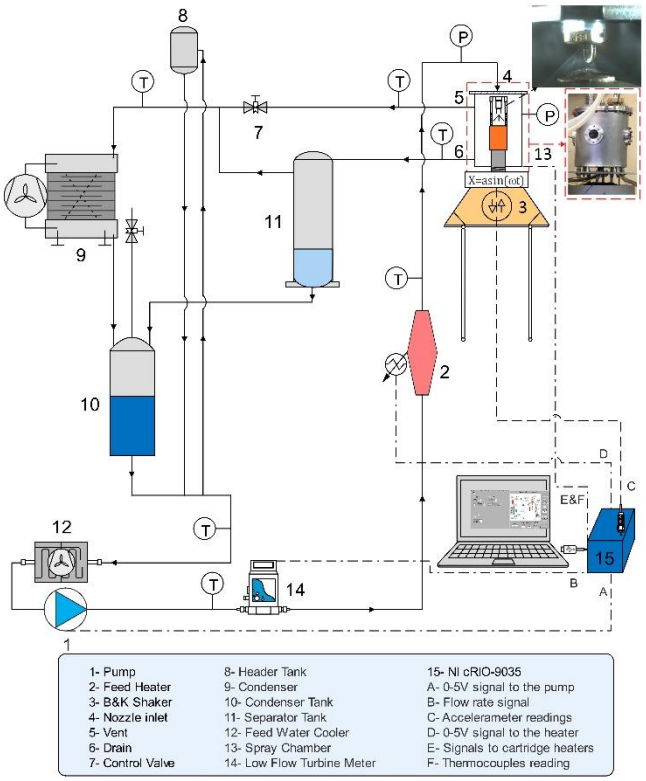

Figure 1 Schematic view of the test setup

As shown in **Figure 2**, the test-piece is located in a chamber mounted on a Bruel & Kjaer V555 mechanical shaker (No. 3 in **Figure 1)**. Thus, the test piece and the nozzle inside the chamber can be simultaneously shaken at different frequencies (f) and amplitudes (a). A Piezotronics PCB A 353B15 accelerometer (10.27 mV/g, 1 Hz - 10 kHz) is attached to the bottom of the drive-shaft attached to the shaker head. Corresponding

acceleration signals (C in **Figure 1)** measured by a National Instruments data acquisition system.

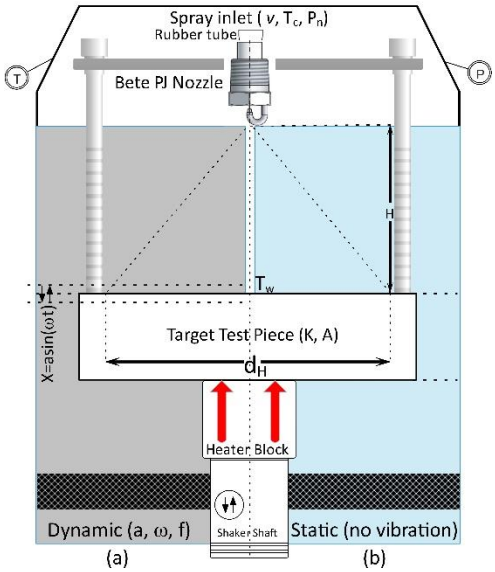

Figure 2 Spray system configuration inside the chamber under: (a) dynamic and (b) static conditions. (Not to scale.)

The amplitude and frequency of the shaker was controlled using a Feedback Instruments FG600 signal generator with pure sine wave option. The test chamber is heated by six Watlow 250W cartridge heaters controlled by 0 to 5 V signals (E in **Figure 1**) from a NI9264 module and a power regulator (EVR-25BF). The test piece is a copper disc with a radius of 10 mm. It has a smooth surface and a thermal conductivity of 385 Wm/K. Three T Type thermocouples are used, the first of which is located 1 millimetre under the coolant surface of the test chamber followed by two more evenly located 5.5 millimetres underneath each other to facilitate the heat flux measurement capabilities.

DATA REDUCTION AND UNCERTAINTY ANALYSIS

A measurement test plan for this empirical study is supplied in **Table 1**. Overall, 32 test runs were undertaken under *static* and *dynamic* conditions (respectively without, and with vibration) at frequencies varying from 2 to 200 Hz, and with amplitude in the range from ±0.04 to ±8 mm. The chamber pressure (1 bar) is kept constant, and two nozzle-to-surface distances of 12 and 21 mm are chosen for two volumetric flow rates of 75 ml/min and 100 ml/min.

At the beginning of each test run (with or without vibration), the power was applied to the cartridge heaters to bring the cooling surface to a condition after incipient boiling and within the two-phase heat transfer mode. Steady-state was assumed when all temperature differences associated with all three thermocouples in time intervals of three minutes were less than 0.3 ˚C (as convergence criterion). Then, the power was gradually increased until the CHF occurred. A test-run for the case study involving *static* cooling surfaces was undertaken twice on two different days for the purposes of checking repeatability of the test facility. The maximum deviation in reproducibility of CHF was 2%, which is less than that produced by the following uncertainty analysis, summarized in **Table 2**.

Table 1 Test plan and spray specification for the operating conditions of the PJ10 nozzle at CHF.

v (ml/min)	H (mm)	a (mm) \ f (Hz)	2	4	8	50	50	100	200	Case
75 and 100	12-21	8	✓	-	-	-	-	-	-	D-1
		4	-	✓	-	-	-	-	-	D-2
		1	-	-	✓		-	-	-	D-3
		1	-	-	-	✓		-	-	D-4
		0.2	-	-	-	-	✓	-	-	D-5
		0.2	-	-	-	-	-	✓	-	D-6
		0.04	-	-	-	-	-	-	✓	D-7

NOZZLE SPRAY SPECIFICATIONS

d_n (mm)	α (◦)	Covering d. (mm)	ΔP (bar)	$u_m(\frac{m}{s})$	d_{05} (μm)	d_{32} (μm)
0.25	90	24	2.9-5.2	24.6-32.9	26-33	117-137

The heat flux was calculated using a solution of the one-dimensional conduction equation:

$$q = -K\frac{dT}{dx} \quad (1)$$

using measurements taken from thermocouples embedded in the test piece, where K, dT, and dx are the thermal conductivity, temperature difference, and the distance between the top and the bottom thermocouples respectively. The uncertainty analysis is based on the method proposed by Moffat [22] which gives:

$$\delta R = \left[\sum_{i=1}^{n}\left(\frac{\partial R}{\partial X_i}\delta X_i\right)^2\right]^{\frac{1}{2}} \quad (2)$$

where δR is the uncertainty of the dependent parameter, $\frac{\partial R}{\partial X_i}$ is sensitivity coefficient, and δX_i is the error of the independent parameter in the measurement. The uncertainty in the determination of heat flux is within 3% for all the test runs.

Table 2 Uncertainties of the calculated and measured parameters.

Parameter	Uncertainty (%)	Units
Thermocouples	±0.4	℃
Flow rate	±0.6 (of full scale)	ml/min
Accelerometer frequency	±5	Hz
Length	±1	mm
Heat flux	±3	MW/m^2

RESULTS AND DISCUSSION

In this section, the combined effects of vibration and surface-to-nozzle distance on the critical heat flux and the effect of frequency and amplitude of vibration will be investigated using dimensionless numbers. The collected data based on the key parameters' trends will then be used to fit the constructed

correlation models using dimensionless numbers to better understand the influence of vibration on the CHF.

The CHF data as a function of the surface-to-nozzle distances of 12 and 21 mm for two flow rates of 75 ml/min and 100 ml/min are shown respectively in **Figure 3** and **Figure 4**. All experiments were undertaken with a constant degree of subcooling of 45 ℃. To make room for inspection, all the dynamic cases are demonstrated with the same data markers and therefore **Figures 2** and **3** can be compared with each other. An effect ratio has been defined as the ratio of the dynamic-CHF/static-CHF. To show the effect of surface-to-nozzle distance for the static cases, the effect ratio also includes corresponding static-CHF/static-CHF (shown by grey data callouts on each figure).

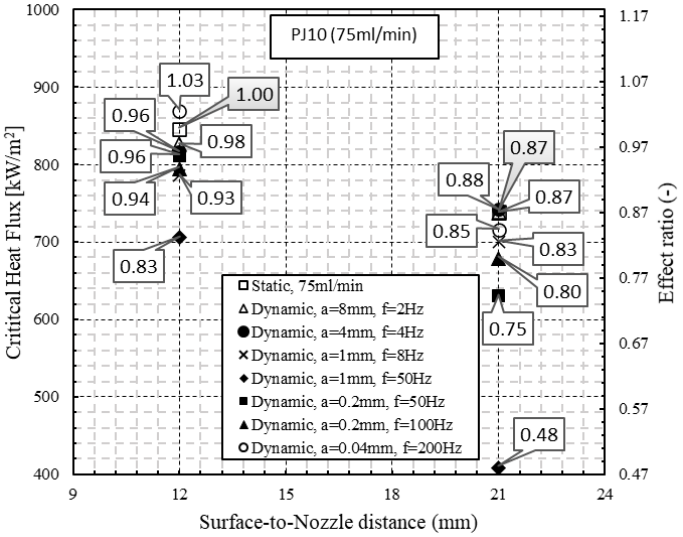

Figure 3 CHF data points against surface-to-nozzle distance at volumetric flow rate of 75 ml/min

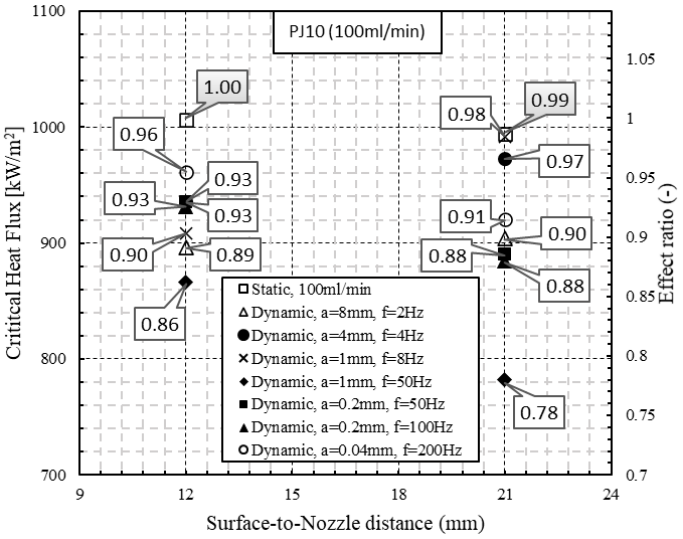

Figure 4 CHF data points against surface-to-nozzle distance at volumetric flow rate of 100 ml/min

Starting with the influence of increasing surface-to-nozzle distance on the static cases, at flow rate of 75 ml/min, the effect is 13% attenuation while for the flow rate of 100 ml/min has almost no effect (1% difference is less than the expected uncertainty and reproducibility). The reason for no influence at higher flow rate can be explained by the dominant effects of three key parameters of nozzle pressure drop ΔP (bar), mean droplet breakup velocities $u_m(\frac{m}{s})$, and Sauter Mean Diameter (SMD) d_{32} (μm). These key parameters are considered to have influences on the CHF in literature [23]. As can be seen in **Table 1** where the spray specifications are supplied, the corresponding greater value for each key parameter is associated with the higher flow rate of 100 ml/min. Therefore, an increased droplet momentum (evident from the greater values for droplet velocity and SMD at 100 ml/min) can be the reason for a reduction in the deteriorating effect of surface-to-nozzle distance for static cases. Hypothetically, increased momentum improves the impinging droplet penetration into the liquid film and reduces the chance of slug propagation. Therefore, this effect delays the incidence of CHF (which when postponed, means heat transfer enhancement).

For all the dynamic cases, at the flow rate of 75 ml/min, the attenuating effect is valid. The maximum decrease in the CHF at both nozzle-to-surface distances are related to a dynamic case with vibrating amplitude of 1 mm and vibrating frequency of 50 Hz which has the highest Acceleration (10.07 g) and Reynolds Number (21360). For the flow rate of 100 ml/min, the same trend is evident for the same dynamic case while the attenuation is less than those for flow rate of 75 ml/min. At a 12 mm nozzle-to-surface distance and 75 ml/min, the effect ratio for this dynamic case is 0.83 while it is 0.86 for the 100 ml/min. At a 21 mm nozzle-to-surface distance the effect ratios for 75 ml/min and 100 ml/min flow rates are respectively 0.48 and 0.78. The reason could be the same as for the static cases. It means the higher values for pressure drop and droplet velocity, as well as a larger droplet SMD, increase the momentum and consequently decrease the identified impeding effect.

By inspecting the trend of CHF results in **Figure 4**, the overall attenuating effect observed for the lower flow rate (75 ml/min) can be seen, however, there are two dynamic cases that have a reverse trend (i.e. they enhance the CHF while the nozzle-to-surface distance increases). Also, it should be noted that the CHF for the dynamic case of a= 8 mm and f=2 Hz remains the same with increasing the nozzle-to-surface distance. These two converse trends are related to dynamic cases with a= 4 mm and f= 4 Hz (shown with a filled circle), and with a= 1 mm and f= 8 Hz (shown with a cross). The former has an enhancement of 4 percent and the latter has an 8 percent increment in the CHF based on their effect ratios. It seems that a reduction in the vibrational amplitude (4 mm to 1 mm) and an increase in vibrational frequency (4 Hz to 8 Hz) for cases D-2 and D-3 result in this behaviour. Both dynamic cases have the same Accelerations of 0.26 g but two different Reynolds Numbers of 6835.2 (also labelled as D-2 in **Table 1**) and 3417.6 (D-3 in **Table 1**). It can be deduced that a higher Reynolds Number has been the reason for less enhancement for the case D-2 (4%) in comparison with the Case D-3 (8%). This trend is also valid for the case D-4 with the highest Reynolds Number (indicated with a diamond) that has the maximum attenuation for both flow rates.

Owing to the nonlinear behaviour of the combined effects of nozzle-to-surface distance and vibration on CHF, it is highly beneficial to develop correlation models for the design of thermal management systems. These correlation models can be constructed using Generalized Buckingham π-theorem [24] to enable prediction of CHF for vibrating surfaces. To develop a functional form, independent key parameters identified for the static conditions in the literature [23] should be considered. These include density ρ_l, latent heat h_{fg}, viscosity μ_l, specific heat C_l, surface density σ, nozzle pressure P_n, chamber pressure P_{ch}, degree of subcooling ΔT_{sub}, mean droplet velocity u_m, volumetric flow rate v, SMD d_{32}, heating area d_H, and finally nozzle-to-surface distance H. However, for dynamic conditions the amplitude (a) and angular frequency ($\omega = 2\pi f$) of vibration also need to be added to the functional form. The next step in generalized Π-Theorem is to define invariant parameters according to the test plan. In this study the chamber pressure ($P_{ch} = 1\ bar$) and the degree of subcooling ($\Delta T_{sub} = 45$°C) are constant and therefore are invariant parameters. In addition, as was discussed in the development of dynamic correlations in the nucleate boiling regime in a previous study by the same authors [25], functional forms can be derived based on modelling requirements and expectations. In the thermal management design process of an evaporative cooling system, pumping flow rate plays an important role on the wall temperature control. In addition, spray specifications should not be included in functional forms based on considerations for measurements (a minimum number of sensors desired to be embedded in an actual thermal management system). Therefore, the functional form is of the form:

$$q_{CHF} = \varphi(\rho_l, h_{fg}, \mu_l, C_l, \sigma, v, d_H, H, a, \omega, g) \quad (3)$$

By performing dimensional analysis, and based on generalized Π-Theorem, the dimensionless Π-parameters for dynamic CHF are obtained as follows:

$$\frac{qH}{\mu_l h_{fg}} = f\left(\frac{{\rho_l}^2 \sigma v}{{\mu_l}^3}, \frac{\rho_l a \omega d_H}{\mu_l}, \frac{a}{H}, \frac{\omega^2 a}{g}\right) \quad (4)$$

where in the LHS, Boiling Number ($Bo = \frac{qH}{\mu_l h_{fg}}$), and in the RHS, vibrational Reynolds Number ($Re_V = \frac{\rho_l a \omega d_H}{\mu_l}$), dimensionless surface-to-nozzle distance ($DH = \frac{a}{H}$), and Acceleration ($Ac = \frac{\omega^2 a}{g}$) Numbers have been derived. Thus, the relation ready for data fitting is according to:

$$Bo = a\,(\frac{{\rho_l}^2 \sigma v}{{\mu_l}^3})^b Re_V^c\, DH^d Ac^e \quad (5)$$

By employing nonlinear least square regression and with the 'bisquare' optimisation method for robustness, the data fitting was achieved using the Levenberg-Marquardt algorithm. Owing to the high dependency of CHF to nozzle-to-surface distance and the trends that were identified previously, and to achieve the highest accuracy, the database is split into two different nozzle-to-surface distances of 12 mm and 21 mm. The optimised parameters resulting in the least root mean square errors are given in **Table 3**.

Table 3 Dynamic correlation parameters for different nozzle-to-surface distances.

H (mm)	Parameters				
	a	b	c	d	e
12	1.92E-03	0.4749	-0.1461	0.0440	0.0485
21	3.93E-06	0.9704	-0.5526	0.2446	0.2241

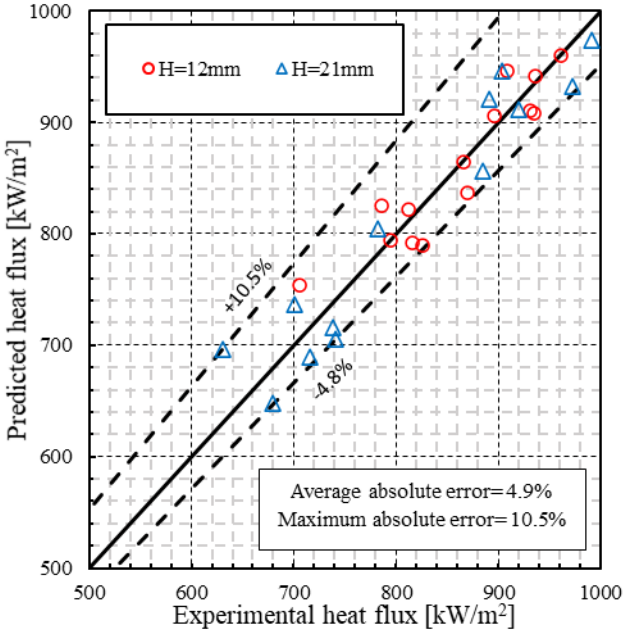

Figure 5 CHF results predicted by correlations with the error bands.

Figure 5 shows the experimental results for CHF versus the predicted data points with error bands as well as average and maximum absolute errors. As can be seen, the dynamic correlation is predicting the data with an average absolute error of 4.9% and maximum absolute error of 10.5%. The predicted CHF results are within the -4.8% and +10.5% error windows. As can be seen, the correlation model represents the best prediction quality for the results of nozzle-to-surface distance of 12 mm which have a higher CHF value and therefore are of more importance for the specific purpose of thermal management. Overall, the model's prediction quality (considering the under- and over-estimations not more than 10.5%) is promising for both nozzle-to-surface distances. The models fitted here offer potentially promising application to future model-based spray evaporative cooling control systems [12].

CONCLUSIONS

Experiment measurements have been undertaken to investigate the effects of surface-to-nozzle distance of vibrational surfaces on the critical heat flux (CHF). In this regard, a flat test-piece made of copper, inside a spray chamber, has been mounted on top of a shaker while heated through a heater block of the same material using cartridge heaters. A wide range of vibrations have been introduced to the test-piece during

spray cooling with different flow rates of 75 ml/min and 100 ml/min. The CHF data points for two nozzle-to-surface distances of 12 mm and 21 mm have been collected. Data analysis and comparisons have been undertaken to investigate the influences of key vibrational parameters and surface-to-nozzles distance in a combined relation using non dimensional numbers. The main conclusions are:

- An increase in surface-to-nozzle distance under static condition for both flow rates was found to cause critical heat flux attenuation.
- For the dynamic conditions at flow rate of 75 ml/min during all vibrational ranges, the impeding effect of surface-to-nozzle distance was still valid.
- The maximum CHF attenuations, for all different nozzle-to-surface distances and flow rates, were found to be related to the dynamic cases with highest Reynolds Number of 21360.
- At a flow rate of 100 ml/min however, by increasing the surface-to-nozzle distance, there were two vibrational cases with reverse trends (i.e. heat transfer enhancement). Vibrational amplitude and frequency in conjunction with Reynolds Number best explain the trend. This nonlinear behaviour encouraged CHF correlation development.
- Developed correlation models, based on the dimensional analysis for prediction of CHF results, were able to predict the experimentally-measured data with maximum absolute errors of 10.5%.

ACKNOWLEDGEMENTS

The authors wish to acknowledge the financial and technical support of the Ricardo Shoreham Technical Centre, UK.

References

[1] Y. Ding, Z.P. Cano, A. Yu, J. Lu, Z. Chen, Automotive Li-ion batteries: current status and future perspectives, Electrochemical Energy Reviews, 2 (2019) 1-28.

[2] Q. Yue, C. He, H. Jiang, M. Wu, T. Zhao, A hybrid battery thermal management system for electric vehicles under dynamic working conditions, International Journal of Heat and Mass Transfer, 164 (2021) 120528.

[3] J.T. Jose, J.F. Dunne, J.-P. Pirault, C.A. Long, Spray Evaporative Cooling System Design for Automotive Internal Combustion Engines, in: ASME 2018 Internal Combustion Engine Division Fall Technical Conference, American Society of Mechanical Engineers, 2018, pp. V002T007A008-V002T007A008.

[4] S. Khandekar, G. Sahu, K. Muralidhar, E.Y. Gatapova, O.A. Kabov, R. Hu, X. Luo, L. Zhao, Cooling of High-Power LEDs by Liquid Sprays: Challenges and Prospects, Applied Thermal Engineering, (2020) 115640.

[5] J. Wang, Y. Li, J. Wang, Transient performance and intelligent combination control of a novel spray cooling loop system, Chinese Journal of Aeronautics, 26 (2013) 1173-1181.

[6] Y. Ding, Y. Li, Y. Li, W. Chen, H. Zhang, D. Li, Intensive cooling method for power electronic component with high heat flux, in: 2014 13th International Conference on Control Automation Robotics & Vision (ICARCV), IEEE, 2014, pp. 163-168.

[7] J.-X. Wang, W. Guo, K. Xiong, S.-N. Wang, Review of aerospace-oriented spray cooling technology, Progress in Aerospace Sciences, 116 (2020) 100635.

[8] Y. Yang, L. Yang, X. Du, Y.J.A.T.E. Yang, Pre-cooling of air by water spray evaporation to improve thermal performance of lithium battery pack, 163 (2019) 114401.

[9] S. Lei, Y. Shi, G. Chen, Heat-pipe based spray-cooling thermal management system for lithium-ion battery: Experimental study and optimization, International Journal of Heat and Mass Transfer, 163 (2020) 120494.

[10] J. Zhang, T.S. Fisher, P.V. Ramachandran, J.P. Gore, I. Mudawar, A review of heat transfer issues in hydrogen storage technologies, JOURNAL OF HEAT TRANSFER, ASME, (2005).

[11] O.V. Kartuzova, M. Kassemi, J.P. Moder, J.H. Agui, Self-pressurization and spray cooling simulations of the multipurpose hydrogen test bed (MHTB) ground-based experiment, in: 50th AIAA/ASME/SAE/ASEE Joint Propulsion Conference, 2014, pp. 3578.

[12] J.T. Jose, A. Sarmadian, J. Dunne, C. Long, J.-P. Pirault, C. Rouaud, An experimentally-verified temperature control simulation model for spray evaporative cooling of vibrating powertrain parts, International Journal of Heat and Mass Transfer, 170 (2021) 121041.

[13] H. Bostanci, S. Altalidi, S. Nasrazadani, Two-phase spray cooling with HFC-134a and HFO-1234yf on practical enhanced surfaces, Applied Thermal Engineering, 131 (2018) 150-158.

[14] S.K. Mishra, A. Arora, H. Chandra, Application of Vibration on Heat Transfer-A Review, i-Manager's Journal on Future Engineering and Technology, 15 (2019) 72.

[15] A. Sathyabhama, S. Prashanth, Enhancement of boiling heat transfer using surface vibration, Heat Transfer—Asian Research, 46 (2017) 49-60.

[16] V. Devahdhanush, I. Mudawar, Review of Critical Heat Flux (CHF) in Jet Impingement Boiling, International Journal of Heat Mass Transfer, 169 (2021) 120893.

[17] I. Mudawar, W. Valentine, Determination of the local quench curve for spray-cooled metallic surfaces, Journal of Heat Treating, 7 (1989) 107-121.

[18] K.A. Estes, I.J.I.J.o.H. Mudawar, M. Transfer, Correlation of Sauter mean diameter and critical heat flux for spray cooling of small surfaces, 38 (1995) 2985-2996.

[19] I. Mudawar, K. Estes, Optimizing and predicting CHF in spray cooling of a square surface, Journal of Heat Transfer, 118 (1996) 672-679.

[20] M. Visaria, I.J.I.j.o.h. Mudawar, m. transfer, Theoretical and experimental study of the effects of spray inclination on two-phase spray cooling and critical heat flux, 51 (2008) 2398-2410.

[21] M. Visaria, I.J.I.j.o.h. Mudawar, m. transfer, Effects of high subcooling on two-phase spray cooling and critical heat flux, 51 (2008) 5269-5278.

[22] R.J. Moffat, Describing the uncertainties in experimental results, Experimental thermal and Fluid Science, 1 (1988) 3-17.

[23] G. Liang, I. Mudawar, Review of spray cooling–Part 1: Single-phase and nucleate boiling regimes, and critical heat flux, International Journal of Heat and Mass Transfer, 115 (2017) 1174-1205.

[24] A.A. Sonin, A generalization of the Π-theorem and dimensional analysis, Proceedings of the National Academy of Sciences, 101 (2004) 8525-8526.

[25] A. Sarmadian, J. Dunne, C. Long, J.T. Jose, J.-P. Pirault, C. Rouaud, Heat flux correlation models for spray evaporative cooling of vibrating surfaces in the nucleate boiling region, International Journal of Heat Mass Transfer, 160 (2020) 120159.